CRACKS AND FRACTURE

Proceedings of the
Ninth National Symposium
on Fracture Mechanics

STP 601

AMERICAN SOCIETY FOR TESTING AND MATERIALS

CRACKS AND FRACTURE

Proceedings of the
Ninth National Symposium
on Fracture Mechanics

A symposium sponsored by
Committee E-24 on
Fracture Testing of Metals
AMERICAN SOCIETY FOR
TESTING AND MATERIALS
University of Pittsburgh,
Pittsburgh, Pa., 25-27 Aug. 1975

ASTM SPECIAL TECHNICAL PUBLICATION 601
J. L. Swedlow and M. L. Williams, symposium co-chairmen

List price $51.75

04-601000-30

AMERICAN SOCIETY FOR TESTING AND MATERIALS
1916 Race Street, Philadelphia, Pa.   19103

Library of Congress Catalog Card Number: 76-1712

Printed in Baltimore, Md.
June 1976

Joseph A. Kies, 1906-1975

Dedication

It was with great sorrow that those concerned with the organization of the Ninth National Symposium on Fracture Mechanics learned that the community of fracture specialists would never again benefit from the wit and wisdom of Joe Kies, one of the pioneers of practical fracture mechanics, highly respected through the world, and held in great affection by those fortunate enough to know him well. The Officers of ASTM Committee E-24 on Fracture Testing of Metals, the members of the Executive Subcommittee, and the members of the National Symposia Task Group of the Executive Committee, all agreed that it would be most *appropriate to dedicate these Proceedings to Joe in recognition that much of our present work rests on foundations that he helped to lay.*

In 1959 the progenitor of ASTM Committee E-24 was established to deal with Vanguard and Polaris motor case problems. Surely standardized tests for the case materials were needed; meantime, the analysis and remedial prescription of the disconcertingly frequent proof test failures had to proceed with deliberate haste. The original master of fracture failure analysis, Kies, got on with this task. With characteristic enthusiasm and sagacity, he would examine the "remains," interrogate witnesses, investigate the background, analyze, and report; dozens upon dozens of cases were handled. It was this wealth of experience that set practical objectives to be met by the ASTM test methods of Committee E-24. This was the Kies contribution; it was vital to Committee E-24.

Joe Kies became a member of ASTM in 1943 and was always an avid proponent of ASTM goals. After graduating from the University of Illinois in 1935, he became a physicist at the National Bureau of Standards. In 1944, he joined the Western Regional Laboratory of the Department of Agriculture in Albany, California, and in 1947, the Oak Ridge National Laboratory. Taking a position at the Naval Research Laboratory in 1948, his collaboration with G. R. Irwin is now recognized to have been the pioneering effort in establishing the discipline of linear elastic fracture mechanics, the primary basis of Committee E-24 activities. He was responsible for basic papers on the interpretation of fracture surface markings, a skill which prepared him for his Committee E-24 essential work on the Polaris submarine missile. He was first to recognize the superior fracture toughness of warm prestretched acrylics, leading to stronger and lighter aircraft glazing materials. Recognizing his contributions, the Department of the Navy bestowed its highest civilian award in 1971, the Distinguished Civilian Service Award. After his retirement Joe contributed generously to the American Society for Metals Handbook, *Volume 9, through membership on the Committee on Use of Fractography for Fracture Analysis. At the time of his death, he was working on Volume 10 as a member of the Committee on Analysis of Brittle and Ductile Failures.*

Foreword

This publication, *Cracks and Fracture,* contains papers presented at the Ninth National Symposium on Fracture Mechanics which was held at the University of Pittsburgh, Pittsburgh, Pa., 25–27 Aug. 1975. The Symposium was sponsored by Committee E-24 on Fracture Testing of Metals of the American Society for Testing and Materials. J. L. Swedlow, Carnegie-Mellon University, and M. L. Williams, University of Pittsburgh, presided as symposium co-chairmen.

The record would not be complete without noting some of the people who lent their talents to the success of the symposium. E. F. Andrews, Corporate Vice President, Materials and Services, Allegheny-Ludlum Industries, spoke at the symposium banquet. His incisive and provocative comments on the criticality of materials supply gave a clear view of many serious problems pertinent to all of us concerned with the concepts and applications of fracture mechanics. Dean M. C. Hawk, University of Pittsburgh, handled many of the arrangements; his devoted efforts were central to the smooth running of the meeting. The Technical Steering Committee did the initial paper selection and much of the early planning; the members were P. C. Paris, Brown University, and E. T. Wessel, Research Center, Westinghouse Electric Corporation. Chairmen of the six sessions were J. E. Srawley, Lewis Research Center, National Aeronautics and Space Administration; H. T. Corten, University of Illinois; J. E. Scott, Bethlehem Steel; C. E. Feddersen, Battelle-Columbus; R. J. Goode, Naval Research Laboratory; and E. K. Walker, Lockheed-California. The symposium co-chairmen wish to express their sincere thanks to these many people.

Related ASTM Publications

Fracture Analysis, STP 560 (1974), $22.75, 04-560000-30

Fracture Toughness and Slow-Stable Cracking, STP 559 (1974), $25.25, 04-559000-30

Fatigue and Fracture Toughness—Cryogenic Behavior, STP 556 (1974), $20.25, 04-556000-30

A Note of Appreciation to Reviewers

This publication is made possible by the authors and, also, the unheralded efforts of the reviewers. This body of technical experts whose dedication, sacrifice of time and effort, and collective wisdom in reviewing the papers must be acknowledged. The quality level of ASTM publications is a direct function of their respected opinions. On behalf of ASTM we acknowledge their contribution with appreciation.

ASTM Committee on Publications

Editorial Staff

Contents

Introduction

The Ninth National Symposium on Fracture Mechanics convened Monday, 26 August 1975, in the Engineering Auditorium at the University of Pittsburgh. Nearly two hundred people were in attendance, representing research and applied activities in industry, government laboratories, and universities. While most of the participants came from establishments within the United States, a few traveled from the United Kingdom and western European countries. As a result, there was a superb opportunity for many practitioners and researchers to exchange views and share their respective experiences.

This symposium was organized under the auspices of ASTM Committee E-24 on Fracture Testing of Metals, and it is now well established as an annual event. A useful aspect of this continuing series is that the presentations combine a number of features: some are new ideas, others give new results, and still others provide progress reports or reviews of continuing, long term efforts, This year, coverage was broadened to materials other than metallic, and papers are found herein dealing with graphite, ceramics, plastics, and wood. Readers of these proceedings have access to an important component of the current literature in this field; owing to both its depth and breadth, the book should serve a wide range of uses in the time ahead.

J. L. Swedlow
Carnegie-Mellon Univeristy, Pittsburgh, Pa. 15213; symposium co-chairman.

M. L. Williams
University of Pittsburgh, Pittsburgh, Pa. 15261: symposium co-chairman.

J. D. G. Sumpter [1] *and C. E. Turner* [2]

Method for Laboratory Determination of J_c

REFERENCE: Sumpter, J. D. G. and Turner, C. E., "**Method for Laboratory Determination of J_c**," *Cracks and Fracture, ASTM STP 601,* American Society for Testing and Materials, 1976, pp. 3–18.

ABSTRACT: Possible methods for evaluating J for a three-point bend specimen are reviewed and the effects of slow crack growth, experimental limit load, and lateral constraint noted. A procedure, compatible with linear elastic fracture mechanics (LEFM) and crack opening displacement (COD) testing, is suggested for finding J_c.

KEY WORDS: crack propagation, fractures (materials), mechanical properties, tests, J-contour integral, linear elastic fracture mechanics, crack opening displacement

The objective of fracture mechanics analysis is to predict the behavior of defects in a large complex structure from the results of a small, easily performed, laboratory test. Most attempts to do this are based on the concept of a fracture characterizing parameter, the critical value of which is postulated to be the same in both the specimen and structure. The two most coherent and generally applicable fracture-safe design procedures put forward in the literature are those based on linear elastic fracture mechanics (LEFM), fracture criterion K_{Ic} [*1*],[3] and on the crack opening displacement (COD) concept, fracture criterion δ_c [*2*]. In this paper, and an associated paper [*3*], the advantages of basing the fracture-safe design procedure on J and its critical value J_c, are discussed.

Experimental work on J [*4–6*] has thus far tended to emphasize evaluation of J_{Ic} as a means of determining K_{Ic}. For this purpose J_{Ic} is identified with initiation of crack growth in a specimen required to meet size constraints less stringent than those demanded in ASTM Test for Plane-Strain Fracture Toughness of Metallic Materials (E 399-72) and its United Kingdom equivalent [*7*]. In this paper, and elsewhere [*3*], J_c is used to designate the point of unstable fracture (which may or may not be

---

[1] Senior scientific officer, Naval Construction Research Establishment, Dunfermline, Scotland.

[2] Professor, Materials in Mechanical Engineering, Imperial College, London, England.

[3] The italic numbers in brackets refer to the list of references appended to this paper.

preceded by slow crack growth) in a specimen having the same thickness as the structure for which the fracture analysis is to be performed. It should be noted here that differences in J_c between the specimen and structure may still arise from variations of in-plane geometry. Although early experimental work [*5*] on center-cracked tension and bend specimens gave promising results, more experimentation is needed to demonstrate convincingly the invariance of J_c in different plastic flow fields. Doubts must also surround the use of J as a characterizing parameter once significant slow crack growth has occurred. But since similar drawbacks and uncertainties also apply to all other one parameter elastic-plastic fracture criteria so far proposed, it is the authors' contention that J_c still provides the most convenient and least ambiguous basis currently available for quantitative fracture-safe design.

In proposing a procedure for laboratory determination of J_c, one of the main objectives has been to devise a method fully compatible with both LEFM and with that already standardized elsewhere [*8*] for COD testing. Emphasis has been given accordingly to the three-point bend geometry ($0.25 < a/W < 0.60$) and to evaluation of J from a load/crack mouth opening displacement record. If this compatibility with COD and LEFM testing is not considered essential, J_c testing based on a direct determination of U (Eq 3) may become the more attractive method.

Determination of *J* Using Finite Element Based Correlations

J is conventionally defined for nonlinear elastic materials as a path independent line integral [*9*]. For a material deforming according to the laws of incremental plasticity, path independence is not guaranteed, but a number of finite element investigations [*10–12*] have shown that near path independence is, in fact, maintained for a large range of cracked-body geometries under monotonic loading, provided that contours are not taken very close to the crack tip. Consequently, J is definable still as the average value of a number of such contours. Naturally enough, most of the fracture-orientated elastic-plastic finite element analyses performed so far have been on specimen geometries. Such computations provide correlations between J and applied displacement which should be directly applicable to fracture toughness testing. Unfortunately, these computations are rather inflexible since each one refers only to a specific geometry and does not in itself give any indication of how the value of J will be affected by minor variations away from this configuration. Crack length, in particular, cannot be specified *a priori* in standard fracture toughness tests. It is, moreover, the authors' experience that the various estimation procedures described below all show very close agreement with computed results for J [*12*]. This, together with their greater flexibility, means that they are more suitable than finite element based correlations for determination of J_c in standard specimen geometries. Numerical analysis still has a major role to play in the analysis of nonstandard specimens such as those containing very shallow notches or those for which the relationship between limit load and ligament length is not known accurately. Computational results are used in the present paper to illustrate the effect of work hardening, lateral constraint, and the relationship between J and COD.

J Estimation Procedures

The most convenient basis for estimation of J in small specimens is that provided by the compliance relationship

$$J = \frac{-1}{B} \left(\frac{\partial U}{\partial a}\right)_q \tag{1}$$

where

U = total absorbed energy (or area under the load/load point deflection curve) at load point deflection q,
B = specimen thickness, and
a = crack length.

Early attempts to establish J_c [4,5] used a series of specimens with different initial crack depths to evaluate J directly from Eq 1; the possibility of obtaining J_c from a single specimen load deflection curve using an estimation procedure based on elastic compliance and slip line field considerations was pointed out subsequently [13]; and more recently [6], attention has focused on the use of a correlation between J and absorbed energy [14]. For specimens in which the uncracked ligament is subject to bending, this takes the form

$$J = \frac{2\,U_{\text{crack}}}{(W - a)B} \tag{2}$$

where U_{crack} denotes the component of energy absorbtion due to the presence of the crack. For deeply cracked ($a/W > 0.6$) three-point bend and compact tension specimens, where the energy absorbtion component of the uncracked body is small, it is suggested elsewhere [6, 12] that Eq 2 can be simplified to

$$J = \frac{2\,U}{(W - a)B} \tag{3}$$

where U is the total area under the load/load point deflection curve.

General Relationship Between *J* and Absorbed Energy

For some applications, such as the testing of weldments [*15*], there can be a requirement for specimens containing relatively shallow surface notches. A more general version of Eq 2, which does not involve subtraction of the uncracked body energy and is applicable to any geometry for which the elastic compliance and limit load are known, is useful in such cases.

$$J = J_e + J_p = \frac{\eta_e U_e}{(W - a)B} + \frac{\eta_p U_p}{(W - a)B} \tag{4}$$

Here the total energy is divided into elastic (including uncracked body energy) and plastic components (Fig. 1), U_e and U_p, respectively. The constants η_e and η_p are geometry dependent; η_e may be calculated easily from the elastic compliance and stress intensity factor [*16*]. Table 1 shows η_e values for the three-point bend and compact tension geometries, based on stress intensity and compliance values given in Refs *13* and *17*, respectively. From a knowledge of the relationship between crack length and limit load Q_L, η_p may be calculated. For example, for the three-point bend specimen, provided that plasticity is confined to the uncracked ligament, the net section yielding (or limit) load is a function of ligament length squared.

$$Q_L = C_n \sigma_Y \frac{B}{S} (W - a)^2 \tag{5}$$

where C_n is a constant; whence, for a nonwork-hardening material

$$J_p = \frac{-1}{B} \left(\frac{\partial U_p}{\partial a}\right)_q = \frac{-1}{B} \left(\frac{\partial [Q_L q_p]}{\partial a}\right)_q \tag{6}$$

$$= 2 C_n \sigma_Y \frac{(W - a)}{S} q_p \tag{7}$$

$$= \frac{2 U_p}{(W - a) B} \tag{8}$$

TABLE 1—*Values of* η_e *for Eq 4.*

a/W	0.2	0.3	0.4	0.5	0.6	0.7
Three-point bend *S/W* = 4	1.4	1.7	1.9	2.0	2.0	1.9
CTS *H/W* = 0.6	3.7	2.7	2.4	2.3	2.2	2.2

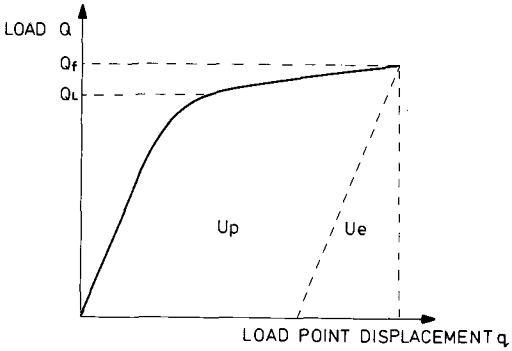

FIG. 1—*Division of load deflection curve into elastic and plastic energies.*

It follows that $\eta_p = 2$ for the three-point bend geometry at all crack to width ratios greater than about $a/W = 0.2$. Limit load for the compact tension specimen (CTS) geometry is less well defined, but η_p might be expected to approach two for deeply cracked specimens where the deformation is predominantly bending.

For the CTS ($a/W > 0.6$), and the three-point bend geometry ($0.4 < a/W < 0.7$) where $\eta_e \approx \eta_p \approx 2$, Eq 4 reduces to Eq 3. It should be re-emphasised, however, that the values of η_e in Table 1 do not involve subtraction of an uncracked body energy. There will, therefore, be a discrepancy between Eq 4 and Eq 2 when the uncracked body energy is significant, as it is in the three-point bend geometry (30 percent of the total elastic at $a/W = 0.5$, 70 percent at $a/W = 0.3$). The source of this discrepancy, an error in the integration limits used to derive Eq 2, has been noted recently [*18*].

Gage Point Location for Deflection Measurement

One problem which arises with the application of Eq 4 is that load-point deflection is not a quantity routinely measured in fracture toughness testing. The standard procedure, ASTM Method E 399-72, is to measure crack mouth opening V [*7,8*]. The solution adopted in the CTS geometry [*6*] is to redesign the specimen so that the clip gage can be located under the loading pins thereby measuring load-point displacement directly. This option is not available for the three-point bend specimen. Rather than attempt to measure load point deflection directly in this specimen, it is probably preferable to convert V to load point displacement, q, by assuming a center of rotation a fixed distance $r(W-a)$ below the crack tip.

Before application of Eq 4, the measured area under a load/mouth opening deflection curve should be factored by

$$F = \frac{q}{V} = \frac{R}{[a + r(W - a)]} \tag{9}$$

It is well known from studies in support of the COD concept [*19*] that r is both load and geometry dependent. After limit load, however, r becomes a fixed value for increments in q and V for a given geometry. Finite element results for the three-point bend geometry in plane strain indicate that this fixed value of r is 0.45 at $a/W = 0.3$ and 0.4 at $a/W = 0.5$. It is suggested that F_p be calculated on this basis. Modifying Eq 4 for use with areas under a load/mouth opening deflection curve by employing separate values of F for elastic and plastic behavior results in

$$J = J_e + J_p = \frac{F_e \, \eta_e \, U_{Ve}}{(W - a)\, B} + \frac{F_p \, \eta_p \, U_{Vp}}{(W - a)\, B} \tag{10}$$

where U_{Ve} and U_{Vp} are the elastic and plastic areas under the load/mouth opening deflection curve; $F_e \, \eta_e$ can be obtained directly from boundary collocation results for elastic mouth opening [*20*].

It should be noted that both F_e and F_p would need modification if mouth opening displacement were monitored using a clip gage mounted on knife edges a distance z above the surface.

Ensuring Compatibility Between J_e and G for Elastic Behavior

Although Eq 10 provides a reasonably satisfactory method of determining J, it is worth questioning whether measurement of absorbed energy really provides the best basis for a new standard test method. The two fracture toughness tests at present in most widespread use are based on load (LEFM) and clip gage measured mouth opening (COD). There is much to be said for providing as close a compatibility as possible with these established test procedures. At the linear elastic end of the range, particularly, it is essential that there should be continuity between J_c and K_c. Discrepancies between experimental and theoretically predicted elastic compliances can easily upset this agreement if K_c is determined in the usual manner from load while J_c is determined from area under the curve. Thus, there seems to be a strong case for forcing compatibility with G in the elastic regime by use of the equality

$$Je = G = \frac{K^2{}_f}{E'} \qquad (11)$$

where

$$K_f = \frac{Q_f S}{BW^{3|2}} \times f\left(\frac{a}{W}\right) \qquad (12)$$

Q_f = final load (Fig. 1),
$f\ (a/w)$ = a function of a/W (ASTM Method E 399-72), and
E' = E for plane stress or $E/(1-\nu^2)$ for plane strain.

Evaluation of J_p from Mouth Opening Displacement

Since J_e is to be evaluated from load in accordance with ASTM Method E 399-72 and Ref *7* it seems consistent to follow COD testing practice [*8*] and to determine J_p from mouth opening displacement. There are two recommended methods for evaluation of COD from mouth opening displacement. The first, due to Ingham et al [*19*], assumes a fixed center of rotation a distance $r(W-a)$ below the crack tip

$$\delta = \left[\frac{r(W-a)}{a + r(W-a)}\right] V \qquad (13)$$

r is put equal to 0.33 for both elastic and plastic behavior. This value was chosen on the basis of experimental investigations to give lower bound values of δ. The second method due to Wells [*21*] uses an estimation procedure very similar to that proposed for J in Refs *13,14*. For elastic behavior, a relationship $\delta = G/2.1\ \sigma_Y$ is assumed, G being linked to V through elastic compliance; at an assumed limit load, derived from slip line field theory, the relationship is changed to Eq 13, but with r chosen as 0.45, again on the basis of slip line field theory. This latter value is much closer to those noted earlier for finite element analysis.

It is fairly straightforward, by a simple rearrangement of Eqs 5,7, and 9 to establish an expression which similarly allows J_p to be presented as a function of clip gage displacement only. One possibility is to substitute for the constant C_n in Eq 7 from slip line field theory as is done in Ref *13*. For three-point bending, the value of this constant is about 1.5 [*22,23*]. Then

$$J_p = 3.0\ \sigma_Y \frac{(W-a)}{S} F_p\ V_p \qquad (14)$$

A better alternative, which does not involved the assumption that the analytical and experimental limit loads will coincide, is to use Eq 5 to substitute for the constant in Eq 7

$$C_n = \frac{Q_L S}{B\ \sigma_Y (W - a)^2} \tag{15}$$

$$J_p = \frac{2\ Q_L\ F_p\ V_p}{(W - a)\ B} \tag{16}$$

The same result for J_p of course, can be obtained by writing U_{Vp} in the plastic term of Eq10 as $Q_L V_p$ and noting $\eta_p = 2$.

Effect on *J* of Work Hardening

Strictly speaking, Eq 16 applies only to a nonwork hardening material where Q_L is both the load at net section yielding and the maximum load reached. In this paper, Q_L is used to signify the net section yielding (not the maximum) load in a work hardening material (Fig. 1). For the three-point bend specimen, at least, this is denoted by an easily definable inflexion in the experimental load deflection curve. Equation 3 indicates that J at a given load point deflection will be higher in a work hardening than in a nonwork hardening material, while Eq 16, unless it includes a slight rise in net section yielding load, will not give this trend. Evidence on the effect of work hardening on J is not conclusive. The J estimation procedures for cracked specimens in tension presented elsewhere [*14*] all predict an increase in J with work hardening, but finite element analysis on this geometry [4] (Fig. 2) does not seem to exhibit this trend. Finite element results for three-point bending show a similarly small effect of work hardening. It would, of course, be fairly simple to replace Q_L in Eq 16 by $(Q_L + Q_f)/2$, or even Q_f, but, at present, it seems more sensible to follow the usual lower bound philosophy of fracture toughness testing and retain Eq 16.

Effect of *J* of Slow Crack Growth

It is noted in Ref *6* that Eq 3 overestimates J when slow crack growth occurs. This point is illustrated in Fig. 3 for which a_i denotes the crack length at the start of the test and a_f, the crack length after slow growth Δa. In so far as J can be said to have any significance to crack tip conditions after slow growth, the absorbed energy, U, in Eq 3 properly should be that appropriate to a crack length a_f monotonically loaded to a given deformation (shaded area in Fig. 3), not the area under the experimental load deflection curve, which represents a crack length a_i growing to length a_f during the course of the test. From Eqs 7 and 9, the value of J_p after slow growth is

$$J_p = 2\ C_n\ \sigma_Y \frac{(W - a_f)}{S} F_p\ V_p \tag{17}$$

---

[4] Work hardening relationship used $\bar{\sigma}/\sigma_Y = 1.0 + (\bar{\epsilon}^p E/186\sigma_Y)^{0.730}$

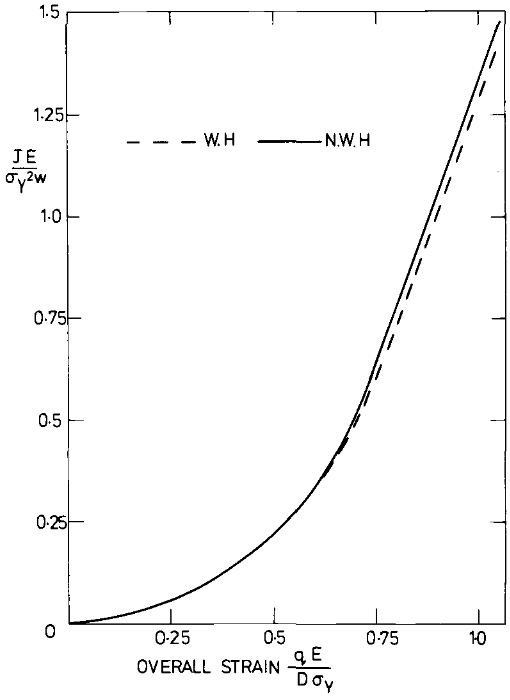

FIG 2—*Effect of work hardening on* J *in a center-cracked plate,* 2a/W = *0.5, gage length,* D = *2.5*W.

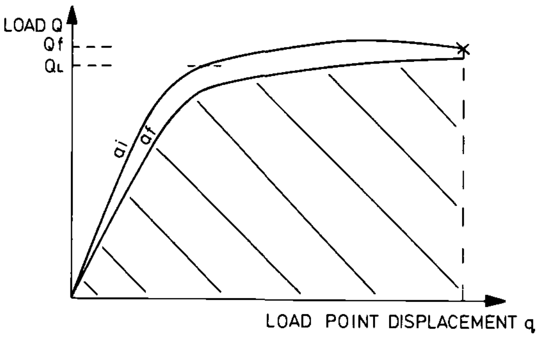

FIG. 3—*Effect of slow crack growth on correlation between* J *and absorbed energy.*

The constant in Eq 17 can be evaluated as before from Eq 15, but, assuming no crack growth before limit load, the relevant crack length is a_i not a_f

$$C_n = \frac{Q_L S}{B\ \sigma_Y B(W - a_i)^2} \tag{18}$$

$$J_p = \frac{2\ Q_L(W - a_f) F_p\ V_p}{B(W - a_i)^2} \tag{19}$$

If there is no slow growth, Eq 19 reduces to Eq 16. If slow growth does take place, Eq 19 does not overestimate J in the way that Eq 3 does. In small specimens, where slow growth causes a significant change in elastic compliance, the measured value of V_p should be adjusted appropriately. This procedure is described more fully in the Appendix; F_p and J_e should, of course, be evaluated on the basis of a_f not a_i.

Effect on *J* of Lateral Constraint

Figure 4 shows finite element computations of J against end displacement for a center-cracked plate in plane strain and plane stress. The curves correspond closely until net section yielding after which

$$\frac{dJ}{dq} = 1.15\,\sigma_Y \text{ plane strain} \tag{20}$$

$$\frac{dJ}{dq} = 1.0\ \sigma_Y \text{ plane stress} \tag{21}$$

In three-point bending there is more pronounced difference between the two cases (Fig. 5). It should be noted at this stage that corresponding values of J in plane stress or plane strain by no means ensure identical crack tip conditions [*12*]. Aside from this, the use of a finite element correlation or an estimation procedure of the type suggested in Ref *13* obviously requires a knowledge of whether the specimen is in plane stress or plane strain. The use of Eq 4 or Eq 16 circumvents this problem, since the lower value of J in plane stress automatically follows from the lower experimental limit load. The only assumption required is that limit load varies as the square of the ligament length in bending or directly with the ligament length in the case of tension.

Relationship Between *J* and COD

There is an obvious similarity between COD defined by Eq 13 and J_p defined by Eq 16 in that both assume a fixed center of rotation r $(W - a)$ below the crack tip. Considering for the moment the plastic component of COD, δ_p

$$\frac{J_p}{\delta_p} = \frac{2\,Q_L W}{rB(W - a)^2} \tag{22}$$

or assuming a specific value for C_n of 1.5 in Eq 5 and putting $r = 0.4$

$$J_p \simeq 2\,\sigma_Y\,\delta_p \tag{23}$$

This relationship has been widely noted in the literature from finite element and other analyses [*24–26*] on the three-point bend geometry. The existence of a similar relationship between J and δ for plane strain small scale yielding has been demonstrated [*24,27*] and has also been

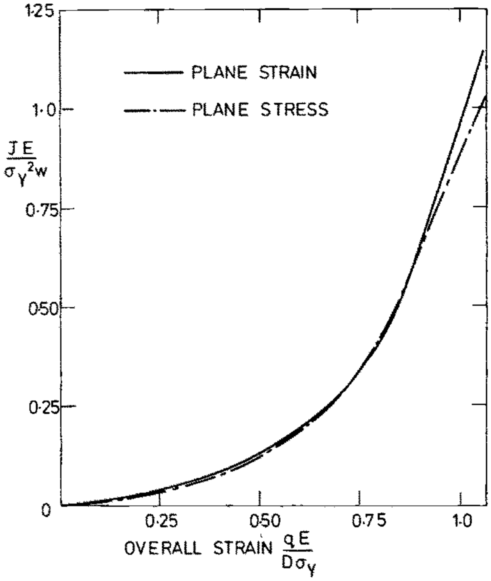

FIG. 4—*J for a center-cracked plate,* 2a/W = *0.3125, gage length,* D = *2.5*W, *plane stress and plane strain.*

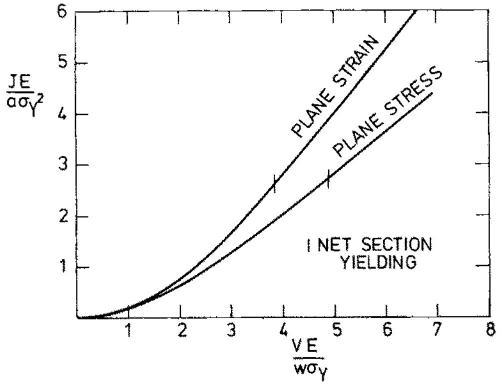

FIG. 5—*J for a three-point specimen,* a/W = *0.5, span,* S = *4*W, *plane stress and plane strain.*

suggested on a more intuitive basis by Wells [*28*]. The assumption of $\delta = G/2.1\ \sigma_Y$ in the Wells COD formula follows from this latter reference and means that near compatibility should exist between total values of J and δ defined in this way. The same conclusion does not hold if a constant center of rotation $r = 1/3$ is assumed throughout the loading range. These points are illustrated in Fig. 6 which compares finite element computed J for three-point bending $a/W = 0.5$ with δ defined by both methods detailed in Ref *8* using the finite element mouth opening as a basis. Robinson and Tetelman [*29*], using a crack infiltration technique on precracked Charpy specimens for relatively high strength materials with rather restricted yielding, found $J \simeq 1\ \sigma_Y\delta$. Further studies by Robinson as yet unpublished, taken to more extensive yielding of rather lower strength steels give $J \simeq 2.2\ \sigma_Y\delta$. These results may indicate the J-COD relationship is material dependent. Comparison with computed results again emphasizes the arbitrary nature of the definition of δ in conventional computational and experimental studies.

Equation 23 does not hold for other geometries. Although a definition of δ in the center-cracked plate is difficult, it is generally accepted, and finite element analysis [*12*] confirms that increments of δ and q are equal after net section yielding. Comparison with Eq 20 shows that the relationship $J_p = 1.15\ \sigma_Y\delta_p$ will apply in plane strain.

Summary and Discussion

The proposed method for determination of J_c for a three-point bend bar is summarized in the Appendix. Few of the ideas used to derive this

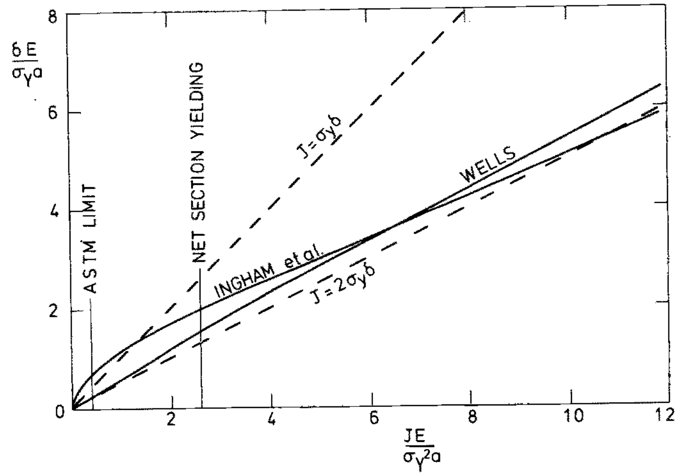

FIG. 6—*Relationship between computed values of* J *and experimental definitions of COD.*

procedure are completely new and can be found in various forms in previous literature on the subject [*13,14*]. It is considered, however, that the method proposed here is an especially appealing one, both in its simplicity for general laboratory use and because of its compatibility and similarity with existing fracture toughness testing standards. This similarity is an obvious advantage in gaining acceptance for a new testing method. Especially in the United Kingdom, where experience and confidence has been gained in the use of COD, there is an understandable reluctance to make radical changes in procedure. As shown here, J_c may be obtained as easily as δ_c using identical specimens and instrumentation. The two major reasons for favoring the use of J over δ are its unambiguous continuity with K for near-elastic behavior, and its greater flexibility and ease of definition in fracture-safe design procedures [*3,30*].

Acknowledgments

The authors wish to thank M. G. Dawes, The Welding Institute, for helpful discussions during the preparation of this paper. C. E. Turner gratefully acknowledges the award of a grant from the Science Research Council for studies of the Micro and Macro Aspects of Fracture.

J. D. G. Sumpter thanks the Superintendent, Naval Construction Research Establishment, for permission to publish this paper, but wishes to note that the views expressed do not necessarily represent those of Ministry of Defense (Navy).

APPENDIX

Proposed Method for Calculating J from the Load/Clip Gage Displacement Curve of a Three-Point Bend Specimen 0.25 < a/W < 0.60

1. From the specimen, measure
   W, B, S—overall specimen dimensions,
   a_i—initial crack length (to end of fatigue crack), and
   a_f—final crack length.

2. Draw a line OA through the elastic part of the load/clip gage deflection (Q/V_g) curve (Fig. 7). Draw a horizontal GF at load Q_f.

Record

Q_F (OG)—final load (may be after maximum load),
Q_L (OH)—limit (net section yielding) load,
V_{ge} (OB)—elastic clip gage displacement (assuming no slow crack growth, and
V_{gt} (OE)—total clip gage displacement.

3. Calculate

$$J_e = \frac{K_f^2}{E'} \qquad (24)$$

where

$$K_f = \frac{Q_f S}{BW^{3|2}} \times f\left(\frac{a}{W}\right) \qquad (25)$$

$$f\left(\frac{a}{W}\right) = \left(\frac{a_f}{W}\right)^{1|2} [2.9 - 4.6\left(\frac{a_f}{W}\right) + 21.8\left(\frac{a_f}{W}\right)^2 - 37.6\left(\frac{a_f}{W}\right)^3 + 38.7\left(\frac{a_f}{W}\right)^4] \qquad (26)$$

4. Calculate

$$J_p = \frac{2Q_L\ (W - a_f)}{B(W - a_i)^2} \left[\frac{W}{a_f + r(W - a_f) + z}\right] \left[V_{gt} - \alpha\ V_{ge}\right] \qquad (27)$$

where z is the height of the clip gage above the specimen surface

$$\alpha = \frac{h\left(\frac{a_f}{W}\right)}{h\left(\frac{a_i}{W}\right)} \qquad (28)$$

$$h\left(\frac{a}{W}\right) = -43.0 + 403.0\ \frac{a}{W} - 1073.2\left(\frac{a}{W}\right)^2 + 1162.8\left(\frac{a}{W}\right)^3 \qquad (29)$$

$$\begin{aligned} r &= 0.45,\ a/W < 0.45 \\ &= 0.4,\ a/W > 0.45 \end{aligned} \qquad (30)$$

5. The value of J at any given clip gage displacement is

$$J = J_e + J_p \qquad (31)$$

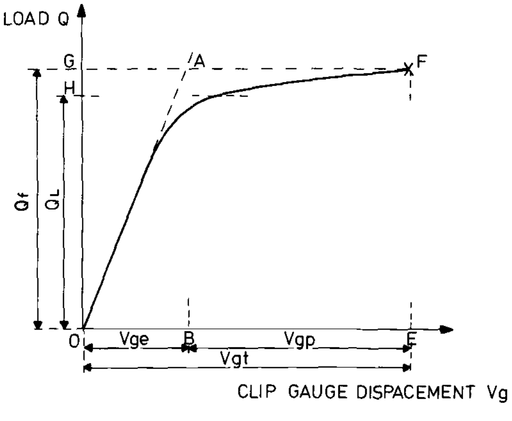

FIG. 7—*Load deflection curve measurements for calculation of* J.

Notes

1. It is necessary to decide whether to use the plane strain or plane stress value of E' in Eq 24. A possible basis for choice might be the criterion for determining J_{1c} validity suggested in Ref *6*

$$\text{plane stress } \frac{B\sigma_Y}{25} < J_c < \frac{B\sigma_Y}{25} \text{ plane strain} \tag{32}$$

2. Equation 27 is not applicable if significant slow crack growth occurs before net section yielding. J_p can be calculated before net section yielding in the absence of slow crack growth by substituting Q_f for Q_L in Eq 27.

3. Equation 29 is a polynomial fit, over the range $0.25 < a/W < 0.6$, to elastic compliance data given in Ref *20*. A slight error might be introduced by applying this to the clip gage as opposed to the mouth opening displacement, but this is likely to be small since α is a ratio, not an absolute quantity.

4. The values of r given in Eq 30 are based on finite element analysis. Alternative values may be used if experimental evidence dictates.

References

[*1*] Wessel, E. T. and Mager, T. R. in *Practical Application of Fracture Mechanics to Pressure Vessel Technology,* Institution of Mechanical Engineers, London, 1971, p. 17.

[*2*] Burdekin, F. M. and Dawes, M. G. in *Practical Application of Fracture Mechanics to Pressure Vessel Technology,* Institution of Mechanical Engineers, London, 1971, p. 28.

[*3*] Sumpter, J. D. G. and Turner, C. E. "Design using Elastic-Plastic Fracture Mechanics," submitted to *International Journal of Fracture.*

[*4*] Begley, J. A. and Landes, J. D. in *Fracture Toughness, ASTM STP 514,* American Society for Testing and Materials, 1972, p. 1.

[*5*] Landes, J. D. and Begley, J. A. in *Fracture Toughness, ASTM STP 514,* American Society for Testing and Material, p. 24.

[*6*] Landes, J. D. and Begley, J. A., "Test Results from *J* Integral Studies—An Attempt to Establish a J_{IC} Testing Procedure," Scientific Research Paper 73-1E7-FMPWR-P3, Westinghouse Research Laboratories, 1973.

[*7*] "Methods for Plane Strain Fracture Toughness (K_{IC}) Testing," Draft for Development, No. 3, British Standards Institution, 1971.

[*8*] "Methods for Crack Opening Displacement (COD) Testing," Draft for Development, No. 19, British Standards Institution, 1972.

[*9*] Rice, J. R. in *Fracture,* Vol. 2, H. Liebowitz, Ed., Academic Press, 1968, p. 191.

[*10*] Hayes, D. J. "Some Applications of Elastic-Plastic Analysis to Fracture Mechanics," Ph.D. thesis, University of London, 1970.

[*11*] Boyle, E. F., "Calculation of Elastic and Plastic Crack Extension Forces," Ph.D. thesis, Queen's University, Belfast, 1972.

[*12*] Sumpter, J. D. G. "Elastic-Plastic Fracture Analysis and Design using the Finite Element Method," Ph.D. thesis, University of London, 1974.

[*13*] Bucci, R. J., Paris, P. C., Landes, J. D., and Rice, J. R. in *Fracture Toughness, ASTM STP 514,* American Society for Testing and Materials, 1972, p. 40.

[*14*] Rice, J. R., Paris, P. C., and Merkle, J. G. in *Progress in Flaw Growth and Fracture Toughness Testing, ASTM STP 536,* American Society for Testing and Materials, 1973, p. 231.

[*15*] Dawes, M. G., *Welding Institute Research Bulletin,* Vol. 14, 1973, p. 157.

[*16*] Turner, C. E., *Materials Science and Engineering,* Vol. 11, 1973, p. 275.

[*17*] Adams, N. J. I. and Munro, H. G. *Engineering Fracture Mechanics,* Vol. 16, 1974, p. 119.

[*18*] Merkle, J. G., Berggren, R. G., and Stelzman W. J. "Compliance and Fracture

Toughness Calculations for Notched Bend Specimens,'' Oak Ridge National Laboratory Report, unpublished, 1974.

[*19*] Ingham, T., Egan, G. R., Elliott, D., and Harrison, T. C. in *Practical Application of Fracture Mechanics to Pressure Vessel Technology,* Institution of Mechanical Engineers, London, 1971, p. 200.

[*20*] Srawley, J. E. and Gross, B., *Engineering Fracture Mechanics,* Vol. 4, 1972, p. 587.

[*21*] Wells, A. A. ''The Status of COD in Fracture Mechanics,'' 3rd Canadian Congress of Applied Mechanics, Calgary, 1971.

[*22*] Green, A. P. and Hundy, B. B., *Journal of Mechanics and Physics of Solids,* Vol. 4, 1956, p. 128.

[*23*] Alexander, J. M. and Komoly, T. J., *Journal of Mechanics and Physics of Solids,* Vol. 10, 1962, p. 265.

[*24*] Tracey, D. M., ''On the Fracture Mechanics of Elastic-Plastic Materials using the Finite Element Method,'' Ph.D. thesis, Brown University, 1973.

[*25*] Hayes, D. J. and Turner, C. E., *International Journal of Fracture,* Vol. 10, 1974, p. 17.

[*26*] Rice, J. R. ''Elastic-Plastic Models for Stable Crack Growth,'' NASA Technical Report NGL 40-002-080/12, National Aeronautics and Space Administration, Washington, D.C., 1973.

[*27*] Levy, N., Marcal, P. V., Ostergren, W. J., and Rice, J. R., *International Journal of Fracture Mechanics,* Vol. 7, 1971, p. 143.

[*28*] Wells, A. A., *Engineering Fracture Mechanics,* Vol. 1, 1969, p. 399.

[*29*] Robinson, J. N. and Tetelman, A. S. in *Fracture Toughness and Slow-Stable Cracking, ASTM STP 559,* American Society for Testing and Materials, 1975.

[*30*] Sumpter, J. D. G. and Turner, C. E., *Second International Conference on Pressure Vessel Technology,* Vol. 2, American Society of Mechanical Engineer, 1973, p. 1095.

N. E. Dowling [1]

Geometry Effects and the J-Integral Approach to Elastic-Plastic Fatigue Crack Growth

---

REFERENCE: Dowling, N. E., "**Geometry Effects and the J-Integral Approach to Elastic-Plastic Fatigue Crack Growth,**" *Cracks and Fracture, ASTM STP 601*, American Society for Testing and Materials, 1976, pp. 19–32.

ABSTRACT: Fatigue crack growth rate data are obtained for center cracked specimens of A533B steel subjected to elastic-plastic cyclic loading. Cyclic J-integral values estimated from load versus deflection hysteresis loops are correlated with these growth rate data. The relationship obtained is in agreement with previous elastic-plastic data on compact specimens and also with linear elastic data on large size compact specimens. These experimental data suggest that the fracture mechanics approach to fatigue crack growth may be extended by the use of the J-integral concept, so that large scale plasticity effects are included.

KEY WORDS: fractures (materials), plastic deformation, cyclic loads, J-integral, cracking (fracturing), fatigue (materials), crack propagation.

The stress intensity parameter, K, is widely used for correlation of fatigue crack growth rates. As the stress intensity concept is based on linear elastic analysis, its validity is restricted to situations where the size scale of the plasticity that occurs is small compared to the other significant dimensions. In this paper, experimental data are presented which suggest that the fracture mechanics approach to fatigue may be extended to situations involving large scale plasticity by the use of the J-integral concept.

As originated by Rice [*1*],[2] the J-integral is analogous to the strain energy release rate, G, except that it is based on nonlinear, rather than linear, elasticity. Thus, for the special case of linear elasticity, J reduces to G, which is in turn directly and simply related to K. For elastic-plastic materials, J loses its physical interpretation in terms of the potential energy available for crack extension, but retains physical significance as a

---

[1] Senior engineer, Mechanics Department, Westinghouse Research Laboratories, Pittsburgh, Pa. 15235.

[2] The italic numbers in brackets refer to the list of references appended to this paper.

measure of the intensity of the characteristic crack tip strain field. This strain intensity interpretation of J accounts for its success as a static fracture criterion for elastic-plastic materials [*2–4*].

In general, the experimental determination of J involves a compliance type procedure using several test members [*3*]. Fortunately, however, simple approximations are available [*5*] for certain geometries which allow J values to be estimated from a single experimental load versus load point displacement curve. Such approximations are illustrated in Fig. 1 for deeply notched compact specimens and also for deeply notched center cracked specimens. Note that these approximations involve certain areas associated with the load versus deflection curve. For center cracked specimens, J is determined by adding elastic and plastic components, the elastic component being G, calculated from the applied load and crack length just as if there were no plasticity.

In an earlier investigation of elastic-plastic fatigue crack growth [*6*], compact specimens were tested, and cyclic J values were estimated from load versus deflection hysteresis loops as illustrated in Fig. 2*a*. Note that the approximation of Fig. 1*a* is applied to only that portion of the hysteresis loop during which the crack is estimated to be open. An analogous operational definition of cyclic J for center cracked specimens is shown in Fig. 2*b*.

In the remainder of this paper, further experimental study of elastic-plastic fatigue crack growth rate versus cyclic J is described. Data are presented for a second specimen geometry, specifically for center cracked specimens. Data are also presented for large size linear elastic compact

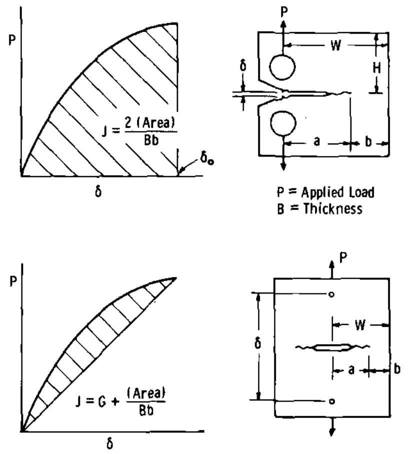

FIG. 1—*Determination of* J *from load versus deflection curves using the Rice et al approximations. Compact specimen above, center cracked specimen below.*

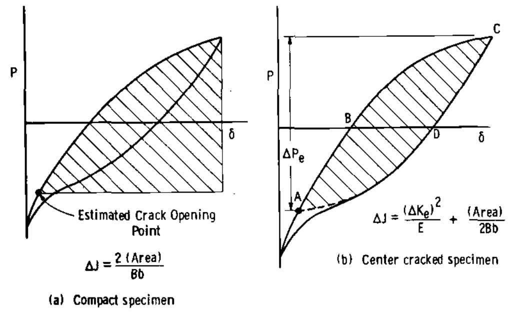

(a) Compact specimen

(b) Center cracked specimen

FIG. 2—*Operational definitions of cyclic* J.

specimens, and all data are compared with the previous data for the same material. Appropriate discussion and conclusions are presented concerning the applicablility of the J-integral concept to elastic-plastic fatigue crack growth.

Laboratory Investigation

In this section, the material and specimens employed are first described. Test procedures, data reduction, and test results are then considered in that order.

Material and Specimens

The material tested was A533B pressure vessel steel having a yield strength of 70 ksi and a Charpy fracture appearance transition temperature (FATT) of 95°F. This material was from the same plate as the material used in an earlier elastic-plastic fatigue crack growth rate study [*6*]. Also, extensive linear elastic fatigue crack growth rate data are given by Paris et al [*7*] for A533B steel having the same nominal properties as that tested here. The data in Ref *6* confirm that the material used here and that of Paris et al [*7*] have essentially identical ambient environment fatigue crack growth rate properties.

Center cracked specimens of the geometry shown in Fig. 3 were tested. The nominal dimensions in inches of the test section, with reference to Fig. 1*b*, were as follows: width $W = 0.967$, uniform section total length 2.00, thickness $B = 0.50$, and machined notch length $a_0 = 0.50$. In designing these specimens, it was necessary to make the uniform test section relatively short to avoid buckling during plastic deformation under compression. However, there is a competing requirement that the test section be sufficiently long to assure at least approximate validity of the elastic and plastic analyses which are available for uniformly stressed

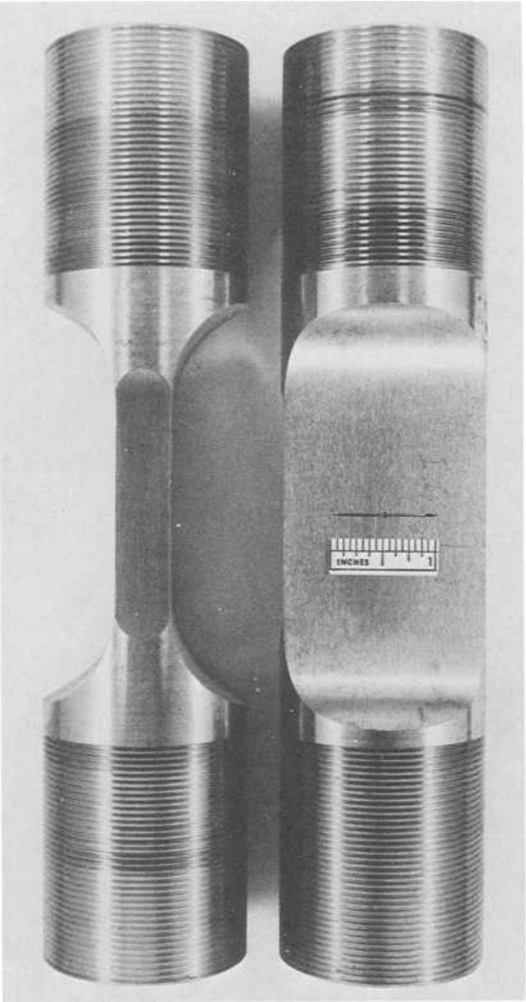

FIG. 3—*Center cracked specimen.*

center cracked members. For the elastic case, it is noteworthy that the specific geometry used at the ends of the test section produces a more uniform stress distribution across the width than is the case for the more common flat plate specimens with pin hole loading or changes in section width. From the viewpoint of elastic analysis, the specimen design adopted is judged to be satisfactory and to have similar validity to specimen designs used previously by others.

For applicability of the available plastic analysis, it is necessary that the deflections used for estimating J be measured over a uniform test section which is sufficiently long so that the plastic deflections approximate those for an arbitrarily long specimen. Note that slip bands 45 deg above and below the plane of the machined notch intersect the surface of the specimen about 1 in. apart, suggesting that plastic deformation is confined to the central half of the test section. Thus, it is reasonable to assume that under plastic deformation the two ends of the test section deflect approximately as rigid bodies so that the plastic deflections measured are largely unaffected by the test section length.

Large size compact specimens of the same proportions as the standard ASTM fracture toughness specimen (ASTM Test for Plane Strain Fracture Toughness of Metallic Materials (E 399-74)) were also tested. With reference to Fig. 1*a*, the nominal dimensions in inches were as follows: width $W = 8.00$, height $H = 4.80$, thickness $B = 4.00$, and machined notched length $a_0 = 3.70$. The compact specimens tested in Ref *6* were of these same proportions, but all dimensions were our fourth of those just given.

Test Procedures

All tests were conducted on closed loop electrohydraulic testing equipment. For the center cracked specimens, a Wood's metal grip was employed so that compressive loads could be applied without backlash. Such grips also aid in alignment and maintain axiality of the threaded ends, hence minimizing any tendency for buckling. Grips similar to those employed here, but smaller, are often used in low cycle fatigue studies as described in detail in Ref *8*.

For all center cracked specimen tests, deflections were controlled to a sloping load versus deflection line as illustrated in Fig. 4. This combined mode of load and deflection control avoids the difficulties which are encountered if either simple load or simple deflection control is employed

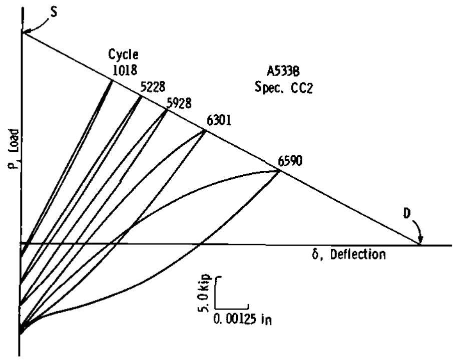

FIG. 4—*Load versus deflection hysteresis loops during deflection control to a sloping line.*

under elastic-plastic conditions. In particular, unstable incremental plastic deflection as in simple load control does not occur. Compared to simple deflection control, sloping line control on center cracked specimens results in a wider range of crack growth rates from each test.

Deflection control to a sloping line was achieved automatically by means of the analog control circuit described in Ref *6*. For each test, the intercepts of the control line, S and D defined in Fig. 4, are listed in Table 1. During each test, the frequency of cycling was decreased several times as the crack growth rate increased so as to maintain a roughly constant rate of crack extension with time. The extreme values of frequency employed for each test are listed in Table 1.

Two large size compact specimens were tested under linear elastic conditions using simple tension to tension constant load cycling. The test conditions for these are also given in Table 1.

TABLE 1—*Description of tests conducted.*

ELASTIC-PLASTIC TESTS ON CENTER CRACKED SPECIMENS

Specimen	Control Line Intercepts		Range of a/W		Test Frequency, Hz	
	D, in.	S, kips	Initial	Final	Initial	Final
CC1	0.0118	24.7	0.52	0.93	1.0	0.1
CC2	0.0154	32.0	0.53	0.93	0.5	0.1
CC3	0.0244	44.0	0.53	0.91	0.1	0.01
CC5	0.0291	56.3	0.52	0.86	0.01	0.005
CC6	0.0293	56.5	0.72	0.94	0.005	0.005

LINEAR ELASTIC TESTS ON LARGE SIZE COMPACT SPECIMENS

Specimen	Load Range, kips	Minimum Load, kips	Range of a/W		Test Frequency, Hz
			Initial	Final	
4T5	72.35	1.85	0.50	0.70	0.8
4T6	135.4	3.47	0.50	0.61	0.2

During all tests, surface crack lengths were monitored visually with a low power travelling microscope. For the center cracked specimens, both ends, and in some cases all four corners, of the crack were monitored. Average crack length versus cycles data were thus obtained, typical examples being shown in Fig. 5. The range of crack lengths over which data were taken are listed in Table 1 for all tests.

Deflections for use in estimating cyclic J for the center cracked specimens were measured along the specimen centerline over a gage length of 2.25 in., that is, between gage points ⅛ in. into the radius at each end of the 2.00-in. uniform section. Load versus deflection hysteresis loops as in Figs. 4 and 6 were recorded periodically during each test. For the two

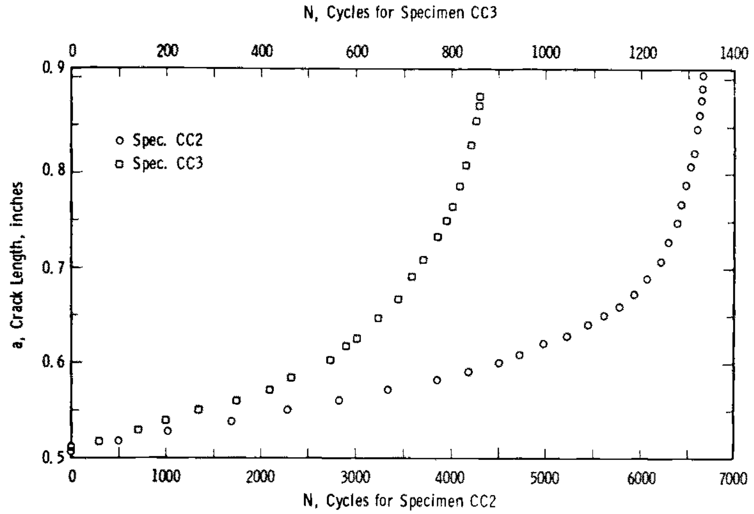

FIG. 5—*Crack length versus cycles data for two elastic-plastic tests on center cracked specimens.*

large size compact specimens, deflections were monitored using a clip gage attached to the front end of the specimen. These were recorded continuously versus time.

Data Reduction

Cyclic crack growth rates were determined for all tests from a versus N data as in Fig. 5 by an incremental polynomial procedure [9]. A second order polynomial was fitted through the first seven a versus N data points

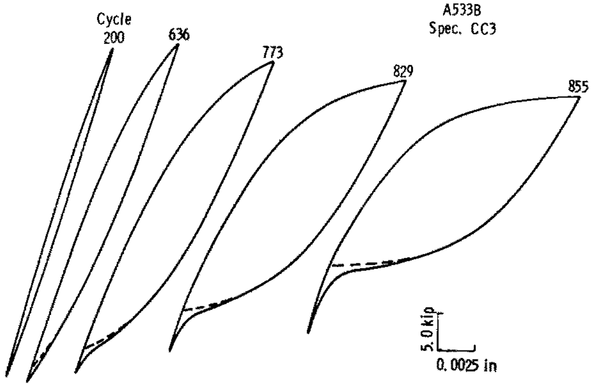

FIG. 6—*The near symmetry of load versus deflection hysteresis loops for a center cracked specimen.*

using least squares regression techniques. The first derivative of this polynomial was then evaluated at the central data point to obtain a crack growth rate, *da/dN*. The same procedure was then applied to the second through eighth, third through ninth, etc., data points so as to obtain crack growth rates at various numbers of cycles during each test.

For the elastic-plastic center cracked specimens, values of cyclic J suitable for correlating with crack growth rates were determined as illustrated in Fig. 2*b*. Note that the mainly elastic load/deflection behavior that occurs while the crack is closed is not expected to significantly affect the crack growth rate. Thus, cyclic J should be calculated from only the loads and deflections that occur while the crack is open.

It is noteworthy that in the previous study of elastic-plastic compact specimens [*6*], local crack tip clip gage measurements were used to estimate crack closure deflections. However, as these measurements were in agreement with estimates made from overall specimen displacement, it was concluded that crack closure under large scale plasticity is a reasonably distinct and easily detected event. This conclusion was further strengthened by visual observations of the specimen surface during tests on both compact and center cracked specimens.

The exact procedure used in estimating cyclic J is best explained by first noting the following: for cyclic plastic deformation of a cracked member where closure effects do not occur, the material behavior is expected to result in a load versus deflection hysteresis loop which is approximately symmetrical with respect to its central point. The asymmetry which does occur (see Figs. 2, 4, and 6) is therefore due mainly to crack closure. It is thus reasonable to make a first order correction for the effect of crack closure by modifying the actual P-δ hysteresis loop so that it has the symmetry expected in the absence of closure effects. Specifically, curves such as CDA in Fig. 2*b* were obtained by tracing curves such as ABC and then rotating 180 deg. Additional symmetrical modified hysteresis loops are illustrated in Fig. 6, and it is noted that in each case the original and modified loops coincide with each other except in the neighborhood of the "tail" associated with crack closure.

In obtaining values of cyclic J for the center cracked specimens, load ranges such as ΔP_e in Fig. 2*b* were measured from the estimated crack opening point. These were then used to determine linear elastic stress intensity ranges, ΔK_e, just as if there were no plasticity. A modified form of the Feddersen secant formula was used which is given in Ref *10* and which is accurate at any a/W. Values of ΔK_e were then employed to compute the elastic component of cyclic J, which is the linear elastic strain energy release rate, G.

$$J_{\text{elastic}} = G = \frac{K^2}{E} \tag{1}$$

where E is the elastic modulus.

The plastic component of cyclic J was estimated as illustrated in Fig. 2*b* from the area inside the modified P-δ hysteresis loop. Due to the symmetry of the modified loop, the area inside is analogous to twice the hatched area in Fig. 1*b*, hence the two in the denominator of the expression of Fig. 2*b*. The elastic and plastic components were of course added as indicated in Fig. 2*b* to obtain values of total cyclic J.

For the two large size compact specimens tested under linear-elastic conditions, stress intensity ranges were determined from the applied load range and crack length by the usual methods of linear elastic fracture mechanics. The polynomial expression in ASTM Method E 399-74, which is accurate [*11*] out to $a/W = 0.7$, was used. So that comparisons on a common basis could be made with the elastic-plastic data from smaller specimens, these stress intensities were convered to J values by Eq 1.

Test Results

Fatigue crack growth rates are plotted versus ΔJ in Fig. 7 for the

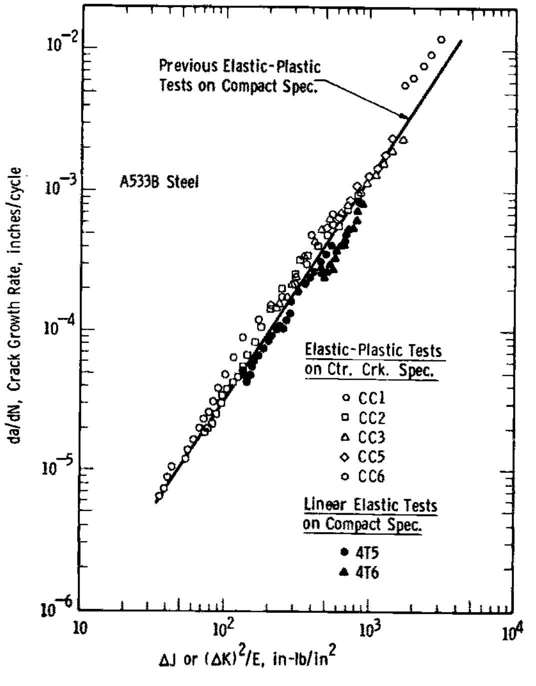

FIG. 7—*Fatigue crack growth rate versus cyclic* J *data for elastic-plastic tests on center cracked specimens and also for linear elastic tests on large size compact specimens.*

elastic-plastic center cracked specimen tests. Growth rates were obtained over three orders of magnitude between 10^{-5} and 10^{-2} in./cycle. Also shown in Fig. 7 are the data from large size compact specimens, these covering a range of growth rate between 5×10^{-5} and 10^{-3} in./cycle.

For center cracked Specimen CC1 (see Table 1), the plastic component of cyclic J did not become larger than the elastic component until a/W reached about 0.85. For the most severe test conditions employed, that is, for Specimens CC5 and CC6, the plastic component of J was dominant for all a/W beyond about 0.6.

As shown by the fracture surfaces for center cracked specimens in Fig. 8, increasing plasticity resulted in a greater tendency for the crack front to be either V-shaped or inclined at about 45 deg. In Specimen CC5, one end of the crack became inclined and grew faster than the other end which developed an apparently less favorable V-shape. This test was terminated early, and Specimen CC6 was tested under the same conditions as CC5 but was first precracked in deflection control to an a/W of 0.72. Symmetrical behavior was obtained, but as can be seen in Fig. 7 the measured growth rates were slightly above the central tendency of the other data.

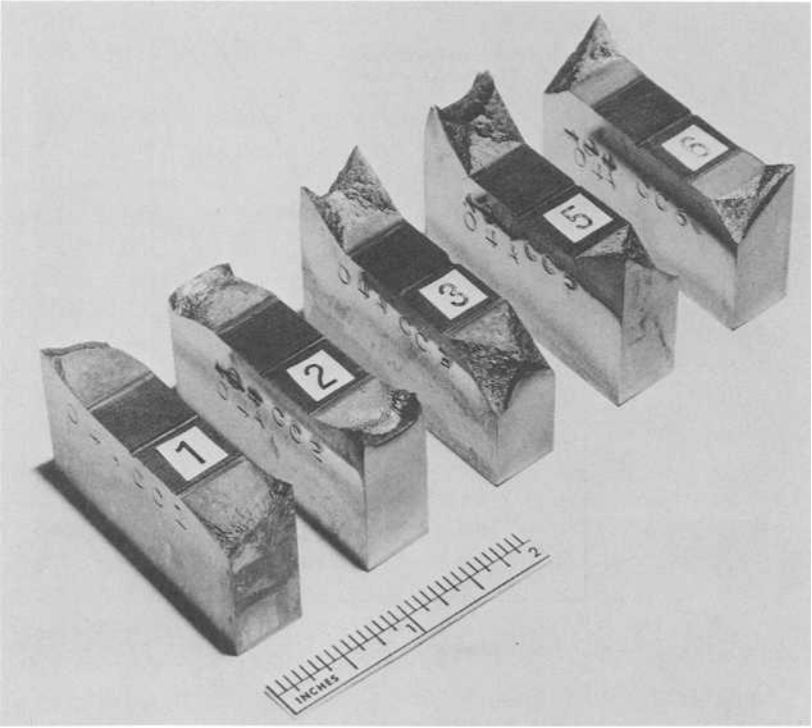

FIG. 8—*Fracture surfaces.*

This is explained by the fact that beyond the precrack the crack grew faster on the surface than on the center, hence the surface measurements did not reflect the average growth rate. Except as just noted for Specimen CC5, little difficulty was encountered with unsymmetrical crack growth.

The large size compact specimens failed catastrophically at values of *a/W* very close to predictions based on fully plastic limit load calculations. Just prior to failure, the deflections at minimum load began to increase rapidly, indicating the onset of ratcheting type gross plasticity. Shear lips occupied only a few percent of the fracture surfaces of these specimens, the fractues being essentially flat.

Discussion

The elastic-plastic fatigue crack growth rate data for both center cracked and compact specimens are plotted in Fig. 9 as solid symbols. Also shown in Fig. 9, as open symbols, are the available linear elastic data. These include the data of this investigation on large size compact specimens, the extensive data on more ordinary size compact specimens from Refs *6* and *7*, and also a small amount of data obtained during the precracking of center cracked Specimen CC6. In Fig. 7, the line fitted in Ref *6* to the elastic-plastic compact specimen data is compared with the high growth rate data reported here.

All of the data in Fig. 9 agree with the central tendency within the scatter expected [*9*] in fatigue crack growth rate testing. For rates above 10^{-7} in./cycle, two parallel straight lines can be drawn on Fig. 9 which include virtually all of the data and which differ by a factor of three in *da/dN*. These crack growth rate data over five orders of magnitude can thus be represented by a simple power relationship

$$da/dN = 2.4 \times 10^{-8} (\Delta J)^{1.56} \tag{2}$$

Thus, the J-integral concept, applied over a range of elastic-plastic fatigue crack growth rates, gives successful correlation for two specimen geometries. The success of this approach is further confirmed by linear elastic data on large size specimens at growth rates which correspond to elastic-plastic behavior in smaller specimens. Also, note from Fig. 9 that the data at high growth rates could have been predicted with reasonable accuracy by extrapolating the small specimen linear elastic data.

Some mention is in order of the relationship between the results reported here and the well known effect of mean stress intensity on fatigue crack growth rate. Although mean stress effects are not well understood, it is likely that crack opening and closure is an important

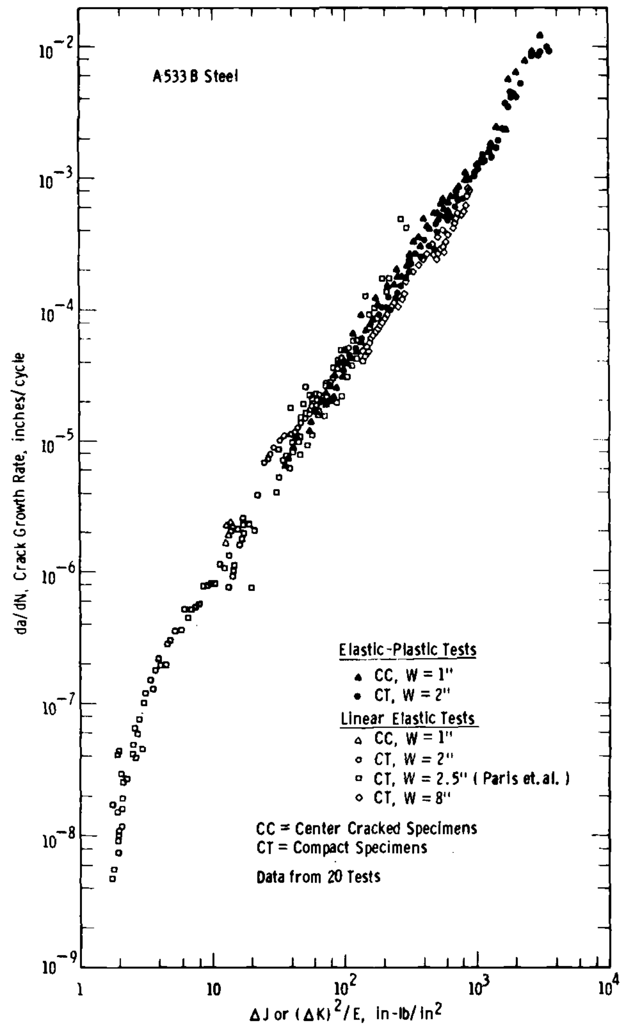

FIG. 9—*Fatigue crack growth rate versus cyclic* J *for various geometries.*

factor [*12–14*], and some speculation in this direction may be useful. Those portions of fatigue cycles which are below the closure level are not expected to contribute to crack extension. Also, if the minimum level during cycling is significantly above the closure level, higher growth rates are expected than for cycling with the minimum at the closure level. For the elastic-plastic tests reported here and in Ref *6*, crack closure occurs near the minimum deflection, and in addition a first order estimate of the crack opening deflection is made which omits deflections below this level from the cyclic J calculation. Thus, these tests primarily investigate the effect of loading range on fatigue crack growth rate. Since crack closure probably occurs near minumum load for zero to tension loading under linear elastic conditions, it is reasonable to compare such results with the elastic-plastic test results reported here and in Ref *6*. Some additional discussion, a recommendation for future work, and preliminary test results relating to mean effects under elastic-plastic conditions are given in Ref *6*.

Additional experimental confirmation of the J-integral approach to elastic-plastic fatigue crack growth is desirable. Test results similar to those already reported are needed for other engineering metals. Also, studies of the behavior of small cracks in elastic-plastic strain fields would be most informative. These studies should include both small surface cracks under uniform strain and small cracks in plastic regions associated with notches.

Due to the current emphasis on static loading and the difficulties inherent in elastic-plastic stress-strain analysis, analytical work specific to cyclic loading has received little attention. Thus, no firm analytical basis exists for the application of the J-integral concept to cyclic loading, but neither can such application be ruled out. The approximate procedures used here in applying J to fatigue were therefore necessarily developed by analogy from static loading analysis.

The successful experimental correlations here obtained suggest that elastic-plastic cyclic loading analysis of cracked members would be a fruitful area of analytical work. Any realistic analysis must be capable of handling both cyclic plasticity and crack closure. Such an analytical capability would of course greatly facilitate the application of J to practical elastic-plastic fatigue problems.

Conclusions and Recommendations

1. Experimental data on one alloy strongly suggest that the J-integral is a valid geometry and size independent correlation parameter for elastic-plastic fatigue crack growth rate. A single correlation is shown to exist between growth rate and cyclic J for elastic-plastic tests on ordinary size specimens of two geometries. From linear elastic tests on large size compact specimens, growth rates which correspond to elastic-plastic behavior in the smaller specimens are obtained, and the correlation between these rates and cyclic J is the same as for the smaller specimens. Additional studies, of other materials and of small crack behavior, are desirable.

2. On a log-log plot of cyclic J versus fatigue crack growth rate for the one material investigated, the elastic-plastic data at high growth rates are

in agreement with the straight line extrapolation of lower growth rate linear elastic data.

3. Increased attention should be given to elastic-plastic stress-strain and fracture mechanics analysis which specifically considers cyclic loading.

Acknowledgments

Gratitude is expressed to J. A. Begley for his advice and constructive comments. D. R. Young aided in planning laboratory tests and in detailed design of experimental apparatus. Technical assistance in conducting the laboratory tests was provided by R. B. Hewlett and F. X. Gradich. This work was made possible by the sponsorhip of Westinghouse Electric Corporation, the atmosphere and facilities which resulted in this paper existing largely due to the efforts of E. T. Wessel, Manager of Mechanics of Materials, Westinghouse Research Laboratories.

References

[1] Rice, J. R. in *Fracture—An Advanced Treatise, Mathematical Fundamentals,* Vol. 2, Academic Press, New York, 1968, pp. 191–311.

[2] Begley, J. A. and Landes, J. D. in *Fracture Toughness, ASTM STP 514,* American Society for Testing and Materials, 1972, pp. 1–20.

[3] Landes, J. D. and Begley, J. A. in *Fracture Toughness, ASTM STP 514,* American Society for Testing and Materials, 1972, pp. 24–39.

[4] Logsdon, W. A. in *Mechanics of Crack Growth, ASTM STP 590,* American Society for Testing and Materials, 1976, pp. 44–61.

[5] Rice, J. R., Paris, P. C., and Merkle, J. G. in *Progress in Flaw Growth and Fracture Toughness Testing, ASTM STP 536,* American Society for Testing and Materials, 1973, pp. 231–245.

[6] Dowling, N. E. and Begley, J. A. in *Mechanics of Grack Growth, ASTM STP 590,* American Society for Testing and Materials, 1976, pp. 83–104; see also Scientific Paper 74-1E7-CREEP-P1, Westinghouse Research Laboratories, Pittsburgh, Pa.

[7] Paris, P. C., Bucci, R. J., Wessel, E. T., Clark, W. G., Jr., and Mager, T. R. in *Strees Analysis and Growth of Cracks, ASTM STP 513,* American Society for Testing and Materials, 1972, pp. 141–176.

[8] Feltner, C. E. and Mitchel, M. R. in *Manual on Low Cycle Fatigue Testing, ASTM STP 465,* American Society for Testing and Materials, 1969, pp. 27–66.

[9] Clark, W. G., Jr. and Hudak, S. J., Jr., *Journal of Testing and Evaluation,* Vol. 3, No. 6, 1975, pp. 454–476.

[10] Tada, H., Paris, P. C., and Irwin, G. R., "The Stress Analysis of Cracks Handbook," Del Research Corporation, Hellertown, Pa., 1973

[11] Wilson, W. K., "Stress Intensity Factors for Compact Specimens Used to Determine Fracture Mechanics Parameters," Research Report 73-1E7-FMPWR-R1, Westinghouse Research Laboratories, Pittsburgh, Pa., July 1973.

[12] Elber, W. in *Damage Tolerance in Aircraft Structures, ASTM STP 486,* American Society for Testing and Materials, 1971, pp. 230–242.

[13] Schmidt, R. A. and Paris, P. C. in *Progress in Flaw Growth and Fracture Toughness Testing, ASTM STP 536,* American Society for Testing and Materials, 1973, pp. 79–94.

[14] Shih, T. T. and Wei, R. P., "A Study of Crack Closure in Fatigue," Report No. IFSM 72-25, Institute of Fracture and Solid Mechanics, Lehigh University, Bethlehem, Pa., Nov. 1972.

D. F. Mowbray[1]

Derivation of a Low-Cycle Fatigue Relationship Employing the J-Integral Approach to Crack Growth

REFERENCE: Mowbray, D. F., "**Derivation of a Low-Cycle Fatigue Relationship Employing the J-Integral Approach to Crack Growth,**" *Cracks and Fracture, ASTM STP 601,* American Society for Testing and Materials, 1976, pp. 33–46.

ABSTRACT: Some recent results from investigations in nonlinear fracture mechanics centering about the J-integral are utilized to derive a low-cycle fatigue relationship. The derived relationship has the form of the well-known Coffin-Manson equation, but differs from it in that the controlling variable is predicted to be applied strain energy density rather than plastic strain range. This predicted controlling variable appears to closely parallel several energy-related functions proposed during the past 15 year period.

KEY WORDS: crack propagation, fractures (materials), stresses, cracks, plastic properties

Nomenclature

a	Crack length
a_0	Initial crack length in low cycle fatigue test
a_f	Final crack length in low cycle fatigue test
C_2	Material constant $= 0.13 \left[\frac{1}{C_1} \left(\frac{a_f^{1-\gamma} - a_0^{1-\gamma}}{1-\gamma} \right)^{1-\gamma} \right]^{1\|\gamma}$
E	Modulus of elasticity
$f(n)$	Function of strain hardening exponent plotted in Ref *14*
$f'(n)$	Function of strain hardening exponent $= (n+1)f(n)$
h	Strip height
J	Path independent integral

---

[1] Manager, Mechanics of Materials, Materials and Processes Laboratory, General Electric Company, Schenectady, N.Y. 12345.

n, C_1	Cyclic stress-strain curve constants
N	Cycles
N_f	Cycles to failure in low cycle fatigue test
W	Strain energy density
W_∞	Strain energy density at infinity
β, ε'_f	Constants in Coffin-Manson relationship (fatigue exponent and fatigue ductility)
γ, C_0	Constants in Dowling-Begley crack growth relationship
Δ	Indicates range of variable
ε	Total strain
ε_p	Plastic strain
ε_y	Yield strain
σ	Stress
$\sigma_{\max}$	Maximum stress in fatigue cycle

The common low cycle fatigue test involves cycling a smooth bar specimen through a constant range of strain until the specimen separates into two pieces, or alternatively until a macrocrack of arbitrary size is present. By definition, low cycle fatigue means that the plastic strain present is a significant part of the total strain range. Life data from a series of such tests can normally be expressed in terms of the plastic strain range by the following relationship

$$N_f^\beta \, \Delta \, \epsilon_p = \epsilon'_f \tag{1}$$

This is the well known Coffin-Manson relationship, proposed roughly 20 years ago independently by Coffin [*1*][2] and Manson [*2*]. $\Delta \, \epsilon_p$ is the plastic strain range, N_f is the cycles to failure or cycles to form an arbitrary size crack, and β and ϵ'_f are material dependent properties. The latter are termed the fatigue exponent and fatigue ductility, respectively. Most metals at moderate temperature will possess values of β in the range 0.45 to 0.60 and ϵ'_f will correspond closely to the value of the true fracture ductility obtained in the common tension test.

The low cycle fatigue damage process appears to be dominated by the growth of cracks [*3–5*]. Nucleation of a multiplicity of cracks on crystallographic planes (Stage I cracks) in the specimen occur at less than 1 percent of the specimen life. These cracks rapidly join to form single dominating cracks which propagate normal to the applied stress (Stage II cracks). The Stage II cracking occupies the major portion of life in the regime commonly considered low cycle fatigue [*5*]. Further, the major portion of the propagation phase is absorbed in producing a crack of area less than 5 to 10 percent of the specimen cross-section area.

---

[2] The italic numbers in brackets refer to the list of references appended to this paper.

Coincident with the crack nucleation period, most metals exhibit a change in plastic flow properties. Either cyclic hardening or softening occurs depending upon the original metallurgical state. Normally, a constant or steady-state response is achieved after a number of cycles small in proportion to the number at failure. This steady-state response can be characterized by the cyclic stress-strain curve, which is the locus of points of the stabilized stress and strain range values from a series of tests. A reasonable representation of the cyclic stress-strain curve is given by the power-type relationship [3]

$$\Delta\sigma = C_0 \ \Delta\epsilon_p{}^n \tag{2}$$

where

$\Delta\sigma$ = stabilized stress range,
C_0 = strength coefficient, and
n = cyclic strain hardening exponent.

Realization that the low-cycle fatigue damage process is predominantly crack growth has led several investigators to formulate derivations of the Coffin-Manson relationship based on crack growth hypotheses [5–8]. A major difficulty in such derivations is in the definition of the non-linear stress and strain fields near the crack tip. However, strong correspondence between crack growth and low cycle fatigue has been demonstrated with modeling employing the Dugdale slip-line model [5], a modified elastic stress intensity factor [6], and the Neuber formula [8]. With these past tie-ins between low-cycle fatigue and crack growth studies it would appear worthwhile at this point in time to investigate the use of the J-integral [9] for describing the non-linear crack tip stress and strain fields in the low cycle fatigue process. *J* has for some time now been successfully employed as a toughness parameter in the non-linear range of material response [10]. More recently Dowling and Begley [11] used *J* to correlate fatigue crack growth rate data. They propose that the value of *J* associated with crack opening is the controlling variable in the high growth rate regime. They obtained data on A533-B steel demonstrating initial confirmation of this proposal.

In the present paper the Dowling and Begley proposal is used in conjunction with a fracture mechanics model of a smooth bar specimen to derive a low cycle fatigue relationship. The same form of equation as the Coffin-Manson relationship is found. However, it differs from the latter in that the predicted controlling variable is applied strain energy density, not plastic strain range. Considering the crack opening to occur at the minimum stress in the cycle and the plastic strain of the order of the total strain, the derived relationship is shown to reduce to the Coffin-Manson relationship. Also, using the Dowling and Begley crack growth rate properties and appropriate cyclic stress-strain data, excellent predictions of the fatigue exponent and fatigue ductility result for A533-B steel.

Derivation

Assumptions

The following assumptions are employed in the analysis.

1. The smooth bar low cycle fatigue specimen can be represented as a semi-infinite space containing an edge crack as illustrated in Fig. 1. The strain is considered to be in the fully plastic regime and uniformly applied remote from the crack.
2. Crack growth occurs during 100 percent of life, initiating from an initial microscopic-size discontinuity and terminating at an arbitrary size macrocrack.
3. The rate of growth of cracks is controlled by the range of J imposed during the crack surface opening. The specific functional form employed is that found in the Dowling and Begley [*11*] work

$$\frac{da}{dN} = C_1 \, \Delta J^{\gamma} \tag{3}$$

where

a = crack length,
N = cycles, and
C_1 and γ = material dependent constants determined by least squares fitting of data.

The significance of ΔJ will be discussed subsequently.

The choice of an edge crack is consistent with the normal mode of initiation from the specimen surface. The semi-infinite space assumption is considered to be realistic in that the cracks remain small in area relative to the total cross section for the major part of life. It is noted that the

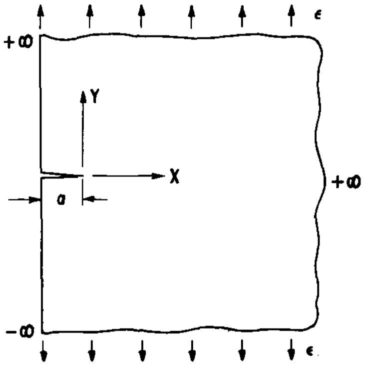

FIG. 1—*Model of low-cycle fatigue specimen.*

modeling does not distinguish between Stage I and Stage II crack orientation. The importance of separating the two stages is difficult to assess with current knowledge of the damage processes. The approach taken is that the Stage I propagation, if it occupies a significant portion of specimen life, is controlled by the same parameters as the Stage II propagation.

The crack growth data obtained by Dowling and Begley for A533-B steel are shown in Fig. 2. Note that the power-type relationship fit to the data reduces to the well-known Paris equation [*12*] (appliable to nominally elastic cases) via the relationship of J to K^2. In fact Dowling and Begley show that the data obtained from the ΔJ testing overlap and extend to higher crack growth rates, data obtained in the nominally elastic range and correlated with ΔK [*11*]. Hence, the same values of material parameters γ and C_1 could be obtained from ΔK testing.

A serious question can be raised as to the applicability of the J-concept to the fatigue crack growth process, because in the strict mathematical sense it is valid only within the confines of deformation plasticity theory [*9*], which does not include unloading. Dowling and Begely have approached this question in the spirit that the concept may have more general applicability than the current mathematical definition indicates. Their operational definition of ΔJ is in a sense equivalent to stating that the process is controlled by the work done in opening the crack surfaces

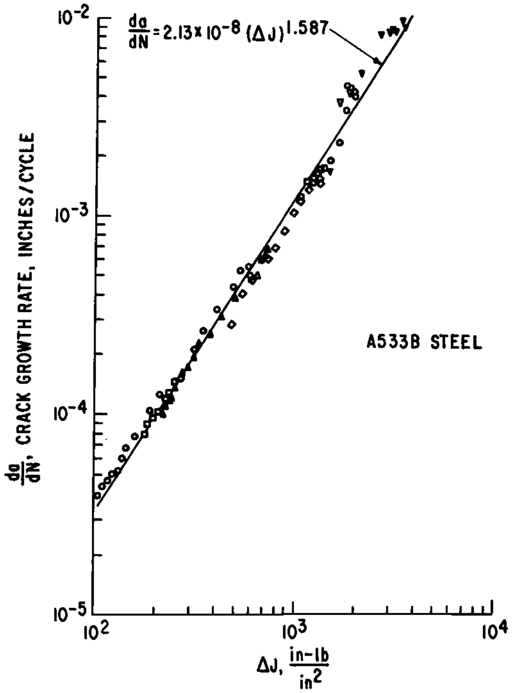

FIG. 2—*Crack growth rate data and correlation (Ref* 11).

and extending the crack an increment da. The implication is that J defines the stress and strain fields near the crack tip during the loading half of the cycle despite intermittent unloading. Their successful correlation of data would appear to confirm this interpretation.

Estimation of J *for a Low-Cycle Fatigue Specimen*

An expression for J as a function of crack length and applied strain for the model of a low cycle fatigue specimen (Fig. 1) is desired. An exact solution for this or similar cases is not presently available, so an estimate will be made. The estimate is based on a unification of available solutions (exact, empirical, and estimated) for cracks in fully plastic strain fields provided by Rice [*9*], Begley et al [*13*] and Goldman and Hutchinson [*14*].

Begley et al [*13*] start with the known J-solution for the geometry of Fig. 3, a uniformly strained infinite strip containing a semi-infinite crack. The J solution is [*9*]

$$J = W_\infty h \tag{4}$$

where W_∞ is the strain energy density at + infinity. W is defined as

$$W = \int_0^{\epsilon_{mn}} \sigma_{ij} d\epsilon_{ij} \tag{5}$$

σ_{ij} and ϵ_{ij} are the stress and strain tensors, respectively. In the linear range, $\sigma = E\epsilon$, and Eqs 4 and 5 combine to yield

$$J = E\epsilon^2 \frac{h}{2} \tag{6}$$

J is therefore proportional to the second power of strain in the linear range. In the nonlinear range where $\epsilon \cong \epsilon_p$, use of the stress-strain law $\sigma = C_0\epsilon^n$ is appropriate and leads to the following for J

$$J = \frac{C_0}{n+1} \epsilon^{n+1} h \tag{7}$$

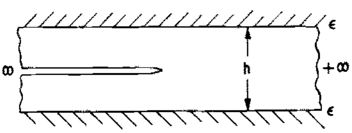

FIG. 3—*Uniformly strained infinite strip.*

Since n is normally small compared with 1, Eq 7 suggests that J is nearly proportional to the first power of strain in the highly plastic range. For the elastic-perfectly plastic idealization ($n = 0$) the direct proportionality is exactly satisfied.

Begley et al reason that the character of the variation of J with ϵ for the cracked strip can be used to estimate J for other crack problems involving a uniform strain field and single length parameter. They consider the example of a Griffith crack, Fig. 4. When loaded in the plastic range under uniform strain at infinity, the effect of the crack on the plastic flow field is negligible, and the effective geometry differs from the previous example only in that the characteristic length parameter is crack length rather than strip height. The elastic solution for J in this case is given by

$$J = E\varepsilon^2 \pi a \tag{8}$$

Because of this reasoning, J should in this case also be roughly proportional to the first power of strain in the fully plastic range. Examining the variation of J with ϵ graphically as in Fig. 5, one expects to see the joining of the parabola defined by Eq 8 with a straight line ($n = 0$ assumed) at the yield strain, ϵ_y. Reasoning that J should be a continuous, smooth function of ϵ, the slopes at ϵ_y for the elastic expression (Eq 8) and the yet to be determined fully plastic expression should be equal. An expression for the fully plastic state which satisfies this criterion is given by Begley et al as

$$J = E\varepsilon_y{}^2 \pi a + 2E\varepsilon_y \, (\varepsilon - \varepsilon_y) \, \pi a$$

or

$$J = E\epsilon_y \, (2\epsilon - \epsilon_y) \, \pi a \tag{9}$$

Begley et al point out that this approximate fully plastic solution should be applicable to other crack problems with appropriate geometry term modification, so long as the problem can be reasonably reduced to that of a crack in a uniform strain field. As one example they work with the case of an edge crack in a semi-infinite space, for which the geometry term is $1.12\pi a$.

Equation 9 possesses an interesting feature which has significance relative to a controlling variable in low cycle fatigue. It can be observed with the help of Fig. 6, that the product of terms $E\epsilon_y \, (2\epsilon - \epsilon_y)$ in Eq 9 is two times the strain energy density at infinity. Hence, J is given by

$$J = 2W_\infty \, \pi a \tag{10}$$

This has the form J = two times the product of the strain energy density at infinity and the square of the geometry term in the stress intensity factor

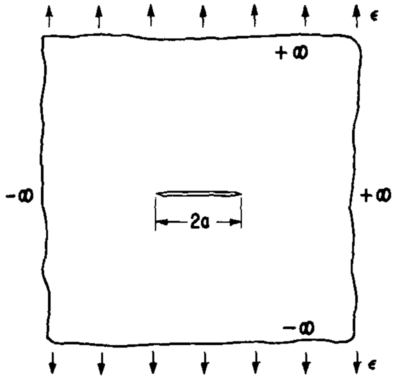

FIG. 4—*Griffith crack geometry.*

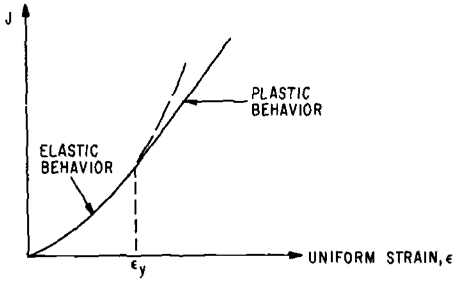

FIG. 5—*Generalized plot of* J *versus* ε *(Ref* 13*).*

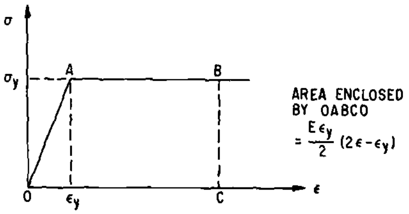

FIG. 6—*Relationship of Eq 9 to strain energy density.*

solution. The cracked strip case described by Eq 7 is of identical form; that is

$$J = 2\,W_{\infty}\,\frac{h}{2} \tag{11}$$

A further indication of this form is found in a solution by Goldman and Hutchinson [*14*] for center cracked panels. For the case where the panel dimensions become infinite compared to the crack length, their solution can be put in the following form

$$J = C_0\,\epsilon^{n+1} f(n) a \tag{12}$$

$f(n)$ is a function of n described graphically in Ref *14*. Defining $f'(n) = (n+1)f(n)$, Eq 12 can be observed to possess the desired form; that is

$$J = \frac{C_0}{n+1}\,\varepsilon^{n+1} f'(n) a = W_{\infty} f'(n) a \tag{13}$$

Agreement with Eq 10 is exactly satisfied if $f'(n) = 2\pi$. The plot of $f(n)$ versus n in Ref *14* does not give values below $n = 0.2$, but at this value, $(n + 1)f(n) \cong 2\pi$.

Although rigorous proof for this suggested form of J-solution is lacking, the examples cited do present a good case for basing an estimate. The geometry term in the stress intensity factor solution for an edge crack is $1.12\sqrt{\pi a}$. Hence, the estimated solution for J becomes

$$J = 2\,W_{\infty}(1.12\sqrt{\pi a})^2 = 7.88\,W_{\infty}\,a \tag{14}$$

Low-Cycle Fatigue Relationship

For purposes of describing low cycle fatigue loading, in which specimens are cycled through a range of controlled variable (normally strain), Eq 14 is converted to range form

$$\Delta J = 7.88 \Delta W_{\infty}\,a \tag{15}$$

The interpretation is added that ΔJ apply only to that part of the cycle in which the crack surfaces are being opened. On substituting Eq 15 in Eq 3, there results

$$\frac{da}{dN} = C_1\,(7.88\,\Delta W_{\infty}\,a)^{\gamma} \tag{16}$$

Since W_∞ is not a function of either a or N, Eq 16 can be set in the integral form

$$\int_{a_0}^{a_f} \frac{da}{a^\gamma} = C_1 (7.88\, \Delta\, W_\infty)^\gamma \int_0^{N_f} dN$$

a_0 is interpreted as an initial microscopic size crack at $N = 0$ and a_f the crack length at which failure is defined, $N = N_f$. Carrying out the integration

$$N_f^{1/\gamma} \Delta W_\infty = \frac{1}{7.88} \left[\frac{1}{C_1} \left(\frac{a_f^{1-\gamma} - a_0^{1-\gamma}}{1-\gamma} \right) \right]^{1/\gamma} \quad (17)$$

Assuming that a_0 and a_f are fixed for a set of experiments, the quantity to the right of the equals sign can be considered a material constant. For convenience this constant is termed C_2 and the derived relationship is

$$N_f^{1/\gamma} \Delta W_\infty = C_2 \quad (18)$$

Discussion

Equation 18 has the same form as the Coffin-Manson low-cycle fatigue relationship. However, it implies that the controlling variable is the range of strain energy density rather than range of plastic strain. Figure 7 gives a schematic illustration of this difference. Observe that when the plastic

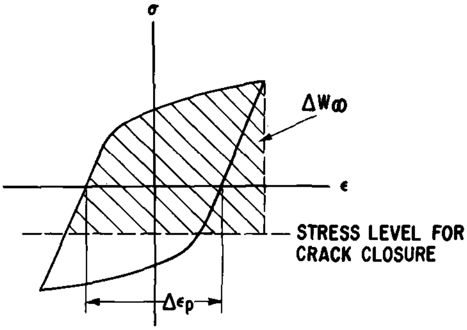

FIG. 7—*Illustration of controlling variables in low cycle fatigue relationships.*

strain is a large fraction of the total strain, there should be a close correspondence between the two variables. Considering the stresses to be completely reversed and the entire stress range effective in opening the crack surfaces, the two are directly related via Eqs 2 and 5 as follows

$$\Delta W_{\infty} = \frac{C_0 \Delta \epsilon_p{}^{n+1}}{n+1} \tag{19}$$

Substituting this result into Eq 18 and rearranging yields the Coffin-Manson form

$$N_f{}^{1/\gamma(n+1)} \Delta \varepsilon_p = \left[\frac{(n+1)\, C_2}{C_0}\right]^{1/(n+1)} \tag{20}$$

This reduction of Eq 18 to the Coffin-Manson relationship implies the following relationships between common material properties and crack length terms

$$\beta = 1/\gamma(n+1) \tag{21}$$

$$\varepsilon_f' = \left\{\frac{0.13(n+1)}{C_0}\left[\frac{1}{C_1}\left(\frac{a_f{}^{1-\gamma} - a_0{}^{1-\gamma}}{1-\gamma}\right)\right]^{1/\gamma}\right\}^{\frac{1}{(n+1)}} \tag{22}$$

Hence, the fatigue exponent, β is predicted to be a function of the crack growth exponent, γ, and the cyclic strain hardening exponent, n. Past analyses [*5–7*] have predicted it to be a function of one or the other, but not both. The fatigue ductility term (ϵ_f') is predicted to be a function of six quantities: the two parameters defining the cyclic stress-strain relationship (n and C_0), the two crack growth parameters (γ and C_1), and the initial and terminal crack lengths (a_0 and a_f).

Of interest is whether these relationships predict reasonable numerical values of β and ϵ_f', and thus, demonstrate the tie-in between crack growth and low-cycle fatigue. A533-B steel properties are used as an example to examine this possibility. Numerical values of the material properties are listed in Table 1. The crack growth constants are from the Dowling and Begley data [*11*] (Fig. 2). Low cycle fatigue information is for A302-B steel [*15*], on older version of A533-B.[3] The values of a_0 and a_f are assumed, having been rationalized in the following fashion: (1) a_f is set at 10 percent of the normal low cycle fatigue specimen diameter (0.250 in.) to maintain consistency with Assumption No. 1 in the analysis. As with linear elastic calculations, the results are quite insensitive to the value of a_f; (2) the value of a_0 should be close in magnitude to some microstructural feature such as grain size, porosity diameter, etc. For the material being considered a value of 0.001 in. appears consistent with this reasoning. Varying this number by a factor of 10 alters the prediction of ϵ_f' by only a factor of 2.

TABLE 1—*Material properties for A533-B/A302-B steel.*

Property	Value	Reference
γ	1.587	*11*
C_0	2.13×10^{-8}	*11*
n	0.15	*15*
C_1	320 000 psi	*15*
β	0.50	*15*
ϵ_f'	0.37	*15*
a_0	0.001 in.	. . .
a_f	0.025 in.	. . .

The predicted values of β and ϵ_f' for A533-B/A302-B steel are compared here with the available measured values:

Property	Prediction	Measured
β	0.55	0.50
ϵ_f	0.56	0.37

The closeness of these results lends considerable support to the analysis and assumptions.

In concluding the discussion it is noted that the predicted controlling variable, strain energy density, corresponds closely to several energy related variables proposed over the years as controlling the low cycle fatigue damage process. Morrow [*16*], for example, proposed the total hysteretic energy. Smith et al [*17*] proposed the function

$$\left(\frac{E}{2}\sigma_{\max}\,\Delta\epsilon\right)^{1/2}$$

---

[3] The standard tensile properties of the materials used in the crack growth [*11*] and low cycle fatigue [*15*] work are near identical.

where $\sigma_{\max}$ is the maximum stress in the cycle and $\Delta\epsilon$, the total strain range. The facility of this function was demonstrated with room temperature data. In yet unpublished work, Ostergren [*18*] has proposed and demonstrated the facility of a similar function for elevated temperature low cycle fatigue. His function is

$$(\sigma_{\max}\ \Delta\epsilon_p)$$

Ostergren postulated that hysteretic energy controls the process, but considered that the crack closure portion of the cycle must be excluded in the calculation. As a first approximation, he considered the crack closed for all negative stress and the hysteretic energy given by the prior product.

Each of the discussed variables, as well as the one derived in this analysis, allow for the inclusion of mean stress bias effects. This is important in considering fatigue near notches [*19*] and creep effects at elevated temperature [*3,18*].

Summary

It has been the objective in this work to derive a low cycle fatigue relationship using some recent developments in nonlinar fracture mechanics centering about the J-integral. In making the derivation, it has been assumed that the low-cycle fatigue damage process is one of crack growth only, that the typical specimen can be modeled as an edge-cracked solid of semi-infinite extent, and that the crack growth rate is controlled by the range of J operative in opening crack surfaces. The specific dependence of crack growth rate on J is assumed to follow the power relationship found by Dowling and Begley. An estimate of J for the model specimen was based on a general form established from available solutions for similar types of loading and geometry.

An equation of the form of the Coffin-Manson relationship was found. It differs from the latter in that the predicted controlling variable is applied strain energy density rather than plastic strain. This predicted controlling variable closely corresponds to several energy related functions proposed over the years, starting with the hysteretic energy proposal of Morrow. Considering the stresses to be completely reversed and fully operative in opening the crack surfaces, the current equation reduces to the Coffin-Manson equation. Using the Dowling-Begley crack growth constants and available cyclic stress-strain constants, very good predictions of the fatigue exponent and fatigue ductility of A533-B steel results.

References

[*1*] Coffin, L. F., Jr., *Transactions,* American Society of Mechanical Engineers, Vol. 76, 1954, pp. 923–949.

[2] Manson, S. S., "Behavior of Materials Under Conditions of Thermal Stress," NACA Technical Note 2933, National Advisory Committee for Aeronautics, 1954.
[3] Coffin, L. F., Jr., *Proceedings,* Institute of Mechanical Engineers, Vol. 188, 1974, pp. 109–127.
[4] Grosskreutz, J. C. in *Metal Fatigue Damage—Mechanism, Detection, Avoidance, and Repairs, ASTM STP 495,* American Society for Testing and Materials, 1971, p. 60.
[5] Tompkins, B., *Philosophical Magazine,* Vol. 18, 1968, pp. 1041–1066.
[6] Boettner, R. C., Laird, C., and McEvily, A. J., *Transactions,* Metallurgical Society of the American Institute of Mining, Metallurgical, and Petroleum Engineers, Vol. 233, 1965, pp. 379–387.
[7] Solomon, H. D., *Journal of Materials,* Vol. 7, No. 3, 1972, pp. 299–306.
[8] Grosskreutz, J. C., "A Theory of Stage II Fatigue Crack Propagation," Report AFML-TR-64-415, Air Force Materials Laboratory, March 1965.
[9] Rice, J. R., "A Path Independent Integral and the Approximate Analysis of Strain Concentration by Notches and Cracks," *Transactions,* American Society of Mechanical Engineers, 1968.
[10] Begley, J. A. and Landes, J. D. in *Fracture Toughness, ASTM STP 514,* American Society for Testing and Materials, 1972, pp. 1–20.
[11] Dowling, N. E. and Begley, J. A. in *Mechanics in Crack Growth, ASTM STP 590,* American Society for Testing and Materials, 1976, pp. 83–104.
[12] Paris, P. C. in *Fatigue—An Interdisciplinary Approach,* Syracuse University Press, 1963, pp. 107–132.
[13] Begley, J. A., Landes, J. D., and Wilson, W. K. in *Fracture Analysis, ASTM STP 560,* American Society for Testing and Materials, 1974, pp. 155–168.
[14] Goldman, N. L. and Hutchinson, J. W., "Fully Plastic Crack Problems: The Center-Cracked Strip Under Plane Strain," AFOSR-TR74-0718, Feb. 1974; copies available from Defense Documentation Center.
[15] Snow, A. L., Langer, B. F., and Gibbons, W. G., "Low Cycle Fatigue Strength of Notched Ni-Cr-Fe Alloy 600 and Low Alloy Steel," WAPD-T-2093, Sept. 1967.
[16] Morrow, J. in *Internal Friction, Damping, and Plasticity, ASTM STP 378,* American Society for Testing and Materials, 1965, pp. 45–87.
[17] Smith, K. N., Watson, P., and Topper, T. H., *Journal of Materials,* Vol. 5, 1970, pp. 767–778.
[18] Ostergren, W. J., "A Damage Function for Predicting Hold Time and Frequency Effects in Elevated Temperature Fatigue," Ph.D. thesis work at Rensselaer Polytechnic Institute, 1974; to be published in the *Journal of Testing and Evaluation,* Sept. 1976.
[19] Mowbray, D. F. and McConnelee, J. E. in *Cyclic Stress-Strain Behavior—Analysis, Experimentation, and Failure Prediction, ASTM STP 519,* American Society for Testing and Materials, 1971, pp. 151–169.

K. M. Nikbin,[1] *G. A. Webster,*[1] *and C. E. Turner*[1]

Relevance of Nonlinear Fracture Mechanics to Creep Cracking

REFERENCE: Nikbin, K. M., Webster, G. A., and Turner, C. E., "**Relevance of Nonlinear Fracture Mechanics to Creep Cracking,**" *Cracks and Fracture, ASTM STP 601,* American Society for Testing and Materials, 1976, pp. 47–62.

ABSTRACT: Creep crack growth tests, conducted on contoured double cantilever beam (DCB) specimens are described for aluminium alloy RR58 and a chromium-molybdenum-vanadium steel. The results are analyzed in terms of $\dot{J}$, the rate equivalent of the J contour integral, which is a nonlinear fracture mechanics parameter. Direct proportionality is found between crack growth rate, $\dot{a}$ and $\dot{J}$. The treatment is shown to reveal a unification of the linear elastic fracture mechanics and net section or reference stress descriptions of creep cracking.

KEY WORDS: crack propagation, mechanical properties, temperature, creep, properties, J contour integral, linear elastic fracture mechanics

It cannot be ensured that engineering components will not contain preexisting flaws or develop cracks during use. For those components operating at elevated temperatures, it is possible that any cracks present may grow by creep. In order to produce a reliable design, therefore, it is necessary to establish the factors controlling the rate of propagation of cracks by creep.

Creep failure is predominantly intercrystalline [*1–3*][2] are usually occurs by the linking up of many individual cracks [*4–6*] (rather than the propagation of one major crack), when the true stress in the material approaches its ultimate tensile strength [*5*]. Observations indicate that cavities and triple point cracks can be present from the early stages of creep [*4–6*] and that they continue to grow with deformation. Mechanisms for the growth of individual cavities and triple point cracks by grain boundary sliding and vacancy diffusion have been proposed by a number of authors [*6–8*]. However, difficulties arise in applying these

---

[1] Research student, senior lecturer, and professor of materials in mechanical engineering, Department of Mechanical Engineering, Imperial College, London, S. W. 7, England.

[2] The italic numbers in brackets refer to the list of references appended to this paper.

theories to creep rupture when cracking is extensive and nucleation is occurring throughout creep.

There is much evidence from conventional tensile creep tests carried out on round bars at constant stress (or load) to show that creep deformation and time to failure are related [*1,2*]. Because of this relation, attempts [*9,10*] have been made to explain tertiary creep and fracture by incorporating a damage factor into conventional secondary creep laws to allow for the progressive loss in area due to cracking. However it is not certain that theories which predict creep fracture where failure is by linking up of many cracks will be satisfactory where failure is by propagation from a single large preexisting flaw. More recently a number of investigators [*11–19*] have attempted to establish the relevance of fracture mechanics to creep cracking in this situation. Their data where obtained over a range of specimen geometries and materials with creep ductilities from <2 percent to 75 percent. It was assumed that creep strain rate $\dot{\epsilon}$ could be described by the secondary creep law written in the form

$$\dot{\epsilon} = C\,\sigma^{n} \tag{1}$$

where

σ = stress,
n = indication of the stress sensitivity of creep, and
C = function of temperature.

In most instances crack growth rate, $\dot{a}$, could be expressed in terms of stress intensity factory, K, by

$$\dot{a}\ \alpha\, K^{\beta} \tag{2}$$

although some investigators claim better correlations with net-section stress [*12*] or with a reference stress [*17*]. Generally, the higher strength low ductility materials correlated better with K and the lower strength high ductility materials, with net-section stress. The values of β were found to lie between approximately 3 and 30, typical of the stress sensitivity, n, of secondary creep rate suggesting that the values of n for creep deformation and β for cracking are closely related.

In most instances, Eq 2 was determined from results which were obtained under conditions of continuously rising K. One series of experi-

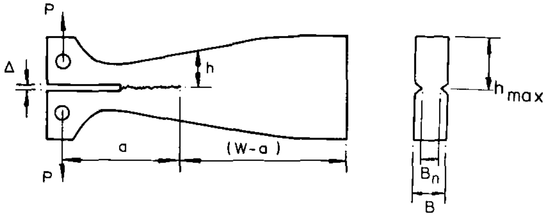

FIG. 1—*Typical contoured DCB geometry.*

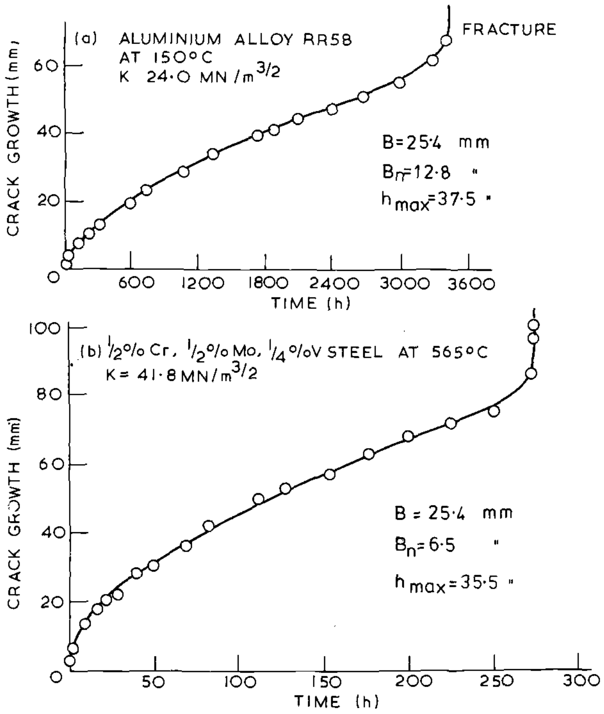

FIG. 2—*Typical creep crack growth,* a, *at constant stress intensity factor,* K.

ments [*18*] was carried out on contoured double cantilever beam (DCB) specimens, Fig. 1, which gave *K* constant at constant load independent of crack length. The results showed that despite the correlation of Eq 2 a constant crack growth rate was not obtained for aluminium alloy RR 58 (Fig. 2*a*). Apparent primary, secondary, and tertiary regions were observed. The tertiary stage was attributed to increasing *K* as the crack approached the end of the specimen. The primary region was found to be reduced by increasing the initial crack length and by soaking the specimen at the test temperature before loading, indicating both geometry and aging complications [*19*].

More recent results [*20*], Fig. 2*b*, on a ½Cr-½Mo-¼V steel which had been heat treated at 1250°C for ½ h and oil quenched to simulate a heat affected zone (HAZ) structure have shown that the just mentioned effects are not peculiar to the aluminum alloy. Again primary, secondary, and tertiary cracking was observed. In spite of the change in crack growth rate at constant *K*, Fig. 3 shows that the crack growth rate in the secondary region, $\dot{a}_s$, when treated as constant, can still be expressed in terms of Eq 2, with a value of β close to n for this material [*21*]. The results are also consistent with other published data [*11,15*] on the same material.

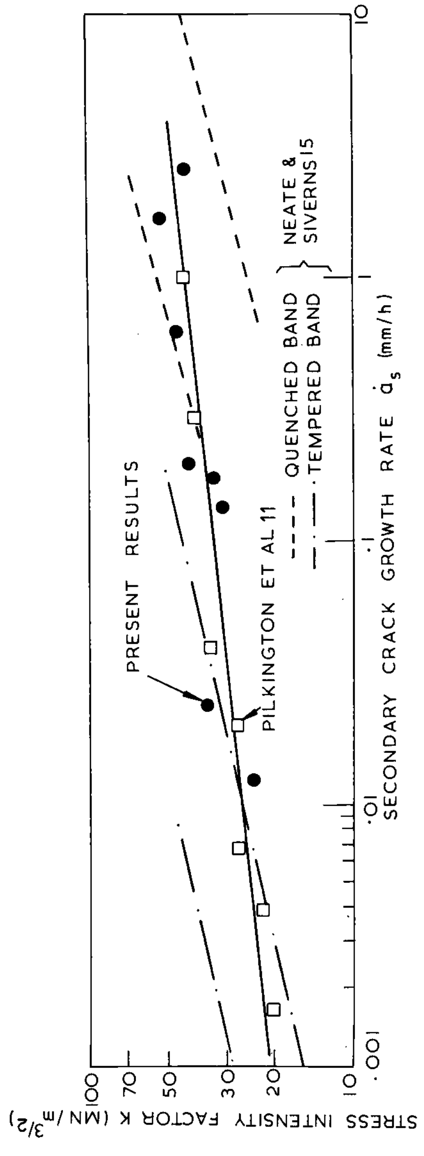

FIG. 3—*Crack growth rate as a function of stress intensity factor for 1/2Cr-1/2Mo-1/4V steel at 565°C.*

It is shown here that the decreasing crack growth rate in the primary region, and the linear elastic fracture mechanics and net section stress approaches to creep cracking, can be rationalized by introducing nonlinear fracture mechanics concepts as suggested by Turner and Webster [20,22]. The approach is consistent with that recently reported by Landes and Begley [23].

Application of Nonlinear Fracture Mechanics to Creep Cracking

The viewpoint of the present paper is that the inadequacy of linear elastic concepts in correlating crack growth rate data under creep conditions at constant stress intensity factor, K, may be due to the nonlinear nature of the constitutive laws for the highly deformed region around the crack tip. The J contour integral has been used to describe the singular terms of stress or strain for a nonlinear elastic material [24,25]. Possible application to the onset of cracking in materials obeying the laws of incremental plasticity has been implied by many workers recently studying elastic-plastic fracture problems although a sure foundation to this approach has not been established. Essential steps in the argument are the retention of the property of path independence, to the extent demonstrated by finite element computation [26–29], and the apparent success of preliminary tests to establish a critical value of the contour integral J_{Ic}, for the onset of cracking in pieces of different geometry [30,31]. If these demonstrations of the usefulness of J for plastic (as distinct from nonlinear elastic) materials are taken to warrant further more extensive studies of the concept then it is here argued that for *steady state creep*, there should likewise be a relevance of J to creep crack growth. The authors are not aware of a proper energy rate balance for the time dependent processes of creep and creep crack growth. The use of J (in a modified form, $\dot{J}$, for reasons of dimensional analysis) as proposed here rests on being able to carry over to steady state creep the characterizing role of J in describing the singular stress and strain rates at the crack tip. As creep rupture in conventional creep testing is related to secondary creep strain rate [1,2], it may be expected that crack growth rate will also depend on secondary creep rate. Following Hutchinson [24], McClintock [32] showed that for nonlinear elastic materials obeying power law hardening of the form

$$\epsilon = A \ \sigma^{n} \tag{3}$$

the stresses and strains around a crack tip are characterized by

$$\sigma \ \alpha \ (J/A)^{1|n \ + \ 1} \tag{4}$$

$$\epsilon \ \alpha \ A(J/A)^{n|n \ + \ 1} \tag{5}$$

For a material obeying the secondary creep rate law, Eq 1, it follows by analogy that the stress and strain rates around a crack tip in a material subjected to steady state creep are

$$\sigma \; \alpha \; (\dot{J}/C)^{1|n + 1} \tag{6}$$

$$\dot{\epsilon} \; \alpha \; C(\dot{J}/C)^{n|n + 1} \tag{7}$$

where $\dot{J}$ is the characterizing parameter for creep. It has the dimensions of J divided by time in order to accommodate the different dimensions of C (Eq 1) and A (Eq 3).

For the case of nonlinear elasticity it has been shown, as reviewed by Rice [*33*], that for a crack of thickness, B_n, and length, a, the numerical value of J can be found from the expression

$$J = -\frac{1}{B_n}\frac{dU}{da} \tag{8}$$

where U is potential energy.

In elasticity, this energy is available to grow the crack. With plasticity, Eq 8 remains a means of evaluating the crack tip parameter J but J is no longer the energy potentially available to grow the crack. This method of evaluating J was used experimentally for plasticity by Begley and Landes [*30*]. For a nonlinear material obeying power law hardening, Eq 3, it is shown [*20*] that for a DCB specimen subjected to a constant load, P

$$J = \frac{P}{B_n\,(n + 1)} \cdot \frac{d\Delta}{da} \tag{9}$$

where Δ is deflection at the loading line (Fig. 1).

Evaluation of $d\Delta/da$ as the crack propagates along the length of the specimen will therefore give J as a function of crack length. Provided the crack length is long enough, shear deflections can be neglected and $d\Delta/da$ obtained from nonlinear bending theory as shown in the Appendix. Substituting in Eq 9 gives

$$J = \frac{2A}{B_n\,(n + 1)} \left[\frac{(2n + 1)}{2nB} \right]^{n} \frac{(aP)^{n + 1}}{(h/2)^{2n + 1}} \tag{10}$$

This equation enables the instantaneous value of J to be calculated for a nonlinear material for any crack length, provided the geometry of the specimen is known. It applies to any DCB specimen contour for which it may be assumed that bending stresses dominate and shear deflections can be ignored. For linear elasticity, $n = 1$, $A = 1/E$, and $J = G$, the elastic strain energy release rate. For plane stress

$$G = K^2/E \tag{11}$$

and for plane strain

$$G = (1 - \nu)^2 K^2/E \tag{12}$$

where ν is Poisson's ratio.

Now consider a material obeying the secondary creep law, Eq 1. The above analysis can obviously be repeated with ϵ replaced by $\dot{\epsilon}$, A by C, and Δ by $\dot{\Delta}$.

For creep, we can define a term with the dimensions of power, $\dot{U}$, and by analogy with Eq 8 a term corresponding to potential power release rate, $\dot{J}$

$$\begin{aligned} \dot{J} &= -\frac{1}{B_n}\frac{d\dot{U}}{da} \\ &= \frac{2C}{B_n(n+1)}\left[\frac{(2n+1)}{2nB}\right]^n \frac{(aP)^{n+1}}{(h/2)^{2n+1}} \end{aligned} \tag{13}$$

This equation is exactly the same as Eq 10 except that $\dot{J}$ has dimensions of power whereas J has dimensions of energy. It is equivalent to replacing ϵ by $\dot{\epsilon}$ in the experimental plasticity evaluation of J as discussed by Landes and Begley [*23*].

Comparison with Experimental Data

The profile of the contoured DCB specimen used by Kenyon et al [*18*] was chosen to give a constant K at constant load independent of crack length. This necessarily implies from Eq 13, however, that $\dot{J}$ will vary with crack length. Figure 4*a* shows the relationship between $\dot{J}$ and crack length for the geometry tested by Kenyon et al for values of n in the range 1 to 25. The ordinate has been normalized with respect to $\dot{J}_i$ the value of $\dot{J}$ at a crack length of 75 mm (the shortest initial crack length used) for ease of comparison. The graph indicates that from the present analysis with $n = 1$, $\dot{J}$ is constant (as it should be for a constant K geometry) until a crack length of 155 mm, after which it rises. For all other values of n, $\dot{J}$ decreases with crack length until 155 mm when it rises again. The decrease is most marked the higher the value of n. Sufficient data have not been obtained yet to enable $\dot{J}$ to be evaluated experimentally to check this trend.

Figure 4*b* shows how crack growth rate decreases experimentally with crack length for the two tests shown in Fig. 2. No truly constant secondary rate exists. The shapes compare very favorably with those shown in Fig. 4*a*, suggesting that the primary stage of cracking may be caused by the decrease in $\dot{J}$ with crack length. Both the experimental and calculated curves have a minimum at a crack length of 155 mm. For crack lengths longer than this, the elastic analysis for this geometry becomes invalid

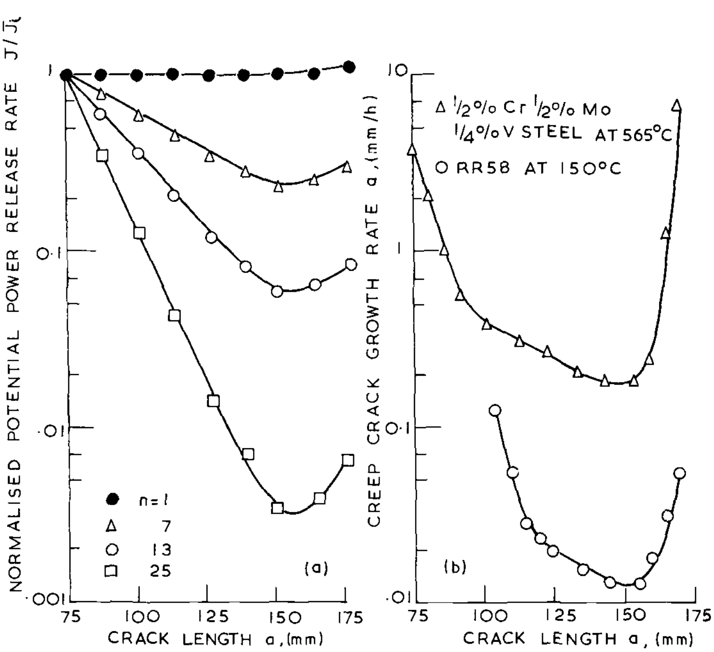

FIG. 4—*Comparison of the change in* (a) *potential power release rate and* (b) *creep crack growth rate with crack length.*

due to the effect of the "remote" free end of the specimen. It is assumed that the same limitation applies to the analysis for J and $\dot{J}$.

Before it is possible to plot crack growth rate against $\dot{J}$, it is necessary to know the value of n in Eq 1 for each material. A value of 10 for n has been estimated for the steel from the tensile creep data of Cummings and King [*21*] and 14 for the aluminum alloy from the results of Kenyon [*19*]. Figure 5 shows the dependence of crack growth rate in the primary and secondary regions on $\dot{J}$ calculated using these values of n. Except in the very early stages of cracking, the results tend to suggest that crack growth rate is approximately proportional to $\dot{J}$. The analysis neglects elastic strains and assumes that both materials exhibit only secondary creep deformation when in fact some primary creep was observed [*19*]. Consequently, some deviation would be anticipated in the early stages of cracking as the stress distribution changes from the initial elastic stress distribution to the settled steady state creep stress distribution. For both materials, this settling down period extended over a crack growth of approximately 5 mm.

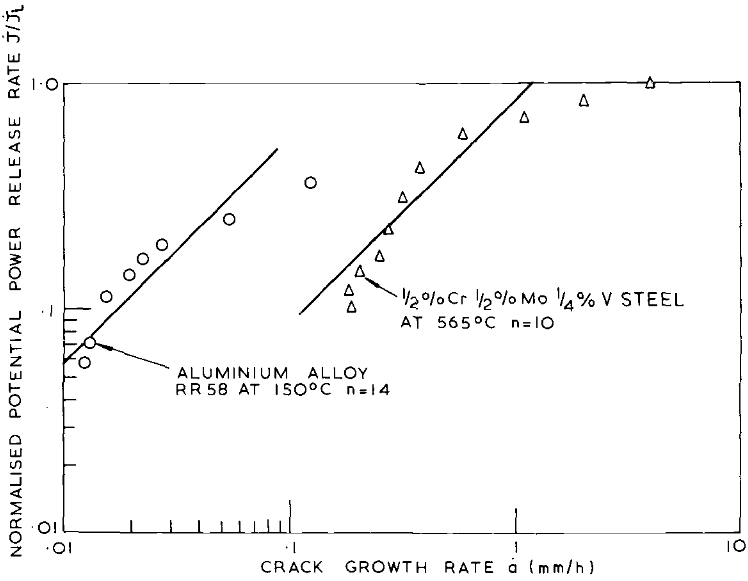

FIG. 5—*Change in crack growth rate with* J *during primary and secondary regions.*

Additional experiments have been carried out to establish more firmly the dependence of crack growth rate on $\dot{J}$. The same experimental procedure as reported by Kenyon et al was used except that fatigue precracking was adopted. All the specimens were 25 mm thick but the groove of the steel specimens was deepened to leave a net thickness of 6.5 mm (compared with 12.6 mm for the aluminum alloy) to prevent breaking off of the specimen leg perpendicular to the crack path. The aluminum alloy was tested at 150°C and the steel, at 565°C. The surfaces of the side grooves in the steel were coated with an alumina-based paint resistant to high temperatures to prevent oxidation and enable crack growth to be monitored visually with the aid of a travelling telescope.

Most of the tests were performed at constant K, but in some instances the load was adjusted during the test to keep $\dot{J}$ constant with crack growth. The results of 9 tests are summarized in Figs. 6 and 7. Figure 6 confims the trend indicated in Fig. 5. It shows that all the results fall on one straight line with a slope of unity with comparatively little scatter (the points furthest from the line are usually those for the early stages of cracking before a settled state has been reached) indicating

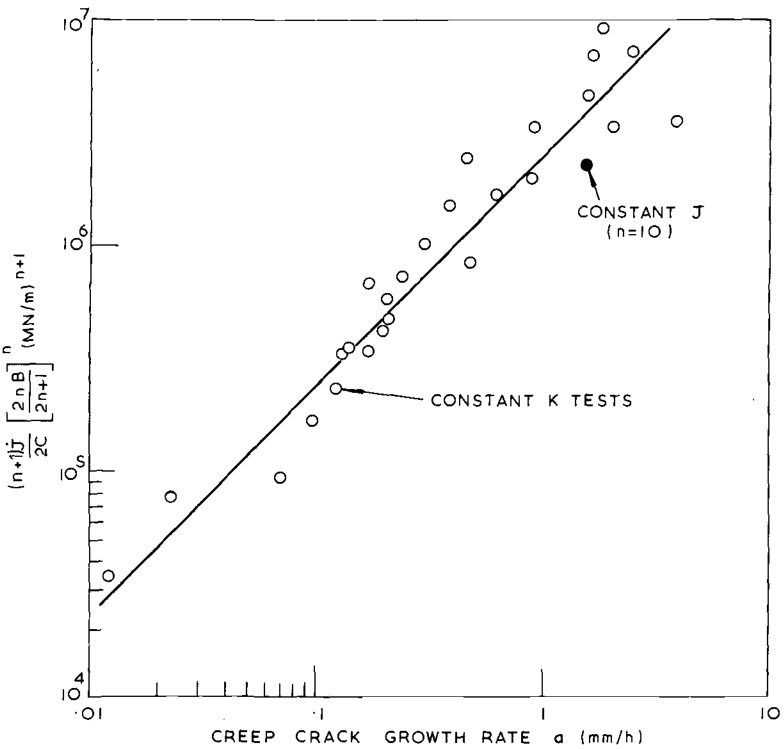

FIG. 6—*Crack growth rate as a function of potential power release rate* J̇ *for 1/2Cr-1/2Mo-1/4V steel at 565°C.*

that creep crack growth rate throughout the primary and secondary regions can be expressed by

$$\dot{a} = F\dot{J} \tag{14}$$

where F is a proportionality factor which could be a function of temperature, since in the creep law, Eq 1, C is, of course, a function of temperature.

A similar observation can be made from the data of Landes and Begley [23] on a superalloy. The characterizing parameter, C^*, used in their paper is equivalent to the $\dot{J}$ used here. Although they show a change in slope in some of their graphs, to a good approximation all their results can be described by Eq 14.

In the present investigation, all the individual constant K tests exhibited primary, secondary, and tertiary regions of cracking whereas Eq 2 predicts a constant crack growth rate. If $\dot{J}$ (rather than K) is the true characterizing parameter, a constant crack growth rate would be expected throughout a test at constant $\dot{J}$. Examples of crack growth curves obtained when load was altered to keep $\dot{J}$ constant are shown in Fig 7. This figure confirms that for both the aluminum alloy and the steel, after a slight curvature

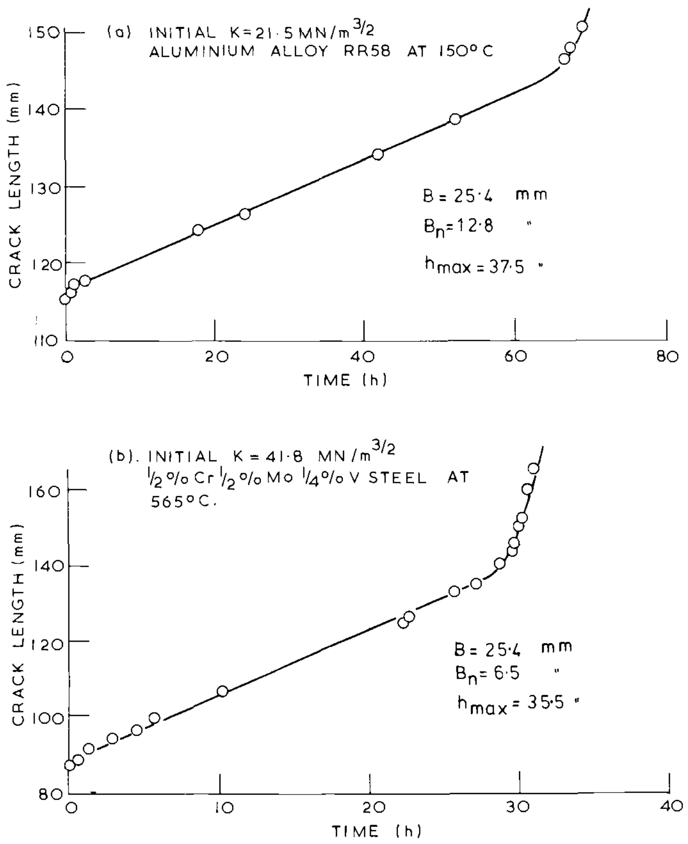

FIG. 7—*Creep crack growth curves at constant* $\dot{J}$.

during an initial settling down stage, the crack growth rate is constant until the test is no longer valid at long crack lengths. The initial *K* value for the constant $\dot{J}$ test of Fig. 7*b* was deliberately chosen to be the same as that of the constant *K* test of Fig. 2*b* for comparison purposes. The initial crack growth rate of the two tests is the same. However, if after the same initial starting conditions the load is either maintained constant to keep *K* constant or alternatively increased to maintain $\dot{J}$ constant for a total crack growth of 50 mm, two quite different behaviors result. In the former case (constant *K*), the crack growth rate decreases gradually (see Fig. 4*b*) by nearly an order of magnitude thus extending the test time to 300 h, whereas in the latter case (constant $\dot{J}$) the growth rate remains constant (Fig. 7) over a crack growth of 50 mm and final fracture is reached in only 30 h. These observations, therefore, reinforce the interpretation of creep crack growth in terms of $\dot{J}$, the creep equivalent of the *J* contour integral.

Discussion

It has been shown that nonlinear fracture mechanics can be used to explain creep crack growth quantitatively. It describes the apparent primary region of cracking which cannot be explained by linear mechanics arguments. No doubt, in some cases, as reported [*19*] for the aluminium alloy, metallurgical changes may also play a role and influence the so-called primary stage of cracking.

Further insight into the cracking process can be obtained by comparing Eq 7 which characterizes the creep strain rates around a crack tip, with the experimental correlation shown in Eq 14. For the materials tested, n was found to be 10 for the steel and 14 for the aluminum alloy. Thus, it is difficult in practice to the distinguish between the ratio $n/n + 1$ and 1. Consequently, although proportionality between crack growth rate and $\dot{J}$ is indicated by the data, it is also clear that a satisfactory correlation could be obtained with $\dot{J}^{n/n + 1}$ to give proportionality between secondary creep rate and creep crack growth at least for the values of n found here.

The successful correlation of creep crack growth with K already reported in the literature calls for comment. Using elastic fracture mechanics $K \alpha P$. From Eq 13

$$\dot{J} \quad \alpha \quad P^{n + 1} \tag{15}$$

therefore

$$\dot{J} \quad \alpha \quad K^{n + 1} \tag{16}$$

Thus Eq 2 could be rewritten

$$\dot{a} \quad \alpha \quad \dot{J}^{\beta/n + 1} \tag{17}$$

Taking β as n gives the correlation with creep strain rate and $\dot{J}^{n/n + 1}$ or K^n. Taking $\beta = n + 1$ gives direct correlation with $\dot{J}$ or $K^{n + 1}$. As already discussed, the difference between these powers cannot be resolved with the present data. It must be noted, however, that the dependence of $\dot{J}$ on crack length, a, (Eq 13) is a function of n so that in general $\dot{J}$ and K will be different functions of crack length. The above discussion holds strictly only for a fixed crack length. It appears that experimental results so far published have been obtained over small changes in crack length and thus do not discriminate between the linear or nonlinear correlations. Another circumstance where K might be more relevant than $\dot{J}$ is where creep ductility is small. The present analysis ignores elastic strains and primary creep. It assumes that sufficient creep occurs to allow a secondary creep stress distribution to be established by redistribution of elastic stresses at the crack tip. For a material of very limited creep ductility this may not happen.

The adoption of nonlinear fracture mechanics can also be used to explain the better agreement of crack growth with net section stress than with K reported by some authors [*12,17*]. It can be shown that the maximum bending stress (neglecting the singularity) at the crack tip in each leg of the DCB specimen is

$$\sigma_{\max} = \frac{(2n + 1)aP}{2nB \times (h/2)^2} \tag{18}$$

Substituting $n = 1$ in this expression gives the net section stress [*12*], and $n = \infty$, the reference stress. Whichever definition of stress is used it will change with crack length in the same way. Comparison of this equation with the expression for $\dot{J}$ (Eq 13), reveals that when $n >> 1$

$$\dot{J} \; \alpha \; (\sigma_{\max})^n$$

Hence, correlation with net section stress or with the reference stress for materials exhibiting high values of n are in agreement with nonlinear fracture mechanics. The value of n for cracking should be the same as that required to describe creep deformation behavior.

Fracture mechanics also provides an explanation of extensive cracking in conventional uncracked creep specimens. By using the infinite plate solution

$$K = \sigma\sqrt{\pi a}$$

an estimate can be made of the size of cracks that will be propagated in these specimens. The lowest value of K at which creep crack growth has been observed in steels and aluminium alloy RR58 is approximately 15 $MN/m^{3/2}$. A typical creep stress for these materials is 300 MN/m^2 giving a crack length $2a = 1.6$ mm. This is far in excess of the sizes of cracks measured [*4,5*]. Even close to fracture, individual cracks seldom exceed a grain facet in length and in aluminium alloy RR58 are typically 30 μm long [*5*]. These figures indicate why, in most materials, crack nucleation is easier than crack propagation and why final creep failure occurs by the linking up of many small cracks when the net section stress approaches the ultimate tensile strength of the material. For creep failure, if a grain facet can be regarded as an incipient flaw, it is likely that grain sizes as large as approximately 1 mm can be tolerated in conventional creep specimens before failure will be by the propagation of one dominant crack. Conversely where large defects exist, such as in weldments or at a major inclusion, good creep toughness in conventional tensile creep tests may not guard against crack growth by creep from the preexisting defect.

Conclusions

Microstructural evidence of the development of voids and triple point cracks during creep deformation suggests that final failure occurs by ligament tearing when the ultimate tensile strength of the material is approached. The stress intensity factors required to propagate creep cracks are sufficiently high that the individual voids or triple point cracks will not be propagated by creep until they reach a size of approximately 1 mm. It is unlikely, therefore, that the failure of round bar creep specimens will be described by fracture mechanics. The creep fracture toughnesses of most materials are too high in relation to their creep strengths for this to happen.

It has been shown that initial flaws which are sufficiently large can be extended by creep. The resulting creep crack growth rate can, for a particular geometry, be correlated in terms of the crack tip characterizing parameter, $\dot{J}$, which corresponds to the J contour integral as used in plasticity for a work-hardening material. Experimental results suggest that creep crack growth rate is approximately proportional to $\dot{J}$. Nonlinear fracture mechanics can describe the previously unexplained apparent primary region of cracking. It is also capable of unifying the linear elastic fracture mechanics and net section stress correlations of creep cracking reported previously.

Acknowledgments

The authors wish to thank the Science Research Council who supported much of the work, The Royal Aircraft Establishment and English Electric for supplying the materials, and their colleague, J. C. Radon, for helpful discussions.

APPENDIX

Analysis of Deflection of DCB Specimen

Consider a cross section of the DCB specimen to be a distance $x < a$ from the loading line. Let the curvature at this section under load, P, be k. Then for plane sections to remain plane, the strain at any distance y from the neutral axis is

$$\varepsilon = ky \tag{19}$$

For moment equilibrium

$$M = \int_{-h/2}^{h/2} \sigma \, B \, y \, dy$$

Therefore, substituting from Eqs 3 and 19

$$\begin{aligned} M &= B \left(\frac{k}{A}\right)^{1/n} \int_{-h/2}^{h/2} y^{1+1/n} dy \\ &= \frac{2nB}{(2n+1)} \left(\frac{k}{A}\right)^{1/n} \left(\frac{h}{2}\right)^{2+1/n} \end{aligned} \tag{20}$$

For small deflections δ, Eq 20 can be rearranged to give

$$k = \frac{d^2\delta}{dx^2} = \left[\frac{(2n+1)M}{2nB}\right]^n \frac{A}{(h/2)^{2n+1}}$$

But $M = Px$, therefore

$$\frac{d^2\delta}{dx^2} = \left[\frac{(2n+1)P}{2nB}\right]^n A \frac{x^n}{(h/2)^{2n+1}}$$

Integrating twice and using the boundary condition $d\delta/dx = 0$ and $\delta = 0$ at $x = a$, the crack tip, gives

$$\delta = \left[\frac{(2n+1)P}{2nB}\right]^n A \left[I_x{}^{**} - I_a{}^{**} - I_a{}^{*}(x-a)\right] \tag{21}$$

where

$$I^{*} = \int \frac{x^n}{(h/2)^{2n+1}} dx$$

and

$$I^{**} = \int\int \frac{x^n}{(h/2)^{2n+1}} dx$$

and the subscripts x and a indicate the values of the integrals at x and a, respectively. For the contoured geometry, h is a function of x.

The loading pin displacement, Δ, required for the evaluation of J, Eqs 4 and 5, is given by

$$\Delta = 2\delta$$

evaluated at $x = 0$; therefore

$$\Delta = \left[\frac{(2n+1)P}{2nB}\right]^n 2A \left[I_0^{**} - I_a^{**} + I_a^{*} a\right]$$

where I_0^{**} is the value of I^{**} at $x = 0$. Therefore

$$\frac{d\Delta}{da} = \left[\frac{(2n+1)P}{2nB}\right]^n 2A \left[- I_a^{*} + I_a^{*} + a\frac{dI_a^{*}}{da}\right]$$

$$= \left[\frac{(2n+1)P}{2nB}\right]^n 2A \frac{a^{n+1}}{(h/2)^{2n+1}} \tag{22}$$

This expression can be substituted into Eq 9 to give J.

References

[1] Garofalo, F., *Fundamentals of Creep and Creep-Rupture in Metals,* Macmillan, New York, 1965.

[2] Penny, R. K., and Marriott, D. L., *Design for Creep,* McGraw-Hill, New York, 1971.

[3] Sullivan, C. P., "A Review of Some Microstructural Aspects of Fracture in Crystalline Materials," *Welding Research Council Bulletin,* No. 122, 1967.

[4] Dyson, B. F. and McLean, D., *Metal Science Journal,* Vol. 6, 1972, pp. 220–223.

[5] Wilson, R. N. and Peel, C. J., RAE Technical Report No. 73149, Royal Aircraft Establishment, Feb. 1974.

[*6*] Greenwood, G. W., *Philosophical Magazine,* Vol. 19, 1969, pp. 423–427.
[*7*] Langdon, T. G., *Philosophical Magazine,* Vol. 22, 1970, pp. 945–948.
[*8*] Heald, P. T. and Williams, J. A., *Philosophical Magazine,* Vol. 24, 1971, pp. 1215–1220.
[*9*] Kachanov, L. M., *Izvestiia Akademii Nauk,* No. 8, 1958, pp. 26–31.
[*10*] Rabatnov, Yn. N., *Creep Problems In Structural Members,* North-Holland, London, 1969.
[*11*] Pilkington, R., Hutchinson, D., and Jones, C. L., *Metal Science Journal,* Vol. 8, 1974, pp. 237–241.
[*12*] Harrison, C. B. and Sandor, G. N., *Engineering Fracture Mechanics,* Vol. 3, 1971, pp. 403–420.
[*13*] Robson, K., "Crack Growth in Two Carbon Steels at 450°C," International Conference on Creep Resistance in Steel, Verein Deutscher Eisenhuttenleute, May 1972.
[*14*] Siverns, M. J. and Price, A. T., *International Journal of Fracture,* Vol. 9, 1973, pp. 199–207.
[*15*] Neate, G. J. and Siverns, M. J., "The Application of Fracture Mechanics to Creep Crack Growth," International Conference on Creep and Fracture in Elevated Temperature Applications, Institution of Mechanical Engineers, Sept. 1973/April 1974.
[*16*] Ellison, E. G. and Walton, D., "Fatigue Creep and Cyclic Creep Crack Propagation in a 1 Cr-Mo-V Steel," Institution of Mechanical Engineers, Sept. 1973/April 1974.
[*17*] Haigh, J. R. and Richards, C. E., "Limits in the Application of Fracture Mechanics to High Temperature Fatigue Crack Propagation in a Turbine Steel," Institution of Mechanical Engineers, Sept. 1973/April 1974.
[*18*] Kenyon, J. L., Webster, G. A., Radon, J. C., and Turner, C. E., "An Investigation of the Application of Fracture Mechanics to Creep Cracking," Institution of Mechanical Engineers, Sept. 1973/April 1974.
[*19*] Kenyon, J. L., "Application of Linear Elastic Fracture Mechanics to Creep Cracking," Ph.D. thesis, University of London, 1975.
[*20*] Webster, G. A., "The Application of Fracture Mechanics to Creep Cracking," Conference on Mechanics and Physics of Fracture, Institute of Physics, Cambridge, England Jan. 1975.
[*21*] Cummings, W. M. and King, R. H., *Proceedings,* Institution of Mechanical Engineers, Vol. 185, 1970/71, pp. 285–299.
[*22*] Turner, C. E. and Webster, G. A., *International Journal of Fracture,* Vol. 10, Sept. 1974.
[*23*] Landes, J. D. and Begley, J. A., "A Fracture Mechanics Approach to Creep Crack Growth," Report 74-1E7-FESGT-P1, Westinghouse Research Laboratory, Dec. 1974.
[*24*] Hutchinson, J. W., *Journal of Mechanics and Physics of Solids,* Vol. 16, 1968, p. 13–31.
[*25*] Rice, J. R. and Rosengren, G. F., *Journal of Mechanics and Physics of Solids,* Vol. 16, 1968, p. 1–12.
[*26*] Hayes, D. J., "Some Applications of Elastic-Plastic Analysis to Fracture Mechanics," Ph.D. thesis, University of London, 1970.
[*27*] Boyle, E. F., "Calculations of Elastic and Plastic Crack Extension Forces," Ph.D. thesis, Queen's University, Belfast, 1972.
[*28*] Sumpter, J. D. G., "Elastic-Plastic Fracture Analysis and Design Using the Finite-Element Method," Ph.D. thesis, University of London, 1973/1974.
[*29*] Sumpter, J. D. G. and Turner, C. E., "Remarks on the Characterising Role of the *J* Contour Integral in Elastic-Plastic Fracture Studies," to be published in *Journal of Mechanical Engineering Science,* April 1976.
[*30*] Begley, J. A. and Landes, J. D. in *Fracture Toughness, ASTM STP 514,* American Society for Testing and Material, 1972, p. 1.
[*31*] Landes, J. D. and Begley, J. A. in *Fracture Toughness, ASTM STP 514,* American Society for Testing and Materials, 1972, p. 24.
[*32*] McClintock, F., *Fracture, An Advanced Treatise,* Vol. 3, H. Leibowitz, Ed., Academic Press, New York, 1971, Chapter 2.
[*33*] Rice, J. R., *Mathematical Analysis in the Mechanics of Fracture,* H. Liebowitz, Ed., Vol. 2, Academic Press, New York, 1968.

E. M. Lenoe[1] *and D. M. Neal*[1]

Assessment of Strength-Probability-Time Relationships in Ceramics

REFERENCE: Lenoe, E. M. and Neal, D. M., "**Assessment of Strength-Probability-Time Relationships in Ceramics,**" *Cracks and Fracture, ASTM STP 601,* American Society for Testing and Materials, 1976, pp. 63–85.

ABSTRACT: In the past few years a number of test procedures have evolved as a result of attempts to observe stable crack growth in ceramics under constant stress conditions. The experimental procedures have included double cantilever, double torsion, in-plane moment, and controlled flaws in beam bending tests. These procedures are briefly reviewed. Available slow crack growth data for hot pressed silicon nitride, which has been presented in the literature, is utilized to estimate survival times for various stress levels. The computations are completed in several ways: (*a*) use of strength data obtained at various loading rates; (*b*) deterministic integration of the equations; and (*c*) in a Monte Carlo sense, wherein the controlling parameters are assumed to possess realistic variability. The end product of each set of computations is a design stress-survival time relationship, and the purpose of this paper is to compare these life estimates and comment on the adequacy of each method.

Additional motivations were to assess the status of properties information, and to establish, if possible, reasonable bounds on the accuracy of these probability-based life estimates. Examination of the data and application of the two probability techniques led to the conclusion that the procedures are appropriate for order of magnitude estimates, which are generally but not necessarily conservative. It was evident that additional data, improved experimental procedures, and further analysis of specimens were required.

Since the exponents of the crack velocity-stress intensity functions in a power law form are large and typically cover a wide range for ceramics of interest, that is, $4 < m < 50$, difficulties were encountered in use of numerical simulation procedures. With $m \leq 10$, for example, the resulting life functions were widely distributed. Furthermore, the mean value estimates were highly unstable and for large m did not appear amenable to economical digital simulation. Accordingly, a number of different trial functions, including logarithmic, exponential, and polynomial approximations were employed to represent subcritical crack behavior. The final function selected was of the form $F = A_0\exp(mK_1)$, where $F = K_1/V$.

This form seemed appropriate since log F versus K_I resulted in reasonable requirements on number of simulations. The m values were appreciably lower than the power law representation. Application of the Monte Carlo method to lifetime estimates of ceramics provided an error tolerance for K_1 and allowed calculation of the probability density function.

---

[1] Chief mechanic of materials and research mathematician, respectively, Army Materials and Mechanics Research Center, Watertown, Mass. 02172.

KEY WORDS: fractures (materials), ceramics, silicon nitrides, fracture properties life (durability) probability theory, Monte Carlo method, crack propagation

At relatively low temperatures the behavior of ceramics is predominantly a strength-controlled phenomena, and the design of ceramic structures is most appropriately based on statistical considerations of strength. However, at elevated temperatures certain ceramics can fail under stresses much lower than those which would ordinarily cause immediate fracture. This condition occurs when the stress/environment combination can cause slow crack growth from existing flaws. In principle, under such circumstances, knowledge of crack velocity and acceleration under a given loading should permit component lifetime estimates to be made.

Several techniques have been developed to estimate lifetimes of ceramic components under either constant or slowly varying stresses. One deterministic method relies on direct integration of crack velocity versus stress intensity relationships. An alternate method of estimating slow crack growth velocity-stress intensity relationships utilizes strength measurements obtained at varying loading rates. Finally, in an effort to provide a probability basis for ceramic structural life calculations, the Weibull strength distribution has been combined with crack velocity-stress intensity functions.

Slow crack growth velocity measurements can be made in a variety of ways, the most popular being the so-called double torsion, edge-notched plate [*1–3*].[2] Constant in-plane rather than out-of-the-plane bending moments can also be applied [*4*]. More recently, flawed beams [*5*], possessing diamond-pyramid-induced defects, have been used to determine the crack velocity-stress intensity function. Each of these test methods yields slightly different parameters, with obvious influence on life estimates. Crack velocity behavior in the majority of structural ceramics can be represented by a power function. Due to the typically large exponent m of this power rule, failure time estimates are extremely sensitive to variability of the input parameters.

Therefore, it is appropriate to consider the experimental procedures and analytical techniques in some detail. This work was prompted in part by Wilkins' [*6*] objections to current life estimating procedures which did not account for variability in materials properties and which did not provide a firm theoretical basis for the use of a power rule.

Obviously an important consideration in life estimates is the shape of the stress intensity, K_I, versus slow crack growth velocity, V. The nature of such stress-corrosion cracking has been examined in detail for various glasses and certain ceramics. Crack growth in silicon nitride materials has not received as much attention. This is partly due to rapid strides in

---

[2] The italic numbers in brackets refer to the list of references appended to this paper.

fabrication technology. During the past four years, rather extensive studies have been completed to produce improved hot pressed, as well as slip cast and injection molded reaction sintered silicon nitrides. These developments have involved use of numerous additives to enhance pressing, molding, and slip casting. Presently, only the relative influence of such processing aids and impurities is known. Their precise role in controlling oxidation, creep rupture and slow crack growth response in severe environments, associated with high-temperature gas turbine operation, remains to be more thoroughly explored. Indeed, elevated temperature slow crack growth observations have not yet been completed on reaction sintered varieties and only limited data is currently available for hot pressed varieties.

Thus as preparation for analytical treatment of data which will be obtained on structural ceramics in the near future, this paper attempts to systematically explore computationally efficient numerical simulation schemes for a number of different slow crack growth formulations.

Experimental Procedures for Slow Crack Growth

The configurations shown in the schematic of Fig. 1 have been used to observe slow crack growth in ceramics. It is worthwhile to consider these methods in turn and outline the basis of data interpretation for each procedure.

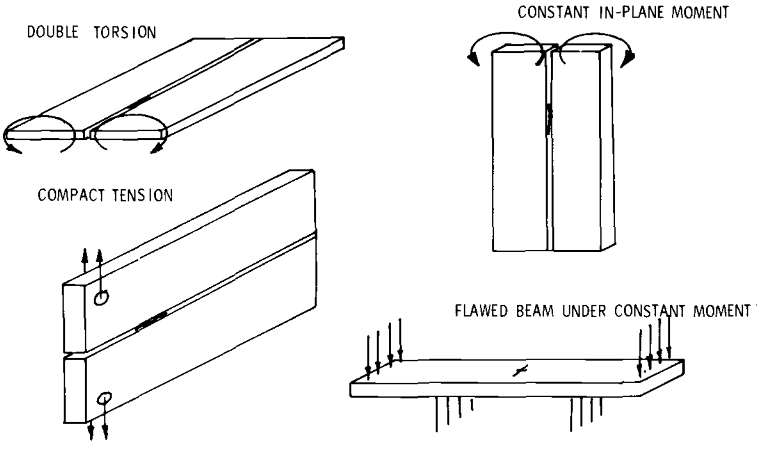

FIG. 1—*Schematic of typical slow crack growth specimens.*

Double Torsion

The double torsion (DT) specimen has been widely reported [*3,7,8*] as suitable for subcritical crack growth. However, the configuration has thus far been subjected only to approximate analysis [3,9] wherein the specimen is treated as two elastic bars. The simple analysis leads to the following nominal form of stress intensity

$$K = PW_m \sqrt{3(1+\upsilon)/(Wt^3t_n)} \qquad (1)$$

The double torsion specimen was subjected to experimental compliance calibration at room temperature for 4340 steel. The experimental results compared within 9 percent of the predictions of Eq 1. Williams and Evans [3], however, point out that crack front curvature can lead to significant error in determination of crack velocities if only surface velocities are used. It appears that additional study is required of such curvature effects. Furthermore, a more accurate estimate of stress intensity is required.

It is also worth noting that compressive stresses develop at the leading edge of the crack and these stresses are larger for thicker specimens.

Constant In-Plane Moment

Rather than apply an edge twisting moment, the edge-notched plate has been also subjected to in-plane moments. Freiman et al [4] have provided an approximate analysis based on a beam-on elastic foundation model, as well as experimental verification of the strain energy release rate expressions. As in the DT specimen, the results were within 10 percent of the analytical model at ambient temperatures. Crack velocity versus stress intensity data were obtained and compared to previous studies on soda-lime glass using the so-called compact tension [10] and double torsion [7] configurations. While the slopes of the resulting relationships are all similar, the curve for DT specimens appears shifted very slightly to the right, whereas the constant moment (CM) results are slightly to the left of those obtained with compact tension test procedures.

Compact Tension

This widely used configuration has been subjected to extensive analyses [11,12]. Theory of elasticity solutions, including corrections for finite geometries and various loading modes, are readily available [13]. Unfortunately, Si_3N_4 does not exhibit slow crack growth except at high temperatures (~ 1800 to 1900°F). This compounds the difficulties of conducting the CT experiment, and at the time of this writing no slow crack growth data have been reported in the open literature for this configuration.

Flawed Beam Under Constant Moment

The cracked beam specimen has been subjected to finite element and other approximate analysis, and estimates can be made for stress intensity factors in a beam under constant moment and containing a semi-elliptical surface flaw [*14–16*]. The difficulty of developing a natural, sharp crack in ceramics has lead to increasing popularity of an artificially induced flaw [*5*]. A diamond indenter under prescribed load (Vickers or Knoop harness tester or both) has been found suitable to introduce small and sharp cracks. Subsequent annealing of the specimen apparently relieves residual stresses so that fracture toughness values are obtained which are identical to those measured using the more acceptable CT specimens [*5*], at least at room temperature.

It is interesting to note that according to rudimentary analysis the stress intensity varies with position along the crack front. Thus if slow crack growth occurs under constant moment, fractography of the failed surfaces can yield a number of crack velocity-stress intensity values from a single specimen.

It is obvious that the experimental procedures, in general, rely on approximate analysis. Undoubtedly, data interpretation would be improved with a more accurate theoretical basis. This is particularly true of the double torsion and flawed beam configurations. It is also worth mentioning that in Si_3N_4 subcritical crack growth occurs at elevated temperatures where the material has a nonlinear stress-strain curve. The ceramic is capable of increased elongation at its highest usage temperature, which suggests the necessity to account for such nonlinearities.

Currently available slow crack growth data for silicon nitride has been obtained with either double torsion [*17,18*] or flawed beam configuration [*19*]. Figure 2 compares the crack velocity observations for the different procedures. A wide variation in behavior is evident. However, it should be noted that the results are dependent on material purity, as well as nominal stress intensity level. Differences in the observed crack velocity versus nominal stress intensity are no doubt exaggerated by deficiencies in theoretical analysis of the different test configuration. This may account for the considerable shift exhibited by the data. With the exception of indicated high purity data, the other results of Fig. 2 were obtained for the HS-130 version of hot-pressed Si_3N_4. Variations of impurity content between billets may also partially account for differences in slope of the data.

Elementary Life Estimating Procedure

Charles [*20,21*] has proposed and experimentally verified analytical fracture mechanics models to describe static fatigue and dynamic strength behavior of glass. The analysis uses a proposed power law form of crack velocity versus stress intensity relation using the Griffith criteria. Experimental verification of the proposed relationship relied on several thousand

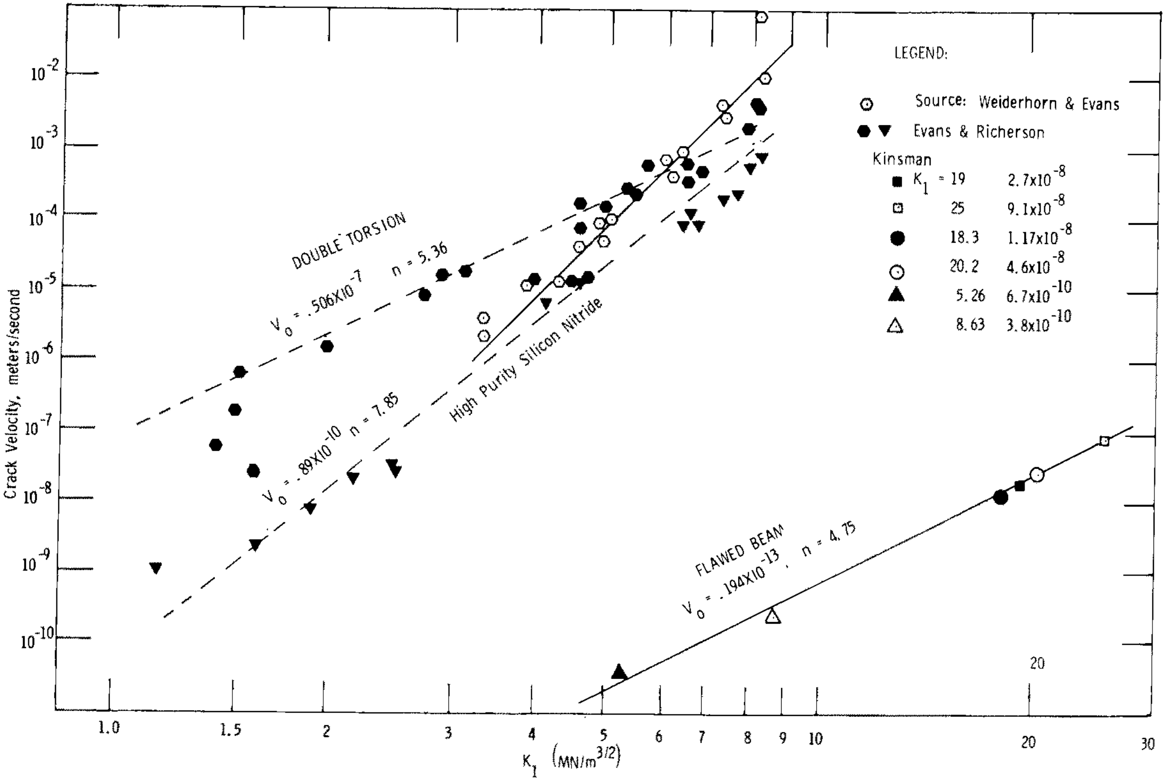

FIG. 2—*Summary of available slow crack growth data for hot-pressed silicon nitride.*

experiments performed on soda-lime glass rods. It is worthwhile to note that the specimens were subjected to severe surface grinding, which ensured sufficient numbers of surface flaws such that failure usually occurred at these surface flaws.

In his preliminary discussion, Charles discussed restrictions as to the measure of dispersion of the critical initial flaws on similar specimens [*21*]. Such restrictions would tend to select similar distributions of critical flaw sizes for the different groups of specimens. It is also noteworthy that the surface grinding preparation no doubt tended to emphasize fracture related to surface integrity rather than inherent material flaws.

Since those early studies, his concepts have been applied to ceramic materials by a number of investigators to estimate slow crack growth parameters [*22–26*].

Using the Griffith equation in the form

$$K_{\text{Ic}} = Y \sigma_f \sqrt{C_0} \tag{2}$$

and assuming a crack velocity versus stress intensity relation

$$\partial C/\partial t = V \; A_0 \; K_I^m \tag{3}$$

results in the simple expression for the ratio of strengths measured at different strain rates, $\dot{\varepsilon}_1$, $\dot{\varepsilon}_2$, and for equivalent failure probabilities

$$(\sigma_1/\sigma_2)^{m+1} = \dot{\varepsilon}_1/\dot{\varepsilon}_2 \tag{4}$$

Therefore, an estimate of the exponent, m, is available.

Alternately, under constant stress, the time to failure τ can be estimated by use of

$$\tau = \int_{C_i}^{C_{\text{Ic}}} dC/V, \tag{5}$$

where it is assumed that times for $C < C_i$ are negligible.

Since
$$dC = [2K_{\text{I}}/(\sigma Y)^2] \; dK_{\text{I}},$$
$$\tau = 2/(\sigma Y)^2 \int_{K_{\text{I}i}}^{K_{\text{Ic}}} (K_{\text{I}}/V) \; dK_{\text{I}} \tag{6}$$

which for a simple power form of crack velocity versus stress intensity form becomes

$$\tau = 2K_{\text{I}i}{}^{2-m}/(\sigma Y)^2 \; \alpha(m-2) \tag{7}$$

For a given batch of N specimens with initial flaw size C_j

$$\tau = \frac{2Y^{2-m} \; \sigma^{2-m} \; C_j^{(2-m)/2}}{(\sigma Y)^2 \alpha(m-2)} = \frac{BC^{(2-m)/2}}{\sigma^m} \tag{8}$$

Then for specimens with the same initial flaw size and the same probability of failure

$$\tau\sigma^{m} = \alpha = \text{constant} = BC_j^{(2 - m)/2} \tag{9}$$

For an individual specimen stressed at σ_1 and failing in τ_1, we now have a relationship for another specimen failing at stress σ_0 in a reference time τ_0. This permits construction of a nomograph, where a family of parallel lines are equi-spaced for equal logarithmic increases in failure time [*26*]. According to this simple theory, creep rupture data can be related to instantaneous or dynamic failures by use of Eqs 4 and 9.

High temperature tension and flexure tests have been performed at various strain rates on hot-pressed silicon nitride [*27*] and the results are presented in Fig. 3. Note in Fig. 3*a* sufficient data were not obtained to construct a probability distribution. The indicated curves were arbitrarily taken to have the same distribution function as the intermediate strain rate (0.001 in./in./min) tests. Equation 4 was applied to these data and the results are presented in Table 1.

Alternate Life Estimating Procedures

We have seen that various test methods have evolved whereby the crack velocity, V, in a specimen can be recorded simply in terms of nominal stress intensity K_I. Crack growth in terms of the K-V relations can be theoretically related to an initial flaw size C. For example, application of a stress, σ, produces a stress intensity factor $K_I = Y\,(C)^{1/2}$ corresponding to a crack velocity, V. If C increases, the corresponding K_I will increase. Therefore, when K_I reaches a particular critical value K_{Ic}, or some lesser value depending on environmental conditions, catastrophic failure occurs.

For constant σ in a delayed fracture test, the time to failure is given by Eq 5. Using a grossly simplifying assumption of a known average initial flaw size leads to Eq 6, where limits of integration are determined from the K-V diagram.

It is evident that a fairly large uncertainty exists as to proper choice of the K-V data. However, let us assume that a particular set of data has been

TABLE 1—*Summary of exponent and spacing ratio estimates.*

Data	Average Exponent, n	Logarithmic Spacing Ratio
2300°F flexure	7.29	1.329
2500°F flexure	4.1005	1.6034
2300°F tension (all data)	9.43	1.31
2300°F tension (Westinghouse data)	11.2125	1.20

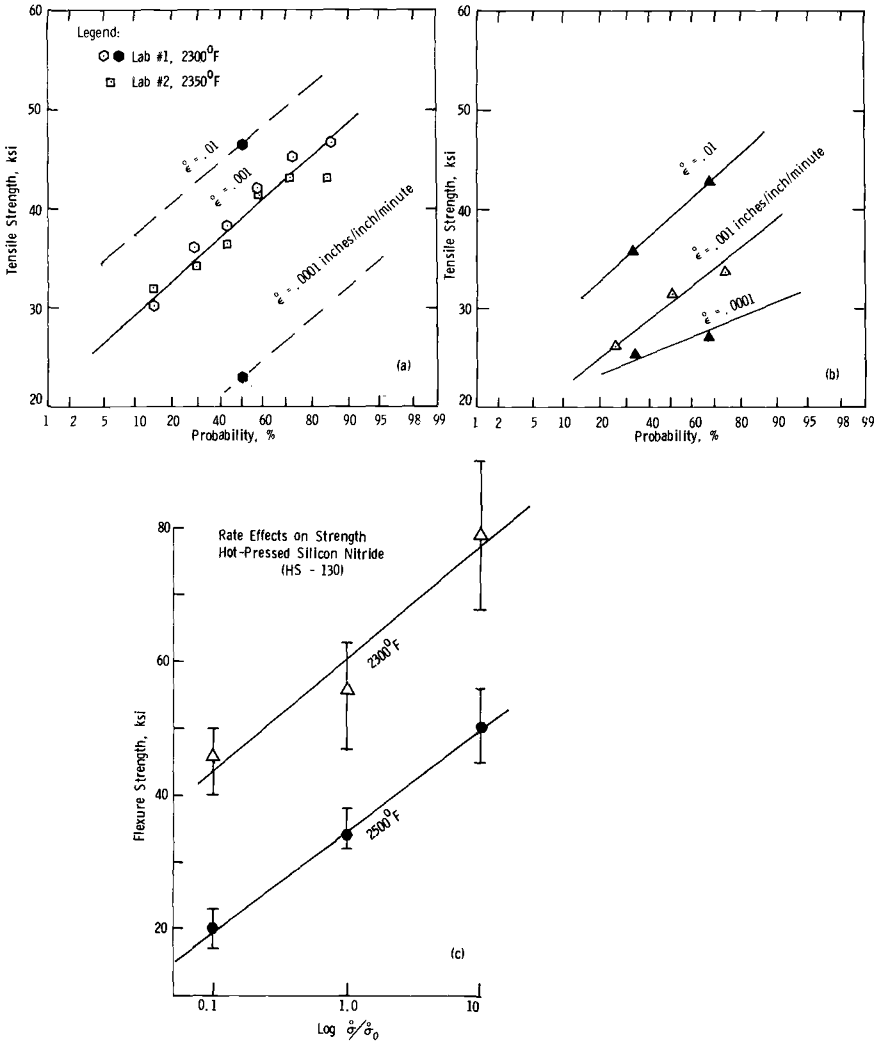

FIG. 3—*Strain rate effects on tensile strength of hot-pressed silicon nitride at 2300 and 2350°F, data from three laboratories.*

chosen as acceptable. Then several decisions must be made in order to proceed even with the deterministic and direct integration of Eq 5. The first question relates to analytical representation of the stress intensity-crack velocity function, whereas the second concern is the range in values of the limits of integration.

Let us apply the commonly used functional relationship for V, the so-called "power law", (Eq 3), where A_0 and m are constants determined from a least-squares fit of data from typical K-V diagrams (Fig. 2). Making appropriate substitutions, τ may be defined as

$$\tau = (2/(m - 2)\,(\sigma Y)^2 A_0)\left[K_{\mathrm{I}}^{\prime\prime(2-m)} - K_{\mathrm{I}}^{\prime(2-m)}\right] \tag{10}$$

An exponential form $V = V_0 e^{mK}{}_{\mathrm{I}}$ has also been used in a similar manner.

Alternatively, if time to failure is defined as

$$\tau = 2/(\sigma Y)^2 \int_{K_{\mathrm{I}}'}^{K_{\mathrm{I}}''} F\, dK_{\mathrm{I}} \tag{11}$$

where $F = K_{\mathrm{I}}/V$, then a plot of log F versus K_{I} reveals a linear relationship, see Fig. 4.

Taking advantage of this fact, one can relate $F(K_{\mathrm{I}})$ as

$$\log F = A_1 K_{\mathrm{I}} + B_1$$

or

$$F = Ae^{BK} \tag{12}$$

Now a least-squares fit of data from F versus K_{I} data determines A and B and can be written as

$$\tau = \frac{2}{(\sigma Y)^2}\int_{K'_{\mathrm{I}}}^{K''_{\mathrm{I}}} Ae^{BK}{}_{\mathrm{I}}\, dK_{\mathrm{I}}$$

or

$$\tau = \frac{2}{(\sigma Y)^2}\left[\frac{A}{B}\left(e^{BK''_{\mathrm{I}}} - e^{BK'}{}_{\mathrm{I}}\right)\right] \tag{13}$$

This form for F is used in analyzing crack growth data presented in this paper.

Using $F(K_{\mathrm{I}})$ instead of power law, V, reduces values of the exponent in the fractional form, K_{I}/V. This is an important consideration because large exponent values ($m \geq 10$) result in an unstable τ value when a simulation scheme is applied.

Available silicon nitride data and the limited slow crack growth results for glass examined in this study have tended to follow this linear relation, whereas with separate representations for crack velocity and stress intensity as contrasted to use of the form $F = K_{\mathrm{I}}/V$ tends to depart from this apparent linear response, see Fig. 5. Therefore it seems more advantageous to fit $F(K_{\mathrm{I}})$ data directly instead of fitting $V(K_{\mathrm{I}})$ data and then defining integrand as K_{I}/V.

In fitting the data, it is not necessary to obtain a fit over the entire range of K_{I}. For the data examined, it was usually possible to consider only three orders of magnitude change in V. That is, if initially $V = 1 \times 10^{-10}$,

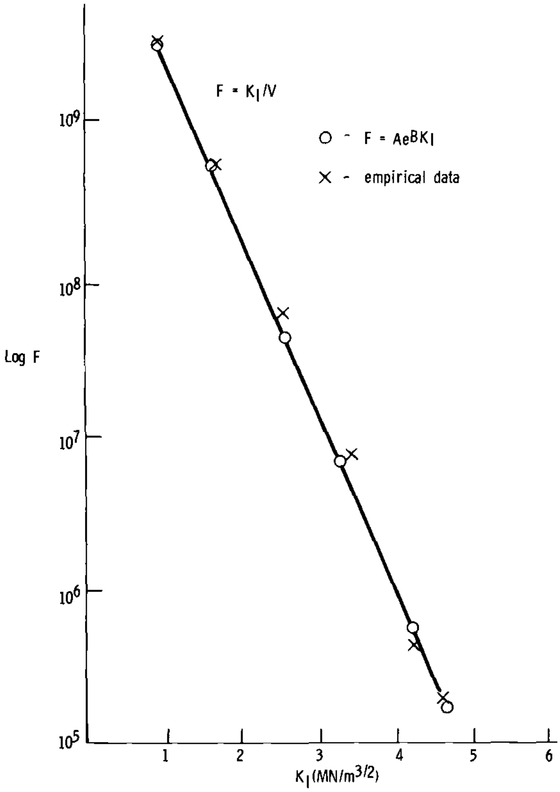

FIG. 4—*Comparison of exponential fit for combined integrand—high purity data for silicon nitride.*

the range of K_I is selected such that V is in the vicinity of 1×10^{-7}. This is possible because the contributions to lifetime τ are negligible beyond the determined range, see Table 2. It may be noted that for each order of magnitude change a significant digit is obtained for τ. This minimizes the need for a large number of data points in the experimentation, at least for the lifetime estimate.

An alternate method, using a polynomial representation in place of the other functional forms, was examined to obtain more flexibility in the curve-fitting procedure. A three-point Lagrangian interpolation scheme proved to be successful. This interpolation process combined with a piecewise integration scheme provides an acceptable method of obtaining τ when the standard functional representations are not acceptable. This method is also adaptable for use with the Monte Carlo method as shown in Fig. 6.

The method involves initially selecting a polynomial form

$$F = C_1 K_I^2 + C_2 K_I + C_3 \tag{14}$$

and fitting three points at a time to F versus K_I data using the Lagrangian process.

Secondly, the time segment τ_2 for the first two points is defined as

$$\tau_2 = \int_{K_{I_1}}^{K_{I_2}} (C_1 K_I^2 + C_2 K_I + C_3)\, dK_I \tag{15}$$

where K_{I_1}, K_{I_2} = first two data value for K_I. The process is repeated N times until desirable convergence for failure time estimate is observed. In general

$$\tau_{(i+1)} = \int_{K_{I_i}}^{K_{I\,(i+1)}} (C_1 K_I^2 + C_2 K_I + C_3)\, dK_I \tag{16}$$

and

$$\tau \approx \sum_{i=1}^{N} \tau_{(i+1)}$$

where C_i's are determined from curve-fitting procedures for each segment. These various formulations were treated both in deterministic ways as well as by use of digital simulation techniques, which are described next.

Monte Carlo Method

The Monte Carlo Method is a desirable means of determining time to failure for slow crack growth since the controlling parameters, for exam-

TABLE 2—*Flaw beam data (piecewise integration).*

	$\tau_{i+1} = \int_{K_{I_i}}^{K_{I\,i+1}} (C_1 K_I^2 + C_2 K_I + C_3) dK_I$	σ = 10 ksi	
i	$K_{I_{i+1}}$	K_{I_i}	τ_{i+1}, days
1	8.63	5.26	200
2	18.3	8.63	114
3	20.2	18.30	3
		$\tau \approx \sum_{i+1}^{3} \tau_{i+1} =$	317

NOTE—τ^* indicates determination over entire range of data using $F = Ae^{BK_I} = 315$.

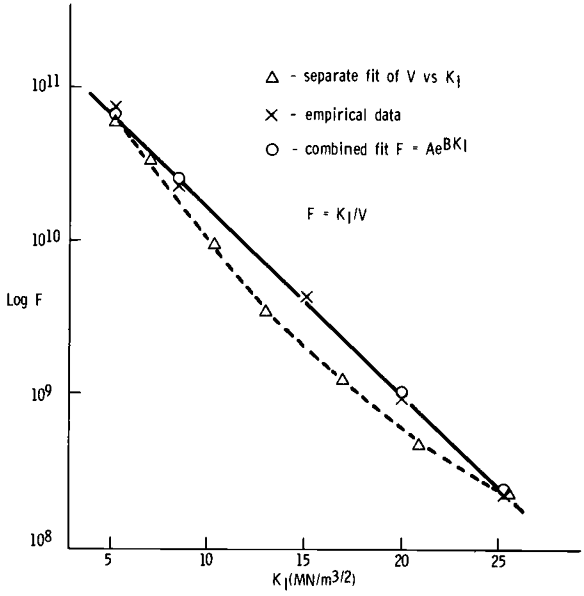

FIG. 5—*Comparison of integrand fitting techniques.*

ple, K_I, V, Y, and σ are inherently variable. The relative complexity of the functional relationship, in addition to the expense of extensive experimentation, further suggest the need for the Monte Carlo method. The method avoids restrictions on the exact specification of the statistical distributions of the variables since simple approximating functions can serve well in the scheme. In general, this prevents formulation of incorrect frequency distributions for the quantities of interest.

In this paper determination of lifetime estimates, τ, by the Monte Carlo method involves representing each of the independent variables by a set of normally distributed random numbers. Use of normal distributions is not a requirement. However, due to resulting simplifications, normal distributions were used in this initial phase of our work. Equation 11 is the pertinent equation.

A value is specified for each variable in the equation by choosing a number at random from its corresponding distribution. The resulting value for τ is determined for each set of randomly selected variables. The computation is repeated, and a probability distribution is obtained for the function of interest.

In the present computations normally distributed random numbers were generated by a Univac 1108 subroutine. The procedure is simply one of generating uniform random numbers and solving for X in the relation

$$\int_{-\infty}^{X} f_i \, dX = R \qquad (17)$$

where

R = uniform random number, and

f_i = normal frequency distribution.

As noted previously, if the probability distributions of the controlling variables are known from some experimental results or from an analytical basis, then the more suitable probability distribution functions f_i may be used.

Results and Discussion

The Monte Carlo simulation scheme proved to be an adequate method for analyzing slow crack growth data to obtain acceptable time to failure results. This is particularly true because of the experimental errors associated with V-K_I determinations. The question of a theoretical basis for the power law or other approximating function to represent data in the lifetime determination remains to be explored for the nitride ceramics.

With regard to application of the Monte Carlo method, we observed that selection of the appropriate number of simulations must rely on considering third and fourth moments of the resulting statistical distribution. This is due to the fact that mean values and standard deviations were fairly constant after a relatively few trials, whereas the third and fourth moments continued to exhibit instability until considerably larger numbers of simulations had been completed. The number of cells in histograms exhibited in Figs. 7 and 8 were determined from Sturgis' equation $NG = 1 + 3.3 \log_{10} (N)$, where N is number of trials and NG number of cells.

In Fig. 5 the effect of using separate fits for $V = V_0 K_I^m$ and then applying them to the integrand $F = K_I/V$ is quite obvious. This weighting of the junction $F = K_I/V$ distorts representation of the integrand in lifetime estimate integral. For this case there is a highly conservative estimate of time. In determining a separate functional relationship for V, one is essentially considering the integrand $F = K_I V$ in a manner that assumes K_I a constant. Weighting of F by separate fitting of V is not necessary if one utilizes the F versus K_I curve shown in Fig. 5. It was quite fortunate that for all data analyzed, log F versus K_I results in a linear plot. This allows for the simple representation $F = A_0 e^{MK}$ to be used in the analysis.

As discussed previously, the Monte Carlo method, using piece-wise integration, was applied to the flawed beam data of Fig. 2 and the results are shown in Table 2. These computations suggest that advantage can be taken of the rapid order of magnitude changes V with respect to K_I. For instance, the third step in the integration contributes little to overall life

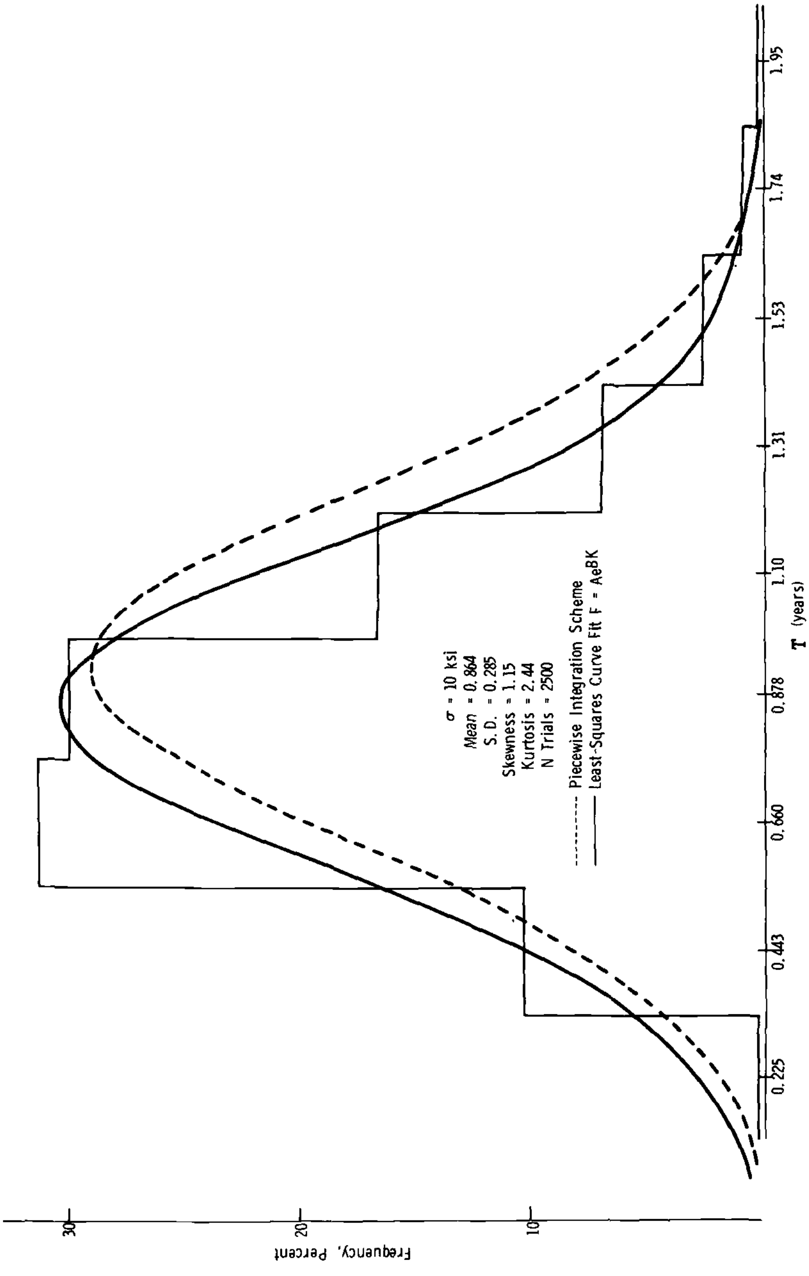

FIG. 6—*Comparison of polynomial and piecewise integration for life estimates, based on flawed beam data.*

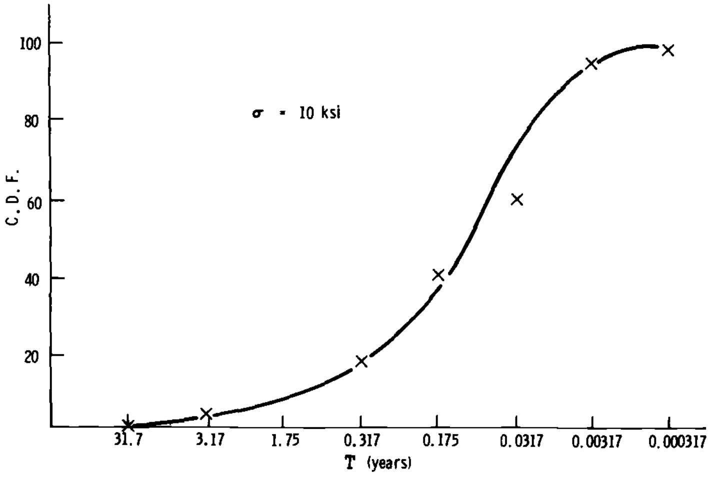

FIG. 7—*Cumulative distribution function for life estimate via high strain rate tests, 10 ksi design stress, HS-130 silicon nitride at 2300°F.*

and the slow crack experiments could have been terminated at an early stage.

In general, one should not attempt to obtain data beyond that necessary to calculate τ accurately to three significant digits. This will also eliminate the need for curve fitting additional data which in some instances results in increasing the exponent value m.

A number of investigators have espoused the use of proof testing in conjunction with slow crack growth concepts [*28–30*]. Unfortunately, the conventional application of such proof test concepts generally involves backward extrapolation of the crack velocity data into time regimes which are exceedingly difficult to define experimentally. In addition, the data have often been analyzed with a power law form, which is a least-squares fit over the entire range of observation. Such procedures perhaps overweigh the trends exhibited by the larger values of K_I, which in reality contribute little to overall life. A more reasonable procedure might be to consider a shorter range of K_I, closer to the region of extrapolation. In any case, it is well worth noting the potential uncertainty introduced by use of proof testing. Furthermore, the estimating method is extremely sensitive to values determined by such extrapolation, and care must be taken in selecting the proof stress ratio. Examination of Wilkins' data [*6*] is indicative of potential disastrous effects of conventional proof test concepts. For instance, the remark that differences for b of 7 or 8 percent in $V = V_0K_I^b$, produces a four- to five-fold difference in $\tau_{\min}$ is not correct. If one evaluates $\tau_{\min}$ at initial K_I value rather than extrapolates, the maximum difference in $\tau_{\min}$ is single-fold. This oversight seems to be fairly common among other researchers in ceramics.

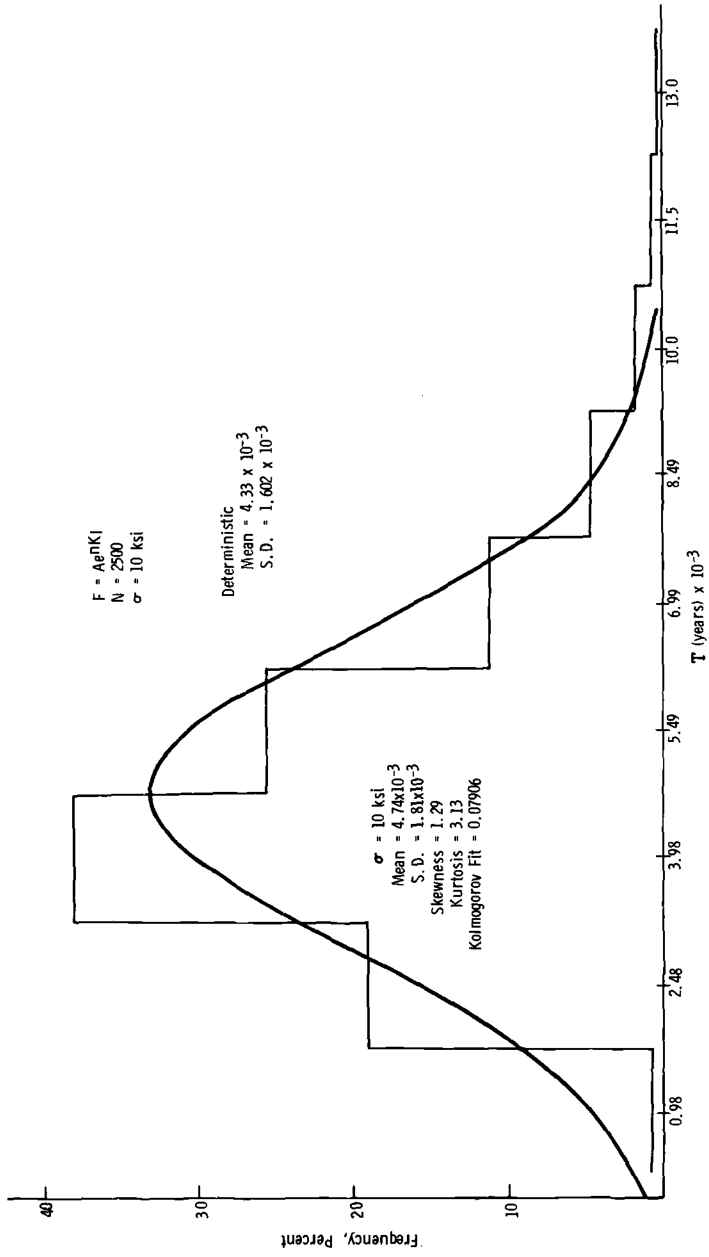

FIG. 8—*Distribution of life estimates for 10 ksi design stress. Ten percent variance in controlling parameters, double torsion test, high purity silicon nitride at 2500°F.*

Summary and Conclusions

Review of the literature has shown that further improvements are desirable in theoretical analysis of subcritical crack growth specimens commonly used for ceramic materials. Available data for hot-pressed silicon nitride were relatively scarce, and the results suggested considerable variation of observed slow crack growth data. Scatter in the data is partly inherent, but is probably also related to variations of controlling impurity contents. It appears that crack velocity observations differed depending on whether they were made on a marco versus a microscale.

A key question relates to the range of integration of the slow crack growth equation. Ordinary concepts utilize the notion of an average critical flaw size as the starting point. In this context it is interesting to refer to Fig. 9, which illustrates typical critical flaws and their distribution as observed by fractography of mechanical properties specimens [*31,32*]. It is also worth observing that in approximately 50 percent of the specimens examined, critical flaws could not be identified via fracture mirror techniques, suggesting the existence of rather small defects. In principle [*33*], the slow crack growth equation could be integrated where distribution of initial flaws and their subsequent growth would be take into account. In reality, the computations are exceedingly difficult, and the matter of whether the crack velocity versus stress intensity relationship is influenced by the area of the crack and the nature of the initial flaw distribution would probably be more easily investigated experimentally.

With reference to the different procedures for estimating life, consider the results shown in Fig. 7 which presents the cumulative distribution function based on tension tests conducted at different strain rates. Figures 8 and 10 illustrate results of the Monte Carlo computation for the different slow crack growth data. The range in mean value of survival time is shown by comparing Fig. 7 near the 40 percent probability level (~ 0.175 year) with Fig. 10*a* (~0.864 year) and Fig. 8 (~0.0047 year). These life estimates exhibit the uncertainties introduced via test procedures, analytical technique, and materials impurity. Figure 10 also indicates the influence of design stress (2, 10, and 20 ksi) for 10 percent variance in all controlling parameters.

With regard to choice of the various life estimating techniques, we see that the strength-probability-time method compared with the flawed beam data provides a conservative estimate, ignoring the temperature difference. Computations for the commercial Norton HS-130 material, based on the double torsion test (see Fig. 2), provide an even shorter life estimate. It would appear reasonable to use the high strain rate data, provided that the nominal surface finish and volume of the specimen is similar to that of the structural component of interest. The choice of double torsion versus flawed beam data must be resolved by further study. In conclusion, it is evident that an improved data base is required and

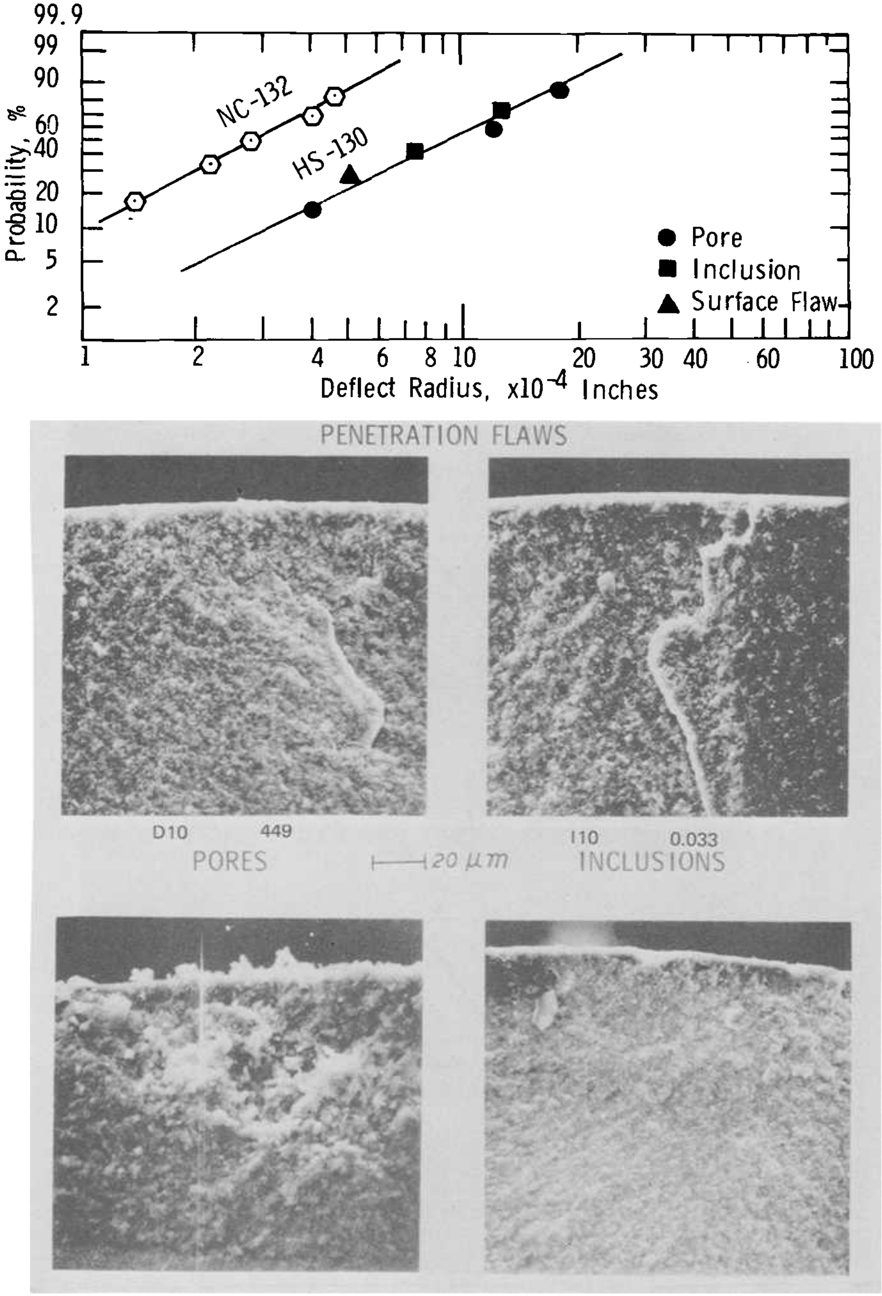

FIG. 9—*Typical flaws and flaw distribution in hot-pressed silicon nitride.*

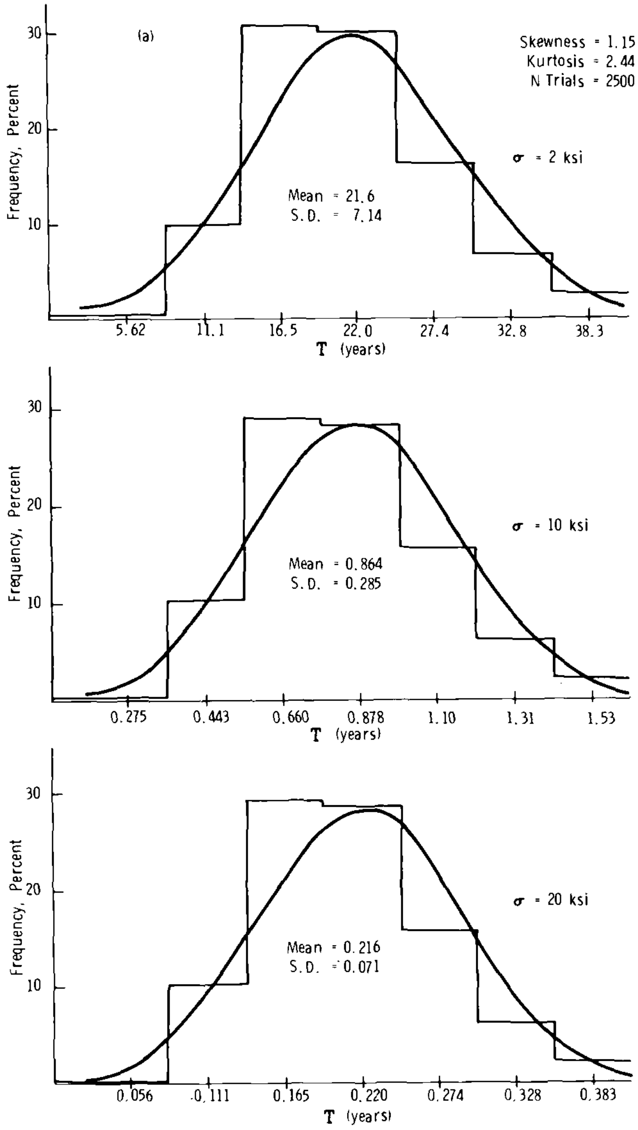

FIG. 10—*Life estimates based on* (a) *flawed beam and* (b) *double torsion test, commercial and high purity silicon nitride, 10 percent variance in parameters at 2500°F.*

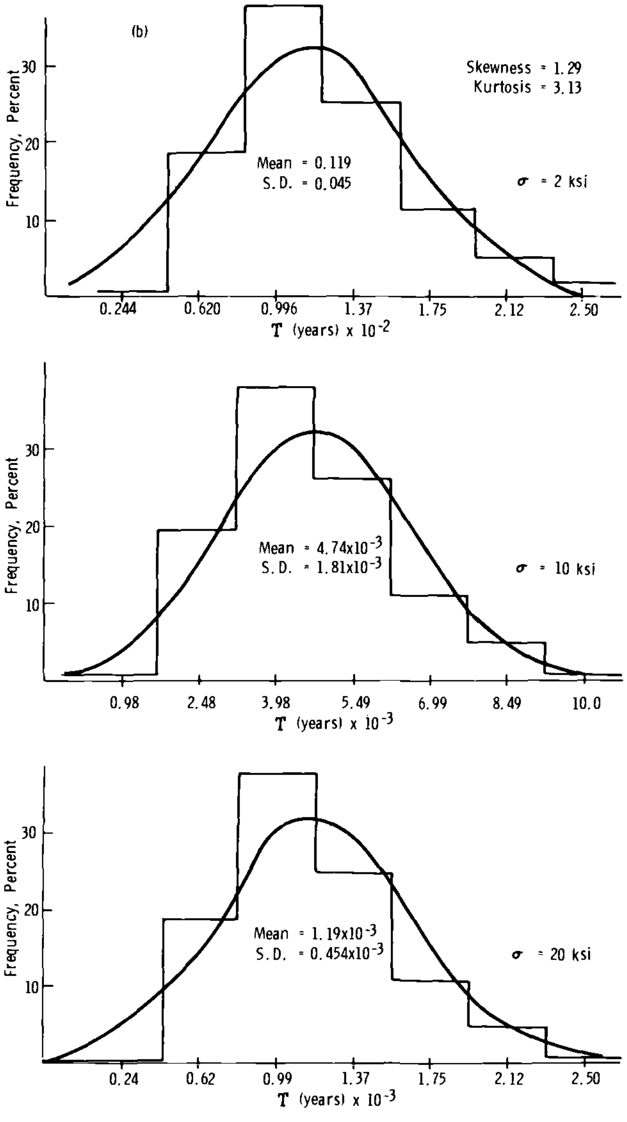

FIG. 10—*Continued.*

further refinements of analysis will be necessary to substantiate or refute the opinions presented in this preliminary assessment.

Acknowledgments

The support of the Advanced Research Projects Agency (APRA) is gratefully acknowledged and the authors wish especially to thank E. C. Van Reuth of ARPA for his support of this study. Further acknowledgments must be extended to C. C. Baird for numerous calculations and preparation of the illustrations, and also to Agnes Travers for typing and editing the manuscript.

References

[*1*] Kies, J. A. and Clark, B. J. in *Fracture—1969,* P. L. Pratt, Ed., Chapman and Hall, London, 1969, pp. 483–491.
[*2*] Beachem, C. D., Kies, J. A., and Brown, B. F., *Materials Research and Standards,* Vol. 11, No. 4, April 1971, p. 30.
[*3*] Williams, D. P. and Evans, A. G., *Journal of Testing and Evaluation,* Vol. 1, No. 4, July 1973, pp. 264–270.
[*4*] Freiman, S. W., Mulville, D. R., and Mast, P. W., *Journal of Materials Science,* Vol. 8, No. 11, Nov. 1973, pp. 1527–1533.
[*5*] Petrovic, J. J., Jacobson, L. A., Talty, P. K., and Vasudevan, A. K., *Journal of the American Ceramic Society,* Vol. 58, No. 5–6, May–June 1975.
[*6*] Wilkins, B. J. S. and Simpson, I. A., *Journal of the American Ceramic Society,* Vol. 57, No. 11, Nov. 1974, p. 505.
[*7*] Evans, A. G., *Journal of Materials Science,* Vol. 7, No. 10, Oct. 1972, pp. 1137–1146.
[*8*] Evans, A. G., *International Journal of Fracture,* Vol. 10, No. 2, June 1974, pp. 251–259.
[*9*] Timoshenko, S. and Goodier, J. N., *Theory of Elasticity,* 2d ed., McGraw-Hill, New York 1951.
[*10*] Wiederhorn, S. M., *Journal of the American Ceramic Society,* Vol. 50, No. 8, Aug. 1967, pp. 407–414.
[*11*] Wiederhorn, S. M., Shorb, A. M., and Moses, R. L., *Journal of Applied Physics,* Vol. 39, No. 3, 15 Feb. 1968, pp. 1569–1573.
[*12*] Gutshall, P. L. and Gross, G. E., *Journal of the American Ceramic Society,* Vol. 51, No. 10, Oct. 1968, p. 602.
[*13*] Sih, G. S., *Handbook of Stress Intensity Factors,* Institute of Fracture and Solid Mechanics, Bethlehem, Pa., 1973.
[*14*] Mars, G. R. and Smith, C. W. in *Stress Analysis and Growth of Cracks, ASTM STP 513,* American Society for Testing and Materials, 1972, pp. 22–36.
[*15*] Grandt, A. F., Jr. and Sinclair, J. M. in *Stress Analysis and Growth of Cracks, ASTM STP 513,* American Society for Testing and Materials, 1972, pp. 37–58.
[*16*] Shah, R. C. and Kobayashi, A. S. in *Stress Analysis and Growth of Cracks, ASTM STP 513,* American Society for Testing and Materials, 1972, pp. 3–21.
[*17*] Evans, A. G., Russell, L. R., and Richerson, D. W., *Metallurgical Transactions A,* Vol. 6A, No. 4, April 1975, pp. 707–716.
[*18*] Evans, A. G. in *Ceramics for High Performance Applications,* J. J. Burke, A. E. Gorum, and R. N. Katz, Eds., Brook Hill Publishing Company, Chestnut Hill, Mass., 1975, pp. 373–396.
[*19*] Kinsman, K. R., "The Varied Role of Plasticity in the Fracture of Inductile Ceramics," Scientific Research Staff Publication, Ford Motor Company, Dearborn, Mich., Oct. 1974.

[20] Charles, R. J., *Journal of Applied Physics,* Vol. 29, No. 11, Nov. 1958, pp. 1549–1553, 1554–1560.

[21] Charles, R. J., *Journal of Applied Physics,* Vol. 29, No. 12, Dec. 1958, pp. 1657–1667.

[22] Wiederhorn, S. M., *Journal of the American Ceramic Society,* Vol. 52, No. 2, Feb. 1969, pp. 99–105.

[23] Evans, A. G. and Wiederhorn, S. M., *International Journal of Fracture,* Vol. 10, No. 3, Sept. 1974, pp. 379–392.

[24] Wiederhorn, S. M., Evans, A. G., and Roberts, D. E. in *Fracture Mechanics of Ceramics,* Vol. 2, R. C. Bradt, D. P. H. Hasselman, and F. F. Lange, Eds., Plenum Press, New York, 1974, pp. 829–841.

[25] Linzer, M. and Evans, A. G., *Journal of the American Ceramic Society,* Vol. 56, No. 11, Nov. 1973, pp. 575–581.

[26] Davidge, R. W., McLaren, J. R., and Tappin, G., *Journal of Materials Science,* Vol. 8, No. 12, Dec. 1973, pp. 1699–1705.

[27] McLean, A. F., Fisher, E. A., and Bratton, R. J., "Brittle Materials Design, High Temperature Gas Turbine," Technical Report AMMRC CTR 72-3, CTR 72-19, CTR 73-9, CTR 73-32, CTR 74-26, CTR 74-59, Ford Motor Company, Dearborn, Mich., Army Materials and Mechanics Research Center Contract DAAG46-71-C-0162, July 1971–Dec. 1974.

[28] Wiederhorn, S. M., "Reliability, Life Prediction and Proof Testing of Ceramics," Interim Report NBSIR 74–486, National Bureau of Standards, Washington, D. C., May 1974.

[29] Evans, A. G., Wiederhorn, S. M. Linzer, M., and Fuller, E. R., Jr., "The Proof Testing of Porcelain Insulators and the Application of Acoustic Emission," Interim Report NBSIR 74–512, National Bureau of Standards, Washington, D. C., 1974.

[30] Evans, A. G., "Understanding the Characteristics of Brittle Materials," ASME Paper 75-GT-87, American Society of Mechanical Engineers, March 1975.

[31] Gruver, R. M., Sotter, W. A., and Kirchner, H. P., "Fractography of Ceramics," Naval Air Systems Command Contract N0019-73-C0356, Ceramic Finishing Company, State College, Pa., Nov. 1974.

[32] Baratta, F. I., Driscoll, G. W., and Katz, R. N., in *Ceramics for High Performance Applications,* J. J. Burke, A. E. Gorum, and R. N. Katz, Eds., Brook Hill Publishing Company, Chestnut Hill, Mass., 1975, pp. 445–476.

[33] Freudenthal, A. M., "New Aspects of Fatigue and Fracture Mechanics," Office of Naval Research Contract N00014-67-A-0214-0011, The George Washington University, Washington, D. C., Dec. 1973.

H. S. Starrett,[1] *A. D. Cull,*[1] *and G. R. Irwin*[2]

Application of Fracture Mechanics to the Thermostructural Failure of Graphite

---

REFERENCE: Starrett, H. S., Cull, A. D., and Irwin, G. R., "**Application of Fracture Mechanics to the Thermostructural Failure of Graphite,**" *Cracks and Fracture, ASTM STP 601,* American Society for Testing and Materials, 1976, pp. 86–108.

ABSTRACT: Thermostructural failure of materials used in reentry vehicles is an important problem. This paper is an experimental and analytical study of a testing facility in which these materials are thermostructurally evaluated. Radio frequency energy is used to induce a steep, radial temperature gradient in a disk-shaped specimen. A K_I solution for this specimen is developed by a semiempirical procedure; it is used to analyze the experimental data. Experiments were performed on ATJ-S (WS) graphite. Comparison of the results from the K_I solution are compared to contemporary K_I values for this graphite. Currently, the K_I solution is inadequate for design purposes; however, it shows the potential of providing a better understanding of the thermostructural fracture process.

KEY WORDS: crack propagation, fracture tests, thermostructural failure, graphite, K_I solution

There are many applications in which a stress field created by a temperature gradient is the primary cause of fracture. For example, in the design of reactor cores, solid fuel elements for rocket motors, turbine blades, and reentry vehicles, fracture resulting from thermal stresses is important. At Southern Research Institute, a unique facility called the temperature/stress test was designed and built to investigate materials experiencing this mode of failure. In using the temperature/stress test to evaluate materials under thermostructural loading, a comparison is made between the strain at failure measured in temperature/stress tests and the

---

[1] Head and research engineer, respectively, Analytical Mechanics Section, Southern Research Institute, Birmingham, Ala. 35205.

[2] Visiting professor, Department of Mechanical Engineering, University of Maryland, College Park, Md. 20742.

strain at failure measured in tension tests. This comparison consistently shows that the strain at failure for thermostructural loading is about 10 percent higher than the tensile value [*1,2*].[3] In an attempt to explain these differences, a program was initiated to analyze the test from the point of view of fracture mechanics. This report is concerned with one phase of the study—the development of a K-solution for a notched temperature/stress specimen.

The material used in this investigation was ATJ-S (WS) graphite. When compared with typical structural materials, graphite is relatively weak from the aspects of both strength and fracture toughness. However, graphite maintains its structural integrity at temperatures in excess of 5000°F and, therefore, it is used in many high temperature applications. Molded graphites, such as the graphite used in this study, are considered

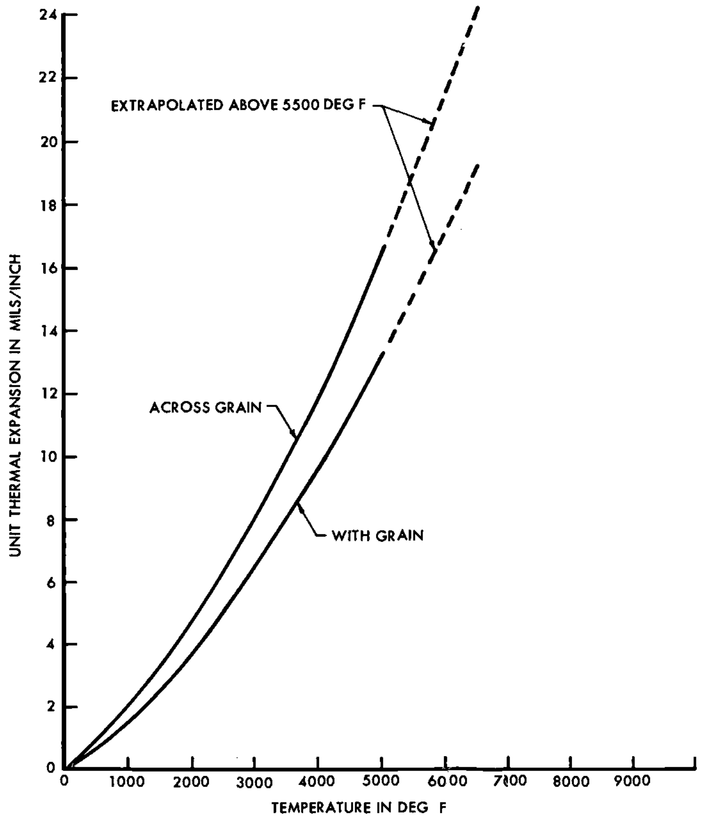

FIG. 1—*Unit thermal expansion of ATJ-S (WS) graphite.*

---

[3] The italic numbers in brackets refer to the list of references appended to this paper.

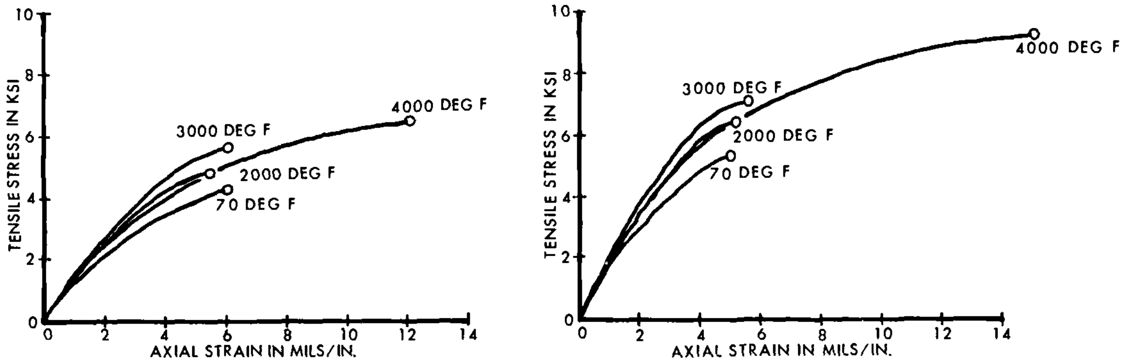

A) ACROSS GRAIN TENSILE STRESS-STRAIN CURVES

B) WITH GRAIN TENSILE STRESS-STRAIN CURVES

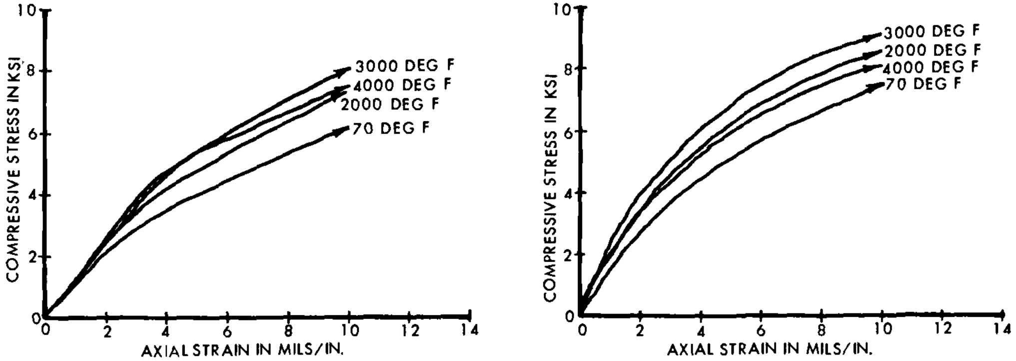

C) ACROSS GRAIN COMPRESSIVE STRESS-STRAIN CURVES

D) WITH GRAIN COMPRESSIVE STRESS-STRAIN CURVES

FIG. 2—*Tensile and compressive behavior of ATJ-S (WS) graphite.*

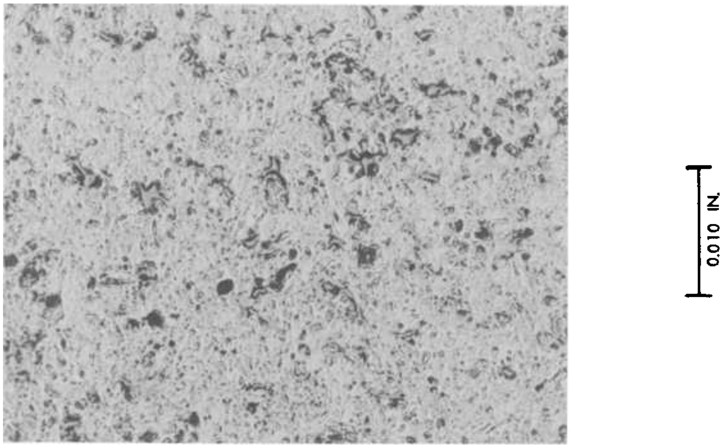

A) STRUCTURE OF ATJ-S(WS) GRAPHITE AT 100X

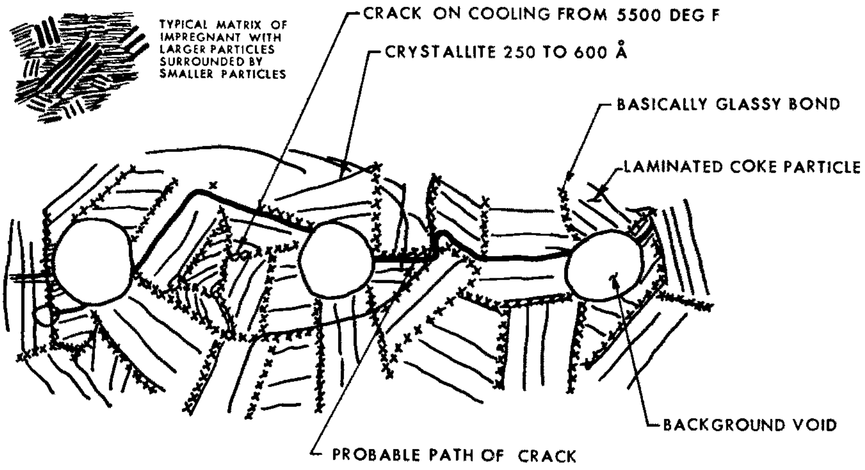

B) SCHEMATIC MODEL FOR CRACK DEVELOPMENT IN POLYGRAPHITES

FIG. 3—*Photomicrograph and schematic model of polygraphite.*

to be transversely isotropic. The direction normal to the plane of isotropy is called "across grain" whereas the directions in the plane are named "with grain." Since fine grained graphite is not a common engineering material, certain properties which are significant in establishing its behavior in thermostructural applications are reviewed in Figs. 1 and 2 where typical expansion curves and stress-strain curves for ATJ-S (WS) are presented. This information establishes the temperature dependent, nonlinear, and anisotropic character of the material.

The structure of ATJ-S (WS) graphite is illustrated by the X100 photomicrograph and the schematic model in Fig. 3. This schematic shows the relatively large background voids, the highly anisotropic, lamellated coke particles, and the impregnant (binder) which acts as the matrix. Although the large voids constitute only a small fraction of the total porosity, they are an important factor in the fracture process.

There are several different theories on the nature of the fracture process in graphites [*3–5*]. One that has gained fairly general acceptance among investigators is that the crack propagates from pore to pore, between the laminae of the coke particles, and around the boundaries of the coke particles following the path of least resistance that is aligned more closely to the direction perpendicular to the principal stress. As noted earlier, the coke particles are highly anisotropic; they exhibit a planar or laminar structure. The strength in the planes is generally considered to be at least 20 times greater than the strength in the direction perpendicular to the planes. In the perpendicular direction, only the Van der Waals forces hold the material together and these forces are quite weak. Perpendicular strengths for the coke particles are nominally 1000 psi. Thus the actual mechanism of separating the laminae occurs at very low nominal stress levels. Precision strain measurements using the Tuckerman gages on graphitic tension specimens have shown that inelastic (nonrecoverable) strain initiates at quite small loads and that significant nonlinear stress-strain response is evident at a nominal tensile stress of about ¼ to ⅓ of the ultimate tensile strength.

The main point, with respect to this study, is that crack formation in graphite starts at low nominal stress levels and continues until catastrophic failure. Furthermore, a single unique crack is not formed, but rather microcracking occurs fairly uniformly through the volume of material subjected to the highest tensile stresses. This has been dramatically illustrated in tension specimens which were tested at 5500°F. Several such specimens were not taken to failure but were removed from the test fixture intact. Post-test X-rays of these specimens showed extensive microcracking throughout their gage volumes. Considerable cracking was also visible on the surfaces.

At temperatures below 3000°F, it is believed that the microcracking occurs at several regions in a tensile volume and that these regions of extensive microcracking grow to a size about five times the background void size (larger pores) before catastrophic failure occurs. This conjecture is based on the fact that measured voids and void clusters, inclusions, and other disparate structures have to be about five or six times the background void size before they act as strength reducers in uniaxial tension specimens. It is believed that this extensive microcracking which takes place prior to failure of graphite can account for the difference in the strains to failure measured in uniaxial tension tests and those measured in the temperature/stress test.

In the temperature/stress test the loading is a result of the differential thermal expansions occurring in the part because of the temperature gradients. As the microcracking occurs in the zones of peak tensile stresses, the stresses are relieved. This relieving mechanism starts at low stress levels and continues during the loading until there is a sufficient build up of elastic strain energy to drive a single crack.

It was the purpose of this effort to characterize the material with the stress intensity factor $K_{I'}$ to see if agreement could be attained between two laboratory tests: the compact tension test, and the temperature/stress test which simulates a thermostructural loading.

Temperature/Stress Test

In the temperature/stress test, inductive heating is used to generate a steep radial temperature gradient in a circular disk-shaped specimen. A schematic representation of the test is shown in Fig. 4. A typical specimen is tapered from the central hole to the outer circumference where it is surrounded by the induction coil. Also identified on the figure are the measurements recorded during a test. Temperatures are measured at the outer and inner circumferences. An optical extensometer measures the inner diametral deformation.

Currently the power supply operates at a frequency of 200 kHz. At this frequency the skin thickness of most polygraphites is about 0.1 in. Thus, approximately 85 percent of the radio frequency (RF) energy is concentrated in a layer about 0.1 in. thick around the outer circumference of the specimen. Consequently, the steep radial temperature gradient develops. The resulting radial distribution of circumferential stress (σ_θ) is tensile at the inside and compressive at the outside. Typical stress and temperature gradients are shown in Fig. 5 where they are superimposed on the cross section of the specific specimen configuration used in this study.

The power supply is rated at 50 kVA at 480 kHz. The induction coil for the specimen shown in Fig. 5 is two turns of flattened copper tubing; its height equals that of the specimen at its outer radius. A small, annular gap ($^1/_{32}$ in.) exists between the specimen and the coil.

The temperatures at the inner and outer radii of the specimen are monitored continuously. An optical pyrometer with a response time of 1 ns (10^{-9} s) is used to measure the outer temperature. A chromel-constantan thermocouple is used to determine the inner temperature. The rise rate of the outer temperature is used to determine the power input to

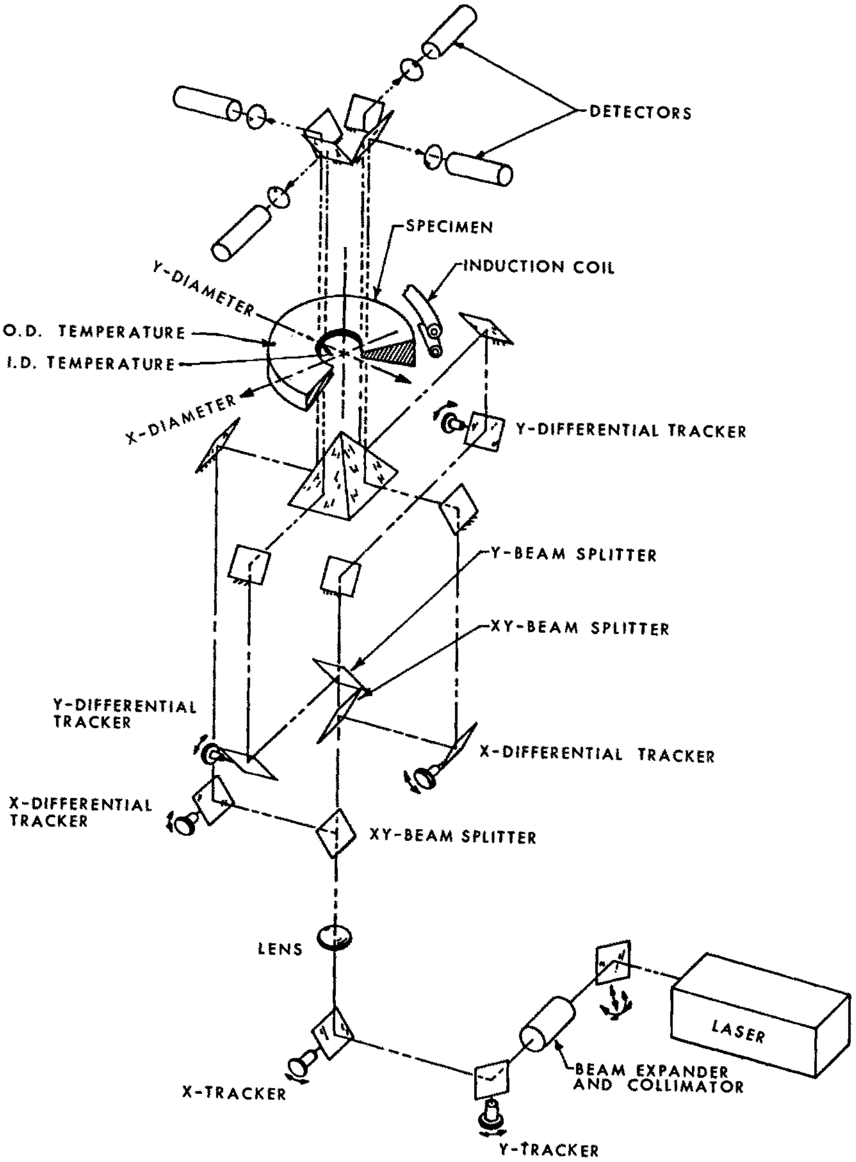

FIG. 4—*Schematic of rapid strain analyzer.*

the specimen, which in turn is used to generate the stress history of the specimen. A two pen recorder with a slewing speed of 0.5 s for full scale movement is used to record both temperatures; time is the independent variable.

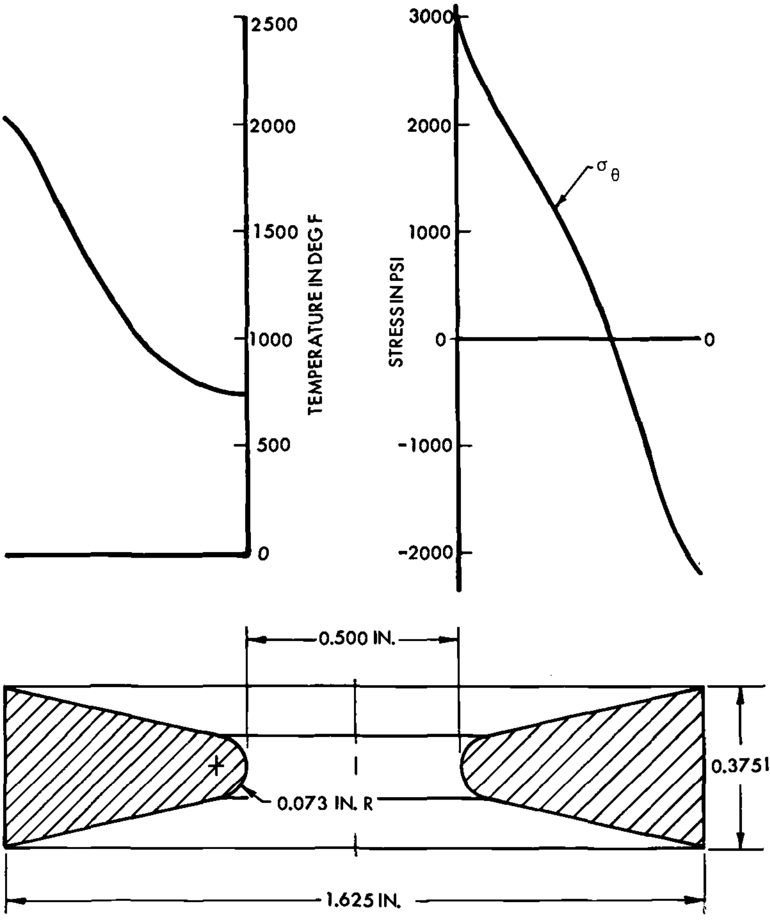

FIG. 5—*Temperature and stress profiles at the time of nominal failure* t = *1.0 s for a 16-kw test condition.*

The deformations of two orthogonal diameters at the inner radius of the specimen also are recorded. The device used for this purpose was developed at Southern Research Institute and is called a rapid strain analyzer (RSA); a schematic representation is provided in Fig. 4. A simple explanation of its operation is as follows. A laser beam is split into four rays. Each ray illuminates one point on the inner edge of the specimen. Two points define the *X* diameter; the other two define the *Y* diameter. A system of moveable mirrors is so arranged that the rays follow the edge of the specimen as it deforms. The apparatus automatically accounts for translations and is insensitive to source intensity. Optical filters are used to eliminate any effects due to radiation when the temperature of the specimen reaches 5000°F.The full scale response (0.1 in.) of the system is currently on the order of 5 ms; the accuracy is on the order of 75 μin. Both diametral deformations are plotted by a two pen recorder identical to the one used for the temperatures; again, time is the independent variable. Typical plots of the diametral deformations for slit and unslit specimens are shown in Fig. 6.

To determine the temperature and stress distributions (unnotched specimens) illustrated in Fig. 5, finite element computer codes are used. The temperature profiles are predicted using a finite element code, MOATS, which has been modified to include internal heat generation terms for each element. This internal heat generation is used to model the induction heating. The distribution of inductive power to each of the elements is based on the mathematical theory of induction heating [*6,7*]. A short computer program is used to input the pertinent material properties, power supply variables, and specimen geometry into the inductive heating equations. The output of this program is the appropriate power distribution curve for the specimen and the magnitude of the heat generation term for each element. Once the relative magnitude of the heat generation term is known for each element, then the temperature distribution as a function of time can be predicted for any level of total power input. The thermal model also accounts for the radiant heat losses from the free surfaces and the reradiation from the work coil. Because of the short test time, 1 to 3 s, convection heat losses are considered insignificant. Confidence in the thermal model used to predict the temperature distributions has been developed by comparing the measured inside diameter (ID) and outside diameter (OD) temperatures during the tests with the analytical predictions at the appropriate power level.

Once the temperature distributions are established for a given input power level, a finite element code is used to predict the distribution of displacements, strains, and stresses. This code accounts for the anisotropic, temperature dependent properties of the graphite [*8*] but does not account for the nonlinear stress-strain response. Comparisons of the predictions of the displacements, strains, and stresses among the linear elastic, deformation plastic, and incremental plastic finite element codes have shown agreement in the displacement and strain predictions within 10 percent, even though the differences in the predictions of the stresses can be greater than 25 percent. In calculating the stress distributions for the K solution, bilinear representations of the stress-strain curves [*8*] were used to convert the strain distributions from the computer code to the stress distributions for the K solution.

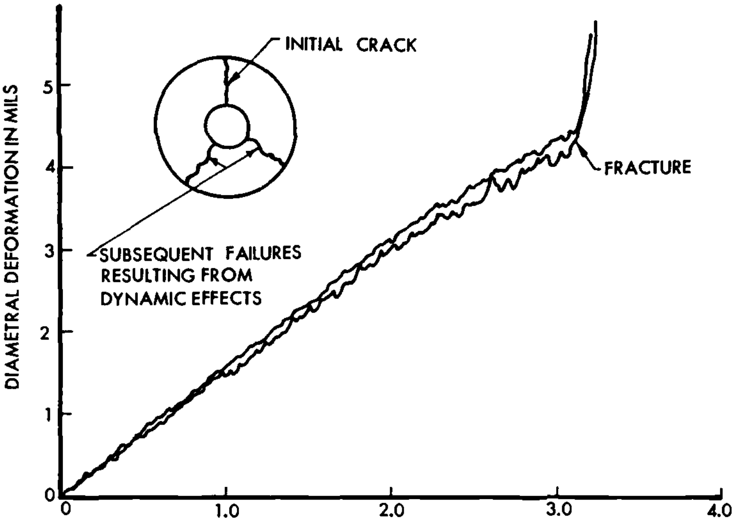

A) UNSLIT DISC

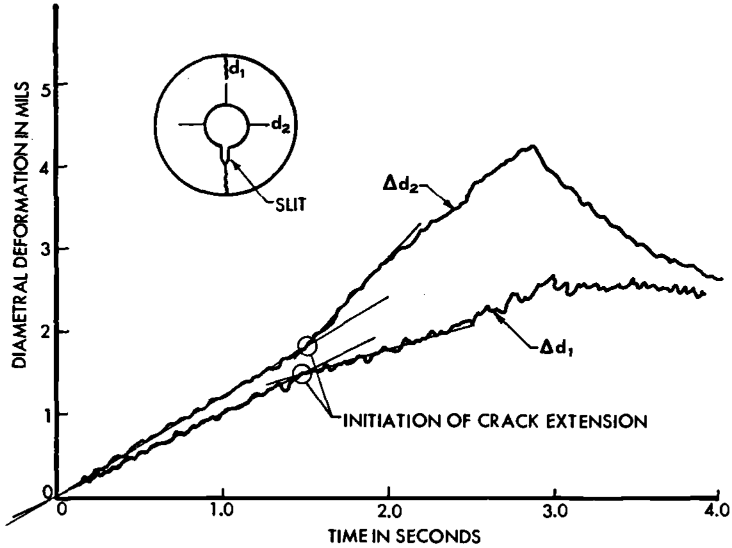

B) SLIT DISC

FIG. 6—*Typical temperature/stress data.*

K_I Solution for the Temperature/Stress Specimen

The basis for the K_I calculations for a temperature/stress specimen with a single radial crack is a model adapted from a known K_I solution by

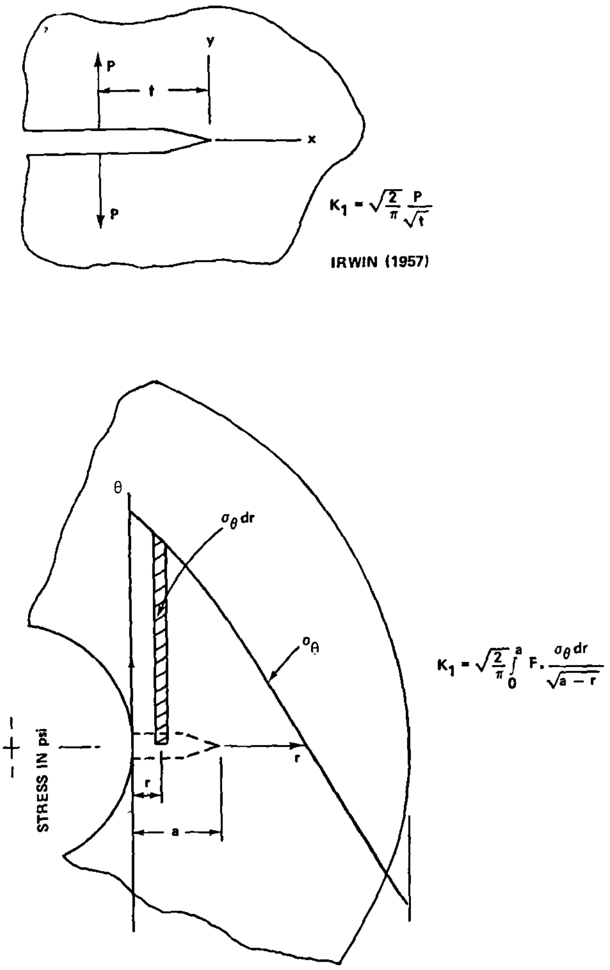

FIG. 7—*Analytical basis for the temperature-stress* K *model.*

means of an experimental procedure. The known solution is that of an infinite plate with a point loaded semi-infinite crack [*9*] which is

$$K_I = \sqrt{\frac{2}{\pi t}}\, P \tag{1}$$

where

P = point load/unit thickness, and

t = distance from P to the crack tip.

The geometry is illustrated in Fig. 7. Figure 7 also shows the distributed load applied to the crack faces of the temperature/stress specimen which models the thermal load. The increment corresponds to P in Eq 1; therefore, the incremental stress intensity factor for the temperature/stress specimen is

$$dK_{\text{I}} = \sqrt{\frac{2}{\pi}}\,\frac{\sigma_\theta dr}{\sqrt{a - r}} \tag{2}$$

where

a = crack length, and
$a - r$ = distance from P to the crack tip.

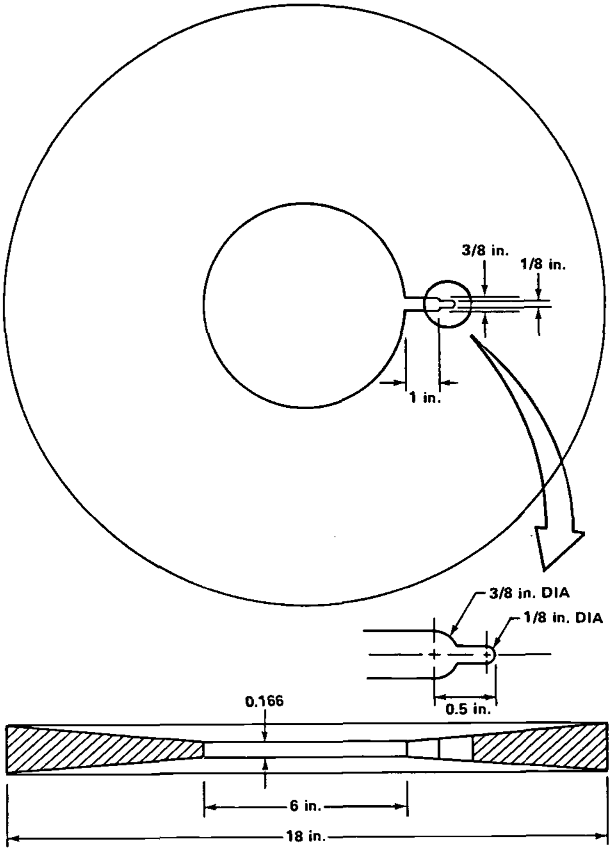

FIG. 8—*Aluminum, large scale model of temperature/stress specimen.*

Integration over the crack length accounts for all the increments; the result is

$$K_{\mathrm{I}} = \sqrt{\frac{2}{\pi}} \int_{o}^{a} \frac{\sigma_{\theta} dr}{\sqrt{a - r}} \qquad (3)$$

Such a direct analogy is insufficient. In order to account for differences between the geometry related to Eq 1 and the actual experimental configuration of the temperature/stress specimen, an influence function, F, is incorporated into Eq 3. Accordingly, the K_{I} model used in the temperature/stress analysis is

$$K_{\mathrm{I}} = \sqrt{\frac{2}{\pi}} \int_{0}^{a} \frac{F \sigma_{\theta} dr}{\sqrt{a-r}} \qquad (4)$$

where F was determined experimentally.

The determination of F involved experiments [*10*] with the large scale aluminum model of the temperature/stress specimen shown in Fig. 8. The specimen was mounted in an Instron machine which was used to apply point loads perpendicular to the slot by means of stirrups mounted in the enlarged portion of the slot. In this manner, the specimen was loaded at successive ½-in. increments from the tip of the slot. For each location of the stirrups the crack opening displacement was recorded. The loads were small enough to prevent inelastic deformation.

The influence function, F, can be related to the load applied to the specimen and the crack opening displacement generated by this load. For a long crack opened by a point load, P, which is distant from the crack tip, the opening displacement adjacent to the crack tip, taken from Ref *9*, is

$$\delta = 4 \sqrt{\frac{2c}{\pi}} \frac{K_{\mathrm{IP}}}{E} \qquad (5)$$

where

c = distance from the tip to the position where δ is measured,
E = elastic modulus, and
K_{IP} = stress intensity due to P.

From Eq 4 the stress intensity factor for a point load on the aluminum model is

$$K_{\mathrm{IP}} = \sqrt{\frac{2}{\pi}} \frac{FP}{\sqrt{a - r}} \qquad (6)$$

The substitution of Eq 6 into Eq 5 yields

$$F = \frac{\pi E}{8} \sqrt{\frac{a - r}{c}} \frac{\delta}{P} \qquad (7)$$

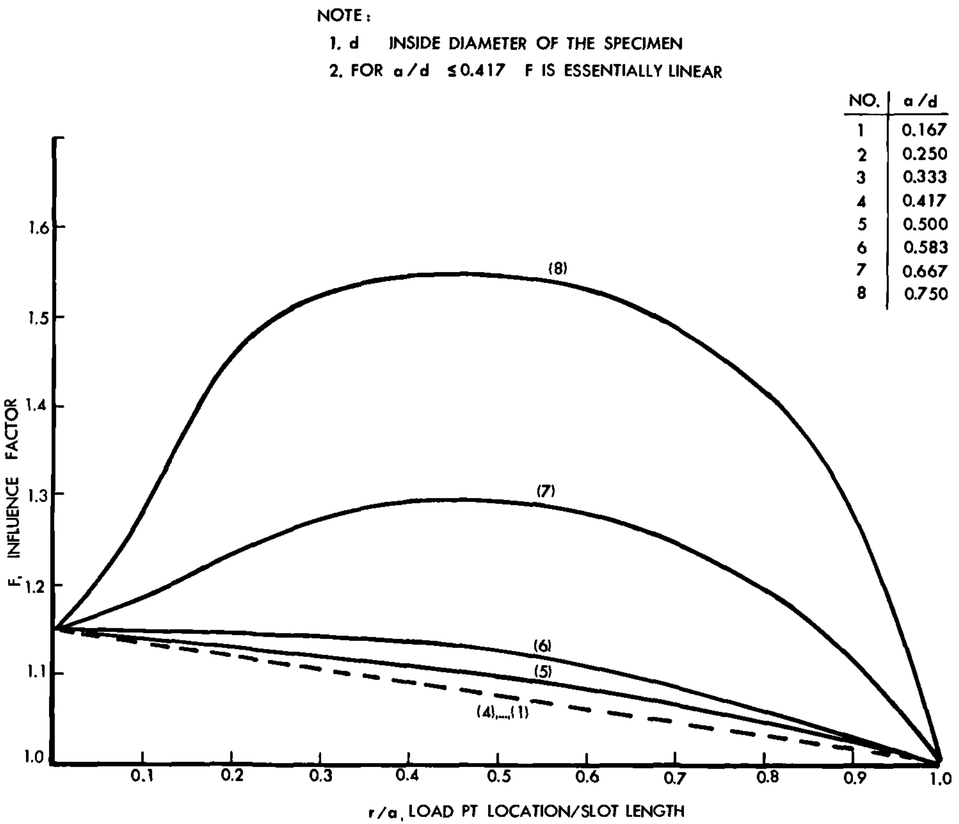

NOTE:

1. d INSIDE DIAMETER OF THE SPECIMEN
2. FOR a/d ≤0.417 F IS ESSENTIALLY LINEAR

NO.	a/d
1	0.167
2	0.250
3	0.333
4	0.417
5	0.500
6	0.583
7	0.667
8	0.750

FIG. 9—F *as a function of* r/a *for a series of slot lengths.*

The mathematical idealization involved in Eq 5 cannot be satisfied experimentally. Consequently, a factor, Q, is introduced to account for such nonideal behavior as the stretch around a finite tip radius, the proximity of the load to the crack tip, and the finite dimensions of the model; therefore

$$F = \frac{\pi E}{8}\sqrt{\frac{a-r}{c}}\;\frac{\delta}{QP} \tag{8}$$

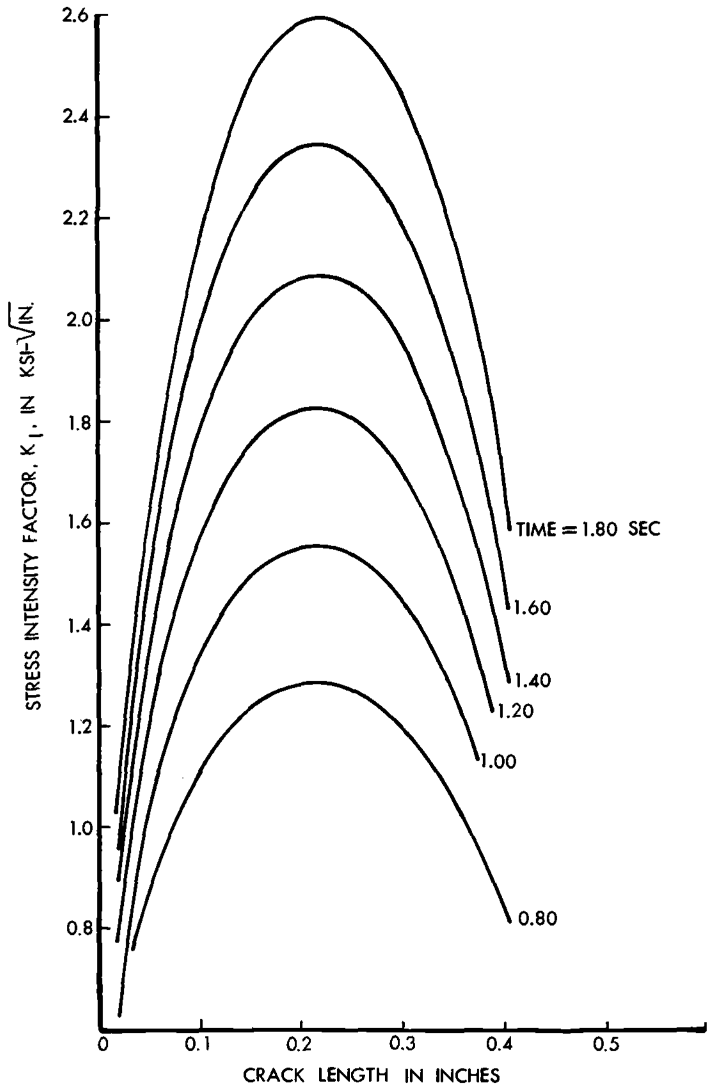

FIG. 10—*Analytical prediction of* K_I *for the 16-kw test condition.*

To estimate a value for Q a series of experiments [10] were performed on a large, center-cracked aluminum plate. This specimen was chosen because of its well documented behavior and known analytical solution [9]. The slit configuration and the loading techniques were identical to those of the large aluminum, temperature/stress model. By comparing the ideal results to the experimental results a value of Q was deduced.

The crack opening displacement was determined from the diffraction pattern generated by passing light from a laser through a narrow slit. This slit was located ⅛ in. from the slot tip.

By increasing the depth of the slot for successive experiments the δ/P-ratio, and thereby the value of F, was evaluated over a wide range of slot lengths. Figure 9 contains the family of curves which describe F as a function of r/a; the parameter of the family is the slot length, a, nondimensionalized by dividing it by the inner diameter, d, of the aluminum model. The common point, $F = 1$ at $r/a = 1$, is required from analytical considerations. The physical limitations of the apparatus prevented the evaluation of F for $r/a < 0.1$; therefore, the common point $F = 1.15$ at $r/a = 0$ was assumed. This point was selected because it allowed a smooth trend for each member of the family of curves as it approached $r/a = 0$.

Reduction of the Data

The σ_θ in Eq 4 and the σ_θ distribution in an unslit specimen are directly related. To arrive at this conclusion, appeal must be made to the concept of linear superposition [11]. The stress field in a slit temperature/stress specimen can be resolved into two parts. One part is the regular field generated in an unslit specimen tested under the same conditions as the slit specimen. The other part is a corrective field due to the presence of the slit. The corrective field is so defined that when it is added to the regular field the resulting field is zero in $r_i \leq r < r_i + a$, that is over the length of the slot. Suppose the regular field is represented as $\sigma_\theta = \Sigma\ (r)$. Then the corrective field is the field generated in a slit specimen by loading the two faces of the slit with the tractions, $p = -\Sigma\ (r)$. It should be noted that the regular field contains no singularities so the corrective field predominates, at least in the vicinity of the slit tip. In other words, the K_I for a slit temperature/stress specimen is determined by the corrective field alone.

Now K_I can be determined by the numerical integration of Eq 4. Figure 10 illustrates the manner in which K_I varies with crack length; this particular analysis is for the 16-kw test condition. A family of curves is necessary for a complete description because σ_θ is changing continuously during the test, and the instant of crack initiation is not known *a priori*. Temperature/stress specimens were manufactured with five slit lengths: 0.056, 0.133, 0.225, 0.282, and 0.338 in. Each was tested at three power levels: 14, 16, and 24 kw. The typical behaviors of specimens with the

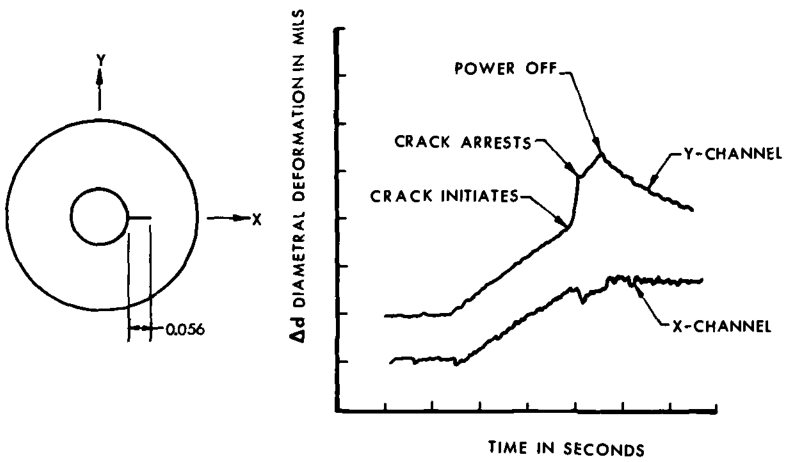

A. SHORTEST SLIT

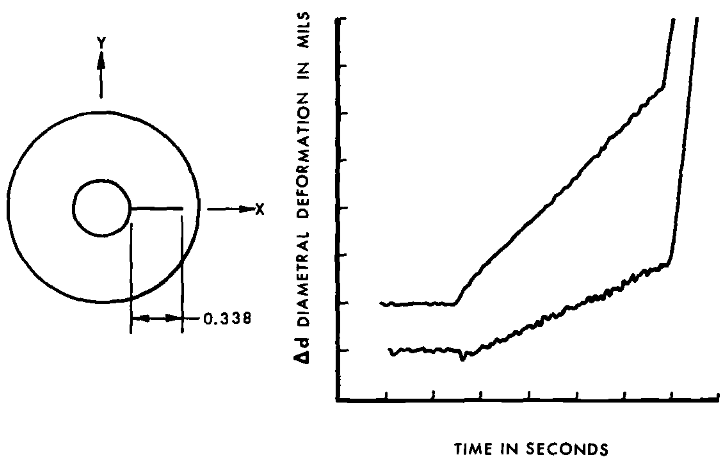

B. LONGEST SLIT

FIG. 11—*Typical experimental data from slit temperature/stress specimen.*

shortest and longest slits are contrasted in Fig. 11. The performances of the other slit lengths lie in between these two extremes. The experimental data for each specimen was examined to determine the instant at which

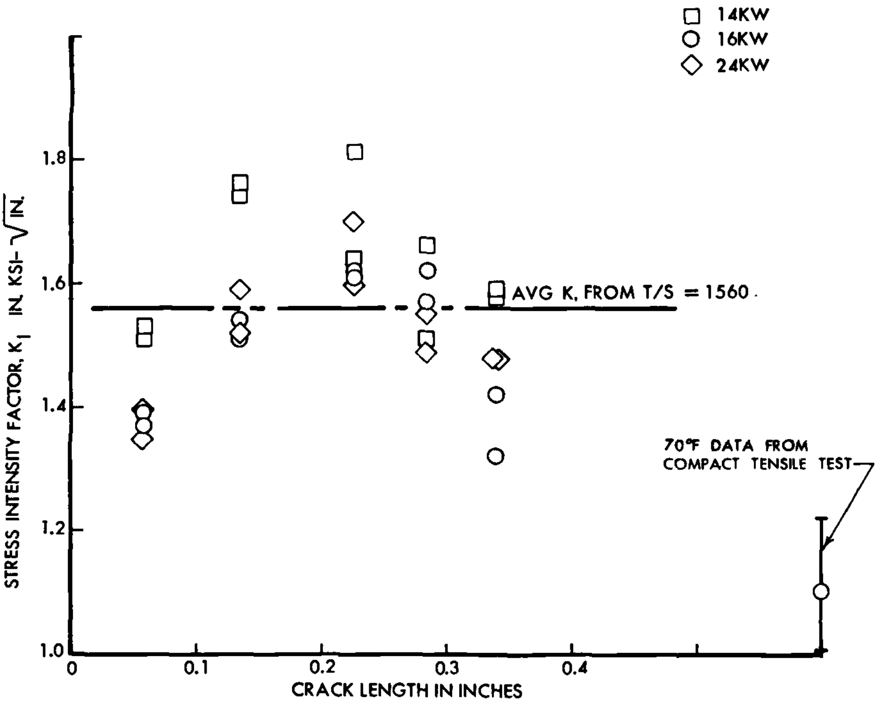

FIG. 12—K *as a function of crack length for the 14, 16, and 24-kw tests.*

the crack started to move. For the 0.056 slit, the initiation time is indicated clearly by the sudden jump in the curve. For the 0.338 slit, the initiation time is less precise since the movement of the crack front is evidenced by a subtle change in slope. These initiation times together with the appropriate calibration curves, such as Fig. 10, define the K_I values for each slit length and power level. The results are collected in Fig. 12 where K_I is plotted as a function of slit length with power level as the parameter.

Discussion

Refer again to the analytical prediction in Fig. 10 which shows plots of K_I versus crack length. Note that each curve in the family peaks at essentially the same value of $a = a^*$. For slits shorter than a^*, the crack is propagating into a region of increasing K; for slits longer than a^*, the opposite is true. The inference is that short and long cracks will exhibit different responses. Figure 11 gives experimental verification of this expectation.

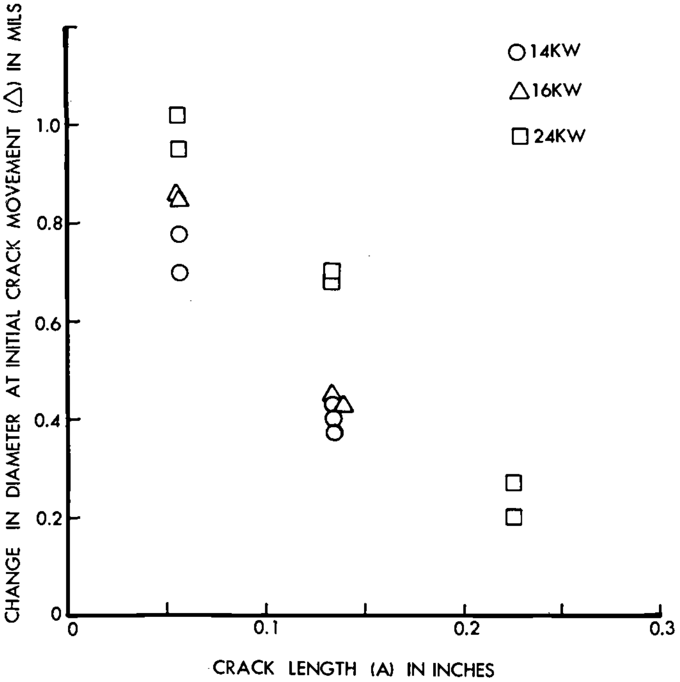

FIG. 13—*Sudden change in diameter as a function of the initial slit length* a *intercepts are the experimental estimates of* a*.

The test data show that for all slits less than a^* the crack moves so precipitously that the recording equipment cannot respond quickly enough to track the changing diameter. However, the crack arrests quickly which permits the recording equipment to start tracking again, but now the graph indicates a lower compliance, that is a longer crack; subsequent extension is stable. On the other hand, when the slit is longer than a^*, no sudden motion is observed; stable crack extension proceeds as long as power is supplied continuously.

For short slit lengths, an estimate of the sudden change in diameter that occurs when the crack initiates can be made from the experimental data. This change, Δ, is plotted against crack length in Fig. 13 for the three power levels at which the tests were performed. The intercepts of these curves with the a axis designate the slit lengths above which no sudden movement is expected. In other words, the a intercepts are experimental estimates of a^*. The analytical predictions for a^* taken from figures such as Fig. 10 are 0.22, 0.22, and 0.24 in. for power levels of 14, 16, and 24 kw, respectively; the corresponding experimental values are 0.22, and 0.23, and 0.28 in.

TABLE 1—*Collection of contemporary stress intensity factors for ATJ-S.*

	K_I, psi $\sqrt{\text{in.}}$				Specimen
	70°F		2000°F		
	AG[a]	WG[a]	AG	WG	Configuration
NRL[b]	830[l]	1110[l]	1210[i,j,l]	1400[i,j,l]	DT[f] (0.25 by 0.04 in.)
Aerospace Corporation[c]	1000	930			CT[g]
NRL[d]	780 to 820	840 to 960	860 to 960[k]	990 to 1090[k]	3B (0.3 by 0.3 by 2.7 in.)
SoRI[e]	818 to 981	960 to 1184	939 to 1022	920 to 1184	CT (0.2 by 0.2 by 0.375 in.)

[a] AG=across grain, WG=with grain.

[b] Freiman, S. W., Mecholsky, J. J., Mast, P., Mulville, D., Beaubien, L., Sutton, S., Wolock, I., "Reentry Vehicle Materials Technology (REVMAT) Program," Quarterly Report #5, Contract P. O. 00087, Naval Surface Weapons Center, Md., 1975.

[c] Quoted Freiman et al, in Quarterly Report #3, REVMAT (details in footnote *b*).

[d] See pp. 109–124.

[e] Each value was determined from 10 to 16 tests at $a/w=0.4$ and 0.5.

[f] DT=double torsion. Dimensions assumed similar to DCB in Report #1 (details in footnote *b*).

[g] CT=compact tension. No dimensions quoted.

[h] 3B=three-point beam.

[i] 2500°F.

[j] Helium purge.

[k] Vacuum furnace

[l] Mecholsky, J. J., personal communication, subsequent to Report #6 (details in footnote *b*)

Figures 10 and 12 show the value of K_I at failure plotted against crack length; the trend in both figures is similar for all power levels. The low values of K_I at short crack lengths could be increased by using an effective crack length rather than the length of the machined slit; this procedure would lower the K_I values for mid-length and long cracks. There are several reasons to justify such a correction procedure.

First, by virtue of the microcracking discussed earlier, the effective crack length is longer than the machined slit. In a recent program [*12*], an attempt was made to establish a constant K_I for graphite for the range of crack lengths $0.2 < a/w < 0.8$ using data collected from tests with compact tension specimens. The corrections required to normalize the K_I values ranged from 0.090 to 0.135 in. which were considered to be unrealistic. As pointed out in the introduction, flaws less than five or six times the background void size do not act as strength reducers in tension specimens. For ATJ-S (WS) this corresponds to a flaw size of about 0.045 in. The implication is that ATJ-S (WS) has a natural flaw of 0.045 in. due to connectivity of the larger pores by microcracking. Thus, a reasonable correction to the slit length is $\Delta a = 0.045$ in.

Secondly, it is reasonable to adjust the K_I value for the shorter crack lengths at the expense of the longer crack lengths because the response of a short crack is more distinct than that of a long crack. The sudden movement of the crack for the shorter notches makes the determination of the time of crack movement much more precise; thus, the accuracy of the time measurement is better. Since the determination of the K_I depends directly on the time of initiation, the values for the shorter notch depths are established more confidently.

If a Δa correction were used, the K_I values for the shorter cracks would increase, the value for the middle crack length might decrease slightly, and the values for the longer cracks also would decrease slightly. The absolute value of K_I shown on Fig. 12 as nominally 1560 ksi $\sqrt{\text{in.}}$ would not change appreciably with a reasonable Δa correction.

The nominal value of K_I for ATJ-S(WS) was determined elsewhere [*12*] to be 1.1 ksi $\sqrt{\text{in.}}$ at 70°F. This value, together with the range of values found in these tests with compact tension specimens, also are shown on Fig. 12. Comparison of the nominal K_I value determined from the temperature/stress tests with that from the compact tests indicates a difference of about 30 percent. Additional results have been obtained by other investigators for the same material; these are listed on Table 1 which shows values both at room temperature and 2000°F. Although values as high as 1.40 ksi $\sqrt{\text{in.}}$ have been measured at 2500°F using double torsion specimens, values as high as 1.56 ksi $\sqrt{\text{in.}}$ have not been reported. The nominal temperature at the crack tip during a temperature/stress test is 1000 to 1200°F; therefore, temperature alone will not account for the 30 percent variation.

Mentioned in the introduction was the 10 percent difference in the strains to failure between the uniaxial tension test and the temperature/stress test. It was expected that localizing the cracking phenomena to the tip of a sharp notch would address this question. Therefore, the comparison between the slit temperature/stress specimen and the compact tension specimen was drawn. Unfortunately, the disparity in the resulting K_I values is greater than the disparity between the two strains to failure. To some degree, refinement of the K_I calculations may reduce the difference between the K_I values of the slit temperature/stress specimen and compact tension specimen. However, significant improvement may require a more complete accounting of the nonlinear, anisotropic character of graphite. The use of a new nonlinear deformation model currently being developed [*13*] may permit a more accurate calculation of the stress distribution.

Conclusion

The motive of this study was to interpret the fracture process in the temperature/stress test by adapting certain concepts of linear elastic fracture mechanics. These concepts were corrupted somewhat to account for the nonideal nature of the material and the physical limitations of the tests. A K-model of the temperature/stress test has been determined.

Initial results with the model show that the response of a temperature/stress specimen can be predicted qualitatively. However, with the present analyses, the differences in the qualitative results between the temperature/stress and compact tensile data are significant, 20 to 30 percent.

Currently, the K_I model could not be used as the basis of a fracture criterion in the design of the leading edge of a reentry vehicle. However, it shows the potential of providing important qualitative insight into the behavior of a crack subsequent to its initiation. The technique has the potential for improvement through the inclusion of such factors as more adequate material modeling and multiaxial stress states.

References

[*1*] Pears, C. D. and Starrett, H. S., "Polygraphites Subjected to Temperature/Stress Loadings," Technical Report No. AFML-TR-73-59, Air Force Materials Laboratory, 1973.

[*2*] Starrett, H. S., Sanders, H. G., Cull, A. D., and Pears, C. D., "Higher Strain Graphites," Technical Report No. AFML-TR-73-186, Air Force Materials Laboratory, 1973.

[*3*] Pears, C. D., Starrett, H. S., and Sanders, H. G., "More on a Strength Analysis of Polygraphites," Contract No. F33615-69-C-1636, Air Force Materials Laboratory, 1969.

[*4*] Smith, M. C., "The Deformation and Fracture Mechanism in Polycrystalline Graphites," *Proceedings*, Conference on Continuum Aspects of Graphite Design, 9-12 Nov. 1970.

[*5*] Zimmer, J. E., White, J. L., Evangelides, J. S., and Meyer, R. A., "Microstructure

and Fracture of Carbon Materials," Vol. 1, Final Report, Contract F04701-75-C-0076, Reentry Vehicle Materials Technology Program, Sept. 1975.

[*6*] Brown, G. H., Hoyler, C. N., and Bierwirth, R. A., *Theory and Application of Radio-Frequency Heating,* Van Nostrand, New York, 1947.

[*7*] Simpson, P. G., *Induction Heating—Coil and System Design,* McGraw-Hill, New York 1960.

[*8*] Starrett, H. S. and Pears, C. D., "Probable and Average Properties of ATJ-S (WS) Graphite," Technical Report No. AFML-TR-73-14, Vol. 1, Air Force Materials Laboratory, Feb. 1973.

[*9*] Tada, H., Paris, P. C., and Irwin, G. R., *The Stress Analysis of Cracks Handbook,* Del Research Corporation, Hellertown, Pa., 1973.

[*10*] Bergreen, Zve, Masters thesis, Department of Mechanical Engineering, University of Maryland, College Park, Md.

[*11*] Bueckner, H. F. in *Methods of Analysis and Solutions of Crack Problems,* Noordhoff, Leyden, The Netherlands, 1973.

[*12*] Cull, A. D. and Starrett, H. S., "A Study of Fracture Mechanics for Graphitic Materials (Interim)," Technical Report No. AFML-TR-75-125, Air Force Materials Laboratory, Oct. 1975.

[*13*] Jones, R. M. and Nelson, D. A. R., "Nonlinear Deformation of Graphitic Materials," Technical Report AFML-TR-74-259, Air Force Materials Laboratory, Feb. 1975.

L. R. Hettche [1] *and T. R. Tucker* [1]

Fracture Toughness of ATJ-S Graphite and CVD Carbon-Carbon Composites at Elevated Temperatures

---

REFERENCE: Hettche, L. R. and Tucker, T. R., "**Fracture Toughness of ATJ-S Graphite and CVD Carbon-Carbon Composites at Elevated Temperatures,**" *Cracks and Fracture, ASTM STP 601,* American Society for Testing and Materials, 1976, pp. 109–124.

ABSTRACT: The fracture toughness and flexural strength of ATJ-S polycrystalline graphite and two chemical-vapor-deposited (CVD) carbon-carbon composites (CVD/felt and CVD/filament wound) are reported for temperatures between 20 and 2000°C. For both the ATJ-S and CVD/felt materials, the toughness and strength are found to rise linearly with increasing temperature. The properties of CVD/filament wound composite exhibit the greatest directional dependence of the materials examined. When the machined notch is oriented perpendicular to the reinforcing filaments, the CVD/filament wound specimens fail by delamination, precluding any fracture toughness determination.

Results of scanning and transmission electron microscopy of the fracture surfaces are also presented. In the case of the polycrystalline graphite, a preference for interfacial separation and, to a lesser extent, cleavage separation are observed.

KEY WORDS: fractures (materials), polycrystalline, graphite, composite materials, graphite composites, high temperature tests, flexural strength, fractography, crack propagation

Because of excellent mechanical property retention at elevated temperature (~2000°C), high sublimation energy, and superior ablation performance, graphitic materials are being developed and evaluated for thermostructural applications, particularly as candidate materials for nose tips and heat shields of advanced reentry systems [*1–3*].[2] The materials of interest include high-density polycrystalline graphite and advanced carbon-carbon composites. The latter category consists of various types

---

[1] Superintendent and research physicist, respectively, Engineering Materials Division, Naval Research Laboratory, Washington, D. C. 20375.

[2] The italic numbers in brackets refer to the list of references appended to this paper.

and geometries of carbon fiber reinforcement in a carbon matrix. Although the fracture behavior of these materials is an important design consideration in the proposed applications, only limited fracture toughness data has been reported for graphite [*4–7*] and even less for carbon-carbon composites [*8,9*]. Moreover, the authors are unaware of any high-temperature fracture toughness measurements for carbonaceous materials.

In this paper, the fracture toughness and flexural strength of polycrystalline graphite (ATJ-S) and two chemical-vapor-deposited (CVD) carbon-carbon composites are reported for temperatures between 20 and 2000°C. Measurements are made on machine-notched (a/W =0.0, 0.3, and 0.5), three-point bend specimens (0.76 by 0.76 by 6.6 cm) heated in vacuum by an induction furnace. Results of scanning and replica transmission electron microscopy of the fracture surfaces are also presented. In addition, both the utility and uncertainty of the critical stress intensity factor as a measure of fracture resistance of carbonanceous materials are discussed.

Material Description

ATJ-S Graphite

ATJ-S graphite is a commercially available material which is used for nose-tips of reentry vehicles and other applications requiring thermal shock resistance and erosion performance. In the fabrication of ATJ-S graphite, the raw coke splinters are oriented with their long axes perpendicular to the molding direction. The final grain structure of the graphitized billet retains the same orientation. Hence, molded polycrystalline graphite has a so-called with-grain plane of isotropy, perpendicular to the direction of the molding pressure, and an across-grain direction, parallel to the direction of molding pressure. Because of the inherent anisotropy of graphite grains and various graphitized artificts, the physical and mechanical properties of polycrystalline graphite are directionally dependent.

The bend-beam specimens of ATJ-S graphite are machined in two orientations, the beam axis parallel to the with-grain plane and the beam axis parallel to the across-grain direction. The crack propagation direction is perpendicular to the with-grain plane for the specimens designated "with-grain" and perpendicular to the across-grain directions for the specimens designated "across-grain." (A third crack propagation direction, coplaner with the with-grain plane, was not examined.)

CVD/Carbon-Carbon Composites

The CVD/carbon-carbon composites examined in this study were developed and evaluated by Sandia Laboratory for reentry heat shield applications [*2,10,11*]. The CVD carbon process involves flowing natural gas (92 percent methane) through a hot (~1100°C) porous carbon substrate or preform. On contact with the hot substrate, the gas cracks, depositing carbon and liberating hydrogen. The carbon substrate is initially molded or formed to the desired shape and is subjected to repeated CVD cycles to achieve high density. CVD densification of the substrate is followed by 2-h heat treatment at approximately 3000°C.

The CVD/felt substrate is made from ~5-cm-long, randomly-oriented viscose rayon fibers which have been carbonized. After densification, the CVD/felt composite contains approximately 9 volume percent substrate fiber and has a bulk density of 1.75 to 1.8 g/cm^3. Bend-beam specimens of this material where excised from the base of a 1.6-cm-thick, full-size cone. The beam axis coincides with the axial direction of the cone, and the crack propagation direction is in the through-thickness (radial) direction. Because of the limited amount of CVD/felt material available for testing and because this material is only slightly anisotropic, the specimens are made in only one direction.

The CVD/filament-wound (CVD/FW) substrate is made from a continuous, five-strand carbon filament of ~0.03-cm diameter. The carbon filament is wound in a helical pattern on a solid conical mandrel. By varying the wrap angle, a constant thickness conical substrate is formed. After repeated CVD carbon cycles, the CVD/FW cone has a density of 1.55 g/cm^3, containing typically a 0.5 fiber volume fraction.

The CVD/FW specimens are cut from the base of a 1.6-cm-thick, full-scale cone (wrap angle of approximately ±80 deg) in two, mutually perpendicular directions. The beam axis coincides with either the circumferential (with-filament) direction of the cone or the axial (across-filament) cone direction. In both specimens, the crack propagation direction is in a through-thickness (radial) direction (perpendicular to the filaments in the with-filament specimens, and parallel to the filaments in the across-filament specimens).

Experimental Procedure

A schematic illustration of the test apparatus is shown in Fig. 1. The specimen is heated by an induction furnace in a vacuum of less than 10 mm of mercury. One end of the test chamber (20-cm inside-diameter stainless steel tubing) mates with the feed-through plate of the water-cooled induction coil. This coil is connected to a 10-kW, 450-kHz power supply. The other end of the test chamber joins with a vacuum subassembly consisting of roughing and diffusion pumps. Optical ports on either side of the test chamber allow continuous monitoring of the specimen temperature by an optical pyrometer. The shaft of the load anvil, protrud-

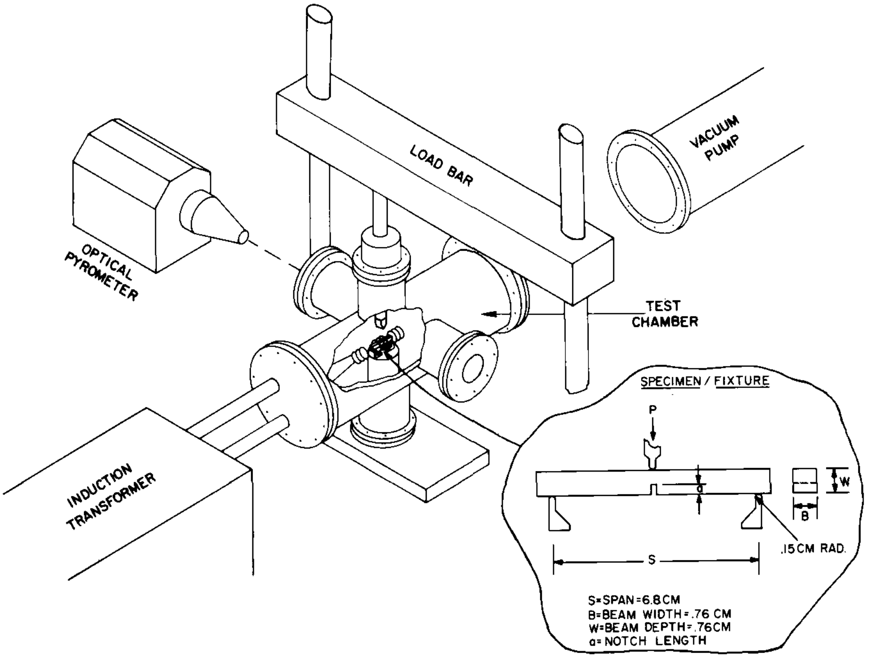

FIG. 1—*Schematic illustrations of test apparatus and specimen/fixture design for determining fracture toughness of graphitic materials at elevated temperatures.*

ing from the top of the test chamber, is displaced at a constant rate of 2.5-cm/min by a screw type testing machine (Instrom TM).

The dimensions of the specimen and bend fixture are also shown in Fig.1. The contact elements of the bend fixture are made of ATJ-S graphite with bearing surfaces machined to 0.154-cm radii. The specimens are notched by a thin, high-speed saw which produces a 0.015-cm-wide, flat bottom flaw.

The load-deflection response of the specimen is determined from the outputs of a load cell and linear variable differential transformer (LVDT) displacement gage. These transducers are located outside of the vacuum chamber. During the free travel of the load train, the friction force of the O-ring vacuum seal equilibrates, and the zero test-load output of the load cell is established. Room temperature tests were also made outside of the test chamber for specimens of each material (a/W = 0.0 and 0.5), in order to examine the effect of O-ring friction on the load-deflection records. In several of these tests, the load-deflection and load crack opening displacement (COD) relationships were simultaneously recorded. The COD gage was held by knife-edge tabs which were bonded to the specimens.

The specimens were heated to 1000°C in approximately 30 s and held at this temperature until the material outgassed (~1 to 2 min). The specimens were then raised to test temperature at a rate of approximately 30 deg/s, held at peak temperature for 15 s, and then tested. Heat transfer to the anvil during loading reduced the specimen temperature by approximately 40°C. For each test, the temperature-time, load-time, and load-deflection relationships were recorded.

Results

Fracture Toughness

Typical load-deflection records for the notched specimens of ATJ-S graphite and CVD/felt materials are shown in Figs. 2 and 3. The peak load and slope of these relationships are seen to increase with increasing temperature. The dotted records of Figs. 2 and 3 represent replica room-temperature tests made outside of the test chamber, and therefore, the load transducer is unaffected by the frictional constraint of the O–ring seal. In all cases examined, the rising load portion of the two room-temperature curves are identical within experimental error. Moreover, in comparison with simultaneously recorded load-COD records, the load-deflection curves are found to be similar in shape and equally sensitive to initial crack extension. After initial crack extension at peak load, however, the two curves are seen to separate. Apparently, the O–ring friction prevented the rapid unloading of the load train when the crack extends. Hence, it is not possible to reliably determine work-of-fracture data from these records.

The rise in slope of the load-deflection curve with increasing temperature is a result of the positive temperature dependence of the elastic

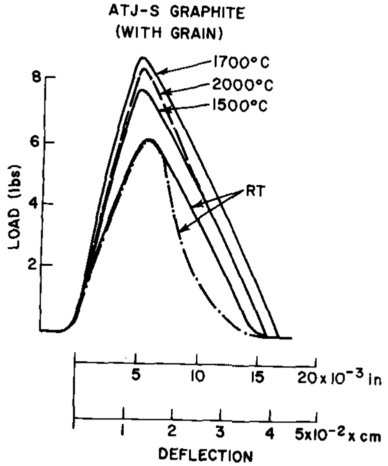

FIG. 2—*Typical load-deflection records for notched specimens* (a/W = *0.5*) *of ATJ-S graphite.*

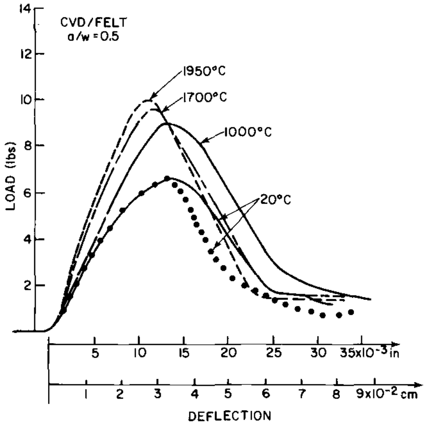

FIG. 3—*Typical load-deflection records for notched specimen* (a/W = *0.5*) *of CVD/felt composite.*

modulus of graphitized materials [*12*]. A similar temperature dependence of the yield strength [*13*] is responsible for the increase in linearity of the load-deflection curves as the test temperature is raised. The yielding behavior of these materials is also evident by a discontinuity in the load-deflection curves. (This behavior is not apparent in the data of Figs. 2 and 3 because of the reduced scale of the reproduction.) It was not possible to satisfy the graphical construction requirement of ASTM Test for Plane-Strain Fracture Toughness of Metallic Materials (E 399-72) for determining K_{Ic} of metals by extrapolation of the initial slope of these records.

Instead, the peak load from the load-deflection relationships is used in the analytical expression given in ASTM Method E 399-72, in order to calculate a critical stress intensity (fracture toughness) for this specimen configuration. The temperature dependence of these values are shown in Fig. 4 for the ATJ-S graphite and in Fig. 5 for the CVD/felt composite. The ATJ-S graphite data exhibit a directional dependence with the with-grain specimens (crack direction perpendicular to with-grain plane axis) possessing the highest fracture toughness. In both directions, the K_I is seen to increase approximately linearly with temperature and to be independent of the a/W ratio. The temperature dependence of the CVD/felt fracture toughness (Fig. 5) is similar to the results of the ATJ-S graphite, and the magnitude of the room-temperature K_I are seen to be in close agreement with the data of Ref *8*.

Using published values of the yield strength (σ_{ys}) of ATJ-S graphite [*13*], the specimen thickness (B) to $(K_I/\sigma_{ys})^2$ ratio is 2.8 at room temperature and 8.8 at 2000°C. Both values are greater than the 2.5 minimum $B/(K_I/\sigma_{ys})^2$ requirement of ASTM Method E 399-72. Although similar

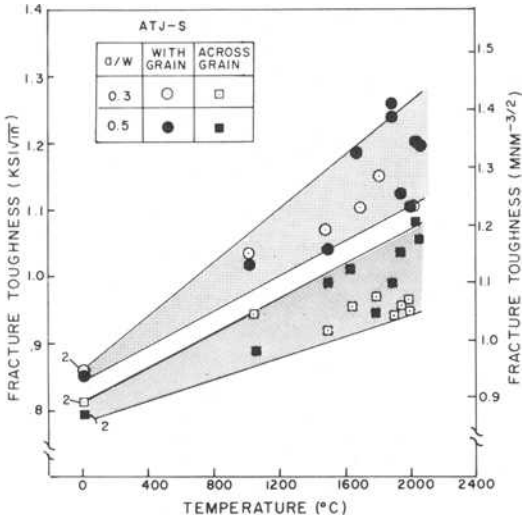

FIG. 4—*Temperature dependence of critical stress intensity factor (fracture toughness) of ATJ-S graphite.*

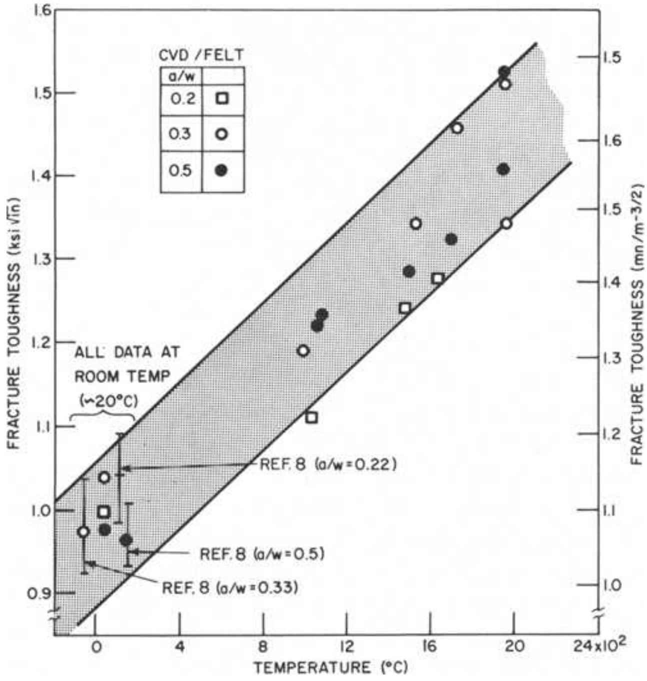

FIG. 5—*Temperature dependence of critical stress intensity factor (fracture toughness) of CVD/felt composite.*

uniaxial data is not available for CVD/felt, the material also appears to satisfy this requirement, judging from a comparison of flexural strengths measured in this study.

When notched specimens of the with-filament CVD/FW material were tested, initial crack extension was perpendicular, rather than colinear, with the machined notch. The crack propagated parallel to the filament at nearly constant loads, resulting in a delamination failure. This behavior is similar to the room-temperature results reported in Ref *8*, and precluded any determination of fracture toughness. Only four specimens of across-filament CVD/FW material were tested, one at each of the following temperatures: 20, 1125, 1500, and 1970°C. In order of increasing test temperature, the K_I of these tests are, respectively: 528, 581, 487, and 649 ksi $\sqrt{\text{in.}}$

Flexural Strength

The results of the flexural strength measurements are presented in Fig. 6 for all materials examined. Here, flexural strength (σ) is defined as the maximum outer fiber stress calculated from the simple beam equation ($\sigma = 1.5\,PS/BW^3$). The load-deflection records for these tests are linear in shape, with a discontinuous drop in load at failure. The CVD/FW material is seen to exhibit the greatest degree of anisotropy of the three materials tested. The strength of CVD/FW differs by nearly an order of magnitude between the two directions examined. Moreover, the with-filament data suggest a maximum at approximately 1100°C, the CVD carbon densification temperature. The flexural strength of the ATJ-S and CVD/felt are seen to rise with increasing temperature. Similar to the fracture toughness properties, the flexural strength of the ATJ-S is found to be directionally dependent, again the with-grain specimen having the highest value.

Fractography

The fracture surfaces of the CVD/felt and ATJ-S graphite specimens were examined by scanning electron microscopy (SEM), and surface replicas were observed by transmission electron microscopy (TEM). The survey included notched and unnotched specimens tested at room temperature and 1500°C. Magnification for the SEM photographs was around ×150 with the TEM micrographs being several orders of magnitude higher. From this limited survey, there was no significant variation in the appearance of the fracture surfaces with temperature.

The SEM micrographs for ATJ-S graphite are shown in Fig. 7 for the two specimen test directions. Micrograph A shows the fracture surface for a with-grain specimen (fracture surface perpendicular to the with-grain plane). Grain size appears to vary from ~20 to 100 μm. A characteristic

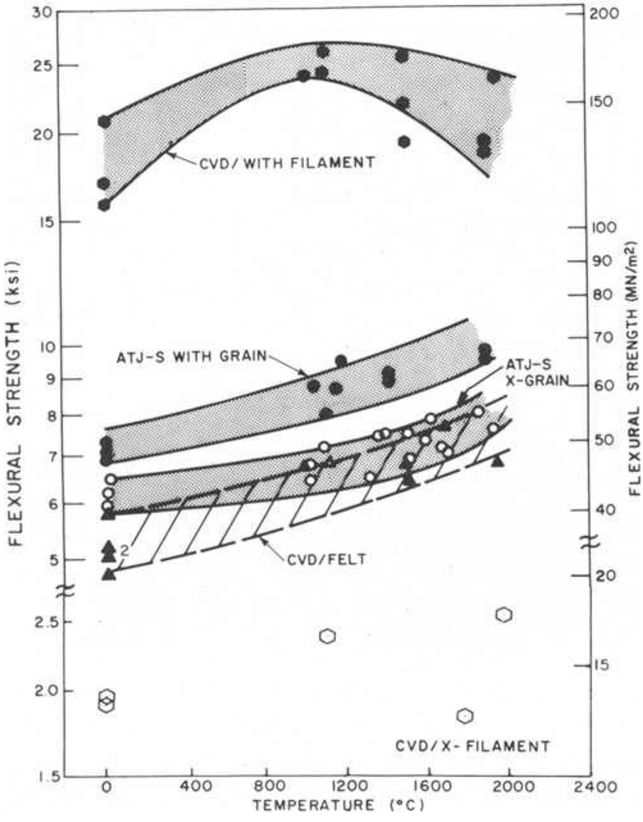

FIG. 6—*Temperature dependence of flexural strength of ATJ-S graphite, and CVD felt and CVD/filament-wound composites.*

feature of fractures in this direction is the irregular undulating topography which gives rise to ridges and troughs. Such a trough is delineated by the two sets of arrows. These irregularities reveal a tendency for the crack to follow intergranular boundaries which in the case lie out of the normal plane of fracture. This type of failure behavior is similar to that described for extruded carbon in Ref *14*.

The fracture surface in Fig. 7*B* is parallel to the with-grain plane. As indicated by the arrows, more grains appear to be oriented in the plane of the figure than in Fig. 7*A*. Striations in these grains indicate that there was substantial cleavage fracture present. Moreover, the directions of the striations represent grain orientations within the plane of the figure. Planar orientation appears to be random as expected for a molded material. On the millimetre scale, the surface is more regular than the surface in Fig. 7*A*, showing a preference of the grains to cleave along their long-axis direction.

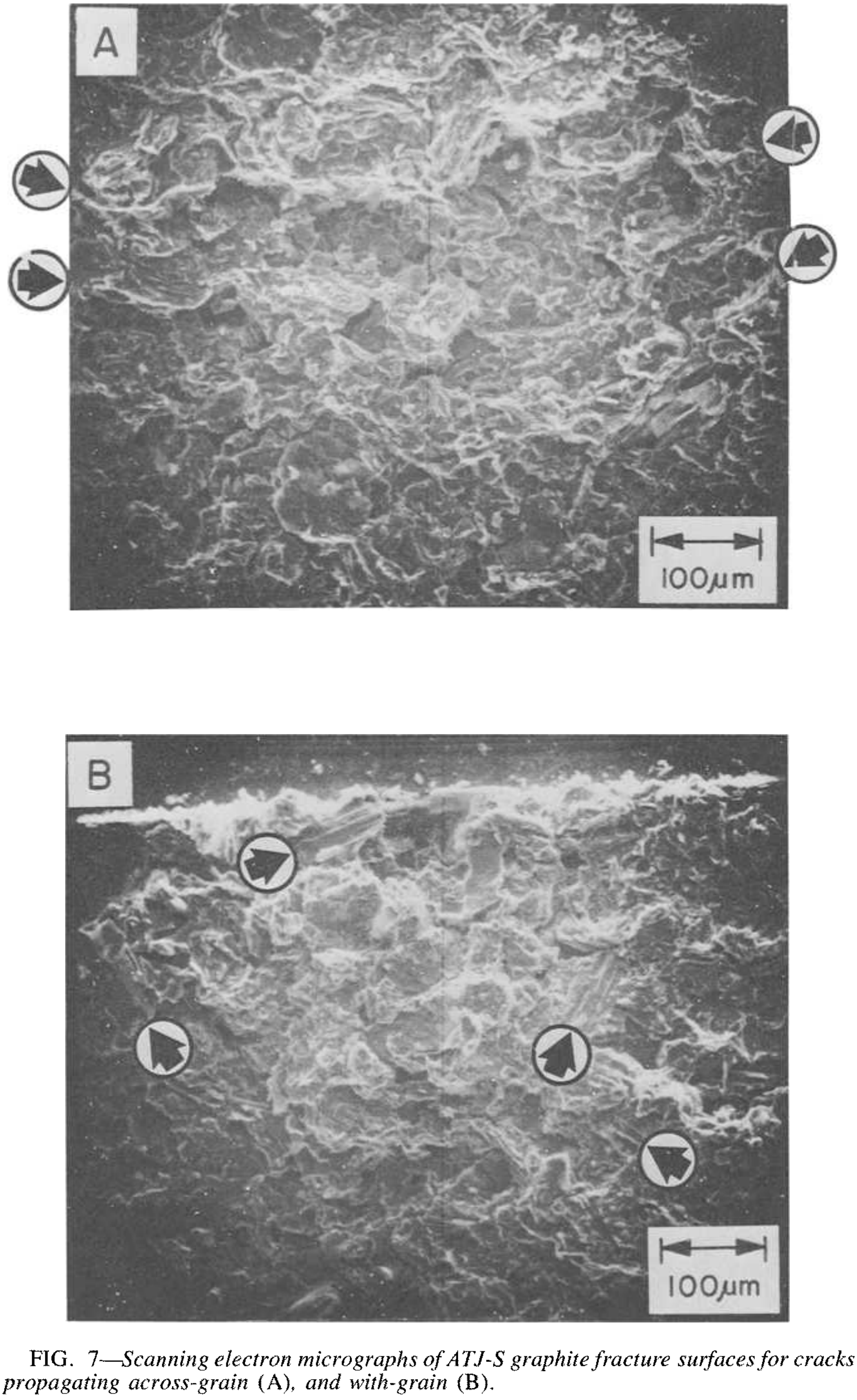

FIG. 7—*Scanning electron micrographs of ATJ-S graphite fracture surfaces for cracks propagating across-grain* (A), *and with-grain* (B).

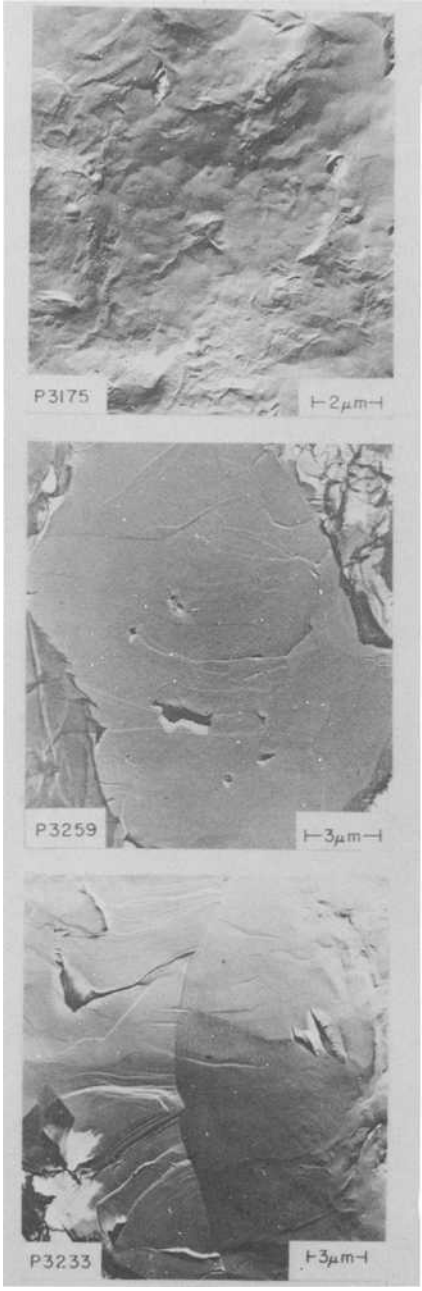

FIG. 8—*Representative features of ATJ-S fracture surfaces as observed by the transmission electron microscope.*

Three representative TEM micrographs for ATJ-S are shown in Fig. 8. The upper figure shows a rather smooth grain surface emerging in intergranular fracture. The central figure indicates transgranular cleavage. The lower photograph shows a rather dramatic combination of the two modes. Here, the fracture proceeds from left to right via cleavage until it reaches the grain boundary near the center of the micrograph. From there, the crack proceeds via interfacial separation along the grain surface.

In general, the majority of the fracture surface areas indicated the intergranular fracture mode. However, some cleavage was present in all cases, and the across-grain tests exhibited more transgranular cleavage fracture than the with-grain tests.

Figure 9 presents a fracture surface SEM micrograph for CVD/felt. The structure is seen to be porous with fiber bundles oriented randomly. The fracture path proceeded both between fibers as in the upper left portion of the figure and through fibers as seen in the lower left quadrant. Fiber cross-sections are made up of a central core of 5 to 8 μm in diameter surrounded by layers of vapor-deposited matrix. The outside diameter of the total fiber ranges from 30 to 40 μm.

The TEM replica surfaces of the CVD/felt fibers are shown in Fig. 10. The fiber cross-section is clearly shown in the upper picture. The core is irregular in shape and has an amorphous appearance. Cracks between the

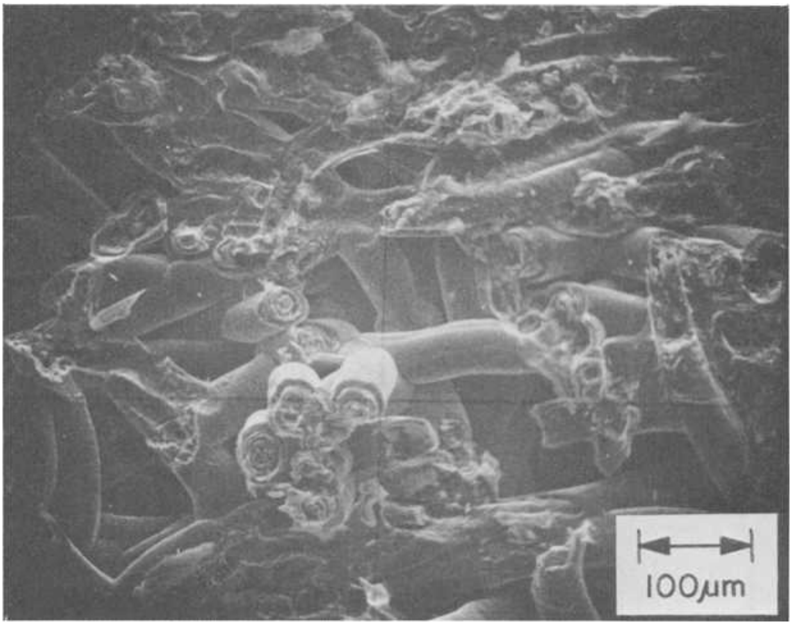

FIG. 9—*CVD felt fracture surface observed by the scanning electron microscope.*

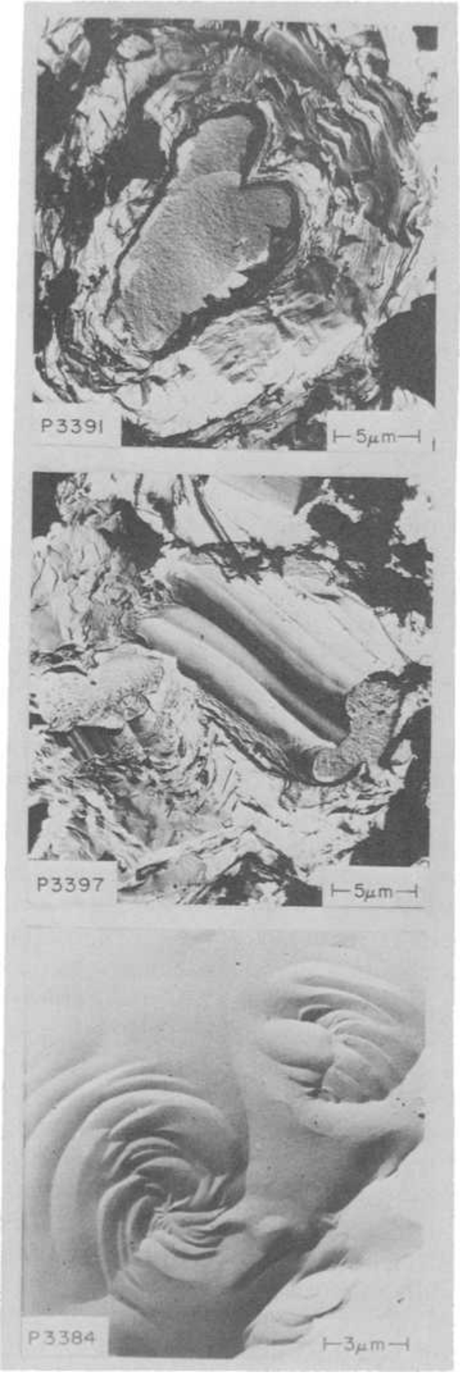

FIG. 10—*Micrographs of CVD felt fiber fracture surfaces.*

surrounding CVD carbon sheaths are shown in detail. In general, the core fractures at a different location from the outer layers, showing delamination of the fiber-matrix interface. This behavior can be noted in Fig. 9 and the center micrograph of Fig. 10.

The bottom micrograph of Fig. 10 shows patterns that were observed frequently on the exterior CVD carbon surfaces. The spiral features when viewed in stereo always appear as depressions. The spiral arms rotate in both directions and the features seem to originate from both points and line segments. These patterns are believed to be related to CVD process either growth spirals originating from surface defects or artifacts of the turbulent gas flow during the deposition cycles.

Discussion

The various explanations which have been offered to account for the positive temperature dependence of the modulus and strength of graphitic materials can also be applied to the temperature response of the fracture toughness. Most of these theories [*12,14,15*] are related to the artificial microstructure which is created by the graphitization process. Porosity in the form of voids and cracks as well as residual stresses are generated on cooling down from the graphitization temperature. This effect is a result of differences in the thermal expansion coefficients of the various graphitized artifacts, including the anisotropic shrinkage of individual crystals. Upon reheating, the cooling defects are closed and the residual stresses relieved, resulting in increases in the modulus, strength, and fracture toughness of the bulk material.

It has also been suggested [*16*] that increased plasticity of graphite at elevated temperature plays an important role in reducing the effectiveness of defects and cracks as points of stress concentration. The localized deformation of graphitic materials is then a superposition of void filling and plastic flow; and therefore, the effects of crack-tip plasticity on the fracture toughness can not be evaluated simply in terms of the macroscopic properties of modulus and yield stress.

The toughness versus strength relationships of CVD/felt and ATJ-S graphite are plotted in Fig. 11 for the range of values measured in this study (Figs. 4–6). This type of data presentation is a useful index for comparing the fracture resistance of materials. A line of constant slope on this plot defines the locus of a constant critical crack depth for that value of K_I/σ and a given stress level. As illustrated in Fig. 11, when the operating stress is 0.5σ, the critical crack depth for a surface flaw is 1 cm for a K_I/σ ratio of 0.63, 0.1 cm for K_I/σ ratio of 0.20, and 0.025 cm for K_I/σ ratio of 0.10. The 0.63 line is provided for reference. This ratio is the recommended highest value of K_{Ic}/σ_{ys} for which a 2.54-cm (1-in.) wide specimen can be used to determine the plane strain fracture tough-

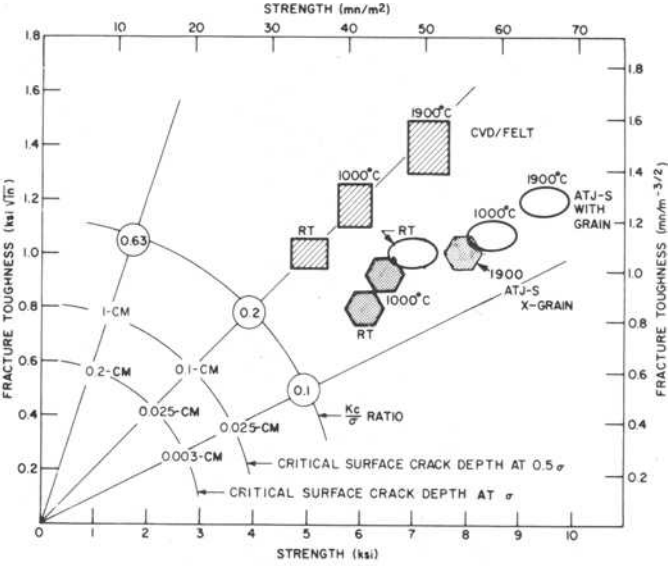

FIG. 11—*Fracture toughness-flexural strength-temperature relationships of CVD/felt and ATJ-S graphite.*

ness of a metal ($B \geq 2.5\ (K_{Ic}/\sigma_{ys})^2$). Above this ratio, the measured value of K_I is affected by crack-tip plasticity.

The CVD/felt data are seen to lie along the 0.2 ratio line. Hence, the increase in strength with temperature is accompanied by a proportional increase in toughness. Insofar as the through-thickness stress gradient developed for a thermostructural application is similar to the stress state of the bend beam specimen, a greater operating stress can be tolerated at higher temperature without any increase in fracture susceptability. In contrast with the CVD/felt data, the K_I/σ ratio for ATJ-S graphite decreases with increasing temperature and the maximum room temperature value is approximately 0.15. In strength critical applications the design stress to ultimate stress ratio of ATJ-S graphite must be less than that for CVD/felt in order to provide the same degree of fracture resistances, based on a critical crack size criterion. This simple example serves to show the utility of determining the toughness-strength-temperature relationships in the developmental evaluation and ranking of candidate materials. It is noted, however, that fracture resistance and strength retention at elevated temperatures are just two of many performance criteria required of thermostructural materials. Usually, a balance of properties are specified, including high resistances to ablation, thermal shock, and erosion.

Acknowledgments

The authors wish to acknowledge A. M. Kummer of the Naval Research Laboratory for his contributions to the design and construction of the apparatus used in this investigation. E. J. Brooks and J. Robinson are also acknowledged for their support with the fractography of this study.

References

[*1*] Stoller, H. M. et al, "Properties of Flight-Tested CVD/Felt, and CVD/FW Carbon Composites," Report SC-DC-71-4046, Sandia Laboratories, Albuquerque, N. Mex. June 1971.

[*2*] McAllister, L. E. and Taverna, A. R. "Development and Evaluation of Mod 3 Carbon/Carbon Composites," Material Review for 1972, Vol. 17, National SAMPLE Symposium, Los Angeles, Calif., April 1972, p. III-A-Three-1-7.

[*3*] Grose, J. G., "Structural Assessment of Carbon-Carbon Materials for the Carbon-Carbon Assessment Program," Report 1011-00-01, Prototype Development Association, Costa Mesa, Calif., Jan. 1974.

[*4*] Corum, J. M., *Journal of Nuclear Materials,* Vol. 22, 1967, pp. 41–54.

[*5*] Davidge, R. W. and Tappin, G., *Journal of Material Science,* Vol. 3, 1968, pp. 165–*173*.

[*6*] Stevens, R., *Carbon,* Vol. 9, 1971, pp. 573–578

[*7*] Vitovec, F. H., *Journal of Testing and Evaluation,* Vol. 1, No. 3, May 1973, pp. 250–254.

[*8*] Guess, T. R. and Hoover, W. R., *Journal of Composite Materials,* Vol. 7, 1973, pp. 2–20.

[*9*] Hoover, W. R. and Guess, T. R., *Journal of Composite Materials,* Vol. 7, 1973, pp. 334–345.

[*10*] Irwin, J. L., "Development and Evaluation of Carbon-Carbon Reentry Heat Shields," SC-DR-70-108, Sandia Laboratories, Albuquerque, N. Mex., April 1972.

[*11*] Frye, E. R. and Rayner, R. M., *Journal of Composite Materials,* Vol. 6, April 1972, pp. 286–292.

[*12*] Mason, I. B. and Knibbs, R. H., *Carbon,* Vol. 5, 1967, pp. 493–506.

[*13*] Starrett, H. S. and Pears, C. D., "Probable and Average Properties of ATJ-S (WS) Graphite," Technical Report AFML-TR-73-14, Air Force Materials Laboratory, Dayton, Ohio, Vol. 1, 1973.

[*14*] Mrozowski, S., in *Proceedings,* First and Second Conferences on Carbon, The Waverly Press, Feb. 1956, pp. 31–45.

[*15*] Roberts, F., Mason, I. B., Price, M. S., and Bromley, J., *Progress in Nuclear Technology,* Vol. 4, Series 4, 1961, p. 105.

[*16*] Martens, V. E., et al in *Proceedings,* 4th Conference on Carbon, Pergamom Press, 1960, pp. 511–529.

J. G. Williams[1] *and M. W. Birch*[1]

Mixed Mode Fracture in Anisotropic Media

REFERENCE: Williams, J. G. and Birch, M. W., "**Mixed Mode Fracture in Anisotropic Media,**" *Cracks and Fracture, ASTM STP 601,* American Society for Testing and Materials, 1976, pp. 125–137.

ABSTRACT: Tests were performed on straight-grained timber to give Mode I fractures in three geometries, and satisfactory K_I data were produced. Mode II tests were more difficult to perform, and the data correlated on a constant net section shear stress basis indicated some form of shear yielding failure. The mixed mode tests used tension specimens with the grain at various angles, and very good data were obtained which gave a constant K_{Ic} fracture criterion independent of K_{II}.

KEY WORDS: crack propagation, fractures (materials), anisotropy, mixed mode

Fracture under combined tension and shear stresses has received considerable attention recently [*1–3*][2] and much has been done to elucidate the behavior of isotropic materials. The loadings are usually expressed as a combination of a symmetric Mode I and an antisymmetric Mode II so that for a crack of length $2a$ in an infinite sheet subjected to a direct stress, σ, normal to the crack and shear stress, τ, we have two stress intensity factors

$$K_I = \sigma \sqrt{\pi a} \tag{1}$$

and

$$K_{II} = \tau \sqrt{\pi a}$$

When crack growth occurs in an isotropic medium with a combination of these two loadings or with K_{II} alone it is never colinear. Probably the most precise expression of the criterion involved is that there is a preferred direction of strain energy release rate other than the colinear one with the presence of shear loading. Recent computations [*3*] show that this condition can be found and that it is very close to the condition of a

---

[1] Professor of polymer engineering and research assistant, respectively, Department of Mechanical Engineering, Imperial College, London, England.

[2] The italic numbers in brackets refer to the list of references appended to this paper.

maximum hoop stress on a line radiating from the crack tip [*1,4*]. Indeed, the solution also agrees well with the concept of a constant strain energy density [*5*], and this is probably not surprising since all three identify with a condition of enhanced stress in that direction.

All the criteria show that on a local level crack growth occurs in Mode I since the maximum energy release rate corresponds closely and the maximum hoop stress corresponds exactly to zero shear stress in the direction of propagation. Thus, although the fracture may be regarded as always Mode I, an apparent relationship exists between the applied K_{I} and K_{II}; Ref *3* shows that this can be represented empirically by the form

$$\frac{K_{\mathrm{I}}}{K_{\mathrm{Ic}}} + \frac{3}{2}\left(\frac{K_{\mathrm{II}}}{K_{\mathrm{IIc}}}\right)^2 = 1 \tag{2}$$

For anisotropic media there is usually a direction of low fracture toughness and in an orthotropic material a crack already in this direction will usually propagate colinearly. It is therefore of interest to study the interaction of Mode I and II loading in such a situation since in principle it removes the ability of the material to choose the local Mode I fracture direction. There have been several studies of this type made in composites and notably Wu [*6*] performed combined loading tests on center-notched plates in glass-fiber reinforced plastic and balsa wood. He reported a curve of K_{I} versus K_{II} indicating a strong interaction and an empirical relationship of the form

$$\frac{K_{\mathrm{I}}}{K_{\mathrm{Ic}}} + \left(\frac{K_{\mathrm{II}}}{K_{\mathrm{IIc}}}\right)^2 = 1 \tag{3}$$

Since in Eq 2 the "apparent" K_{IIc} of the isotropic case is $\sqrt{2/3} \times K_{\mathrm{Ic}}$, then it is clear that this result is very close to the isotropic prediction in form. It is worth noting in this data, however, that results from angled crack tension tests do not show a strong K_{II} dependence and that those in tests involving shear applied directly show greatly enhanced scatter compared with those without shear.

McKinney [*7*] confirms Eq 3 in tests on unidirectional graphite/epoxy laminates although the experimental data appears to contain very few mixed mode results. There is also no justification given for the use of the stress intensity factor to describe the results obtained in shear.

Anisotropy in fracture toughness is, of course, usually associated with anisotropy in stiffness and the elastic relationships for energy release rates and stress intensity factors have been derived [*8*]. For orthotropic media with cracks in a direction of "principal" modulus, the stress intensity factors are the same as for the isotropic case (as are the various finite width correction factors [*9*] and the strain energy release rates are given by

$$\begin{aligned} G_{\mathrm{I}} &= K_{\mathrm{I}}^2 \sqrt{\frac{a_{11}\,a_{22}}{2}} \times \phi \\ G_{\mathrm{II}} &= K_{\mathrm{II}}^2 \times \frac{a_{11}}{\sqrt{2}} \times \phi \end{aligned} \tag{4}$$

where

$$\phi = \left[\sqrt{\frac{a_{22}}{a_{11}}} + \frac{2a_{12} + a_{66}}{2a_{11}}\right]^{\frac{1}{2}}$$

and a_{11}, a_{22}, etc., are the usual anisotropic compliances. Sih et al [*8*] suggest that mixed mode fracture may be deduced from a critical G obtained by G_{I} and G_{II} so that

$$G_c = \sqrt{\frac{a_{11}\,a_{22}}{2}} \times \phi \quad \left(K_{\mathrm{I}}^2 + \sqrt{\frac{a_{11}}{a_{22}}} \times K_{\mathrm{II}}^2\right) \tag{5}$$

This implies a relationship between K_{Ic} and K_{IIc} such that

$$K_{\mathrm{IIc}} = \left(\frac{a_{22}}{a_{11}}\right)^{1/4} \times K_{\mathrm{Ic}} \tag{6}$$

For most woods $(a_{22}/a_{11})^{1/4}$ is approximately 2.5, and this agrees quite well with published data [*6*].

Sanford and Stonesifer [*10*] in tests on glass-fiber reinforced plastic (GRP) have also used a critical strain-energy release rate to describe their mixed mode data and conclude that Mode II behavior can be deduced from this criterion.

It seemed a useful exercise, therefore, to pursue this method, and in an attempt to model the fracture behavior of anisotropic materials, a small number of mixed mode tests were performed on wooden specimens. Although the preliminary results showed good consistency, they did not appear to agree with the reported relationship between the two fracture modes.

Therefore, it was decided to enlarge the initial experimental program and to include pure Mode I and II loading. Firstly, Mode I tests were performed in four geometries to establish the general validity of using K_{I} as a description of fracture since some publications had indicated significant discrepancies [*11*]. Some Mode II tests were then tried and finally a set of angled crack tension tests were carried out to determine a K_{I}, K_{II} locus.

Experiments

The specimens were made from two types of timber which were chosen because of straight grain and freedom from knots. One is a mahogany type hardwood called Utile (*Entandrophragma Utile*) and the other a softwood, Scots pine or European redwood (*Pinus Sylvestris*). Trees are cylindrically anisotropic so that there are three principal elastic directions; that along the axis of the trunk and termed longitudinal (L); that in a radial direction (R) and the tangential direction (T), as shown in Fig. 1*a*. Planks cut away from the center therefore have a modulus E_L along the axis, E_T across the width and E_R through the thickness (see Fig. 1*b*).

The direction of crack propagation in an orthotropic material is conventionally represented by two coordinates, the first indicating the direction normal to the plane of the crack and the second the direction of crack propagation. The tests in this study were confined to the TL system with the exception of the surface notch tests which produced crack propagation in the TR direction.

Mode I Test

Four types of specimens frequently used for fracture studies in polymers [*12*] were made in Utile for these tests, as shown in Fig. 2. The double torsion and tapered cleavage tests are both designed to give fixed G values independent of crack length for a constant load since

$$G = \frac{P^2}{2B} \times \frac{dC}{da} \tag{6}$$

where

P = applied load,

B = crack width, and

dC/da = rate of change of compliance with crack length which is normally constant for these geometries.

In both cases the compliances were determined for a number of crack lengths so that dC/da could be found directly. The constant value was found for only just over half the specimen length as opposed to isotropic materials which give constancy for almost the entire length. On loading to fracture, there was no uniform slow growth since there was some shredding of the surface but a reasonably flat surface was produced. The tests were performed at a number of crosshead speeds in the range 0.02 to 0.5 cm/min but no evidence of rate effects was found. In both, quite steady loads were achieved as the crack grew so that it was possible to determine G_c directly from Eq 6.

Although side grooves had been machined in these specimens in order to constrain the crack along the line of symmetry, it was found that the crack often deviated slightly from this axis in the tapered cleavage tests. As reasonably steady loads were still obtained, values of G_c have been calculated using the thickness of material through which the crack actually propagated, and these results are included in Table 1.

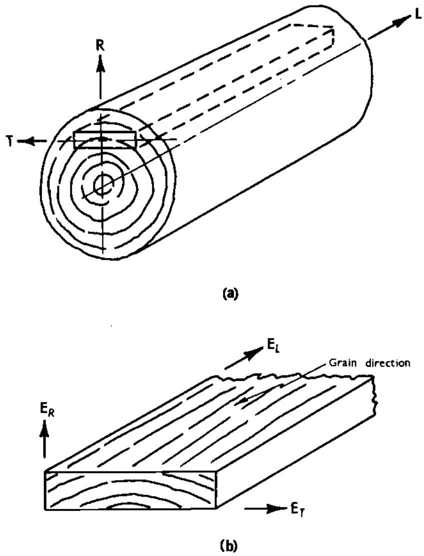

FIG. 1—*Anisotropy directions.*

The G_{Ic} values are converted to K_{Ic} by means of Eq 4 using measured values of E_L and E_T but the other constants were taken from the literature (see Appendix for values).

Single-edge notch specimens were manufactured in both species of wood so that the crack again ran in the TL direction, and this time K_{Ic} was measured directly at a crosshead speed of 0.5 cm/min. There was no steady growth here but an unstable fracture giving a much cleaner surface than the cleavage test. A similar type of fracture behavior was observed in the surface notch tests although the values of K_{Ic} and G_{Ic} were significantly lower.

Although the values of K_{Ic} in the TL plane are reasonably consistent, it can be seen from Table 1 that the variation in the results appear to be

TABLE 1—*Mode I fracture data for Utile.*

Test Method	Fracture Energy, G_{Ic}, J/m^2	K_{Ic}, MN/m$^{3/2}$	Mean Thickness, mm
Double torsion	626 →	0.96 [a]	2.9
Tapered cleavage	467 →	0.84 [a]	4.7
Single-edge notch	151 ←	0.48 [a]	6.4
Surface notch	177 ←	0.35 [b]	15.9 [c]

NOTE— → conversion (see Appendix).

[a] In the TL direction.

[b] In the TR direction.

[c] Effective thickness.

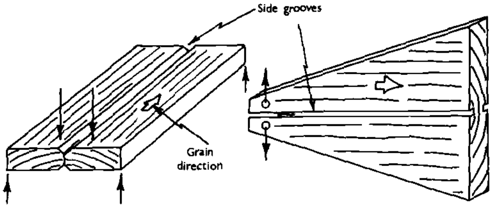

(a) Double Torsion (b) Tapered Cleavage

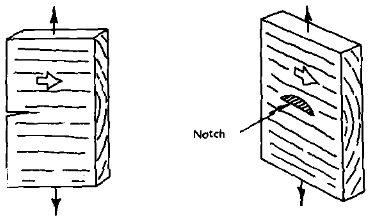

(c) Single Edge Notch (d) Surface Notch

FIG. 2—*Specimen geometries and anisotropy directions.*

related to the thickness of the specimens used in the three types of test. To confirm this trend over a wider range, further tests were performed on single-edge notch specimens varying in thickness from 3 to almost 50 mm.

The results of these tests confirm that a relationship exists between fracture toughness and material thickness (a phenomenon also found in thermoplastic polymers), and it is intended to investigate this effect in more detail in a future experimental program.

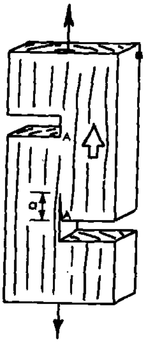

FIG. 3—*Mode II test geometry.*

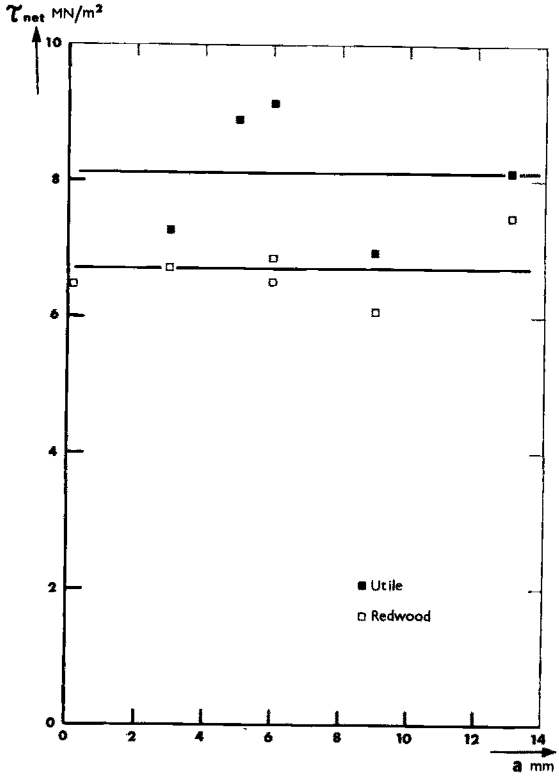

FIG. 4—*Mode II tests, net section shear stress as a function of crack length.*

Mode II Tests

Great difficulty was encountered in producing a Mode II fracture. This had been the common experience in isotropic materials and, indeed, this led to the work described here. Beam tests using longitudinal cracks were prone to Mode I failures at sites other than the crack, and finally the geometry shown in Fig. 3 was used and unstable fractures were produced along the A-A line as shown. Attempts to describe these in terms of K_{II} values resulted in considerable scatter as compared with the Mode I tests, and an analysis using the compliance method suggests that this specimen in fact, does not produce true Mode II fractures. When the net section stress was calculated, however, it was found that this was reasonably consistent as shown in Fig. 4. Redwood showed little scatter in the results and gave an average value of shear stress of 6.7 MN/m^2 while Utile showed more scatter with an average of 8.1 MN/m^2. The conclusion here is that the failure is a form of catastrophic yielding in shear along the fibers and not an unstable crack propagation as in Mode I. The data given by Wu [*6*] appears to be described quite well by this concept also and probably accounts for the enhanced scatter in shear noted previously.

Mixed Mode Tests

In these tests, specimens were manufactured with the grain at various angles to the specimen axis as shown in Fig. 5. In the first series of tests, termed "angled cracks," edge notches were machined parallel to the grain direction. It was not possible to do this precisely because of difficulty in defining the grain direction, but crack propagation was usually within ±2 deg of the crack direction. In this case, the K values may be computed directly from

$$\begin{aligned} K_{\mathrm{I}} &= \sigma \sqrt{\pi a} \times \cos^2 \theta \\ K_{\mathrm{II}} &= \sigma \sqrt{\pi a} \times \cos \theta \sin \theta \end{aligned} \tag{7}$$

and the locus of K_{I} versus K_{II} at fracture determined.

A second series of tests called "straight cracks" was used also since the specimens were easier to make. In these the notches were cut normal to the edge of the specimen as shown in Fig. 5*b*. No precise solution is available for this geometry, but the simple view was taken that an effective crack length a' projected by a along the grain direction would be appropriate so that

$$a' = a/\cos \theta$$

and the expressions for K become

$$\begin{aligned} K_{\mathrm{I}} &= \sigma \sqrt{\pi a} \times \cos^{3|2} \theta \\ K_{\mathrm{II}} &= \sigma \sqrt{\pi a} \times \sin \theta \cos^{1|2} \theta \end{aligned} \tag{8}$$

In both cases, the measured fracture angle was used for θ. For $\theta \rightarrow \pi/2$ there was a problem in that the fractures ran into the specimen grips, and some special long specimens were tested to see if this affected the results. There was no apparent difference in the tests.

Tests were performed at a number of angles such that groups were produced in reasonably narrow angular ranges, and Fig. 6 and 7 show the data for redwood plotted as σY versus $1/\sqrt{a}$ for both sorts of specimens. Y is the isotropic finite width correction factor computed on the basis of the true width and the crack length in the width direction. Only the longer crack lengths were affected significantly, but the correction did give

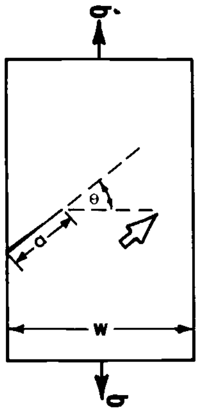

(a) 'Angled Crack'

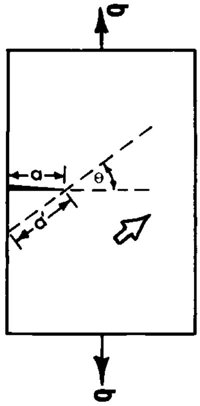

(b) 'Straight Crack'

FIG. 5—*Mixed mode tests.*

improved linearity. The data show good linearity for both materials and both geometries so that the K_I and K_{II} values could be computed from Eqs 7 and 8. These are shown in Figs. 8 and 9. The simple correction for the straight cracks does bring them in line with the angled cracks, and it is clear that in both materials the fractures are essentially at constant K_I with almost no effect of K_{II}. There is some decrease in K_I for Utile for high K_{II} values but it is only slight.

Discussion and Conclusions

The picture which emerges from the data is that Mode I fractures are

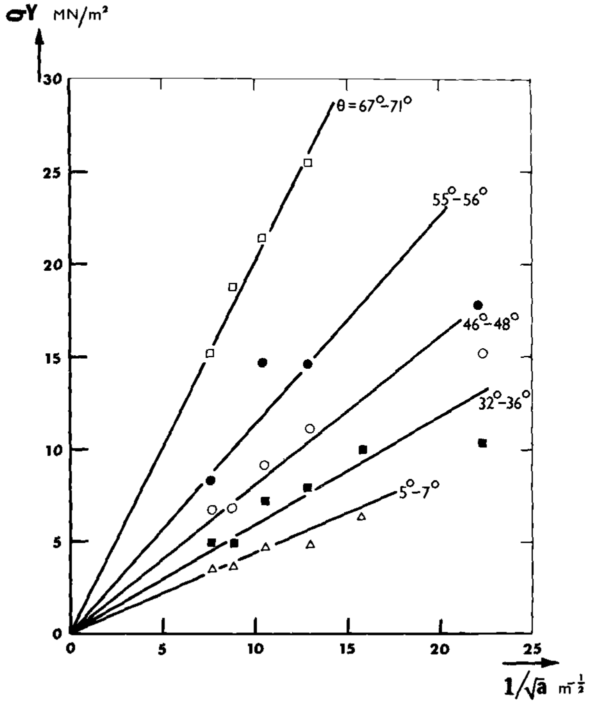

FIG. 6—*Mixed mode data for redwood (straight cracks).*

accurately described by a K_I value, but attempts to produce Mode II fractures result in shear yielding. In mixed mode the shear appears to have no effect and failures occur in pure Mode I. The edge-notch geometry does limit the range of K_{II} and K_I values which can practically be applied. $\theta \approx 75$ deg is the working upper limit giving $K_{II}/K_I \approx 3.5$, and it seems likely that for angles greater than this, shear failures would result. It is interesting to note that if a mean K_{IIc} is calculated from the results of the shear tests then a value of around 1.1 MN/m$^{3|2}$ is produced such that $K_{IIc}/K_{Ic} \approx 2.4$ which agrees quite well with the concept of summing the G_I and G_{II} values as noted previously. In addition the relative contributions of G_I and G_{II} can be assessed from

$$\frac{G_{II}}{G_I} = \left(\frac{K_{II}}{K_I}\right)^2 \times \sqrt{\frac{a_{11}}{a_{22}}}$$

from Eq 4. Since $\sqrt{a_{11}/a_{22}} \approx 0.2$ the effect of the anisotropic elasticity

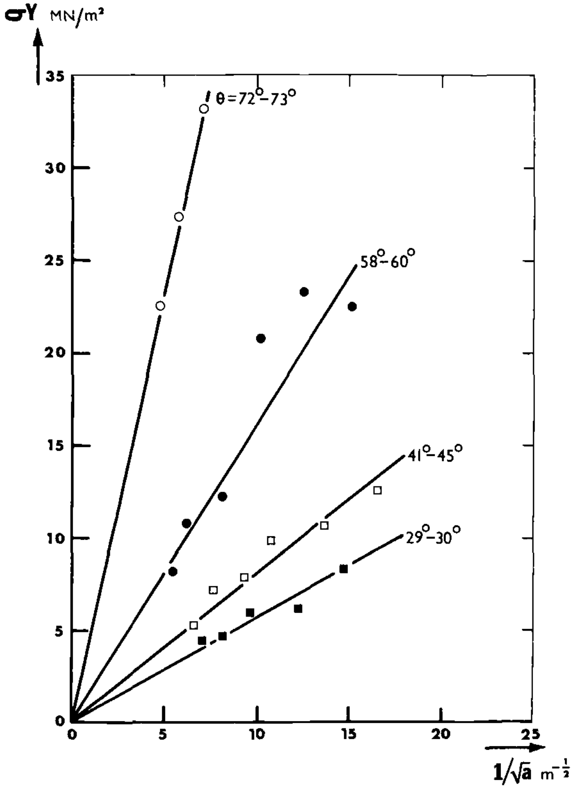

FIG. 7—*Mixed mode data for redwood (angled cracks).*

is to reduce the effect of $G_{\rm II}$ and hence $K_{\rm II}$. However, the data shown here indicate a consistency in $K_{\rm I}$ not in accordance with this theory. When $K_{\rm II}$ effects are noted (for example, see Ref *6*), it is probably the onset of shear failures which would be crack length dependent lines on the $K_{\rm I}$–$K_{\rm II}$ graphs of the type reported. The agreement of $K_{\rm IIc}/K_{\rm Ic}$ is presumably coincidental. The same must also be true of the agreement of Wu's locus of $K_{\rm I}$ and $K_{\rm II}$ and the isotropic solution of Knauss unless there is local non-colinear crack growth in balsa wood.

This work has given a very simple picture of mixed mode failure and raised several questions on the nature of the fractures produced. It also gives a new perspective on previously reported $K_{\rm IIc}$ values and on mixed mode data in anisotropic media. The pursuit of a valid Mode II failure has been unsuccessful since it appears that even when cracks are constrained to grow colinearly they do so in Mode I as in the isotropic case.

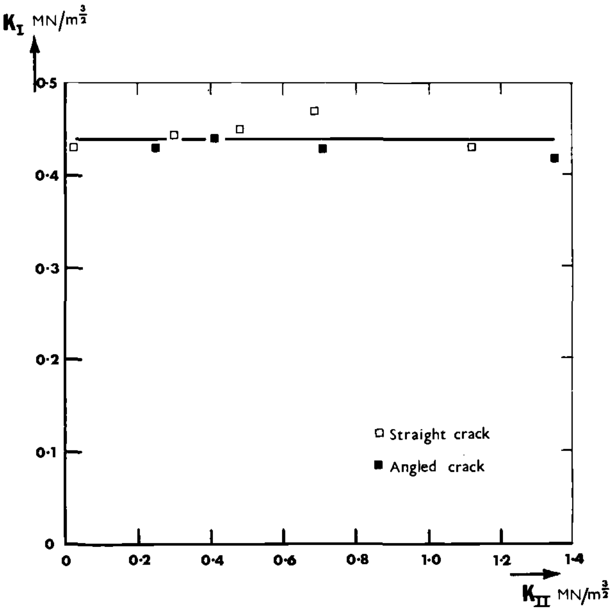

FIG. 8—$K_I - K_{II}$ *locus for redwood.*

APPENDIX

For Utile, the following elastic constants were used

$$a_{11} = \frac{1}{E_L} = 7.37 \times 10^{-5}\ \mathrm{m^2/MN}$$

$$a_{22} = \frac{1}{E_T} = 1.49 \times 10^{-3}\ \mathrm{m^2/MN}$$

$$a_{12} = -\frac{\nu_{LT}}{E_T} = -\ 8.20 \times 10^{-4}\ \mathrm{m^2/MN}$$

$$a_{66} = \frac{1}{G_{LT}} = 2.13 \times 10^{-3}\ \mathrm{m^2/MN}$$

From Eq 4 we have

$$G_I = K_I^2 \times \sqrt{\frac{a_{11}\,a_{22}}{2}} \times \left[\sqrt{\frac{a_{22}}{a_{11}}} + \frac{2a_{12} + a_{66}}{2a_{11}}\right]^{1/2}$$

$$G_I = K_I^2 \times 6.55 \times 10^{-4}\ \mathrm{MN/m}$$

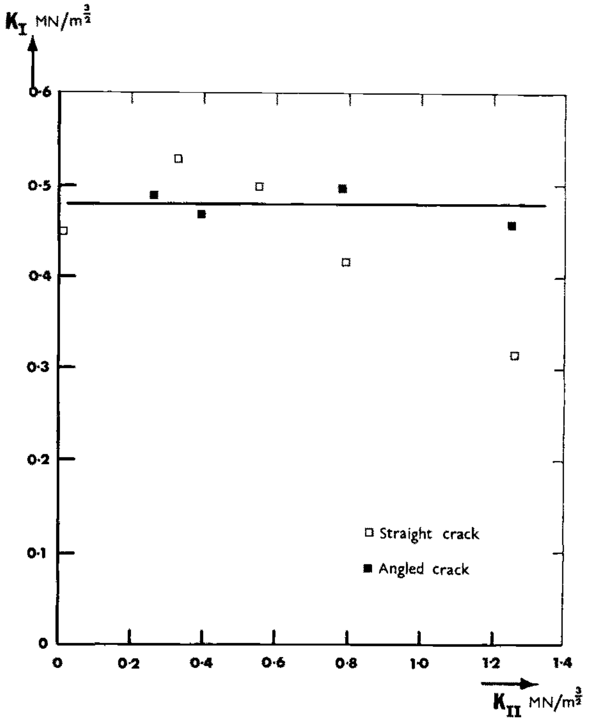

FIG. 9—K_I − K_{II} *locus for Utile.*

References

[1] Ewing, P. D. and Williams, J. G., *International Journal of Fracture Mechanics*, Vol. 8, 1972, pp. 441–446.

[2] Hussain, M. A., Pu, S. L., and Underwood, J. H. in *Fracture Analysis, ASTM STP 560*, American Society for Testing and Materials, 1974, pp. 2–28.

[3] Palaniswamy, K. and Knauss, W. G., "On the Problem of Crack Extension in Brittle Solids Under General Loading," Report SM 74–8, Graduate Aeronautical Laboratories, California Institute of Technology, 1974.

[4] Erdogan, F. and Sih, G. C., *Journal of Basic Engineering*, Vol. 85D, 1963, pp. 519–525.

[5] Sih, G. C. in *Methods of Analysis and Solutions of Crack Problems*, Nordhoff International Publishing, Leyden, 1973, pp. 21–24.

[6] Wu, E. M., *Journal of Applied Mechanics*, Vol. 34, Series E, No. 4, 1967, pp. 967–974.

[7] McKinney, J. M., *Journal of Composite Materials*, Vol. 6, Jan. 1972, pp. 164–166.

[8] Sih, G. C., Paris, P. C., and Irwin, G. R., *International Journal of Fracture Mechanics*, Vol. 1, No. 3, 1965, pp. 189–203.

[9] Mandell, J. F., McGarry, F. J., Wang, S. S., and Im, J., *Journal of Composite Materials*, Vol. 8, 1964, p. 106.

[10] Sanford, R. J. and Stonesifer, F. R., *Journal of Composite Materials*, Vol. 5, April 1971, pp. 241–245.

[11] Schniewund, A. P. and Pozniak, R. A., *Engineering Fracture Mechanics*, Vol. 2, 1971, pp. 223–233.

[12] Marshall, G. P., Coutts, L. H., and Williams, J. G., *Journal of Materials Science*, Vol. 9, 1974, pp. 1409–1419.

W. G. Clark, Jr.[1]

Applicability of the K_{Iscc} Concept to Very Small Defects

REFERENCE: Clark, W. G., Jr., "**Applicability of the K_{Iscc} Concept to Very Small Defects,**" *Cracks and Fracture, ASTM STP 601*, American Society for Testing and Materials, 1976, pp. 138–153.

ABSTRACT: Stress corrosion threshold (K_{Iscc}) data were generated for 180 and 215-ksi yield strength Type 4340 steel exposed to a 5 psig hydrogen sulfide gas environment. Tests were conducted with three-point-bend specimens containing both edge cracks and surface cracks ranging from 0.010 to 0.200 in. deep. The effect of defect size on K_{Iscc} was evaluated and the results compared to K_{Iscc} data generated with 1-in.-thick compact toughness specimens. Results show that absolute defect size (to as small as 0.010 in. deep) does not impose a limitation on the applicability of linear-elastic fracture mechanics concepts to small defect problems.

KEY WORDS: crack propagation, stress corrosion, fracture tests, toughness, steels, environment, hydrogen sulfide

The application of linear-elastic fracture mechanics concepts to the characterization of environment induced cracking under static loading conditions (stress corrosion cracking) provides a unique quantitative design approach to the prevention of stress corrosion failures. Specifically, it has been well established that the crack tip stress intensity factor, K_{I}, can be used to describe the mechanical driving force required for the development and growth of stress corrosion cracks [*1,2*].[2] Although the rate of cracking is sometimes an important engineering consideration, the rate of crack growth associated with stress corrosion is often very rapid and, once cracking begins, failure is imminent. For this reason, much of the current emphasis in the fracture mechanics approach to stress corrosion is focused on the determination of the critical stress intensity required for the onset of stress corrosion cracking. This parameter is commonly referred to as the stress corrosion threshold, K_{Iscc}, and is considered an inherent property of the particular material-environment system being

---

[1] Fellow engineer, Mechanics Department, Westinghouse Research Laboratories, Pittsburgh, Pa. 15235.

[2] The italic numbers in brackets refer to the list of references appended to this paper.

evaluated. Once the appropriate value of K_{Iscc} has been determined, this parameter is used in design considerations to establish the critical combination of applied stress and defect size below which stress corrosion cracking will not occur. This information can be used then to establish limiting design stresses and nondestructive inspection criteria.

Although the use of the K_{Iscc} parameter to characterize stress corrosion performance has been well established, one problem consistently develops when applying this concept to practical engineering structures. Specifically, questions arise concerning the applicability of the K_{Iscc} concept to small defect problems. Due to the fact that most potential stress corrosion problems involve high stress applications as well as high strength materials which exhibit low values of K_{Iscc}, the defect sizes of concern can be very small. For example, at a stress level of 100 ksi, the critical surface crack depth required to induce stress corrosion in a material which has a K_{Iscc} of 50 ksi $\sqrt{\text{in.}}$ is on the order of 0.06 in. Aside from the problems related to the detection of such small defects, the question remains as to how well the K_{Iscc} concept and the concepts of linear-elastic fracture mechanics in general apply to the analysis of fracture performance in the presence of such small defects.

A limited amount of work concerning the effect of crack size on fracture performance has been conducted by Brown and Srawley [*3*]. Their work shows that when the defect size being considered is on the order of at least fifty times the size of the respective crack tip plastic zone, ($r_p \approx 1/6\pi\ (K_I/\sigma_{ys})^2$), linear elastic fracture mechanics concepts apply to the analysis. However, these results were developed with cracks only as small as about 0.200 in. deep, and it has not yet been established if further limitations exist due to the absolute size of the defect itself. In addition, sufficient data have not been developed for a wide range of materials to substantiate the 50 to 1 crack size to plastic zone ratio requirement.

This paper presents the results of an investigation conducted to evaluate the applicability of the K_{Iscc} concept to small defect problems. K_{Iscc} data were generated for 180 and 215-ksi yield strength Type 4340 steel exposed to a 5-psig hydrogen sulfide gas environment. Tests with the 215-ksi yield strength material were conducted with three-point-bend specimens containing both edge cracks and surface cracks ranging from approximately 0.010 to 0.200 in. deep. Tests with the 180-ksi yield strength material were limited to edge-cracked specimens. The effect of defect size on the measured value of K_{Iscc} was evaluated and the results compared to K_{Iscc} data generated with 1-in.-thick compact toughness specimens.

Material

The material involved in this investigation consisted of quenched and tempered AISI 4340 type steel heat treated to 180 and 215-ksi yield strength levels. The 180-ksi yield strength material was supplied as 3-in.-thick forged plate and the 215-ksi yield strength material was supplied as 7.5-in.-diameter forged bar stock. The nominal chemical composition, heat treatment, and room temperature tensile properties of the forgings are summarized in Table 1.

Experimental Procedure

Specimen Preparation

The $K_{\rm Iscc}$ tests conducted in this investigation involved both edge-cracked and surface-cracked three-point-bend specimens. The respective specimen blank geometries are shown in Figs. 1 and 2. Note that two different length to depth ratio electrical discharge machining (EDM) surface notch configurations were used in the surface cracked tests (Fig. 2). Prior to $K_{\rm Iscc}$ testing, all specimen blanks were subjected to low stress sinusoidal cyclic loading in air to develop fatigue cracks at the notches. The stress intensity range associated with the precracking operation did not exceed 15 ksi $\sqrt{\rm in.}$ (R = 0.1). After precracking to various predetermined crack depths,[3] the specimen blanks were further machined to remove the crack starter notches. In both cases, the finished specimen height was 0.394 in. (0.100 in. of material was removed from the blank height). This specimen preparation technique allowed the development of extremely small precracks (to about 0.01 in. deep) and also eliminated any complications which might arise due to the influence of the crack starter notch on subsequent fracture behavior.

K_{Iscc} *Testing*

All $K_{\rm Iscc}$ testing reported in this investigation was conducted under very slow loading rate ($\dot{K} \approx 2$ ksi $\sqrt{\rm in.}$/min), rising load conditions in a 5-psig hydrogen sulfide gas environment (99.6 volume percent H_2S, typically 31-ppm water). This technique of $K_{\rm Iscc}$ testing essentially involves a procedure identical to the more conventional $K_{\rm Ic}$ test (ASTM Test for Plane-Strain Fracture Toughness of Metallic Materials (E 399-72)) except that a slower rate of loading is used and the specimen is exposed to the environment of interest while being loaded [*4*]. Under these conditions, the onset of cracking can be determined easily from the load-deflection test record, and the corresponding stress intensity level provides an accurate estimate of $K_{\rm Iscc}$. Although this method of estimating $K_{\rm Iscc}$ can have severe

---

[3] For the case of the surface notched specimens, the crack depth was estimated from crack length measurements made on the specimen surface.

TABLE 1—*Chemical composition, heat treatment, and room temperature tensile properties of materials investigated (modified Type 4340 steel).*

CHEMICAL COMPOSITION, WEIGHT PERCENT

Material	C	Mn	Si	P	S	Ni	Cr	Mo	V
180 yield	0.36	0.63	0.25	0.010	0.010	2.54	0.86	0.39	0.093
215 yield	0.41	0.81	0.27	0.006	0.009	1.88	0.91	0.37	. . .

HEAT TREATMENT

180 yield	austenitized 4 h at 1560°F, water quenched; double tempered 4 h at 1080°F and furnace cooled.
215 yield	austenitized 2 h at 1500°F, oil quenched; tempered at 600°F for 10 h and air cooled.

TENSILE PROPERTIES AT 75°F

	0.2% Yield Strength, ksi	Tensile Strength, ksi	Elongation in 2 in., %	Reduction in Area, %
180 yield	179	194	14	46
215 yield	215	250	10	38

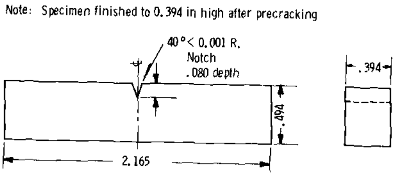

FIG. 1—*Three-point bend edge notched specimen blank.*

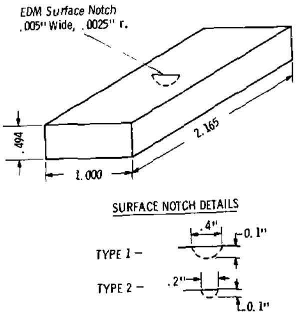

FIG. 2—*Surface notched bend specimen blank.*

limitations depending upon the rate of crack growth encountered just beyond reaching K_{Iscc},[4] sufficient data have been developed which clearly illustrate that this technique is directly applicable to high strength Type 4340 steel exposed to hydrogen sulfide gas. Specifically, long time "bolt loaded" K_{Iscc} tests involving 180 and 215-ksi yield strength 4340 steel exposed to hydrogen sulfide gas yield K_{Iscc} values identical to those developed as the result of rising load testing *[4]*.[5]

Figure 3 shows the three-point-bend test fixture used for the K_{Iscc} testing. A glass bell jar was used to contain the low pressure hydrogen sulfide gas. In all cases, a load-deflection (ram displacement) record was generated during the test, and this record was used to determine the onset of cracking. The stress intensity factor associated with the first indication of cracking (deviation from linearity on the load-deflection curve) was computed and is reported here as the apparent K_{Iscc}. All tests conducted in this study yielded linear load-deflection records and the onset of cracking was characterized by a sharp break in the test record. In all cases, the load corresponding to the onset of cracking was essentially identical to the failure load. This behavior reflects the extremely rapid rate of crack growth

---

[4] The faster the rate of crack growth, the more accurate this procedure becomes.

[5] Westinghouse Research Laboratories, unpublished data.

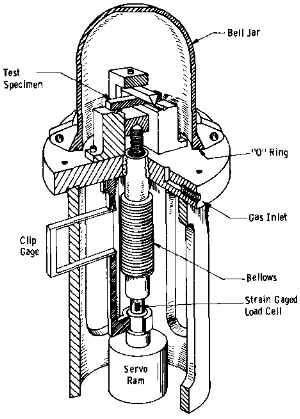

FIG. 3—*Fixture used for three-point bend testing in gaseous environments.*

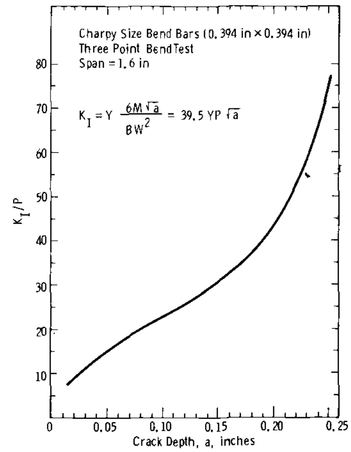

FIG. 4—K_I/P *calibration for charpy size bend bars.*

encountered in high strength 4340 steel exposed to hydrogen sulfide gas. The typical rate of crack growth was on the order of 5 in./min. No evidence of plastic flow prior to the onset of cracking was observed in any test.

The stress intensity expression used to compute the apparent K_{Iscc} values for the edge-notched bend specimens was that developed by Gross and Srawley [*3,5*]. A graphical presentation of this expression for the Charpy size bend specimens and 1.6-in. span used in this investigation is presented in Fig. 4. The stress intensity calibration used to evaluate the

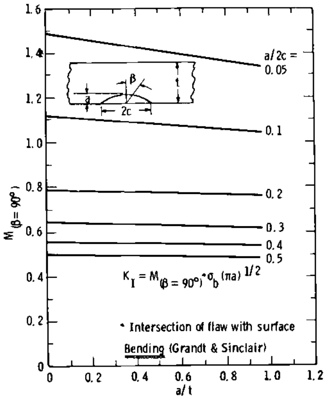

FIG. 5—*Stress intensity calibration for a surface flaw in bending (β = 90 deg).*

surface-flawed bend tests is illustrated in Fig. 5 [*6*]. Note that this analysis yields the stress intensity at the point of intersection of the crack with the specimen surface (β = 90 deg).

Experimental Results

The results of the slow loading rate, rising load K_{Iscc} tests conducted with the 180 and 215-ksi yield strength 4340 steel edge-notched bend specimens, are presented in Figs. 6 and 7, respectively. The load at failure (onset of crack growth) is plotted as a function of crack depth. The apparent K_{Iscc} values measured in each test are given in parentheses and the smooth curve represents the load versus crack depth relationship calculated for a K_{Iscc} value equivalent to the average K_{Iscc} for all test results presented on the respective figure. Note that for both materials, the average "a versus P" curve provides an excellent fit of all the data.

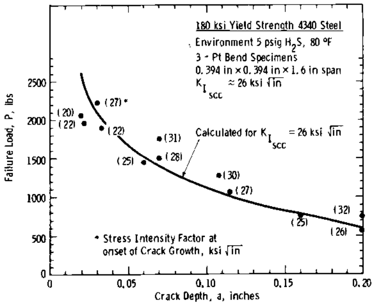

FIG. 6—*Failure load versus crack depth, 180-ksi σ_{ys} 4340 steel (edge-notched specimens).*

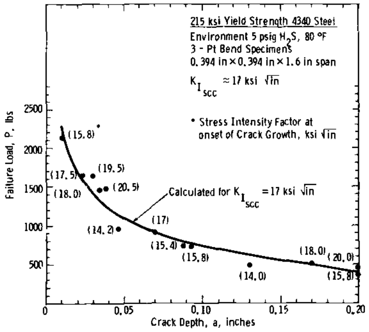

FIG. 7—*Failure load versus crack depth, 215-ksi σ_{ys} 4340 steel (edge-notched specimens).*

Figure 8 presents the apparent K_{Iscc} versus crack depth for both the 180 and 215-ksi yield strength materials. Note that for the 180-ksi yield material, the K_{Iscc} values ranged from 20 to 32 ksi $\sqrt{in}$. with an average of 26 ksi $\sqrt{in}$. The K_{Iscc} data generated for the 215-ksi yield strength material ranged from 14 to 20.5 ksi $\sqrt{in}$. with an average of 17 ksi $\sqrt{in}$. Figure 9 shows the fracture appearance of several 215-ksi yield strength 4340 steel edge-notched bend specimens used to evaluate the effects of defect size on K_{Iscc}. Note the absence of "shear-lip" development and the straight crack fronts associated with the precracks.

Table 2 presents the results of the K_{Iscc} testing conducted with the 215-ksi yield strength 4340 steel surface-cracked bend bars. Note that surface cracks ranging from 0.008 in. deep by 0.054 in. long to 0.180 in. deep by 0.618 in. long were included in these tests. The crack depth to specimen thickness ratios (a/t) ranged from 0.02 to 0.36, and the crack depth to length ratios ($a/2c$) ranged from 0.078 to 0.324. Note also that three tests (169-21, 23, and 33) were conducted with specimens 0.494 in. high rather than 0.394 in. high. In these tests, the crack starter notches

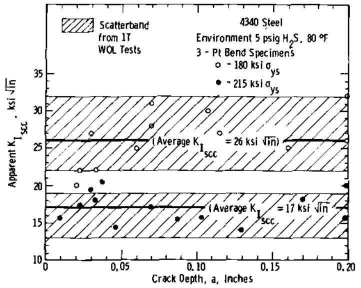

FIG. 8—K_{Iscc} *versus crack depth (edge-notched specimens).*

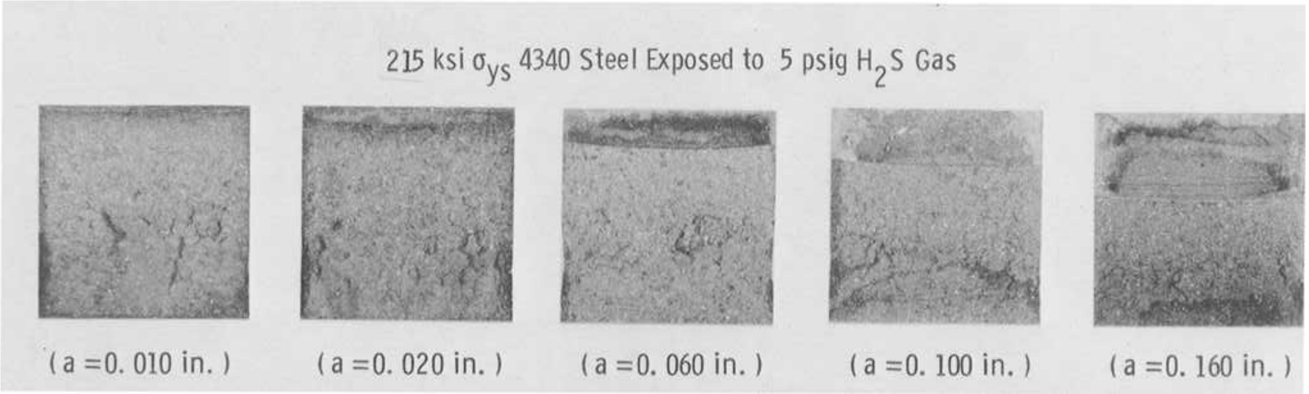

FIG. 9—*Fracture appearance of bend specimens used to evaluate small defect* K_{Iscc}.

were not removed prior to K_{Iscc} testing. Table 2 shows that the K_{Iscc} values computed for $\beta = 90$ deg (the stress intensity at the intersection of the defect with specimen surface, Fig. 5, ranged from 12.5 to 19.0 ksi $\sqrt{\text{in.}}$ with an average value of 15 ksi $\sqrt{\text{in.}}$ In those cases where the surface-crack length ($2c$) exceeded one half of the specimen width (Specimens 169-21 and 23), a width correction based on data available for the center-cracked plate in tension problem was incorporated into the analysis [*3*]. This correction amounted to about a 20 percent increase in the stress intensity factor over that computed from Fig. 5. Figure 10 shows the apparent K_{Iscc} versus crack depth relationship for the 215-ksi yield strength 4340 steel surface-cracked specimens exposed to 5-psig H_2S gas. Figures 11 and 12 show the typical fracture appearance of the surface-cracked specimens. Note the uniform development of the fatigue cracks from the crack starter notches (Fig. 11).

Discussion

The K_{Iscc} versus crack depth data summarized in Figs. 8 and 10 for the 215-ksi yield strength 4340 steel clearly show the absence of a crack size effect on the apparent K_{Iscc} as measured with edge-cracked and surface-cracked bend bars. In both cases, the K_{Iscc} values measured in the presence of defects ranging from about 0.01 to 0.20 in. deep were essentially identical. The grand average of all K_{Iscc} data generated in this investigation with the 215-ksi yield strength material (Figs. 8 and 10) is 16 ksi $\sqrt{\text{in.}}$ with a range of 12.5 to 20.5 ksi $\sqrt{\text{in.}}$ for twenty-two tests (range of variability is approximately ±25 percent). These results are essentially identical to the K_{Iscc} data generated with 1-in.-thick compact toughness specimens prepared from the same heat of material (average $K_{Iscc} = 15$ ksi $\sqrt{\text{in.}}$, range 13 to 19 ksi $\sqrt{\text{in.}}$) (see footnote 5).

The K_{Iscc} data generated for the 180-ksi yield strength material (Fig. 8, average $K_{Iscc} = 26$ ksi $\sqrt{\text{in.}}$, range 20 to 32 ksi $\sqrt{\text{in.}}$, variability ±23 percent) do not clearly reveal the absence of a crack size effect on K_{Iscc}. Specifically, the lowest values of K_{Iscc} measured were those associated with the smallest cracks. This would imply that for the case of cracks on the order of 0.02 in. to 0.03 in. deep, the stress intensity expression used to compute K_{Iscc} underestimates the crack tip stress conditions. However, in view of the amount of scatter in the K_{Iscc} data encountered at all crack lengths studied, it is possible that the lower values of K_{Iscc} measured for the shallow cracks are only a reflection of data scatter. In fact, an extensive amount of rising load and long time bolt loaded K_{Iscc} data generated with 1-in. compact toughness specimens of the same material show that the K_{Iscc} in hydrogen sulfide gas ranges from 22 to 32 ksi $\sqrt{\text{in.}}$ with an average value of 25 ksi $\sqrt{\text{in.}}$ [*4*]. In view of these results, it appears that like the 215-ksi yield material, cracks ranging from about

TABLE 2—*Summary of surface flawed bend tests.*[a]

Specimen	Crack Size, in.	Bar Thickness, t, in.	Failure Load, lb	Failure Stress, ksi[b]	a/t	$a/2c$	K_{Iscc},[c] ksi $\sqrt{\text{in.}}$
169-21	0.180 by 0.618	0.494	2000	19.2	0.365	0.292	12.6[d]
169-22	0.058 by 0.448	0.394	2400	36.0	0.148	0.130	15.4
169-23	0.139 by 0.507	0.494	2500	24.0	0.280	0.275	13.0[d]
169-24	0.030 by 0.294	0.394	2980	44.8	0.076	0.101	15.5
169-25	0.013 by 0.167	0.394	4125	62.0	0.033	0.078	16.5
169-31	0.019 by 0.279	0.394	3690	54.0	0.048	0.068	19.0
169-32	0.008 by 0.054	0.394	5060	76.0	0.020	0.148	12.5
169-33	0.107 by 0.333	0.494	4625	44.5	0.218	0.324	15.8
169-34	0.015 by 0.110	0.394	4310	64.8	0.038	0.136	14.2
							avg (15)

[a] Three-point bend tests, 1 in. wide, 1.6-in. span, 215-ksi yield strength; 4340 steel exposed to 5-psig H_2S gas, loading rate ($K \approx 2$ ksi $\sqrt{\text{in.}}$/min).

[b] Outer fiber bending stress.

[c] Calculated for $\beta = 90$ deg, intersection of flaw with surface.

[d] Includes width correction.

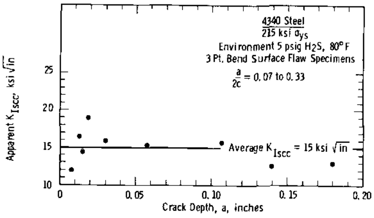

FIG. 10—K_{Iscc} *versus crack depth (surface flaw specimens).*

0.02 to 0.200 in. deep do not have a significant effect on the measured value of K_{Iscc} for the 180-ksi yield strength 4340 steel. Consequently, we can conclude that at least for the yield strengths and respective K_{Iscc} levels involved in this study, the existing concepts of linear elastic fracture mechanics and specifically the K_{Iscc} parameter can be used to characterize the fracture behavior in the presence of very small defects. This conclusion must be qualified as to both the material strength level (σ_{ys}) and the K_{Iscc} values being considered since it is likely that the applicability of existing fracture mechanics concepts to small defects is limited by the relationship between the defect size and the respective plastic zone size (r_p) which is proportional to the material's yield strength and the applied K_I level [$r_p \approx 1/6\pi\ (K_I/\sigma_{ys})^2$]. Thus, it is reasonable to assume that when the defect being considered is on the order of the same size as the respective plastic zone, the plastic zone will engulf the defect and linear elastic fracture mechanics concepts will not apply directly. For the case of the Type 4340 steels involved in this investigation, the plastic zones developed at the respective K_{Iscc} values are about 0.0003 and 0.001 in. for the 215 and 180-ksi yield strength materials, respectively. Thus, the data reported here for the smallest defects studied represent about a 25 to 1 ratio between defect size and plastic zone. Consequently, this study shows that when the defect size-plastic zone ratio is at least on the order of 25 to 1, fracture mechanics concepts can be used to accurately describe the crack tip stress conditions. This observation varies somewhat from the work of Brown and Srawley which indicates that a 50 to 1 defect size-plastic zone ratio is required to produce consistent K_{Ic} values for high strength steels [*3*]. This variation in results may reflect differences in material properties as well as other factors, and it is obvious that additional information is required before a firm limit on defect size-plastic zone ratio can be established. The determination of this limiting ratio becomes increasingly important for the case of lower strength alloys which exhibit susceptibility to stress corrosion cracking. Specifically, as the plastic zone size associated with the onset of cracking increases, the

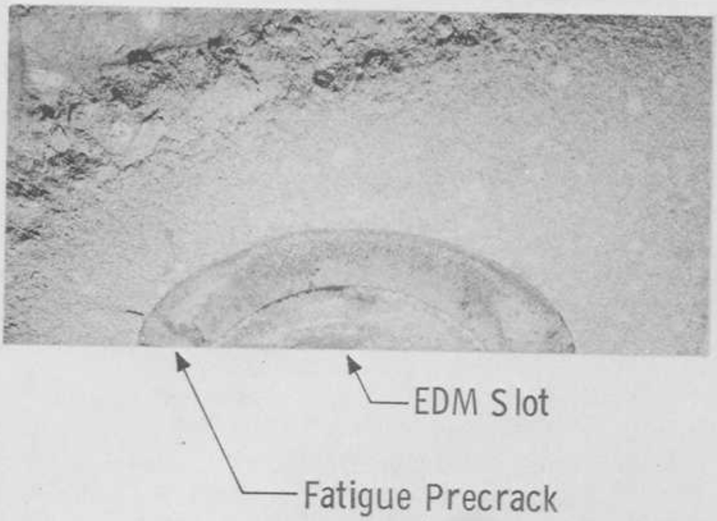

4:1 Crack Starter Notch

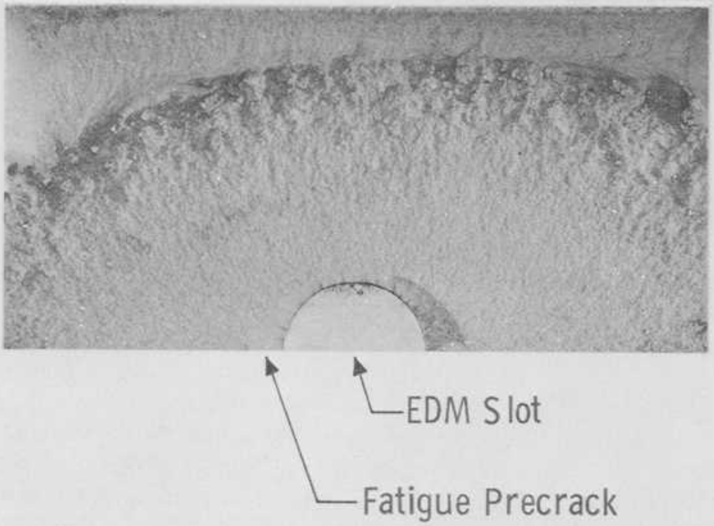

2:1 Crack Starter Notch

FIG. 11—*Surface flawed specimens used to evaluate small defect* K_{Iscc}.

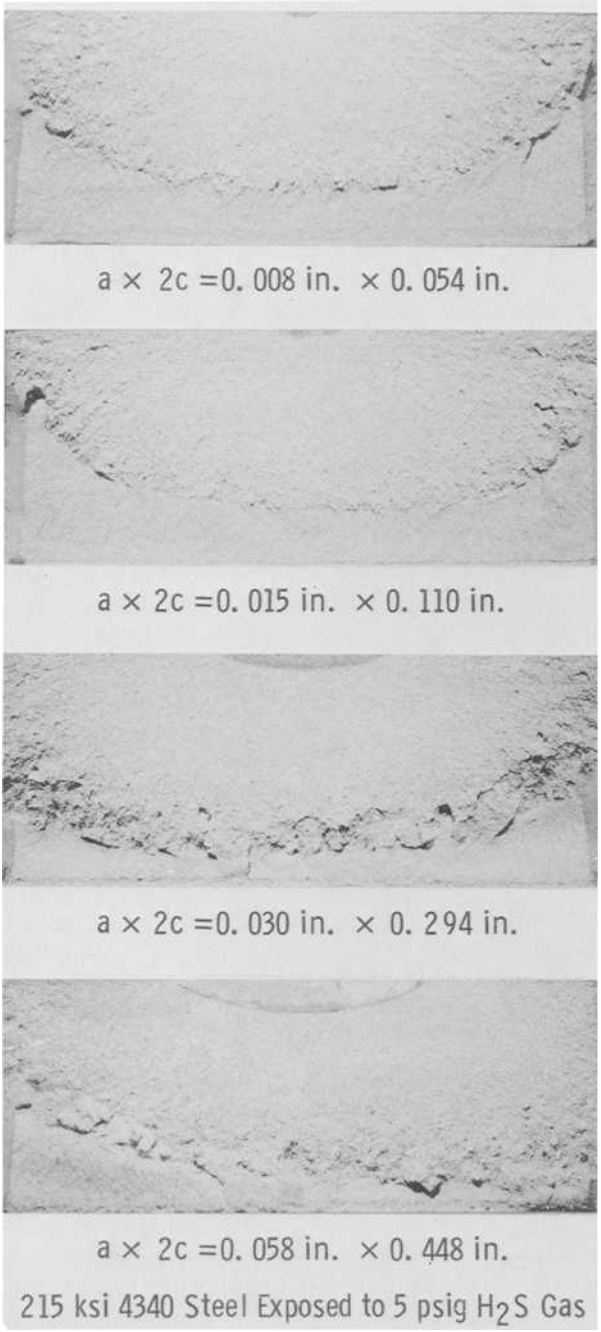

FIG. 12—*Fracture appearance of surface flawed specimens used to evaluate small defect* K_{Iscc}.

limiting size of the defect which can be characterized in the fracture mechanics analysis also increases, thus limiting the applicability of the fracture mechanics approach to design. Additional testing involving lower strength ferrous alloys is currently in progress, and it is expected that the results of this work will more accurately establish the limits of the applicability of linear elastic fracture mechanics concepts to small defect problems.

It was noted previously that the stress intensity calibration developed by Grandt and Sinclair for the case of β = 90 deg (Fig 5, K_I at the point along the crack front where the crack intersects the specimen surface) was used to compute the K_{Iscc} values reported for the 215-ksi yield strength 4340 steel surface-cracked specimen (Table 2). The K_{Iscc} values were also computed with the stress intensity calibration developed by Shah and Kobayashi for the case of β = 0 deg (K_I at the deepest point along the surface crack front) [7]. However, for the crack sizes and shapes involved in this program, the β = 0-deg analysis generally yielding K_{Iscc} values 20 percent lower than those determined from the β = 90-deg analysis. In a few cases, both analyses yielded the same values. Since the β = 90-deg analysis yielded results similar to the edge-cracked bend bars and the 1-in.-thick compact toughness tests, it was concluded that this analysis best represents the fracture behavior encountered for the conditions studied in this program.

The K_{Iscc} data generated in this program as well as the data developed with the 1-in.-thick compact toughness specimens indicate that for relatively high strength steels exposed to a very reproducible environment, we can expect as much as ±25 percent variability in K_{Iscc}. This extensive amount of data scatter implies that the onset of stress corrosion cracking is very susceptible to small variations in metallurgical conditions. Obviously, additional information as well as a detailed examination of existing K_{Iscc} data is required to determine if ±25 percent variability is typical of K_{Iscc} test results. However, in view of the large amount of variability encountered in this program, it is apparent that when characterizing the K_{Iscc} of a given material-environment system, a sufficient number of tests must be conducted in order to develop a statistically accurate value suitable for use in design.

Summary and Conclusions

The results of this investigation show that the K_{Iscc} concept and the concepts of linear-elastic fracture mechanics in general are applicable to the characterization of fracture performance in the presence of defects as small as 0.010 in. deep. Thus, we can conclude that absolute defect size itself (to as small as 0.010 in.) does not impose a limitation on the applicability of fracture mechanics to design considerations. However, it does appear that the ratio of defect size to crack tip plastic zone size should impose a limitation on the fracture mechanics analysis of small defect problems. The results of the work presented here show that when the defect size-plastic zone ratio is at least on the order of 25 to 1; fracture mechanics concepts are directly applicable to the problem. Further testing with lower strength materials is required to more accurately establish the lower bound of this limitation.

It has been shown that even for relatively high strength steels exposed to a reproducible environment, the K_{Iscc} can vary by as much as ±25 percent. This observation indicates that K_{Iscc} is strongly dependent on small variations in metallurgical conditions and, therefore, several tests are required to establish useful K_{Iscc} values.

The K_{Iscc} data generated with surface-cracked bend bars show that the stress intensity calibrations developed by Grandt and Sinclair for the case of the stress intensity at the point of intersection of the defect with the specimen surface accurately describes the fracture performance encountered in this study. Evaluation of the test results in terms of the stress intensity at the deepest point of the surface flaw generally yielded lower K_{Iscc} values.

Acknowledgments

The experimental testing associated with this investigation was conducted by P. J. Barsotti and W. H. Halligan under the direction of D. R. Young of the Fracture Mechanics Laboratory. The work was sponsored by the Westinghouse Large Rotating Apparatus Division.

References

[*1*] Johnson, H. H. and Paris, P. C., "Sub-critical Flaw Growth," *Engineering Fracture Mechanics*, Vol. 1, No. 1, 1968.

[*2*] Wei, R. P., Novak, S. R., and Williams, D. P., *Materials Research and Standards*, Vol. 12, No. 9, 1972, p. 25.

[*3*] Brown, W. F., Jr. and Srawley, J. E., *Plane Strain Crack Toughness Testing of High Strength Metallic Materials, ASTM STP 410*, American Society for Testing and Materials, 1967.

[*4*] Clark, W. G., Jr. and Landes, J. D., "An Evaluation of Rising Load K_{Iscc} Testing," presented at the Symposium on New Approaches to Stress Corrosion Testing, 1975 Annual Meeting of the American Society for Testing and Materials, Montreal, 1975.

[*5*] Gross, B. and Srawley, J. E., "Stress-Intensity Factors for a Single-Edge-Notch Specimen in Bending or Combined Bending and Tension by Boundary Collocation of a Stress Function," Technical Note D-2603, National Aeronautics and Space Administration, Jan. 1965.

[*6*] Grandt, A. F., Jr. and Sinclair, G. M. in *Stress Analysis and Growth of Cracks, ASTM STP 513*, American Society for Testing and Materials, 1972, p. 37.

[*7*] Shah, R. C. and Kobayashi, A. S. in *Stress Analysis and Growth of Cracks, ASTM STP 513*, American Society for Testing and Materials, 1972, p. 3.

Julius Mautz[1] *and Volker Weiss*[1]

Mean Stress and Environmental Effects on Near Threshold Fatigue Crack Growth

REFERENCE: Mautz, Julius and Weiss, Volker, "**Mean Stress and Environmental Effects on Near Threshold Fatigue Crack Growth,**" *Cracks and Fracture, ASTM STP 601,* American Society for Testing and Materials, 1976, pp. 154–168.

ABSTRACT: The effect of mean stress and environment on the threshold and near threshold fatigue crack propagation behavior has been studied for D6ac steel and for 7050-T73651 aluminum. Fatigue crack propagation experiments were conducted in the range of 10^{-7} to 10^{-9} in./cycle (2.5×10^{-9} to 2.5×10^{-11} m/cycle) at 375 Hz.

A mean stress effect on the threshold stress intensity factor range, ΔK_{th}, is only observed for low mean stresses, in the regime of the minimum stress intensity factor, K_{min}, $0 \leq K_{min} \leq 2$ ksi $\sqrt{\text{in.}}$ (2.2 $\text{MN/m}^{3/2}$), typically $0 \leq R \leq 0.5$. For higher values of K_{min}, the fatigue crack propagation threshold is controlled by ΔK_{th}. For the high test frequency used, no effects of humid argon and room air as compared to a dry argon environment were observed on the fatigue crack propagation threshold ΔK_{th}. Environmental effects were noted in the near threshold region. For D6ac steel room air produced the highest crack propagation rate while dry and wet argon produced identical but lower crack propagation rates for the same ΔK values. For 7050-T73651 alumium both wet argon and room air environments produced the highest crack propagation rates, while dry argon produced lower crack propagation rates. Changing the test frequency for 375 to 100 Hz had no noticeable effect on the threshold and near threshold region results for D6ac steel in room air but in dry argon 100 Hz gave slightly higher crack propagation rates with respect to 375 Hz.

KEY WORDS: fatigue (materials), crack propagation, stress ratio, environmental tests, argon, alloy steels, aluminum alloys, fractures (materials)

An understanding of the threshold condition for fatigue crack propagation is of both fundamental and practical concern. The fundamental aspect relates to the existence of a threshold below which a crack will not propagate in fatigue. This question requires a deeper understanding of the

---

[1] Research assistant and professor, respectively, Department of Chemical Engineering and Materials Science, Syracuse University, Syracuse, N. Y. 13210.

micromechanical processes at and near the crack tip. The practical aspects are obvious to the materials engineer and to the designer, particularly in connection with the requirements for quality control procedures for parts that are to be designed for long lives in the range of 10^{10} to 10^{12} cycles. The sharp increase in the number of papers dealing with the subject of fatigue crack propagation threshold attests to these concerns. A partial bibliography on the subject has recently been published by Weiss and Lal [*1*][2] which contains 75 references.

Models proposed to date fall into two categories, those based on a critical strength concept and those based on a crack closure concept. The present work is concerned with an experimental study of the effect of mean stress and environment on fatigue crack propagation in the near threshold region for an ultra high strength steel and a high strength aluminum alloy. Threshold has been shown to vary with mean stress [*2–5*], temperature [*3*], and frequency [*5*]. Pook [*6*] has shown environmental effects for brine, tap water, and oil (SAE 30) on mild steel. No environmental effects were reported by Paris [*3*] for A533-B-1 steel in distilled water or by Bucci [*4,7*] for A577 steel in distilled water and in dry hydrogen and for Ti-6Al-4V in dry argon.

Experimental

The test materials were D6ac steel and 7050-T73651 aluminum. The chemical composition and pertinent mechanical properties data are given in Table 1. The specimen is illustrated in Fig. 1. Crack propagation data were taken in the region $0.3 < a/W < 0.7$ and the stress intensity factor was calculated from [*8*]

$$K = \frac{P}{B\sqrt{W}}\left[29.6\left(\frac{a}{W}\right)^{1/2} - 185.5\left(\frac{a}{W}\right)^{3/2} + 655.7\left(\frac{a}{W}\right)^{5/2} - 1017\left(\frac{a}{W}\right)^{7/2} + 638.9\left(\frac{a}{W}\right)^{9/2}\right]$$

where

K = stress intensity factor,
P = applied load,
B = thickness,
W = width, and
a = crack length.

The specimen thickness was nominally 0.10 in. (2.5 mm) for both materials. The original stock size of the aluminum alloy was 0.25 in. (6.35 mm) and that of the D6ac was 0.187 in. (4.75 mm). The specimen orientation was longitudinal-transverse (L-T), that is, crack growth oc-

---

[2] The italic numbers in brackets refer to the list of references appended to this paper.

TABLE 1—*Chemical composition and mechanical properties of the materials studied.*

Material	Chemical Composition, %	Yield Strength, ksi(MN/m^2)	Ultimate Tensile Strength, ksi(MN/m^2)	K_Q, ksi $\sqrt{in.}$ $(MN/m^{3/2})$
D6ac Steel (HRC 50) 1675°F (913°C) for 40 min air cooled, 1575°F (857°C) for 40 min oil quenched 400°F (205°C) for 2 h 500°F (260°C) for 2 h	0.48C, 0.83Mn 0.010P, 0.005S 0.28Si, 0.15Cu 0.58Ni, 1.06Cr 1.01Mo, 0.10V Fe, balance	238 (1640)	286 (1970)	34.5 (37.9) for 1.00-in. (25.4-mm) thick compact specimens
7050-T73651 aluminum	0.12Si max, 0.15Fe max 2.0 to 2.8Cu, 0.10Mn max 1.0 to 2.6Mg, 0.04Cr max 5.7 to 6.7Zn, 0.06Ti max 0.08 to 0.15Zr others, 0.15 max Al, balance	64 (441)	72 (497)	32.2 (35.4) for 1.00-in. (25.4-mm) thick compact specimens

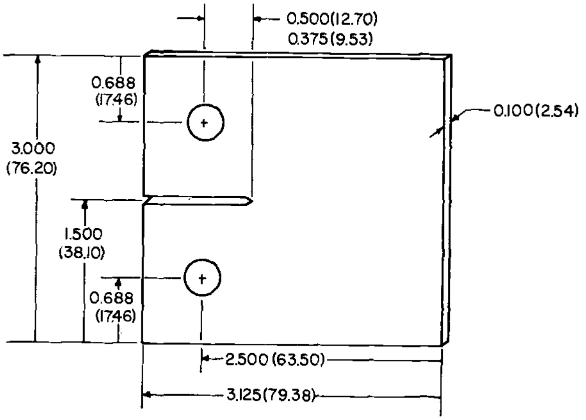

FIG. 1—*Dimensions of compact specimen in inches (millimetres).*

curred at right angles to the rolling direction. Nine specimens were involved in the program.

The tests were conducted at 375 Hz in an electrodynamic shaker. The load was obtained from a quartz load crystal connected in series just above the upper specimen holder. Displacements were monitored with the help of two accelerometers located near each end of the specimens. The mean load was applied with dead weights connected in series with a soft spring so as not to affect the alternating load. The dead weight system allowed the mean load to be changed easily.

Crack growth was followed with a nine-power traveling microscope on the polished specimen surface. The crack length could be read with an accuracy of 0.001 in. (0.025 mm). At low $K_{\min}$ values and in the threshold region it occasionally became very difficult to locate the crack tip particularly with the aluminum alloy. In these cases, crack growth was similar to that observed in initiation phases where slip lines mask the exact crack tip location for a while. After a relatively short time, approximately 100 000 cycles, the crack tip appeared clearly delineated. This uncertainty may have contributed to the scatter in the experimental data.

Crack initiation was accomplished in the shaker with the lowest possible combination of mean and alternating load. These conditions were maintained until the operating crack length of $a/W = 0.3$ was reached. Data were taken by reducing the load successively in approximately 10 percent increments. Crack extensions of the order of 0.03 in. (0.75 mm) were produced between load reductions in the high load region and of approximately 0.005 in. (0.125 mm) in the low load region. Near the threshold region the incremental load drop chosen was considerably less than 10 percent and principally determined by the running time, approximately 2 h (2.7×10^6 cycles). In the air environments, threshold was considered to be obtained when the crack growth curves became nearly vertical. This corresponds to a crack growth rate of nearly 10^{-8} in./cycle (2.5×10^{-10} m/cycle). Since some of the curves for dry and wet argon did not show a vertical section, threshold was considered to be obtained for crack growth rates of less than 10^{-8} in./cycle (2.5×10^{-10} m/cycle). For the major part of the study the load program for each specimen was such that da/dN values could be obtained as a function of the stress intensity factor range, ΔK, with the minimum stress intensity factor, $K_{\min}$, remaining constant.[3]

There were several reasons for conducting constant $K_{\min}$ tests rather than the conventional constant R tests. Constant $K_{\min}$ tests decrease the interaction effects which occur in a decreasing load sequence. Testing control is increased, since crack growth at large constant R values would be limited to small values of ΔK. There also appears to be an added importance to an absolute stress intensity factor in the high and low crack growth rate ranges with respect to the middle range. For large rates, K_Q or K_{Ic} is relevant whereas at threshold $K_{\min}$ or $K_{\max}$ is relevant, that is, documented support for a constant $K_{\max}$ hypothesis [5,9] at threshold. Also K_Q and K_{Iscc}, which may be relevant since long testing times are usually involved for very long life applications, can easily be denoted on ΔK_{th} versus $K_{\min}$ diagrams. The main disadvantage in choosing a $K_{\min}$ control is in the life calculation of nonredundant structures where R remains constant. For this case "constant R plots" could be obtained from the data by interpolating between the proper constant $K_{\min}$ plots for the desired values of ΔK.

All tests were conducted at room temperature. The environments were laboratory air (relative humidity approximately 40 to 50 percent), dry argon, and moist argon (relative humidity larger than 85 percent). For the controlled atmospheric tests the specimen was enclosed in a flexible plastic chamber which would not affect the load and which had a plate glass window to allow observation of crack advance. A continuous flow of argon slightly above atmospheric pressure was maintained to avoid leakage of air into the test chamber. To achieve dry argon, the gas was pumped through a 1.3-m-long glass tube filled with ⅛-in. molecular sieves. Before starting each test, the system was checked for leaks and the specimen was "dried" for at least 1 h with infrared lamps (approximately 140°F (60°C)).

---

[3] For a check on the testing procedure, eight tests were conducted at a constant mean load with load reduction of less than 3 percent. In this case, $K_{\min}$ increases, whereas for constant R tests, $K_{\min}$ decreases with a decrease in the alternating load. The results are given in Figs. 4 and 8 which show only a small decrease at low $K_{\min}$. The reproducibility of the results can be observed in Figs. 2, 3, and 6.

Results and Discussion

The experimental results for D6ac steel are presented in Figs. 2 through 5 and for 7050-T73651 aluminum in Figs. 6 through 8. Data on the effect of test frequency on D6ac steel are presented in Fig. 9.

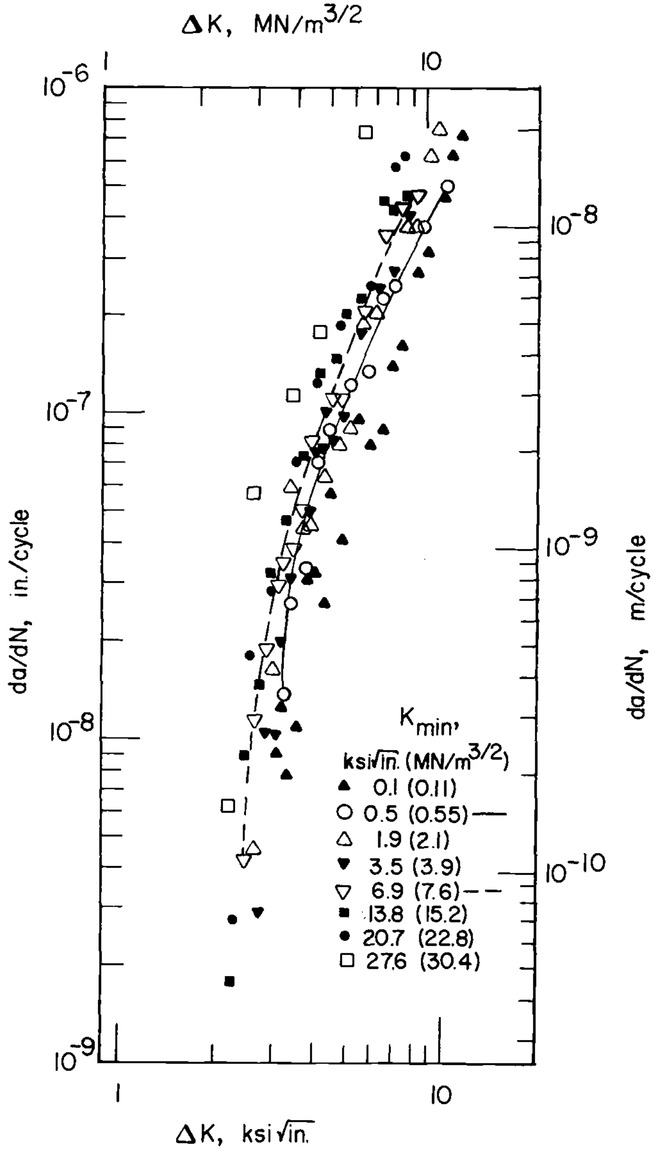

FIG. 2—*Effect of K_{min} on fatigue crack growth rate of D6ac steel (HRC 50) in room air and at 375 Hz.*

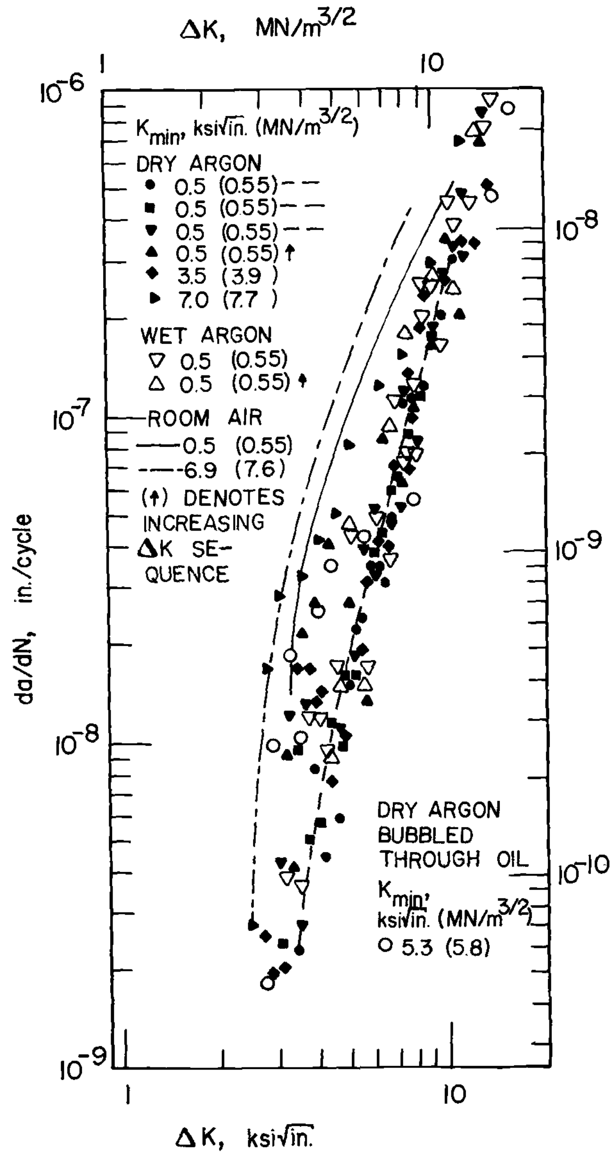

FIG. 3—*Environmental effect on fatigue crack growth rate of D6ac steel (HRC 50) at 375 Hz.*

Mean Stress Effects

For both materials the threshold condition appears to be dominantly controlled by ΔK_{th}, except for the region of low K_{min} values, approaching $K_{min} = 0$, where a maximum stress intensity factor, K_{max}, control might operate (Figs. 4, 5, and 8). This effect is more pronounced in the

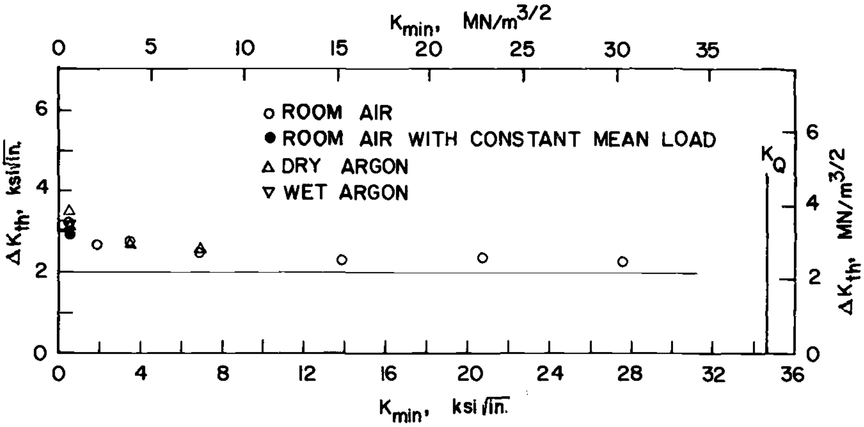

FIG. 4—*Threshold stress intensity factor range versus minimum stress intensity factor for D6ac steel (HRC 50) at 375 Hz.*

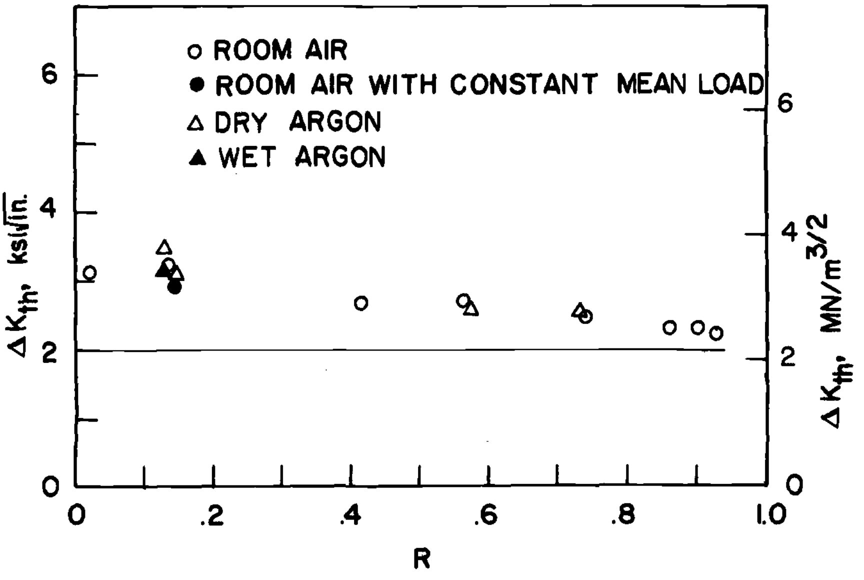

FIG. 5—*Threshold stress intensity factor range versus* R *for D6ac steel (HRC 50) at 375 Hz.*

aluminum alloy than in the steel, as also indicated by Figs. 2 and 6 which depict the near threshold region in terms of *da/dN* versus ΔK plots. The range where a K_{max} criterion for threshold might apply is limited to K_{min} < 2 ksi $\sqrt{in.}$ (2.2 MN/m$^{3/2}$), that is R typically <0.5. The K_{max} control mechanism has been supported by crack closure [*5*], the theoretical strength model [*9*], and an environmentally based model [*10*].

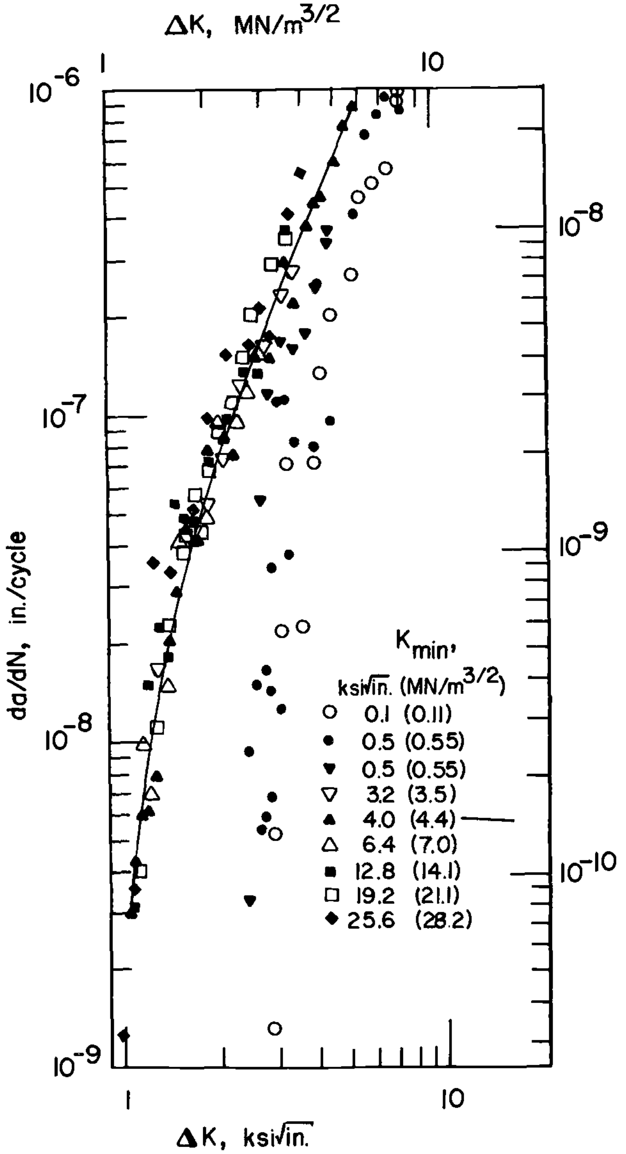

FIG. 6—*Effect of* K_{min} *on fatigue crack growth rate of 7050-T73651 aluminum in room air at 375 Hz.*

The dominance of ΔK control of fatigue crack propagation threshold for high values of K_{min} suggests some form of plastic relaxation in the near crack tip region. This means that the plastic zone size as calculated from K_{max} has no effect on the cyclic plastic zone size due to ΔK. This is

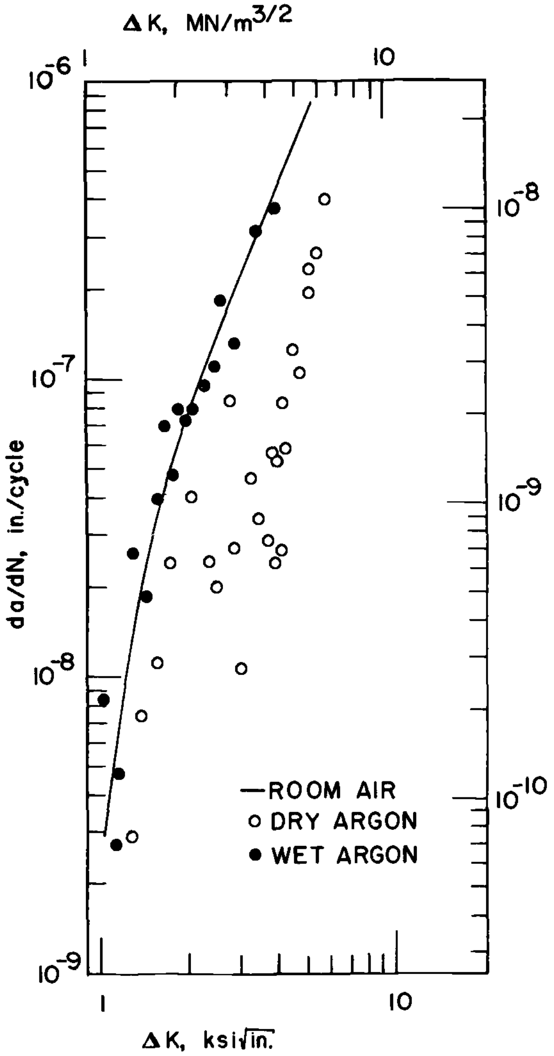

FIG. 7—*Effect of environment on fatigue crack growth rate of 7050-T73651 aluminum with* K_{min} *= 4 ksi* $\sqrt{\text{in.}}$ *(4.4 MN/m*$^{3/2}$*) and at 375 Hz.*

similar to the mechanism operating in the middle region of fatigue crack growth rates where *R* has little effect on the crack growth curves.

Environmental Effects

Environmental effects at the high testing frequency of 375 Hz due to the presence or absence of water vapor and air are observed in the near threshold region, but not for threshold conditions as defined by crack

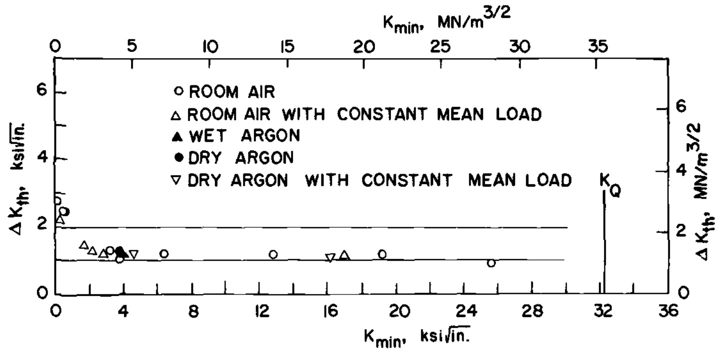

FIG. 8—*Threshold stress intensity factor range versus* K_{min} *for 7050-T73651 aluminum at 375 Hz.*

propagation rates at or below 3×10^{-9} in./cycle (7.5×10^{-11} m/cycle). The effects observed in D6ac steel differ from those observed in 7050-T73651 aluminum. In the former (Fig. 3), the crack propagation rates on specimens conducted in dry or wet argon were less than those observed on specimens tested in air for the same ΔK values in the region da/dN between 10^{-8} in./cycle (2.5×10^{-10} m/cycle) and 10^{-6} in./cycle (2.5×10^{-8} m/cycle). For the aluminum alloy, on the other hand (Fig. 7), the crack propagation rates obtained in air and in wet argon were approximately the same, while those obtained in dry argon were substantially lower, for the same ΔK values in the da/dN region between 10^{-8} and 10^{-6} in./cycle (2.5×10^{-10} and 2.5×10^{-8} m/cycle). From the present data (Fig. 3), it appears that D6ac steel is not very sensitive to the presence of water vapor as far as the fatigue crack growth rate near threshold is concerned.

It has been shown that water, either in vapor or liquid form, can have a significant effect on the crack propagation rates in alumium and aluminum alloys [*11–14*]. Dry air and air with various amounts of water vapor have also been shown to affect crack growth rates [*11,14*] down to 10^{-7} in./cycle (2.5×10^{-9} m/cycle). Wadsworth [*15*] determined that water vapor alone was as effective as oxygen in decreasing the fatigue life of aluminum as compared with that obtained in a vacuum. The observed increased crack growth rates in wet argon with respect to dry argon (Fig. 7) agree with Wadsworth's results. Bradshaw and Wheeler [*14*] showed that the slope of da/dN versus partial pressure of water vapor curves for constant ΔK showed a maximum variation at a critical pressure. It is suggested that this critical pressure was experienced in the dry argon tests since there is significant scatter (Fig. 7).

The fatigue crack propagation rates for high strength steels have also been shown to be very susceptible to water, either in vapor or liquid form [*16–19*]. Statically loaded specimens have shown that oxygen inhibits the

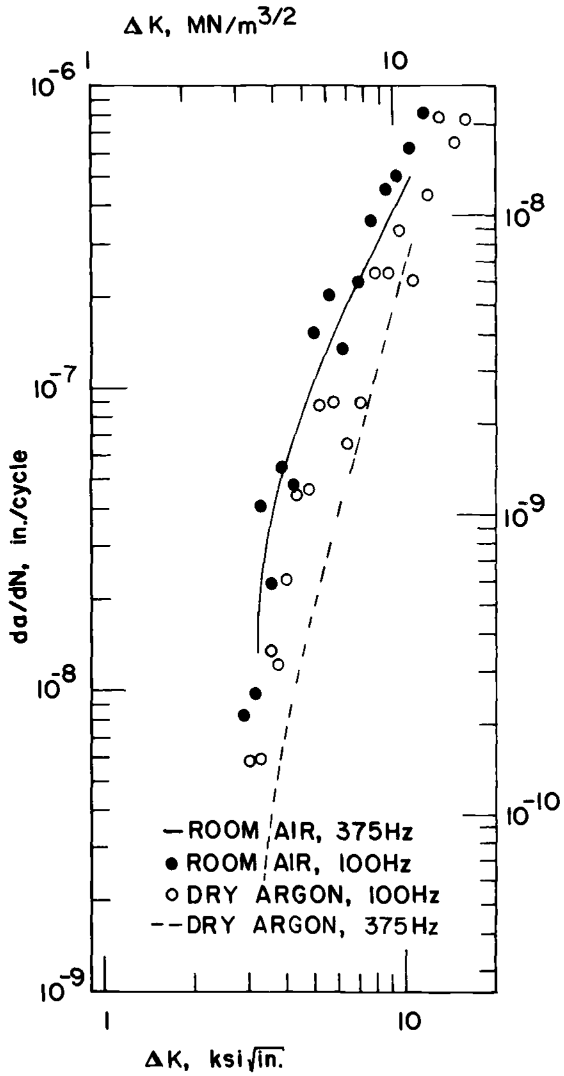

FIG. 9—*Fatigue crack growth rate of D6ac steel (HRC 50) with* K_{min} *= 0.5 ksi* $\sqrt{\text{in}}$. *(0.55* $MN/m^{3/2}$*).*

effect of water vapor [*20*], but it has also been deduced that oxygen does not affect the rate of fatigue crack growth in moist environments [*21*]. Li et al [*18*] and Wei et al [*19*] showed a detrimental effect of humid argon with respect to dry argon for some high strength steels in the range of 6 × 10^{-7} to 10^{-5} in./cycle (1.5 × 10^{-8} to 2.5 × 10^{-7} m/cycle) at 125 Hz. Previous tests on D6ac steel [*22,23*] between 10^{-4} and 10^{-6} in./cycle (2.5

$\times 10^{-6}$ to 2.5×10^{-8} m/cycle) have shown nearly identical behavior with respect to dry and room air at frequencies up to 10 Hz, although a definite detrimental effect of distilled water was observed at 3 Hz, which was the highest test frequency. These findings, unfortunately, do not aid in the analysis of the observed results for D6ac at 375 Hz. Perhaps the statement by Smith and Shahinian [*24*] with respect to fatigue lives might be applied to the very low growth rate regime: "Most of the metals investigated have been found to be affected more by oxygen than water vapor except aluminum and its alloys which are reported to be equally susceptible to water vapor."

Frequency Effect

Tests were conducted on D6ac steel at 375 and 100 Hz, both in air and in dry argon. The results are shown in Fig. 9. A frequency effect between 375 and 100 Hz for D6ac steel in dry argon is observed (Fig. 9). Therefore, it is suggested that the resulting threshold values could be environmentally affected and vacuum results could be different. Recently Cooke et al [*25*] have found lower fatigue crack growth rates and larger threshold values for a medium carbon alloy steel in vacuum with respect to air.

For the tests conducted in room air at 100 and 375 Hz no frequency effect was observed (Fig. 9) and none was expected. No environmental effect was expected since both frequencies are considered high and the partial pressures of water vapor and oxygen in room air are large. Also, an intrinsic material effect such as creep due to crack tip heating was not expected since Schmidt and Paris [*5*] have implied that for 2024-T3 aluminum this was only effective between 342 and 832 Hz.

Summary and Conclusions

The effect of mean stress and environment on the threshold and near threshold fatigue crack propagation behavior of D6ac steel and 7050-T73651 aluminum was studied. From the experimental data the following conclusions can be drawn.

1. A mean stress effect on fatigue crack propagation threshold, in terms of K_{max}, is only observed in the regime $0 \leq K_{min} \leq 2$ ksi $\sqrt{\text{in.}}$ (2.2 MN/$m^{3/2}$), that is, R is typically greater than zero and less than 0.5. For higher values of K_{min} the fatigue crack propagation threshold is determined by the stress intensity factor range, ΔK_{th}.

2. At the high testing frequency of 375 Hz, no effect of wet argon and room air as compared to a dry argon environment were observed on the fatigue crack propagation threshold, ΔK_{th}. Environmental effects are noted in the near threshold region. For D6ac steel room air produced the highest crack propagation rate while dry and wet argon produced identical

but lower crack propagation rates for the same ΔK values. For 7050-T73651 aluminum both wet argon and room air environments produced the high crack propagation rates, while dry argon produced lower crack rates.

3. Changing the test frequency of 375 to 100 Hz had no noticeable effect on the threshold and near threshold region results for D6ac steel in room air. But in dry argon, 100 Hz gave slightly higher crack propagation rates compared to 375 Hz.

Acknowledgments

The work reported here was sponsored under Army Research Office Grant No. DA-ARO-D-31-124-72-G136. The authors gratefully acknowledge the support of the Army Research Office for this program. They also wish to acknowledge the valuable comments made by Keith Miller of Cambridge University, England, and H. W. Liu of Syracuse University.

References

[*1*] Weiss, V. and Lal, D. N., *Metallurgical Transactions,* Vol. 5, 1974, p. 1946.
[2] Frost, N. E., Pook, L. P., and Denton, K., *Engineering Fracture Mechanics,* Vol. 3, 1971, pp. 109–126.
[*3*] Paris, P. C., Bucci, R. J., Wessel, E. T., Clark, W. G., and Mager, T. R. in *Stress Analysis and Growth of Cracks, ASTM STP 513,* American Society for Testing and Materials, 1972, pp. 141–176.
[*4*] Bucci, R. J., Clark, W. G., and Paris, P. C. in *Stress Analysis and Growth of Cracks, ASTM STP 513,* American Society for Testing and Materials, 1972, pp. 177–195.
[*5*] Schmidt, R. A. and Paris, P. C. in *Fracture Toughness Testing, ASTM STP 536,* American Society for Testing and Materials, 1973, pp. 79–94.
[*6*] Pook, L. P. in *Stress Analysis and Growth of Cracks, ASTM STP 513,* American Society for Testing and Materials, 1972, pp. 106–124.
[*7*] Bucci, R. J., Paris, P. C., Hertzberg, R. W., Schmidt, R. A., and Anderson, A. F. in *Stress Analysis and Growth of Cracks, ASTM STP 513,* American Society for Testing and Materials, 1972, pp. 125–140.
[*8*] Wessel, E. T., *Engineering Fracture Mechanics,* Vol. 1, No. 1, 1968, pp. 77–103.
[*9*] Lal, D. N., "A New Model for the Threshold Condition for the Initiation and Propagation of Fatigue Cracks," Ph.D. thesis, Syracuse University, 1974.
[*10*] Cooke, R. J. and Beevers, C. J., *Engineering Fracture Mechanics,* Vol. 5, 1973, pp. 1061–1071.
[*11*] Hartmann, A., *International Journal of Fracture Mechanics,* Vol. 1, 1965, pp. 167–188.
[*12*] Bradshaw, F. J. and Wheeler, C., *Applied Materials Research,* Vol. 5, 1966, p. 112.
[*13*] Wei, R. P., *International Journal of Fracture Mechanics,* Vol. 4, 1968, pp. 159–170.
[*14*] Bradshaw, F. J. and Wheeler, C., *International Journal of Fracture Mechanics,* Vol. 5, 1969, pp. 255–268.
[*15*] Wadsworth, N. J. in *Internal Stresses and Fatigue in Metals,* G. M. Rassweiler and W. L. Grube, Eds., Elsevier Publishing Company, New York, 1959, pp. 382–396.
[*16*] Dahlberg, E. P., *Transactions,* American Society for Metals, Vol. 58, 1965, p. 46.

[*17*] Van Der Sluys, W. A., *Journal of Basic Engineering, Transactions,* American Society of Mechanical Engineers, Series D, Vol. 89, 1967, p. 28.

[*18*] Li, C. Y., Talda, P. M., and Wei, R. P., *International Journal of Fracture Mechanics,* Vol. 1, 1968, p. 155.

[*19*] Wei, R. P., Taldà, P. M., and Li, C. Y. in *Fatigue Crack Propagation, ASTM STP 415,* American Society for Testing and Materials, 1967, p. 460.

[*20*] Hancock, G. G. and Johnson, H. H., *Transactions of the Metallurgical Society,* American Institute of Mining, Metallurgical and Petroleum Engineers, Vol. 236, 1966, p. 513.

[*21*] Johnson, H. H. and Paris, P. C., *Engineering Fracture Mechanics,* Vol. 1, 1968, pp. 3–45.

[*22*] Paris, P. C., Bucci, R. J., and Little, C. D. in *Stress Analysis and Growth of Cracks, ASTM STP 513,* American Society for Testing and Materials, 1972, pp. 196–217.

[*23*] Unpublished research of Del Research Corporation, 1970, and data connected with F-111 Test Program, General Dynamics Corporation, Fort Worth Division, 1970; as quoted from previous reference.

[*24*] Smith, H. H. and Shahinian, P. in *Effect of Environment and Complex Load History on Fatigue Life, ASTM STP 462*, American Society for Testing and Materials, 1970, pp. 217–233.

[*25*] Cooke, R. J., Irving, P. E., Booth, G. S., and Beevers, C. J., *Engineering Fracture Mechanics,* Vol. 7, 1975, pp. 69–77.

J. G. Kaufman,[1] *G. T. Sha,*[1] *R. F. Kohm,*[1] *and R. J. Bucci*[1]

Notch-Yield Ratio as a Quality Control Index for Plane-Strain Fracture Toughness

REFERENCE: Kaufman, J. G., Sha, G. T., Kohm, R. F., and Bucci, R. J., **"Notch-Yield Ratio as a Quality Control Index for Plane-Strain Fracture Toughness,"** *Cracks and Fracture, ASTM STP 601,* American Society for Testing and Materials, 1976, pp. 169–190.

ABSTRACT: The ratio of notch-tensile strength to tensile-yield strength (the notch-yield ratio) is correlatable with plane-strain fracture toughness, K_{Ic}. As a result of that fact and relative simplicity of notch-tension testing, it is suitable for plant quality control testing for fracture toughness. The test procedures and quality control testing practices are described, and data showing the correlation between K_{Ic} and notch-yield ratio from both ½ and 1$\frac{1}{16}$-in.-diameter notched tension specimens for several aluminum alloys are presented. The 1$\frac{1}{16}$-in.-diameter specimen provides a more discriminating correlation at high toughness levels than does the ½-in.-diameter specimen. It is emphasized that this is not a procedure for estimating K_{Ic} directly, but for providing assurance that K_{Ic} equals or exceeds a stated value.

KEY WORDS: crack propagation, fracture properties, quality control, notch sensitivity, notch tests

The increased emphasis on the use of fracture mechanics concepts in the design of fracture critical structural elements in aircraft has made it necessary to incorporate fracture toughness minima in certain material procurement documents. In general, the minima are expressed in terms of the plane-strain fracture toughness, K_{Ic}, determined in accordance with ASTM Test for Plane Strain Fracture Toughness of Metallic Materials (E 399-74).

The complexity of plane-strain fracture toughness testing, the time involved, and the problems in interpretation of the test data all combine to greatly increase the expense of material procurement testing, and there is a great need for simpler, less expensive indicator tests for quality control of fracture toughness. The tension test of a sharply notched round bar is

---

[1] Senior engineering associate, senior engineer, statistical analyst, and group leader, respectively, Aluminum Company of America, Alcoa Laboratories, Alcoa Center, Pa. 15069.

an effective way of accomplishing this for aluminum alloy products, as described herein.

Scope

The scope of this paper includes (*a*) a description of the notch-tension test and its advantages for quality control testing for aluminum alloys, (*b*) plane-strain fracture toughness and notch-tensile data for a number of lots of several aluminum alloys, 2024, 2124, 7075, and 7475, illustrating the useful correlation between the two, and (*c*) a description of the specific manner in which quality control for fracture toughness can be carried out utilizing the notch-tension test.

Background

The notch-tension test has been used for a number of years to evaluate the relative notch toughness (or the inverse, notch sensitivity) of various metals and alloys [*1,2*],[2] including aluminum alloys [*3,4*]. It has been considered and utilized in a few cases for the direct measurement of plane-strain fracture toughness [*3,5–8*], but there are size limitations and complications with such things as fatigue cracking that make it less attractive than other available procedures [*9*].

The notch-tension test is relatively simple, in that the only datum generated is the notch-tensile strength, (NTS) determined simply by dividing the maximum load supported by the specimen by the original net cross-sectional area. No extensometry is involved, nor is there any interpretation of load-deformation curves; the only raw data are the initial net-section diameter and the ultimate load. It has the additional advantage that little new or unusual equipment is involved, as the specimens can be machined and tested in the equipment currently available in most plant laboratories, with only a few added accessories to adequately machine the notch and control alignment as described later. The test results are obtained in units of stress and, thus, are related readily to other properties.

The tensile strength of the notched specimen itself does not provide much information about the inherent toughness of a material.[3] More useful information is obtained by comparison of this NTS with the tensile properties of the material. For example, the ratio of the NTS to the tensile strength of the material (notch-strength ratio) is a measure of tensile efficiency and for many years was also considered a measure of notch

---

[2] The italic numbers in brackets refer to the list of references appended to this paper.

[3] Although it is possible to attempt to calculate a K_{Ic} estimate directly from the NTS (see footnote 5), this is not recommended because of the fact that the specimen is not fatigue cracked and is far below reasonable estimates at adequate constraint for plane-strain conditions [*9*].

toughness. More recently, the ratio of NTS to the tensile yield strength (TYS) of the material (notch-yield ratio (NYR)) has been recognized [*10,11*] (ASTM Standard Method of Sharp-Notch Tension Testing of High Strength Sheet Materials (E 338-68(1973)) as that providing more meaningful information about the inherent notch toughness of the material, that is, its ability to deform plastically in the presence of a severe stress raiser and thus avoid the development of a free-running crack and the catastrophic failure of the component. The TYS of the material, though arbitrarily defined, is a measure of the stress at which appreciable plastic deformation first takes place and, thus, is a reasonable basis for comparison to determine whether the NTS was developed with or without appreciable plastic deformation. It is this characteristic that has been shown to be related to other measures of fracture toughness [*3*], and it is upon this basis that the notch-tension test is proposed as a quality-control test for fracture toughness.

Specimen and Test Procedure

The major aspects of the test are presented as follows. Since previous work [*8,9,12*] has shown that relatively careful control of alignment to minimize bending stresses is one of the most important features of the notch-tension test, considerable attention is given to that problem. It is imperative that bending stresses be kept to a minimum, preferably no more than about five percent in the normal range of operating loads (the draft ASTM method [4] allows 10 percent at 30 ksi on a control specimen), to avoid influencing the results. The effect of excessive bending stresses is always negative, downgrading the apparent toughness of the material.

Specimen Design

The standard test sections of the notched-round specimens are of the design in Fig. 1 (see footnote 4). The standard specimen utilized at Alcoa Laboratories for most high strength alloys has been the tapered seat version of the ½-in.-diameter specimen (see footnote 4) shown in Fig. 2, though the threaded end version in Fig. 3 is also acceptable. For very tough materials and exceptionally high toughness minima, the 1$\frac{1}{16}$-in.-diameter specimen in Fig. 4 is useful; the larger diameter provides greater restraint to plastic deformation, and a greater ratio of diameter/root

---

[4] Proposed Method for "Sharp-Notch Tension Testing of Thick High-Strength Aluminum and Magnesium Alloy Products with Cylindrical Specimens," *Annual Book of ASTM Standards,* July 1974, Part 10, pp. 657–668.

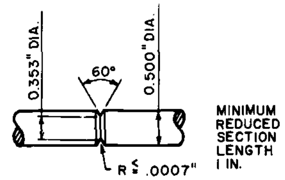

0.500 IN. DIA TEST SECTION

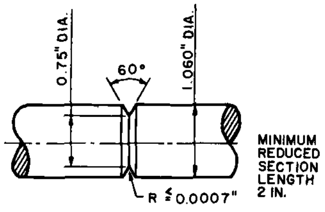

1.060 IN. DIA TEST SECTION

FIG. 1—*Standard test sections of notched-tension specimens.*

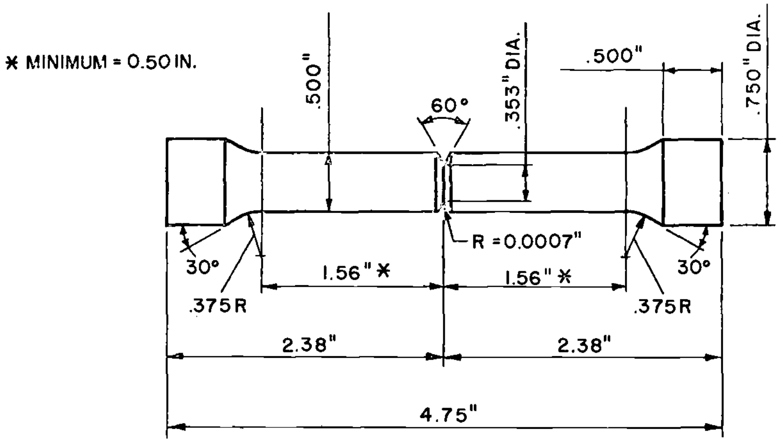

FIG. 2—*0.500 in. diameter tapered seat notched-tension specimen.*

radius, which should minimize variations in data due to variations in notch tip radius.

The notch tip radius is 0.0007 in. maximum, and in normal machining operations, radii from 0.0002 to 0.0005 in. are obtained. Data in Ref *12* suggest only a small range in NTS will result from the resultant range in radii from 0.0002 to 0.0007 in., though recent unpublished data from Brown and Jones at NASA-Lewis Research Center [5] illustrate that this

---

[5] Brown, W. F., Jr., private communication, 22 May 1974.

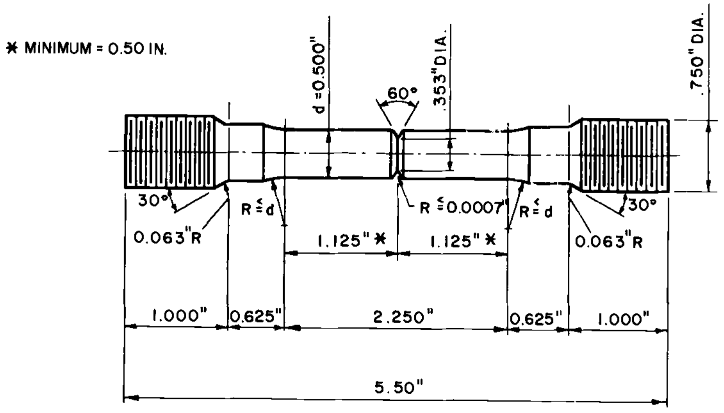

FIG. 3—*0.500 in. diameter threaded end notched-tension specimen.*

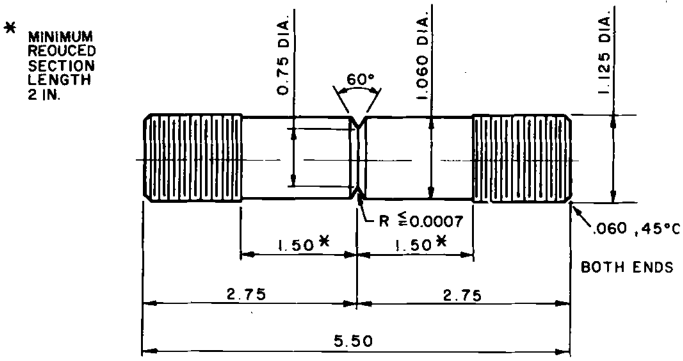

FIG. 4—*1.060 in. diameter threaded end notched-tension specimen.*

will vary from alloy to alloy and may be as large as five percent. The diameter of each individual specimen is measured within 0.0005 in. and the notch tip radius checked with a microprojector to be within the required limit; usually notch tip radii are between 0.0002 and 0.0005 in. and are obtained readily with carbide tools sharpened to a point.

Specimen Preparation

Maximum control of specimen alignment can be achieved if the entire specimen, including the notch, is machined in a single lathe setup [*13*].

Alignment Devices

Alignment devices should be used in conjunction with the normal tensile loading system. These include in-line systems for accommodating bending such as the NASA double collet fixture [*14*], or the use of parallel-bar aligners (Fig. 5) in conjunction with precision-machined tapered seat holders (Fig. 6) [*12,15*] or spherically seated tension bolts and head blocks. All components of such systems should be machined with extreme care [*16*] as no alignment system will work if the specimens or connections between specimens and other components are not precisely aligned. Representative bending stress measurements with ½-in. tapered seat and threaded end specimens in the precision machined holders are shown in Fig. 7.

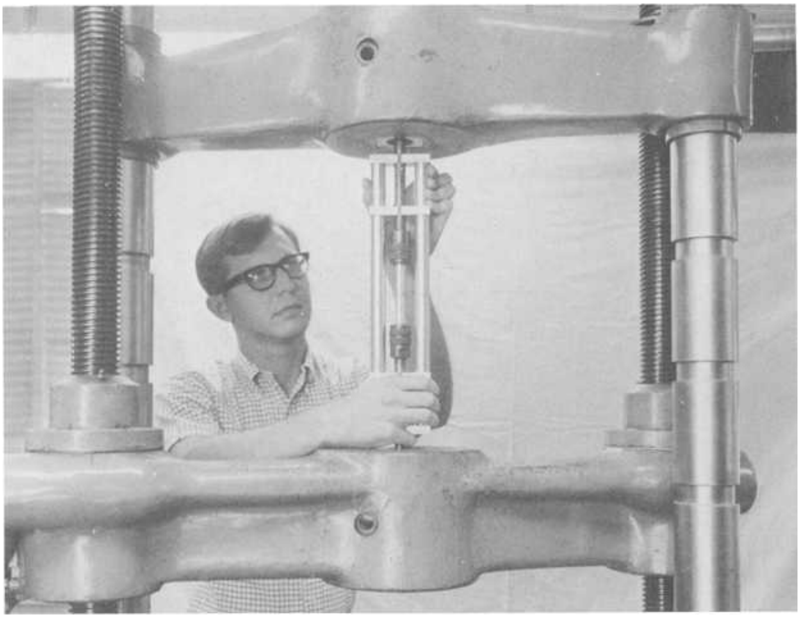

FIG. 5—*Use of parallel-bar aligners to control alignment of tension bolts during notch-tension test (squeezed tightly together, with 500 to 1000-lb. load on specimen).*

Loading Rate

The specimens may be tested at stressing rates up to 100 000 psi/min [*12*].

Data Reduction

Measure the maximum load supported by the specimen, $P_{\max}$, normally the fracture load, and calculate the NTS by dividing $P_{\max}$ by the original net cross-sectional area. Calculate the NYR by dividing NTS by the TYS of the material determined at 0.2 percent offset, in a tension test conducted per ASTM Standard Methods of Tension Testing of Metallic Materials (E 8-69).

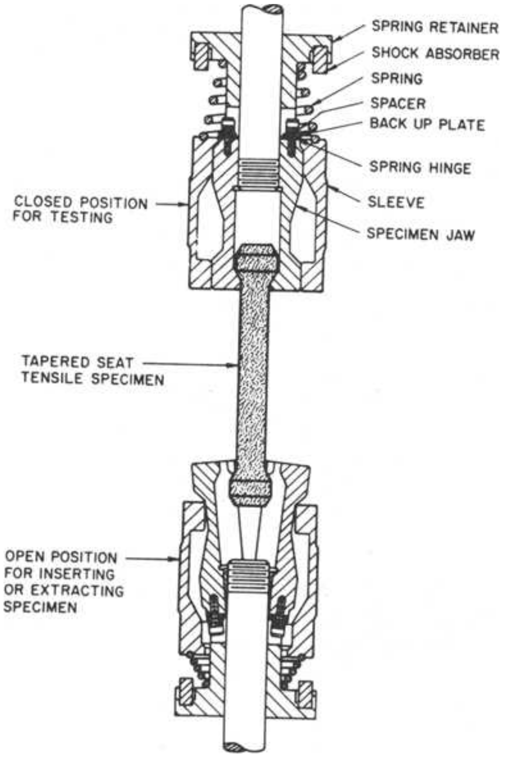

FIG. 6—*Tapered seat specimen holder.*

Correlation with Plane-Strain Fracture Toughness

The heart of the usefulness of the notch-tension test for quality control of fracture toughness is the reasonably good correlation between NYR and K_{Ic}. Representative data from plane-strain fracture toughness tests and tension tests of ½-in.-diameter notched specimens are provided in Table 1 for 2X24 (2024 and 2124) and Table 2 for 7X75 (7075 and 7475); data for both the ½-in. and 1$\frac{1}{16}$-in.-diameter specimens from tests of 2124-T851 are shown in Table 3.

In all cases for which data are shown, the K_{Ic} and notch-tension tests were made of each lot of material, with both types of specimens taken from identical locations through the thickness. The tests were conducted in strict accordance with the respective methods (ASTM Method E 399-74) (see also footnote 4).

The K_{Ic} values from Tables 1 and 2 are plotted as a function of NYR in Figs. 8 and 9 for 2X24 and 7X75, respectively; corresponding plots of the data in Table 3 are shown in Fig. 10. (Plots of K_{Ic} versus NTS are similar and could also be used for correlative purposes.) The data for 7075 and

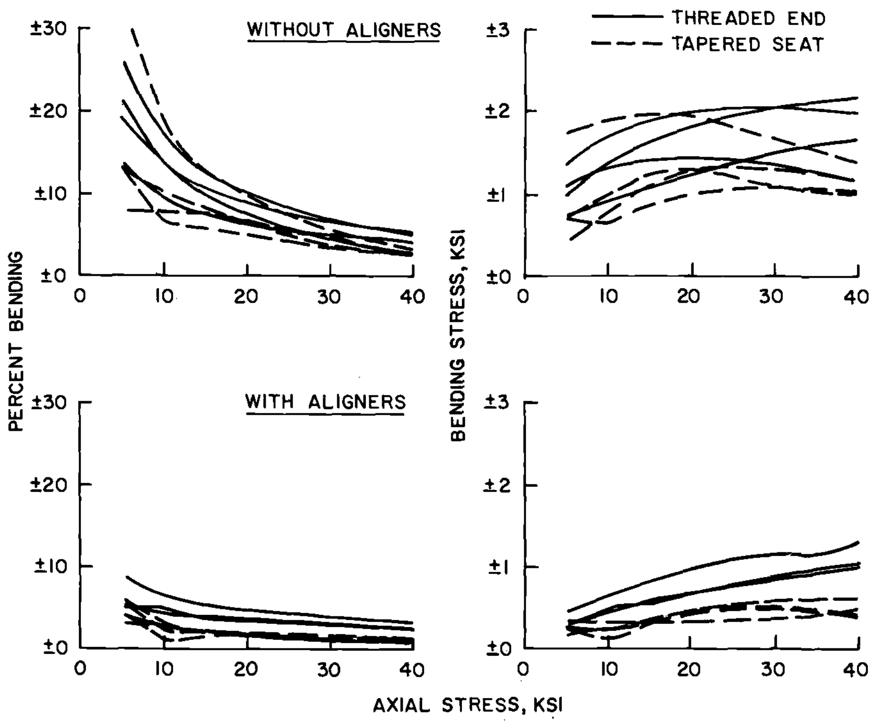

FIG. 7—*Bending stresses and percent bending in ½-in.-diameter tension specimens loaded through precision-machined head blocks and tension bolts.*

7475 are identified by temper (*a*) T651, (*b*) T7651, and (*c*) T7351, but a separate analysis does not appear to be necessary or justified when a large population of data are available. Actually, it would be preferred for some purposes to separate data for specific orientations of K_{Ic} specimens, for it is obvious that each notch-tension specimen is associated with two orientations of fracture toughness specimens (for example, L versus LT and LS). The inclusion of similar alloys or tempers or both is helpful, as it provides a wider range of toughnesses in the correlation and, thus, assistance in establishing the values of NYR associated with limiting values of K_{Ic}.

W. F. Brown (see footnote 5) has noted that the data from the two types of test can be plotted as in Figs. 11 and 12, which have the advantage that the two sets of data are dimensionally consistent (in.) and the basic linear elastic fracture mechanics (LEFM) relation between the two tests is displayed clearly. The data for both alloys do scatter about the theoretical line until general yielding occurs. The finite root radius would be expected to result in values slightly the theoretical level, and test misalignment, however small, would contribute to scatter on the low side. While this type of relationship is helpful in analyzing the theoretical aspects of

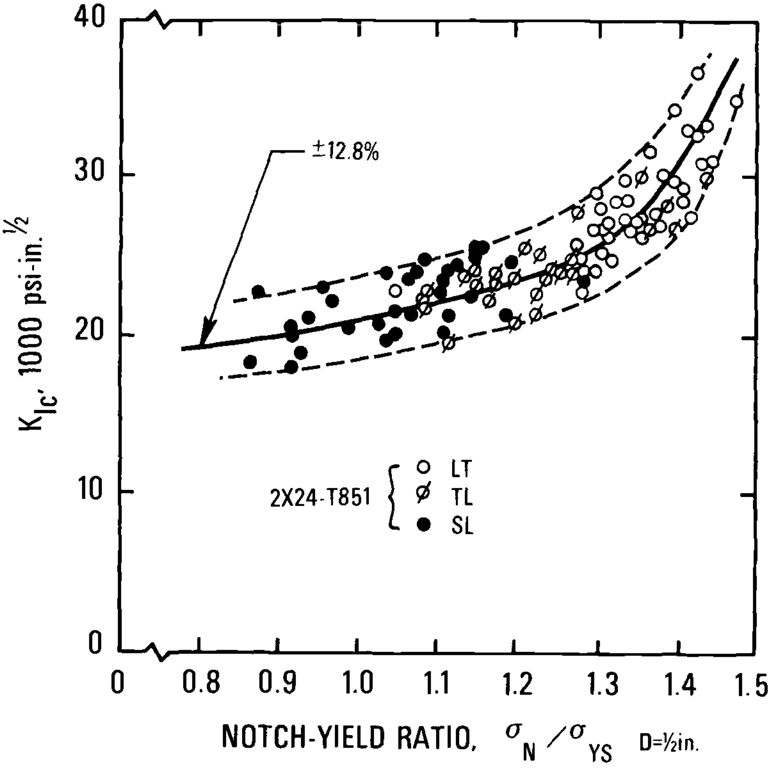

FIG. 8—*Correlation of plane strain fracture toughness and NYR for 2024 and 2124 plate.*

the correlation, plots such as in Figs. 8, 9, and 10 are those most useful in plant test laboratory applications of the data.

Several potential problems in applying these data to quality control are illustrated by the correlations in Figs. 8 through 10. First, and most obvious, the correlations are bands, not single lines. This is to be expected in any correlation relationship and particularly for two fracture tests which are subject to greater variability than regular tension tests. The width of the band is relatable not only to the inherent scatter in the two tests (for example, alignment, crack or notch tip control), but also sampling factors as the fact that a notch-tension specimen samples a smaller portion of the thickness of the material than a fracture toughness specimen. A second problem is illustrated by the manner in which the plots curve upward indicating a lessening of sensitivity of the notch-tension test above ratios of about 1.3 associated with more general yielding. As illustrated by the data in Fig. 10, the use of the larger

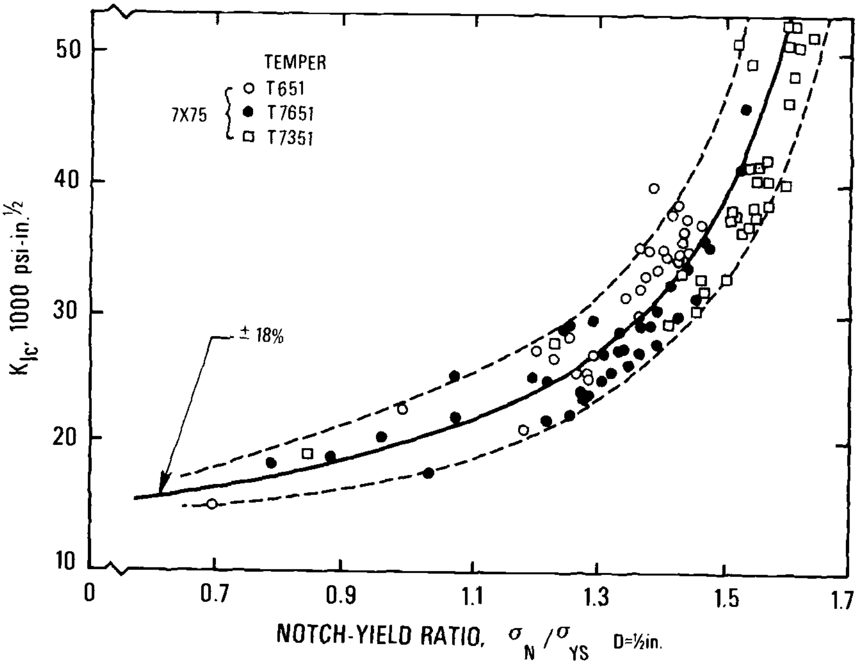

FIG. 9—*Correlation of plane strain fracture toughness with NYR for 7075 and 7475 plate.*

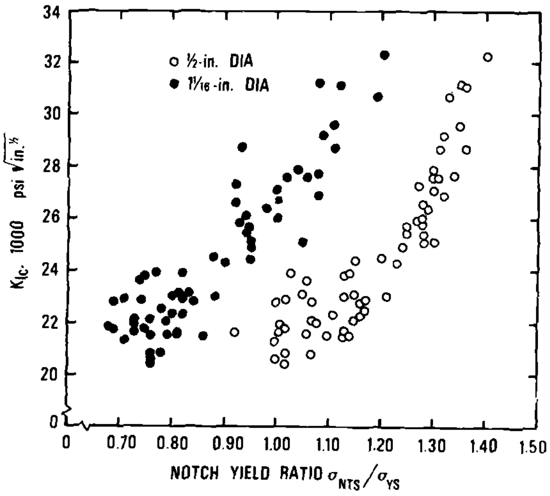

FIG. 10—*Correlation of plane strain fracture toughness with NYR (*½ and 1¹⁄₁₆*-in.-diameter specimens) for 2124-T851.*

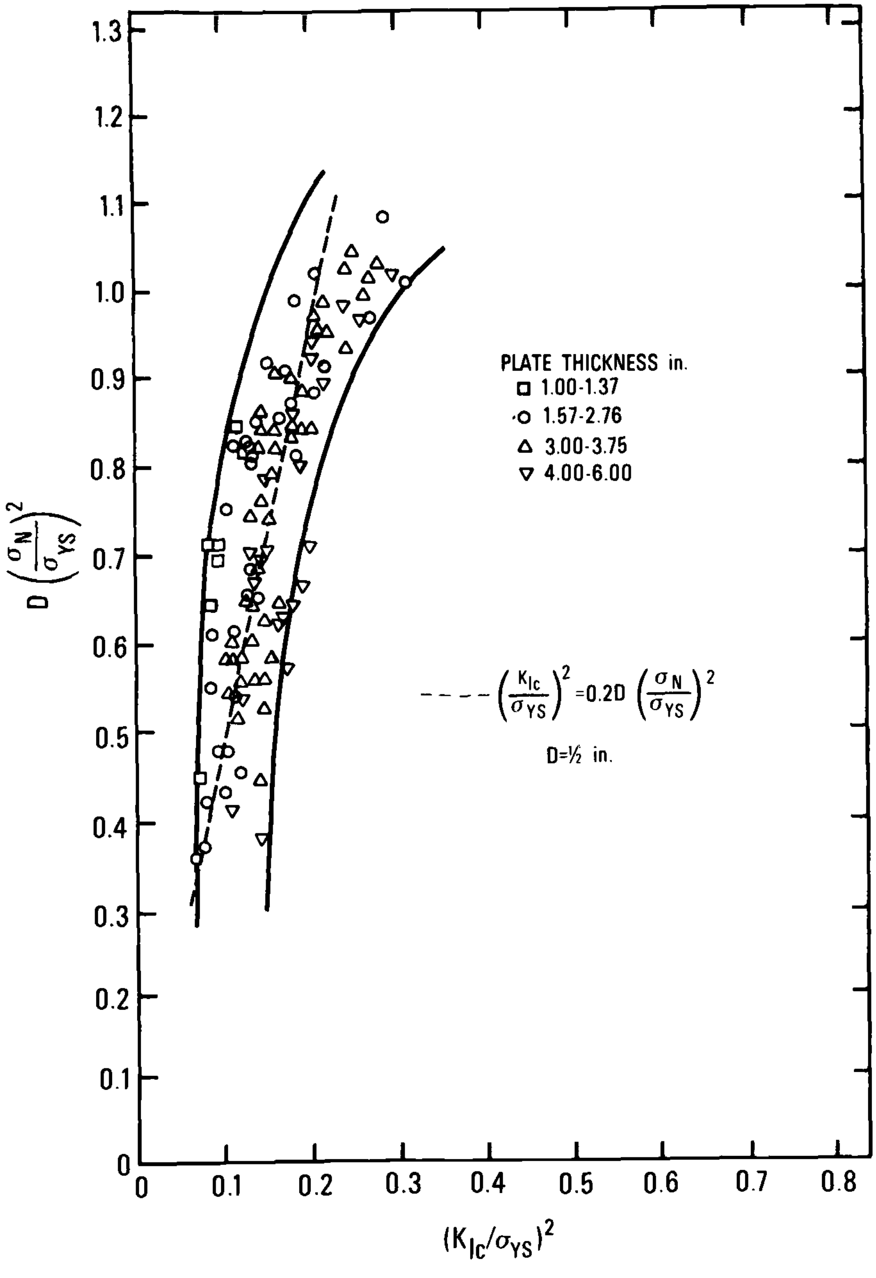

FIG. 11—*Dimensionally consistent correlation between notch-tensile and fracture toughness data for 2024 and 2124 plate* [16].

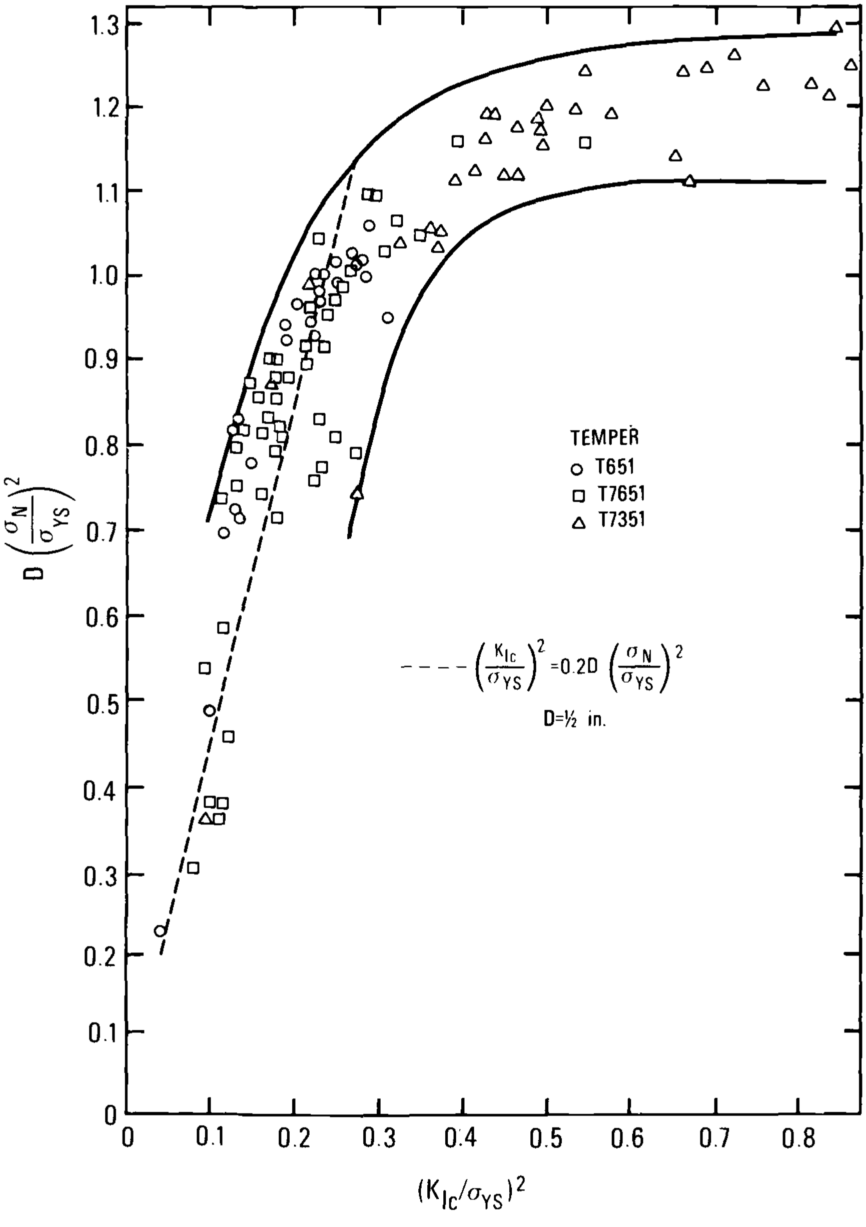

FIG. 12—*Dimensionally consistent correlation between notch-tensile and fracture toughness data for 7074 and 7475 plate* [16].

diameter of notched specimen results in lower NTS for a given level of toughness and hence a wider range of K_{Ic} values before the transition ratio of 1.3 is reached, so that while the same general behavior is evident, the larger diameter specimen provides more discriminating ability at the higher levels of toughness.

The width and shape of the bands of data result in the fact that the NYR is not very useful for determining the absolute value of K_{Ic} associated with a given NYR. For this reason, a lower limit from the data defined in a one-way probability analysis at 75 percent confidence that 90 percent of lots will exceed the stated K_{Ic} minimum is utilized in the quality-control situation, as described as follows. In this situation, the width and shape of the band of data are not critical, since what is sought is assurance that the K_{Ic} value is equal to or greater than the stated minimum value. The use of a lower limit of the data (that is, the highest NYR associated with the stated minimum K_{Ic} value) will provide the high degree of assurance that the K_{Ic} of a material with that ratio has a K_{Ic} equal to or greater than the minimum.

In early use of this method, when too few data were available for meaningful statistical analysis, the lower limit of the band was established by ''eyeball'' fitting of a line to the lower limit of the data, as suggested by Figs. 8 to 10. More recently, a statistical model incorporating material thickness and TYS has been developed for the lower limit based upon 75 percent confidence that 99 percent will exceed the resultant values, namely

$$\log K_{Ic} = A_0 \text{ (thickness)} + A_2 \text{ (yield strength)} + A_3 \text{ (NYR)}$$

Technically, all data should be for a single size of specimen, or a factor for specimen size should be incorporated, since significant specimen size effects are noted for high-toughness alloys with rapidly rising crack-resistance curves.

Acceptance or Rejection

Given the correlation in Fig. 8 as an example and assuming the use of a lower limit from the data, however, established, the following steps would be involved in utilizing the notch-tension test.

Example—For 7475-T7651 plate in the T-L orientation, the minimum value of K_{Ic} is 30 ksi $\sqrt{\text{in.}}$ The equivalent range of NYR for long-transverse (LT) ½-in.-diameter specimens of 7475-T7651 from Fig. 8 is 1.25-1.43; a minimum value of 1.42 might be used as a quality-control minimum. Thus, for quality control testing the following steps must be taken.

1. Conduct a tension test of a single-notched specimen from the specification location, calculate the NTS and determine the NYR by

TABLE 1—*Results of plane-strain fracture toughness and notched-round-bar specimen tension tests of 2024-T851 and 2124-T851 plate.*

Alloy and Temper	Product	Product Thickness, in.	Specimen	Location and Orientation [a]	K_{Ic}, ksi $\sqrt{\text{in.}}$	Specimen Thickness, in.	Crack Length, in.	NTS, ksi	TYS, ksi	TS, ksi	$\frac{\text{NTS}}{\text{TYS}}$	$\frac{\text{NTS}}{\text{TS}}$	Valid K_{Ic} Tests in avg
2024-T851	plate	1.00	369550	LT	20.9	0.75	0.74	79.8	70.5	73.0	1.13	1.09	3
				TL	18.7	0.75	0.75	65.0	68.6	73.0	0.95	0.89	3
		1.37	301840	TL	18.6	1.00	1.08	76.8	64.4	70.8	1.19	1.08	2
			301841	LT	22.6	1.00	0.98	85.2	65.6	71.8	1.30	1.19	3
				TL	20.0	1.00	1.01	76.8	64.4	70.8	1.19	1.08	3
			301999	LT	23.1	1.00	1.04	83.7	65.6	71.8	1.27	1.17	5
				TL	20.1	1.00	1.04	76.3	64.8	71.2	1.18	1.07	6
2124-T851	plate	1.57	369722	CLT	34.7	1.50	1.50	95.8	65.2	70.6	1.47	1.36	2
				CTL	29.8	1.50	1.53	93.0	65.2	70.4	1.43	1.32	2
				CSL	21.3	0.50	0.49	65.6	63.0	67.1	1.04	0.98	1
			369724	CLT	27.4	1.50	1.59	90.2	64.2	71.4	1.41	1.26	1
				CTL	25.2	1.50	1.59	87.6	67.2	72.8	1.30	1.20	2
				CSL	18.8	0.50	0.47	60.1	65.4	69.7	0.92	0.86	1
			369726	CLT	26.2	1.50	1.56	90.9	67.2	72.8	1.35	1.25	2
				CTL	24.0	1.50	1.56	86.5	67.2	72.6	1.29	1.19	2
				CSL	20.9	0.50	0.50	59.9	64.4	68.2	0.93	0.88	2
		1.75	410675	CLT	28.4	1.50	1.58	88.4	67.0	72.0	1.32	1.23	2
				CTL	24.0	1.50	1.57	76.8	65.7	71.5	1.17	1.07	2
				CSL	18.2	0.50	0.46	56.3	65.3	70.4	0.86	0.80	1
		2.50	410676	MLT	27.2	1.00	1.01	88.0	65.4	71.5	1.35	1.23	2
				MTL	26.2	1.00	1.04	83.9	64.2	70.7	1.31	1.19	2
				CSL	22.0	1.00	0.96	60.7	63.5	69.2	0.96	0.88	2
		2.52	410799	MLT	25.6	1.00	0.96	88.7	69.7	74.9	1.27	1.18	3
				MTL	22.8	1.00	0.97	86.6	67.6	73.9	1.28	1.17	2
				CSL	19.7	1.00	0.96	69.6	66.3	73.7	1.03	0.92	2
		2.50	410852	MLT	34.3	2.00	2.16	91.9	66.2	71.5	1.39	1.29	2
				MTL	27.9	2.00	2.14	82.5	64.8	70.8	1.27	1.17	2
				CSL	21.2	1.00	0.93	69.6	62.9	68.5	1.11	1.02	2
			410853	MLT	36.6	2.00	2.10	92.9	65.6	70.8	1.42	1.31	2

				MTL	30.0	2.00	2.18	86.9	64.4	70.5	1.35	1.23	2
				CSL	22.4	1.00	0.95	71.0	62.1	67.6	1.14	1.05	2
			410854	MLT	29.8	2.00	2.18	87.4	65.8	70.6	1.33	1.24	1
				MTL	24.0	2.00	2.10	73.4	64.4	69.8	1.14	1.05	1
				CSL	20.3	1.00	0.93	61.9	63.1	67.6	0.98	0.92	1
		2.76	410796	MLT	24.8	1.00	0.95	85.5	67.4	72.9	1.27	1.17	2
				MTL	24.0	1.00	0.96	84.6	66.1	72.5	1.28	1.17	2
				CSL	20.5	1.00	0.93	62.9	64.2	69.2	0.98	0.91	1
		3.00	340903	MLT	28.4	1.00	1.00	85.3	60.8	68.6	1.40	1.24	2
				MTL	26.6	1.00	1.00	81.9	58.8	66.8	1.39	1.23	2
				CSL	24.7	1.00	1.02	67.6	62.6	68.0	1.08	0.99	2
			370130-2	MLT	25.0	0.50	0.52	85.9	66.2	72.2	1.30	1.19	1
				MLT	26.5	1.00	1.02	85.9	66.2	72.2	1.30	1.19	1
				MLT	28.9	1.00	1.53	85.9	66.2	72.2	1.30	1.19	1
				MLT	28.9	1.41	1.53	85.9	66.2	72.2	1.30	1.19	1
				MTL	21.8	0.50	0.52	70.0	64.8	71.3	1.08	0.98	1
				MTL	21.5	1.00	1.03	70.0	64.8	71.3	1.08	0.98	1
				MTL	22.7	1.00	1.54	70.0	64.8	71.3	1.08	0.98	1
				MTL	22.2	1.41	1.55	70.0	64.8	71.3	1.08	0.98	1
		3.15	410798	MLT	26.4	1.00	0.96	88.2	65.7	71.1	1.34	1.24	2
				MTL	24.8	1.00	0.99	85.2	65.0	71.1	1.31	1.20	2
				CSL	22.9	1.00	0.96	68.8	62.6	67.2	1.10	1.02	1
		3.39	410797	MLT	27.2	1.00	0.96	81.8	61.6	68.5	1.33	1.19	2
				MTL	28.0	1.00	0.96	84.1	61.0	68.4	1.38	1.23	2
				CSL	23.9	1.00	0.95	76.3	59.6	65.9	1.28	1.16	1
		3.50	410677	MLT	31.6	1.50	1.52	87.2	63.9	70.3	1.36	1.24	2
				MTL	26.6	1.50	1.55	80.8	62.7	69.9	1.29	1.16	2
				CSL	25.0	1.00	0.99	69.7	61.4	68.5	1.14	1.02	2
2124-T851	plate	3.50	410816	MLT	27.9	1.50	1.54	85.2	65.4	71.0	1.30	1.20	1
				MTL	23.0	1.50	1.54	73.1	64.2	70.2	1.14	1.04	2
				CSL	20.6	1.00	0.99	60.9	59.9	64.6	1.02	0.94	2
			279264	CLT	31.0	2.00	2.09	89.6	62.1	69.5	1.44	1.29	2
				CTL	23.5	2.00	2.06	76.0	61.6	68.2	1.23	1.11	2
				CSL	20.1	1.00	0.94	66.4	60.4	64.9	1.10	1.02	2
			279266	CLT	30.9	2.00	2.16	89.9	62.9	69.6	1.43	1.29	2
				CTL	23.3	2.00	2.10	73.3	62.6	68.9	1.17	1.06	2

TABLE 1—*Continued.*

Alloy and Temper	Product	Product Thickness, in.	Specimen	Location and Orientation [a]	K_{Ic}, ksi $\sqrt{\text{in.}}$	Specimen Thickness, in.	Crack Length, in.	NTS, ksi	TYS, ksi	TS, ksi	$\frac{NTS}{TYS}$	$\frac{K_{Ic}}{TS}$	Valid Tests in avg
				CSL	21.2	1.00	0.98	64.0	60.6	65.4	1.06	0.98	2
			279268	CLT	32.6	2.00	2.12	89.4	62.9	69.6	1.42	1.28	2
				CTL	24.7	2.00	2.12	78.2	62.2	69.0	1.26	1.13	2
				CSL	22.9	1.00	1.04	57.3	60.6	64.6	0.95	0.89	2
			279270	CLT	33.0	2.00	2.00	91.0	64.6	71.0	1.41	1.28	2
				CTL	24.9	2.00	2.08	76.9	63.2	69.7	1.22	1.10	2
				CSL	23.9	1.00	1.01	63.8	62.2	65.9	1.03	0.97	2
			279272	CLT	33.2	2.00	2.08	90.1	62.9	70.2	1.43	1.28	2
				CTL	24.1	2.00	2.09	69.6	62.2	77.4	1.24	1.11	2
				CSL	22.8	1.00	1.00	70.2	61.8	69.6	1.14	1.01	2
			279274	CLT	30.0	2.00	2.10	87.9	63.8	71.2	1.38	1.23	2
				CTL	22.6	2.00	2.04	75.8	62.2	69.4	1.22	1.09	2
				CSL	20.0	1.00	0.98	63.2	60.6	64.8	1.04	0.98	2
		3.75	410795	MLT	27.0	1.00	1.00	86.2	64.2	69.9	1.34	1.23	2
				MTL	23.2	1.00	1.00	80.7	63.0	69.5	1.28	1.16	2
				CSL	23.4	1.00	0.99	65.9	62.2	66.9	1.06	0.99	2
		4.00	340900	MLT	29.2	1.00	1.00	83.1	59.4	67.2	1.40	1.24	2
				MTL	23.4	1.00	1.03	71.2	60.0	67.8	1.19	1.05	1
				CSL	24.0	1.00	0.98	66.1	59.3	66.1	1.11	1.00	2
		4.31	340896	MLT	26.8	1.00	1.00	81.3	59.3	67.2	1.37	1.21	2
				MTL	23.8	1.00	1.00	76.3	60.8	68.3	1.25	1.12	2
				CSL	24.3	1.00	0.96	66.7	59.6	66.6	1.12	1.00	2
		4.50	410678	MLT	27.0	1.50	1.53	83.0	63.4	70.2	1.31	1.18	2
				CSL	22.6	1.50	1.52	52.2	59.8	65.6	0.87	0.80	2
		5.50	410679	MLT	28.4	1.50	1.50	81.5	61.1	68.2	1.33	1.20	2
				MTL	22.0	1.50	1.52	68.6	59.3	67.5	1.16	1.02	2
				CSL	23.8	1.50	1.48	61.5	57.5	63.6	1.07	0.97	2
		6.00	358103	CSL	23.6	0.50	0.52	63.4	56.0	63.5	1.13	1.00	2

			358105	MTL	20.4	0.50	0.51	65.6	55.4	65.4	1.19	1.00	2
				CSL	21.1	0.50	0.51	64.8	55.0	62.8	1.18	1.03	1
2124-T851	special process plate	2.04	410681	MLT	21.2	0.75	0.75	80.1	65.4	70.8	1.22	1.13	2
				MTL	19.4	0.75	0.74	72.1	65.2	70.9	1.11	1.02	2
				CSL	17.8	0.75	0.73	57.0	67.2	67.8	0.91	0.84	2
		4.00	410682	MLT	22.8	1.50	1.57	68.1	65.5	70.2	1.04	0.97	2
				CSL	20.0	1.50	1.55	54.8	60.2	65.9	0.91	0.83	2
		4.50	410683	MLT	32.5	1.50	1.52	85.2	59.8	67.8	1.42	1.26	2
				MTL	26.5	1.50	1.57	79.3	58.5	67.5	1.36	1.17	1
				CSL	25.4	1.50	1.52	66.0	57.3	64.1	1.15	1.03	2
		6.00	410684	MLT	29.4	1.50	1.54	79.3	57.1	65.2	1.39	1.22	2
				MTL	23.9	1.50	1.57	69.5	55.0	64.6	1.26	1.08	2
				CSL	24.5	1.50	1.53	65.4	54.8	60.6	1.19	1.08	2

NOTE—TS = tensile strength.

[a] M and C refer to quarter and half-thickness locations; the last two letters refer to standard orientation (ASTM Method E 399-74).

TABLE 2—*Results of plane-strain fracture toughness and notched-round-bar specimen tension tests of 7075-T651 and 7475-T651 plate.*

Alloy and Temper	Product	Product Thickness, in.	Specimen	Location and Orientation[a]	K_{Ic}, ksi$\sqrt{\text{in.}}$	Specimen Thickness, in.	Crack Length, in.	NTS, ksi	TYS, ksi	TS, ksi	$\frac{\text{NTS}}{TYS}$	$\frac{NTS}{\text{TS}}$	Valid K_{Ic} Tests in avg
7075-T651	plate	1.37	301742	LT	28.0	1.00	1.05	97.8	78.2	86.2	1.25	1.14	2
				TL	24.0	1.00	1.08	94.7	74.2	83.3	1.28	1.14	1
			301920	LT	26.7	0.75	0.76	103.7	80.4	88.8	1.29	1.17	2
				TL	26.4	0.75	0.77	95.1	77.4	86.6	1.23	1.10	3
		1.75	323102	CLT	27.0	1.00	1.05	98.2	81.5	89.5	1.20	1.10	3
				CTL	22.3	1.00	1.03	73.8	74.4	85.1	0.99	0.87	3
				CSL	14.8	0.50	0.50	48.1	70.2	80.8	0.69	0.60	3
7475-T651	plate	1.30	410760	LT	32.8	1.28	1.61	111.7	81.3	88.1	1.37	1.27	2
				TL	33.2	1.28	1.61	108.7	78.1	86.8	1.39	1.25	1
			410761	LT	37.4	1.29	1.61	110.8	78.5	86.0	1.41	1.29	1
				TL	36.4	1.29	1.60	110.6	77.3	86.0	1.43	1.29	1
			410762	LT	35.0	1.30	1.60	108.6	77.4	86.1	1.40	1.26	2
				TL	34.2	1.30	1.60	107.2	77.9	84.3	1.43	1.27	2
			410763	LT	34.8[b]	1.34	1.62	109.1	77.0	85.2	1.42	1.28	2
				TL	33.8	1.33	1.61	107.0	75.5	84.9	1.42	1.26	1
				TL	38.4	1.34	2.68	107.0	75.5	84.9	1.42	1.26	2
			410764	LT	35.2	1.31	1.61	107.8	79.0	85.8	1.36	1.26	1
				TL	34.7	1.31	1.60	107.1	76.7	85.8	1.40	1.25	1
			410765	LT	37.2	1.28	1.60	107.0	75.0	82.8	1.43	1.29	2
				TL	36.8	1.28	1.58	105.4	72.3	81.7	1.46	1.29	2
		1.75	411082	CLT	39.8[b]	1.78	2.25	103.2	74.6	81.2	1.38	1.27	2
				CTL	29.6	1.78	2.18	99.5	73.1	82.8	1.36	1.20	1
				CSL	20.8	0.50	0.49	78.2	66.3	82.0	1.18	0.95	2
		2.00	411052	CLT	35.8[b]	2.02	2.08	102.3	71.5	79.1	1.43	1.29	2
				CTL	34.5	2.03	2.12	101.3	70.5	80.9	1.44	1.25	2

NOTE—TS = tensile strength.

[a] M and C refer to quarter and half-thickness locations; the last two letters refer to standard orientation (ASTM Method E 399-74).

[b] Indicates close to being valid.

dividing the NTS by the TYS at the same location, obtained in a test of a smooth specimen in accordance with ASTM Method E 338-68(1973).

2. If LT NYR $\geqq$ 1.43, lot is accepted as having $K_{Ic} \geqq 30$ ksi $\sqrt{\text{in.}}$

3. If NYR <1.43, test two additional notched-tension specimens. If NYR of both $\geqq$1.43, lot is accepted. If either NYR <1.43, lot is subject to K_{Ic} testing per ASTM Method E 399-74.

4. If $K_{Ic} \geqq 30$ ksi $\sqrt{\text{in.}}$, lot is accepted. If $K_{Ic} < 30$ ksi $\sqrt{\text{in.}}$, lot is rejected.

It is apparent from Fig. 8 that the use of a value of 1.45 as the limiting ratio would ensure with high confidence that no lots with K_{Ic} equal to or less than 30 ksi $\sqrt{\text{in.}}$ would be accepted. It is true that some lots could have ratios from 1.25 to 1.42 with K_{Ic} equal to or greater than 30 ksi $\sqrt{\text{in.}}$ and that K_{Ic} testing would be required to prove that However, such tests would be required of only a small part of the population, saving a considerable amount of expense.

Summary

A quality control procedure for the fracture toughness of aluminum alloys based upon notched round bar testing has been described, and illustrative data presented. Substantial economies in quality control testing costs are possible in cases where useful correlations can be established between K_{Ic} and NYR from the tension test. It must be emphasized that this is not a substitute for a plane-strain fracture toughness test if a value of K_{Ic} is desired; ASTM Method E 399-74 is the proper way to obtain K_{Ic} and all criteria of validity should be carefully adhered to. The value of the notch-tension test is in providing high reliability that K_{Ic} is equal to or greater than a specified value, for which a useful correlation relatively between K_{Ic} and NYR or NTS has been obtained.

TABLE 3—*Results of plane-strain fracture toughness and notch-tension tests of 2124-T851 plate.*

Product Thickness, in.	Specimen	Location and Orientation [a]	K_{Ic}, ksi$\sqrt{\text{in.}}$	Specimen Thickness, in.	Crack Length, in.	NTS [b], ksi		TYS, ksi	TS, ksi	NTS/TYS		NTS/TS	
						½ in. dia	1 1/16 in. dia			½ in. dia	1 1/16 in. dia	½in. dia	1 1/16 in dia
3.00	109-368	MLT	27.7	1.50	1.54	86.9	70.2	64.9	70.4	1.34	1.08	1.23	1.00
		MTL	23.0	1.50	1.54	77.4	56.2	63.9	69.8	1.21	0.88	1.11	0.81
		CSL	21.5	1.00	1.00	67.8	50.0	61.4	67.3	1.10	0.81	1.01	0.74
	109-369	MLT	26.9	1.50	1.54	85.6	69.9	64.7	70.3	1.32	1.08	1.22	0.99
		MTL	22.5	1.50	1.53	74.6	49.7	63.7	69.8	1.17	0.78	1.07	0.71
		CSL	20.8	1.00	1.00	62.8	48.0	61.8	68.0	1.02	0.78	0.92	0.71
	109-371	MLT	25.1	1.50	1.54	82.5	67.5	64.4	70.2	1.28	1.05	1.18	0.96
		MTL	21.5	1.50	1.54	72.8	54.9	63.7	69.8	1.14	0.86	1.04	0.79
		CSL	20.4	1.00	1.00	62.6	46.7	61.2	67.1	1.02	0.76	0.93	0.70
3.25	461-821	MLT	29.2	1.50	1.53	87.6	72.4	66.2	71.4	1.32	1.09	1.23	1.01
		MTL	24.5	1.50	1.53	77.9	57.0	64.7	70.7	1.20	0.88	1.10	0.81
		CSL	23.1	1.00	1.00	65.9	50.5	62.6	67.4	1.05	0.81	0.98	0.75
	461-831	MLT	28.7	1.50	1.53	89.2	72.7	65.7	71.3	1.36	1.11	1.25	1.02
		MTL	25.1	1.50	1.56	84.6	61.5	64.9	71.3	1.30	0.95	1.19	0.86
		CSL	23.9	1.00	1.02	64.6	48.0	62.6	69.3	1.03	0.77	0.93	0.69
3.50	461-951	MLT	29.6	1.50	1.52	88.6	72.7	65.4	70.9	1.35	1.11	1.25	1.03
		MTL	25.8	1.50	1.55	81.7	59.6	63.9	70.4	1.28	0.93	1.16	0.85
		CSL	22.9	1.00	1.01	62.8	43.7	61.4	68.6	1.02	0.71	0.92	0.64
4.00	109-607	MLT	32.3	1.50	1.53	85.8	73.6	61.1	68.9	1.40	1.20	1.25	1.07
		MTL	27.6	1.50	1.56	79.7	61.8	60.8	68.8	1.31	1.02	1.16	0.90
		CSL	24.4	1.00	1.01	69.0	56.6	59.8	67.2	1.15	0.95	1.03	0.84
	109-627	MLT	30.7	1.50	1.53	84.3	74.9	63.2	70.1	1.33	1.19	1.20	1.07
		MTL	24.3	1.50	1.55	76.6	56.0	62.4	69.7	1.23	0.90	1.10	0.80
		CSL	23.6	1.00	1.01	64.9	45.6	61.3	66.0	1.06	0.74	0.98	0.69
	109-628	MLT	31.1	1.50	1.53	89.3	73.5	65.5	71.7	1.36	1.12	1.25	1.03
		MTL	26.1	1.50	1.55	82.0	60.1	64.2	71.2	1.28	0.94	1.15	0.84
		CSL	23.9	1.00	1.00	69.7	50.3	61.4	67.4	1.14	0.82	1.03	0.75
4.50	448-031	MLT	27.1	1.50	1.54	83.8	64.9	64.7	71.0	1.30	1.00	1.18	0.91
		MTL	22.9	1.50	1.53	73.8	51.6	63.2	70.4	1.17	0.82	1.05	0.73

		CSL	21.5	1.00	1.00	69.2	46.7	61.1	67.3	1.13	0.76	1.03	0.69
	448-041	MLT	26.0	1.50	1.52	82.5	65.2	64.9	71.0	1.27	1.00	1.16	0.92
		MTL	21.8	1.50	1.53	67.2	51.2	63.2	70.0	1.06	0.81	0.96	0.73
		CSL	21.6	1.00	1.00	62.1	41.3	61.1	65.8	1.02	0.68	0.94	0.63
	448-051	MLT	25.7	1.50	1.53	82.8	63.4	66.5	72.4	1.25	0.95	1.14	0.88
		MTL	22.0	1.50	1.53	70.5	51.4	65.0	71.5	1.08	0.79	0.99	0.72
		CSL	20.6	1.00	1.00	62.5	47.5	62.6	66.7	1.00	0.76	0.94	0.71
	448-061	MLT	24.9	1.50	1.52	79.7	61.2	64.2	70.3	1.24	0.95	1.13	0.87
		MTL	20.8	1.50	1.53	67.2	47.6	62.9	69.6	1.07	0.76	0.97	0.68
		CSL	21.6	1.00	1.00	55.6	43.9	60.4	64.7	0.92	0.73	0.86	0.68
	448-071	MLT	26.4	1.50	1.52	83.8	63.6	64.9	71.7	1.29	0.98	1.17	0.89
		MTL	22.8	1.50	1.54	72.8	53.1	62.9	70.6	1.16	0.84	1.03	0.75
		CSL	22.8	1.00	1.00	64.8	45.0	60.6	66.2	1.07	0.74	0.98	0.68
	448-081	MLT	25.4	1.50	1.52	81.5	61.6	65.4	71.5	1.25	0.94	1.14	0.86
		MTL	21.7	1.50	1.53	71.9	47.3	63.4	70.2	1.13	0.75	1.02	0.67
		CSL	21.7	1.00	1.01	62.2	42.4	61.7	66.3	1.01	0.69	0.94	0.64
	448-091	MLT	27.9	1.50	1.53	83.9	67.0	64.7	71.2	1.30	1.04	1.18	0.94
		MTL	23.1	1.50	1.55	71.8	52.1	62.6	69.8	1.15	0.83	1.03	0.75
		CSL	22.8	1.00	1.01	60.5	42.0	60.7	67.0	1.00	0.69	0.90	0.63
	448-101	MLT	26.6	1.50	1.52	83.7	60.1	65.2	71.5	1.28	0.92	1.17	0.84
		MTL	22.3	1.50	1.53	73.4	50.8	63.2	70.3	1.16	0.80	1.04	0.72
		CSL	21.3	1.00	1.00	61.6	43.9	61.7	66.4	1.00	0.71	0.93	0.66
	448-111	MLT	31.2	1.50	1.55	87.3	70.1	64.9	71.1	1.35	1.08	1.23	0.99
		MTL	25.4	1.50	1.55	81.8	59.8	63.7	70.6	1.28	0.94	1.16	0.85
		CSL	21.5	1.00	1.01	67.6	48.3	61.2	68.1	1.10	0.79	0.99	0.71
4.75	461-871	MLT	28.7	1.50	1.55	86.1	66.5	65.7	71.4	1.31	0.93	1.21	1.01
		MLT	23.0	1.50	1.55	72.0	56.2	63.9	70.1	1.13	0.80	1.03	0.88
		CSL	23.8	1.00	1.00	70.2	49.3	61.9	66.1	1.13	0.75	1.06	0.80
	461-881	MLT	27.3	1.50	1.53	84.3	66.3	66.2	72.1	1.27	0.92	1.17	1.00
		MTL	22.1	1.50	1.55	74.1	52.3	64.7	71.3	1.15	0.73	1.04	0.81
		CSL	21.9	1.00	1.01	63.6	49.0	62.9	67.3	1.01	0.73	0.95	0.78
	461-891	MLT	27.6	1.50	1.54	84.8	68.9	65.2	71.4	1.30	1.06	1.19	0.96
		MTL	22.3	1.50	1.55	70.0	51.6	63.2	70.2	1.11	0.82	1.00	0.74
		CSL	22.1	1.00	1.01	65.6	46.9	61.4	65.8	1.07	0.76	1.00	0.71

NOTE—TS = tensile strength.

[a] M and C refer to quarter and half-thickness locations; the last two letters refer to standard orientation (ASTM Method E 399-74).

[b] For ½-in. and $1\frac{1}{16}$-in.-diameter notched round specimens.

References

[1] Sachs, G., Ebert, L. J., and Brown, W. F., Jr., *Transactions,* American Institute of Mining, Metallurgical, and Petroleum Engineers, Iron and Steel Division, 1948, p. 424.

[2] Baker, J. F. and Tipper, C. F., *Welding Research Council Bulletin,* No. 37, June 1957.

[3] Kaufman, J. G. and Johnson, E. W., *Advances in Cryogenic Engineering,* Vol. 6, 1960, pp. 637–649.

[4] Kaufman, J. G. and Holt, Marshall, "Fracture Characteristics of Aluminum Alloys," Technical Paper No. 18, Alcoa Laboratories, 1965.

[5] Irwin, G. R., "Onset of Fast Crack Propagation in High Strength Steel and Aluminum Alloys," Report 4763, Naval Research Laboratories, 24 May 1956.

[6] Wei, R. P. and Lanta, F. J., *Materials Research and Standards,* June 1965, p. 307.

[7] Carman, C. M., Armiento, D. F., and Markus, H., *Journal of Basic Engineering,* Vol. 87, No. 4, 1965, pp. 904–916.

[8] Brown, W. F., Jr. and Srawley, J. E., *Plane Strain Crack Toughness Testing of High Strength Metallic Materials, ASTM STP 410,* American Society for Testing and Materials, 1966.

[9] Brown, W. F., Jr., "The Circumferentially Notched Cylindrical Bar as a Fracture Toughness Test Specimen," presented at the G. R. Irwin Symposium on Linear Fracture Mechanics, Lehigh University, 29–30 July 1974.

[10] Kaufman, J. G. and Johnson, E. W., *Proceedings,* American Society for Testing and Materials, Vol. 62, 1962, pp. 778–793.

[11] ASTM Special Committee on Fracture Testing of High Strength Materials, *Materials Research and Standards,* Vol. 2, No. 3, March 1962, pp. 196–203.

[12] Kaufman, J. G. in *Fracture Toughness, ASTM STP 514,* American Society for Testing and Materials, 1972, pp. 82–97.

[13] March, J. L., Ruprecht, W. J., and Reed, George, *ASTM Bulletin,* No. 244, 1960, pp. 52–55.

[14] Jones, M. H., Bubsey, R. T., Succop, G., and Brown, W. F., Jr., *Journal of Testing and Evaluation,* Vol. 2, No. 5, Sept. 1974, pp. 378–386.

[15] Babilon, C. F. and Traenkner, H. A., *Proceedings,* American Society for Testing and Materials, Vol. 64, 1964, pp. 1119–1127.

[16] Jones, M. H. and Brown, W. F., Jr., *Journal of Testing and Evaluation,* Vol. 3, No. 3, May 1975, pp. 179–181.

F. Erdogan,[1] *G. R. Irwin,*[2] *and M. Ratwani* [3]

Ductile Fracture of Cylindrical Vessels Containing a Large Flaw

REFERENCE: Erdogan, F., Irwin, G. R., and Ratwani, M., "**Ductile Fracture of Cylindrical Vessels Containing a Large Flaw,**" *Cracks and Fracture, ASTM STP 601,* American Society for Testing and Materials, 1976, pp. 191–208.

ABSTRACT: The fracture process in pressurized cylindrical vessels containing a relatively large flaw is considered. The flaw is assumed to be a part-through or through meridional crack. The flaw geometry, the yield behavior of the material, and the internal pressure are assumed to be such that in the neighborhood of the flaw the cylinder wall undergoes large-scale plastic deformations. Thus, the problem falls outside the range of applicability of conventional brittle fracture theories. To study the problem, plasticity considerations are introduced into the shell theory through the assumptions of fully-yielded net ligaments using a plastic strip model. Then a ductile fracture criterion is developed which is based on the concept of net ligament plastic instability. A limited verification is attempted by comparing the theoretical predictions with some existing experimental results.

KEY WORDS: fractures (materials), pressure vessels, cylindrical shells, plastic deformation, crack propagation, surface defects, failure

In this paper the phenomenon of fracture propagation in relatively thin-walled cylindrical pressure vessels and pipes is examined. In particular, the consideration is restricted to the problem in which the area of the localized defect zone is sufficiently large so that the net ligament and the cylinder wall in some close neighborhood of the defect is fully yielded. The "defect" is assumed to be located in a meridional plane. In a problem such as this, because of the expected large-scale plastic deformations in the crack region of the cylinder, the standard toughness and stress intensity-oriented factors in units of G or K do not seem to be suitable for studying the problem. In this paper, after discussing the application of the

---

[1] Professor of mechanics, Lehigh University, Bethlehem, Pa. 18015.

[2] Professor of mechanics, Lehigh University, Bethlehem, Pa. 18015, and University of Maryland, College Park, Md. 20740.

[3] Research engineer, Northrop Corporation, Hawthorne, Calif. 90250.

"crack opening stretch" concept to cylindrical vessels and presenting some results, some ideas regarding the "net ligament plastic instability" are developed and the method of their application to the fracture of thin-walled cylindrical vessels with a part-through crack is indicated.

Analytical Model

In order to analyze the problem it is assumed that the defect, which may consist of a crack or a cluster of cracks with arbitrary shape and orientation, is replaced by a part-through crack of equivalent size located in a meridional plane of the cylinder and characterized by the distance, c, and the length parameters, $2a$ and d (Fig. 1). It is further assumed that the thickness-to-radius ratio h/R is sufficiently small so that the cylindrical vessel may be treated as a "shallow shell" and the internal pressure p_0 and the ratios d/h and a/h are sufficiently large so that the cylinder wall in some close neighborhood of crack ends and the net ligament of thickness h-d around the crack are fully yielded. The problem may then be solved by approximating the yield zones ahead of the crack tips by a Barenblatt-Dugdale type plastic strip of length p (Fig. 1*b*) by assuming that the net ligament of length $2a$ and thickness h-d carries only a membrane stress of magnitude σ_y, and by using the shallow shell equations. The plastic strip $a < |x| < a + p, \ - h/2 < z < h/2$ is assumed to carry a membrane load $N_{yy} = N$ and a moment resultant $M_{yy} = M$. Yielding starts on the outer surface of the shell when the sum of the membrane and bending stresses reaches σ_{ys}, the yield strength of the material. However since in the meridional strips $a < |x| < a + p$ the shell wall is assumed to be fully yielded, a more appropriate yield condition may be the one which is based on the assumption of a plastic hinge developing in the region. Thus, from the equilibrium equations this condition may be expressed as

$$\left[\frac{N}{h\sigma_y}\right]^2 + \frac{|M|}{\left(\frac{h}{2}\right)^2\sigma_y} = 1 \qquad (1)$$

where σ_y, which is defined as the "flow stress" [*1*][4] and which is somewhat greater than σ_{ys}, is a measure of the yield behavior of the material. Recommendations for the selection of σ_y include $\sigma_y = (\sigma_{ys} + \sigma_u)/2$ or $\sigma_y = \sigma_{ys} + \sigma_0$ where σ_u is the ultimate strength and σ_0 is a fixed value [*1*]. However, for the general purpose it is sufficient to assume that

$$\sigma_y = (1 + n)\sigma_{ys} \qquad (2)$$

---

[4] The italic numbers in brackets refer to the list of references appended to this paper.

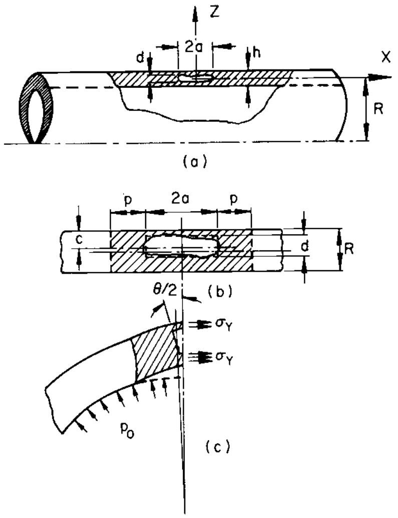

FIG. 1—*Internal flaw in the shell with fully-yielded net ligaments.*

where the percentage n depends on the strain hardening behavior of the material.

In practical applications the yield condition (Eq 1) is linearized by approximating the parabola by the straight lines going through the intercepts on N and M axes. For $N > 0$ this leads to the following commonly used condition

$$\frac{N}{h\sigma_y} + \frac{4|M|}{h^2\sigma_y} = 1 \tag{3}$$

In the shell problem under consideration, since bending effects are small compared to the membrane stresses, for our purpose a more realistic linearized approximation to the parabola (Eq 1) would be its tangent at the point ($M = 0, N = h\sigma_y$) which may be expressed as

$$\frac{N}{h\sigma_y} + \frac{2\,|M|}{h^2\sigma_y} = 1 \tag{4}$$

The solution of the shell problem is obtained by adding to the homogeneous solution given by $N_{yy} = N_0 = Rp_0$ (with remaining N_{ij} and M_{ij}, $i,j = x,y$, zero) the perturbation solution obtained from the following crack surface tractions (Fig. 1)

$$N_{yy} = (h - d)\,\sigma_y,\; N_{xy} = 0,\; M_{xy} = 0,$$
$$M_{yy} = \frac{\sigma_y}{2}\left[\left(h - c - \frac{d}{2}\right)\left(c + \frac{d}{2}\right) - \left(h - c + \frac{d}{2}\right)\left(c - \frac{d}{2}\right)\right] \quad (5a\text{–}d)$$
$$(-\,a < x < a,\; y = 0)$$
$$N_{yy} = N,\; N_{xy} = 0,\; M_{yy} = M,\; M_{xy} = 0 \quad (6a\text{–}d)$$
$$(a < |x| < a + p,\; y = 0)$$

where x, y, and z refer to the rectangular coordinates, and a, h, c, d, and p are the dimensions shown in Fig. 1. In this perturbation problem the crack is assumed to extend from $x = -\,(a + p)$ to $x = a + p$. In addition to the usual field quantities such as the displacements and the stress and moment resultants, the perturbation problem contains the unknowns M,N (the yield zone tractions), and p (the plastic zone size). Therefore, to solve the problem, in addition to the usual field equations of the shell, three more conditions are needed. The yield condition given by Eq 4 provides one such relation. The remaining two relations are provided by the condition of finiteness of the stress and moment resultants N_{yy} and M_{yy} at the ends of the plastic zones $x = \pm(a + p)$, $y = 0$. This is equivalent to the statement that

$$K_{\mathrm{m}} = 0, \qquad K_{\mathrm{b}} = 0 \quad (7a,b)$$

where K_{m} and K_{b} are the membrane the bending components of the stress intensity factor at the auxiliary crack tips $x = \pm(a + p)$.

The crack problem is solved by using the following linearized shallow shell equations with Kirchhoff type boundary conditions

$$\frac{Eha^2}{R}\,\frac{\partial^2 w}{\partial x^2} + \nabla^4 F = 0$$
$$\nabla^4 w - \frac{a^2}{RD}\,\frac{\partial^2 F}{\partial x^2} = \frac{q}{D}\,a^4,\; D = Eh^3/12(1 - \nu^2) \quad (8a,b)$$

where $w(X,Y)$ is the displacement in z-direction, $F(X, Y)$ is the stress function, q is the normal traction on the shell surface, and $X = x/a$, $Y = y/a$. By expressing w and F in terms of appropriate Fourier integrals, the problem may be reduced to a system of singular integral equations [2, 3] which is then solved in a somewhat straightforward manner [4]. The present solution is obtained by closely following the superposition technique described in Ref 5.

After solving the problem the total crack opening stretch δ_t may be obtained from

$$\delta_t(x,z) = \delta(x,0) + z\theta(x)\,, \quad \left(|x|<a+p,\ |z|<\frac{h}{2}\right)$$
$$\delta(x,0) = v(x,+0) - v(x,-0)$$
$$\theta(x) = \frac{\delta(x,0)}{R} + \theta_2(x)$$
$$\theta_2(x) = 2\frac{\partial}{\partial y}w(x,0) \qquad (9a\text{–}d)$$

where $v(x,y)$ and $w(x,y)$ are, respectively, the y and z-components of the displacement vector (on the neutral surface) and $\theta(x)$ is the (relative) crack surface rotation (Fig. 1). The crack opening displacements of particular practical interest are the following:

$\delta_0 = \delta(0,0)$: the crack opening displacement at the midpoint of the crack $x = 0$ on the neutral surface.

δ_c: the crack opening stretch at the midpoint $x = 0$ and the leading edge $z = h/2 - d$ of a part-through (external) surface crack given by

$$\delta_c = \delta_0\left[1 + \left(\frac{h}{2} - d\right)/R\right] + \left(\frac{h}{2} - d\right)\theta_2(0) \qquad (10)$$

δ_ϵ: the "average" net ligament stretch evaluated at the midpoint of the net ligament $x = 0$, $z = -d/2$ of a part-through (external) surface crack given by

$$\delta_\epsilon = \delta_0(1 - d/2R) - \theta_2(0)d/2 \qquad (11)$$

$\delta_a = \delta(a,0)$: the (conventional) crack opening stretch at the (actual) crack tips $x = \pm a$ for a through crack.

It is seen that for practical applications it is sufficient to calculate the quantities δ_0, δ_a, and $\theta_2(0)$. Figures 2 thru 5 show some sample calculated results. Figures 2 and 3 show δ_0 and δ_a for a through crack. In these figures N_0/h, d_1, and λ are, respectively, the hoop stress, the normalization factor, and the shell parameter and are given by

$$N_0 = p_0R\,, \quad d_1 = 4a\sigma_Y/E\,, \quad \lambda = [12(1-\nu^2)]^{1/4}\frac{a}{\sqrt{Rh}} \qquad (12a\text{–}c)$$

where E and ν are the elastic constants.[5] The case of $\lambda = 0$ corresponds to flat plate for which

---

[5] The Poisson's ratio υ appears in the shell analysis independent of λ also and was taken to be ⅓ in the present numerical work.

$$\frac{\delta_0}{d_1} = \frac{2}{\pi}\log[(1 + \sin\beta)/\cos\beta]$$

$$\frac{\delta_a}{d_1} = -\frac{2}{\pi}\log(\cos\beta), \quad \beta = \frac{\pi N_0}{2h\sigma_y} \qquad (13a\text{–}c)$$

Figures 4 and 5 show δ_0 and $\theta_2(0) = \theta_2$ for a part-through (external) surface crack in the shell. The normalizing factor for θ_2 shown in Fig. 5 is defined by

$$d_2 = 4a\sigma_y/(Eh) \qquad (14)$$

The figures give the results for $d/h = 0.5$. More complete results covering the range of $0.3 \leq d/h \leq 0.8$ for external surface cracks, $0.3 \leq d/h \leq 0.5$ for symmetrically located imbedded part-through cracks, and a sample result for an internal surface crack may be found in Ref *6*.

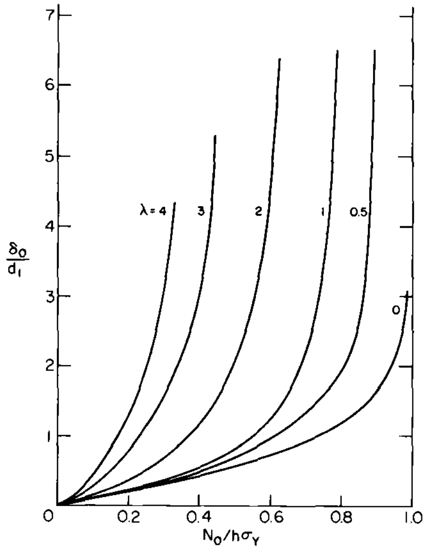

FIG. 2—*Crack opening displacement in the neutral surface and at the mid-section of the crack* (x = 0, z = 0) *for the cylindrical shell containing a through crack.*

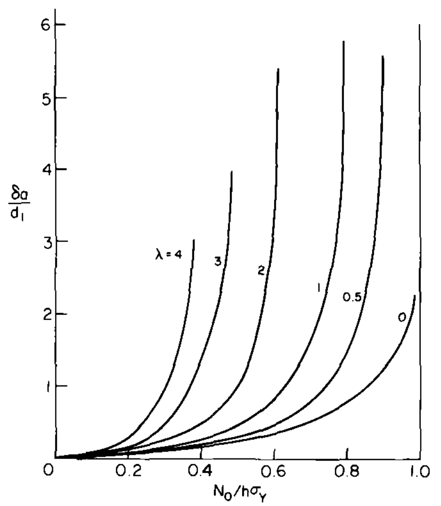

FIG. 3—*Crack opening stretch in the neutral surface and at the crack tip* ($x = a$, $z = 0$) *for a cylindrical shell containing a through crack.*

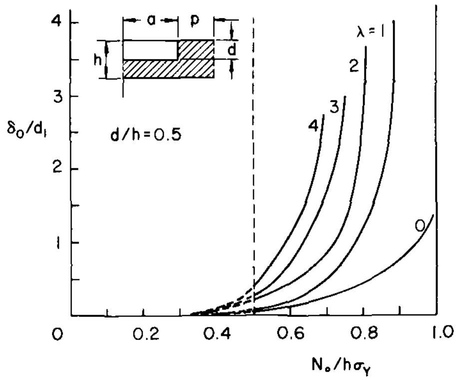

FIG. 4—δ_0 *versus* N_0 *at* ($x = 0$, $z = 0$) *for an external surface crack,* $d/h = 0.5$.

Load Carrying Capacity for Constant Crack Opening Stretch

If one takes the simple view that in the presence of large-scale plastic deformations the fracture process at the leading edge of a flaw will be controlled primarily by the magnitude of local strains and if one assumes

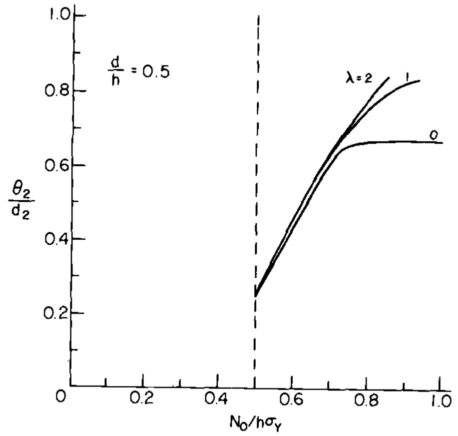

FIG. 5—*θ_2 versus* N_0 *at* $x = 0$ *for an external surface crack,* $d/h = 0.5$.

that the "crack opening stretch" along the crack front is a fairly good measure of these strain magnitudes, results similar to those presented in this paper may be used, as a first approximation, to estimate the load carrying capacity of relatively thin-walled pressurized vessels containing part-through or through cracks. For this it is sufficient to generate a set of hoop stress $\sigma_H = N_0/h$ versus crack size curves for constant crack opening stretch. Figure 6, for example, shows the results for a shell containing a through crack which is essentially a series of σ_H versus a curves for constant δ_a (see Eq 12*c*). The figure also gives some idea (in the quasi-static case) about the necessary rate of pressure drop with increasing crack size in order to have crack arrest. Some sample results for the part-through (external) crack for $\lambda = 1 - 4$ are shown in Figs. 7 thru 10. In this case the crack opening stretch of critical interest is δ_c which is calculated at the midsection of the leading edge of the crack and is given by Eq 10. Note that for $d = 0$, $\sigma_H = N_0/h = \sigma_y$, that is, the critical load corresponds to the "plastic flow" of the entire shell. The small circles shown in the figure for $d = h$ give the load level for the corresponding crack opening stretch δ_a at the tips of a through crack of same length $2a$. Generally, the extrapolated value of the load N_0/h_y for constant δ_c curves at $d = h$ is smaller than the load corresponding to an equal crack opening stretch δ_a at the crack tip $x = a$ in a through crack. This means that, at least theoretically, if one ignores the dynamic effects (largely on δ_{cr}) it is possible to have leak before burst or before any additional crack extension beyond $x = \pm a$ (provided that, when the net ligament ruptures, N_0 has the value corresponding to the constant δ_c and $d = h$). Thus, once the critical fracture resistance parameter $\delta = \delta_{cr}$ of the material and the crack

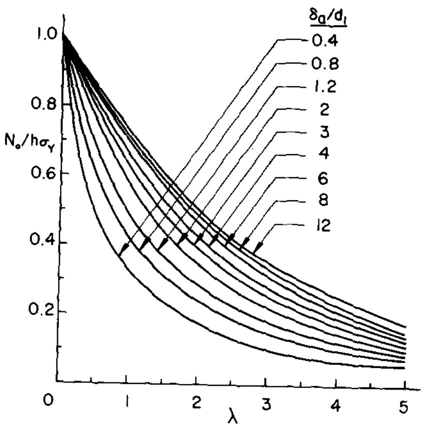

FIG. 6—N_0 *versus* λ *for a constant crack opening stretch* δ_a *at the crack tip* x = a *in a cylindrical shell containing a through crack.*

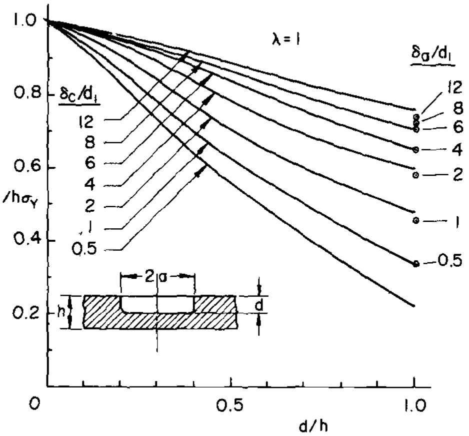

FIG. 7—N_0 *versus* d *for constant total crack opening stretch,* δ_c *at the leading edge of the crack in the mid-section* (x = 0, z = h/2 − d) *in a cylindrical shell with an external surface crack,* $\lambda = 1$.

geometry are specified an estimate of the load-carrying capacity of the vessel may be obtained by interpolating the results such as these[6] given in Figs. 6 and 7 thru 10.

---

[6] In order to calculate δ_c in these figures, it was assumed that $h/R = 0.465/19$. However, in most cases, the contribution coming from $\delta_0\, a/R$ is relatively small and may be neglected.

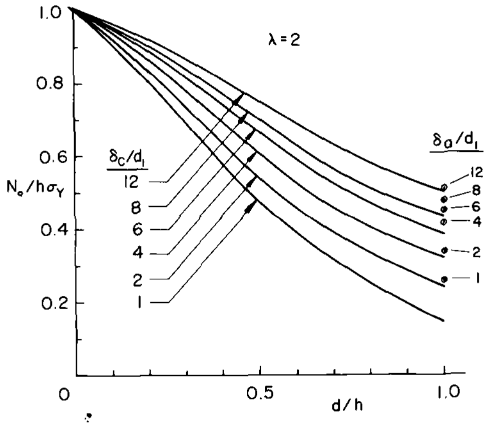

FIG. 8—N_0 *versus* d *for constant total crack opening stretch,* δ_c *at the leading edge of the crack in the mid-section* ($x = 0$, $z = h/2 - d$) *in a cylindrical shell with an external surface crack,* $\lambda = 2$.

Another technique for obtaining an estimate of the load-carrying capacity of a pressurized cylinder with a relatively large flaw by using the present analysis would be the following. From the crack opening stretch results such as those shown in Figs. 3 and 4 it may be observed that for a given crack geometry, in the neighborhood of a certain value of the applied load N_0 any small increase in $N_0/h\sigma_y$ causes a very large increase in δ_a or δ_c. This suggests that near this particular load the phenomenon which takes place around the crack front may be similar to the "necking" phenomenon observed in a ductile tensile bar, when the material experiences plastic instability. Morever, around a certain applied load, the slope of the related stretch curve increases so rapidly that the load corresponding to the plastic instability may be determined from these curves within an acceptable degree of accuracy by assuming a hypothetically selected high slope (say, between 5 and 20). Figure 11 shows the results for a slope of approximately 20. Figures 12, 13, and 14 show the comparison of theoretical results given in Fig. 11 with the experimental results reported in Ref *1* on pipes of various steels. Figure 12 shows the comparison for through cracks where the (theoretical) solid curve is obtained from Fig. 11 (with $d = h$) and the points represent the experimental results. In calculating the experimental results from the burst pressure, it was assumed that $\sigma_y = \sigma_{ys} + 10\ 000$ psi which was suggested in Ref *1*. This corresponds to $0.11 < n < 0.115$ in Eq 1. The Figs. 13 and 14 show the comparison of the theoretical and the experimental results for part-

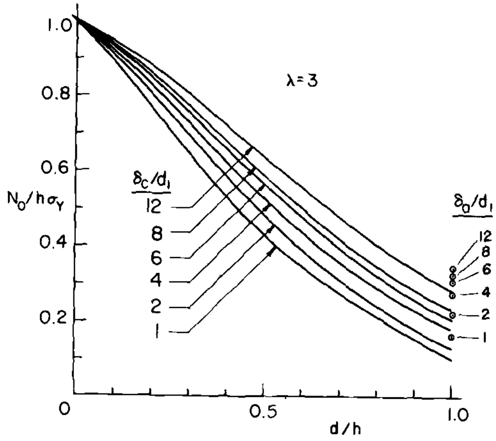

FIG. 9—N_0 *versus* d *for constant total crack opening stretch,* δ_c *at the leading edge of the crack in the mid-section* (x = *0,* z = h/2 − d) *in a cylindrical shell with an external surface crack,* λ = *3.*

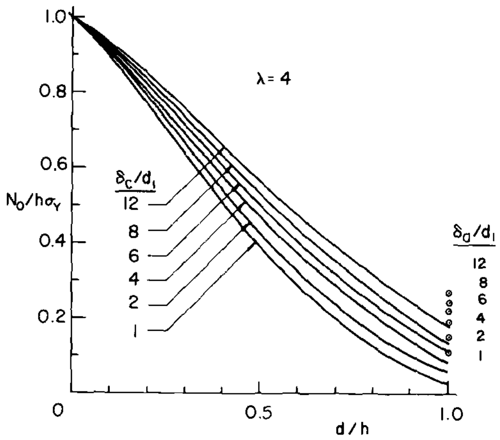

FIG. 10—N_0 *versus* d *for constant total crack opening stretch,* δ_c *at the leading edge of the crack in the mid-section* (x = *0,* z = h/2 − d) *in a cylindrical shell with an external surface crack,* λ = *4.*

through cracks where the solid curves are obtained from Fig. 11 for $d = h/2$ and in the experiments $0.492 < d/h < 0.511$. In these figures the

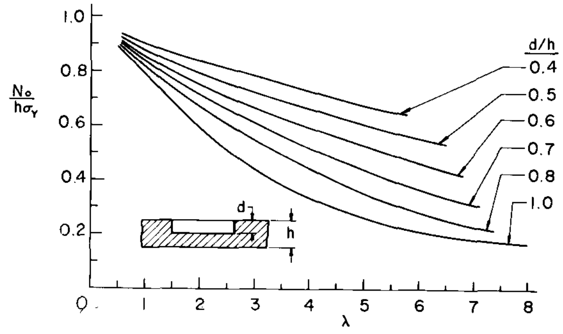

FIG. 11—*Load carrying capacity of pressurized cylidrical shells with a part through or through crack based on the plastic instability criterion.*

experimental results are calculated from the burst pressure by using n = 0.05 and n = 0.10, respectively (see Eq 1). In spite of the simplicity of the approach, the agreement seems to be encouraging.

Further Consideration of Fracture Failure by Net Ligament Plastic Instability

Referring to the results given in Ref *1*, it was found that for near-failure conditions in pressurized cylinders δ_c is generally greater than $0.1(h - d)$. On the other hand, investigations regarding the J-integral method [*7*] suggest that δ_c would need to be less than $0.04(h - d)$ for the applicability of that method of characterization. It is therefore apparent that relative to δ_c the net ligament is not large enough to characterize its failure in terms of a progressive crack extension model. A simple alternative model to study the phenomenon would be one in which the net ligament separation is regarded as controlled by plastic instability.

A nominal value of the average tensile strain in the net ligament may be estimated as

$$\epsilon = \delta_\epsilon(h - d) \tag{15}$$

where δ_ϵ is the (average) net ligament stretch given by Eq 11. Using the results of this paper and referring to the failure conditions given in Ref *1* for steel cylinders, ϵ is found to be above 0.15 which is moderately less than the expected maximum load strain for an unnotched tensile bar but greater than that for a deeply notched bar or plate. Since the net ligament geometry corresponds more nearly to the deeply notched situation, one may assume that during the increase of pressure toward a condition of net ligament failure the tensile load across the net ligament is decreasing.

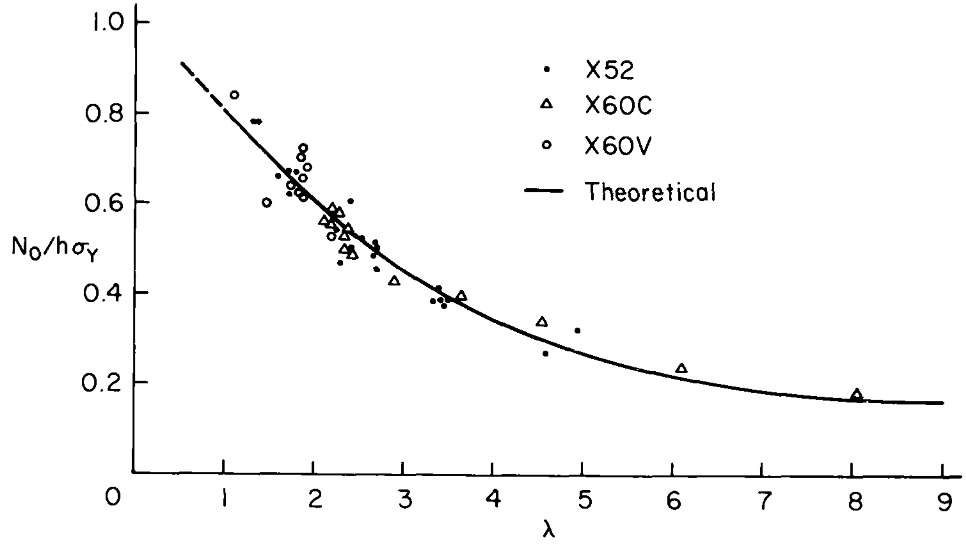

FIG. 12—*Comparison of the results of the fracture tests in steel pipes with a through crack* [1] *with that given by the plastic instability criterion: flow stress* $\sigma_y = \sigma_{ys} + 10$ *ksi.*

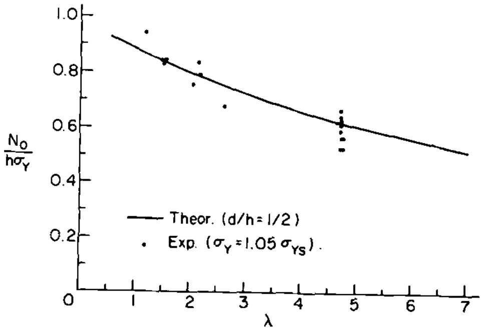

FIG. 13—*Comparison of the theoretical and experimental results for fracturing steel pipes with a part-through crack: flow stress* $\sigma_y = 1.05\ \sigma_{ys}$.

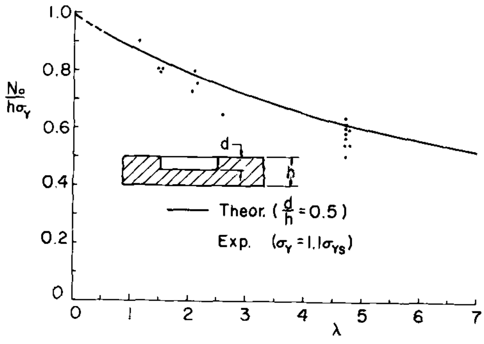

FIG. 14—*Comparison of the theoretical and experimental results for fracturing steel pipes with a part-through crack: flow stress* $\sigma_y = 1.1\ \sigma_{ys}$.

This may not necessarily mean that the net ligament separation will occur. Due to the redistribution of the load it may be possible to have a stable ϵ value for a fixed internal pressure.

A model can be constructed to illustrate this stability behavior in the following manner. Assume that for any value of ϵ greater than, say 0.1, the effective crack depth may be expressed as

$$d = d_0 + \alpha(\epsilon)\delta_\epsilon \tag{16}$$

where d_0 is the initial crack depth prior to loading and $\alpha(\epsilon)$ is a coefficient approaching unity as ϵ increases into 0.3 to 0.5 range. Assuming that $\alpha(\epsilon)$ is a known function and noting that for given dimensions R, h, and a and pressure p_0 δ_ϵ is a function of d, with Eqs 15 and 16 provides a (highly nonlinear) equation to determine d which can best be solved by successive approximations as follows

$$d(0) = d_0,\ d(N) = d_0 + \alpha[\epsilon(N-1)]\delta_\epsilon\,(N-1),\quad N = 1, 2, \ldots \tag{17}$$

Referring to Eq 11, it is seen that the iteration in Eq 17 becomes particularly simple if the results giving δ_0 and θ_2 are properly parametrized and expressed in algebraic form. Clearly, divergence of the successive approximations expressed in Eq 17 implies net ligament plastic instability, and convergence may be interpreted as a stable state.

The basic mechanics of the foregoing stability model is dependent, among other minor factors, primarily on the selection of $\alpha(\epsilon)$ and the flow stress σ_Y. Using fixed values of α between 0.4 and 0.8, it was found that roughly equivalent failure conditions could be predicted by using small α and σ_Y well above σ_{YS} or large α and σ_Y close to σ_{YS}.

As an illustration, certain test results obtained in the Battelle Columbus Laboratories on a pressurized line-pipe steel cylinder with an external axial part-through crack were considered.[7] During the experiment the crack opening displacement δ_e of the notch at the external surface was measured (at various values of the pressure p_0) which is related to δ_0 and θ_2 by

$$\delta_e = \delta_0\left(1 + \frac{h}{2R}\right) + \frac{h}{2}\,\theta_2 \tag{18}$$

These measurements and other relevant information are: $R = 18$ in., $h = 0.403$ in., $d_0 = 0.201$ in., $2a = 3.8$ in., $\sigma_{YS} = 64.6$ ksi; p_0(ksi): 1.0, 1.2, 1.25, 1.29; and δ_e(mils): 29, 60, 80 failure.

The successive approximation results for δ_0/h were obtained by assuming

$$\sigma_Y = \sigma_{YS} + 2 \text{ ksi},\quad \alpha(\epsilon) = 0.46 + 0.54\,(1 - 0.1/\epsilon) \tag{19}$$

and are given in Fig. 15. Curves A, B, and C correspond to the pressures 1.0, 1.2, and 1.25 ksi, respectively. Curve D corresponds to $p_0 = 1.267$ ksi where the quantities δ_e and ϵ shown in the figure are for $N = 14$. It may be seen that while Curves A, B, and C stabilize, δ_0/h corresponding to Curve D diverges, increasing in nearly linear fashion with N and indicating plastic instability at this pressure. The stable limits of δ_e and ϵ

---

[7] The information was supplied by J. F. Kiefner and refers to Battelle Experiment 70–13.

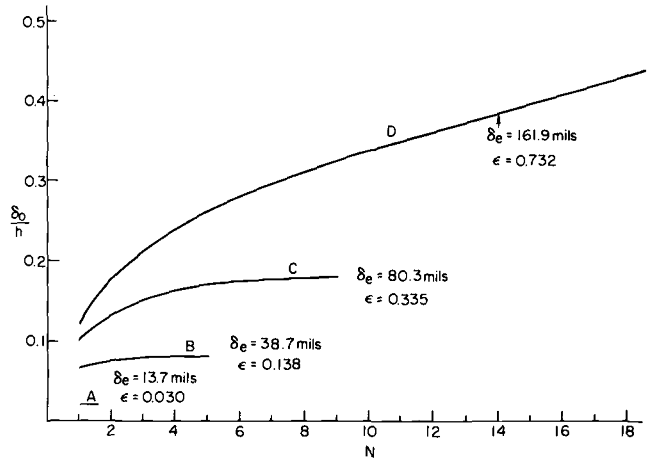

FIG. 15—*Successive approximation values of* δ_0/h *for the conditions of Battelle Experiment No. 70–13. Curves A, B, C, D correspond respectively to internal pressure of 1000, 1200, 1250, and 1267 psi.* N *is the successive approximation number.*

for Curves A, B, and C are shown in the figure. Although the values of δ_e comparable to those observed in the experiment were predicted by the calculation close to failure pressure, the predicted δ_e becomes increasingly too small for pressures below 1.25 ksi. Aside from all the approximations regarding the modeling and the analysis of the elastic-plastic shell problem, this may primarily be due to inadequate representation of δ_0 and θ_2 curves at the range of smaller pressures or N_0/h_y which was used in the calculations. With regard to the trends of the successive approximation curves, if one assumes that the plastic strains represented by approximately the first five iterations correspond to the initial "small time" response, it may be interesting to note that the calculated trend lines show a resemblance to the experimentally observed creep of the crack opening displacement.

In general, the results obtained from the simple plastic instability model are encouraging. They suggest that large net ligament strains can develop in a stable manner at pressures less than the failure pressure. Even though a complete study over a wide range of λ and d_0/h was not made, the comparison of selected trials at $\lambda = 3$, $d_0 = 0.6h$ and $\lambda = 1.5$, $d_0 = 0.5h$ with Battelle experiments 70-13 indicated that, with proper parameter adjustments approximate agreement with experimental data should be no problem. It should also be pointed out that a more rigorous analysis leading to a theoretically acceptable "valid" representation of the displacements and stresses in the net ligament is a major task which at this point does not appear to be tractable. However, as the foregoing example demonstrates, the concept certainly has a great deal of merit as an alternative approach to model part-through deep crack problems in thin plate and shell structures and needs to be described in the hope of attracting further research.

Conclusions

1. Formidable analytical complexities cannot be avoided when plasticity is included into the shell theory. Nevertheless, by means of a simple model a substantial set of results were produced which permit useful estimates of crack opening stretch, net ligament strain, and crack opening rotation.

2. For internal pressures near the value corresponding to failure, that is, for near-failure conditions, estimates based on the shell model show that the crack opening stretch is too large relative to net ligament size for applicability of a failure criterion of the customary fracture mechanics type.

3. For near-failure conditions, estimates of the net ligament strain are clearly large enough to indicate that a loss of tensile force across the net ligament accompanies the approach of the internal pressure toward the failure value.

4. The criterion for net ligament separation based upon plastic instability corresponds approximately with experimental observations.

5. As a first approximation, a less complex method of using the results of the shell model for prediction of failure conditions may be justified. One such criterion based on a critical slope of crack opening stretch versus hoop stress appears to show good agreement with experimental results.

Acknowledgments

The work reported in this paper was supported by the Materials Division, NASA, Langley (Grant NGR39–007–011) and by Battelle Memorial Institute, Columbus Laboratories, Columbus, Ohio. In particular, we would like to express our thanks to W. Illg of NASA and R. J. Eiber of Battelle for their interest and support.

References

[1] Kiefner, J. F., Maxey, W. A., Eiber, R. J., and Duffy, A. R. in *Progress in Flow Growth and Fracture Toughness Testing, ASTM STP 536,* American Society for Testing and Materials, 1973, pp. 461–481.

[2] Erdogan, R., and Kibler, J. J., *International Journal of Fracture Mechanics,* Vol. 5, 1969, pp. 229–237.

[*3*] Yuceoglu, U. and Erdogan, F., *International Journal of Solids Structures,* Vol. 9, 1973, pp. 347–362.
[*4*] Erdogan, F. and Gupta, G. D., *Quarterly of Applied Mathematics,* Vol. 30, 1972, pp. 525–534.
[*5*] Erdogan, R. and Ratwani, M., *International Journal of Fracture Mechanics,* Vol. 8, 1972, pp. 413–426.
[*6*] Erdogan, F. and Ratwani, M., *Nuclear Engineering and Design,* Vol. 27, 1974, pp. 14–29.
[*7*] Landes, J. D. and Begley, J. A. in *Fracture Toughness, ASTM STP 514,* American Society for Testing and Material, 1972, pp. 24–39.

G. T. Hahn,[1] *R. G. Hoagland,*[1] *M. F. Kanninen,*[1] *and*
A. R. Rosenfield[1]

Pilot Study of the Fracture Arrest Capabilities of A553B Steel

---

REFERENCE: Hahn, G. T., Hoagland, R. G., Kanninen, M. F., and Rosenfield, A. R., "**Pilot Study of the Fracture Arrest Capabilities of A533B Steel,**" *Cracks and Fracture, ASTM STP 601,* American Society for Testing and Materials, 1976, pp. 209–233.

ABSTRACT: The arrest properties of A533B steel are derived from measurements of the crack velocity and crack length at arrest using: (*a*) 140 by 400-mm duplex double-cantilever-beam (DCB) specimens with hardened and welded-on AISI 4340 steel starter sections, (*b*) a wedge-loading procedure, and (*c*) the Timoshenko beam-on-a-generalized-foundation dynamic analysis. Propagation and arrest events were studied at temperatures from −18 to 33°C (nil ductility temperature + 61°C) and involved fractures propagating in the A533B at velocities up to 710 ms^{-1} and for distances up to 159 mm. The arrest capability of the steel is expressed in terms of the propagating crack fracture energy for the corresponding toughness, K_D, and the velocity dependence of these quantities. The thickness, crack velocity, and temperature dependences of K_D and its relation to K_{Ic} and K_{Ia} are examined. At −18°C, $K_D = 129\ \text{MNm}^{-3/2}$, and $K_a = 76\ \text{MNm}^{-3/2}$. This method of evaluation promises to provide access to the full range of arrest properties of low and medium strength structural steels.

KEY WORDS: crack propagation, fractures (materials), velocity, double-cantilever-beam specimen, steels

Nomenclature

A	Area of crack
$A(v)$	Function relating G and K for a rapidly moving crack
a_0	Initial crack length
a_1	Crack length at end of starter section in DCB specimen
b	Specimen thickness

---

[1] Manager, Metal Science Section, principal metallurgist, Metal Science Section, senior mathematician, Applied Mathematics and Mechanics Section, and associate manager, Metal Science Section, respectively, Battelle Columbus Laboratories, Columbus, Ohio 43201.

b_n	Specimen thickness at root of sidegroove
C_0, C_1, C_2, C_R	Wave speeds
DCB	Double cantilever beam
E	Young's modulus
e	Distance from end of specimen to center line of loading pins
G_I	Crack-tip energy release rate
G_Ia	Strain energy release rate at the instant of crack arrest
h	DCB specimen half height
$K_\mathrm{a}, K_\mathrm{Ia}$	Stress intensity at crack arrest
$\bar{K}_\mathrm{D}$	Average value of K_D
$K_\mathrm{D}, K_\mathrm{ID}$	Instantaneous value of propagating crack fracture toughness
K_Ic	Static plane strain fracture toughness
$K_\mathrm{D,min}, \mathrm{K}_\mathrm{ID,min}$	Minimum value of K_D or K_ID
K_Q	Stress intensity at the onset of rapid crack propagation
L_1	Length of starter section
L_2	Length of test section
L_3	Overall specimen length
NDT	Nil-ductility temperature
P	Load
$R_\mathrm{D}, R_\mathrm{ID}$	Instantaneous value of propagating crack fracture energy
$R_\mathrm{ID,min}$	Minimum value of R_ID
RW	Specimen orientation where load is applied normal to the rolling direction and crack travels in long transverce direction
T	Kinetic energy
T^D	Kinetic energy associated with dynamic crack propagation
U	Strain energy
U^D	Strain energy associated with dynamic crack propagation
V	Crack velocity
w	Beam deflection
W	External work done on specimen
WR	Specimen orientation where load is applied normal to the long transverse direction and crack travels in rolling direction
ν	Poisson's ratio
σ_{ys}	Yield strength
ψ	Beam rotation

Fracture arrest properties of steels have been measured with contoured-DCB [*1–3*] [2] and rectangular-DCB [*4–8*] specimens. More recently, the authors have described a rectangular, duplex-DCB wedge-loading procedure [*9–11*]. The method lends itself to a fully dynamic analysis [*12–14*] from which toughness values for the propagating crack can be inferred from measurements of the crack velocity as well as the

---

[2] The italic numbers in brackets refer to the list of references appended to this paper.

crack length at arrest. Secondly, a high strength-low toughness starter section welded to the specimen (see Fig. 1) reduces specimen size requirements at initiation.[3] Finally, the low toughness of the starter section makes it possible to initiate fast fractures over a wide range of temperature independent of the transition temperature of the specimen [*10*]. The method can be used to measure a broad range of arrest properties displayed by low and medium strength structural steels.

The duplex-DCB procedure has been applied to the A517F steel [*9*] and more recently to A553 and to the ABS-C, E, and EH grades [*10*]. The present paper describes the adaptation of the method to the A533B grade used in nuclear pressure vessels. Preliminary measurements of R_D and K_D, the propagating crack fracture energy and toughness, and the thickness, temperature, and crack velocity dependence of these quantities are presented. Agreements between theory and experiment support R_{ID} (or K_{ID})

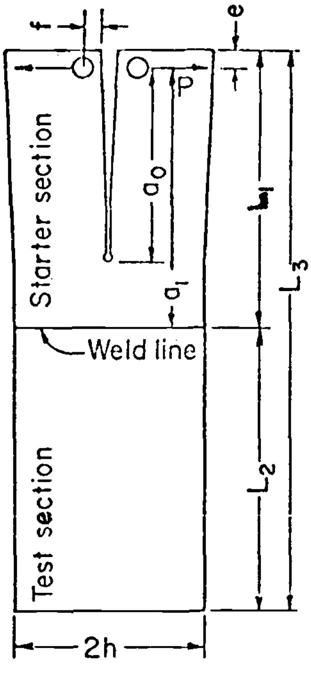

$a_0 \approx 3.3$ in. (84 mm)
$a_1 = 4.54$ in. (115.3 mm)
b (Specimen Thickness) = 0.5-2 in. (12.7-50.8 mm)
e = 1.0 in. (25.4 mm)
f = 0.94 in. (23.9 mm)
h = 2.75 in. (70 mm)
$L_1 = 5.54$ in. (141 mm)
$L_2 = 10.03$ in. (256 mm)
$L_3 = 15.62$ in. (396.7 mm)
Pin Hole Dia. = 1.5 in. (38 mm)
Pin Length = 4.5 in. (115 mm)

FIG. 1—*Wedge loaded rectangular duplex-DCB test procedure:* (a) *specimen configuration showing the wedge (A), the loading pins (B), the starting slot (C), the point of arrest (D), and the weld line (E);* (b) *wedge loading arrangement; and* (c) *record of the variation of grid voltage with time during crack propagation. In* (c)*, each step change corresponds to the rupture of one of the conducting strips shown in* (b)*.*

---

[3] The minimum size requirement for a given toughness level is reduced by the factor (σ_{ys} (starter section)/σ_{ys} (specimen)) ^{2}, which, for a A553B specimen and a 4340 steel "starter section" amounts to about X9. The symbol σ_{ys} stands for the yield strength.

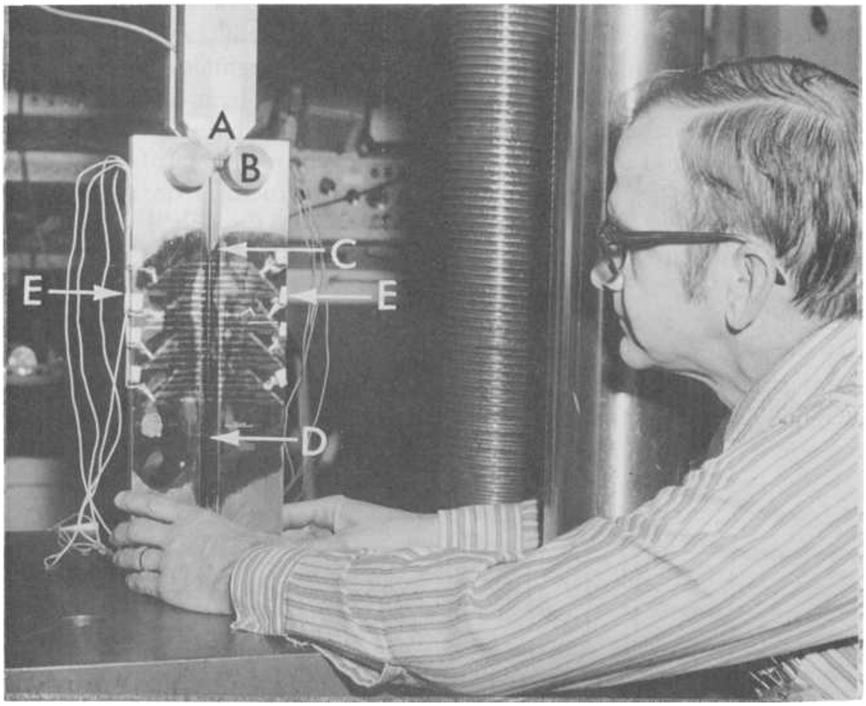

FIG. 1—(*Continued.*)

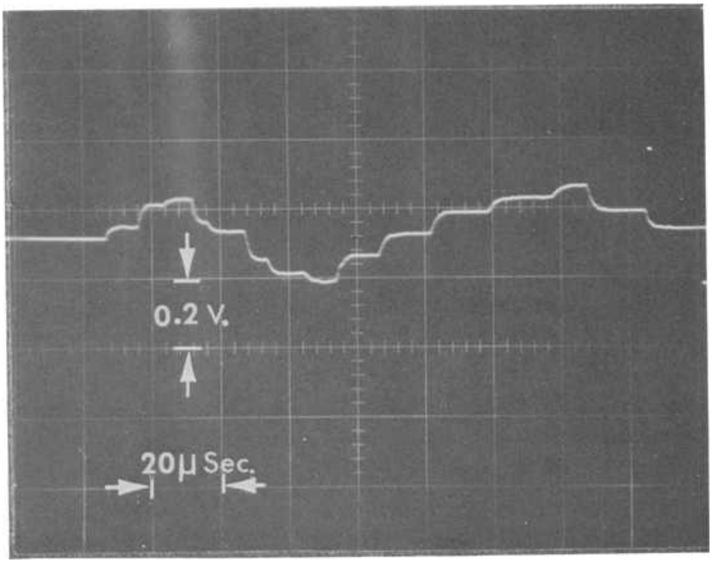

FIG. 1—(*Continued.*)

as the material property governing fast fracture and crack arrest. Relations between K_{ID} and K_{Ia} are derived from the analysis.

Experimental Procedure

The duplex-DCB specimen consists of a high strength/low toughness Society of Automotive Engineers (SAE) 4340 steel "starter section" containing a blunt starting slot which is electron beam welded to the A533B specimen (see Fig. 1*a*). Specimens of the A553B steel were taken from a rector nozzle cut out with a WR orientation. The composition and the tensile, (RW) Charpy, and (WR) fracture toughness properties of the A533B steel are given in Tables 1 and 2. The NDT of the material is −29°C. The A533B blanks were joined to quenched and tempered (R_c = 48), AISI 4340 steel starter-section blanks [4] in a 150 kVA electron beam welder. Cracking and delayed cracking in the weld were initially encountered, particularly in 50.8-mm-thick blanks. This problem was eliminated by preheating 50.8-mm-thick starter and specimen blanks 1 h at 260°C, and welding and postheating 1 h at 316°C, all without intermediate cool downs.

As shown in Fig. 1*b*, the specimens are loaded by slowly forcing a wedge between the loading pins. Stress intensity values are calculated

TABLE 1—*Tensile and fracture toughness properties of the A533B steel.*

Temperature, °C	Yield Stress		Ultimate Stress			K_{Ic}
	ksi	MNm^{-2}	ksi	MNm^{-2}	% EL	$MNm^{-3/2}$ [a]
−18	...	...	...	...	...	148,153
+10	...	...	...	...	...	243,254
+21	...	...	...	...	...	277,305
+24	68.5,77.0	471,530	88.5,91.5	609,630	24,25	... ...

[a] The K_{Ic} values were obtained from 2TCT specimens of WR orientation by the equivalent energy method.

TABLE 2—*Charpy-V properties (RW orientation).*[a]

Temperature, °C	Energy		Lateral Expansion		% Shear
	ft/lb	J	10^{-3} in.	mm	
−62	8,9	11,12	7,8	0.18,0.20	1,1
−34	17,21	23,29	16,16	0.41,0.41	20,20
−12	55,77	75,104	46,58	1.2,1.5	30,40
+4	71,88,75	96,119,102	66,54,56	1.4,1.4	50,50,50
+66	124,138	168,187	92,93	2.3,2.4	98,99

[a] Composition of the A533B steel [*15*]: 0.23C, 1.26Mn, 0.010P, 0.014S, 0.14Cu, 0.18Si, 0.65Ni, 0.54Mo.

---

[4] The AISI 4340 steel starter sections were austenized 1 h at 843°C, oil quenched, and tempered 1 h at 204°C.

from the slot or crack length and the displacement measured with a clip gage mounted on top of the specimen in a hollow space in the wedge. The relations employed are derived from Ref *12*. At a critical stress intensity K_Q, a sharp crack emerges from the blunt slot in the starter section. Because the starter slot is purposely blunted, the fracture immediately becomes unstable, since $K_Q > K_{Ic}$. The crack propagates at high speed, typically ~ 800 ms^{-1} (2500 ft/s), into the specimen, where it may continue to propagate for some distance before arresting. Step changes in the voltage measured across a series of conducting strips (vapor deposited on the specimen surface over a thin epoxy layer) are used to measure the crack velocity (see Figs. 1*b* and *c*). Additional details of the testing procedure can be found in Refs *9* and *11* and in Tables 3 and 4.

The initial experiments (Series I in Tables 3 and 4) revealed a strong tendency for the crack to branch after entering the A533B specimen (see Fig. 2). The possibilities that branching is caused either by residual stresses in the locale of weld or by a wave reflection or that the branching could be avoided by large compression stresses as high as 35 000 psi were shown to be remote by the experiment illustrated in Fig. 3. The specimen in Fig. 3 and the other experiments of Series II and III, Table 3, show that branching can be prevented with deep side grooves cut into the specimen.

A photograph of the specimen configuration that evolved from the experiments of Series I and II is shown in Fig. 1*b*. The design differs slightly from that employed in Series II in that the side grooves run the entire length of the specimen—a feature that eliminates costly spark machining operations. The depth of each of the v-shaped side grooves is 30 percent of the total thickness, a value selected on the basis of previous experience. One has an included angle of 45 deg, the other is 90 deg to facilitate deposition of the velocity measuring conducting strips.

In the Series III experiments, duplicate 12.7, 25.4, and 50.8-mm-thick specimens were successfully tested at −18°C, individual specimens, at both 10 and 32°C. Detailed descriptions of the Series I, II, and III experiments are given in Table 3, but only those of Series III lend themselves to analysis of A533B properties.

Dynamic Analysis

Kanninen [*13,14*] has derived a fully dynamic analysis of crack propagation and arrest in wedge-loaded rectanglar DCB-specimens with finite dimensions. The analysis is based on the type of energy balance first used by Mott [16] and is expressed in terms of G_I, the dynamic crack tip energy release rate, and R_{ID}, the propagating crack fracture energy or K_I and K_{ID}, the corresponding stress intensity parameters [*17–20*]. These quantities are defined more fully in the Appendix. Criteria for crack propagation and arrest dictated by energy conservation can be expressed in these terms

$$\text{criteria for crack propagation} \left.\begin{array}{l} G_I = R_{ID}(V) \\ K_I = K_{ID}(V) \end{array}\right\} \qquad (1)$$

$$\text{criteria for crack arrest} \left.\begin{array}{l} G_I < R_{ID,\ min} \\ K_I < K_{ID,\ min} \end{array}\right\} \qquad (2)$$

Note that inequality ($G_I < R_{ID,min}$) the dynamic fracture arrest criterion, reduces to the static arrest criterion employed by Crosley and Ripling [*1*,*2*] and others [*7*] when kinetic energy and dynamic effects are neglected (see Appendix).

The equations governing dynamic crack propagation in the rectangular-DCB specimen were obtained from the fundamental equa-

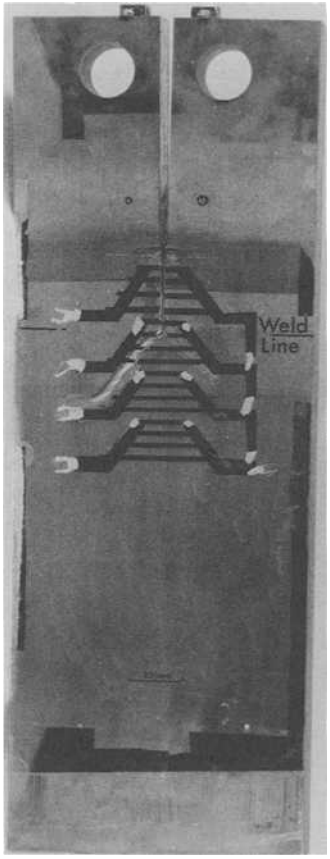

FIG. 2—*Specimen 3V4B-A4, tested at* $-16°C$, *30-deg wedge,* $K_Q = 286\ MNm^{-3/2}$.

TABLE 3—*Results of fracture arrest experiments.*

Specimen	Side Groove Configuration	Thickness, mm	a_0, mm	Notch Root, dia mm	Wedge Angle, deg	Test Temperature, °C	Critical Load, MN[b]	Critical Displacement, mm[c]	Arrest Displacement, mm[d]
				SERIES I					
3V4B-B2[a]	no grooves	25.4	88.9	1.32	30	11	0.210	4.62	7.21
3V4B-A4[a]	no grooves	25.4	87.6	1.32	30	−16	0.184	4.01	5.79
3V4B-A2[a]	no grooves	25.4	88.4	0.50	45	−16	0.182	2.57	crack ran to side
3V4B-B3	no grooves	25.4	97.5	0.71	80	10	0.351	2.44	4.45
3V4B-B4	no grooves	25.4	96.8	1.12	80	10	0.342	2.54	3.38
				SERIES II					
3V4B-A5	no grooves	25.4	94.0	1.22	100	11	0.627	2.64	5.79
3V4B-B1	partial side grooves[e]	25.4	62.7	1.52	100	−16	0.827	3.10	arm broke
3V4B-B5	2 side grooves[g]	25.4	83.6	1.52	45	−17	0.198	2.62[f]	3.84
3V4B-A1	1 side groove[g]	25.4	82.8	1.42	80	−19	0.574	2.95	6.22
3V4B-B6	1 side groove[g]	25.4	83.6	1.52	80	10	0.661	3.38	arm broke
3V4B-A3	2 side grooves[g]	25.4	84.3	1.27	80	11	0.538	3.00	6.10

				SERIES III					
3V4B-AC5	2 side grooves[h]	12.7	85.6	1.85	80	−17	0.158	1.52	2.90
3V4B-AC6	2 side grooves[h]	12.7	79.8	1.85	80	−21	0.156	1.55	2.92
3V4B-C6	2 side grooves[h]	25.4	83.8	1.85	80	−18	0.262	1.55	3.05
3V4B-C5	2 side grooves[h]	25.4	82.0	1.85	80	−19	0.247	1.50	2.09
3V4B-C2	2 side grooves[h]	50.8	83.8	1.91	80	−16	0.476	1.40	4.83
3V4B-C7	2 side grooves[h]	50.8	84.8	1.88	80	−17	0.506	1.63	5.00
3V4B-C4	2 side grooves[h]	25.4	83.8	2.13	80	10	0.289	1.65	3.25
3V4B-C3	2 side grooves[h]	25.4	83.8	2.49	80	32	0.298	1.70	2.72

[a] Pin dimensions, diameter 25.4 mm, length, 88.9 mm; other specimens, diameter 38.1 mm, length, 114.3 mm.

[b] Compressive load at the onset of propagation.

[c] Displacement gage reading at the onset of propagation.

[d] Displacement gage reading after crack arrest.

[e] 25.4-mm-long side groove beginning in starter section near weld line and extending 19.1 mm into test section.

[f] Previously loaded to 889 600 N and a displacement of 3.68 mm which were not sufficient to initiate the crack.

[g] Side grooves beginning in starter section about 6 mm from weld line and running full length of specimen.

[h] Side grooves cut full length of specimen.

TABLE 4—*Results of fracture arrest experiments.*

				4340 Steel Starter Section			A533 Steel Specimen			
Specimen	$K_Q{}^a$ MNm$^{-3/2}$	$K_a{}^b$ MNm$^{-3/2}$	$\overline{K_D}{}^c$ MNm$^{-3/2}$	V, ms^{-1}	a_1-a_0, mm	$K_D{}^d$ MNm$^{-3/2}$	V, ms^{-1}	a_a-a_1, mm	$K_D{}^d$ MNm$^{-3/2}$	$K_D{}^e$ MNm$^{-3/2}$
					SERIES I					
3V4B-B2 [a]	324	. . .	. . .	900	31.75	180	. . .	5.1+25.4/30.5 [f]	. . . [h]	. . . (h)
3V4B-A4 [a]	286	. . .	. . .	700	33.02	180	560 [g]	1.27+33.0/34.3 [f]	. . . [h]	. . . (h)
3V4B-A2 [a]	181	. . .		610	32.26	120	959 [g]	5.1+25.4/30.5 [f]	. . . [h]	. . . [h]
3V4B-B3	154	(97)	122	400	23.11	120	~200 [g]	1.78/18.8 [i]	. . .	>100 [j]
3V4B-B4	162	(106)	131	~400	23.88	127	. . .	1.27/14.2 [i]	. . .	>112 [j]
					SERIES II					
3V4B-A5	174	(105)	135	~750	23.88	110	~900	21.34	. . .	>140
3V4B-B1	220	. . .	. . .	1250	27.43	~110	520	20.3+76.2/96.5	. . . [h]	. . . [h]
3V4B-B5	. . . [k]	. . . [k]	. . . [k]	. . . [k]	. . . [k]	. . . [k]	. . . [k]	. . . [k]	. . . [k]	. . . [k]
3V4B-A1	224	(103)	152	910	34.04	120	500	85.34	260	253
3V4B-B6	254	(183) [l]	170 [l]	720 [l]	1.10 [l]	160 [l]	520 [l]	43.18	290 [l]	315 [l]
3V4B-A3	223	(123)	166	640	30.73	150	~400	72.15	275	207

Series III

3V4B-AC5	120 (189)	68	113	800	33.02	111	710	72.64	118	120
3V4B-AC6	124 (196)	74	120	. . .	34.80	. . .	540	54.61	137	131
3V4B-C6	118 (186)	83	124	880	30.48	105	555	54.86	129	131
3V4B-C5	116 (184)	74	117	930	32.51	101	510	90.93	132	123
3V4B-C2	106 (168)	. . .	. . .	. . .	31.75	. . .	. . .	118.87	. . .	>79
3V4B-C7	114 (180)	80	120	880	30.73	101	500	128.27	130	122
3V4B-C4	125 (198)	87	131	980	30.99	105	380	83.31	168	143
3V4B-C3	132 (209)	(101)	145	820	31.24	122	. . .	33.78	. . .	>174

[a] K_Q values are calculated from the end displacement neglecting the presence of side grooves and reflect the energy stored in the specimen at the onset of propagation. K_Q values in parenthesis are corrected for the presence of side grooves by the factor $(b/b_n)^{0.5}$, where b is the thickness of the plate, and b_n the thickness of the reduced section.

[b] K_a values are based on the initial displacement and the crack length at the first halt. Values in parentheses are lower bound estimates based on the crack length at final arrest.

[c] $\bar{K}_D = \sqrt{K_Q \times K_a}$.

[d] K_D values calculated from crack velocity measurements and dynamic analysis assuming A-type $K_{ID}(V)$ by way of Fig. 5*c*.

[e] K_D values calculated from crack length at first halt, or lower bound from crack length at arrest, by way of dynamic analysis for A-type $K_{ID}(V)$ by way of Fig. 5*c*.

[f] Cracked branched; approximate length of the two branches is quoted.

[g] Crack velocity of one of the two branches.

[h] Analysis invalidated by branching.

[i] Values indicate penetration on the surface and on the midsection, respectively.

[j] Lower bound value based on furthest penetration at center of plate.

[k] Weld fractured before crack could penetrate A533B specimen.

[l] Values unreliable because DCB arm fractured at weld line during propagation event.

[m] Values in parenthesis show crack length in specimen corresponding to the first halt.

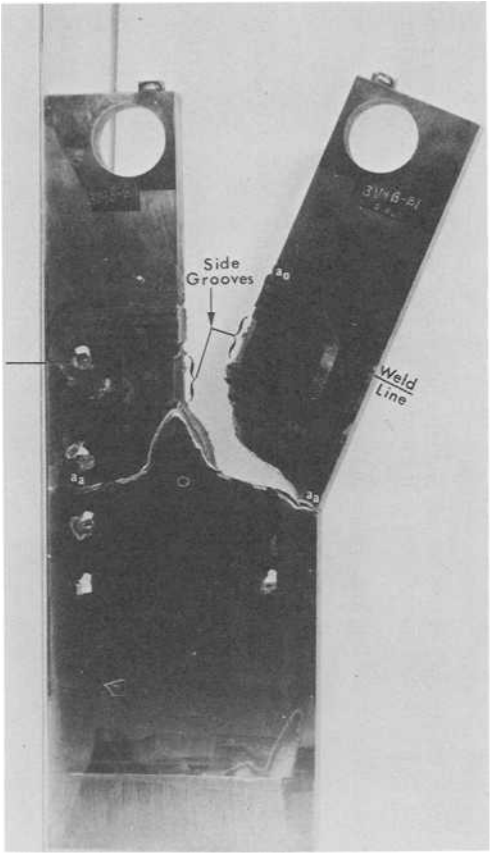

FIG. 3—*Specimen 3V4B-B1 tested at −18°C (NDT + 11°C).*

tions of mechanics (that is, equations of motion, constitutive equations, and kinematic equations) [*13,14*]. The resulting treatment gives equations that are similar to those of a Timoshenko beam-on-a-generalized-elastic-foundation. The calculations assume an infinitely stiff loading system (no wedge movement or energy transfer between loading system and specimen after the crack initiates; $dW^D/dA = 0$) although the arms of the specimen are free to oscillate subject to the constraint of wedge loading; that is, the displacement of the loading points can never be less than at the onset of propagation. For a given DCB-specimen geometry, K_Q value and the material elastic properties, density and R_{ID} (V) or K_{ID} (V), the equations determine the time variation of crack length, a, crack velocity, V, and the energy components U^D and T^D by direct computation of the dynamic crack driving force, G_I. The program also computes K_{Ia}, the stress intensity parameter for the conditions at arrest after vibrations in the system are damped out.

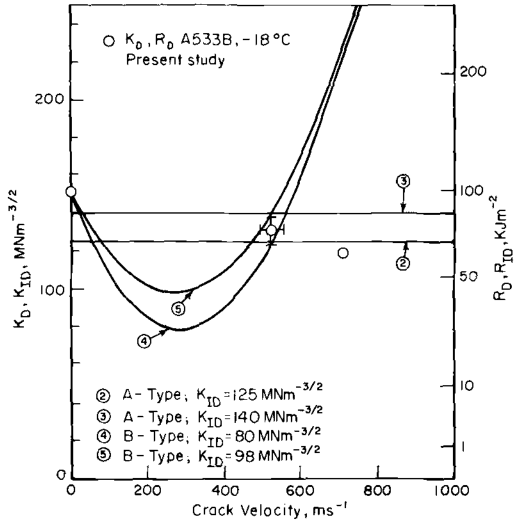

FIG. 4—*K_{ID} crack velocity dependencies employed in the calculations for the A533B specimens and K_D values derived from the measurements.*

Calculations were performed for A-type (crack velocity independent) and B-type (parabolic) K_{ID} crack velocity dependences [*11,21,22*]

starter section
  Dependence 1 A-type, $K_{\mathrm{ID}} = 104\ \mathrm{MNm}^{-3|2}$
specimen
  Dependence 2 A-type, $K_{\mathrm{ID}} = 125\ \mathrm{MNm}^{-3|2}$
  Dependence 3 A-type, $K_{\mathrm{ID}} = 140\ \mathrm{MNm}^{-3|2}$
  Dependence 4 B-type, $K_{\mathrm{ID,min}} = 80\ \mathrm{MNm}^{-3|2}$
  Dependence 5 B-type, $K_{\mathrm{ID,min}} = 90\ \mathrm{MNm}^{-3|2}$

The four dependences for the specimen are illustrated in Fig. 4. Results of the calculations for the A-type dependence are presented in Fig.5. The crack length-time curves and the variations of the energy components with crack length are qualitatively the same for the A- and B-type dependencies [*11,14*]. The main difference is that the oscillations [5] in the crack length-time curves are more prominent for the A-type dependence and make it more difficult to assign a single average velocity to the specimen (see Refs *2,3,* and *11*). The uncertainty associated with velocity

---

[5] The oscillations are connected with the way blunting is treated in the analysis and may be an artifact of the theoretical model [*13,14*].

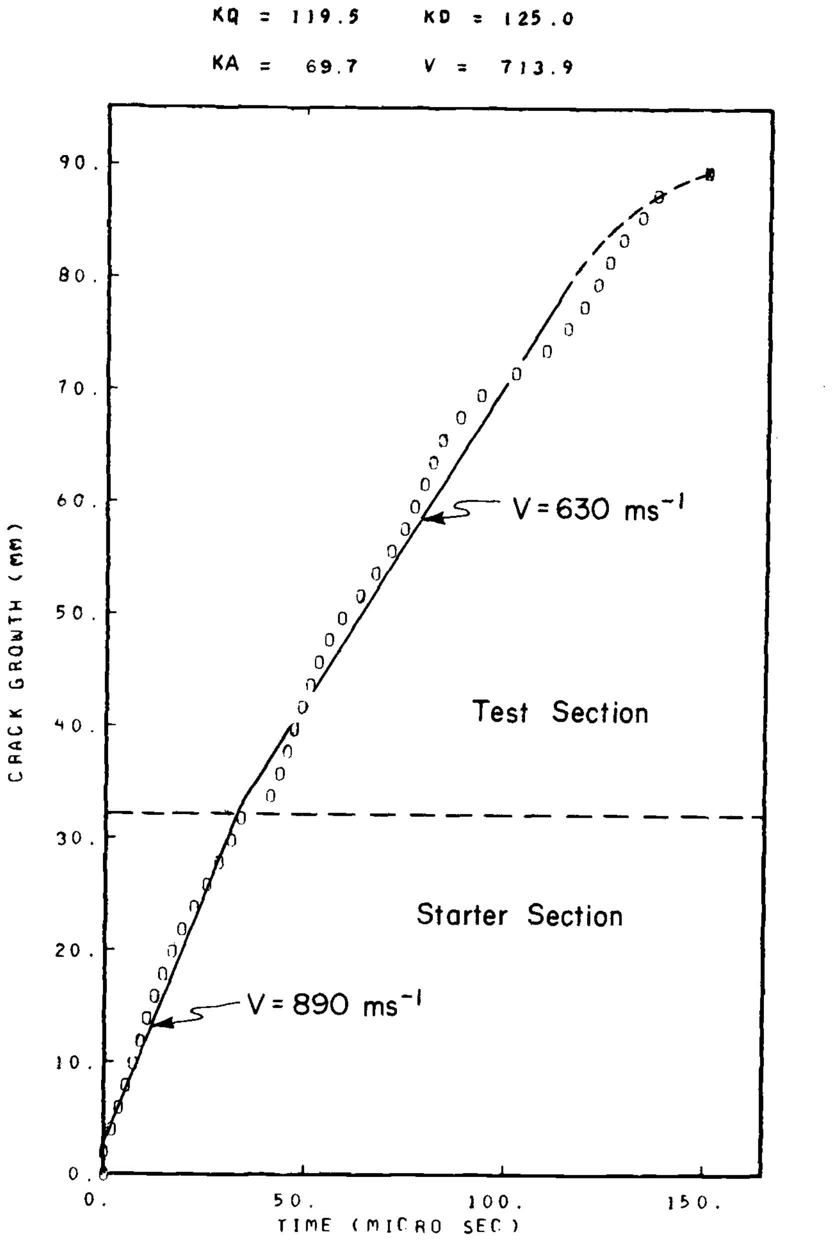

FIG. 5—*Results of the Timonshenko-beam-on-a-generalized-elastic-foundation analysis for the duplex DCB specimen and A-type material behavior.*

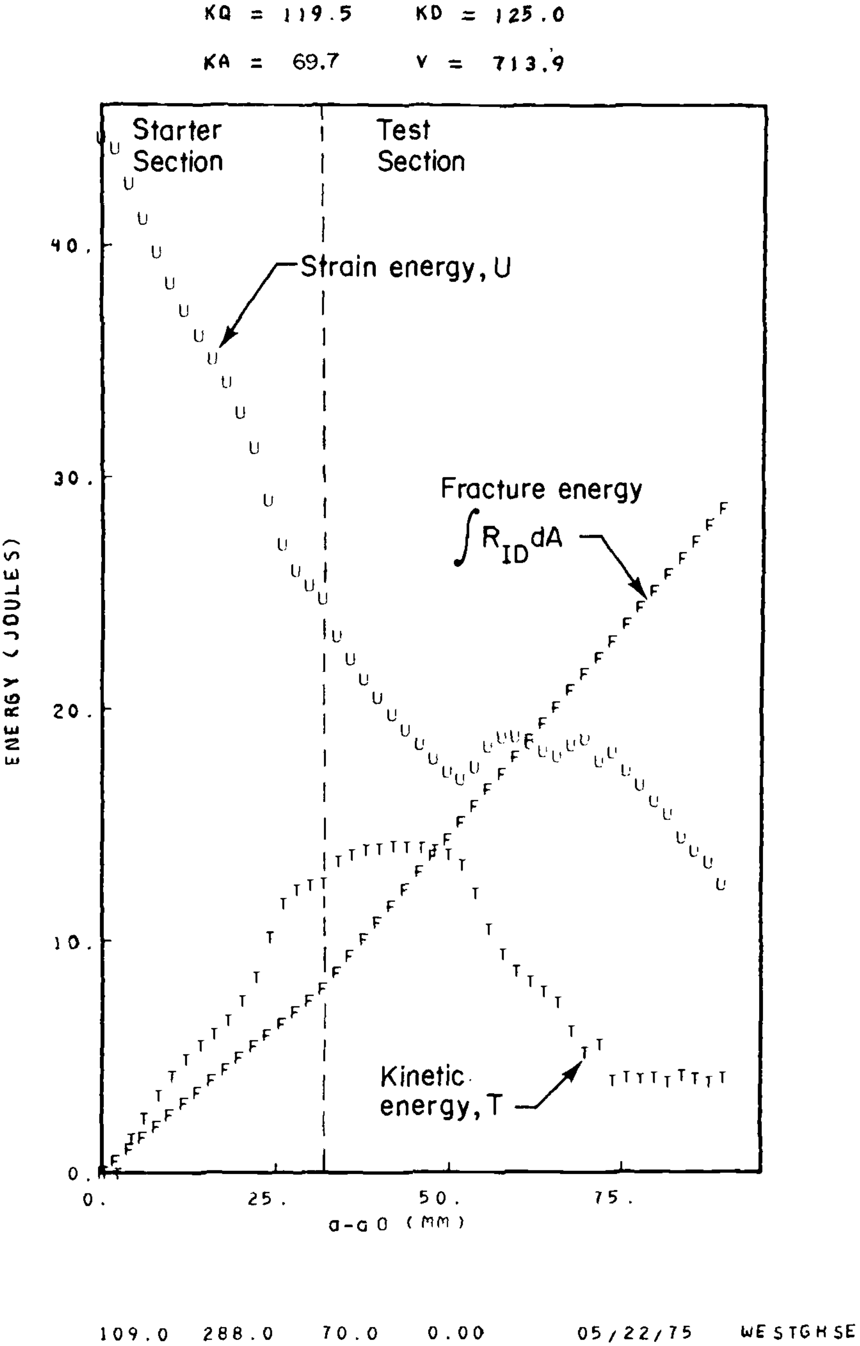

FIG. 5—*(Continued.)*

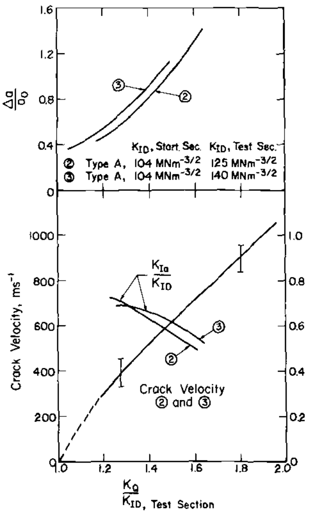

FIG. 5—*(Continued.)*

values calculated for A-type dependences is indicated by the bracket in Fig. 5*c* or by a band in other figures.

Figure 5*c* presents in graphical form the analytically derived characteristics of crack propagation and arrest in the duplex-DCB specimen. The main features are that crack velocity and the distance propagated during an event increase with K_Q. At the same time, the stress intensity at arrest, K_{Ia} decreases with K_Q; K_{Ia} does not correspond with any point on the K_{ID} velocity dependence. Previous calculations [*11,14*] have shown that the relation between $K_Q/K_{ID(\text{specimen})}$ and crack velocity is relatively insensitive to the nature of the K_{ID} velocity dependence, while the relation between K_Q/K_{ID} and $\Delta a/a_0$ is affected by the nature of the dependence. For this reason, crack velocity measurements can be interpreted without prior knowledge of $K_{ID}(V)$.

Experimental Results

The crack propagation events produced in six DCB specimens tested at −18°C (NDT + 11°C) were nearly identical and independent of thickness. Figure 6, which compares the velocity measurements, shows that fractures, which initiated at about the same K_Q level, propagated at nearly the same speed and halted (at least momentarily) after comparable extensions. Specimens C2 and C6, not shown for clarity, essentially reproduce these same features (see Table 4). Results for Specimen AC5

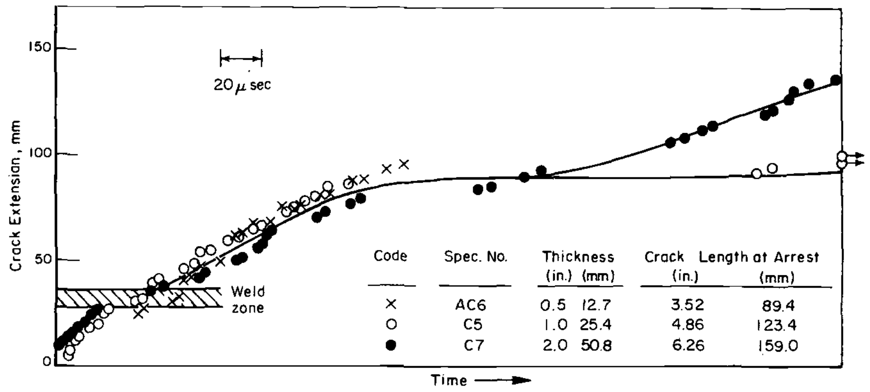

Code	Spec. No.	Thickness (in.)	Thickness (mm)	Crack Length at Arrest (in.)	Crack Length at Arrest (mm)
×	AC6	0.5	12.7	3.52	89.4
○	C5	1.0	25.4	4.86	123.4
●	C7	2.0	50.8	6.26	159.0

FIG. 6—*Crack length versus time records derived from the conducting grids of the 4340/A533B duplex DCB specimens tested at −18°C (NDT + 11°C).*

are somewhat atypical, as the crack propagated at a higher speed. The crack in the 12.7-mm-thick AC6 specimen arrested after propagating 89.4 mm in about 90 μs. Cracks in the 25.4 and 50.8-mm-thick specimens reinitiated after halts of ~100-μs duration, propagating an additional increment before finally arresting. Detailed measurements that have since been performed [*23*] show (*a*) reinitiation is a consequence of additional wedge movement (relative to the pins) that occurs after the crack begins to propagate [6] and (*b*) the effects of this movement are not communicated to the crack tip in time to affect the speed and duration of the propagation event up to the first halt. In other words, the first halt corresponds with crack arrest for the case where the wedge does not move once the crack begins to propagate, namely, the condition treated by the present analysis. Subsequent extensions, halts, and the final arrest involve the additional pin displacements produced by the wedge after the crack begins to propagate. Consistent with this, the Series III K_{Ia} values quoted in Table 4 were calculated for the initial pin displacement and the crack length at the initial halt.

Figure 7 illustrates the K_D and K_a values relative independence on thickness over the range examined. The ratio $K_a/K_D = 0.59$, indicated by Fig. 7*a* is close to the value predicted (see Fig. 5*c*) for the K_Q levels obtained in these experiments ($K_Q/K_{ID} \approx 1.43$). The temperature de-

---

[6] Part of the movement arises from the interaction between the DCB specimen and the testing machine, which increases with greater applied loads and larger amounts of energy stored in the testing machine. Consistent with this, the difference between the final and initial wedge-opening displacement and the second increment of crack extension increase with specimen thickness (see Table 1), and reinitiation can be eliminated entirely by reducing the wedge angle [*23*].

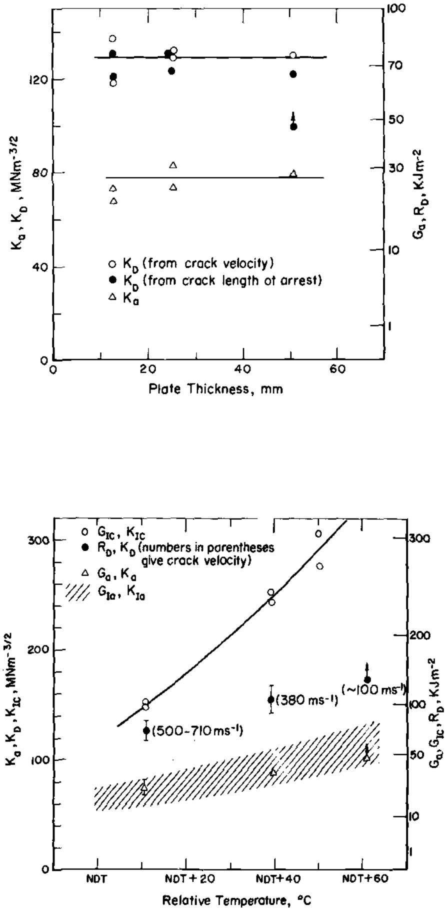

FIG. 7—*Influence of specimen thickness and test temperature on measured* K_D *and* K_a *values.*

pendence of K_D, K_a, and K_{Ic} is shown in Fig. 7*b*. The present K_a values fall into the band reported for K_{Ia} measurements by Crossley and Ripling [*24*].

An effort was made to distinguish whether the A-type or B-type K_{ID} velocity dependence is appropriate for the A533B steel. As shown in Fig. 8*a*, either A-type 2 or B-type 4 (together with A-type 1 for the starter section) provide a reasonable description of the velocity measurements. However, A-type 2 is in somewhat better accord with the crack length measurements than B-type 4 (see Fig. 8*b*). It is true that B-type 5 offers a good description of crack length, but its description of the velocity in the specimen is inferior to the A-type 2. These results, together with the K_D values in Fig. 4, are an indication that the rate independent A-type behavior may be more appropriate than the B-type at 18°C for the range of velocity examined.

Discussion

The present experiments, which were instrumented more completely than previous crack arrest studies of the A533B grade [*1*, *2*], show that the specimens are not in static equilibrium at the time of arrest. The 90 μs duration of the propagation and arrest event in Specimen AC6 is shorter than the period of the longest standing wave in the DCB-specimen arm which is estimated to be ~400 μs [7] for the crack length corresponding to arrest. It follows that the crack propagation and arrest events that were measured here cannot be treated with a static analysis.

The Timoshenko beam-on-a-generalized-foundation, though one dimensional, is a first principle, dynamic analysis accounting for both the kinetic energy *and* the translational and rotational inertia. The fact that the analysis, together with the two disposable R_{ID} (V) [or K_{ID} (V)] characteristics for the starter section and specimens, accounts for (*a*) the observed crack velocity profile, (*b*) the absolute magnitude of the velocity in the starter section and (*c*) specimen section, and (*d*) the crack length at arrest, as well as (*e*) the observed variation of these quantities with K_Q level in other tests [*6*], is strong evidence that the approach is sound. Further evidence, demonstrating the specimen geometry independence of $K_{ID}(V)$ is currently being sought. In the meantime, it should be noted that the analysis shows a significant amount of kinetic energy in the duplex specimen is converted into fracture energy. Figure 5*b* shows this and illustrates that the kinetic energy release rate, $-dT^D/dA$ (the slope of the kinetic energy curve), makes a significant contribution to the crack driving force. For this reason, K_{Ia} does not emerge either as an invariant or as a good approximation of $K_{ID,min}$, which it is intended to represent [*21*,*22*]. At −18°C, the K_a values underestimate K_{ID} by 41 percent.[8]

One finding of the present study is that the duplex-DCB test method can be useful for measuring the heavy section fracture arrest capabilities of A533B and other medium strength steels above the NDT with modest specimen size and load requirements. At −18°C, initiation levels of $K_Q \approx 115$ $MNm^{-3/2}$ succeeded in producing about 80-mm-long crack jumps [9] which could be well characterized and appear to be quite reproducible. These jumps reflect a propagating crack toughness $K_D \approx 129$ $MNm^{-3/2}$. The AISI 4340 steel starter section can probably sustain

---

[7] From simple vibration theory for one-dimensional beams.

[8] Note that for the A-type dependence $K_{ID} = K_{ID, min}$.

[9] Note counting reinitiation.

higher K_Q values, possibly up to 250 MNm$^{-3|2}$ without excessive yielding.[10] This means that K_D measuring capacity of the 140 by 400 mm duplex specimens (with side grooves) could be as high as 250 MNn$^{-3|2}$, and even higher if smaller crack jumps are analyzed. Some difficulties may arise at high K_Q levels from the yielding of the specimen adjacent to the weld line when the distance between the starting slot and the weld line (a_1 in Fig. 1*a*) is inadequate. This may account for the discrepancy between the K_D values obtained from Specimens A1 and A3 ($K_Q \approx 224$ MNm$^{-3|2}$) of Series II and C5, C6, and C4 of Series III ($K_Q \approx 120$ MNm$^{-3|2}$).

It is not clear that the K_D values extracted from the present experiments reflect the minimum, plane-strain level. For this reason the designation K_{ID} has been purposely avoided when reference is made to actual measurements. The ASTM Test for Plane-Strain Fracture Toughness for Metallic Materials (E 399-74) thickness requirement would call for a 216-mm-thick specimen to assure plane strain at a (static) toughness level

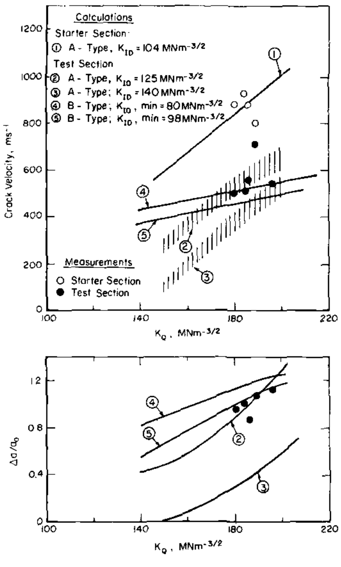

FIG. 8—*Comparison of measured crack velocity and crack extension increments (to the first halt) with theoretical expectations for different* K_{ID} *crack velocity dependence for the specimen.*

---

[10] The crack tip plastic zone undergoes a transition from a crack-like zone to a beam-like zone when the zone size-to-beam height ratio exceeds 0.09 [*25*]. The corresponding minimum beam height requirement is $H \geq$ '1.5 $(K_Q/\sigma_{ys})^2$, which is consistent with recommendations for CT-specimens [*26*].

of 129 $MNm^{-3/2}$ in A533B (σ_{ys} = 482 MNm^{-2}). The fact that the K_D values obtained for the 12.7 to 50.8-mm-thick specimens were the same may be a sign that plane strain conditions are more easily sustained at the tip of a propagating crack (for example, that propagation is accompanied by a more than three-fold elevation of the dynamic yield stress). This possibility, which remains to be verified by examining a range of thickness encompassing the ASTM Method E 399-74 requirement, implies that plane strain, propagating crack toughness values up to about $K_{ID} \approx$ 250 $MNm^{-3/2}$ may be accessible with the 50-mm-thick specimens. Additional questions raised by large compression loads and the relatively deep side grooves needed to stabilize the crack path are currently being examined.

The present set of measurements tend to discount the B-type (parabolic) K_{ID} crack velocity dependence postulated by the authors [*21*] and others [*22*] in recent discussions. If the existence of the A-type of dependence is supported by further research, the measurement task could be greatly reduced. However, measurements over a wider range of crack velocities and temperatures are needed to establish this print. Information reported here on the temperature dependence of K_D is too fragmentary for comment, except to note that K_D values fall below K_{Ic} in the range NDT + 11°C to NDT + 61°C.

Addendum

Following the symposium and preparation of the manuscript, a study of the effect of wedge angle on the experimental results was undertaken. It was concluded that all of the measured K values (K_Q, K_D, K_a) decrease linearly with wedge angle. As a result

$$K = \frac{K'}{1 - \frac{\theta}{500}} \qquad (3)$$

where

K = actual value,

K' = value calculated using the methods described in this paper, and

θ = wedge angle in degrees.

For the results reported here on Series III, the wedge angle is 80 deg and the K values should be multiplied by 1.19. Details are given in Ref *27*.

In order to analyze these results a new series of calculations may be required. However, since the model scales with K_Q/K_D, and this ratio is unchanged, the agreement between theory and experiment will not be affected.

Conclusions

1. The duration of crack propagation and arrest events in the duplex-DCB specimens, ~ 100 μs, is relatively short compared to the relaxation time. For this reason, these events require a dynamic analysis.

2. The Timoshenko beam-on-a-generalized-foundation dynamic analysis provides a good description of propagation and arrest events in duplex-DCB specimens. The analysis identifies R_{ID} (or K_{ID}), the propagating crack fracture energy (or toughness) and its variation with crack velocity as material property contolling crack arrest. It also shows that K_{Ia} values for the duplex-DCB specimen substantially underestimate, $K_{\text{ID,min}}$, the minimum propagating crack toughness.

3. Propagating crack toughness values derived from A533B specimens 12.7 to 50.8 mm thick are independent of thickness and relatively insensitive to velocity at −18°C. At this temperature K_{D} = 129 MNm$^{-3|2}$, K_{Ic} = 150 MNm$^{-3|2}$ and K_{a} = 76 MNm$^{-3|2}$. The K_{D} values appear to be intermediate between K_{Ic} and K_{a} in the temperature range NDT + 11°C to NDT + 61°C.

4. The rectangular, duplex DCB, wedge-loading procedure is a promising approach to measuring the fracture arrest capabilities of the A533B and other medium strength grades over a wide range of temperatures.

Acknowledgments

The authors wish to thank the Westinghouse Nuclear Power Systems Division for their support of this program and permission to publish. They are grateful to P. Riccardella and C. Buchalet for guidance and useful discussion. They also wish to acknowledge the technical assistance of C. R. Barnes and P. N. Mincer, and thank C. Pepper for her assistance with the manuscript.

APPENDIX

Analysis of Dynamic Fracture Propagation and Arrest Events

The Timoshenko beam-on-a generalized-elastic foundation dynamic analysis employs the type of energy balance first used by Mott [*16*]. It is expressed in terms of the energy released by the propagating crack under dynamic conditions and the energy consumed in the vicinity of the propagating crack tip. The dynamic energy release rate

$$G_{\text{I}} \equiv \frac{dW^D}{dA} - \frac{dU^D}{dA} - \frac{dT^D}{dA}$$

where W, U, and T and A are the external work, the elastic strain energy, the kinetic energy, and the crack area, respectively. The superscripts, D, emphasize that the evaluation of these quantities requires dynamic analyses. A much more attractive relation for G_I for computational purposes can be derived from the energy balance relation above. This relation expresses G_I in terms of parameters computed at the crack tip (the point $x = a$) in the Timoshenko beam generalized elastic foundation model as

$$G_I = \frac{E}{6} \left[\frac{12}{h} w^2 + h \Psi^2\right]_{x = a}$$

where w and Ψ are the beam deflection and rotation, respectively, $2h$ is the beam height, and E is Young's modulus.

The quantity R_{ID} is the engery consumed by plastic deformation and fracture processes at the tip of a propagating crack per unit area of crack advance. R_{ID} (V) signifies the R_{ID} can be a function of crack velocity. Note that $R_{ID} \rightarrow G_{Ic}$ as $V \rightarrow 0$. The quantities G_I and R_{ID} are related to K_I and K_{ID} by expressions of the form

$$K_I = A^{1/2}(V) \sqrt{\frac{EG_I}{1 - \nu^2}}$$

and

$$K_{ID} = A^{1/2}(V) \sqrt{\frac{ER_{ID}}{1 - \nu^2}}$$

where the function $A(V)$ depends on C_1, C_2, C_R, and on the crack speed V. Using a technique similar to that of Broberg [*28*], Freund [*17–19*] has evaluated $A^{1/2}$ (V) for an infinite plate and it is close to unity for low crack speeds: $1 \leq A^{1/2}$ (V); $V \leq 1500$ ms^{-1} (0.3 C_0) for steel. To facilitate comparisons with K_{Ic} and K_{Ia} values, R_{ID} values are here expressed in terms of K_{ID} assuming $A^{1/2}$ $(V) = 1$.

The (dynamic) criteria for crack propagation and arrest (Eq 1 and inequality 2) are

$$R_{ID} = \frac{dW^D}{dA} - \frac{dU^D}{dA} - \frac{dT^D}{dA} \equiv G_I \tag{4}$$

and

$$R_{ID,min} > \frac{dW^D}{dA} - \frac{dU^D}{dA} - \frac{dT^D}{dA} \equiv G_I \tag{5}$$

These expressions of energy conservation reduce to the more familiar (static) criteria for crack extension and crack arrest when kinetic energy and dynamic effects are neglected

$$R_{I(V = 0)} \leq \frac{dW}{dA} - \frac{dU}{dA} \equiv G_{IC} \tag{6}$$

$$R_{ID,min} > \frac{dW}{dA} - \frac{dU}{dA} \equiv G_{Ia} \tag{7}$$

when $dT^D/dA \rightarrow 0$, $dW^D/dA \rightarrow dW/dA$, and $dU^D/dA \rightarrow dU/dA$.

The quantity G_{Ia} the strain energy release rate derived from a static analysis for the conditions at arrest, that is, after oscillations in the system are damped out, is related to the so called arrest toughness

$$K_{\text{Ia}} = \sqrt{\frac{EG_{\text{Ia}}}{1 - \nu^2}}$$

It is important to recognize that G_{Ia} can only be equated with $R_{\text{ID,min}}$ in the static case, and not in the dynamic case when $dT^D/dA \neq 0$ or $dU^D/dA \neq dU/dA$ or $dW^D/dA \neq dW/dA$.

References

[1] Crosley, P. B. and Ripling, E. J., *Transactions,* American Society of Mechanical Engineers, Vol, 10, 1965, p. 223.
[2] Crosley, P. B. and Ripling, E. J., *Nuclear Engineering and Design,* Vol. 17, 1971, p. 32.
[3] Kawaguchi, Y., *The Sumitomo Search,* No. 10, Nov. 1973, p. 44.
[4] Hoagland, R. G., Rosenfield, A. R., and Hahn, G. T., *Metallurgical Transactions,* Vol. 3, p. 123.
[5] Hahn, G. T., Hoagland, R. G., Kanninen, M. F., and Rosenfield, A. R. in *Dynamic Crack Propagation,* G. C. Sih, Ed., Noordhoff, 1973, p. 649.
[6] Hahn, G. T., Hoadland, R. G., Rosenfield, A. R., and Sejnoha, R., *Metallurgical Transactions,* Vol. 5, 1974, p. 475.
[7] Turner, C. E. and Radon, J. C. in *Fracture 1969,* P. L. Pratt, Ed., Chapman, 1969, p. 165.
[8] Burns, S. J. and Bilek, Z. J., *Metallurgical Transactions,* Vol. 4, 1973, p. 975.
[9] Hahn, G. T., Hoagland, R. G., Kanninen, M. F., and Rosenfield, A. R., *Pressure Vessel Technology,* Part II, American Society of Mechanical Engineers, New York, 1974, pp. 981–984.
[10] Hahn, G. T., Hoagland, R. G., and Rosenfield, A. R., "Dynamic Crack Propagation and Arrest in Structural Steels," Final Report on Project SR-201 to Ship Structure Committee, Battelle Columbus Laboratories, 1975.
[11] Hoagland, R. G., Kanninen, M. F., Rosenfield, A. R., and Hahn, G. T., "Critical Experiments, Measurements, and Analyses to Establish a Crack Arrest Methodology for Nuclear Pressure Vessel Steels," Report BMI-1933, Battelle Columbus Laboratories, 1974.
[12] Kanninen, M. F., *International Journal of Fracture,* Vol. 9, 1973, p. 83.
[13] Kanninen, M. F., *International Journal of Fracture,* Vol. 10, 1974, p. 415.
[14] Kanninen, M. F., *Proceedings,* Conference on Prospects of Fracture Mechanics, G. C. Sih et al Eds., Noordhoff, 1974, p. 251.
[15] Riccardella, P., Westinghouse Nuclear Systems Division, private communication, 1973.
[16] Mott, N. F., *Engineering,* Vol. 165, 1948, p. 16.
[17] Freund, L. B. in *Dynamic Crack Propagation,* G. C. Sih, Ed., Noordhoff, 1973, p. 553.
[18] Freund, L. B., *Journal of the Mechanics and Physics of Solids,* Vol. 20, 1972, p. 129.
[19] Freund, L. B., *Journal of the Mechanics and Physics of Solids,* Vol. 20, 1972, p. 141.
[20] Freund, L. B., *Journal of the Mechanics and Physics of Solids,* Vol. 21, 1973, p. 47.
[21] Hahn, G. T., Hoadland, R. G., Kanninen, M. F., and Rosenfield, A. R., *Pressure Vessel Technology,* Part III, American Society of Mechanical Engineers, New York, 1974, p. 121.

[22] Crosley, P. B., and Ripling, E. J., *Pressure Vessel Technology,* Part III, American Society of Mechanical Engineers, New York, 1974, p. 126.

[23] Hahn, G. T. et al, "Critical Experiments, Measurements, and Analyses to Establish a Crack Arrest Methodology for Nuclear Pressure Vessel Steels," Report BMI-1934, Battelle Columbus Laboratories, 1975.

[24] Crosley, P. B. and Ripling, E. J., *Pressure Vessel Technology,* Part II, American Society of Mechanical Engineers, New York, 1974, p. 995.

[25] Hahn, G. T., Sarrate, M., and Rosenfield, A. R., *International Journal of Fracture Mechanics,* Vol. 7, 1971, p. 43.

[26] Wessel, E. T., *Engineering Fracture Mechanics,* Vol. 1, 1968, p. 77.

[27] Hahn, G. T. et al, "Critical Experiments, Measurements, and Analyses to Establish a Crack Arrest Methodology for Nuclear Pressure Vessel Steels," Report BMI-1937, Battelle Columbus Laboratories, 1975.

[28] Broberg, B., *Journal of Applied Mechanics,* American Society of Mechanical Engineers, 1964, p. 546.

S. Mostovoy,[1] *P. B. Crosley,*[1] *and E. J. Ripling*[1]

Note on the Dependence of Crack Velocity on Driving Force for an Epoxy Adhesive

---

REFERENCE: Mostovoy, S., Crosley, P. B., and Ripling, E. J., "**Note on the Dependence of Crack Velocity on Driving Force for an Epoxy Adhesive,**" *Cracks and Fracture, ASTM STP 601,* American Society for Testing and Materials, 1976, pp. 234–244.

ABSTRACT: The dependence of crack velocity, $\dot{a}$, on driving force for an adhesive system was shown to be described by a curve having the shape of an inverted L. That is, at high values of $\dot{a}$, large increases in G caused small increases in $\dot{a}$ while at low velocities, small increases in G cause large increases in $\dot{a}$. Since the data in the literature on polymethylmethacrylate (PMMA) and mild steel can also be represented by such a curve shape, the inverted L may represent the general dependence of $\dot{a}$ on driving force.

The high velocity branch appears to be associated with rough fracture surfaces and the low velocity branch, with smooth fracture surfaces.

KEY WORDS: crack propagation, cracking (fracturing), adhesives, epoxy resins, limiting velocity

Interest in fast cracking has been largely limited to identifying the stress intensity factor, K (or crack extension force, G), associated with the transition point at which a stationary or slowly extending crack abruptly jumps ahead. More recently some interest has developed also in other transition or critical points including those at which a running crack is arrested or begins to branch. An identification of these points is generally sufficient for solving engineering problems. Each of these critical points is thought to represent a point on a curve of crack velocity, $\dot{a}$, as a function of the driving force, where the latter is described by K or G. Hence, understanding how the critical points are related and influenced by test and service variables would be assisted by a better understanding of the dependence of $\dot{a}$ on K or G. Clark and Irwin discussed this dependence of crack velocity on driving force and described the stress fields associated with crack division and onset and arrest of rapid crack exten-

---

[1] Senior project director, senior project director, and director of research, respectively, Materials Research Laboratory, Inc., Glenwood, Ill. 60425.

sion [*1*].[2] They suggest that for each material there is a limiting crack velocity equal to about one-half the shear wave velocity, $C_2/2$, and a minimum stable crack speed just prior to arrest. For polymethylmethacrylate (PMMA), the latter is 48 m/s. Other investigators have also observed limiting velocities for fracture propagation. Cotterell reviewed this topic in 1965 and suggested a maximum velocity of about $2C_2/3$ [*2*].

A rather large number of investigators studied the effect of driving force on $\dot{a}$ for PMMA. In one of the more recent studies, Green and Pratt [*3*] compared their data with that presented in some earlier studies and showed that at high crack velocities, the fracture toughness was increased five to ten-fold while $\dot{a}$ increased by one order, Fig. 1*a*. At low crack

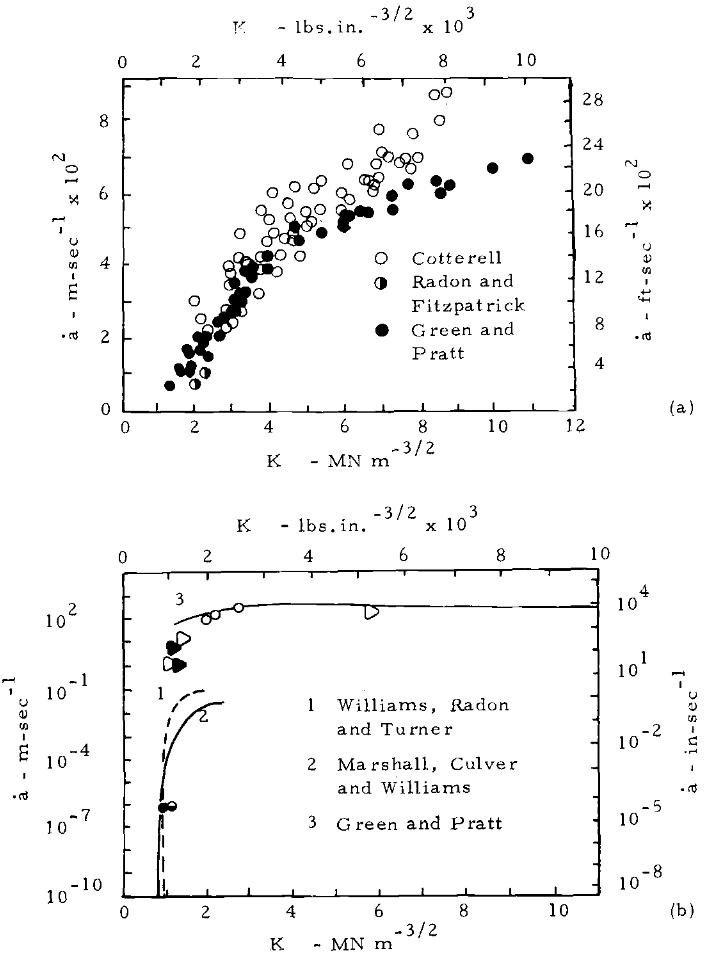

FIG. 1—*Dependence of crack velocity on driving force for PMMA* [3].

---

[2] The italic numbers in brackets refer to the list of references appended to this paper.

velocities, on the other hand, large changes in $\dot{a}$ were associated with very small changes in toughness, Fig. 1*b*. Broutman and Kobayashi [*4*] showed a similar behavior over this same range of velocities although they described a second discontinuity at $\dot{a}$ of approximately 50 m/s in addition to the one at 10^{-1} m/s. Nevertheless, if one ignores the low velocity discontinuities, the dependence of $\dot{a}$ on driving force can be described by an inverted L-shaped curve.

Cotterell [*2*] also measured the fracture surface roughness of his PMMA specimens, and his plot of roughness versus $\dot{a}$ had the same shape as his toughness versus $\dot{a}$ plot.

Less data are available on the dependence of $\dot{a}$ on driving force for nonpolymeric materials although one such relationship was presented by Eftis and Krafft [*5*] for a mild steel, Fig. 2. The curve in Fig. 2 is drawn as a smoothed best fit to the data although Krafft et al [*6*] suggested that the dynamic initiation toughness (and hence, possibly, the *K* value associated with running cracks) varies harmonically over a rate interval ratio of about 20 for steels. Nevertheless, on a coarse scale, at least, the dependence of $\dot{a}$ on driving force is again represented by an inverted L-shaped curve.

Direct measurements of the dependence of crack velocity on the driv-

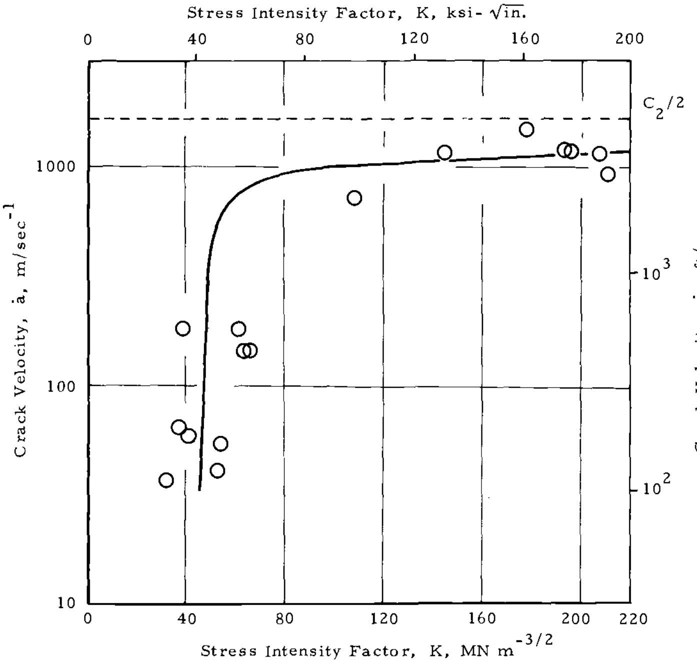

FIG. 2—*Dependence of crack velocity on stress intensity factor for AISI 1020 steel at* $-11°C$ *(12°F)* $(\sigma_{ys} = 236$ *MPa (34.3 ksi), nil ductility temperature* $\approx -7°C$ *(20°F)* [5].

ing force is relatively simple for the polymeric adhesives since the limiting crack velocities are relatively low, and high cracking rates can be obtained with moderate displacement rates because of the high modulus of the metal adherends. This paper describes the dependence of $\dot{a}$ on the driving force, G, for such bonded specimens.

Material and Test Procedure

All tests were conducted with contoured double cantilever beam (DCB) specimens of the type shown in Fig. 3 using 12.7-mm (0.5-in.) thick 2024-T4 aluminum alloy adherends. This type of specimen is helpful in studies of rapid cracking because the crack extension force, G, is a function of load, P, only, independent of crack length, a; and the crack growth rate, $\dot{a}$, at constant load is proportional to the displacement rate, $\dot{\Delta}$ [7]. That is

$$G = \frac{P^2}{2B^2} \frac{8}{E} m' \qquad (1)$$

where

P = load,
B = specimen thickness,
E = modules of adherends,
m' = experimentally derived shape factor having dimensions of length^{-1}, and
$\dot{\Delta}$ = displacement rate.

$$a = \Delta \frac{EB}{8\,Pm'} \qquad (2)$$

where $\dot{a}$ = cracking rate. Hence, a constant driving force is obtained by maintaining P constant as the crack extends. Further, $\dot{a}$ need not be measured directly, but can be implied from $\dot{\Delta}$ (so long as a static analysis can be used and the crack is driven by the crosshead). The proportionality between $\dot{a}$ and $\dot{\Delta}$ depends on m'. Thus, at a given crack length, the lower values of m' give lower specimen compliance and higher values of $\dot{a}$ for a specific value of $\dot{\Delta}$ at a given applied G_i. To obtain the large variation in $\dot{a}$ needed in this study, the two specimen shapes shown in Fig. 3, designated $m' = 3.54$ mm^{-1} (90 in.$^{-1}$) and $m' = 0.215$ mm^{-1} (5.45 in.$^{-1}$) were used. The $m' = 3.54$ mm^{-1} specimen was used for $a \leqslant 30.5$ m/s (100 ft/s), and $m' = 0.215$ mm^{-1} for $\dot{a} \geq 3.05$ m/s (100 ft/s).

A single adhesive system was used: DER 332 epoxy resin, hardened with tetraethylenepentamine (TEPA), and post-cured for 5 h. The shape of the P-Δ curve, on slow loading, depends on the ratio of hardener to resin content, and post-cure temperature for the contoured DCB specimen. One series of specimens was made with 10 parts of hardener per hundred of

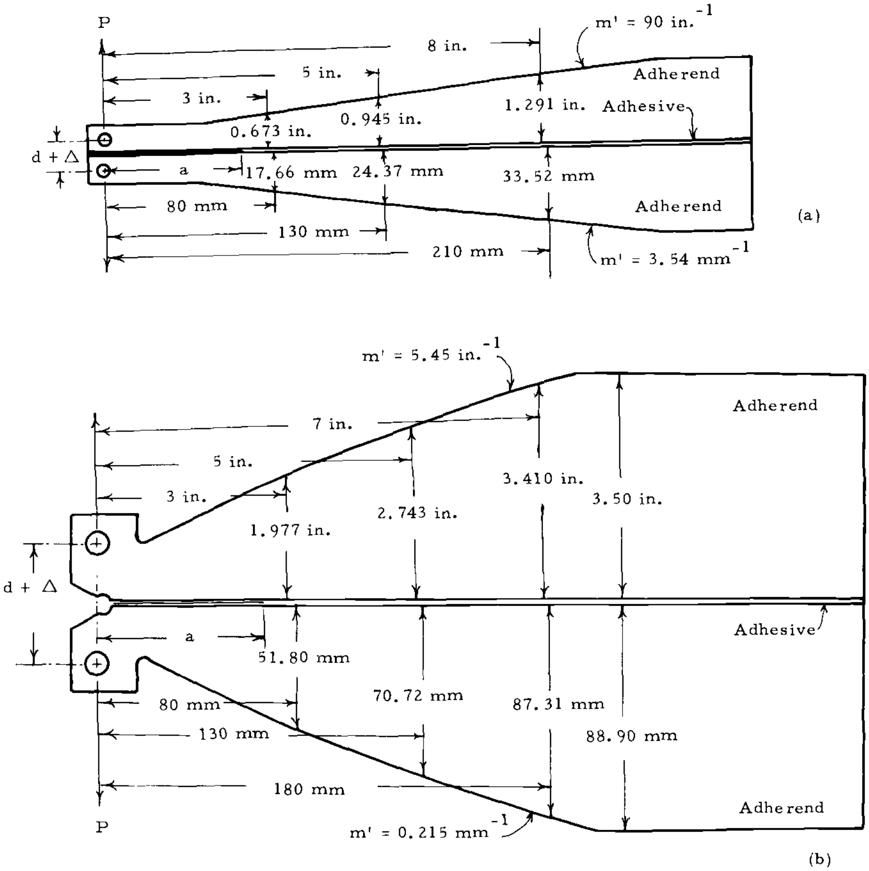

FIG. 3—*Contoured DCB specimen shapes:* (a) m′ = *90 in.*$^{-1}$ *(3.54 mm*$^{-1}$*) and* (b) m′ = *5.45 in.*$^{-1}$ *(0.215 mm*$^{-1}$*).*

resin (PHR), post-cured at 82°C (180°F), and the other with 12.5 PHR, post-cured at 132°C (270°F). These are designated as 10/180 and 12.5/270, respectively. The former develops a "flat" P-Δ curve, Fig. 4*a*, and the latter, a "peaked" curve. Peaked curves generally show two discontinuities, the upper one, P_c, is associated with crack initiation, and the lower one, P_a, with crack arrest, Fig. 4*b*. The cracking rate for materials that show flat P-Δ curves depend on $\dot{\Delta}$ as given in Eq 2. For those that show peaked P-Δ curves, which is typical of most metals, $\dot{a}$, at least in the initial portion of a crack jump, exceeds the value given by Eq 2.

Loads were measured with an in-line load cell for the $m' = 3.54$ mm^{-1} (90 in.$^{-1}$) specimens for $\dot{a} < 30.5$ m/s (100 ft/s). For higher crack velocities, using either $m' = 3.54$ or 0.215 mm^{-1} specimens, the low frequency response of the load cell prevented its use. Satisfactory load-time records were obtained at these higher cracking rates by mounting

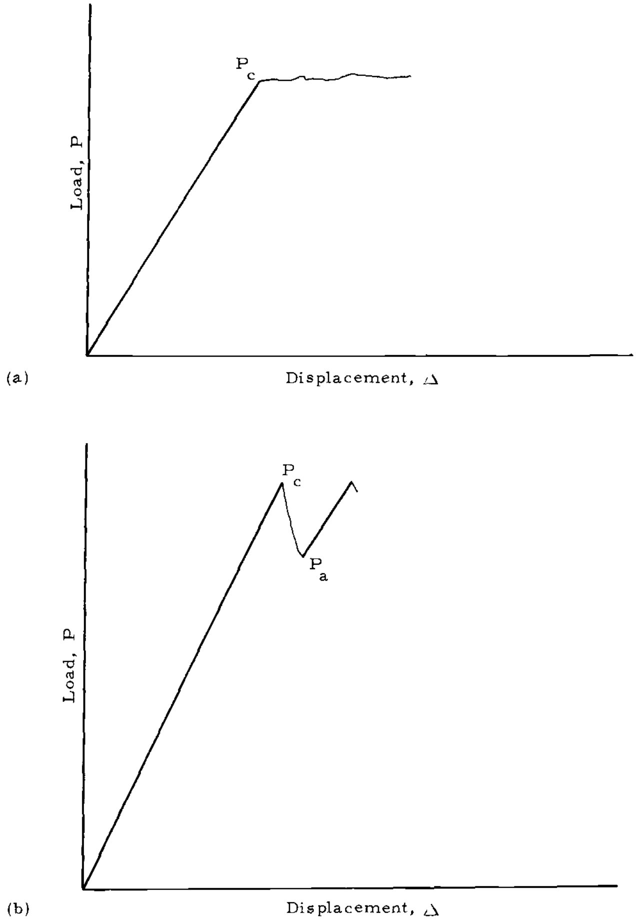

FIG. 4—*Schematic* P–Δ *curves:* (a) *flat, and* (b) *peaked.*

strain gages on the arm of the aluminum adherends. The gages were calibrated for each specimen by use of the in-line load cell at loads less than the critical one prior to conducting the test.

Three methods were used for measuring $\dot{a}$ depending on the time scale needed for the measurements. For the coarsest time scale, where $\dot{a}$ was thought to be reasonably constant over a range of crack lengths, $\dot{a}$ was implied from $\dot{\Delta}$ by using Eq 2. For the finest time scale, over the course of a run-arrest segment of crack extension where velocities are expected to change rapidly, $\dot{a}$ was measured by using ripple markings on the fracture surface as described in Ref *8*. An intermediate time-scale measurement was used to check the accuracy of the ripple marking. This consisted of painting equally spaced conductive lines on an epoxy layer on the side of the specimen. These lines were connected through a battery powered resistance bank so that as the crack passed through each line a step appeared on the oscilloscope plot of voltage versus time. By counting the ripple markings over the interval between two painted lines, it was found that $\dot{a}$ measured by the two methods were accurate within a factor of two. A schematic diagram of the specimen and two ripple markings patterns taken from Ref *8* are shown in Fig. 5.

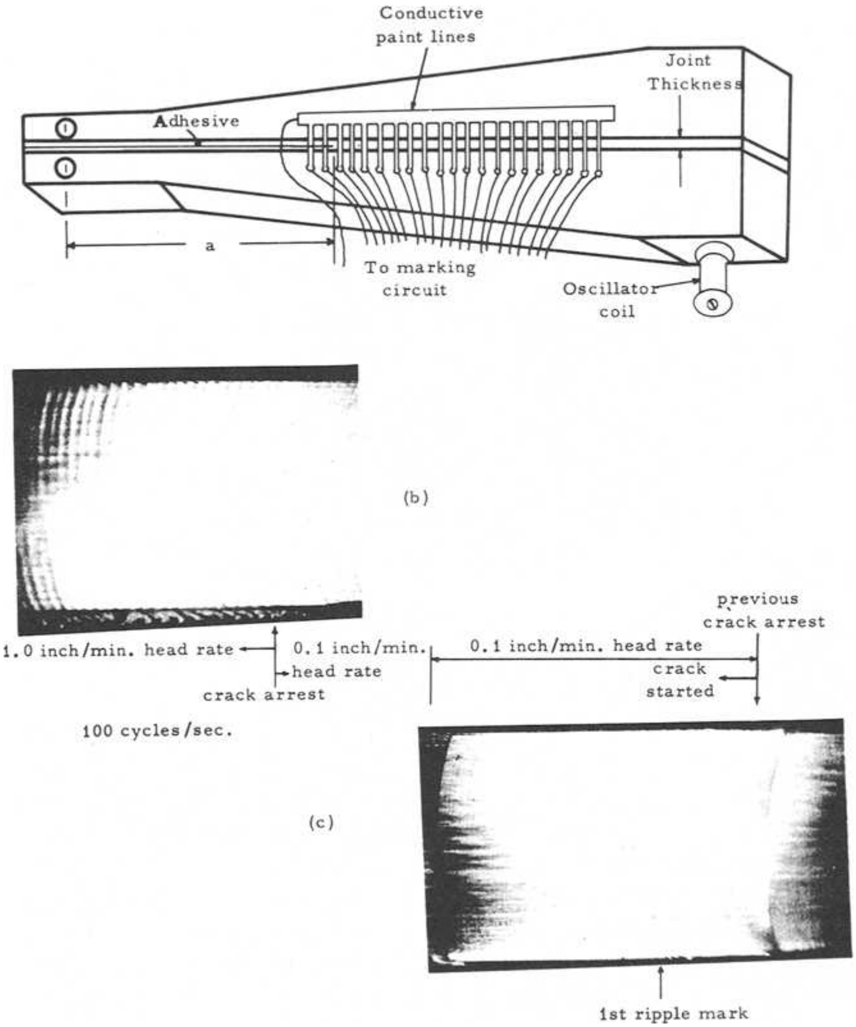

FIG. 5—(a) *Schematic diagram of conductive paint lines and bell coil attached to a tapered DCB specimen for measuring strain rate,* (b) *ripple pattern for slow running crack, and* (c) *ripple pattern for fast (jumping) crack.*

Results and Discussion

At constant $\dot{\Delta}$, ripple markings on the 10/180 specimens were uniformly spaced (see Fig. 5) as expected for a material that develops a flat P-$\dot{\Delta}$ curve. Hence, no attempt was made to measure $\dot{a}$ on a fine scale. Instead, it was obtained from $\dot{\Delta}$ by the use of Eq 2. The highest velocity measured on this material was approximately 152 m/s (500 ft/s), Fig. 6. Since this is less than 15 percent of the shear wave velocity for the epoxy, the error in using this static calculation is thought to be small.

The fracture surfaces for $\dot{a}$ less than about 30 m/s (100 ft/s) were glassy smooth, that is, highly reflective, while at higher velocities, the fracture surfaces were smooth but nonreflective, for example, frosted or silky.

Crack velocity, $\dot{a}$, over the course of the jump is plotted as a function of change in crack front location in Fig. 7. It is apparent that over the first half of the jump, $\dot{a}$ was relatively high, but it decreased abruptly, and over the last half of the jump, a was relatively high, but it decreased

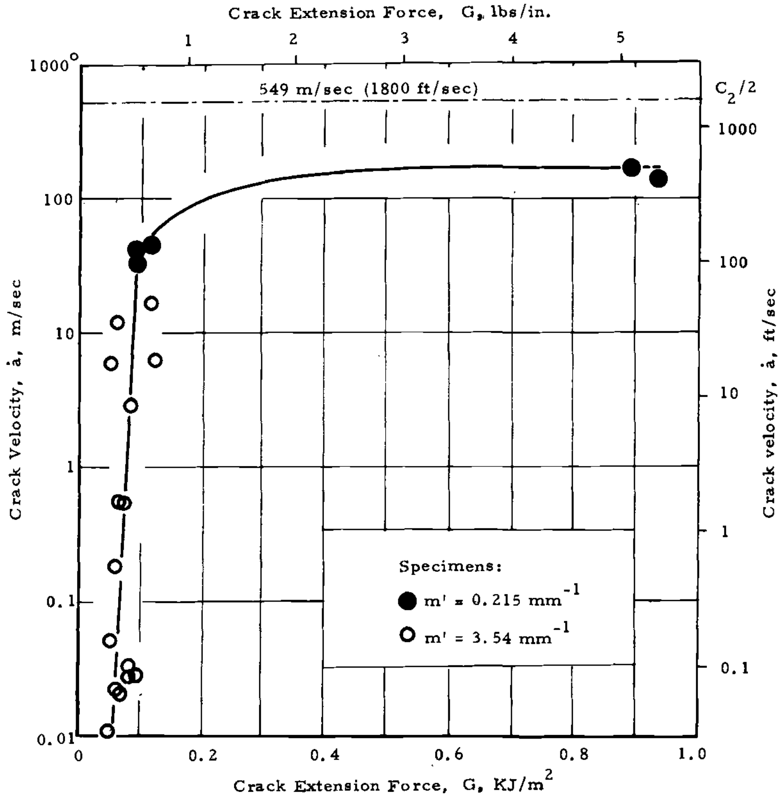

FIG. 6—*Dependence of crack speed,* ȧ, *on driving force,* G *for 10/180 adhesive joint (*G *from Eq 1,* ȧ *from Eq 2).*

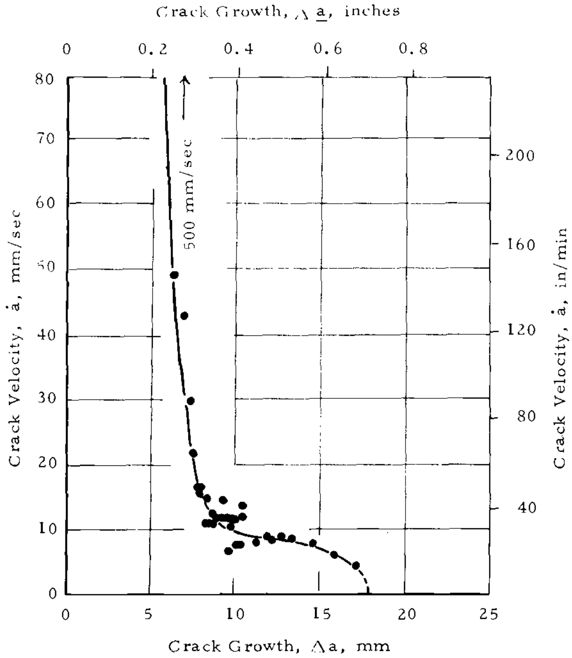

FIG. 7—*Crack velocity versus crack growth for a run-arrest segment (12.5/270 adhesive,* $m' = 3.54$ *mm*$^{-1}$ *specimen).*

abruptly, and over the last half of the jump, $\dot{a}$ was very low, of the order of creep velocities, until the crack decelerated to an arrest. This very slow extension prior to a complete stop was also found by Clark and Irwin [*1*] for PMMA, but the speed was higher and the amount of slow crack extension was lower than is the case for the 12.5/270 epoxy. The first ripple mark indicated that the average velocity over the first 5 mm (0.2 in.) was 0.5 m/s (1180 in./min). All of these velocities are relatively low so that again it appears to be safe to do a static analysis of the specimen behavior over the course of the jump.

Knowing Δ_0, that is, Δ when $P = P_c$, the change in specimen compliance with crack length, dC/da, Δ, and a for each ripple mark, it was possible to calculate the manner in which G decreased over the jump, Fig. 8. G decreases smoothly from its value of G_{Ic} to G_{Ia}.

This $\dot{a}$ versus G relationship obtained over the run-arrest segment is added to data for the driven crack in Fig. 9. The latter were obtained on the 12.5/270 epoxy bonds using the same method as used for collecting driven crack data on the 10/180 epoxy bonds.

Some rapid loading tests were also conducted on the 12.5/270 adhesive. These are shown as Xs in Fig. 9 by plotting the pseudo cracking rate, based on $\dot{\Delta}$ from Eq 2 as a function of dynamic crack extension force, G.

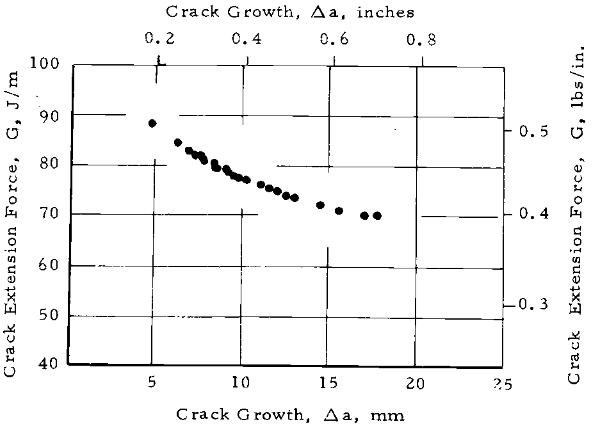

FIG. 8—*Crack extension force for a run-arrest segment (12.5/270 adhesive,* m′ = *3.51 mm^{-1} specimen).*

All of these specimens showed a silky band on the fracture surface at the point of crack initiation suggesting that all the cracks initiated at an $\dot{a}$ of at least 30.5 m/s (100 ft/s). The cracks driven at the high velocity had a silky appearance over the complete fracture surface.

Conclusions

1. A single epoxy system was used for these tests. One group of specimens (12.5/270) had a higher hardener content and post-cure temperature than the other (10/180). The 12.5/270 adhesive showed a "pop" on room temperature slow loading, while the 10/180 adhesive did not. In spite of this difference in the shape of the load-displacement curves, the dependence of $\dot{a}$ on driving force for the two was essentially identical.
2. The dependence of crack velocity on driving force for the adhesive system can be represented by a curve having the shape of an inverted L. At high crack velocities, large increases in G cause small increases in $\dot{a}$, while at low velocities, small increases in G cause large increases in $\dot{a}$. This inverted L shape was also found for PMMA and mild steel (although these may be some low amplitude peaks in the low velocity branch of the curve) suggesting that this is a general shape found for all materials.
3. The high velocity branch of the $\dot{a}$-driving force curve is associated with rough fracture surfaces, and the low velocity branch with smooth fracture surfaces.

References

[1] Clark, A. B. J. and Irwin, G. R., *Experimental Mechanics*, June 1966, p. 321.

[2] Cotterell, B., *Applied Materials Research,* Vol. 4, 1965, p. 227.

[3] Green, A. K. and Pratt, P. L., *Engineering Fracture Mechanics,* Vol. 6, No. 1, 1974.

[4] Broutman, L. J. and Kobayashi, T., "Dynamic Crack Propagation Studies in Polymers," *Proceedings, Dynamic Crack Propagation,* G. C. Sih, Ed., Noordhoff International, Publishing, 1973.

[5] Eftis, A. and Krafft, J. M., *Journal of Basic Engineering, Transactions,* Series D., American Society of Mechanical Engineers, Vol. 87, 1965, p. 1.

[6] Krafft, J. M., Hettche, L. R., Sullivan, A. M., and Loss, F. J., "Fracture-Flow Relationships for A533-B Pressure Vessel Steel," *Journal of Engineering for Industry,* 1970.

[7] Mostovoy, S., Crosley, P. B., and Ripling, E. J., *Journal of Materials,* Vol. 2, No. 3, 1967, p. 661.

[8] Mostovoy, S. and Ripling, E. J., *Journal of Applied Polymer Science,* Vol. 10, 1966.

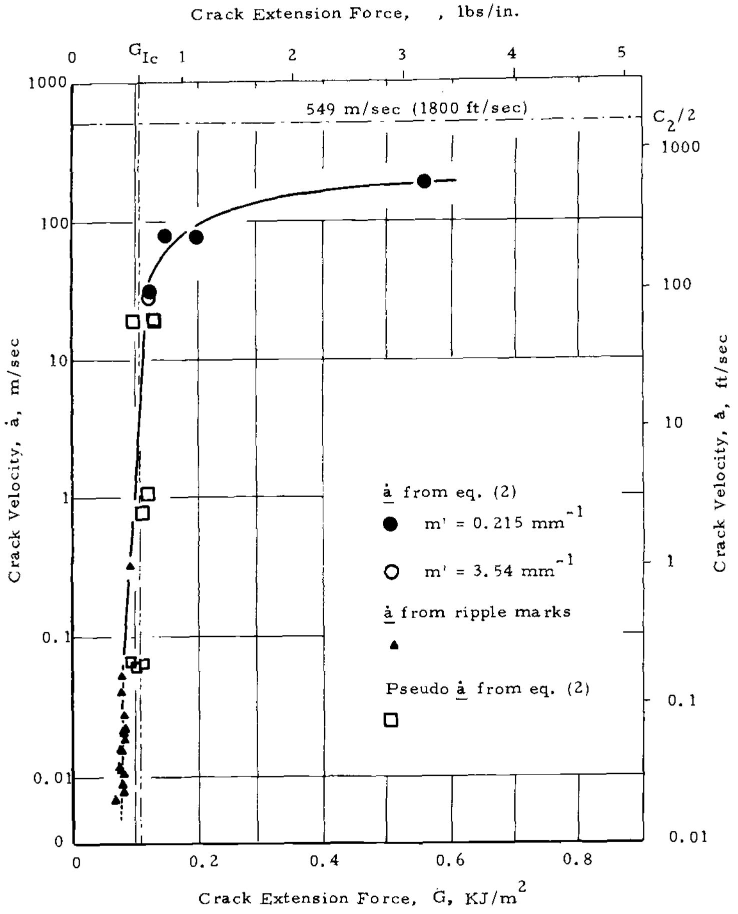

FIG. 9—*Dependence of crack speed,* a, *on driving force,* G, *for 12.5/270 adhesive joints, as well as pseudo-cracking rate as a function of dynamic driving force,* G_{ID}.

K. N. Morman, Jr.[1] *and R. G. Dubensky*[2]

Predicting Fatigue Crack Retardation Under Single and Intermittent Overloading

REFERENCE: Morman, K. N., Jr. and Dubensky, R. G., **"Predicting Fatigue Crack Retardation Under Single and Intermittent Overloading,"** *Cracks and Fracture, ASTM STP 601,* American Society for Testing and Materials, 1976, pp. 245–261.

ABSTRACT: An expression which simulates both retardation and delayed retardation in crack propagation subsequent to tensile overloading is presented and related to test data for Man Ten, Hadfield, and AISI 1020 steels, and Ti-8A1-1Mo-IV titanium alloy.

The crack growth expression is then generalized to predict the crack growth life in specimens for a variety of intermittent overload conditions. Agreement between the predicted and test data values for the four materials is within 20 percent for approximately one half of the more than 80 overload conditions studied.

KEY WORDS: fatigue (materials), retarding, predictions, crack propagation, alloys, fractures (materials)

Nomenclature

a	Crack length, mm
a^*	Incremental crack length affected by overload
a_I	Initial crack length
a_F	Crack length at fracture
a_{01}	Crack length at point of overload
Δa	Crack growth from a_{01}, $a - a_{01}$
Δa^*	Crack growth from a_{01} to minimum crack growth rate
da/dN	Crack growth rate, mm/cycle
$(da/dN)_\infty$	Constant amplitude crack growth rate
A	Empirical constant
B	Specimen thickness, mm
c	Fatigue ductility exponent

---

[1] Principal research engineer associate, Advanced Methods and Technology, Car Engineering Group, Ford Motor Company, Dearborn, Mich. 48121.

[2] Associate professor, Oklahoma State University, Stillwater, Okla.

d	Constant reflecting stress state
$f(\Delta K)$	Constant amplitude crack growth rate function
K	Maximum stress intensity factor, $MNm^{-3/2}$
K_c	Fracture toughness
K_{ol}	Maximum stress intensity during overload
ΔK	Stress intensity range
ΔK_{ol}	Stress intensity range during overload
m	Empirical constant
n	Empirical constant
N	Number of cycles
N_D	Number of delay cycles under a single overload
N_F	Number of cycles to fracture
ΔN	Number of cycles between intermittent overloads
N_I	Number of cycles to grow a crack to a_I
p	Empirical constant
P	Applied load, N
P_{ol}	Applied overload
ΔP	Applied load range
ΔP_{ol}	Overload range
$2r_{oy}$	Plastic zone size due to overloading, mm
R	P_{min}/P_{max}
W	Specimen width, mm
S_y	Yield strength, MN/m^2

The phenomena of delay in fatigue crack propagation under single and intermittent tensile overloading has been the subject of several publications over the past 15 years [*1–13*].[3] It has long been recognized that the development of a fundamental understanding of delay under these somewhat simplified loading conditions represents a first step toward understanding the more complex phenomena of fatigue crack propagation under spectrum loading.

Detailed in Figs. 1*a, b,* and *c* are schematics showing three of the most commonly observed types of retardation behavior following a tensile overload, as illustrated in Fig. 1*d*. In some instances, researchers have observed immediate retardation following the overload cycle as shown in Fig. 1*a* [*10*]. In other instances, the minimum growth rate did not occur immediately after the overload cycle. Instead, the minimum rate is reached only after the crack has grown a small distance (Fig. 1*b*); this phenomenon is referred to as delayed retardation [*1,5–9*]. Still others [*6,13*] have noted an initial acceleration in crack extension immediately following the overload (Fig. 1*c*). The dotted curve indicates the crack growth behavior if no overload were applied, termed constant-amplitude growth.

---

[3] The italic numbers in brackets refer to the list of references appended to this paper.

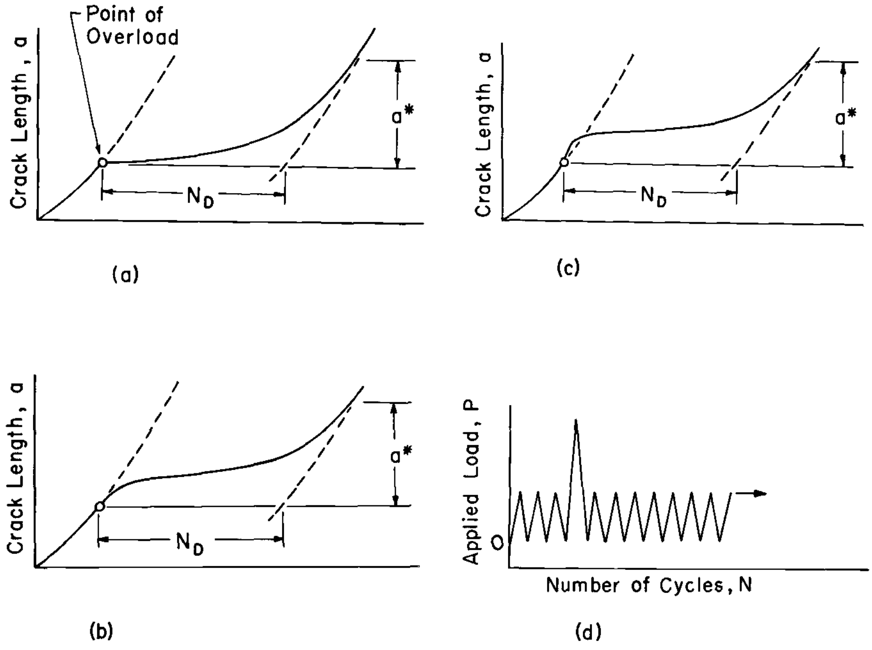

FIG. 1—*Schematic of observed crack growth curves following single tensile overload:* (a) *retardation,* (b) *delayed retardation,* (c) *initial acceleration, and* (d) *load schedule.*

Crack growth retardation can be characterized by the parameters a^* and N_D, where a^* is the crack length from the point of overload to the point of tangency of constant-amplitude growth, and N_D is the difference between the number of cycles of retarded growth and the number of cycles of constant-amplitude growth during crack extension to a^*. This definition of delay cycles is similar to the one employed by Wei and Shih [*11*].

The behavior of crack growth under intermittent tensile overloading is somewhat less documented than single overload behavior [*8–10*]. For materials exhibiting no delayed retardation, intermittent overloads produce more retardation than single overloads of the same magnitude [*10*]. These experiments revealed a significent interaction effect on delay when overloads were applied before the crack was allowed to propagate beyond the interaction zone, a^*, produced by a previous overloading. The results are more complicated in materials exhibiting delayed retardation, where, under certain circumstances, intermittently repeated overloads produce less retardation than single overloads of the same magnitude [*8,9*]. Furthermore, a decrease in the number of cycles between overloads results in a further decrease in retardation or crack growth life.

Several empirical models have been proposed to account for the effect of retardation [*14–16*]. The basis for these models is some expression for constant-amplitude growth which relates the rate of crack growth to the change in stress intensity factor: $da/dN = f(\Delta K)$. In each model, retardation due to overloading is simulated by modifying one of the constant parameters associated with the constant-amplitude law or by modifying ΔK. These models have met with some success in predicting crack growth under randomized load spectra, but not for deterministic loading. One of the principal reasons for this lack of quantitative agreement is that none of the models are capable of reproducing the effects of delayed retardation.

This paper presents a simple crack growth law which simulates both retardation and delayed retardation in crack growth under single tensile overloading. Like previous models the proposed law has its basis in an expression for constant-amplitude growth. It is demonstrated that the growth expression can be generalized to predict growth under intermittent overloads using single overload data. Numerical values for the empirical constants associated with the crack growth expression were obtained from single overload data for three steel alloys (Man Ten, Hadfield, AISI 1020) and one titanium alloy (Ti-8A1-1Mo-1V). Using the correlation between the stress intensity parameter $(\Delta K/K_{\mathrm{ol}})^{1|c}K$ and the number of delay cycles, N_{D} suggested in Ref *17*, the crack growth expression was then applied to predict intermittent overload data for each of the four materials. Agreement between tests results and analytical predictions was good.

Theoretical Development

Single Overload Formula

Analysis of test data for crack growth subsequent to the application of a single overload at crack length, a_{ol} suggests the following formula

$$N = N_{\mathrm{D}} \left\{ 1 - \exp \left[-q \left(\frac{\Delta a}{2r_{\mathrm{oy}}} \right) \right] \right\}^{m} + \int_{a_{\mathrm{I}}}^{a} \frac{da}{f(\Delta K)} + N_{\mathrm{I}} \quad (1a)$$

where m and q are empirical constants, $f(\Delta K)$ is any of the crack propagation expressions for constant amplitude loading, $\Delta a = a - a_{\mathrm{ol}}$, and $2r_{\mathrm{oy}}$ is the monotonic plastic zone size caused by the overload. For small-scale yielding the plastic zone size is calculated as follows

$$2r_{\mathrm{oy}} = \frac{2}{d\pi} \left(\frac{\Delta K_{\mathrm{ol}}}{S_{\mathrm{y}}} \right)^{2} \quad (1b)$$

where $d = 2$ for plane stress and $d = 6$ for plane strain. Equation 1*a* is the result of plotting and cross-plotting a versus N data and da/dN versus Δa data and intuitive reasoning.

Differentiation of Eq 1a and some manipulation yields

$$\frac{da}{dN} = f(\Delta K)\Lambda(\Delta a, \Delta K_{\text{ol}}, N_{\text{D}}, f(\Delta K)) \tag{2}$$

where

$$\Lambda = \left\{1 + \left(\frac{mqN_{\text{D}}}{2r_{\text{oy}}}\right)\left[l - \exp\left(-\frac{q\Delta a}{2r_{\text{oy}}}\right)\right]^{m-1} \exp\left(-\frac{q\Delta a}{2r_{\text{oy}}}\right) f(\Delta K)\right\}^{-1} \tag{3}$$

The minimization of Λ with respect to Δa results in an expression which relates crack extension between overload application and minimum growth rate, Δa^*, to overload plastic zone size as follows

$$\Delta a^* = \frac{\ln(m)}{q} \bullet (2r_{\text{oy}}) \tag{4}$$

For no delayed retardation, $\Delta a^* = 0$ and thus $m = 1$. For the case of delayed retardation, $m > 1$. Typical plots of Eqs 1 and 2 are shown in Figs. 2a and b for both cases.

The empirical constants m and q may be evaluated from standard curve fitting procedures.

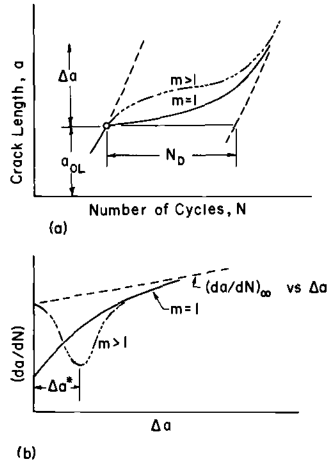

FIG. 2—*Schematic of Eq 1 predictions of crack growth following single overload:* (a) *crack length versus cycles, and* (b) *crack growth rates versus crack growth subsequent to overload.*

Generalization to Intermittent Overloads

A superposition rule may be used to calculate the delay or retardation produced by the common action of several overloads which are applied in an intermittent fashion. In the spirit of which Eq 1*a* was derived, the combined effect of these overloads may be represented in terms of a corresponding set of delay cycles, N_{D_j} ($j = 1,2, \ldots$) of different magnitudes applied successively. As an example, consider the case shown in Fig. 3 which is a schematic representation of a material exhibiting no delayed retardation ($m = 1$). At $a = a_{ol}$, an overload is applied, which produces a delay in crack growth equal to $N_{D_1} \{1 - \exp [-q (\Delta a_1/2r_{oy_1})] \}$ where $\Delta a_1 = a = a_{ol_1}$. If no other overloads are applied, this equation will describe retardation for the remaining crack life; but if at $a = a_{ol_2}$, another overload is applied, then for $a > a_{ol_2}$ the influence of the previous overload will be terminated and additional delay will be produced which is proportional to N_{D_2}. The total number of applied cycles, if no further overloading occurs, is, therefore

$$N = N_{D_1} \left\{1 - \exp\left[-q\left(\frac{\Delta a_1}{2r_{oy_1}}\right)\right] \exp\left[q\left(\frac{\Delta a_2}{2r_{oy_1}}\right)\right]\right\} +$$

$$N_{D_2} \left\{1 - \exp\left[-q\left(\frac{\Delta a_2}{2r_{oy_2}}\right)\right]\right\} + \int_{a_I}^{a} \frac{da}{f(\Delta K)} + N_I$$

where $\Delta a_1 = a - a_{ol_1}$ and $\Delta a_2 = a - a_{ol_2}$. From this equation it is but one step to a very general case of M overloads including delayed retardation ($m > 1$). Thus, the total number of applied cycles at crack length a is then the constant-amplitude growth plus the sum of the retardations caused by each single overloading that has taken place at crack lengths $a = a_{ol_j}$ ($j = 1, 2, \ldots M$), that is

$$N = \sum_{j=1}^{M-1} N_{D_j} \left\{1 - \exp\left[-q\left(\frac{\Delta a_j}{2r_{oy_j}}\right)\right] \exp\left[q\left(\frac{\Delta a_{j+1}}{2r_{oy_j}}\right)\right]\right\}^m +$$

$$N_{D_M} \left\{1 - \exp\left[-q\left(\frac{\Delta a_M}{2r_{oy_M}}\right)\right]\right\}^m + \int_{a_I}^{a} \frac{da}{f(\Delta K)} + N_I \qquad (5)$$

This formula can be used to predict crack growth under intermittent overloading once an expression for constant-amplitude growth, $f(\Delta K)$, has been decided upon and m, q, and N_{D_j} have been correlated with single tensile overload data. The correlation of the N_{D_j}'s with overload parameters is discussed in a subsequent section of this paper.

Correlation Procedure and Results

To evaluate the m and q parameters of Eq 1a, a computer program was developed to apply this equation to single overload data. Starting with encoded a versus N data, and using the Paris equation $f(\Delta K) = A\Delta K^n$ for constant-amplitude growth, this program fits the rate expression, Eq 2, to calculated da/dN versus Δa values in the following steps:

1. Crack growth rates are calculated by the two-point secant method.
2. Maximum stress intensity factor values are calculated using the appropriate formula for the given test specimen type.

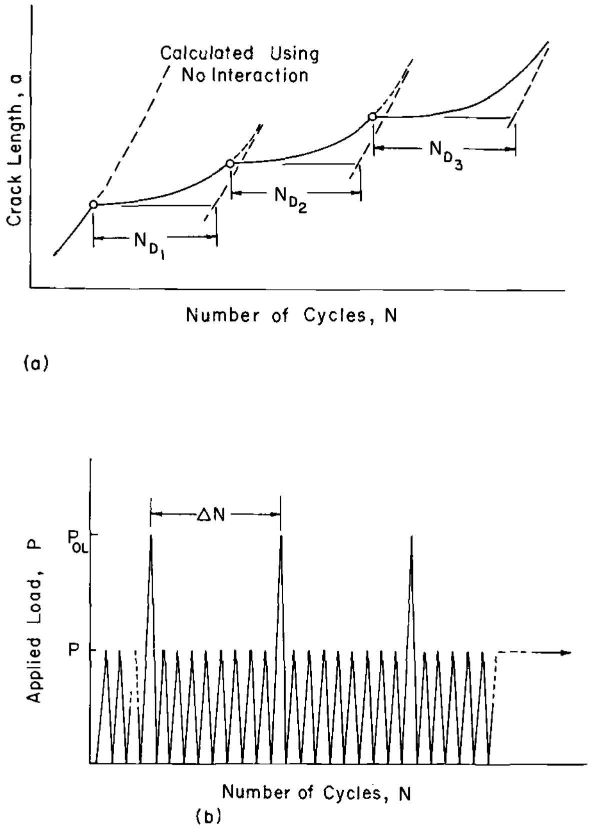

FIG. 3—*Schematic of delay in crack growth due to intermittent single overloads:* (a) *delays in crack growth from intermittent overloads, and* (b) *overload schedule.*

3. Equation 2 is fitted to the calculated *da/dN*, Δa values by least-squares regression.

A separate computer program was used to fit the Paris equation to constant-amplitude test data.

Nominal values for K_c were established by inspection of the data sets for the maximum values of K. N_D values were obtained from a versus N plots of data from single overload tests. Data on four material were analyzed: Man-Ten [*7*], Hadfield [*8*], and AISI 1020 steels [*9*], and Ti-8Al-1Mo-1V alloy [*10*]. All data on the steel alloys were taken from compact tension specimens and the data on the titanium alloy, from center-cracked panels. In all test cases, overloading was preceded and followed by constant-amplitude loading with positive R ratios.

Maximum stress intensities for the compact tension specimens were calculated from

$$K = \frac{P\sqrt{a}}{BW}\left[29.6 - 185.5\left(\frac{a}{W}\right) + 655.7\left(\frac{a}{W}\right)^2 - 1017\left(\frac{a}{W}\right)^3 + 638.9\left(\frac{a}{W}\right)^4\right]$$

and those for the center cracked panel specimens from

$$K = \frac{P\sqrt{a}}{BW}\left[1.77 + 0.227\left(\frac{2a}{W}\right) - 0.510\left(\frac{2a}{W}\right)^2 + 2.7\left(\frac{2a}{W}\right)^3\right]$$

where in both cases P is the applied load, B is tne net thickness, W is the specimen width, but a is the total crack length in the compact specimen and is one half the total crack length in the center cracked panel.

Detailed results of the correlation study performed are presented in Table 1. The values shown represent the average of values fitted from individual overload tests. For a given material, the fitted values of m and q were essentially constant for different single overload magnitudes.

Following the work of Adetifa and Gowda [*17*], a stress intensity parameter of the form $(\Delta K/K_{ol})^{1|c}K$ was plotted against the number of delay cycles, N_D for all four metals. In this parameter, expression c is the absolute value of the fatigue ductility exponent of the material; K and K_{ol} are calculated for the crack length at the point of overload. The log-log plots shown in Fig. 4 demonstrate reasonably good linear trends and therefore suggest a relationship between N_D and the stress intensity parameter of the form

TABLE 1—*Correlation of empirical parameters with single overload data.*

Material	Reference	Paris Equation Parameters		S_y, MN/m^2	K_c, MNm$^{-3/2}$	Eq 1 Parameters		Eq 6 Parameters	
		A	n			q	m	C_o	p
Man Ten steel	*7*	2.3308×10^{-9}	3.251	317	166	3.912	3.798	309.6	0.2771
Hadfield steel	*8*	0.02159×10^{-9}	4.350	420	148	3.361	4.434	220.4	0.1955
AISI 1020 steel	*9*	1.6182×10^{-9}	3.353	627	104	5.780	8.174	445.1	0.4291
Ti-8Al-1Mo-1V titanium alloy	*10*	9.7581×10^{-9}	2.913	883	125	2.072	1.000	291.3	0.3399

$$N_D = \left[\frac{C_0}{(\Delta K/K_{ol})^{1/c_K}} \right]^{1/p} \qquad (6)$$

C_0 and p values for the four alloys under study are also presented in Table 1.

Predictions and Discussion

Computer Program

A computational scheme for the prediction of crack growth under intermittent overloading using Eq 5 has been devised and incorporated into a digital computer program. The algorithm keeps track of overload magnitude, crack tip location, and overload plastic zone size and numerically integrates the function $1/f(\Delta K)$ by quadratures. For each overload application, the various quantities are computed, for example, stress intensity factors, overload plastic zone size, etc. The delay cycle, N_D, is computed according to Eq 6 and then the number of cycles, N, is updated according to Eq 5. This simple summing and integration process is repeated until all the overloads are exhausted, the crack reaches a specified critical length, or the stress intensity factor reaches the critical value, K_c.

Numerical Results

Figures 5 through 8 show the comparison of sample predicted crack growth behavior with test results. For the three steels, crack growth behavior, following a single overload consisted of a delayed retardation period, a nearly constant crack growth rate, and final fracture. Delayed

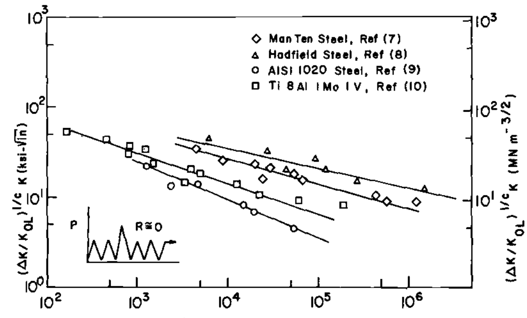

FIG. 4—*Correlation of number of delay cycles with stress intensity parameter.*

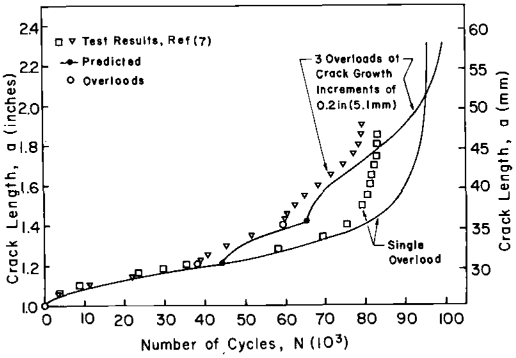

FIG. 5—*Comparison of predicted and actual overload effects on crack growth, Man Ten steel:* $\Delta P = 17\ 793$ *N,* $\Delta P_{ol} = 35\ 586$ *N.*

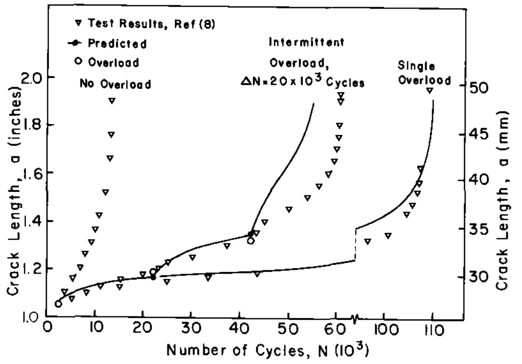

FIG. 6—*Comparison of predicted and actual overlaod effects on crack growth, Hadfield steel:* $\Delta P = 17\ 793$ *N,* $\Delta P_{ol} = 31\ 138$ *N.*

retardation is also detectable in the intermittent overload predictions as well as in the test data. The Ti-8Al-1Mo-1V titanium alloy exhibited no delayed retardation (Fig. 8).

Both the analytical and test results for the Man-Ten and Hadfield steels indicate that intermittent overloading to the same level can produce less retardation than a single overload of equal magnitude. In contrast, the results for the AISI 1020 steel and the Ti-8Al-1Mo-1V titanium exhibit increases in retardation subsequent to intermittent overloading.

In both sets of results in which intermittent overloading produced less retardation, it is observed that the crack growth between overloads is nearly equal to or less in magnitude than that of the crack extension Δa^* required to achieve minimum crack growth rate. For example, from the

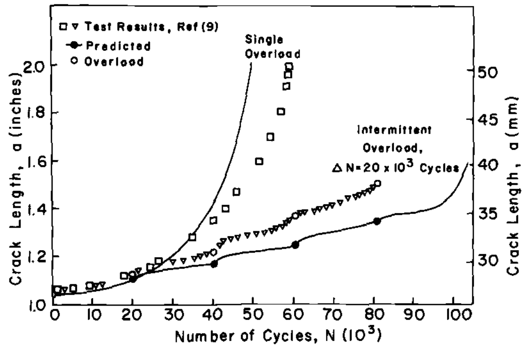

FIG. 7—*Comparison of predicted and actual overload effects on crack growth, AISI 1020 steel:* $\Delta P = 11\ 121$ *N,* $\Delta P_{ol} = 22\ 241$ *N.*

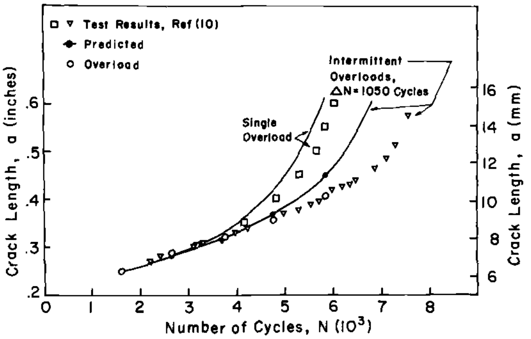

FIG. 8—*Comparison of predicted and actual overload effects on crack growth, Ti-8Al-1Mo-1V titanium alloy:* $\Delta P = 27\ 801$ *N,* $\Delta P_{ol} = 36\ 142$ *N.*

results for Man-Ten steel illustrated in Fig. 5, it is observed that the overloads were applied at 0.2 in. (5.1 mm) increments of crack growth while Δa^* was computed, using Eq 4, to be $\Delta a^*_1 = 0.2$ in. (5.1 mm) and $\Delta a^*_2 = 0.247$ in. (6.28 mm), corresponding to the first and second overloads, respectively.

It may be observed from the plotted AISI 1020 steel analytical and test results (Fig. 7) that the intermittent overloads were applied at increments greater than Δa^* and, thus, more retardation was produced than with the single overload alone.

Tables 2 through 5 contain the crack life predictions for each of the four materials analyzed under a variety of intermittent overload conditions. Included also, for comparison purposes, are the test values. Although some large deviations are indicated in the tables, approximately one-half of the 83 predictions are within 20 percent of the test values.

TABLE 2—*Comparison of predicted and actual crack growth life cycles,* (N_F-N_I) *under intermittent overloading, Man Ten steel.*

				Increment of Crack Growth Between Overloads, mm		
ΔP, N	ΔP_{ol}, N	No Overload	Single Overload	3.8	5.1	7.6
22 241	31 138	9 040	12 920	. . .	14 090	14 380
		(5 630) [a]	(9 940)		(12 610)	(12 200)
	40 034		27 050	. . .	26 220	27 950
			(25 550)		(22 650)	(21 650)
17 793	26 689	18 940	32 180	40 160	. . .	38 330
		(16 690)	(25 100)	(34 060)		(31 480)
	35 586		95 830	. . .	99 400	
			(83 670)		(79 000)	. . .
13 345	22 241	48 620	119 820	. . .	. . .	. . .
		(37 650)	(61 320)			
	31 138		606 080	. . .	774 780	. . .
			(596 480)		(816 380)	

[a] Test values are in parentheses.

TABLE 3—*Comparison of predicted and actual crack growth life cycles,* (N_F-N_I) *under intermittent overloading, Hadfield steel.*

				Number of Cycles Applied Between Overloads, ΔN				
ΔP, N	ΔP_{ol}, N	No Overload	Single Overload	40 000	20 000	10 000	4 000	2 000
17 793	22 241	7 270	16 380	. . .	. . .	19 400	18 900	16 290
		(13 000)[a]	(19 300)			(20 100)	(25 800)	(21 400)
	26 689		44 450	. . .	. . .	42 290	27 730	. . .
			(40 800)			(40 900)	(32 900)	(27 700)
	31 138		106 950	. . .	54 500	46 880	28 900	. . .
			(107 700)		(60 500)	(52 500)	(37 700)	(27 500)
	35 586		129 720	78 240	51 970	36 920	23 020	14 970
			(134 900)	(91 600)	(80 000)	(58 600)	(45 800)	(33 800)
13 345	22 241	25 720	64 850	72 790	66 350	58 050	41 520	. . .
		(24 300)	(69 000)	(138 200)	(94 900)	(109 300)	(88 900)	
	26 689		258 300	. . .	112 852	91 820	54 870	40 500
			(297 300)		(70 800)	(173 100)	(163 200)	(149 300)
	31 138		1 016 780	. . .	. . .	100 740	. . .	. . .
			(1 535 800)			(524 300)		

[a] Test values are in parentheses. For consistency of presentation, the test values appearing in Table 2 of Ref *8* were modified by adding the no overload life cycles corresponding to ΔP = 17 793 N (13 000 cycles) and ΔP = 13 345 N (24 300 cycles) and included in this table.

TABLE 4—*Comparison of predicted and actual crack growth life cycles,* (N_F-N_I) *under intermittent overloading, AISI 1020 steel.*

				Number of Cycles Applied Between Overloads, ΔN		
ΔP, N	ΔP_{ol}, N	No Overload	Single Overload	20 000	10 000	5 000
15 569	26 689	9 760 (18 610) [a]	13 390 (23 410)	13 390 (23 410)	15 490 (31 310)	20 580 (36 930)
	22 241		11 050 (19 910)	11 050 (19 900)	11 520 (20 018)	12 660 (24 810)
13 345	26 689	17 090 (29 270)	29 590 (44 190)	38 680 (64 690)	61 890 (82 710)	59 000 (63 500)
	22 241		21 520 (31 680)	22 890 (37 580)	27 170 (42 690)	37 250 (53 800)
11 121	26 689	32 410 (48 070)	86 320 (105 560)	196 390 (186 080)	184 870 (155 800)	152 550 (140 430)
	22 241		50 050 (67 760)	109 000 (86 050)	132 290 (96 300)	125 290 (125 110)

[a] Test values are in parentheses.

TABLE 5—*Comparison of predicted and actual crack growth life cycles,* (N_F-N_I) *under intermittent overloading, Ti-8Al-1Mo-1V titanium.*

				Number of Cycles Applied Between Overloads, ΔN			
ΔP, N	ΔP_{ol}, N	No Overload	Single Overload	2 640	1 320	1 050	550
22 241	36 142	11 000 (10 200) [a]	12 960 (12 000)	23 230 (26 740)	22 670 (23 230)	. . .	. . .
27 801	36 142	(3 820)	4 200 (4 600)	. . .	. . .	5 200 (5 950)	7 660 (7 220)

[a] Test values are in parentheses.

The differences between the predicted and test results are due largely to the sensitivity of N_D to small changes in the stress intensity parameter $(\Delta K/K_{ol})^{1/c} K$ as expressed by Eq 6. Small deviations from the actual tests value for this parameter are produced within the computational scheme when number of cycles is the criteria for overload application and not crack length. These small deviations produce large differences between the values of N_D computed by Eq 7 and those obtained from tests. This error is cumulative when the procedure is applied to predicting crack growth under intermittent overloading.

Conclusions

1. A crack growth law which simulates both retardation and delayed retardation under single tensile overloads was presented. Parameters associated with this law appear to be constant for different single overload magnitudes for a given material.
2. The single overload crack growth law was generalized to predict crack propagation under intermittent tensile over-loading. Although some large deviations are indicated, approximately one-half of the 83 predictions are within 20 percent of the test values.

Acknowledgments

The authors would like to express their appreciation to R. Little of the University of Michigan, Dearborn Campus, and R. I. Stephens of the University of Iowa. Prof. Little provided the algorithm for data fitting. We are indebted to Prof. Stephens for providing us with the data on the Hadfield, AISI 1020, and Man-Ten steels.

References

[*1*] Schijve, J., "Fatigue Crack Propagation in Light Alloy Sheet Material and Structures," Report, MP 195, National Luchtvaartlaboratorium, Amsterdam, Aug. 1960.

[*2*] Hudson, C. M. and Hardrath, H. F., "Effects of Changing Stress Amplitude on the Rate of Fatigue—Crack Propagation in Two Aluminum Alloys," TN D-960, National Aeronautics and Space Administration, Sept. 1961.

[*3*] Christensen, R. H., *Proceedings,* Crack Propagation Symposium, Cranfield, England, 1962.

[*4*] Hudson, C. M. and Raju, Kn. N., "Investigation of Fatigue—Crack Growth Under Simple Variable-Amplitude Loading," TN D-5702, National Aeronautics and Space Administration, March 1970.

[*5*] von Euw, E. F. J., Hertzberg, R. W., and Roberts, R. in *Stress Analysis and Growth of Cracks, ASTM STP 513,* American Society for Testing and Materials, 1972, pp. 230–259.

[*6*] Corbly, D. M. and Packman, P. F., *Engineering Fracture Mechanics,* Vol. 5, July 1973, pp. 479–497.

[*7*] Stephens, R. I., unpublished data on Man-Ten steel received by the authors, March 1975.

[*8*] Rice, R. C. and Stephens, R. I. in *Progress in Flaw Growth and Fracture Tough-*

ness Testing, ASTM STP 536, American Society for Testing and Materials, 1973, pp. 95–114.

[*9*] Gardner, F. H. and Stephens, R. I. in *Fracture Toughness and Slow-Stable Cracking, ASTM STP 559,* American Society for Testing and Materials, 1974, pp. 225–244.

[*10*] Dubensky, R. G., ''Fatigue Crack Growth Delays,'' SAE Paper 740223, Society of Automotive Engineers, 1974.

[*11*] Wei, R. P. and Shih, T. T., *International Journal of Fracture Mechanics,* Vol. 10, No. 1, 1974, pp. 77–85.

[*12*] Gallagher, J. P. and Hughes, T. F., ''Influence of Yield Strength on Overload Affected Fatigue Crack Growth Behavior in 4340 Steel,'' AFFDL-TR-74-27, Air Force Flight Dynamics Laboratory, July 1974.

[*13*] Chanani, G. R., *Metals Engineering Quarterly,* Vol. 15, No. 1, Feb. 1975, pp. 40–48.

[*14*] Willenborg, J., Engle, R. M., and Wood, H. A., ''A Crack Growth Retardation Model Using an Effective Stress Concept,'' AFFDL-TM-71-1-FBR, Air Force Flight Dynamics Laboratory, Jan. 1971.

[*15*] Wheeler, O. E., *Transactions, Journal of Basic Engineering,* American Society of Mechanical Engineers, Vol. 94, Series D, No. 1, March 1972, pp. 181–186.

[*16*] Gray, T. D., ''Fatigue Crack Retardation Following a Single Overload,'' AFFDL-TM-73-137-FBR, Air Force Flight Dynamics Laboratory, Oct. 1973.

[*17*] Adetifa, O. A. and Gowda, C. B., *International Journal of Fracture,* Vol. 10, No. 4, 1974, pp. 614–616.

W. F. Kirkwood [1] *and M. E. Prado* [1]

Three-Dimensional Stress Distribution of a Double-Cantilever Beam with a Side Notch

REFERENCE: Kirkwood, W. F. and Prado, M. E., "**Three-Dimensional Stress Distribution of a Double-Cantilever Beam with a Side Notch,**" *Cracks and Fracture, ASTM STP 601,* American Society for Testing and Materials, 1976, pp. 262–273.

ABSTRACT: The effect of a side notch used as a crack guide in a double-cantilever-beam specimen is investigated. The resulting stress distribution along the section of symmetry ahead of the notch is obtained from a three-dimensional photoelastic model. The effect of the side notch through the thickness and down the side of the specimen is determined. After stress freezing, the model was sliced along principal planes. Along the x-x plane of symmetry, the principal stresses were determined by graphical integration of Filon's transformation of the Lamé-Maxwell equations and by subslicing along the x-z plane. Results of the investigation are in good agreement with those of other investigators. The side notch increases the value of the maximum tensile stress at the intersection of the starter notch and the side notch by approximately 22 percent.

KEY WORDS: crack propagation, double cantilever beams, notch test stresses, stress-intensity factor, photoelasticity, fractures (materials)

Nomenclature

a	Distance from loading pin center line to notch tip, mm
B	Minimum through-the-thickness distance between side notches, mm
d	Distance from the notch tip to the end of the specimen, mm
P	Load, N
R_N	Notch root radius, mm
W	Distance from loading pin center line to the end of the specimen, mm
K_I	Stress intensity factor for Mode I type of displacement, $\text{MPa}\sqrt{\text{m}}$
$\sigma_x, \sigma_y, \sigma_z$	Cartesian system stress components

---

[1] Mechanical engineers, Materials Test and Evaluation Section, Materials Engineering Division, Mechanical Engineering Department, Lawrence Livermore Laboratory, University of California, Livermore, Calif. 94550.

n Fringe order
f Material fringe value, N/mm per fringe
t Thickness of the model slice, mm
σ_n Nominal combined bending and tensile stresses, Pa

Experimental work in determining stress-intensity factors and three-dimensional effects has been conducted on compact specimens. Schroedl and Smith [*1*][2] have performed analyses on compact specimens for *W/B* and *a/W* ratios as recommended in ASTM Test for Plane-Strain Fracture Toughness of Metallic Materials (E 399-74). However, although other geometries are often used to characterize material toughness, the effort to determine the three-dimensional effects on the stress intensity of other geometries has not been made to the same degree as in the case of compact specimens. Specifically, the use of the side notch in the double-cantilever beam (DCB) has not been explored to determine the effect of the notch on the through-thickness stress-intensity factor. Mostovoy [*2*] presents the general approach for the use of this class of specimens, and Gallagher [*3*] and Dull [*4*] discuss the determination of experimentally determined stress intensity factors and the compliance calibration for these specimens. The use of the contoured double cantilever beam specimen is for determining fatigue properties, material stress-corrosion resistance, and fracture toughness. Because of the geometric advantage which the DCB specimen offers, a program for determining the fracture toughness of beryllium was initiated in 1970 at Lawrence Livermore Laboratory (LLL) using DCB specimens [*5*]. This work served to motivate the present study. The DCB specimens used in Ref *5* were side notched, but no attempt was made to determine the influence of a side notch on fracture toughness. The present study is thus aimed at evaluating side-notched specimens with the goal of determining their three-dimensional stress distribution.

This study is restricted to one-notch geometry with a specific crack length. However, a thorough experimental stress analysis of this geometry has been made, and it is believed that the conclusions reached in this study should be relevant to other side-notched geometries.

Experimental Procedure

The photoelastic specimens employed in these experiments are machined from readily available epoxy resins which exhibit excellent characteristics for use in three-dimensional models. Leven [*6*] has detailed the techniques and procedures for successfully employing phthalic-anhydride cured resins, and the authors have had good results with these materials. After casting and fabrication, the model is placed in

---

[2] The italic numbers in brackets refer to the list of references appended to this paper.

an oven and loaded with dead weights. The oven is slowly heated to 165°C, which is the desired "stress freezing" [7] temperature for this material, and then slowly cooled to ambient temperature. At this point the stresses are premanently locked into the specimen, and it is ready for slicing and analysis.

Model Slicing and Fringe Evaluation

Figure 1 shows the coordinate system employed in this investigation. The specimen geometry is described in Fig. 2, and the slicing plan is shown in Fig. 3. Figure 4 shows the stress patterns in the center slice, $2Z/B = 0$. These patterns are similar at $2Z/B = 0.4$ and 0.6. The numbers in the field of these photographs refer to fringe order, n. Figure 5 is a slice taken at the edge of the specimen and includes the side notch. Figure 6 shows stress patterns of two slices removed tangent to the starter notch for determining the fringe orders along the z axis. By determining the fringe order at an initial slice thickness and determining n/t through a series of machining operations, the final values of the stress differences $\sigma_y - \sigma_z$ may be extrapolated to the free boundary along the starter notch.

From the stress patterns shown in Figs. 4 and 5, the principal stresses in the region of the starter notch were determined and are plotted in dimensionless form in Fig. 7. Separation of the principal stresses was accomplished using the slope equilibrium method [7], Filon's tranformation of the Lamé-Maxwell equations [8] and by subslicing. The determination of fractional fringe orders was accomplished using Tardy Compensation [9], a Babinet compensator, and by extrapolation to a boundary.

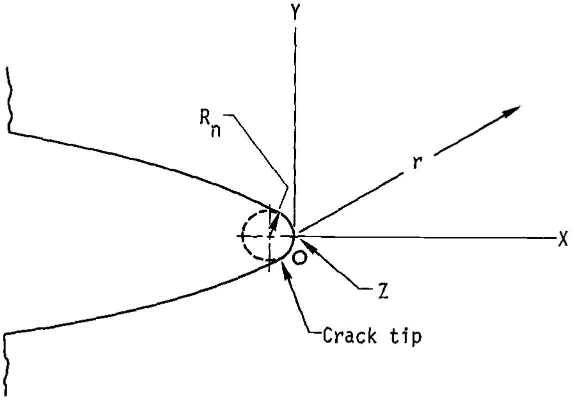

FIG. 1—*Coordinate system for the stress field near the crack tip. The* z *axis is perpendicular to the page.*

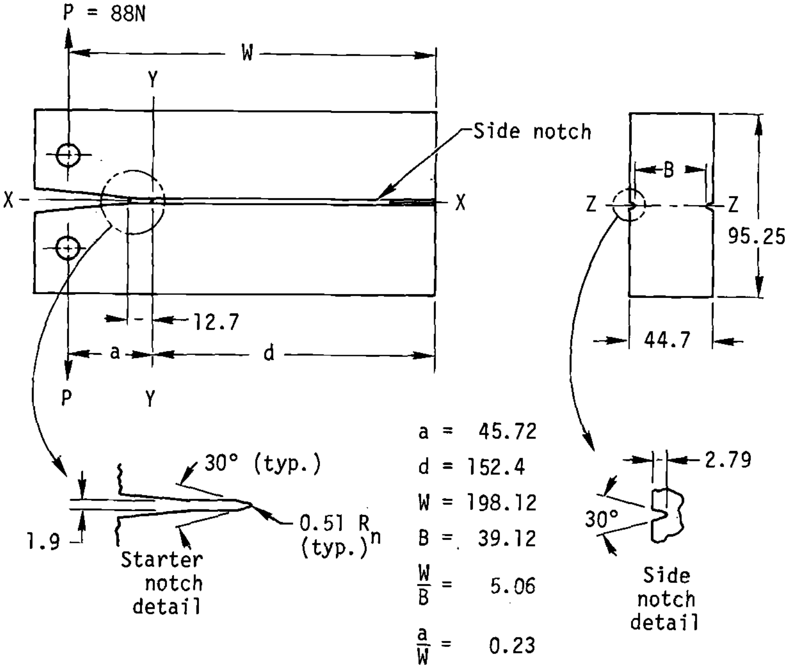

FIG. 2—*Dimensions of photoelastic model, all dimensions in millimetres. Starter notch and side notch have same radius.*

Discussion of Experimental Analysis and Results

Figure 4 shows a light field photograph of a slice removed from the center or mid-thickness of the model. Along the x axis, the fringe pattern (see numbers on field of photograph) ranges from an order of zero at the isotropic point to a maximum of 5.6 at the root radius. Along this principal axis, σ_x and σ_y are principal stresses. In each case the stress pattern was analyzed by applying the stress optic law [*8*]

$$\sigma_x - \sigma_y = \frac{nf}{t} \qquad (1)$$

The determination of the principal stresses through the thickness (along the z axis at the root of the notch) is handled in the same manner with

$$\sigma_y - \sigma_z = \frac{nf}{t} \qquad (2)$$

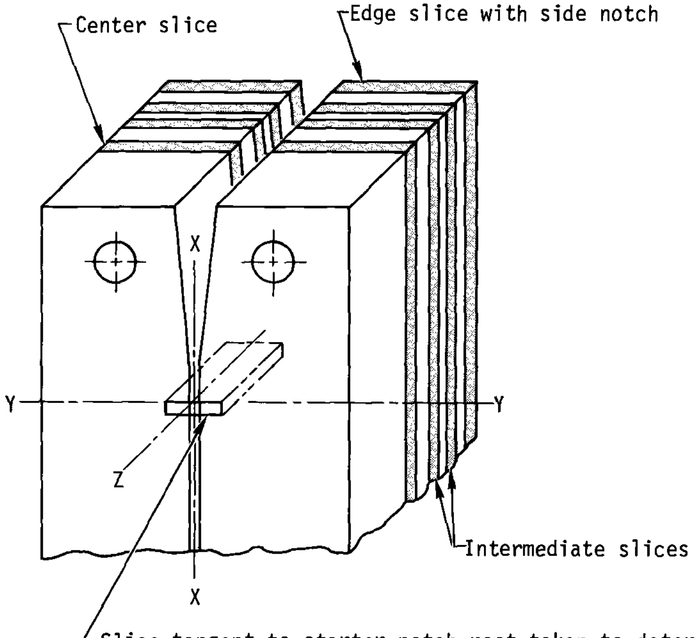

Slice tangent to starter notch root taken to determine $\sigma_y - \sigma_z$ at the root. Values were extropolated to the free boundary by thinning several times and recording the fringe values.

FIG. 3—*Specimen-slicing plan.*

The general form for the elastic-stress field near a crack tip of zero root radius by Irwin [*10*] is

$$\sigma_y = \frac{K_\mathrm{I}}{(2\pi r)^{1/2}} \cos \frac{\theta}{2} \left(1 + \sin \frac{\theta}{2} \sin \frac{3\theta}{2}\right) \tag{3}$$

As our model has a small finite root radius, it does not satisfy Eq 3 because r never approaches zero. Bowie and Neal [*11*] performed investigations employing finite root radius with results showing that for a notch-length-to-root-radius ratio greater than 2.0, there is introduced a maximum 2 percent error in determining K_I. Kobayashi [*12*] determined through a series of photoelastic experiments that K_I reaches a stationary value when the minimum value of r is approximately 1.85 mm. The boundary stress σ_y/σ_n determined at the notch root through the thickness from $2Z/B = 0$ to 0.75 varies approximately 3½ percent, which is an acceptable span for experimental error. Therefore, it will be assumed for this investigation that σ_y/σ_n is constant through this thickness.

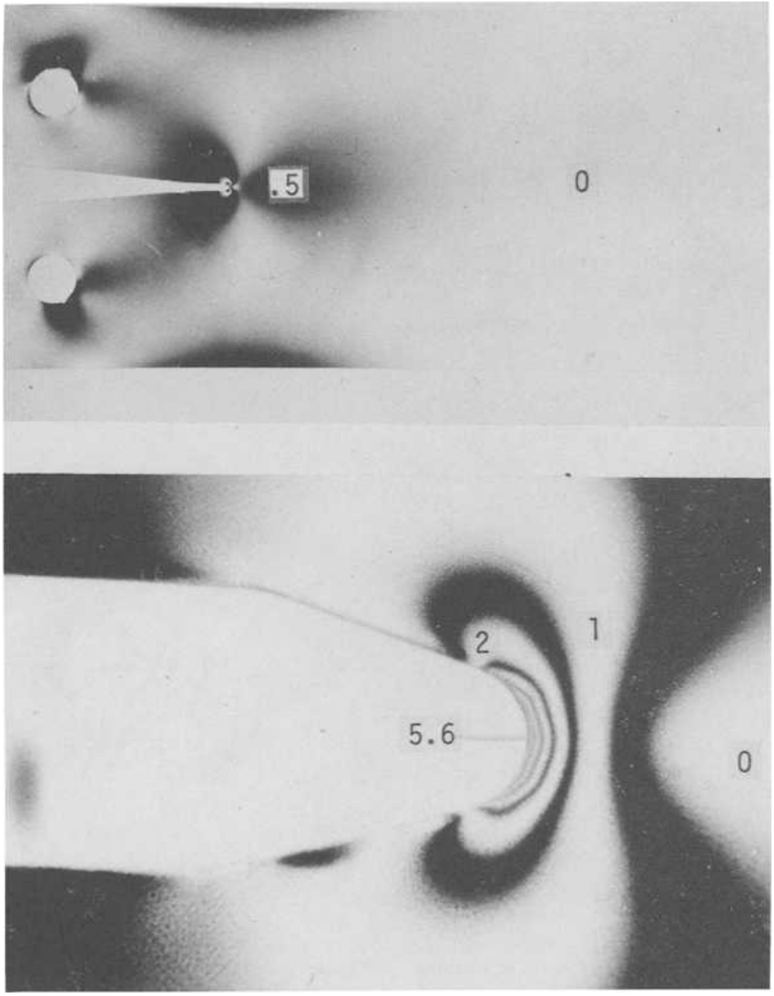

FIG. 4—*Light-field photographs of center slice and enlargement of stress pattern at crack tip. Slice is at 0.89 mm thickness. Notch-tip enlargement is ×20. Numbers in field refer to fringe order,* n.

The stress intensity factors were determined using the dimensionless form suggested by Marloff et al [*13*] in which

$$\sigma_n = \frac{P}{Bd}\left(4 + \frac{6a}{d}\right) \tag{4}$$

Setting $\theta = 0$ in Eq 3 leads to an apparent stress intensity

$$K_I = (2\pi r)^{1/2}\sigma_y \tag{5}$$

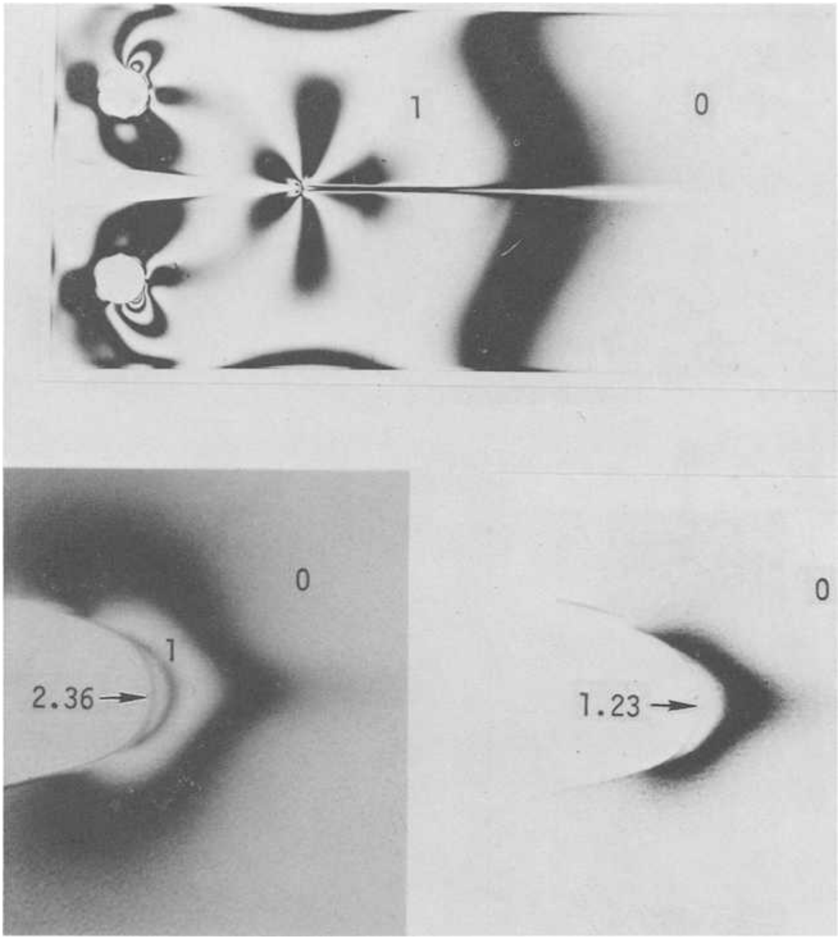

FIG. 5—*Light-field photographs of edge slice, showing side notch. Top section is 4.11 mm thick. Lower left section showing crack tip* (×20) *is 0.41 mm thick. Lower right section showing crack tip* (×20) *is 0.18 mm thick. The thinning of the sections was used in:* (a) *determination of values of* $\sigma_y - \sigma_x$ *down the side notch axis and* (b) *determining maximum values of* σ_y *at the intersection of the crack tip and the notch. Numbers in field refer to fringe order,* n.

By setting $r = x$ and dividing numerator and denominator by $d^{1|2}$, a convenient equation for both stress analysis and plotting may be developed

$$K_{\rm I} = (2\pi d)^{1|2} \left(\frac{x}{d}\right)^{1|2} \sigma_y \qquad (6)$$

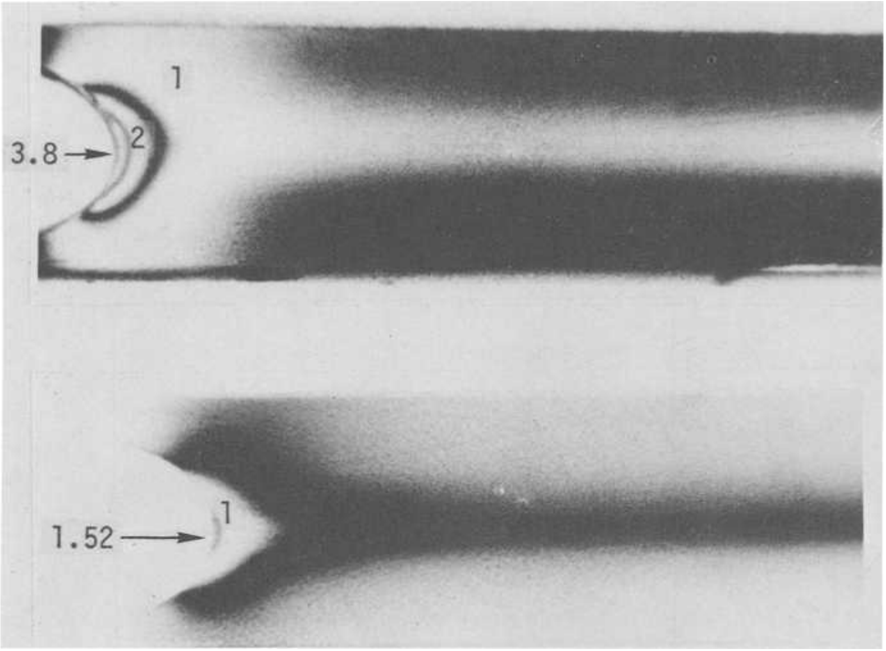

FIG. 6—*Stress pattern looking along trace of starter notch out to the side notch along the z-z plane. Upper slice thickness = 0.58 mm (×20). Lower slice thickness = 0.21 mm (×20).*

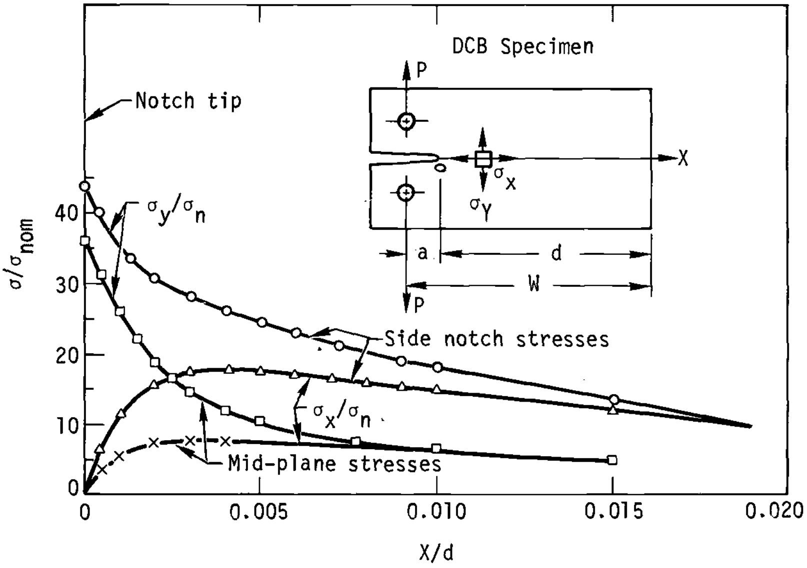

FIG. 7—*Distribution of the principal stresses (σ_y/σ_n and σ_x/σ_n) near the notch tip.*

By substituting $a^{1/2}/\sigma_n$ into both sides of Eq 6, the apparent stress intensity factor may be expressed in dimensionless form

$$\frac{K_I(a)^{1/2}B}{P} = 7.97 \left(\frac{x}{d}\right)^{1/2} \left(\frac{\sigma_y}{\sigma_n}\right) \tag{7}$$

Figures 8 and 9 show the stress distribution along the z axis from the

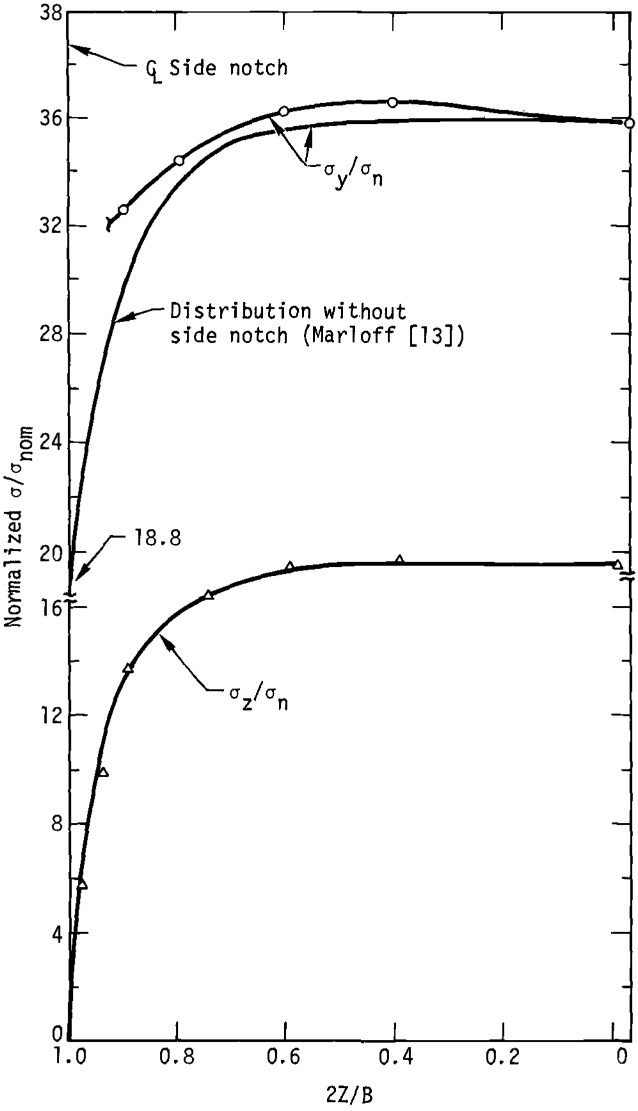

FIG. 8—*Through-the-thickness variations of the principal stresses along the* z-z *axis.*

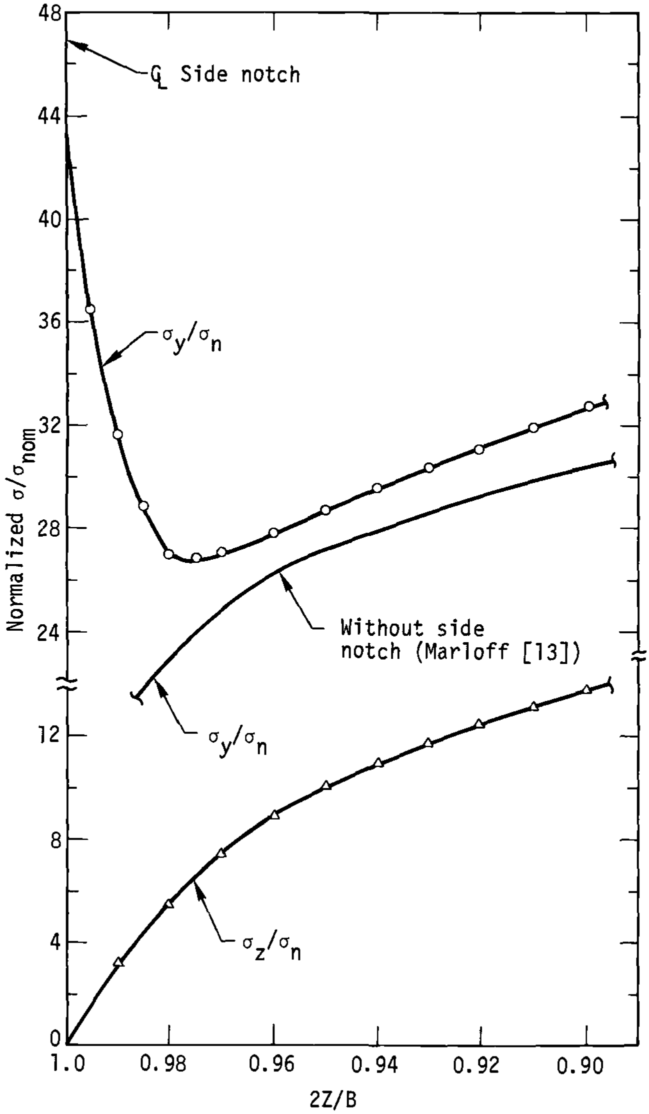

FIG. 9—*Through-the-thickness variation of the maximum starter-notch stresses near the side notch.*

center of the specimen out to the side notch. For most of this distance it behaves as though it does not know the side notch is there, but the discontinuity slowly influences it and by 2Z/B = 0.97, a minimum value is reached with the σ_y/σ_n stress rapidly increasing to the side notch. So for a value of R_N = 0.51 mm with a 30-deg flank angle, the side notch influences the distribution of principal stresses for a distance of approximately 1.3 times the side notch radius. The effects of the side notch may be beneficial in maintaining a more even stress distribution through the specimen thickness and ensuring a more uniform crack length through the thickness.

The values of σ_z/σ_n were higher than anticipated, but this is probably due to the high Poisson's ratio of the model material (0.48) at the stress-freezing temperature. Also the triaxial state of stress near the notch tip indicates that the condition of plane strain exists. Figure 8 shows the principal stresses in the x-y plane at the center and along the side notch of the specimen. Starting at the notch root and going along the x axis, the values of σ_y/σ_n are always higher along the side notch compared to the center, a condition which should be expected at a free boundary and probably guarantees good crack guidance.

Figure 10 is a plot of the apparent stress intensity factors near the starter notch. These plots were made for values of x/d between 0.001 to 0.015. It appears that these values become constant beyond x/d = 0.007.

Conclusions

The results of this investigation indicate that the use of a side notch in symmetrical fracture-toughness specimens provides the crack the guidance for which it was intended. Furthermore, the side notch, although it acts as a stress riser, tends to raise the average boundary stress from the

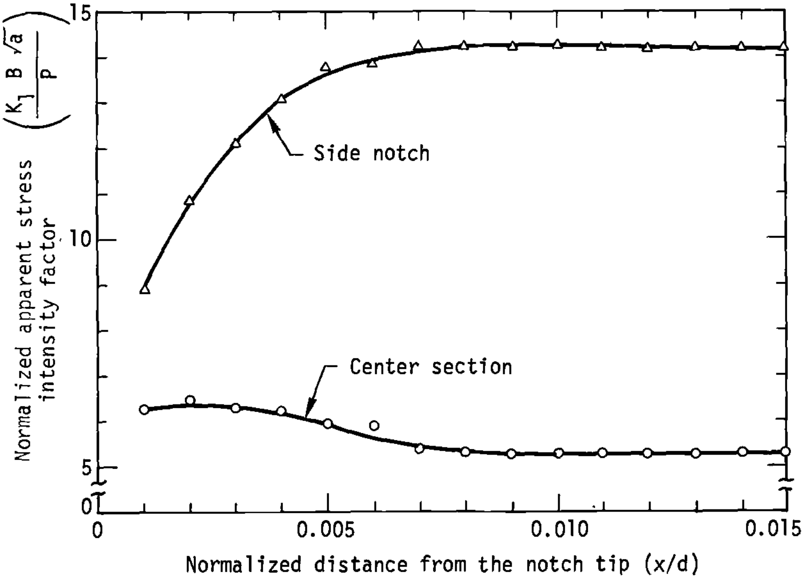

FIG. 10—*Plot of apparent stress-intensity factors at center section and at side notch.*

region $z/B = 0.75$ to 1.00 to nearly the same as the mid-thickness value and will guarantee a more constant crack length throughout the complete thickness.

Acknowledgments

The authors wish to acknowledge the contribution of J. C. Stone for his skill in machining, testing, and photographing the model. This work was performed under the auspices of the U. S. Energy Research & Development Administration, under Contract No. W-7405-Eng-48.

References

[*1*] Schroedl, M. A. and Smith, C. W. in *Fracture Analysis, ASTM STP 560,* American Society for Testing and Materials, 1974, pp. 69–80.
[*2*] Mostovoy, S., Crosley, P. B., and Ripling, E. J., *Journal of Materials,* Vol. 2, 1967, p. 661.
[*3*] Gallagher, J. P., *Engineering Fracture Mechanics,* Vol. 3, No. 1, 1971, pp. 27-43.
[*4*] Dull, D. L., Buch, J. D., and Raymond, L., *Engineering Fracture Mechanics,* Vol. 4, 1972, pp. 523-531.
[*5*] Prado, M. E., "Evaluation of Fracture Toughness of Beryllium," Report UCID-15970, Lawrence Livermore Laboratory, 1970.
[*6*] Leven, M. M., "Epoxy Resins for Photoelastic Use," Proceedings, International Symposium on Photoelasticity, Chicago, 1961, MacMillan Company, New York, 1963.
[*7*] Hetenyi, M. in *Handbook of Experimental Stress Analysis,* Wiley, New York, 1950, pp. 933-936.
[*8*] Frocht, M. M. in *Photoelasticity,* Wiley, New York, 1941, Chapter 1.
[*9*] Gorasen, R. W. and Adams, L. H., *Journal of the Franklin Institute,* Vol. 216, No. 4, 1933, pp. 475-504.
[*10*] Irwin, G. R., Kies, J. A., and Smith, H. L., *Proceedings,* American Society for Testing and Materials, Vol. 58, 1958, pp. 640-657.
[*11*] Bowie, O. L. and Neal, D. M., *International Journal of Fracture Mechanics,* Vol. 3, No. 2, 1967, pp. 111-119.
[*12*] Kobayashi, A. S. in *Handbook of Fracture,* Vol. 3, Academic Press, New York, 1971, pp. 311-369.
[*13*] Marloff, R. H., Leven, M. M., Ringler, T. N., and Johnson, R. L., *Experimental Mechanics,* Vol. 11, No. 12, 1971, pp. 529-539.

A. S. Kobayashi,[1] *S. Mall,*[1] *and M. H. Lee* [1]

Fracture Dynamics of Wedge-Loaded Double Cantilever Beam Specimen

REFERENCE: Kobayashi, A. S., Mall, S., and Lee, M. H., "**Fracture Dynamics of Wedge-Loaded Double Cantilever Beam Specimen,**" *Cracks and Fracture, ASTM STP 601,* American Society for Testing and Materials, 1976, pp. 274–290.

ABSTRACT: Dynamic photoelasticity was used to analyze the Battelle-type wedge-loaded double cantilever beam (DCB) specimen machined from Homalite-100 sheets of 3/8-in. (9.5 mm) thickness. Dynamic stress intensity factors, dynamic energy release rate, crack velocities of straight and curved cracks were determined. Corresponding static stress intensity factors were calculated by the method of finite element analysis. These results were compared against Kanninen's analytical results and experimental results by Hahn et al using steel specimen. While dynamic photoelasticity results show qualitative agreement with Kanninen's results, the two differ in detail.

KEY WORDS: crack propagation, fractures (materials), stresses, steels, cracks

The wedge-loaded DCB (double-cantilever-beam) specimen developed by Hahn et al [*1,2*] [2] is a compact specimen where the crack, which is initiated under a constant wedge-opening, propagates into a diminishing field of stress intensity factor and could eventually arrest. A distinct characteristic of a wedge-loaded DCB specimen is the existence of compressive stresses parallel to the crack plane, which tend to stabilize the crack path. Hence, with an appropriate wedge angle the side-grooving, which is necessary in ordinary DCB specimen, can be eliminated in some specimens. The wedge-loaded DCB specimen is thus a two-dimensional specimen which can be adequately analyzed by available two-dimensional techniques such as two-dimensional dynamic photoelasticity and finite element analysis.

---

[1] Professor, graduate student, and former graduate student, respectively, Mechanical Engineering Department,University of Washington, Seattle, Wash. 98195.

[2] The italic numbers in brackets refer to the list of references appended to this paper.

In terms of evaluating the fracture characteristics of materials, the wedge-loaded DCB specimen is an efficient specimen which can be used to determine both fracture initiation and fracture arrest properties in a relatively short span. By using a blunt notch tip at the starter crack, strain energy release rates can be raised high above the fracture toughness of the material to simulate fracture dynamics in highly loaded structures. Recently, a wedge-loaded duplex DCB specimen has been used to study fracture dynamics in ductile material, such as A517-F steel. In this duplex specimen, the crack initiates in a brittle 4340 steel, which is electron-beam welded to the A517-F test section, and runs into this ductile test section at which point the running crack branches and arrests [*3*]. Such crack branching can also be eliminated at the expense of reintroducing relatively deep side grooves (of the magnitude of 60 percent of the net thickness) [*4*].

Experimental analysis of the wedge-loaded DCB specimen consists mainly of crack velocities measured by grids of conducting strips mounted on the specimen surface. Crack velocities in 4340 steel and polymethyl-methacrylate DCB specimens were found to be approximately 10 to 20 percent of the longitudinal wave velocity and remained almost constant for most of the length of the specimens [*2,5*]. Higher crack velocities were related to the higher initial stress intensity factors associated with blunt initial starter notches. Crack velocities were also observed to decrease abruptly just prior to crack arrest.

The only available theoretical analysis of the wedge-loaded DCB specimen is by Kanninen who modeled this specimen by a one-dimensional augmented beam partly supported by an elastic foundation [*6,7*]. The crack propagates in discrete jumps when the spring at the crack tip reaches a critical energy level at which time it ruptures and the crack tip advances by an increment of length. The stored spring energy is then dissipated during this time. Crack velocities and the energy rates are determined for ratios of statically released energy versus energy absorption rate at the propagating crack tip which extends either by a velocity independent [*6*] or a velocity dependent [*7*] dynamic fracture criterion. Kanninen's results show that more than half of the static strain energy released by the propagating crack in the initial stage of crack propagation can be converted into kinetic energy which is later fed back into the crack tip and supplies approximately 90 percent of the fracture energy just prior to fracture arrest.

This brief review of the current theoretical and experimental knowledge on wedge-loaded DCB specimen indicates that further detailed dynamic analysis of this specimen is necessary, particularly if this specimen is to be used as a standard specimen for characterizing fracture dynamic properties of materials. The objective of this paper is to analyze, statically and dynamically, the wedge-loaded DCB specimen and compare these results with the extensive analysis conducted by the Battelle researchers. Dynamic photoelasticity was used for the latter and static finite element analysis was used for the former.

Experimental Procedure

The modified Cranz-Schardin 16 spark-gap camera and associated dynamic polariscope used in this investigation have been described in numerous previous papers (see, for example, Refs *8* and *9*). The wedge-loaded DCB photoelastic specimens used in this investigation consisted of ⅜-in. (9.5 mm) thick Homalite-100 plates, 3 by 6 in. (76.2 by 152.4 mm) loaded with a 31-deg wedge as shown in Fig. 1. At fracture load, the crack propagated from a single, edge-notched starter crack of length ¾ to

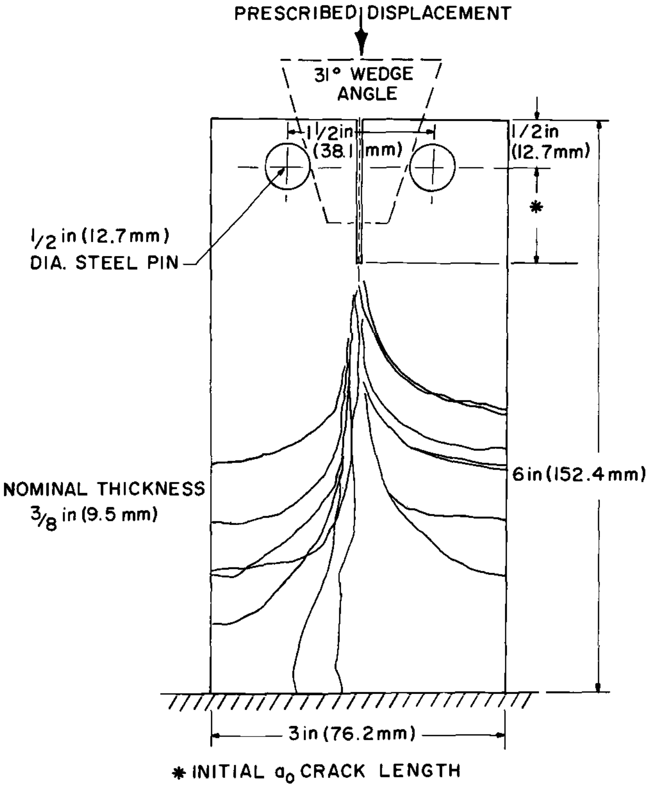

FIG. 1—*Wedge-loaded DCB specimen and curved crack paths.*

1½-in. (13.05 to 38.1 mm) with either a sawed crack tip [3] or a crack tip blunted by a drilled hole or prescribed radius.

The Homalite-100 sheets used in these experiments were calibrated by Bradley [*8*] and Wade [*10*], who reported an average dynamic modulus of elasticity, Poisson's ratio, stress-optic coefficient, and static fracture toughness of 657 ksi (4.65 GPa), 0.345, 155 psi-in. fringe (27.1 Pa-m/fringe) and 580 psi $\sqrt{\text{in.}}$ (636 Pa$\sqrt{\text{m}}$), respectively.

Dynamic stress intensity factors, K_D, were determined from the dynamic photoelasticity patterns using a variation of the original procedure suggested by Irwin [*11*]. This approximate procedure is based on the assumption that the dynamic near-field state of stress can be obtained by scaling the corresponding static near-field state of stress with a scaling factor, K_D/K, which is the ratio of dynamic to static stress intensity factors. This assumption was validated to some extent in Ref *12* by the equivalence in the shapes of the theoretical dynamic and corresponding theoretical static isochromatics surrounding a crack tip extending at constant velocity up to 15 000 in./s (381 m/s) in a plate of infinite extent. Further investigation on possible errors due to this usage of a two-parameter static near-field solution for characterizing a one-parameter dynamic near-field stress, however, are needed before a rigorous error estimate of the experimental procedure used in this paper can be made. Since the maximum distances of the dynamic isochromatic loops used in data reduction varied form 0.02 to 0.1 in. (0.5 to 2.5 mm), our experiences indicate that the estimated accuracy of dynamic stress intensity factor, K_D, could be of the order of ±10 percent of its true values.

Additional effects of the superposed reflected compression stress waves and vertically polarized shear-stress waves impinging on the propagating crack tip in the actual finite specimen can be accounted for by studying the dynamic near-field solution of a propagating semi-infinite crack in these stress wave fields. Fortunately, Chen and Sih [*13*] have shown that this dynamic near-field solution is identical in form to that of a crack tip extending at constant velocity in an infinite plate [*14*]. Thus, the analysis in Ref *12* can be used to reach the same conclusion that the shape of isochromatics surrounding a propagating semi-infinite crack impinged by compression and vertically polarized shear stress waves is similar to that of isochromatics surrounding a static crack in a static stress field. The estimated errors due to the finite distances of the dynamic isochromatic loops from the moving crack tip in this impinging stress wave field is thus estimated to be of the same order of ±10 percent of its true value.

The remaining unresolved question is the possible differences in the shapes of dynamic and static isochromatics surrounding an accelerating or decelerating crack tip. This effect for most of the dynamic photoelastic

---

[3] Sawed and chiseled crack tip which represents a sharp crack tip was not used in this analysis since the crack would immediately arrest in such DCB specimens.

analysis is considered small since the crack in Homalite-100 is observed to run at a relatively constant velocity of 10 000 to 15 000 in./s (254 to 381 m/s).

Returning to the approximate procedure for determining dynamic stress intensity factors, Bradley's procedure was used where more than two distinct isochromatic loops could be observed at the crack tip. For low dynamic stress field where only one distinct dynamic isochromatic loop could be observed, another modification of Irwin's procedure was used where the dynamic stress intensity factor can be represented as

$$K_{\mathrm{D}} = \tau_{\mathrm{max}} \frac{2\sqrt{2\pi r_m}}{[\sin^2\theta_m + 2\delta\sqrt{\frac{2r_m}{a}} \sin\ \theta_m\ \sin\frac{3\theta_m}{2} + \left(\delta\sqrt{\frac{2r_m}{a}}\right)^2]^{1|2}} \tag{1}$$

where r_m and θ_m represent, in terms of the polar coordinates, the location at the furthest point of the isochromatics; a is the crack length of the edge-notched DCB specimen, and δ is the ratio of the remote stress component to the applied stress [*15*].

The extreme condition for τ_{max} provides a relation between $\delta\sqrt{2r_m}/a$ versus θ_m without the knowledge of the crack length, a. The denominator in Eq 1 is relatively insensitive to the variations in $\delta\sqrt{2r_m}/a$ for 90 deg $\leqslant \theta_{\mathrm{m}} \leqslant$ 130 deg which fortunately was the range in which the isochromatic loops appeared in the low dynamic stress field. Thus, this alternate procedure was used with relative success in evaluating the low dynamic stress intensity factors in this investigation.

The dynamic energy release rate, $\mathcal{G}_{\mathrm{D}}$[4], was computed by the following plane stress relation by Freund for a propagating crack in an infinite solid [*16,17*] and for also an initially stationary crack impacted by a plane pulse [*18*] as

$$\mathcal{G}_{\mathrm{D}} = \frac{1}{2G} K_{\mathrm{D}}^2\, A(d) \tag{2a}$$

where

$$A(d) = \frac{b^2d^2\ (1 - a^2\mathrm{d}^2)}{4d^2\ \sqrt{d^2 - a^2}\sqrt{d^2 - b^2} - (2d^2 - b^2)^2} \tag{2b}$$

$$a = 1/c_1,\ b = 1/c_2,\ d = 1/c$$

c_1, c_2, and c = velocities of the dilatational wave, distortional wave and crack, respectively, and

G = shear modulus of elasticity.

---

[4] Freund and others refer to this quantity as the energy flux, E, into the crack tip. Although this designation may be more appropriate, the $\mathcal{G}_D$ notation implies that $\mathcal{G}_D$ is a simple dynamic extension of the well-known static strain energy release rate, $\mathcal{G}$.

To reiterate again, the dynamic stress intensity factor, K_D, determined by dynamic photoelasticity will incorporate all dynamic effects due to crack propagation and impinging stress waves, and will completely characterize the elasto-dynamic stress field surrounding a moving crack tip within the constraints just discussed. The dynamic energy release rate, $\mathcal{G}_D$, computed by Eq 2, must in theory be equal to the specific dynamic fracture energy of the material or R_D in the Battelle analysis. Previous experimental results indicate that this specific dynamic fracture energy of the material is far from being constant or a monotonic function of the crack velocity as assumed by the others [*6,7*].

The static stress intensity factor, K, and static strain energy release rate, $\mathcal{G}$, were obtained by finite element analysis. This procedure has been well documented and therefore will not be repeated here (see, for example, Refs *8, 9,* and *10*).

When a global energy balance of the specimen is considered, the kinetic energy as well as the work done must be accounted for in addition to the preceding dynamic and static energy released. For a conservative system, the kinetic energy is fed back into the crack tip so that it can continue to extend even in a region where the dynamic energy release rate is less than the critical strain energy release rate, $\mathcal{G}_c$, which is a material property. In actual experiments, some of the kinetic energy is dissipated through specimen and loading pin movements as the loading pins separate from the loading wedge of the wedge-loaded DCB specimens [*17*].

Results

Of a total 31 tests conducted, the crack path curved in approximately half of the specimens. Figure 1 shows some of the curved paths observed in this wedge-loaded DCB specimen. Although small misalignment of the specimen could have caused some crack curving, this predominance in curved cracks shows that the wedge angle of 31 deg probably did not decrease the normal stress in the crack direction enough to stabilize the crack path.

The preceding conjecture was verified by a static analysis of this specimen. A conventional finite element code with constant strain elements was used to analyze the not-so-near field normal stresses which should otherwise be a hydrostatic state in the singular region ahead of the crack tip. Figure 2 shows that the ratio of normal stresses, σ_{yy}/σ_{xx}, approximately $0.015b$ distance ahead of the crack tip, for a conventional DCB specimen and for a wedge-loaded DCB specimen with wedge angles of $\alpha = 31$ deg, are approximately 1.05 to 1.10 throughout most of the crack length. For conventional DCB specimens the increase in the ratio of σ_{yy}/σ_{xx} at crack length of $a/b > 0.7$ indicates that the crack path should stabilize if the crack can reach this length without prior curving.

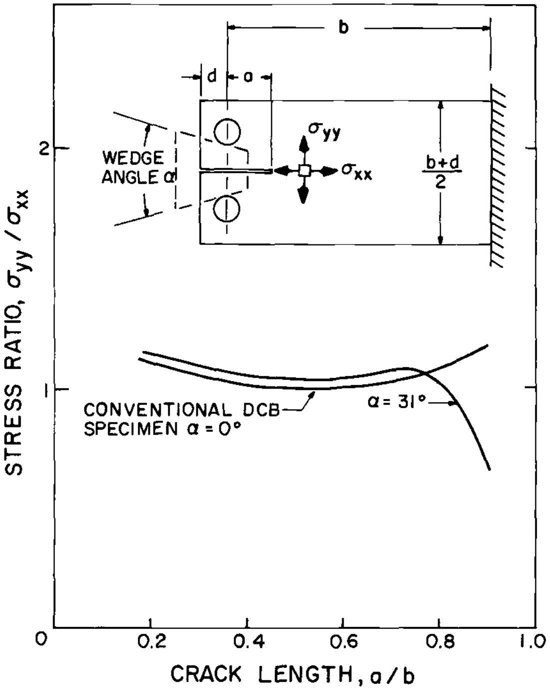

FIG. 2—*Normal stress ratios immediately ahead of the crack tip in a conventional and a wedge-loaded DCB specimen.*

The curved crack phenomenon was further studied by analyzing statically an idealized curved crack in the wedge-loaded DCB specimen. Figure 3 shows that the normal stress ratio ahead of the crack tip, $\sigma_{yy}'/\sigma_{xx}'$ continuously decreases as the crack turns. Also, the Modes I to II stress intensity factor ratio, K_I/K_{II}, continuously decreases with crack curving. The net result of this static analysis indicates that when the crack curves, it will probably continue to run until it is oriented almost perpendicular to its original crack path. The principal stress direction, also shown in Fig. 3, appears to have rotated 70 or 80 deg from the original crack path once the crack curves. Thus, only some chanced dynamic stress field generated by irregular reflected and refracted stress waves can return the crack to its original straight path.

Figures 4 and 5 show typical dynamic isochromatic patterns in fracturing wedge-loaded DCB specimens with a slotted starter crack. The curved crack path in Fig. 5 was idealized and analyzed in Fig. 3. Both cracks arrested sometime during the last four frames of recording.

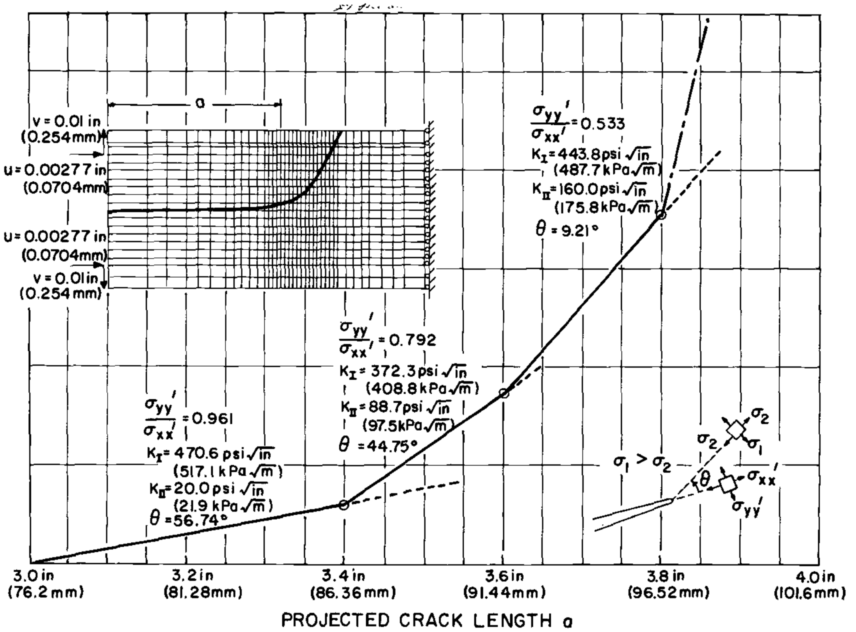

FIG. 3—*State of stress immediately ahead of a curved crack in a wedge-loaded DCB specimen.*

Figures 6 and 7 show the dynamic stress intensity factors [5] and dynamic energy release rates for the two specimens shown in Figs. 4 and 5. The gradual increase in K_D during the initial phase of crack propagation is in accordance with the results in Refs *8* and *9* for cracks with sharp initial crack tip radius. Figures 8 and 9 show the dynamic stress intensity factors and dynamic energy release rates in wedge-loaded DCB specimens with blunt cracks of known initial radius. The rapid increase in K_D during the initial phase of crack propagation in these tests are in qualitative agreement with those results for blunt initial crack tip radius in Refs *5* and *6*. The dynamic stress intensity factor and dynamic energy release rate at the onset of crack propagation were assumed to be equal to the corresponding static critical values on the basis that fracture initiated from some minute crack at the end of a rough saw-cut slot or a rough drilled hole. Although such assumption may be questionable in ductile material, empirical findings in high strength aircraft structures [*19*] appear to justify this assumption. Also shown in these four figures are curves of equivalent

---

[5] K_{IID} and G_{IID} were not determined in the 31S-030274.

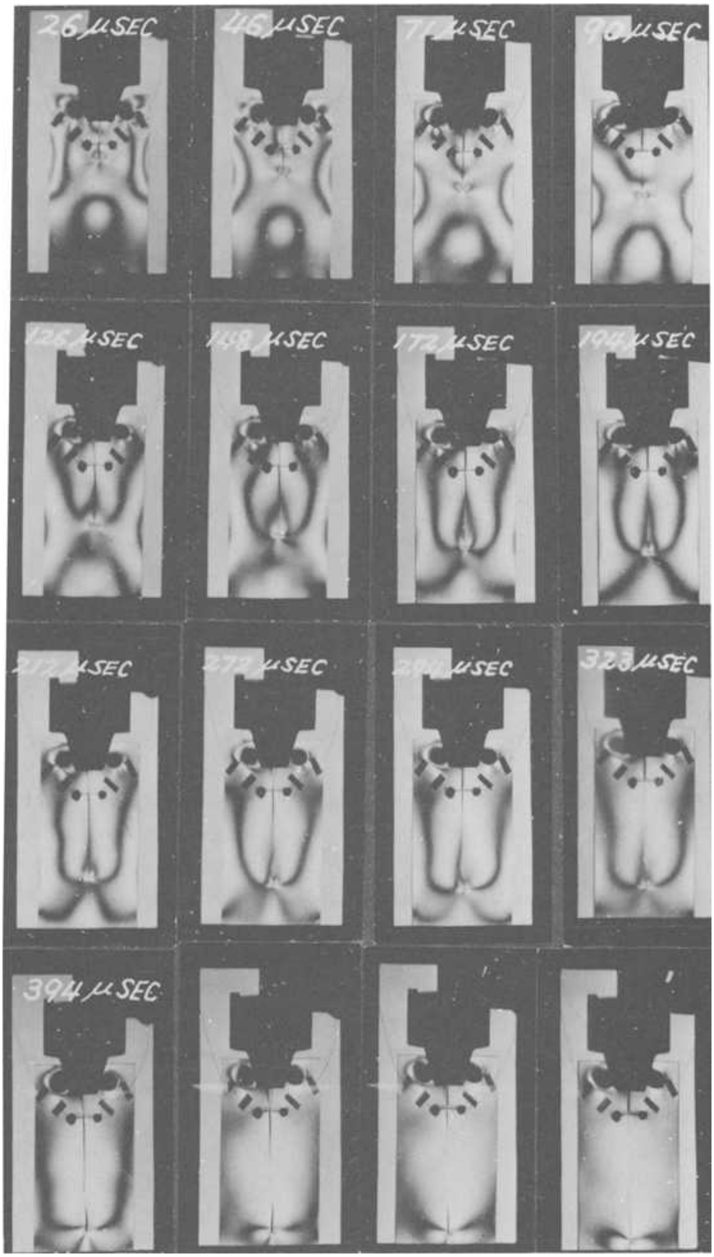

FIG. 4—*Dynamic photoelastic patterns of a propagating crack in a wedge-loaded DCB specimen, 1S-031273.*

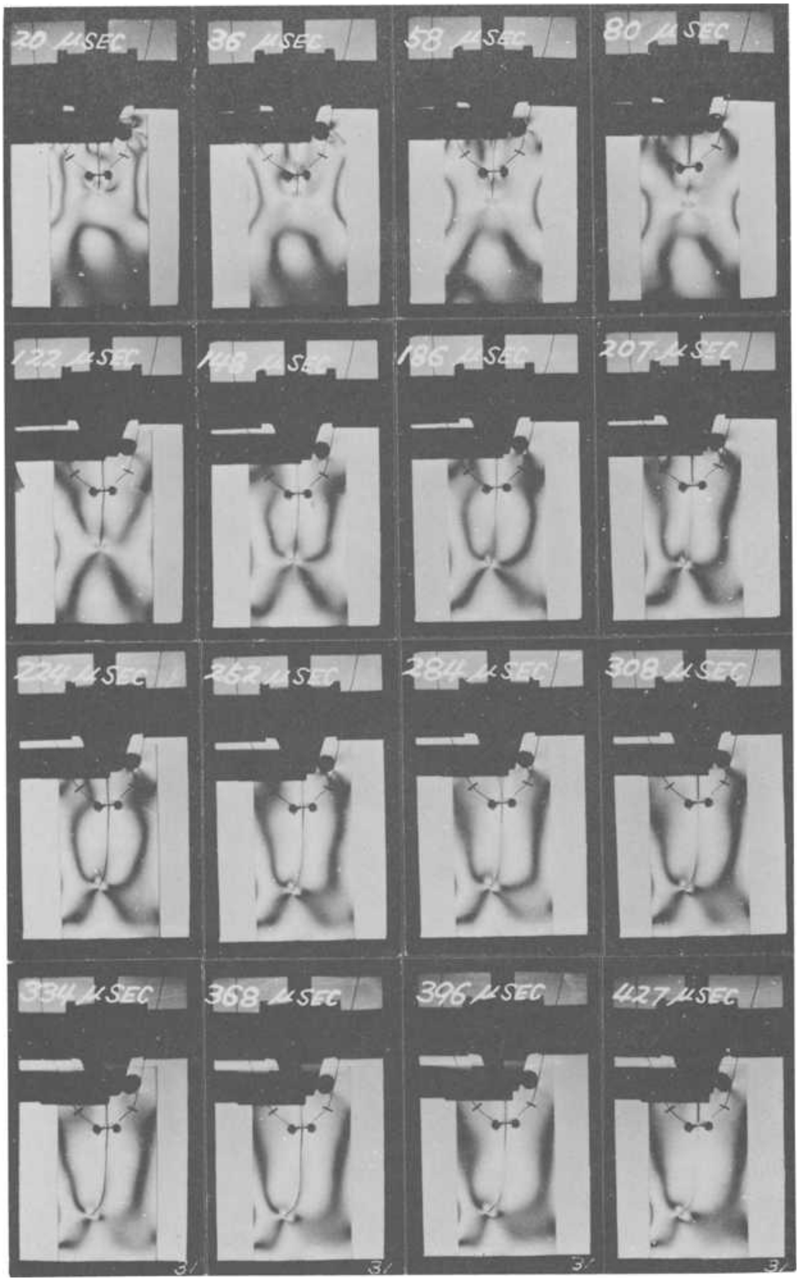

FIG. 5—*Dynamic photoelastic patterns of a propagating crack in a wedge-loaded DCB specimen, 31S-030274.*

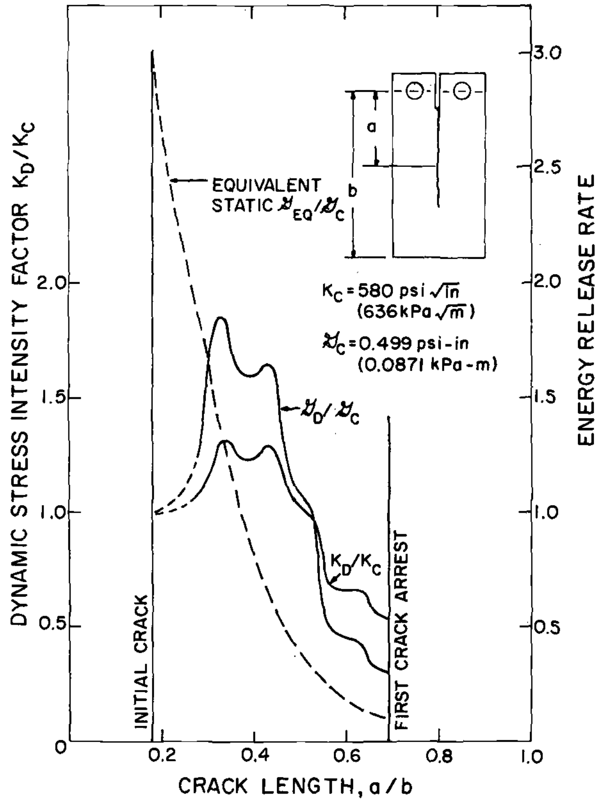

FIG. 6—*Dynamic stress intensity factors and dynamic energy release rates in wedge-loaded DCB specimen; initial crack tip was sawed; Specimen 1S-031273.*

static energy release rate, $\mathcal{G}_{EQ}$, which was computed by matching the total static strain energy released by a slowly growing crack in a wedge-loaded DCB specimen with the measured total dynamic energy released during the entire crack propagation. The equivalent static strain energy release rate thus obtained can be used to isolate the dynamic effects during crack propagation.

The average dynamic energy release rate, $\mathcal{G}_D|_{avg}$, which is the total dynamic total energy released during crack propagation divided by the total newly created crack surface was also computed. The four average dynamic energy release rates, together with the four equivalent static strain energy release rates at the onset of crack propagation, $\mathcal{G}_{EQ}|_{t=0}$, are tabulated in Table 1. The latter $\mathcal{G}_{EQ}|_{t=0}$ corresponds to the strain energy release rate of the initial blunt crack, $\mathcal{G}_Q$, in the Battelle analysis.

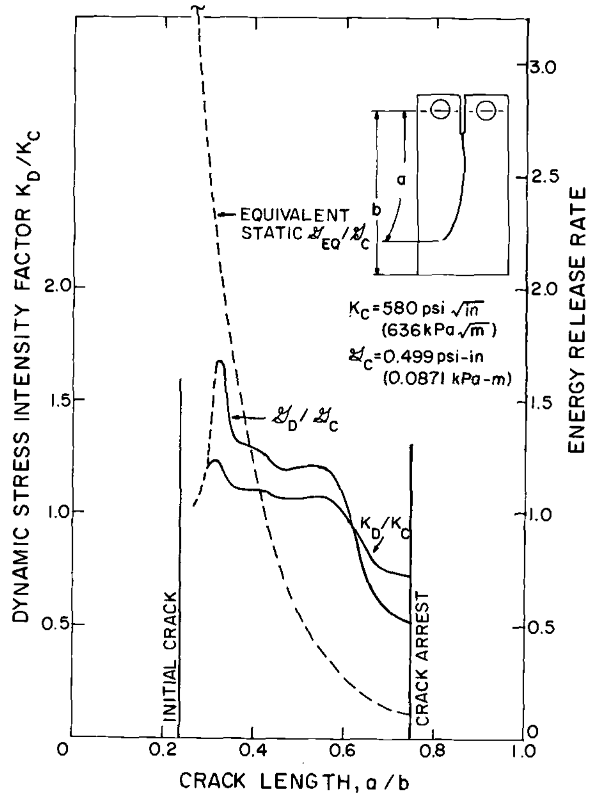

FIG. 7—*Dynamic stress intensity factor and dynamic energy release rates in wedge-loaded DCB specimen; initial crack tip was sawed; Specimen 31S-030274.*

Figure 10 shows the crack velocities at discrete crack length in six specimens. The crack velocities in these specimens ranged from 10 to 20 percent of the dilatational wave velocity and are in general agreement with the results reported by Hahn et al [*1,2*]. The crack velocity, however, reached a maximum value immediately after crack propagation, leveled to a constant velocity, and then dropped prior to crack arrest. This general trend is slightly different from Battelle results which show almost constant velocity crack propagation throughout their specimens without the trailing low-velocity crack propagation prior to crack arrest. This difference could be attributed in part to the extremely brittle Homalite-100 used in this investigation where the crack could continue to propagate in the low stress field as well as our experimental procedure which

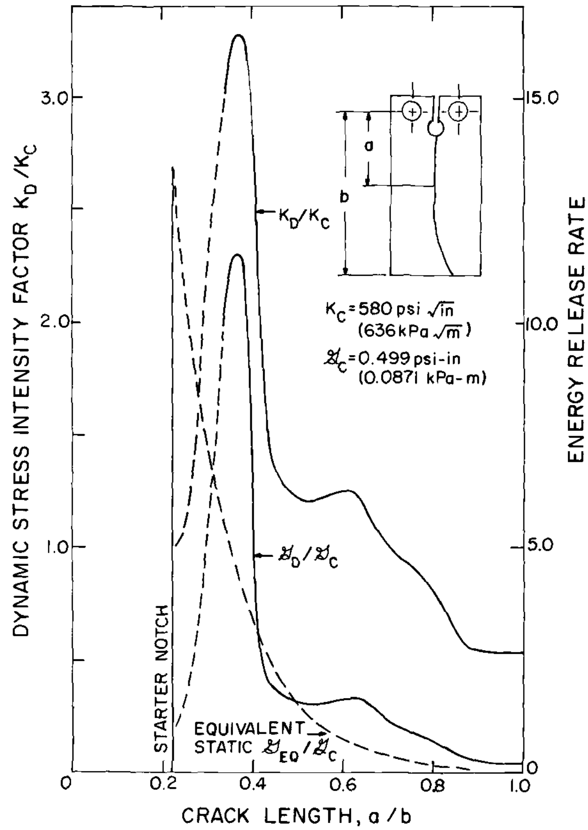

FIG. 8—*Dynamic stress intensity factors and dynamic energy release rates in wedge-loaded DCB specimen; initial notch tip radius, ⅛ in.; Specimen 21B-020874.*

possibly resulted in larger experimental errors in crack velocity determination immediately preceding crack arrest.

Discussion

Comparison of Figs 6 through 9 and Fig. 10 show that dynamic stress intensity factor and the dynamic energy release rate generally increased with increased crack velocity as assumed by Kanninen in one of his analyses [*20*]. The wider scatter in these values, however, makes it impossible to fit a unique functional relation between the dynamic stress intensity factor (or dynamic energy release rate) and the crack velocity.

For the two specimens where crack arrest occurred (see Figs. 6 and 7),

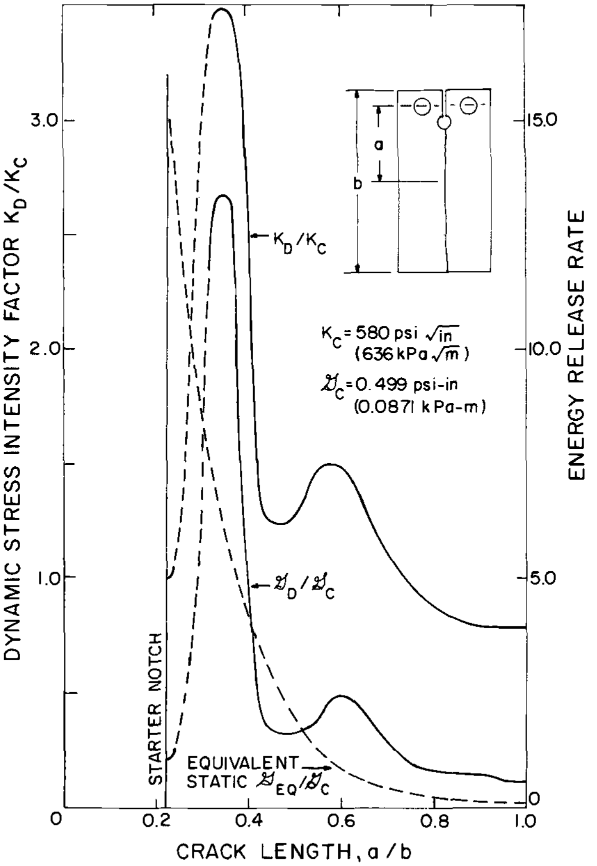

FIG. 9—*Dynamic stress intensity factors and dynamic energy release rates in wedge-loaded DCB specimen; initial notch tip radius, 1/8 in.; Specimen 26B-022474.*

the dynamic stress intensity factors and dynamic energy release rates decrease below their corresponding static critical values and at arrest are approximately 50 to 70 and 30 to 50 percent of their static critical values. Again, these results are in qualitative agreement with those shown in Table 1 of Ref *20*. Following the trend in previous investigations [*12, 21*], the arrest values are expected to vary with test specimens. Such variation indicates that the dynamic stress intensity factor and dynamic energy release rate at crack arrest are not material properties but are problem-dependent quantities.

It is interesting to note in Table 1 that the averaged dynamic energy release rate, $\mathcal{G}_D|_{avg}$, in the two specimens, 1S-031273 and 31S-030274, is

TABLE 1—*Energy release rates.*

Specimen	1S-031273	31S-030274	21B-020874	26B022474
$\mathcal{G}_D\|_{avg}/\mathcal{G}_c$	1.08	1.08	2.36	2.78
$\mathcal{G}_{EQ}\|_t = 0/\mathcal{G}_c$	3.00	4.72	12.6	14.9

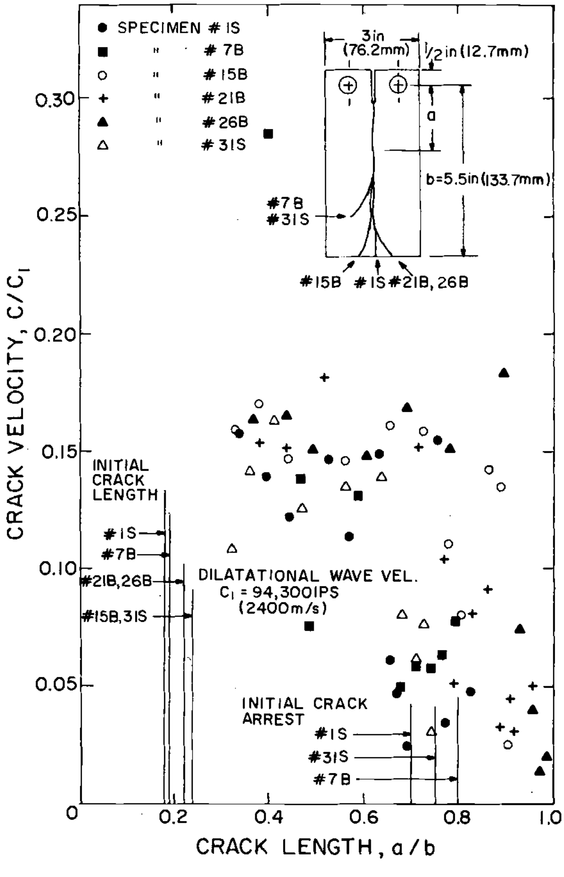

FIG. 10—*Crack velocities in wedge-loaded DCB specimen.*

approximately equal to the critical strain energy release rate. This same conclusion was reached when reviewing the authors' many experiments in Ref *21*. Since most of the total strain energy released during crack propagation is absorbed by the running crack tip and little is lost to the surroundings in this wedge-loaded DCB specimen, such total energy balance appears reasonable at first. This empirical finding could, however, indicate that the dynamic energy release rate determined by the procedure described in this paper is not exactly equal to the dynamic resistance of the material during crack propagation, but should be regarded as the energy flux through the small region bordered by the isochromatic loop surrounding the moving crack tip.

For the two specimens with slotted cracks, $\mathcal{G}_{EQ}|_{t=0} = 4\mathcal{G}_c$ and is comparable to one of the specimen with $K_{IQ} = 2K_{Ic}$ which was analyzed by the Battelle group [20]. Their predicted crack velocity of 20 percent of the compression wave velocity is in approximate agreement with the crack velocities observed in the two specimens of 1S-031273 and 31S-030274. Their predicted point of crack arrest is at $a = 0.6b$ which again is in approximate agreement with the experimental results. The estimated dynamic stress intensity factor at arrest would be about half of the critical stress intensity factor which again is in approximate agreement with the experimental results. It should be noted that the dynamic stress intensity factor varies considerably irrespective of the crack velocity in this investigation and thus differs considerably with the postulated dynamic fracture criterion by the Battelle group. Nevertheless, the observable physical data in this investigation and Battelle's analysis are in essential agreement irrespective of the apparent differences in the dynamic fracture criterion.

Acknowledgments

The results obtained in this investigation were obtained in a research contract funded by the Office of Naval Research (ONR) under Contract No. N00014-67-0103-0040. The authors wish to acknowledge the support and encouragement by N. R. Perrone and H. Basdegas of ONR. Particular gratitude is due to G. T. Hahn, M. F. Kanninen, A. R. Rosenfield, and R. G. Hoagland for their many hours spent in discussing the wedge-loaded DCB specimens with the senior author and offering many helpful suggestions in fracture dynamics.

References

[1] Hahn, G. T., Hoagland, R. G., Kanninen, M. F., and Rosenfield, A. F. in *Dynamic Crack Propagation*, G. C. Sih, Ed., Noordhoff International Publishing, 1973, pp. 649–662.

[2] Hahn, G. T., Hoagland, R. G., Kanninen, M. F., and Rosenfield, A. F., "The Characterization of Fast Fracture and Arrest in Structural Materials," *Proceedings*, Third International Conference on Fracture, 1973.

[3] Hahn, G. T., Hoagland, R. G., Kanninen, M. F., Rosenfield, A. R., and Sejnoka, R., "Fast Fracture Resistance and Crack Arrest in Structural Steel, " SSC-242, Project SR-201, U. S. Coast Guard, 1973.

[4] Hahn, G. T., Hoagland, R. G., Kanninen, M. F., and Rosenfield, A. R., in this publication.

[5] Kanninen, M. F., Rosenfield, A. R., and Hoagland, R. G. in *Deformation and*

Fracture of High Polymers, H. H. Kausch, J. A. Hassel, and R. I. Jaffee, Eds., Plenum Press, New York, 1973, pp. 471–486.

[*6*] Kanninen, M. F., *International Journal of Fracture,* Vol. 10, No. 3, Sept. 1974, pp. 415–431.

[*7*] Kanninen, M. F., "An Analysis of Dynamic Crack Propagation and Arrest for a Material Having a Crack Speed Dependent Fracture Toughness," *Proceedings,* Conference on the Prospects of Fracture Mechanics, J. C. Sih, H. C. van Elst, and D. Broek, Eds., Noordhoff International Publishing, 1974.

[*8*] Bradley, W. B. and Kobayashi, A. S., *Experimental Mechanics,* Vol. 10, No. 3, March 1970, pp. 106–113.

[*9*] Bradley, W. B. and Kobayashi, A. S., *Engineering Fracture Mechanics,* Vol. 3, 1971, pp. 317–332.

[*10*] Wade, B. G., "A Photoelastic and Numerical Study on Fracture Dynamics of Stressed Panels," Ph.D. thesis, University of Washington, Seattle, Wash., Dec. 1973.

[*11*] Irwin, G. R., Discussion and Author's Closure of the Paper, "The Dynamic Stress Distribution Surrounding a Running Crack—A Photoelastic Analysis," *Proceedings,* Society for Experimental Stress Analysis, Vol. XVI, No. 1, 1958, pp. 91–96.

[*12*] Kobayashi, A. S., Wade, B. G., and Bradley, W. B. in *Deformation and Fracture of High Polymers,* H. H. Kausch, J. A. Hassell, and R. I. Jaffee, Eds., Plenum Press, New York, 1973, pp. 487–500.

[*13*] Chen, E. P. and Sih, G. C., *International Journal of Solids and Fracture,* Vol. 9, 1973, pp. 897–919.

[*14*] Sih, G. C. in *Inelastic Behavior of Solids,* M. F. Kanninen, W. F. Adler, A. R. Rosenfield, and R. I. Jaffee, Eds., McGraw-Hill, New York, 1970, pp. 608–639.

[*15*] Kobayashi, A. S. and Wade, B. G. in *Dynamic Crack Propagation,* G. C. Sih, Ed., Noordhoff International Publishing, 1973, pp. 663–677.

[*16*] Freund, L. B., *Journal of the Mechanics and Physics of Solids,* Vol. 20, 1972, pp. 129–140.

[*17*] Freund, L. B., *Journal of the Mechanics and Physics of Solids,* Vol. 20, 1972, pp. 141–152.

[*18*] Freund, L. B., *Journal of the Mechanics and Physics of Solids,* Vol. 21, 1973, pp. 47–61.

[*19*] Wood, H. A. and Kirby, W. T. in *Fracture Mechanics of Aircraft Structures,* H. Liebowitz, Ed., AGARDograph No. 176., Jan. 1974, pp. 3–13.

[*20*] Hoagland, R. G., Rosenfield, A. R., Kanninen, M. F., and Hahn, G. T., "Rectangular-DCB Specimens for Fast Fracture and Crack Arrest Measurements," Report Under Task Agreement No. 62 under Contract No. 2-7405-eng-92, Battelle Columbus Laboratories, Dec. 1974.

[*21*] Kobayashi, A. S., "Criteria for Crack Branching and Crack Arrest," *Progress in Experimental Mechanics—The Durelli Aniversary Volume,* V. J. Parks, Ed., Catholic University of America, 1975.

K. E. Stahlkopf,[1] *R. E. Smith,*[1] *W. L. Server,*[2] *and*
R. A. Wullaert[2]

Preliminary Results of a Program for Developing Fracture Toughness Data on Ferritic Nuclear Pressure Vessel Steels

---

REFERENCE: Stahlkopf, K. E., Smith, R. E., Server, W. L., and Wullaert, R. A., "**Preliminary Results of a Program for Developing Fracture Toughness Data on Ferritic Nuclear Pressure Vessel Steels,**" *Cracks and Fracture, ASTM STP 601,* American Society for Testing and Materials, 1976, pp. 291–311.

ABSTRACT: A comprehensive fracture toughness testing program focused principally at providing statistical assurance of the American Society of Mechanical Engineers (ASME) K_{IR} fracture toughness design curve is presently underway. While the overall program represents testing of 50 heats of typical production materials, including A533-B, Class 1 plate; A508, Class 2 forging; A540-B-23 and B-24, Class 3 bolting material; submerged arc, manual metal arc, and shielded metal arc weldments; and associated heat-affected zone material, the data presented herein represent the initial results of an interlaboratory round robin program and the first seven heats of A533-B Class 1 plate tested in the program. Mechanical tests performed include tension, drop weight-nil ductility transition (NDT) temperature, Charpy V-notch, instrumented precracked Charpy, static and dynamic compact fracture, and dynamic three-point bend. Of these tests, instrumented precracked Charpy, dynamic three-point bend, and dynamic compact fracture are nonstandard procedures. Methodology for performance of these nonstandard tests is outlined. The fracture mechanics tests were performed on specimens up to 1-in. thick (4-in.-thick specimens will be tested later). Loading rates ranging from quasistatic to stress intensity rates ($\dot{K}$) of 5×10^5 ksi $\sqrt{\text{in.}}$/s were applied.

Testing and data analysis procedures for dynamic fracture toughness testing were developed. Special emphasis was placed on the assurance of adequate electronic response in conjunction with control of the time to fracture for ensuring reliable test results. Elastic-plastic data analysis techniques were applied to test results and included both the J-integral and the equivalent energy approaches. Maximum load was used in the J-integral and equivalent energy analysis for lack of an experimental technique for determining crack initiation over a range of loading rates. It is recognized that this approach can lead to nonconservative toughness

---

[1] Program manager and project manager, respectively, Electric Power Research Institute, Palo Alto, Calif. 94303.

[2] Vice president and president, respectively, Fracture Control Corporation, Goleta, Calif. 93017.

values when crack growth occurs prior to maximum load. However, for completeness elastic-plastic data analyzed using this criteria are included.

KEY WORDS: crack propagation, fractures (materials), pressure vessels, steels

In January 1971, the Pressure Vessel Research Committee (PVRC), at the request of the American Society of Mechanical Engineers (ASME) Boiler and Pressure Vessel Committee, formed a task group to review current knowledge and prepare recommendations on toughness requirements for ferritic materials in nuclear power plant components. The PVRC recommendations [*1*] [3] were presented to the ASME in August of the same year. The following January, the ASME Boiler and Pressure Vessel Committee approved revisions to the toughness requirements of Section III of the Code based on the PVRC recommendations. These revisions, which for the first time encompassed the K_{IR} concept, became part of the Code with the issuance of the Summer 1972 Addenda to Section III [*2*]. Although the K_{IR} curve was based upon all applicable data which were available, it became evident to the Atomic Energy Commission (AEC) (now Nuclear Regulatory Commission) and the majority of the technical community, that there was a definite need to obtain additional fracture toughness data to determine if the published K_{IR} curve represents the fracture toughness of production heats of ferritic nuclear pressure vessel steels.

In October 1972, the AEC, in a meeting with representatives of the Metal Properties Council (MPC), the PVRC, and industry, stated its belief that additional research was needed to demonstrate that toughness requirements for ferritic materials in nuclear power plant components, as specified in the Summer 1972 Addenda to Section III, were representative of actual production heats of materials used in reactor pressure vessel construction. A task group under the joint sponsorship of PVRC and MPC was formed in response to this meeting to define the required research. The Joint PVRC/MPC Task Group formulated a program which addressed these needs and recommended the program to the AEC and the Electric Power Research Institute (EPRI) in the summer of 1973 [*3*]. The EPRI modified and expanded the recommended program, and work was begun in March 1974.

The objectives of the modified program are threefold:

1. Measure the fracture toughness properties of 50 heats or weldments of reactor pressure vessel steel and bolting material including: A533-B, Class 1 plate; A508 Class 2 forging; A302-B modified plate; and A540 bolting material;
2. Evaluate the applicability of the use of the instrumented precracked Charpy test to measure meaningful fracture toughness data; and

---

[3] The italic numbers in brackets refer to the list of references appended to this paper.

3. Establish a data base of acoustic emission signatures for reactor pressure vessel steels and evaluate the effect of specimen thickness, temperature, microstructure, and crack surface lubrication on these signatures.

Under the program management of EPRI, five contractors were chosen. Effects Technology, Inc., Babcock & Wilcox, and Combustion Engineering were chosen to perform a coordinated fracture toughness measurement program with Effects Technology, Inc., additionally serving as a Program Office Coordinator. Naval Research Laboratory undertook an adjunct program of fracture toughness measurement utilizing their unique capability to test large three-point dynamic bend specimens. Acoustic Emission Technology was chosen to perform the acoustic emission portion of the program.

The fracture toughness measurements presented in this paper include the initial results of an interlaboratory test program and the first seven heats of A533-B, Class 1 plate tested. A final presentation of all data, including a statistical analysis, will be presented within a year.

Background

The analytical procedures (as given in the *ASME Boiler and Pressure Vessel Code*) to predict the behavior of postulated flaws in Class 1 components require some knowledge of the fracture toughness of the materials used to fabricate those components. Generating the required toughness properties for each heat of material is impractical because the type and number of required tests would result in substantial material requirements and prohibitive costs. Consequently, a reference curve approach is used. This approach utilizes an artificial toughness-temperature relationship which is adjusted along the temperature axis according to an index reference temperature (T-RT_{NDT}), where T is the temperature of interest and RT_{NDT} is the reference temperature. The drop weight-nil ductility transition (NDT) temperature and Charpy V-notch energy and lateral expansion values are used to determine the value of RT_{NDT} [2]. In concept, the RT_{NDT} is fixed by the NDT. Subsequently, a set of three Charpy V-notch specimens are tested at a temperature 60°F higher than the NDT in order to assure the upswing in toughness with temperature (that is, the toughness relationship assumed by the K_{IR} curve). Charpy values of 50 ft·lb impact energy absorbed and 35-mils lateral expansion are the criteria required to assure this condition. If the Charpy values equal or exceed these levels, then the NDT becomes the reference temperature. Should the measured Charpy values at NDT + 60°F be lower than required, then additional tests are performed at higher test temperatures until requirements are met. For these cases, the reference temperature becomes the temperature at which the Charpy 50/35 criteria (CV50/35) are assured minus 60°F. Thus, the reference temperature is the higher temperature of either the NDT or the $T_{CV50/85}$-60°F.

The reference K_{IR}-temperature curve, when properly indexed to the RT_{NDT}, is assumed to describe the fracture toughness properties of that heat of material. The reference curve, which applies to all ferritic materials having a minimum specified yield strength of 50 ksi or less, is construed to be a lower bounding function of all available measures of fracture toughness for such materials. It includes both ''static'' and ''dynamic'' fracture toughness and crack arrest data. Although a great deal of data were used to establish the K_{IR} curve, the data unfortunately represented a large amount of testing on only a few heats of material. Consequently, adequate heat-to-heat variability statistics were not available to provide a rational basis for establishing a statistically significant lower bound curve. Thus, graphical procedures were applied. The program described in this paper has been designed to provide these statistics. A variety of tests and testing procedures have been encompassed to include both standard and nonstandard procedures. Variabilities due to test procedures and interlaboratory differences are determined in order to form a sound basis for factoring heat-to-heat variability and to assist in evaluating results from nonstandard tests.

Materials and Test Matrix

Table 1 identifies the various materials studied in the overall program and also identifies the materials whose property measurements are de-

TABLE 1—*Summary of materials studied in EPRI fracture toughness program.*

Laboratory and Material	Heats
Babcock & Wilcox	
A508-2 forging	5
A508-2 submerged arc weldment	5
A508-2 manual metal arc weldment	5
A540 bolting	5
Combustion Engineering	
A533-B-1 plate	5
A533-B-1 submerged arc weldment	5
A533-B-1 manual metal arc weldment	5
Effects Technology, Inc.	
A533-B-1 plate [a]	9
A533-B-1 shielded metal arc weldment	4
A302-B plate	1
Naval Research Laboratory	
A533-B-1 plate	1
A508-2 forging	1
A302-B plate	1
All laboratories	
A533-B-1 plate (HSST 02) [a]	1

[a] Test results for these materials presented in this paper.

TABLE 2—*Minimum text matrix.*

Test	Minimum Tests/Heat
1. Tension (ASTM Method A-370)	6
2. Drop weight-NDT (ASTM Method E-208)	6
3. Charpy V-notch (ASTM Method E-23) (instrumented)	34 to 51
4. Static compact or three-point bend, 1 in. thickness (ASTM Method E 399)	4
5. Instrumented, precracked Charpy	17
6. Dynamic compact or three-point bend, 1 in. thickness	4
7. Dynamic 4-in. compact[a]	1

[a] Results of the dynamic 4-in. compact fracture tests remain to be analyzed and will be presented in a later paper.

scribed in this paper. Table 2 identifies the minimum test matrix performed on each heat of material. In many cases, the matrix has been extended to provide additional data. Testing was accomplished according to a scheme of test temperatures which have been referenced directly to the drop weight-NDT temperature. In this way, results of different heats can be evaluated with respect to the variability of results for a given portion of the K_{IR} curve.

It should be noted from the test matrix (Table 2) that toughness testing was accomplished at three different rates of loading. Quasistatic testing has been performed according to standard procedures developed for such tests (ASTM Test for Plane-Strain Fracture Toughness of Metallic Materials (E 399)). These tests were loaded at stress intensification rates $\leq$ 2.5 ksi $\sqrt{\text{in.}}$/s. Intermediate loading rates were obtained with the dynamic compact test (approximately 10^3 ksi $\sqrt{\text{in.}}$/s), and rapid loading rates were obtained with dynamic three-point bend tests, precracked Charpy and 1-in. bend (approximately 10^5 ksi $\sqrt{\text{in.}}$/s).

The development of a simple, yet reliable, fracture toughness test was considered an important part of the program. Potential uses include irradiation surveillance programs, materials evaluations, and qualification of pressure vessel materials. Because standard testing procedures were not available to perform the dynamic fracture tests, program procedures were established. These procedures will be discussed later. Where the test record indicated that the elastic assumption had been violated, an elastic-plastic analysis based upon maximum load was used. Both the "equivalent energy" concept and the one-specimen J-integral approximation have been applied. Four-in. dynamic compact tests were included as a check point in evaluating both dynamic procedures and size effects. Results of the 4-in. compact tests are not yet available for the material presented in this paper.

The other tests indicated in the minimum matrix (tension, drop weight, and Charpy V-notch) are standard tests and have been included for the following reasons. First, these properties were needed to fully characterize the behavior of the materials and represent those properties which are normally measured. Secondly, the data were needed to both index subsequent tests (drop weight) and to assist in evaluating the results of other tests. All Charpy V-notch tests were instrumented to provide background data on well-characterized heats for future studies and to determine dynamic yield strengths with which to evaluate the results of dynamic fracture tests. Thirdly, the statistical variation in the results of standard tests could be determined and used as a basis for evaluating variabilities associated with nonstandard tests. Although the testing variability of one test would not be expected to be identical to the variability of a different test, it was anticipated than an effective benchmark could be developed with which to evaluate the nonstandard testing procedures. Lastly, it was believed to be important to sort out material variabilities by more than one test, because different tests measure different properties, and the distribution in the measurement of one property may differ from that of another.

Testing and Data Analysis Procedures

Whenever possible, existing ASTM standards were used to perform the tests and analyze the data (see Table 2). New procedures for dynamic fracture toughness testing were drafted based on recent papers [*4,5*] the work of ASTM [*6*], PVRC/MPC [*7*], and International Institute of Welding (IIW) [*8*] working groups. Both standard and nonstandard test procedures, along with detailed data analysis techniques and specified test record reports, were provided by the Program Office to all program participants. This document [*9*] has been commonly referred to as the "EPRI procedures." Only the highlights of the nonstandard procedures (dynamic fracture toughness) will be discussed here to give the reader an understanding of the overall methodology. Details of the procedure development will be provided in a subsequent publication.

Test Procedures

Until recently [*10*], interpretation of the force-time record for dynamic fracture toughness tests, particularly impact tests, has not been a simple task, and much of the brittle fracture data generated before 1971 is suspect because of various ambiguities of the apparent force record with respect to that for independent measurements derived from the specimen [*8,11–13*]. Problems which clouded the understanding and acceptance of the instrumented impact test were related to inertia loading, frequency response, and actual time to fracture. These problems are now sufficiently understood [*4,5,14*] to specify reliable test procedures with which to generate meaningful values of dynamic fracture toughness K_{Id}.

The EPRI dynamic fracture toughness procedures cover the precracked

Charpy sample, the precracked three-point bend specimen, and the compact fracture specimen. These procedures are, in fact, modifications to existing standard methods and include: (*a*) increased loading rate for the ASTM Method E 399; (*b*) precracking the Charpy specimen and adding instrumentation for derivation of load records for the ASTM Method E 23; and (*c*) combining the above modifications of Methods E 399 and E 23 for use of drop tower techniques, using three-point bend specimens.

Although the requirements for instrumentation in dynamic testing are better understood for pendulum Charpy-type testing than for either drop tower or dynamic compact specimen testing, the procedures developed for this program have been applied to all three types of tests. Brief discussions of the salient features of the test procedures follow.

A test system used for dynamic testing must not only have adequate electronic frequency response, but the specific characteristics of the response must also be documented for each test. It is convenient to state these characteristics in terms of a limiting response time T_R [5] which is inversely proportional to the 0.9 dB frequency cutoff (10 percent attenuation) for an RC circuit. Because of the techniques employed for monitoring the effective load on the specimen, it is helpful to specify minimum, as well as maximum, T_R values for a given test. Specifying a minimum T_R is an electronic technique (filtering) for producing the equivalent of a least-squares curve fit to the oscillating tup signal.

The requirement for an acceptable load-time response can result in the need to decrease impact velocity from the usual full capacity of 17 ft/s (pendulum machines). This causes a decrease in the energy (E_0) available to break the specimen. Consequently, the toughness of the test specimen at the testing temperature needs to be considered. The reduction in tup velocity during the elastic or elastic-plastic loading of the sample should be minimized. This requirement may be expressed

$$E_0 \geq 3 W_I \tag{1}$$

and

$$E_0 > \Delta E_0 \tag{2}$$

where W_I is the energy required to initiate fracture and ΔE_0 is the total energy required to completely fracture the specimen.

Velocity specifications are stated in terms of an acceptable time to fracture (t_f) or an acceptable time to general yield (t_{GY}). This is illustrated in Fig. 1. An acceptable time to a given load measurement is referenced to the characteristic wave length of vibration for the specific specimen-tup interaction. That is, t_f or t_{GY} must be greater than or equal to some multiple of the period of this oscillation. It has been found [15] that the period of the oscillations can be predicted from

$$t = 1.68 \frac{S}{C_0} \left(\frac{W}{S}\right)^{1|2} (EBC_s)^{1|2} \tag{3}$$

where

S = support span,
W = beam width,
B = beam thickness,
C_s = specimen compliance,
E = Young's modulus, and
C_0 = speed of sound in the specimen.

For the Charpy test, t is calculated to be 31 μs. Preliminary experimental work has shown excellent agreement with this calculated value.

The impact of an unsupported specimen will create inertial oscillations in the contact load between tup and specimen. A time approximately equal to $2t$ is required for the load to be dissipated into the specimen. The appearance of the tup signal both in magnitude and frequency during the time $2t$ is nearly the same as that for a supported specimen. Thus, when the time to fracture, t_f, is less than $2t$, it is not possible to use the tup signal to determine fracture toughness. For the Charpy test a conservative specification for reliable load or t_f evaluation is

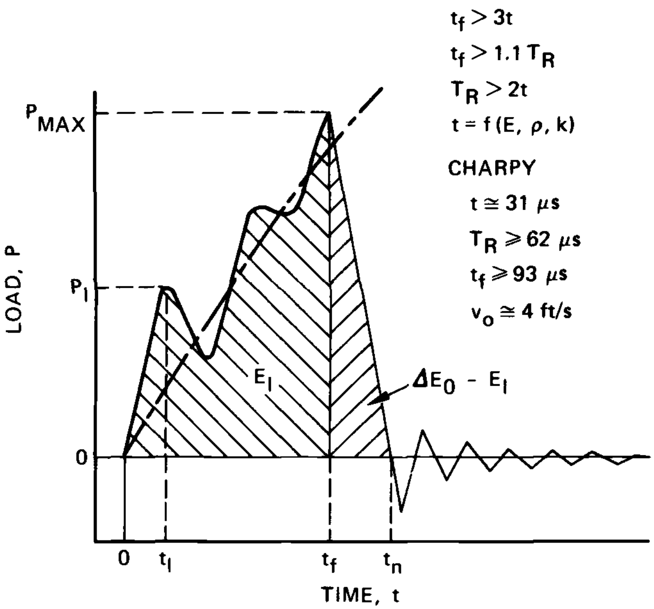

FIG. 1—*Test acceptance requirements for fracture before general yield in impact loaded bend specimen.*

$$t_f \geq 3t \quad (4)$$

which reduces to

$$t_f \geq 93 \ \mu s \quad (5)$$

if t is taken to be 31 μs for the Charpy case.

The potential problem of limited frequency response of the dynamic response system is avoided by specifying

$$t_f > 1.1 \ T_R \quad (6)$$

where T_R is as defined earlier. A minimum T_R can also be specified such that the amplitude of the oscillations is reduced electronically to make a minimal disparity between tup contact force load and the effective specimen load at midspan. For the bend test, it has been empirically found [15] that:

$$T_R > 2t \quad (7)$$

or for the Charpy specimen

$$T_R > 62 \ \mu s \quad (8)$$

Therefore Eq 6 requires that the signal is not over filtered, and Eq 7 dictates that the filtering is sufficient to electronically curve-fit the signal oscillations. Instrumented impact tests meeting the requirements represented by Eqs 1, 2, 4, 6, and 7 are believed to produce acceptable results. Complete evaluation of all program data should define more accurately the general applicability of these test requirements.

Data Analysis

Special data record forms [9] were designed to ensure that complete records for each individual test were maintained by all laboratories. In addition, daily proof checks were performed to ensure that reliable data were being obtained. In order to facilitate rapid data retrieval and because of the large number of tests, a computer data bank was established with which to store processed data. The specific data sets stored for each test are listed in Table 3.

The equivalent energy and J-integral calculations were used for evaluating instrumented impact data showing post-general yield behavior. These calculations are based upon maximum load and also take into account "machine-interaction" compliance contributions. The static and dynamic compact specimen tests directly measure load-line displacement so that the machine compliance is not used in toughness calculations.

Since an experimental technique was not available for detecting crack initiation in the dynamic tests, it was assumed that the onset of cracking occurred at maximum load. Thus the energy to maximum load was used to calculate equivalent energy (K_c^*, K_d^*) and J-integral (K_{Jc}, K_{Jd}) fracture

TABLE 3—*Data order within the data bank.*

		Data Order			
Column 1	Column 2	Column 3	Column 4	Column 5	Column 6
T ≡ *Tensile*					
Temperature, °F	σ_{ys}, ksi	σ_{ts}, ksi	uniform elongation, %	total elongation, %	reduction of area, %
IV ≡ *Instrumented Standard Charpy*					
Temperature, °F	dial energy, ft•lb	lateral expansion, mils	fracture appearance, percent shear	blank	blank
IP ≡ *Instrumented Precracked Charpy*					
Temperature, °F	K_{Id}, ksi $\sqrt{\text{in.}}$	K^*_d, ksi $\sqrt{\text{in.}}$	K_{Jd}, ksi $\sqrt{\text{in.}}$	W/A, in. lb/in.^{2}	$\dot{K}$, ksi $\sqrt{\text{in.}}$/s
D ≡ *Drop Weight-NDT*					
Temperature, °F	break ≡1 no break ≡2 no test ≡3				
C1S, C1D, ≡ *1T Static and Dynamic Compact Tests, 1T Dynamic Bend Tests, and 2T, 3T, and 4T Dynamic Compact Tests* B1D, C2D, C3D, C4D					
Temperature, °F	$K_{Ic,d}$, ksi $\sqrt{\text{in.}}$	$K^*_{c,d}$, ksi$\sqrt{\text{in.}}$	$K_{Jc,d}$,ksi$\sqrt{\text{in.}}$	blank	$\dot{K}$, ksi$\sqrt{\text{in.}}$/s

NOTE—

σ_{ys}=static 0.2 percent offset yield strength,

σ_{ts}=static tensile strength,

K_{Ic}, K_{Id}=static or dynamic plane-strain fracture toughness; for impact tests, fractures are before general yield, and for static and dynamic compact tests, fractures meet the relationship $P_{max}/P_Q \leqslant 1.10$,

K_{Jc}, K_{Jd}=static or dynamic toughness estimated using the J-integral approach at maximum load for fractures past general yielding or when $P_{max}/P_Q > 1.10$,

K_c*, K_d*=static or dynamic toughness estimated using the equivalent energy approach at maximum load for fractures past general yielding or when $P_{max}/P_Q > 1.10$,

W/A=dial impact energy per unit ligament area, and

$\dot{K}$=the stress intensity rate; the approximate toughness divided by the time to maximum load.

toughness. If crack initiation occurs before maximum load, the elastic-plastic values generated in this program will be higher than normal K_{Ic} and K_{Id} values because of different measurement points. Although the use of energy to maximum load was an acceptable technique for measuring elastic-plastic toughness (equivalent energy) at the start of this program, the authors recognize the need for future work in this area. The elastic-plastic toughness values based on maximum load are included in this paper for completeness, even though they may not represent the most conservative values.

Interlaboratory Program

As previously mentioned, the basic test matrix embraced several test techniques which have not been standardized. In order to evaluate the experimental procedures and to determine the statistical interlaboratory variability, a control material round robin testing format was used [*16*]. This program involved a double test matrix for each testing laboratory (see Table 2) on a pedigreed pressure vessel material—HSST Plate 02. A statistical analysis of the data was conducted. Only the analysis of the prescribed Charpy tests will be described. A detailed analysis of the full test matrix is in progress [*16*].

Instrumented Precracked Charpy Results

At first sight, an attractive approach to the task of data reduction was through the use of polynomial and multiple regression procedures. The data were therefore analyzed using polynomial functions of the second, third, and fourth order. Although these were later augmented to include other test variables, the approaches proved unsuccessful. Higher order fits often produced useless curves, because even though scatter about the curve was minimized, no physical meaning could be extracted from the curves.

It was concluded that some consideration of the physical phenomena must be incorporated into a useful curve-fitting procedure. In this way the procedure would be capable of providing a satisfactory engineering interpretation to the test results.

Several approaches were attempted, and an approach [*17*] was selected in which the test response (Y) was transformed prior to curve fitting procedures. The data were assumed to be represented by a curve of the form

$$Y = A + B \tanh \left(\frac{T - T_0}{C} \right) \tag{9}$$

Thus, the variables in the regression, A, B, T_0, and C have physical significance as follows:

lower shelf = $A - B$,

upper shelf $= A + B$,
transition temperature $= T_0$ (the midpoint of the transition temperature range), and
slope at $T_0 = B/c$.

The mathematical techniques required to fit this relationship are somewhat novel, and are described in detail by Oldfield [*17*].

As a preliminary to the main analytical tasks, regression curves with 2σ and 3σ limits were fitted both to the dynamic toughness data meeting the acceptance criteria as defined in the EPRI procedures, and to the whole of the data, including test results not meeting these criteria. The EPRI acceptance criteria are listed in Table 4. The combined results are shown graphically in Fig. 2. Unacceptable tests have been identified by an "X." The error code appropriate to each unacceptable test result is flagged with the appropriate code number (Table 4). (Acceptable tests are identified by ▣). There were negligible differences observed between the curve fit parameters determined independently for the data with and without unacceptable results. Thus, the unacceptable data did not, overall, alter the shape of the curve. From a statistical standpoint, no difference exists between these two cases. It should be noted that the EPRI acceptance criteria were primarily derived from standards concerned with elastic fracture, and thus they may not be pertinent to the elastic-plastic data (as Fig. 2 appears to indicate). Hopefully, acceptance criteria for elastic-plastic fracture data will be developed by ASTM in the near future.

Preliminary Results on A533-B-1 Steel

The statistical approach used to analyze the control material was also applied to the first seven heats of A533-B-1 steel tested in the overall program. It is important to emphasize at this point that the primary purpose

TABLE 4—*EPRI acceptance criteria.*

Data Bank Code	Acceptance Criteria	Source or Problem Avoided
0	acceptable	. . .
1	thickness criteria not met (only when $P_{max}/P_Q \leq 1.10$)	ASTM Method E 399-74 ($K_Q \neq K_{Ic}$)[a]
2	crack too long ($a/w > 0.55$)	ASTM Method E 399-74
3	crack too short ($a/w < 0.45$)	ASTM Method E 399-74
4	crack skewed	ASTM Method E 399-74
5	K_f(max) over last 2.5 percent too high	ASTM Method E 399-74
6	t_f, $t_{GY} < 3t$, 1.1 T_R (Eqs 4 and 6)	inertia, frequency response
7	$3W_I > E_0$ (Eq 1)	velocity change
8	material condition questionable	. . .
9	anomalous result for unknown reasons	. . .

[a] K_Q is therefore identified as a K_{Ic} with an error code 1.

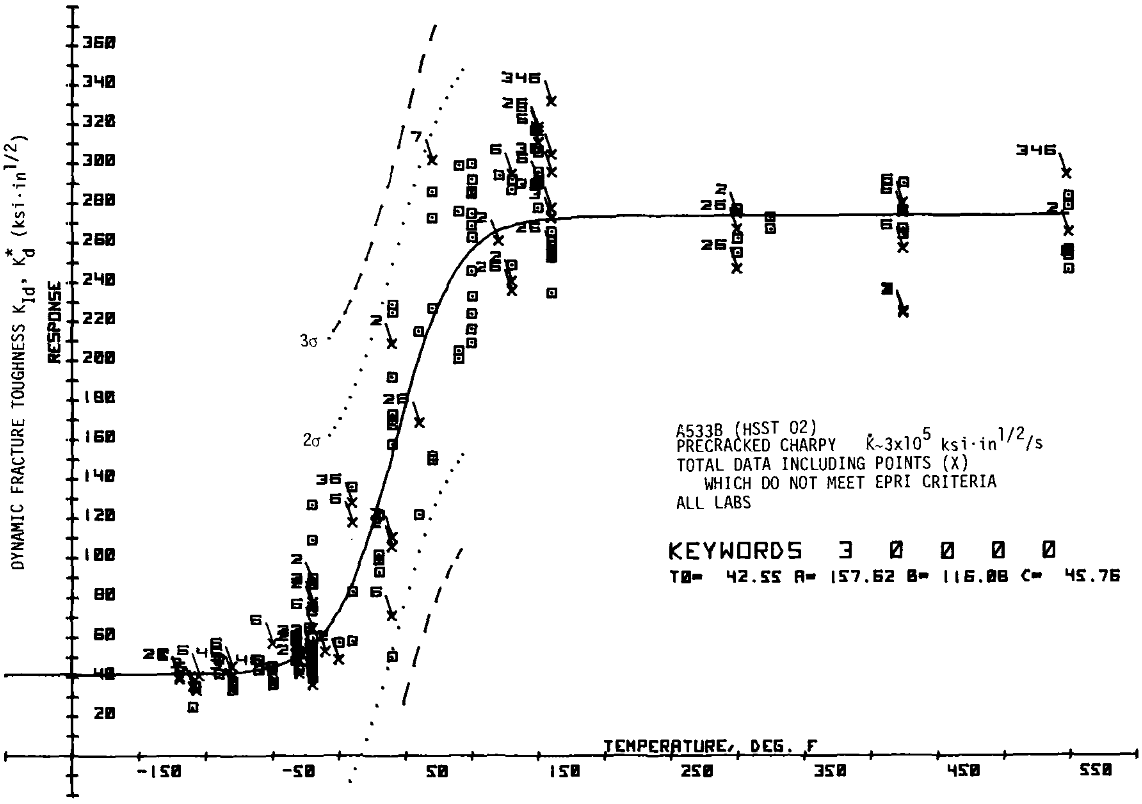

FIG. 2—*Summary of total precracked Charpy dynamic fracture toughness results obtained by the interlaboratory participants.*

of the statistical analysis is to help evaluate all 50 heats in this program and to determine the heat-to-heat variations in mechanical properties. The data presented herein are provided to allow the reader to evaluate the methodology used in testing and data analysis for the overall program. A brief preview of the curve fitting results and statistical analysis on the toughness of heats A thru G (tested at Effects Technology, Inc. (ETI) is presented here.

Charpy V-Notch Tests

Standard Charpy V-notch tests were performed over the temperature range of −150 to 550°F for both the transverse and longitudinal orientations. The relevant data stored in the data bank are dial impact energy, lateral expansion, and percent shear.

All of the impact energy data were fitted using the tanh model described in the last section. Typical Charpy V-notch energy results are shown in Fig. 3 (ETI Heat D). The 2σ and 3σ confidence limits have been drawn for the transition temperature region ($T_0 \pm 50°F$). Similar results (not shown) were obtained for both lateral expansion and percent shear.

Note that in Fig. 3 the temperature corresponding to $RT_{NDT} + 60°F$ has been marked in relation to the 50 ft·lb level. In most cases, the impact energy governed the RT_{NDT} fix as is common for most A533-B-1 steels. Hopefully, the statistical analysis and the use of the tanh fit parameters will yield insight into the use and meaning of RT_{NDT}.

Fracture Toughness Tests

Precracked Charpy tests were performed in accordance with the EPRI procedures [*9*] over the temperature range of NDT-90 to 550°F. The specimens were machined from the transverse orientation except for Heat D which was longitudinal. The fracture mechanics tests (including the precracked Charpy) are judged to be acceptable or unacceptable after post-test analysis. All of the data contained in the data bank have been coded with regard to acceptance criteria, and these codes are carried through to all graphs which contain data that do not meet the acceptance criteria. It is important to emphasize that at the end of the program, after 50 heats are analyzed, it may be evident that acceptance criteria should be changed. Thus, some of the unacceptable tests may become acceptable, or vice versa. The data developed with the precracked Charpy test which have been stored in the data bank are the dynamic plane-strain fracture toughness K_{Id} (fracture before general yield), equivalent energy toughness K_d^* and J-integral toughness K_{Jd} (fractures after general yield and based upon maximum load), W/A, and $\dot{K}$.

The tanh curve fitting technique described earlier was used to analyze both the precracked Charpy W/A and fracture toughness results. Figure 4

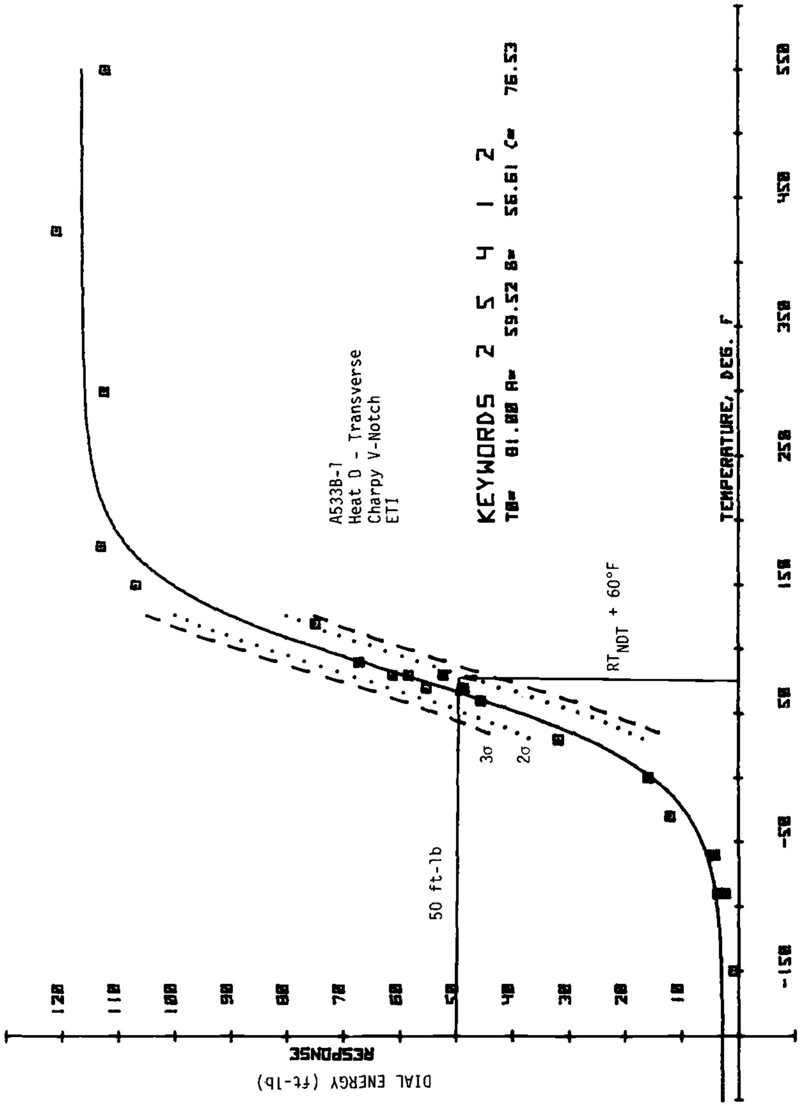

FIG. 3—*Charpy impact energy for ETI Heat D (transverse).*

shows the *W/A* data for ETI Heat B. Note that three tests are flagged with a number 2 indicating that *a/w* for the specimen was greater than 0.55. Also shown in Fig. 4 is the drop weight-NDT temperature and the two extrapolated lines from the lower shelf and the transition region; the intersection of these two lines usually gives a temperature very near the NDT as observed by Hartbower [*18*]. Since K_{Id} cannot be measured over the whole temperature range, either K_{Jd} or K_d^* was selected for the analysis, as appropriate. Since K_d^* and K_{Jd} values are almost identical, the K_{Jd} data were not plotted. Figure 5 includes all of the precracked Charpy toughness data from ETI Heats A thru G referenced to the RT_{NDT} of each heat. A comparison with the K_{IR} curve in the same figure indicates that the toughness values dip below the K_{IR} curve only at the low temperature end (below $T\text{-}RT_{NDT}$ = 20°F.).

The 1-in. static compact specimens and 1-in. dynamic bend specimens were tested in the temperature range of −150°F to NDT +120°F. As before, all specimens were in the transverse orientation except for Heat D. The temperature range (that is, no points on the upper shelf) and the small number of tests per heat make the tanh model more difficult to apply, but with appropriate programming, the data can be fit with the tanh model. Figure 6 shows the tanh regression for the 1-in. static compact results when several heats are analyzed together.

Combining all of the fracture toughness values for all seven heats of A533-B-1 steel gives the tanh regression curve shown in Fig. 7. For the same thickness specimen, it was observed that the dynamic toughness was lower than the static, as would be expected. Also, all of the data fall above the K_{IR} curve except at very low temperatures. The data indicate that the K_{IR} curve predicts conservative toughness values. The data represented in Fig. 7 includes only seven of the more than 50 heats of steel to be analyzed in this program.

Conclusion

The purpose of this paper has been to acquaint the reader with the overall test program and briefly present some of the nonstandard test techniques and data analysis methods which were used. Because of the complexity and size of the overall program, final results will not be available for some time. Final conclusions should not be drawn until a complete analysis of all data has been made.

References

[*1*] "PVRC Recommendation on Toughness Requirements for Ferritic Materials," Welding Research Council Bulletin 175, Aug. 1972.

[2] "Nuclear Power Plant Components," *ASME Boiler and Pressure Vessel Code, Section III,* Summer 1972 Addenda, American Society of Mechanical Engineers, June 1972.

[3] "PVRC-MPC Proposed Initial Program on Fracture Toughness Properties of Nuclear Components' Material," Report to the Atomic Energy Commission, Aug. 1973.

[4] Saxton, H. J., Ireland, D. R. and Server, W. L. in *Instrumented Impact Testing, ASTM STP 563*, American Society for Testing and Materials, Oct. 1974, pp. 59–73.

[5] Ireland, D. R. in *Instrumented Impact Testing, ASTM STP 563*, American Society for Testing and Materials, Oct. 1974, pp. 1–29.

[6] ASTM Task Group E24.03.03 on Precracked Charpy Standardization, C. E. Hartbower, Chairman, 1974.

[7] PVRC/MPC, Working Group on Instrumented Precracked Charpy Test, C. Buchalet, Chairman, Task Group on Fracture Toughness Properties for Nuclear Components, 1974.

[8] Buys, E. C. J. and Cowan, A. "Interpretation of the Instrumented Impact Test," Document X-458-68, International Institute of Welding, July 1968.

[9] Ireland, D. R., Server, W. L. and Wullaert, R. A., "Procedures for Testing and Data Analysis," ETI Technical Report 75-43, Effects Technology, Inc., Oct. 1975.

[10] *Instrumented Impact Testing, ASTM STP 563*, American Society for Testing and Materials, 1973.

[11] *Impact Testing of Metals, ASTM STP 466*, American Society for Testing and Materials, 1969.

[12] Turner, C. E., Kennish, P., Culver, L. E. and Radon, J. C. "A Study of the Mechanics of Notched-Bar Impact Tests," Mechanical Engineering Department, Imperial College, London, June 1970.

[13] Nash, G. E., "An Analysis of the Forces and Bending Moments Generated During the NRL Dynamic Tear Test,"Report 6864, Naval Research Laboratory, Jan. 1969.

[14] Hoover, W. R. in *Instrumented Impact Testing, ASTM STP 563*, American Society for Testing and Materials, Oct. 1974, pp. 203–214.

[15] Ireland, D. R. "Comments on EPRI Instrumented Impact Test Procedures," ETI Technical Report 75-37, Effects Technology, Inc., May 1975.

[16] Oldfield, W., Wullaert, R. A., Server, W. L., and Wilshaw, T. R. "Fracture Toughness Data for Ferritic Nuclear Pressure Vessel Materials; Task A—Program Office, Control Material Round Robin Program," ETI Technical Report 75–34R, Effects Technology, Inc., July 1975.

[17] Oldfield, W., *ASTM Standardization News*, Vol. 3, No. 11, Nov. 1975.

[18] Orner, G. M. and Hartbower, C. E. *The Welding Journal*, Vol. 40, No. 9, Oct. 1961, p. 459-S.

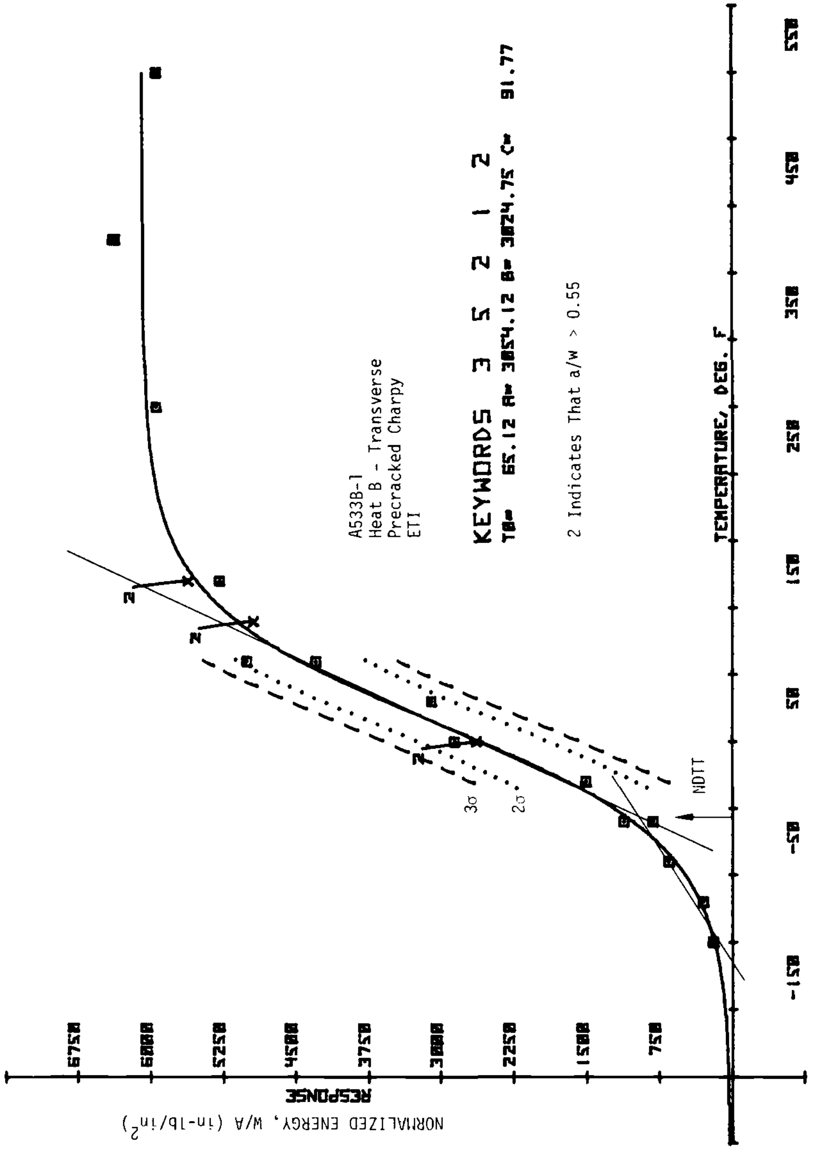

FIG. 4—*Precracked Charpy normalized energy results for Heat B.*

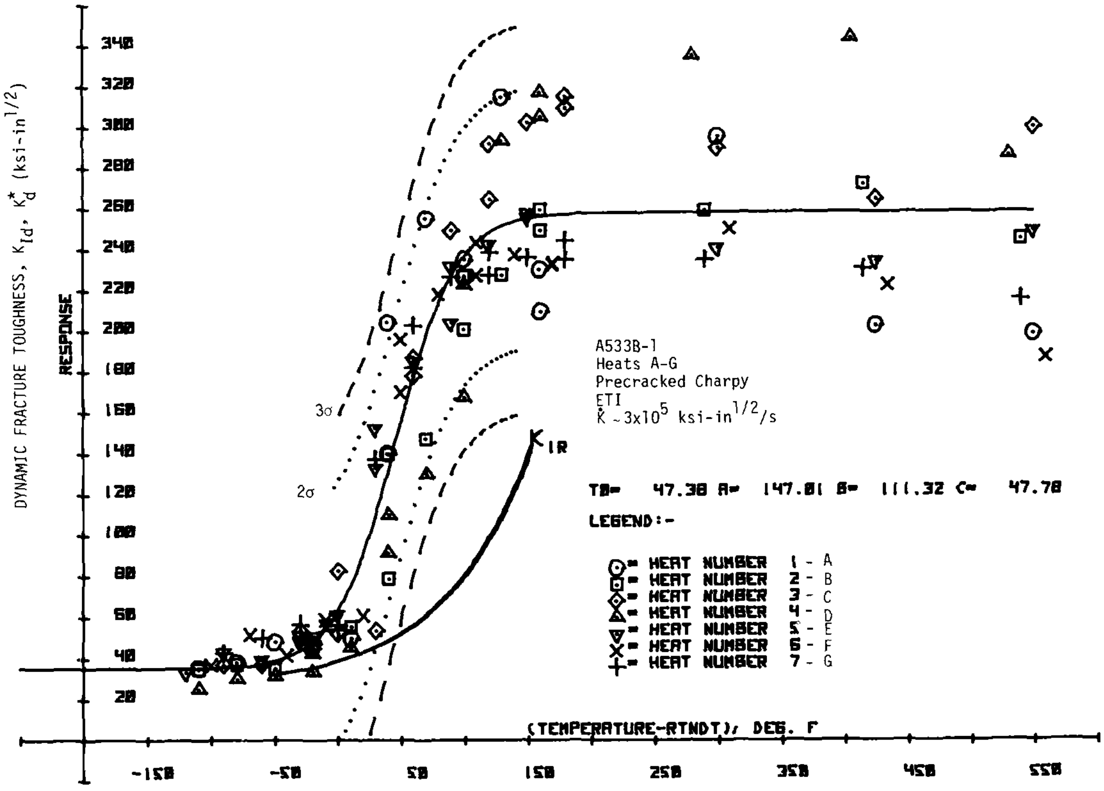

FIG. 5—*Total precracked Charpy dynamic fracture toughness results for ETI Heats A thru G.*

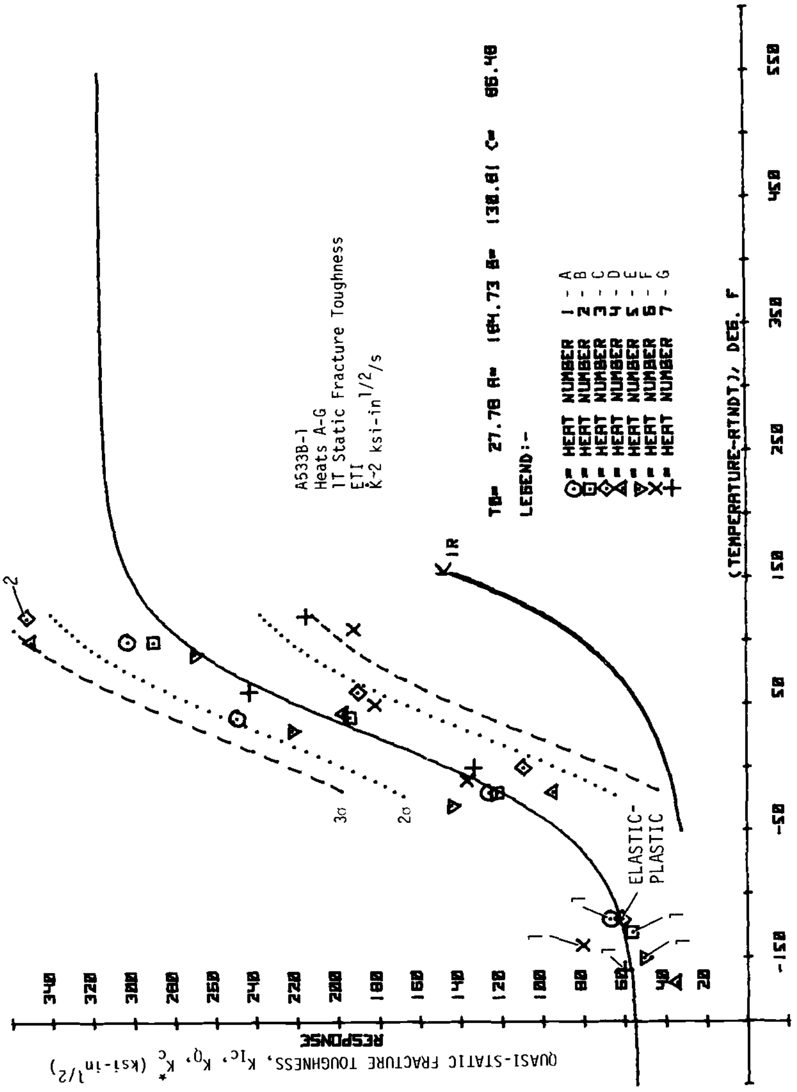

FIG. 6—*Total static fracture toughness results for ETI Heats A thru G.*

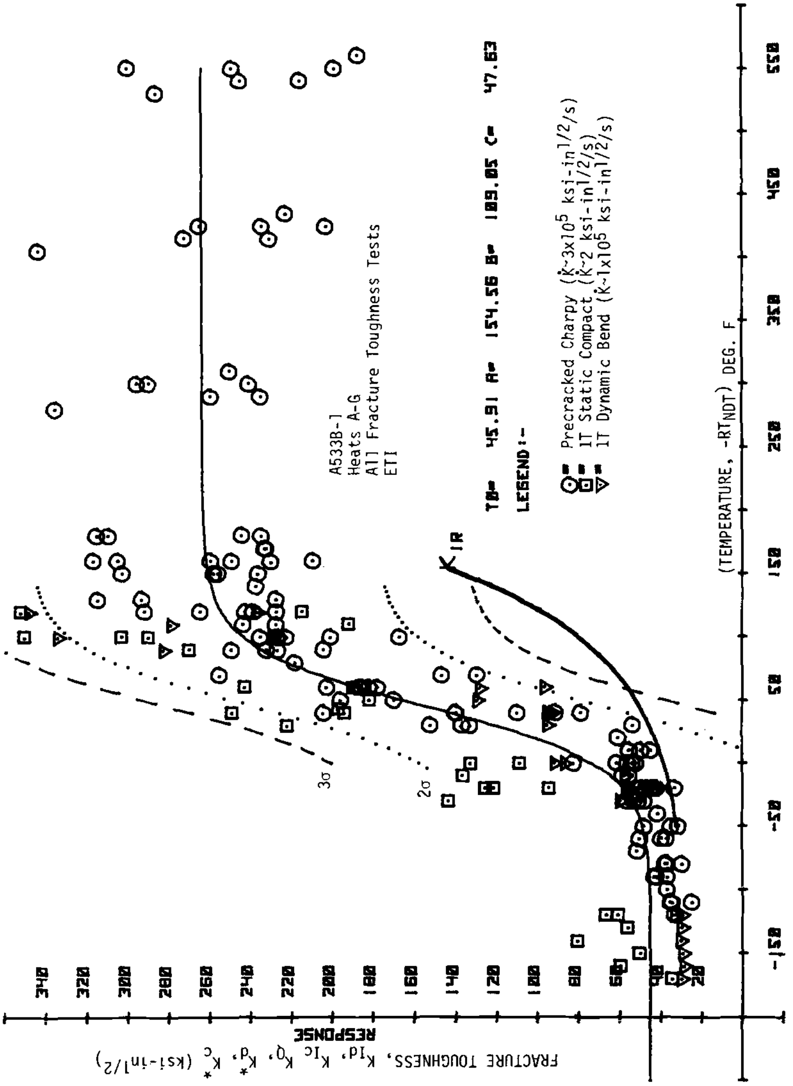

FIG. 7—*Fracture toughness results from all toughness tests on ETI Heats A thru G.*

J. H. Underwood [1]

J_{Ic} Test Results From Two Steels

REFERENCE: Underwood, J. H., "**J_{Ic} Test Results From Two Steels,**" *Cracks and Fracture, ASTM STP 601,* American Society for Testing and Materials, 1976, pp. 312–329.

ABSTRACT: Fracture toughness tests were performed with 10 by 20-mm, deeply notched bend specimens of a mild steel and a nickel-chromium-molybdenum steel. Using the recently proposed J-integral test method, critical values of the energy line integral for Mode I crack growth, J_{Ic}, were determined for the two materials. The J_{Ic} results were discussed in relation to various specimen geometry criteria and critical crack growth criteria which have been proposed for a standardized J_{Ic} test procedure. The J_{Ic} results from the nickel-chromium-molybdenum steel are found to be in excellent agreement with the known K_{Ic} value when the elastic deflection corresponding to the uncracked specimen is taken into account.

The J_{Ic} results from both steels are shown to be closely approximated by a one-specimen J_{Ic} test procedure, which is described and suggested for use as a fracture toughness screening test.

An analysis is presented of the error which arises in J_{Ic} determination when the effect of uncracked deflection in bend specimens is ignored. The error can be significant for materials with large values of yield strength relative to fracture toughness, even for deeply cracked specimens.

KEY WORDS: crack propagation, fracture properties, tests, compliance, steels

Nomenclature

A	Total area under P-δ curve
A'	Corrected area under P-δ curve; $A' = A - A_{\text{no crack}}$
A_{Ic}	Total area under P-δ curve at J_{Ic}
$A_{\text{no crack}}$	Area under P-δ curve due to uncracked deflection
a	Crack length
Δa	Crack growth in a J_{Ic} test
Δa_c	Critical crack growth at J_{Ic}
B	Specimen thickness
b	Minimum remaining ligament length
C	Compliance; calculated from K calibration
C_m	Compliance; measured from P-δ curve
D	Moment arm in four-point loading

---

[1] U. S. Army fellow, National Engineering Laboratory, East Kilbride, Scotland.

E	Elastic modulus
f	P_f/P_ℓ
J_f	Approximation for energy line integral
J_{Ic}	Critical value of energy line integral for Mode I crack growth
K_{Ic}	Critical value of K for plane strain Mode I crack growth
L	Moment arm in three-point bending
ℓ	Limit load constant for bending
P_f	Approximation for maximum load on P-δ curve
P_ℓ	Limit load
P_{max}	Maximum load on P-δ curve
P_u	Load at point of unloading on P-δ curve
W	Specimen depth
Y	$KBb^{3/2}/PW$; from K calibration
δ	Load-point deflection
δ_u	δ at point of unloading on P-δ curve
ν	Poisson's ratio
σ_F	Flow stress; $(\sigma_y + \sigma_u)/2$
σ_u	Ultimate stress
σ_{ys}	Yield stress

Introduction and Objective

The test procedure for determining plane strain fracture toughness, K_{Ic}, is well accepted and documented [*1*] [2] (and ASTM Test for Plane-Strain Fracture Toughness of Metallic Material (E 399-74)). The main limitation of the procedure is the minimum size of the specimen that can be tested. The size requirement given in the K_{Ic} test procedures [*1*] (and ASTM Method E 399-74) is also suitable for discussion and is the following equation

$$a,\ b,\ B \geqslant 2.5\ K_{Ic}^2\ /\sigma_{ys}^2 \qquad (1)$$

Figure 1 shows the dimensions a, b, and B for a bend specimen, a common fracture mechanics specimen, and the specimen of interest here. This size requirement, in effect, limits the size of the crack-tip plastic zone relative to the specimen dimensions, since the plastic zone is proportional to the ratio K_I^2/σ_{ys}^2. Only when the specimen dimensions are larger than the minimum of Eq 1 can one expect that the plastic zone has negligible effect on the stresses around the crack and thus on the measured value of K_{Ic}.

The J-integral test procedure promises to overcome this size limitation in K_{Ic} measurement and allow the consistent measurement of fracture toughness in much smaller specimens than is possible with the K_{Ic} procedure. A definition of J which provides a good physical understanding of the concept, taken from Ref *2*, is

[2] The italic numbers in brackets refer to the list of references appended to this paper.

$$J = -\partial U / \partial a \tag{2}$$

where ∂U is the change in strain energy per unit thickness corresponding to an infinitesimal increase in crack length of a loaded body. This change in strain energy can be visualized as the decrease in area under a load-deflection curve corresponding to an increase in crack length at constant deflection, see Fig. 2. The change in strain energy is negative, so J is a positive quantity. The critical J value corresponding to a critical amount of Mode I crack growth in a loaded body is the quantity of interest, J_{Ic}. When plastic deformation is negligibly small, J is equivalent to G, the strain energy release rate. This situation corresponds to the initial straight-line portions of the load-deflection curves in Fig. 2. The great

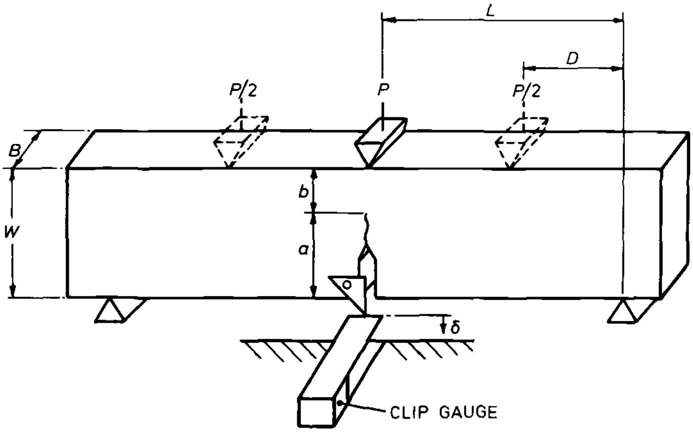

FIG. 1—*Bend specimen and test arrangement.*

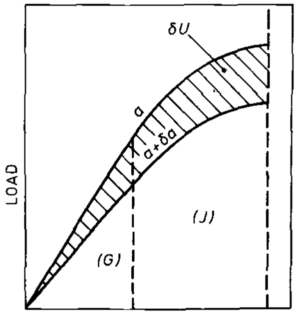

FIG. 2—*Generalized load-deflection plot.*

importance of the J-integral method is that it applies as well to geometries with large scale plastic deformation. There is growing experimental evidence that J_{Ic} values measured from small specimens with significant plastic deformation are the same as the linear elastic G_{Ic} values measured from larger specimens of the same material.

Rice et al [3] have described a simple and reliable approximation for J which makes the differentiation process indicated by Eq 2 unnecessary. The approximation applies to any specimen in which the uncracked ligament is subjected primarily to bending stresses and in which yielding of the specimen is confined to the uncracked ligament and can be expressed as the following equation taken from Ref 3

$$J = \frac{2}{bB} \int_{0}^{\delta_{\text{crack}}} P d(\delta_{\text{crack}}) = \frac{2A'}{bB} \tag{3}$$

A' is the area under a load versus load-point-deflection curve, where the deflection, δ_{crack}, is due only to the introduction of the crack. In a J_{Ic} test, the area under the curve is somewhat larger, because the total measured deflection is the sum of δ_{crack} and the elastic deflection of the specimen which would occur with no crack present [3]

$$\delta = \delta_{\text{crack}} + \delta_{\text{no crack}} \tag{4}$$

However, the value of $\delta_{\text{no crack}}$ can be calculated easily from the test results. In those cases where it corresponds to a significant portion of the total area under the P-δ curve, a correction can be made, as is shown later. For the bend specimens used here with $a/W > 0.6$, the correction is, in some cases, small enough to ignore. In all cases, bend specimens with $a/W > 0.6$ clearly satisfy the ligament conditions mentioned previously, that is, there is primarily bending in the ligament and yielding is confined to the ligament.

Recently, Merkle et al [4] described an analysis which leads to an approximation for J in the same form as Eq 3, but the result is quite different in that δ and A correspond to total deflection and total area under the load-deflection curve. For certain test conditions, there is a significant difference between the Merkle et al approach using the total area under the load versus load-point-deflection curve and the Rice et al approach using the area under the curve due to the presence of the crack only. For the present, the question of which approach is correct has no clear answer. In this work, the latter approach is used.

The objectives of this work are to (*a*) describe the test procedures and results from J-integral tests of a low strength and a medium strength steel, (*b*) compare the results with some of the proposed criteria for the J_{Ic} test procedure, and (*c*) propose a simplified test procedure which could be used as a J_{Ic} screening test.

General J_{Ic} Test Method

Since J can be easily measured as $2A/bB$ for certain conditions, the most significant problem in measuring J_{Ic} is determining which value of J is the critical value corresponding to some critical amount of crack growth. The crack-growth-resistance curve or R-curve method used by Landes and Begley [5] is a good basic test method. With this method, a series of identical precracked specimens are loaded to various values of δ, and the measured $2A/bB$ values are plotted versus the crack growth which is measured after the test from the fracture surfaces. Then, J_{Ic} can be taken as a point on the J versus Δa curve which corresponds to a calculated or preselected critical Δa value. The measuring points for the critical Δa which are considered here are: (*a*) the Landes and Begley proposal [5] of the intersection of the R-curve with the calculated crack-opening-stretch curve; and J_{Ic} value so determined can be thought of as the value beyond which true crack growth begins, over and above an effective crack growth corresponding to crack-tip stretching or blunting; (*b*) Corten's proposal [6] of the J value corresponding to the point of maximum load on the P-δ curve; for near limit load conditions and for the ratio $B/b \geqslant 2.0$ the critical amount of crack growth, Δa_C, is proposed to occur at or very near $P_{\max}$; and (*c*) Paris' proposal [7] of the J value at $\Delta a_C = 0.025 K_{Ic}{}^2/\sigma_{ys}{}^2$.

J_{Ic} Test Procedure

An outline of tests performed is (*a*) Tests 1 and 2, both of four specimens each from two different samples of a carbon-manganese steel, at a nominal a/W of 0.6, and (*b*) three tests of four specimens each from a single sample of a nickel-chromium-molybdemum steel, Test 3 at a nominal a/W of 0.75, Test 5 at an a/W of 0.6, and Test 4 at an a/W of 0.75 under four-point bending. The material properties of the two steels are listed in Table 1.

All of the bend specimens from both materials were made to the following dimensions: $B = 10.0$ mm, $W = 20.0$ mm, length $= 90$ to 100 mm. All specimens were tested with the outer supports spaced at $2L = 82.4$ mm. The four-point bend specimens were tests with a moment arm of $D = 21.4$ mm, see Fig. 1. A 3.2-mm-wide notch was cut in each specimen, 8.0 mm deep, and with a 60-deg by 0.1-mm radius notch tip. The specimens were preloaded in compression to negative K values of 50 and 80 MN/m$^{3|2}$ for the mild and alloy steels, respectively. The tensile residual stress generated ahead of the notch by this preloading produces quicker and more uniform fatigue crack initiation from the notch. Fatigue cracks were grown to the lengths indicated in Table 2 at $K_{\max}$ values not exceeding 70 MN/m$^{3|2}$. Both the fatigue loading and the subsequent monotonic loading were performed at room temperature.

The specimens were loaded monotonically in about 2 min up to various values of δ_u and then unloaded. A continuous plot of load versus load-point displacement was obtained for each specimen; Fig. 3 shows a plot for each material. The load-point displacement was measured using a standard clip gage [1] (ASTM Method E 399-74) between a knife point attached to the specimen and a fixed knife edge, as shown schematically in Fig. 1. Then, the cracks were grown further by fatigue loading, and finally the specimens were broken apart. The crack growth, Δa, which occurred during monotonic loading was distinguished easily from the areas of fatigue precracking and postcracking on the fracture surface.[3] Figure 4 shows the fracture surface of a mild steel and an alloy steel specimen. From top to bottom of each fracture surface is the starter notch, the fatigue precrack, the area of monotonic crack growth, the fatigue postcrack, and the final portion of the fracture surface produced when the specimen was broken apart. The minimum remaining ligament after precracking b and the maximum value of Δa were measured from each fracture surface using a X7 lens. The area, A, under each load-deflection curve was measured and converted to energy units.

The values of δ_u, b, Δa, and A which were determined as described in the preceding paragraph are listed in Table 2.

Discussion of Test Results

Correction for Uncracked Deflection

The areas under a P-δ curve which correspond to the elastic deflection

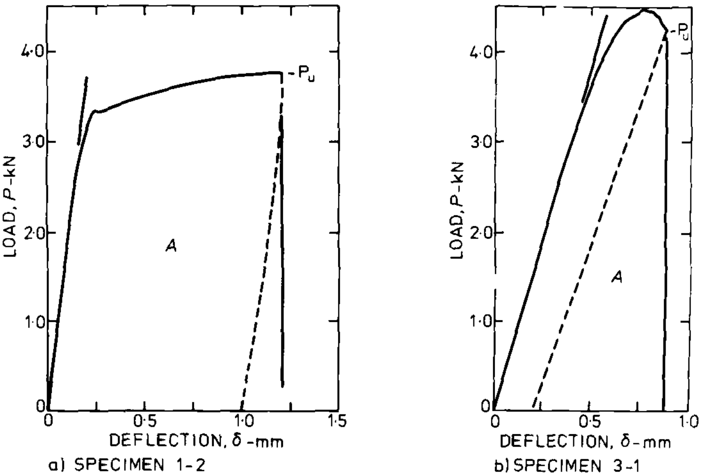

FIG. 3—*Load versus load-point-displacement measurements for two specimens.*

---

[3] It should be noted that heat tinting processes are used more commonly and quite successfully to mark the area of monotonic crack growth in J-integral tests.

TABLE 1—*Material properties.*

Test	Composition	σ_{ys}, MN/m^2	σ_u, MN/m^2	Elongation, %	Reduction of Area, %	E nominal, MN/m^2	ν, nominal	K_{Ic}, MN/m$^{3/2}$
1	0.27C, 0.9Mn	386	538	40	. . .	207 000	0.30	. . .
2		443	566	37	. . .			
3, 4, 5	0.35C, 3.4Ni, 1.8Cr, 0.6Mo, 0.5Mn, 0.1V	1213	1366	16	60	207 000	0.30	145

TABLE 2—*J-integral test data.*

For all tests B = 10.0 m, W = 20.0 mm

Test and Specimen	C_m/C	P_{max}, kN	P_u, kN	δ_u, mm	b, mm	Δa, mm	A, N m
1-1	0.94	. . .	3.98	0.61	7.8	0.1	1.99
1-2	1.07	3.78	3.76	1.21	7.5	0.6	3.98
1-3	1.07	3.65	3.61	1.79	7.3	1.2	5.94
1-4	0.96	. . .	4.07	0.81	7.8	0.3	2.72
2-1	1.02	4.47	4.37	1.15	7.5	1.2	4.47
2-2	0.96	4.34	4.32	0.79	7.5	0.5	2.78
2-3	0.98	. . .	3.56	0.63	6.7	0.05	1.72
2-4	1.03	. . .	3.96	0.72	7.1	0.1	2.24
3-1	1.04	4.48	4.28	0.87	5.0	0.65	2.54
3-2	1.00	4.89	4.88	0.81	5.1	0.50	2.49
3-3	1.05	. . .	4.85	0.72	5.3	0.25	2.06
3-4	1.01	. . .	4.52	0.59	5.2	0.10	1.48
4-5 [a]	0.93	. . .	10.30	0.86	5.5	0.25	2.26
4-6 [a]	0.96	9.83	9.83	0.85	5.2	0.40	2.69
4-7 [a]	0.92	10.15	10.10	0.73	5.3	0.70	2.87
4-8 [a]	0.96	. . .	8.90	0.58	5.4	0.05	1.41
5-9	1.06	. . .	8.05	0.46	7.6	0.10	1.95
5-10	1.06	10.38	10.30	0.72	7.9	0.50	4.27
5-11	1.04	9.90	9.90	0.68	7.6	0.35	3.89
5-12	1.02	. . .	9.00	0.58	7.5	0.20	2.78

[a] Four-point bend test.

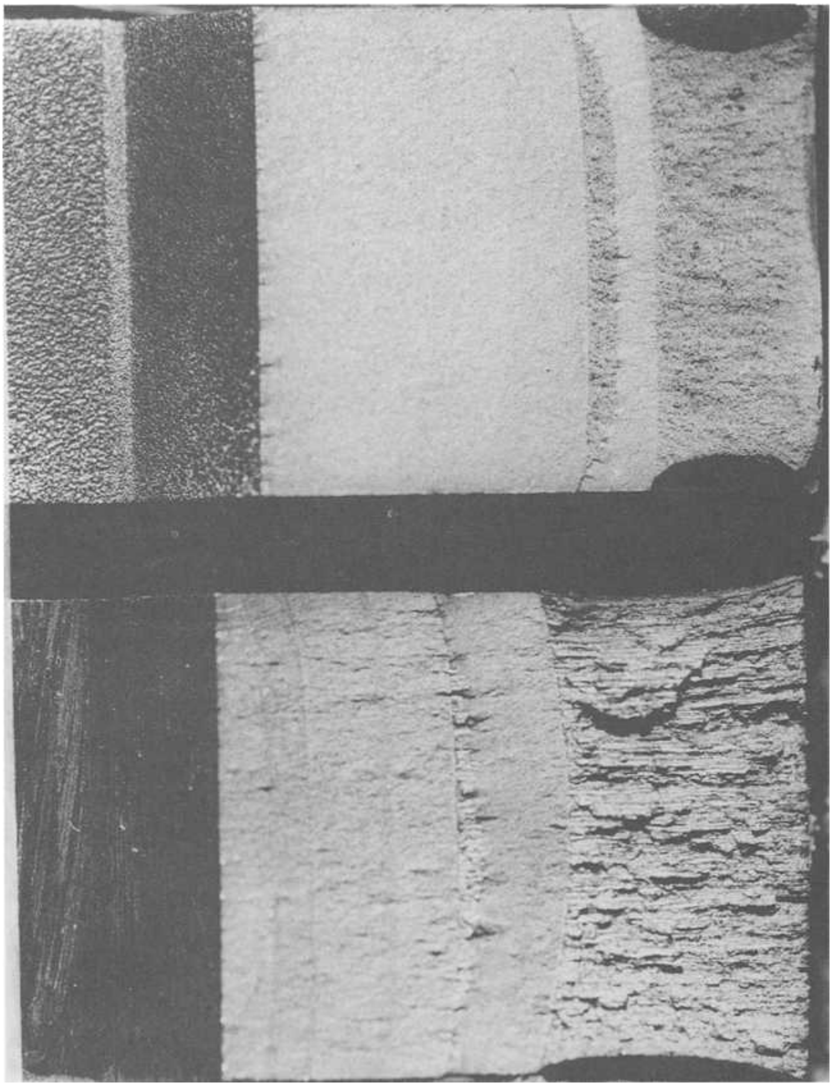

FIG. 4—*Photograph of fracture surfaces; Specimen 1-2 on the left, Specimen 3-1 on the right.*

of three- and four-point bend specimens with no crack are given in Eqs 5 and 6, respectively

$$A_{\text{no crack}} = \frac{P_u}{2}\left\{\frac{P_u(2L)^3}{48E(BW^3/12)}\right\} = \frac{P_u{}^2(L/W)^3}{EB} \tag{5}$$

$$A_{\text{no crack}} = \frac{P_u}{2}\left\{\frac{P_uD^2(6L-4D)}{12E(BW^3/12)}\right\} = \frac{P_u{}^2(D/W)^3(3L/D-2)}{EB} \tag{6}$$

where P_u is the load at the point of unloading, see Fig. 3. The bracketed terms can be recognized as the expressions for the elastic deflection of uncracked three- and four-point bend specimens. A plot of the ratio $A_{\text{no crack}}/A$, calculated from Eqs 5 and 6 using the measured values of P_u and A in Table 2, is shown as Fig. 5. The large values of this ratio and the variation between tests can be explained using the following argument.

For the purpose of the argument, P_u can be taken equal to the limit load for a three-point bend specimen [5]

$$P_\ell = 2\ell Bb^2\sigma_{ys}/L \tag{7}$$

where $\ell=0.364$, the appropriate constant for bending. Then combining Eqs 5 and 7 and using $J_{Ic} = K_{Ic}{}^2/E = 2A_{Ic}/bB$ results in

$$A_{\text{no crack}}/A_{Ic} = 1.06L\ (b/PW)^3\ (\sigma_{ys}/K_{Ic})^2 \tag{8}$$

Although Eq 8 applies only for three-point bend tests at limit load, it does explain qualitatively the results in Fig. 5. As an example, the largest difference in $A_{\text{no crack}}/A$ is between the Test 5 and the Tests 1 and 2 conditions, and Eq 8 predicts a significant difference for these conditions due to the different σ_{ys}/K_{Ic} ratios. The values from Eq 8 are 0.167 and 0.034 for Test 5 and Test 1 and 2, respectively, not a great deal different from the values in Fig. 5.

R-Curves and Measurement Points

The R-curves drawn from the data in Table 2 are shown in Figs. 6 and 7. The mild steel results in Fig. 6 are corrected for the uncracked deflection of the specimen, that is, $A' = A - A_{\text{no crack}}$. The only measuring point for J_{Ic} which seems appropriate for the mild steel tests is the Landes and Begley [5] intercept method. Corten's maximum load proposal can not be applied because the $B/b > 2.0$ requirement is not met. And Paris' proposal [7] in the form of the straight line $\Delta a_c = 0.025EJ/\sigma_{ys}{}^2$ has too low a slope to intercept the R-curves within the range of the data in Fig. 6.

The R-curves from the alloy steel tests are shown in Fig. 7 both before

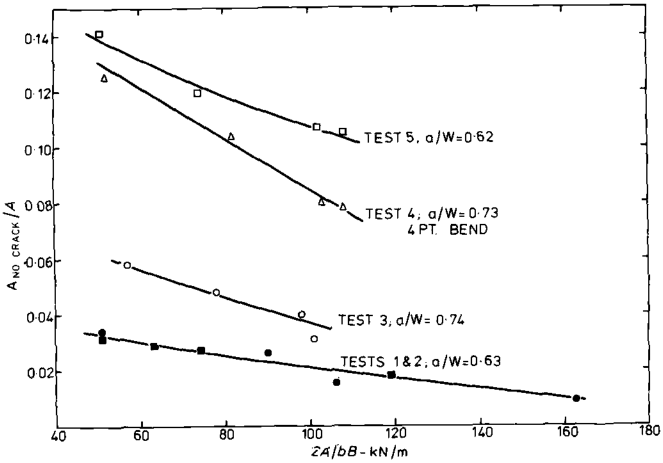

FIG. 5—*Ratio of area under P-δ curve which corresponds to uncracked deflection.*

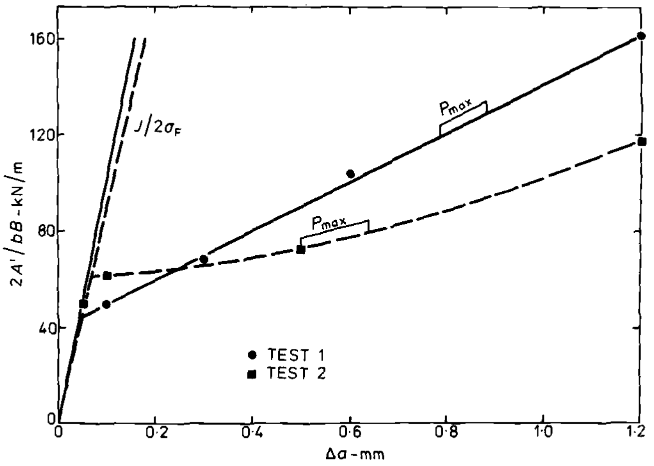

FIG. 6—*R-curves for mild steel tests.*

and after correction for the uncracked deflection. The intercept method is not recommended for these results, because the Δa values at the intercept point are significantly lower for the alloy steel due to its high yield strength and are therefore below the minimum which can be measured with reasonable accuracy. The Corten and Paris proposals can be applied. Since the corrections for uncracked deflection are quite large and the corrections result in a good representation of the three alloy steel tests

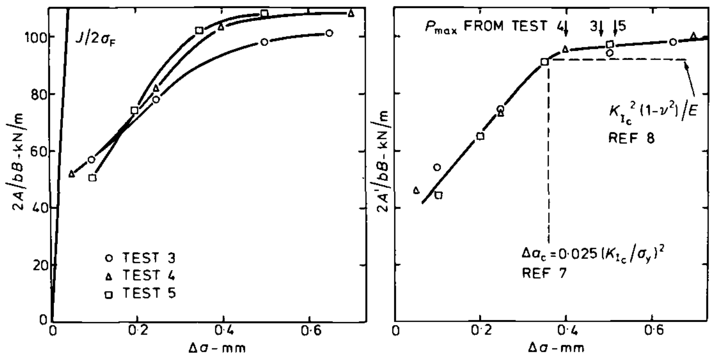

FIG. 7—*Uncorrected and corrected R-curves for nickel-chromium-molybdenum steel tests.*

with a single curve, the Corten and Paris proposals are applied to this single, corrected R-curve.

J_{Ic} *Test Results*

Table 3 lists the critical J values determined from the R-curves using the three measurement points under discussion. For the mild steel tests, the intercept J values, 61 and 44 kN/m, are taken as J_{Ic} values. These values are at the low end of the range expected for this material, but in the mild steel tests, crack growth is in a transverse direction, so a low J_{Ic} value is expected.

For the alloy steel, K_{Ic} is known quite certainly from the results of seventeen laboratories testing this material [*8*]. The specimens tested here were taken from a single K_{Ic} specimen from that previous work. The corresponding J_{Ic} value is $K_{Ic}^2\ (1 - \nu^2)/E = 92$ kN/m. The so-called "plane strain" conversion to J_{Ic} is used, because the critical B/b ratio is greater than unity. In addition, the ratio of plastic zone size to b is quite small

$$\frac{1}{6\pi}\left[\frac{K_{Ic}}{\sigma_{ys}}\right]^2 \Bigg/ b = 0.15$$

where b is taken as 5 mm, and K_{Ic} and σ_{ys} are from Table 1. The average of the five critical J values which can be considered J_{Ic} values is 93 kN/m. Such excellent agreement with the value of 92 kN/m calculated from the known K_{Ic} value is probably fortuitous to some extent. But if the J_{Ic} test and analysis procedures are correct, good agreement is expected because the K_{Ic} value and its conversion to J_{Ic} are quite certain, and the test material is known to possess highly uniform properties. This good agreement is interpreted as an indication that the test procedure is correct and that the Corten and Paris measurement point criteria apply to this material.

J_{Ic} *Test Criteria*

With regard to the size and loading criteria proposed for valid J_{Ic} tests, the following comments are offered. Referring to Table 3, all specimens were within the Landes and Begley criteria [*5*] of $b \geqslant 25\, J_{\text{Ic}}/\sigma_F$. In Tests 1, 2, and 5, one or both of the criteria proposed by Corten for valid maximum load determination of J_{Ic} were clearly violated; $B/b \geqslant 2.0$ and $P_{\text{max}}/P_{\ell} \geqslant 0.85$. These were the tests with the apparent discrepancies in the maximum load J values. So if any conclusion can be drawn from these tests, it would support Corten's size and loading criteria.

A criteria for a "good" J_{Ic} test which is seldom discussed is the ratio of measured compliance to calculated compliance. Compliance can be calculated from a known K calibration in the usual manner starting with Irwin's equation taken from Ref *9*

$$dC = \frac{2BK^2}{EP^2}da = -\left[\frac{KB}{PW}\right]^2 \frac{2W^2}{EB}db$$

The bracketed term in the preceding equation is a function of b and a/W and can be obtained from the Srawley and Gross K calibration for the bend specimen [*10*].

So that
$$C = Y^2\left[\frac{L}{2W}\right]^2 \frac{W^2}{EBb^2} + C_1 \qquad (9)$$

where $Y = KBb^{3/2}/PW$ is the parameter used by Srawley and Gross, the $(L/2W)^2$ term accounts for the slightly greater than unity $L/2W$ ratio used in these tests, and the constant of integration, C_1 is evaluated from Eq 9 by setting $b = W$ and $C = 2L^3/EBW^3$, the conditions for an uncracked elastic beam. The result is

$$C = \frac{Y^2L^2}{4EBW^2}\left[\frac{W^2}{b^2} - 1\right] + \frac{2L^3}{EBW^3} \qquad (10)$$

The ratio of the measured compliance to the value calculated from Eq 10 is listed in Table 2 for each of the specimens tested. The agreement is not unreasonable considering the difficulties in measuring the slope on a P-δ curve and in measuring the remaining ligament, b.

Finally, the differences in analyzing the four-point bend specimens should be mentioned. In addition to Eq 6 already noted, Eq 7 and 10 will also be different for four-point bend specimens. But the most important difference in analyzing four-point bend tests is that the center-point displacement from a four-point bend specimen is not, in fact, a load-point displacement. When the center-point displacement is reduced by the ratio D/L, that is $\delta = (D/L)\ \delta_{\text{center}}$, it becomes an effective load-point displacement. Applying this ratio to the center-point displacement is equivalent to measuring the displacement at the load points of a four-point bend specimen, see Fig. 1. For the four-point bend tests in this report the center-point displacements were reduced according to the above expression, thus A and J were reduced by the same ratio. A verification that this procedure is correct is the fact that the three- and four-point bend J_{Ic} results from Tests 3 and 4, respectively, were nearly identical.

Proposed J_{Ic} Screening Test

The proposed screening test is based on the observation that the area under a P-δ curve can be closely approximated by replacing the curve with two straight lines, see Fig. 8. Line OA is along the elastic portion of the P-δ curve. Line AB is at a load value, denoted P_f, such that Area 1 = Area 2, and thus the area under OAB is the same as the area under the P-δ curve up to $P_{\max}$.[4] An expression for the area under OAB leads to an expression for J which can be used for a one specimen screening test.

The area under the two lines OAB can be written as

$$A_f = P_f\delta - \tfrac{1}{2}P_f^2C$$

Then using the experimental observation that the ratio $P_f/P_\ell = f$ is essentially constant for a given geometry and material, an approximate form of Eq 10, $C = Y^2L^2/4EBb^2$, Eq 7 to define P_ℓ, and $J = 2A/bB$, the result is

$$J_f = \frac{4f\ell\sigma_{ys}b\delta}{L} - \frac{f^2\ell^2Y^2\sigma_{ys}{}^2b}{E} \tag{11}$$

Inspection of Eq 11 shows that, if the value of f is known, then J can be determined by measuring only the single value of load-point displacement at a load near the maximum load. This is the essential idea of the proposed screening test. First a standard R-curve J_{Ic} test is performed to determine J_{Ic} and the characteristic value of f for the particular material and geometry. Then additional screening or quality control J_{Ic} tests in the same material can be performed by loading one specimen of the same geometry with any given value of b up to the δ value in Eq 11 which corresponds to the prior-determined J_{Ic}. By comparing the Δa measured on

---

[4] This is a convenient method of measuring the area under P-δ curves and was used for most of the curves here.

TABLE 3—*J-Integral test results.*

Test	Material	$\frac{a}{W}$	$\frac{B}{b}$	$\frac{P_{\max}}{P_\ell}$	J, kN/m			$\frac{b\sigma_F}{J_{Ic}}$
					At Intercept	At Δa_c	At $P_{\max}$	
1	C-Mn	0.62	1.3	0.99	61 [a]	...	75	59
2	C-Mn	0.64	1.4	1.00	44 [a]	...	125	79
3	Ni-Cr-Mo	0.74	2.0	0.86	...	92 [a]	94 [a]	70
4 [b]	Ni-Cr-Mo	0.73	1.9	0.88	...	92 [a]	95 [a]	72
5	Ni-Cr-Mo	0.62	1.3	0.79	...	92 [a]	97	108

[a] J_{Ic} values.

[b] Four-point bend test.

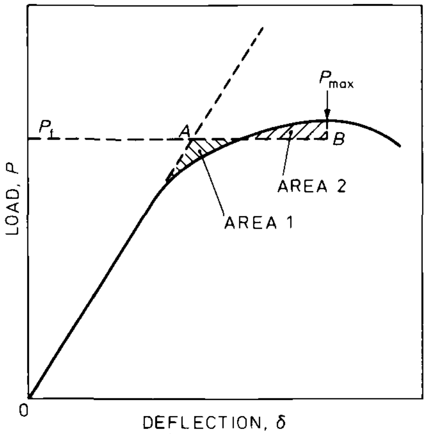

FIG. 8—*Schematic P-δ plot showing approximation for maximum load.*

the fracture surface of the additional specimen with the prior-determined Δa_{Ic} value, one can at the least determine if the J_{Ic} of the additional specimen is above or below the prior-determined value. And this determination simply involves loading the specimen to a preselected δ value with no load measurement or data plotting required.

An indication that Eq 11 is an appropriate approximation of J is its similarity with the Bucci et al approximation for J for a rigid-plastic bend bar taken from Ref *11*

$$J = \frac{4\ell\sigma_u b\delta}{L} \tag{12}$$

In addition, for the rigid-plastic case where $E \to \infty$, $\sigma_u = \sigma_{ys}$, and $f = 1$, Eq 11 becomes identical to Eq 12.

A further, direct indication that Eq 11 is a good approximation is the comparison of J_f values with measured $2A/bB$ values. Table 4 shows such

TABLE 4—*J-integral screening test results.*

Test and Specimen	P_f, kN	$\frac{P_f}{P_\ell}$	f	J_f, kN/m	$\frac{2A}{bB}$, kN/m
1-1	...	...	0.94	51	51
1-2	3.56	0.93	0.94	107	106
1-3	3.46	0.95	0.94	158	163
1-4	...	...	0.94	72	70
3-1	4.22	0.79	0.81	105	101
3-2	4.64	0.83	0.81	96	98
3-3	...	...	0.81	84	78
3-4	...	...	0.81	58	57

a comparison, calculated from the δ, b, and A values in Table 2. Two significant aspects of the comparison are that it remains good for two quite different materials and for J values significantly above and below the J value corresponding to $P_{\max}$.

Conclusions

In determining J_{Ic} using the $2A/bB$ approach with bend bars, the uncracked deflection contribution can be significant for materials with large values of $\sigma_{ys}/K_{\mathrm{Ic}}$ particularly near limit load, and even for $a/W >$ 0.6. The relative error in J_{Ic} which results when uncracked deflection is ignored can be expressed directly from Eq 8 as

$$J_{\text{no crack}}/J_{\mathrm{Ic}} = 1.06L \left(\frac{b}{W}\right)^3 \left(\frac{P_{\mathrm{Ic}}}{P_\ell}\frac{\sigma_{ys}}{K_{\mathrm{Ic}}}\right)^2 \tag{13}$$

where the addition of P_{Ic}/P_ℓ accounts for tests below limit load. Size criteria can be easily written from Eq 13. As an example, for standard three-point bend tests at limit load and for the specimen size and the alloy steel used here the minimum crack length for which the error in J_{Ic} is below two percent is $(a/W)_{\min}=0.81$. Thus, for bend bar tests in material such as this with large $\sigma_{ys}/K_{\mathrm{Ic}}$ ratios, the effect of uncracked deflection must be included for accurate results. For compact specimens [*1*] (ASTM Method E 399-74), with their inherent much smaller uncracked deflection, corrections are seldom if ever required.

For the particular tests and materials studied here, some additional conclusions can be drawn. Clip-gage center-point displacements can be used successfully to conduct three- and four-point bend J_{Ic} tests. For determining the value of J_{Ic}, it appears that none of the three measuring point criteria investigated here is generally applicable to *both* the relatively low strength mild steel and the relatively high strength alloy steel. A one specimen test, which involves only single measurements of load-point displacement and remaining ligament, can be used with both materials to conduct J_{Ic} screening tests for comparison with standard R-curve J_{Ic} results.

Acknowledgments

The author is happy to acknowledge the helpful comments and suggestions of L. P. Pook, National Engineering Laboratory, during all phases of this work.

References

[*1*] "Methods for Plane Strain Fracture Toughness ($K_{I,C}$) Testing," DD 3:1971, British Standards Institution.

[2] Rice, J. R., *Journal of Applied Mechanics, Transactions,* American Society of Mechanical Engineers, Vol. 35, 1968, pp. 379–386.
[3] Rice, J. R., Paris, P. C., and Merkle, J. G. in *Progress in Flaw Growth and Fracture Toughness Testing, ASTM STP 536,* American Society for Testing and Materials, 1973, pp. 231–245.
[4] Merkle, J. G., Berggren, R. G., and Stelzman, W. J., "Compliance and Fracture Toughness Calculations for Notched Bend Specimens," Quarterly Progress Report on Reactor Safety Programs sponsored by the National Research Council Division of Reactor Safety Research, Oct.-Dec. 1974, Heavy Section Steel Technology Program, ORNL-TM-4805, Vol. 2, Oak Ridge National Laboratory, March 1975.
[5] Landes, J. D. and Begley, J. A. in *Fracture Analysis, ASTM STP 560,* American Society for Testing and Materials, 1974, pp. 170–186.
[6] Corten, H. T., discussion presented at the meeting of Committee E-24 on Fracture Testing of Metals, American Society for Testing and Materials, Atlanta, Ga., March 1974.
[7] Paris, P. C., discussion presented at the meeting of Committee E-24 on Fracture Testing of Metals, American Society for Testing and Materials, Pittsburgh, Pa., Oct. 1973.
[8] Wilkinson, T. and Walker, E. F., "Draft of Final Report on the Collaborative Fracture Toughness Testing of the Fracture Toughness High Strength Steels Working Group,"MG/EB/32/72, Corporate Laboratories, British Steel Corporation, unpublished report.
[9] Irwin, G. R., *Applied Materials Research,* Vol. 3, 1964, p. 65.
[10] Srawley, J. E. and Gross, B., *Engineering Fracture Mechanics,* Vol. 4, 1972, pp. 587–589.
[11] Bucci, R. J., Paris, P. C., Landes, J. D., and Rice, J. R. in *Fracture Toughness, ASTM STP 514,* American Society for Testing and Materials, 1972, pp. 40–69.

N. J. Adams [1]

Influence of Configuration on R-Curve Shape and G_c When Plane Stress Conditions Prevail

---

REFERENCE: Adams, N. J., "**Influence of Configuration on R-Curve Shape and G_c When Plane Stress Conditions Prevail,**" *Cracks and Fracture, ASTM STP 601*, American Society for Testing and Materials, 1976, pp. 330–345.

ABSTRACT: Following a brief introduction, an examination is presented of the factors which define the fracture toughness, R-curve relationships, and the extent of stable crack extension. Use is made of the compliance calibrations for a center cracked sheet and a compact tension specimen to show how configuration influences the shape of the R-curve in specimens of equivalent width and identical thickness. The change in the shape of the R-curve is shown to affect stable crack extension and the G-curve tangency requirement to result in differing toughness levels in the different configurations.

In support of the analytical results, tests have been conducted on two high strength aluminium alloys to establish the variations in the shape of R-curves, using both compliance-indicated and measured absolute values of crack length. Various toughness values which highlight the influence of plastic deformation on toughness have been calculated.

KEY WORDS: crack propagation, fracture (materials), R-curves, metals, aluminum, plane stress, evaluation

The plane stress fracture mode, that is, separation resulting in slant mode fracture surfaces, has been a common problem in the application of both medium and high strength materials, for example, low pressure pipelines and aircraft structures. To a large extent, the problem has taken second place to the generally more serious problem of plane strain fracture, that is, the brittle mode associated with flat fracture surfaces. The state of the art of the latter has now reached the stage of a standard test procedure being recommended [*1*] [2] (ASTM Test for Plane-Strain Fracture Toughness of Metallic Materials (E 399-74)). More research effort is now being focused on plane stress fracture, and one possible method of analysis is the resistance R-curve concept. The concept was

---

[1] Senior inspector, Nuclear Installations Inspectorate, Millbank, London, England.

[2] The italic numbers in brackets refer to the list of references appended to this paper.

originated by Irwin [2] and later discussed in depth by Kraft [3] and Srawley and Brown [4]. More recently, the subject was considered by Heyer and McCabe [5,6] and Bradshaw [7].

In this paper, the R-curve concept is discussed, with particular reference to the nature of the R-curve in relation to specimen configuration and to how the results will influence the application of the concept to structures in general.

Initially, consideration of the R-curve as a test configuration dependent quantity is dicussed. The implication of the variation in stress intensity for two different specimen types is reviewed and the ensuing results are discussed in the light of available evidence. Tests were conducted on two high strength aluminium alloys the results of which substantiate the analytical findings.

The R-Curve Concept

The basis of the resistance R-curve concept is that a crack extends under the action of a crack extension force, which increases progressively as the stress in a structure increases. As a crack extends, elastic strain energy is released by the cracked structure. The rate of energy release with respect to crack extension, G, is frequently referred to as the crack driving force. The resistance, R, respresents the amount of work which must be done to produce a crack increment, *da*. Rapid propagation of a crack is prevented by an increasing resistance, R, exhibited by the material which will yield at the crack tip. Thus equilibrium exists between G and R up to the point of structural instability. The G-R concept is shown schematically for a sheet of infinite width in Fig. 1. At points where a G-line intercepts the R-curve, equilibrium is maintained, but, when a G-line becomes tangential to the R-curve, crack instability will occur. That is, the elastic energy release by the structure for a crack increment, *da*, is greater than the increase in resistance offered by the material.

At the point of specimen or structure instability, it was shown that [4]

$$\frac{\partial G}{\partial a}_{s = s_c} = \frac{\partial R}{\partial a}_{s = s_c}$$

where S_c denotes the value of the applied stress, the subscript c denoting a critical or stationary value. In terms of the elastic analysis of a cracked body, the quantity G can be readily calculated, and, because of equilibrium, the value of R is equal to the instantaneous value of G. From this information, an R-curve can be constructed. From the analysis, it is also possible to calculate a critical value of G_c based upon the critical applied stress S_c.

In considering the practical application of the R-curve concept, it is essential to know if a material, at some specified thickness, will exhibit a nominally constant G_c value or R-curve shape, or both. In Fig. 1, the case is presented for a center cracked sheet of infinite width. However, if finite width effects are introduced, then the point of tangency of a G-curve will move down the R-curve with diminishing specimen width [*4*]. Clearly then, G_c is not constant but depends on specimen width, hence size effect is of considerable consequence in practical applications.

An important question to be resolved concerns the influence of specimen or structural configuration on toughness. Since resistance curves can only be derived from laboratory test data, an analytical approach is not possible. The method adopted was to consider, on two different configurations, several different conditions of failure and to examine their implications in the light of practical experience.

The stress intensity factor K is generally expressed in the following form

$$K = \frac{Pa^{1/2}}{BW} Y \tag{1}$$

where the function $Y = f(a/W)$ accounts for configuration. The function Y has been determined for many types of loading and configuration [*8*]. For plane stress conditions, the energy release rate G is related to the stress intensity factor K, by the relationship $G = K^2/E$. Thus the shape of a G-curve is defined by the appropriate Y function.

In what follows, an examination was made of the implications of considering certain types of material behavior and the consequence of the variation in Y functions. Two simple configurations were considered, the center cracked sheet (CCS) and the compact tension (CT) form. The respective Y functions for these two specimen configurations are

$$Y = 1.77 \quad \left[1 + 0.1 \frac{2a}{W} - \frac{2a^2}{W}\right] \quad \text{for CCS} \tag{2}$$

and

$$Y = 29.6 - 185.5 \frac{a}{W} + 655.7 \frac{a^2}{W} - 1017 \frac{a^3}{W} + 638.9 \frac{a^4}{W} \quad \text{for CT} \tag{3}$$

At this point, the analytical implications will be presented, and comparison with experimentally determined results will be deferred to a later section.

As a starting point, it was considered that a CT specimen was equivalent in width to half a CCS specimen, as shown schematically in Fig. 2. The following proposals will now be discussed.

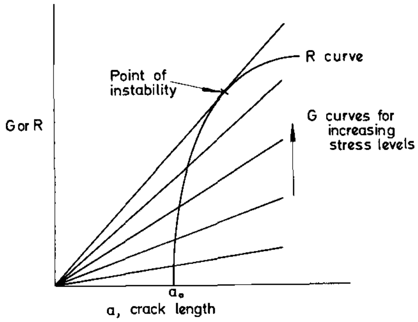

FIG. 1—*Schematic representation of G/R-curve relationship for a sheet of infinite width.*

Unique Material G_c *Value Exists*—If it was considered that fracture instability would occur at a unique G_c value in specimens of equivalent width, then some information on the nature of the R-curve could be derived. The slope of hypothetical G-curves is shown in Fig. 3 for CCS and CT specimens of equal width and crack length past a point of considered instability. Recalling that instability is defined by the tangent point of the G- and R-curve, it can be seen from Fig. 3 that, if stable crack extension is to take place, then, at the critical point, the R-curve for the CT specimen must be steeper than that for the CCS specimen to fulfill the tangency requirement. Clearly, the implication is that, if a unique G_c value exists, then the R-curves must be different for the two specimens at the particular width considered. Also, since the R-curve for a CT specimen must be steeper, it implies a reduction in stable crack extension up to instability.

Unique Material R-Curve Exists—If, at a specified thickness, a material exhibited an R-curve of unique shape, then, in terms of the two specimens considered, a CT will always have a lower value of G_c than a CCS. This follows from the fact that the rate of change of the Y function, with aspect ratio as reflected by the G-curves of Fig. 3, is greater for a CT and will, as a consequence, result in a tangent point lower down on the R-curve. This result will also imply less stable crack extension from an initial value a_0.

Unique Material R-Curve and G_c *Value Exist*—Consider now the circumstances when a material R-curve and G_c value are taken as independent of configuration. In the two previous cases, it has been shown what the consequences of assuming equivalent width does to the R-curve and G_c value. By virtue of Y calibration variation, applying these two

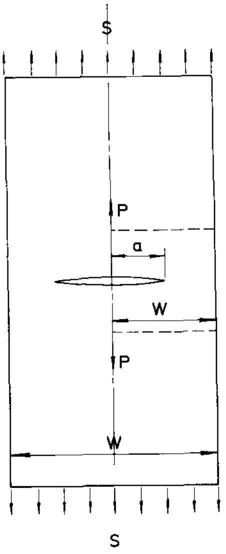

FIG. 2—*Idealization of CCS and CT specimens with applied loads.*

constraints simultaneously to the fracture behavior leads to a relative change in equivalent specimen width.

Consider a CCS to be 100 units wide with a crack length $2a = 50$ units at failure. By constraining the R-curve and G_c value, the CT specimen can only meet the tangency requirement at the same crack length if the width is different. Such action would change the load at failure and the G-curve to a point where the gradient is less than previously shown in Fig. 3. Solving for the imposed conditions, the resulting width of a CT specimen would be approximately 82 units. The conditions considered here also mean that the extent of stable crack growth will be the same in both specimen types.

It should be borne in mind that the preceding discussion has been based on linear elastic analysis at one aspect ratio only. Since the Y functions vary with aspect ratio, the slopes of the curves will also vary. In particular, the adjusted width of the third proposal would change if an initial aspect ratio different from 0.5 were selected. However, in addition to possible elastic variations, it must be acknowledged that plane stress fracture is associated with considerable plastic deformation prior to instability such that, if nominal net section stress distributions change significantly with configuration, then the yielding process may be influenced. It was shown by Wilson [*9*], using modified elastic analysis, and experimentally by Hahn [*10*] that the size of the yield zone ahead of a crack in a

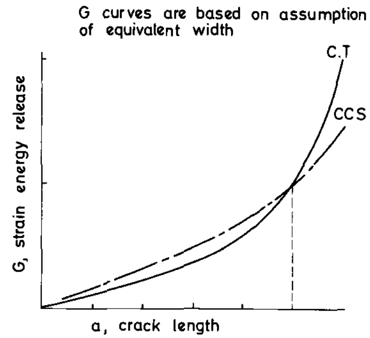

FIG. 3—*Variation in slopes of G-curves for CCS and CT specimen at a common G-value and crack length.*

CT type specimen was approximately one half of the size in a CCS specimen at the same stress intensity level. Since crack tip yield plays a significant part in the fracture process, then large changes with configuration could have some effect on the R-curve shape and G_c value.

Tests and Results

Results have been obtained from tests conducted on two aluminium alloys: a high strength weldable alloy Hiduminium 48 and an alloy L 104. The mechanical properties of these alloys are given in the following table.

Alloy	Ultimate Tensile Strength, MN/m^2	0.2% Proof Stress, MN/m^2	% Elongation, 50 mm
Hiduminium 48	491	445	12
L 104	496	450	9

The tests were conducted on both CCS specimens and CT specimens nominally 3 mm thick, the latter to the configuration required for plane strain specimens [*1*]. The CCS were tested at widths of 100, 200, and 300 mm for the L 104, and 50, 100, 200 mm for the Hiduminium 48. For the CT specimens, the widths were 25, 50, 100, and 150 mm, representing half the widths of the CCS, thus providing comparable ligament sizes. Prior to fracture testing, all specimens were precracked from a machined notch by constant amplitude stress cycling. The tests were performed at crack aspect ratios moninally 0.2, 0.32, and 0.5.

For each fracture test, a record of applied load against crack opening displacement was obtained. A servohydraulic test machine was used, and the load cell output was supplied to the Y axis of an X-Y plotter. For the CCS specimens, a displacement transducer was used to measure crack opening displacement on the centerline at points 6 mm to either side of the crack plane. For the CT specimens, the load pin separation was measured. A pair of displacement transducers, located either side of the loading shackles, were used and the output of the two transducers was averaged to cancel any effects of misalignment. For all CT tests, guide plates were used to prevent out-of-plane displacement of the specimens. Displacement transducer output was used to drive the X axis of the plotter.

On each test record, a calibration of both load and displacement was completed. It was then possible to determine the load and displacement at any stage of a test. A typical test record commences with an initial straight line, the slope of which relates elastic crack opening to the applied load. As yielding at the crack tip occurs, the record deviates from linearity. Depending on the fracture characteristics of the material, failure may occur when the point of maximum load is reached. However, ductile materials frequently sustain maximum load for some period, while crack opening displacement continues to increase before final failure occurs. Following the initial deviation from linearity, due to yield at the crack tip, subsequent deviation can be attributed to greater amounts of yielding which may be combined with stable tearing of the material. It is not possible to separate these two effects from the test record alone. During many of the tests, an additional photographic record was taken. The specimen surface was painted matte black and the area of the crack illuminated. As load was applied, the fatigue crack opened up, and light reflected from the bright surface could be easily distinguished, as could the edge of the subsequent fracture surface during stable crack extension. During tests on L 104, photographs were taken as the test progressed and were related to their appropriate points on the load-displacement record by an event marker. For the tests on Hiduminium 48, the photographs included a digital meter displaying the instantaneous load; however, this was not related to the test record.

The initial linear portion of the test record is due to overall elastic behavior, and the slope is related to the length of the fatigue crack. At any point on the nonlinear portion of the record, an indicated crack length can be determined with the aid of a compliance calibration, the initial slope, and the slope of a line drawn from the origin to intercept that point. This apparent crack length, a_m, can include crack extension beyond the fatigue crack length, a_0' together with the influence of plastic deformation at the crack tip. By considering a number of points on the load displacement record, the relationship between apparent crack length and applied load can be established. This relationship defines the shape for the crack growth resistance curve, based on apparent crack length.

The compliance curves used in the analysis of the CCS were derived from tests on a range of specimen widths [*11*]. It was later found that the curves agreed closely with the modified ASTM Recommended Practice for R-Curve Determination (E 561-75T) equation suggested by Eftis [*12*] which has the form

$$\frac{Ev}{\sigma W} = \left(\frac{\pi a/w}{\sin \pi\, a/w} \right)^{1|2} \left\{ \frac{2}{\pi} \cos h^{-1} \left[\frac{\cos h\, \pi\, y/w}{\cos\, \pi\, a/w} \right] - \frac{(1-\nu)}{W} * \left[1 + \left(\frac{\sin \pi\, a/w}{\sin h\, \pi\, y/w} \right)^{2} \right]^{-1|2} + \frac{\nu y}{W} \right\}$$

This equation will result in indicated crack lengths marginally smaller than ASTM Method E 561-75T at aspect ratios over 0.45. The compliance curve for CT specimens was calculated from the displacement equation given elsewhere [*13*]. Subsequent experimental results from specimens up to 500 mm wide confirmed the validity of the analysis.

Since it has been established that $G = R$ up to instability, it is possible to construct the R-curves for the materials making use of the fact that $EG = K^2$, where

$$K = \frac{P}{BW} Y_1 \sqrt{a_m} \tag{4}$$

for CCS and

$$K = \frac{P}{BW^{1|2}} Y_2 \tag{5}$$

for CT specimens

where

B = specimen thickness,
W = width, and
Y_1 and Y_2 = appropriate functions for each specimen type and are given by Eqs 2 and 3.

The R-curves derived from compliance indicated crack lengths are presented in Figs. 4 to 6, (for example, $R_m = \sigma^2 * Y^2(a_m) * a_m$ for a CCS).

For L 104 they are presented separately for CCS and CT types due to their initial similarity at lower values of R_m, while both types are shown for Hiduminum 48 in Fig. 6.

From the photographic records, additional crack growth resistance curves were also computed in terms of the absolute crack lengths, and these are shown in Figs. 7 and 8 for L 104 and Hiduminium 48, respectively (for example, $R_m = \sigma^2 * Y^2(a_m) * a_m$ for a CCS). It is emphasized here

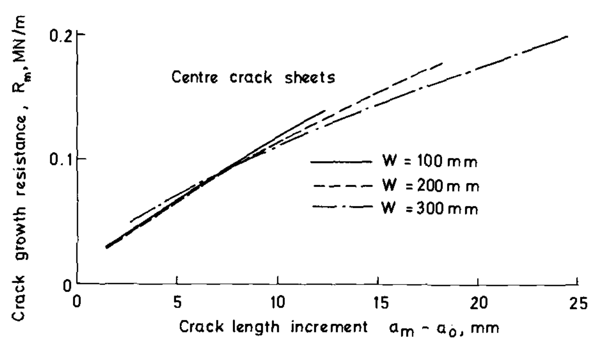

FIG. 4—*Crack growth resistance curves for compliance indicated crack lengths in L 104.*

that while a_m is a compliance indicated crack length and includes yield effects, a_a is an absolute crack length actually measured on the specimen surface and does not include the influence of crack tip yielding. It must be borne in mind that in these two figures the value of R_a is calculated in terms of the applied stress and absolute crack length a_a. Hence, for any particular stress level or applied load, the value of R_a in Figs. 7 and 8 is lower than the calculated value of R_m in Figs. 4, 5, and 6, since the latter is based on a compliance indicated crack length. As a consequence, direct comparisons between the results of Figs. 4 to 6, 7 and 8 cannot be made.

Values of fracture toughness can be calculated in a number of ways from the available data. The following three methods have been used.

1. Fracture toughness G_{c0} based on maximum gross stress and initial fatigue crack length, a_0.

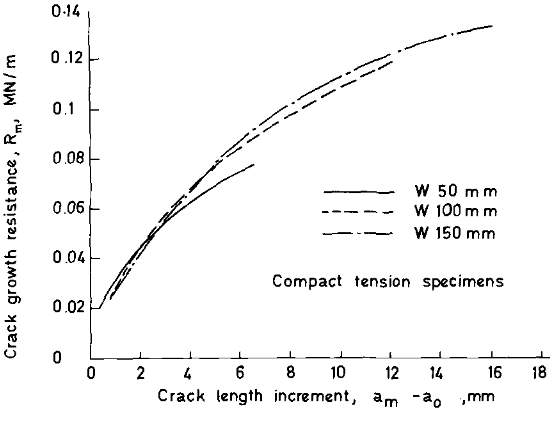

FIG. 5—*Crack growth resistance curves for compliance indicated crack lengths in L 104.*

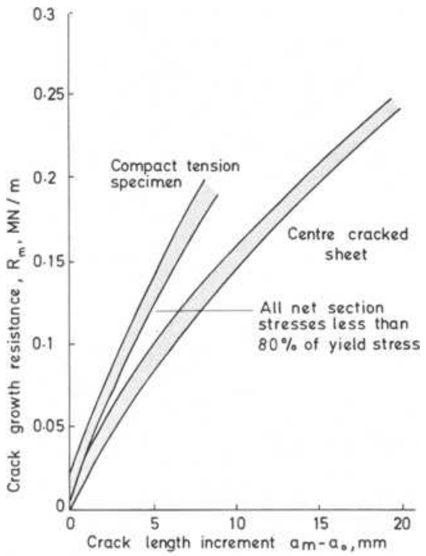

FIG. 6—*Scatter bands of crack growth resistance curves for compliance indicated crack lengths in Hiduminium 48.*

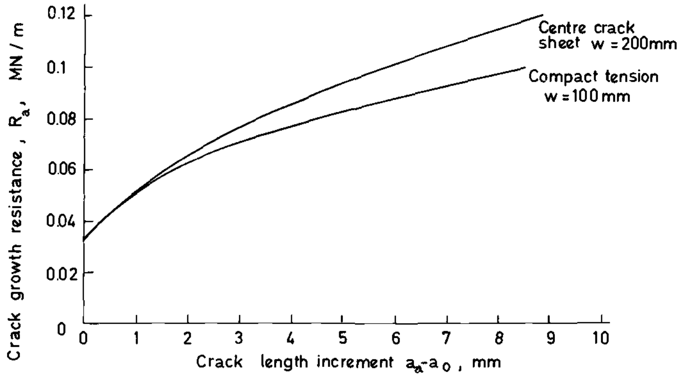

FIG. 7—*Crack growth resistance curves as a function of absolute crack length for L 104.*

2. Fracture toughness G_{cm} calculated on the basis of maximum gross stress and apparent crack length at instability, a_m, determined using the load-displacement record and the experimental compliance calibration.

3. Fracture toughness G_{ca} calculated on the basis of maximum gross

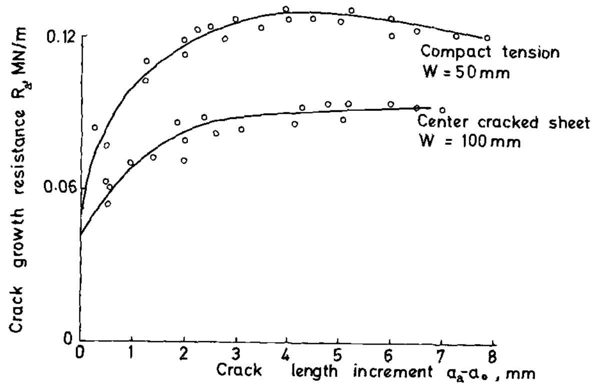

FIG. 8—*Crack growth resistance curves as a function of absolute crack length in Hiduminium 48.*

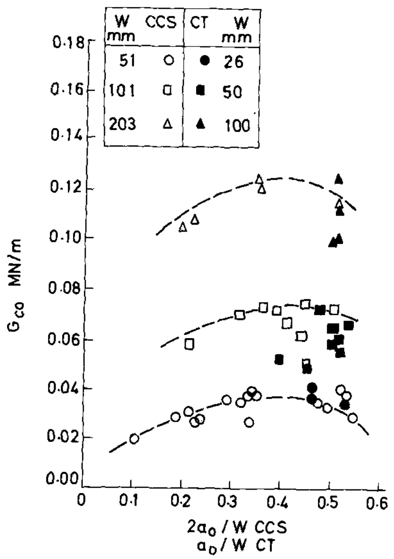

FIG. 9—*Variation in* G_{co} *with crack aspect ratio for CCS and CT specimens at various widths for Hiduminium 48.*

stress and absolute crack length a_a determined from the photographic records.

Finally the results for the toughness of Hiduminium 48 as expressed in

TABLE 1—*Comparison of average* G *values at instability for Hiduminium 48 and L 104.*

Alloy	Specimen Width, mm	G_{co} MN/m	G_{cm}, MN/m	G_{ca}, MN/m
Hiduminium 48	50	0.035	0.087	...
CCS	100	0.073	0.147	0.079
	200	0.115	0.240	...
CT	26	0.036	0.052	...
	50	0.063	0.103	0.10
	100	0.110	0.210	...
L 104				
CCS	100	0.056	0.122	0.076
	200	0.088	0.160	0.093
	300	0.112	0.212	0.132
CT	50	0.043	0.065	...
	100	0.068	0.104	0.089
	150	0.084	0.119	0.109

terms of G_{co} are presented graphically in Fig. 9, while average values of the three methods are given for both materials in Table 1.

Discussion of Results

Before proceeding to a detailed discussion of the relationship between experimental and analytical results, it is of value to put the experimental results in context with regard to the general conditions of failure. The resistance curve concept is an extension of linear elastic fracture mechanics to situations of contained yielding. At this time, the commonly accepted criterion for defining the limit of application of elastic analysis is that net section stress levels at instability should not exceed 80 percent of the yield stress. This criterion was not satisfied in all the tests reported.

For the CCS specimens all the test results on L 104 were acceptable with the exception of the 100 mm-wide specimens which failed at approximately 85 percent of the yield stress. For Hiduminium 48, the net section stresses at failure exceeded the 80 percent level but remained below general yield. Photographic records for Hiduminium 48 indicate the onset of stable tearing to commence at approximately 80 to 85 percent of the instability load. For the CT specimens, application of the 80 percent limit can not be applied readily due to the complex stress distribution across the ligament.

In Figs. 4 and 5 the resistance curves for L 104 based on compliance indicated crack lengths are presented for CCS and CT specimens, respectively. If these two figures were overlaid, certain differences between the resistance curves would be apparent. At lower R-values the CT curves are steeper. As the R-value increases, however, the slope of the resistance curves for the CT specimens decreases suggesting that, eventually, a plateau will be reached, that is, a limiting value of R. The CCS resistance curves do not exhibit this feature but show continually increasing values of R. In Fig. 6, the R-curves are shown for Hiduminium 48 and because of the greater differences both CCS and CT are shown together. In addition, the area on the curve below where net section stresses do not exceed 80 percent of yield is indicated. These results show no tendency to approach a plateau. The R-curves of Figs. 4 to 6 comprise all widths and initial crack lengths tested and indicate that, for each particular specimen type and material tested, when allowance is made for experimental scatter, there is a single R-curve within each category for the materials at the particular thickness. Thus for each material and specimen type, the shape of the R-curve is independent of the initial crack length and aspect ratio. However, because the toughness at failure, G_c, is defined by the tangency condition, it will vary as a function of crack aspect ratio.

Figures 7 and 8 show R-curves for both materials when calculated in terms of the absolute crack length. However, when presented in this manner, the relative behavior for the CCS and CT specimens varies with the material, but, it must be emphasized that in the case of Hiduminium 48 stable tearing was occuring at net section stresses about 80 percent of yield.

One feature that both Figs. 7 and 8 indicate is that, although the R-curves and final toughness G_c vary with specimen type and crack aspect ratio, respectively, the initiation of actual crack extension detected on the specimen surface does not appear to be influenced by these variables. The singular advantage of R-curves presented in the form of Figs. 7 and 8 is that they permit failure, at a specified stress level, to be characterized in terms of the absolute crack length and thus give a measure of the amount of stable tearing that will be visible on the structure surface.

In discussing the experimental results in relation to the analytical considerations, reference will be made to the previous section on the R-curve concept with the three specific conditions being referred to for brevity as: (*a*) a unique material G_c value exists, (*b*) a unique material R-curve exists, and (*c*) both a unique material R-curve and G_c value exist. Whether R-curves are plotted in terms of compliance indicated crack length or absolute crack length, there are differences between the two specimen types considered. Clearly a unique material R-curve does not exist, thus the conditions derived for (*b*) are invalid under those circumstances.

It was pointed out earlier that finite width effects lead to a variation in G_c, that is, G_c increases with increasing specimen width. It can be seen from Fig. 9 and Table 1 that such behavior is substantiated. That a unique value of G_c, as used in (*a*) for a given width shall exist for different configurations is contradicted by the results shown in Table 1 and the variation of G_{co} shown in Fig. 9 for Hiduminium 48.

The condition (*a*) indicated different R-curves for different configurations, and furthermore implies that the CT shall be steeper than the CCS. This condition is supported by both materials although it does change at higher values of R for L 104. The fact that in CT specimens the R-curve for L 104 approaches a plateau is a most significant feature. The implication is that the maximum toughness of a material will vary with the nominal net section stress distribution. This characteristic may well be allied to the influence of stress distribution on yield zone size.

As pointed out earlier in the paper, the final failure of Hiduminium 48 specimens appeared to be close to the onset of net section yielding. Thus, it was of some value to consider the relationship between the plastic zone size, r_y, and the crack length. This was done using the proposals of [*4*] relating r_y/a and $2a_m/w$ to describe reasonable limits of accuracy for G_c determination. The plastic zone size can be calculated iteratively using

$$r_y = \frac{1}{2\pi}\left(\frac{K}{\sigma_y}\right)^2 \tag{6}$$

in conjunction with K as described by Eqs 4 and 5. It would appear that at low aspect ratios r_y/a has reached a value at which accurate determination of G_c becomes questionable. Such a problem does not arise in the case of L 104 material. A point worth bearing in mind at this stage is that even if one questioned the final accuracy of the G_c value because of the plastic zone size at instability, the R-curve derived from the load-displacement record will still be valid up to that point on the load scale when the modified elastic analysis could be said to have broken down.

Applying the r_y correction of Eq 6 to CT specimens leads to values or r_y greater than the remaining ligament size in almost every Hiduminium 48 specimen, although this does not occur with L104. It is felt that this does not imply necessarily an inadequate specimen size, but poses more questions about the validity of the correction to CT specimens. It has been shown by analysis [*9*], etch techniques [*10*], and compliance and strain measurements [*5,6*] that the plastic zone is smaller in CT specimens than in CCS at comparable G values. In fact, just simple consideration of the state of stress and the steeper normal stress gradient ahead of the crack in CT and bend specimens will lead qualitatively to the same conclusion. In fact, confirmation that the yield zone sizes do differ with configuration is reflected in the difference between the compliance and absolute crack length R-curves of Figs. 4, 5, and 7 for L104 and Figs. 6 and 8 for Hiduminium 48. That is, if the yield zones were the same for both specimen types, then the R-curves of the two configurations would have the same relative shape whether plotted against absolute or compliance indicated crack length. Clearly this is not the case.

Finally, since the yield zone size influences the amount of irrecoverable work done prior to failure, it seems logical that CT specimens with their smaller plastic zones should not lead to such a high value of toughness as that measured in CCS and that the limiting value of resistance should begin to appear in narrower widths of specimen.

Concluding Remarks

By using the Y calibrations appropriate to CCS and CT specimens, it has been shown that in specimens of equivalent width a material cannot have both unique G_c values and an identical R-curve. The implications of the analysis were that if an R-curve were independent of the specimen configuration, then the toughness must vary or vice versa. Assuming a material to have characteristic G_c value at a particular width implies a steeper R-curve with smaller amounts of crack extension in CT specimens.

The experimental results from tests on two materials indicate that both the R-curve and G_c are dependent on specimen configuration. For the CCS, the nominal net section stress is wholly tensile, while for the CT specimen, the nominal net section stresses are predominantly bending. It has been shown previously that the plastic zone size is affected by the net section stress distribution. Because of the interaction of yield zone size and variation in Y function it is not possible to say which has the greater influence on R-curve shape. However, since the elastic analysis is not strictly applicable to plane stress failure it may well be that the plastic zone is the dominating factor.

The test results of L 104 show the CT R-curve to be rapidly approaching a plateau, while this is not evident in CCS. This behavior was not revealed in Hiduminium 48, but this may well be due to the fact the very wide specimens necessary to reduce the net section stress well below 80 percent yield could not be tested.

The test results for different crack lengths and crack aspect ratios, suggest that within experimental scatter the R-curve in a particular specimen type is independent of initial crack length.

Because failure is defined by the tangency of a G-curve to the material R-curve, it becomes important to analyze a structure, bearing in mind that both the R-curve and the Y function (and thus the resulting G-curves) vary with significant changes in the nominal net section stress distribution. Use of an inappropriate R-curve may well lead to very significant errors in estimated G_c values and amounts of permissible stable crack extension.

Acknowledgments

The author wishes to thank G. Munro for many useful discussions and his aid in conducting the experiments. This work was carried out under the sponsorship of a contract supported by Military Vehicles Engineering Establishment. Crown copyright reserved.

References

[1] "Methods for Plane Strain Fracture Toughness (K_{Ic}) Testing," DD3, British Standards Institution, 1971.

[2] Irwin, G. R., "Fracture Testing of High Strength Materials Under Conditions Appropriate for Stress Analysis," Report 5486, Naval Research Laboratory, July 1960.

[3] Kraft, J. W., Sullivan, A. M., and Boyle, R. W., *Proceedings,* Crack Propagation Symposium, College of Aeronautics, Cranfield, Vol. 1, Sept. 1961, pp. 8–28.

[4] Srawley, J. E. and Brown, W. F., *Symposium on Fracture Toughness and Its Application, ASTM STP 381,* American Society for Testing and Materials, 1965.

[5] Heyer, R. H. and McCade, D. E., *Engineering Fracture Mechanics,* Vol. 4, 1972, p. 393.

[6] Heyer, R. H. and McCade, D. E., *Engineering Fracture Mechanics,* Vol. 4, 1972, p. 413.

[7] Bradshaw, F. J., Lacey, D., and Wheeler, C., "The Effect of Section Thickness on the Crack Resistance of Aluminum Alloy L93 with Measurements of Plastic Strain," Technical Report 72039, Royal Aeronautical Establishment, March 1972.

[8] *Plane Strain Crack Toughness Testing of High-Strength Metallic Materials, ASTM STP 410,* American Society for Testing and Materials, 1967.

[9] Wilson, W. K., "Geometry and Loading Effects on Elastic Stress at Crack Tips," Research Report 67-ID7-BTLPV-RI, Westinghouse, 1967.

[10] Hahn, G. T., Sarrate, M., and Rosenfield, A. R., *International Journal of Fracture Mechanics,* Vol. 7, pp. 435–446.

[11] Adams, N. J., Munro, H. G,, Webber, D., and Roberts, C., "Fatigue and Fracture of an 18 Percent Nickel Maraging Steel Used for Military Bridging," Final Contract Report MVEE TR 72515, Military Vehicles Engineering Establishment, July 1972.

[12] Eftis, J. and Liebowitz, H., *International Journal of Fracture Mechanics,* Vol. 8, 1972, p. 383.

[13] Adams, N. J. and Munro, H. G., *Engineering Fracture Mechanics,* Vol. 6, 1974, p. 119.

R. L. Tobler [1]

Fatigue Crack Growth and J-Integral Fracture Parameters of Ti-6Al-4V at Ambient and Cryogenic Temperatures

REFERENCE: Tobler, R. L., "**Fatigue Crack Growth and J-Integral Fracture Parameters of Ti-6A1-4V at Ambient and Cryogenic Temperatures,**" *Cracks and Fracture, ASTM STP 601,* American Society for Testing and Materials, 1976, pp. 346–370.

ABSTRACT: Fatigue crack propagation and fracture parameters for 2.03-cm-thick compact specimens of an extra-low-interstitial Ti-6A1-4V alloy were measured at temperatures between 295 K (70°F) and 4 K (−453°F). Plane-strain linear-elastic and J-integral fracture toughness test results were in good agreement: the K_{Ic} values for this alloy decreased from 105 MN/m$^{3/2}$ at room temperature to 54 MN/m$^{3/2}$ at 4 K, and a ductile-to-brittle fracture transition occurred in the range 125 to 76 K (−235 to −323°F). Despite this transition, the fatigue crack growth rates (*da/dN*) of this alloy remained temperature insensitive over the entire ambient-to-cryogenic range. These fatigue and fracture results are compared with data previously reported for a normal-interstitial Ti-6A1-4V alloy.

KEY WORDS: crack propagation, fatigue (materials), fracture properties, J-integral, low temperature tests, titanium alloys

High ratios of strength-to-density and strength-to-thermal conductivity make titanium-6 percent aluminum-4 percent vanadium (Ti-6A1-4V) an attractive aerospace and cryogenic structural material. Often, service temperatures span the ambient-to-cryogenic range, and the mechanical properties at low temperatures may be critical in design.

Temperature reductions increase the yield strength and decrease the ductility of Ti-6A1-4V [*1*],[2] resulting in flaw-sensitive mechanical behavior. The normally ductile material may fail in a relatively brittle

---

[1] Metallurgist, Properties of Solids Section, Cryogenics Division, Institute for Basic Standards, National Bureau of Standards, Boulder, Colo. 80302.

[2] The italic numbers in brackets refer to the list of references appended to this paper.

manner in the presence of a fatigue crack under conditions of plane strain. A fracture mechanics analysis is often the best means of assuring structural reliability and design efficiency.

The few fracture data for Ti-6Al-4V (extra-low-interstitial (ELI)) alloys at cryogenic temperatures are insufficient: crack growth rate data at low temperatures are rare [2], fracture toughness data for thin sheet or plate [*3–5*] do not provide valid K_{Ic} data over the entire cryogenic to ambient range, and no data exist below liquid hydrogen temperature. The present paper provides some needed fracture toughness and crack growth rate parameters with emphasis at the temperatures 295, 76, and 4 K. Linear-elastic fracture mechanics and J-integral test results are compared, and the existence of a fracture transition in this material is demonstrated.

Experimental

Linear Elastic Fracture Mechanics

If a negligible amount of plastic deformation occurs prior to fracture, the ASTM Method of Test for Plane-Strain Fracture Toughness of Metallic Materials (E 399-74) can be applied. This method utilizes the stress intensity factor, K, to describe fracture behavior. For specimens of a standard geometry, K is calculated from the relation

$$K = \frac{P}{BW^{1|2}}[f(a/W)] \qquad (1)$$

where

P = applied load,
B = specimen thickness,
W = specimen width,
a = crack length, and
$f(a/W)$ = factor dependent on relative crack length.

Linear elastic conditions prevail for thick specimens where the plastic zone at the crack tip is constrained by the surrounding bulk of elastically loaded material. Under these conditions, materials loaded in tension exhibit a critical stress intensity factor, K_{Ic}, at which failure occurs spontaneously without significant plastic deformation.

The parameter K_{Ic} is a material property and a useful design criterion. Provided that specimen size requirements are met, K_{Ic} can be calculated from Eq 1 using the secant load, P_Q, determined from the fracture test record according to ASTM Method E 399-74. The size criterion assuring linear elastic behavior and valid K_{Ic} data is

$$a,\ b,\ B \geqslant 2.5 \left(\frac{K_{Ic}}{\sigma_{ys}}\right)^2 \qquad (2)$$

where

σ_{ys} = 0.2 percent offset yield strength of the material, and
b = specimen ligament ($b = W\text{-}a$).

Subsized specimens yield invalid fracture toughness measurements that are denoted K_Q.

J-Integral Analysis

Specimens that do not satisfy the thickness requirement of Eq 2 may exhibit nonlinear load-deflection behavior due to plastic deformation at the crack tip. In such a case, elastic stress field descriptors are not relevant, but the path-independent J-integral formulated by Rice [*6*] may be used to characterize fracture.

For nonlinear elastic materials, J represents the rate of change of potential energy with respect to crack area. Experimentally, the J-integral can be evaluated as an energy proportional to the area (A) under the load-versus-loadline deflection (δ) curve of a precracked specimen tested in tension or bending. The critical value, J_{Ic}, has been defined as the value of J required to initiate crack extension. Although a standard test procedure has not yet been developed, experiments by Begley and Landes [*7–9*] and others demonstrated that J_{Ic} is a meaningful fracture parameter for linear elastic, elastic-plastic, or fully plastic behavior. Recent applications include tests of Ti-6Al-4V at room temperature [*10,11*].

For standard compact specimens, J can be calculated using either of two equations. Assuming the specimen is in a state of pure bending, the following expression was derived [*12*]

$$J = \frac{2A}{Bb} \tag{3}$$

Although conservative to some degree, this expression yields adequate results for deeply cracked specimens where the assumption of pure bending is more appropriate [*12*]. Merkle and Corten pursued a more exact solution for the compact specimen, accounting for axial force as well as bending [*13*]. For linear elastic behavior

$$J = \frac{\lambda_J A}{Bb} \tag{4}$$

Here, λ_J is a factor ranging from 2.55 to 2.31, dependent on relative crack length [*13*]. This expression applies to a wider range of a/W, but data quantifying the scope and accuracies of Eqs 3 and 4 are lacking. Therefore, the present paper includes a comparison of critical J values calculated from both equations. The comparison is made for a range of a/W, in the linear-elastic case, where K_{Ic} data are also calculated using ASTM Method E 399-74.

Since the J-integral applies to plane strain, a size criterion is necessary to ensure that results will be independent of specimen dimensions and geometry. A tentative criterion is [*9*]

$$a,\ b,\ B \geqslant \alpha\left(\frac{J_{\text{Ic}}}{\sigma_{ys}}\right) \tag{5}$$

where α a may be a factor of 50. The specimen need not be as large as that required for linear-elastic tests; yet, the parameter J_{Ic} can be converted to K_{Ic} using the relation [*7*]

$$K_{\text{Ic}}{}^2 = \frac{E}{1-\nu^2} \times J_{\text{Ic}} \tag{6}$$

where E is Young's modulus, and ν is Poisson's ratio. Thus, it is possible to derive the linear-elastic fracture toughness value from smaller, plastic J-integral specimens. In this paper, the symbol K_{Ic} (J) distinguishes values obtained using Eq 6 from K_{Ic} data determined according to ASTM Method E 399-74.

Material and Specimen

Stock of an ELI Ti-6Al-4V alloy produced to aeronautical materials specification (AMS) 4930 was obtained in the form of a 2.54-cm-thick forged ring, 101.6 cm inside diameter (ID) by 106.7 cm outside diameter (OD). The material was annealed commercially at 1200 ± 14 K for 4 h, furnace cooled, and descaled. The microstructure, shown in Fig. 1, was primary alpha and beta with an average alpha grain diameter of 0.013 mm. The chemical analysis is listed in Table 1, and mechanical properties at primary temperatures of interest are listed in Table 2. The tensile properties were measured at room temperature according to ASTM Tension Testing of Metallic Materials (E 8-69) or estimated at cryogenic temperatures from handbook data [*1*].

All tests were performed using compact specimens of the geometry shown in Fig. 2. The specimen proportions were in general accordance with ASTM Method E 399-74, but a modified notch was introduced to enable loadline deflection measurements. The specimen thickness was 2.030 cm, the width-to-thickness ratio, *W/B*, was 2.0, and the orientation was LT [*15*].

Procedure

Young's modulus and Poisson's ratio were measured at room temperature using the ultrasonic pulse-superposition method. The results were equivalent (±1 percent) to those reported for a similar heat [*14*]. Since the

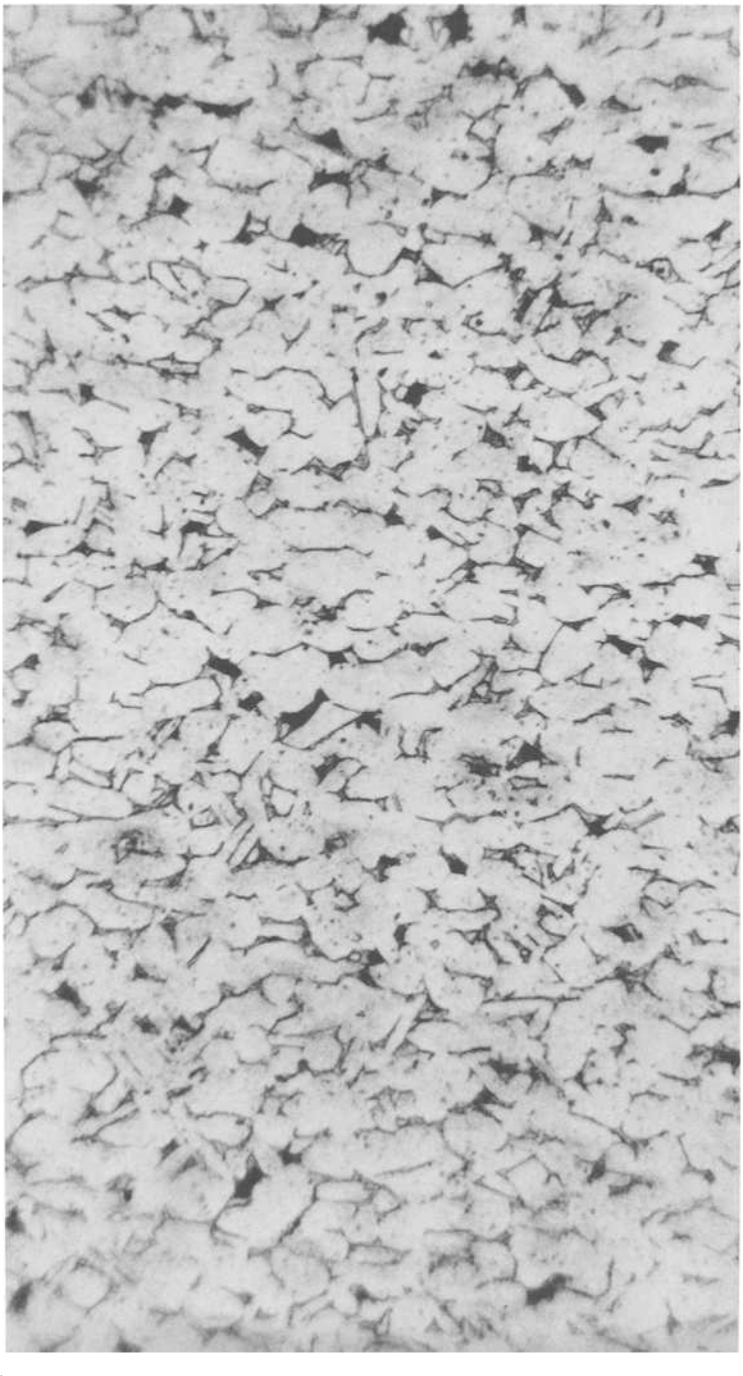

FIG. 1—*Microstructure of ELI Ti-6Al-4V alloy (etchant 10 HF, 5* HNO_3*, 85* H_2O*) X 250.*

TABLE 1—*Chemical analysis (weight percent).*

Ti	Al	V	Fe	O	C	N	H
Balance	5.91	3.94	0.103	0.110	0.018	0.014	52 ppm

TABLE 2—*Representative mechanical properties.*

Temperature, K	0.2 percent Yield Strength, 10^8 N/m^2	Ultimate Strength, 10^8 N/m^2	Elongation, %	E [14], 10^{11} N/m^2	ν [14]
295	8.3	8.9	14	1.11	0.323
76	14.9	15.0	10	1.21	0.310
4	16.6	17.1	4	1.22	0.309

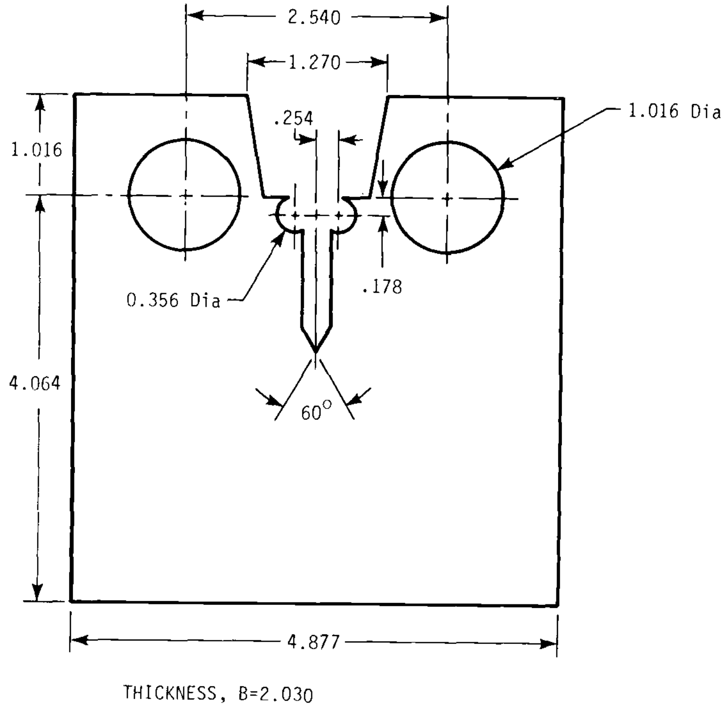

FIG. 2—*Compact specimen (cm).*

elastic properties of Ti-6Al-4V are regular functions of temperature, the low temperature elastic constants presented by Naimon et al could be used with good accuracy [*14*].

Fatigue and fracture tests were performed using a 100-kN capacity servohydraulic testing machine and cryostat. As described elsewhere [*16*], a vacuum-insulated dewar containing liquid nitrogen or liquid helium encloses the load frame, specimen, and clip gage during tests at 76 or 4 K. In this study, intermediate temperatures were obtained by admitting cold nitrogen vapor to the dewar. A chromel-constantan thermocouple was attached to the specimen during these tests and a servomechanical temperature controller regulated the vapor flow such that temperatures of 200, 125, and 110 K were maintained within ±3 K. Clip gage calibrations at temperatures from 295 to 4 K verified that the gage sensitivity changed by only 1.5 percent and linearity corresponded to ASTM Method E 399-74 requirements.

Using load control, the specimens were precracked and then fractured at identical temperatures. The loading rate to fracture corresponded to a stress intensity factor increase of about 1.0 $MN/m^{3/2}/s$. Critical stress intensity factors were calculated using the ASTM Method E 399-74 solution for f (a/W). The J-integral calculations were performed for the same specimens using Eqs 3 and 4 where the area, A, was measured with a planimeter at points of interest, and λ_J values were interpolated from the published solution [*13*].

For low temperature tests, fracture toughness calculations were performed at the load point, P_Q, in accordance with ASTM Method E 399-74, and at other points described in the text. At room temperature, stable crack extension occurred and the J-resistance curve (J versus Δa) was determined following a procedure outlined by Begley and Landes [*9*]. Six identical specimens ($a/W = 0.578 \pm 1$ percent) were loaded to cause decreasing amounts of crack extension. These specimens were then unloaded and heat tinted 10 min at 900 K to oxidize the surfaces where crack extension had taken place. The specimens were finally fractured into halves and the increments of crack extension, Δa, were measured with a traveling microscope at locations corresponding to 25, 50, and 75 percent of specimen thickness. The values of J were calculated using Merkle and Corten's method [*13*].

Most fatigue crack growth data were obtained during precracking of fracture toughness specimens. The maximum fatigue stress intensity, K_f, was maintained within ASTM Method E 399-74 specifications. At two temperatures (295 and 76 K), additional specimens were tested solely for crack growth data at higher stress intensity factors.

Fatigue crack growth was monitored by elastic compliance measurements, an approach based on the fact that specimen compliance, δ/P, increases with increasing crack length. The correlation between crack length and compliance was determined experimentally by plotting the crack lengths of fractured specimens versus the dimensionless parameter $EB\ \delta/P$. Changes in clip gage sensitivity and Young's modulus with temperature were accounted for in the term $EB\ \delta/P$, and a single correlation curve was obtained as shown in Fig. 3.

Crack growth rates were determined by plotting the static compliance with an X-Y recorder at intervals during the fatigue tests. Using the correlation shown in Fig. 3, the average crack length could be inferred at any time. The crack lengths were plotted versus cycles, N, and the growth rates, da/dN, were obtained by graphical differentiation. Stress intensity factor ranges, ΔK, were calculated as the difference between the maximum and minimum fatigue stress intensities.

The loads during fatigue were measured to ±1 percent by means of a digital peak load indicator. The load cycle was sinusoidal at a frequency of 20 Hz and a minimum/maximum load ratio of 0.1.

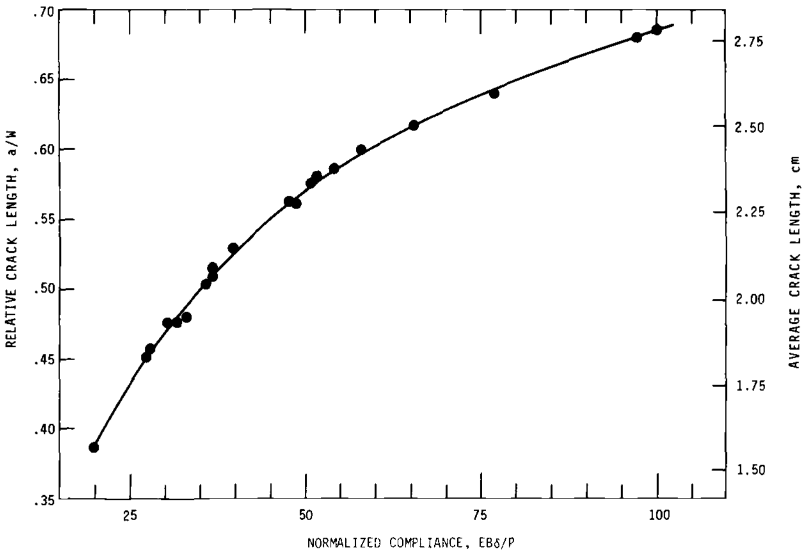

FIG. 3—*Crack length versus compliance.*

Results

Fatigue Crack Growth

Fatigue crack growth rates are shown in Fig. 4. The data define a slightly curved scatter band that increases in width at higher stress intensity ranges. The results at 295, 200, 76, and 4 K are nearly equivalent, and no pronounced temperature effects can be distinguished from the scatter among specimens.

As shown in Fig. 4, the data trend is best approximated by two straight line segments intersecting at $\Delta K = 20$ MN/$m^{3|2}$. The equations describing these linear segments are of the form suggested by Paris and Erdogan [*17,18*]

$$da/dN = C(\Delta K)^n \tag{7}$$

Although a single Paris equation is sometimes preferred to describe crack growth rates over wide ranges of ΔK, the results in Fig. 4 and elsewhere [*19–21*] do not conform rigorously with a single-equation format. The empirical constants, C and n, which correspond to the linear approximations of Fig. 4, were determined graphically and are specified in that figure.

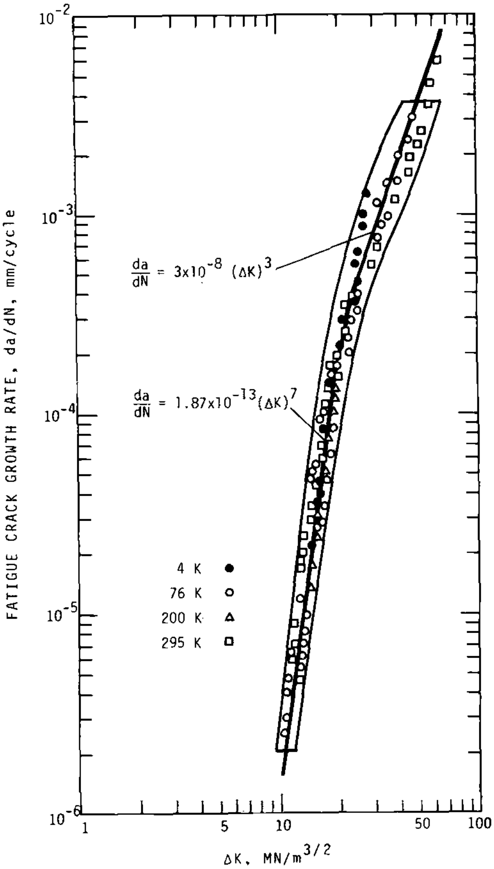

FIG. 4—*Growth rate data of ELI Ti-6Al-4V alloy.*

A band representing data for a normal interstitial grade of Ti-6Al-4V is superimposed on the present results in Fig. 5. Similarly, data for the normal grade were obtained at 295, 76, and 4 K, but the results were temperature independent over the range of Δ*K* investigated [*16*]. The overlap of bands in Fig. 5 suggests that a variation in the level of interstitials does not significantly influence the growth rates of these alloys. Note that these results were obtained using identical test procedures.

Fracture Toughness

Macroscopic features of specimens loaded directly to failure are shown

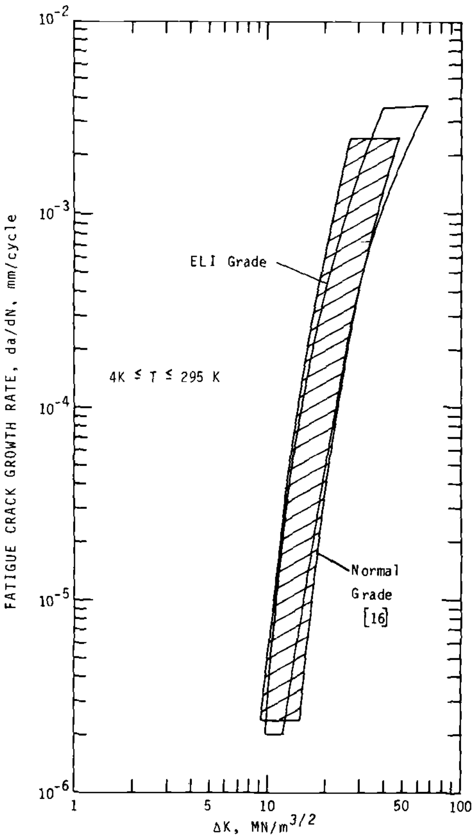

FIG. 5—*Growth rate data of Ti-6Al-4V alloys.*

in Fig. 6. The fracture surfaces indicate decreasing toughness at cryogenic temperatures. Slant and flat fracture modes are evident at each temperature, but the proportion of slant fracture at specimen edges decreases from 23 percent at room temperature to 5 percent at 4 K. Also, the flat fracture region becomes progressively smoother as temperature is lowered from 295 to 4 K. Similar trends but less noticeable changes were reported for the normal-interstitial alloy [*16*].

The variety of P-δ behaviors observed is shown in Fig. 7. A transition from elastic-plastic to linear-elastic behavior occurs at about 125 K, and at 110 K the behavior is ideally linear elastic. At more extreme temperatures, fast fracture terminates the curves after a series of pop-ins, increments of unstable crack extension. The pop-ins, which were faint and sometimes barely perceptible, produced small step-like discontinuities

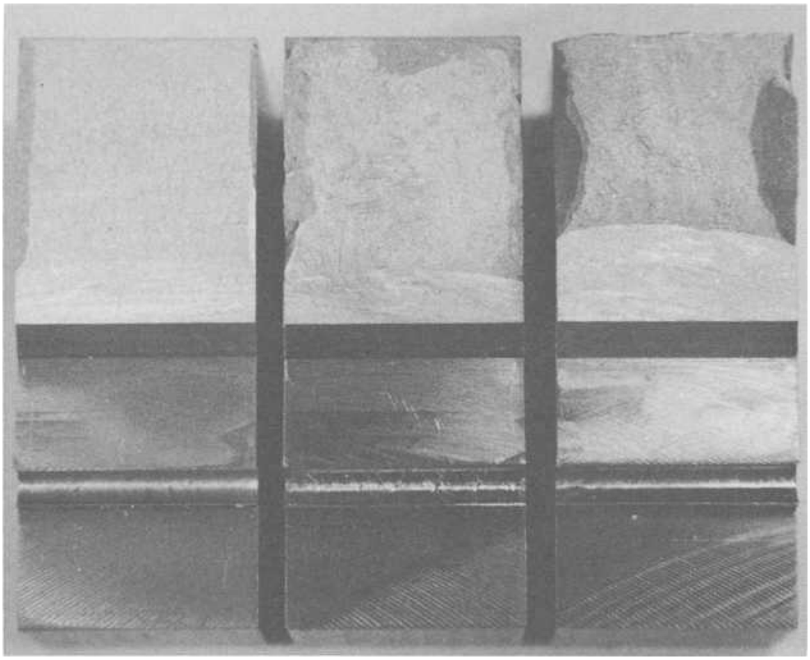

FIG. 6—*Surface appearances of 2.030-cm-thick ELI Ti-6Al-4V fractured at (left to right) 4 K, 110 K, and 295 K.*

beginning at about 0.95 P_Q. Thus, specimens at 76 and 4 K failed in linear-elastic plane strain but deviations from the initial P-δ slopes are evident. Table 3 cites the relationships among P_Q, $P_{\max}$, and the load at the first noticeable pop-in, P_p.

Linear-Elastic Fractures

Of all the results summarized in Tables 4 and 5, the test at 110 K affords the simplest interpretation. The K_{Ic} and J_{Ic} measurement point at

TABLE 3—*Summary of load-deflection behaviors.*

Temperature, K	ASTM Method E 399 Classification	Category	Order of Load Points
295,200	no designation	elastic-plastic	$P_Q<P_{\max}<P_p$
125	Type I	linear-elastic	$P_Q<P_{\max}=P_p$
110	Type III	linear-elastic	$P_Q=P_{\max}=P_p$
76, 4	Type II	linear-elastic	$P_p<P_Q\leq P_{\max}$

TABLE 4—*ASTM Method E 399-74 test results.*

Specimen	Temperature, K	K_f, MN/m$^{3/2}$	a, cm	a_e/a^a, %	a/W	P_{max}/P_Q	K_Q, MN/m$^{3/2}$	K_{Ic}, MN/m$^{3/2}$	R_{Sc}
6 [b]	295	32.0	2.352	0.95	0.579	N/A	N/A	N/A	N/A
7 [c]	295	32.0	2.364	0.93	0.582	N/A	77.5	invalid [d]	N/A
8	295	34.6	2.349	0.93	0.578	1.41	83.2	invalid	1.31
9 [c]	295	35.0	2.337	0.96	0.575	N/A	78.9	invalid	N/A
10 [c]	295	29.6	2.372	0.92	0.584	N/A	82.3	invalid	N/A
15 [c]	295	29.5	2.320	0.93	0.570	N/A	85.9	invalid	N/A
17 [c]	295	29.5	2.337	0.94	0.575	N/A	88.5	invalid	N/A
20	200	29.0	2.151	0.90	0.529	1.17	84.5	invalid [d]	0.87
19	125	25.0	1.956	0.96	0.481	1.03	$K_Q = K_{Ic}$	100	0.70
18	110	24.0	2.096	0.92	0.516	1.00	$K_Q = K_{Ic}$	78.0	0.55
1	76	26.3	2.085	0.93	0.513	1.06	$K_Q = K_{Ic}$	61.7	0.46
2	76	34.4	2.337	0.91	0.575	1.00	$K_Q = K_{Ic}$	61.0	0.47
3	76	24.5	2.618	0.95	0.644	1.00	$K_Q = K_{Ic}$	61.6	0.54
4	76	24.0	2.746	0.97	0.675	1.00	$K_Q = K_{Ic}$	59.9	0.53
11	4	25.9	2.319	0.95	0.570	1.06	$K_Q = K_{Ic}$	54.0	0.39
12	4	30.9	2.057	0.97	0.506	1.00	$K_Q = K_{Ic}$	53.7	0.33
13	4	29.6	1.854	0.95	0.454	1.04	$K_Q = K_{Ic}$	54.6	0.33

NOTE—N/A = not applicable.

[a] a_e = crack length at specimen edge.

[b] Unloaded prior to P_Q.

[c] Unloaded prior to P_{max}.

[d] $P_{max}/P_Q > 1.10$ and insufficient thickness.

TABLE 5—*J-integral results at cryogenic temperatures.*

Specimen	Temperature, K	a/W	λ_J	$E/(1-\nu^2)$, 10^{11}N/m^2	$J_Q{}^a$, kJ/m^2	$K_Q(J)/K_{Ic}$	$J_{Ic}{}^b$, kJ/m^2	$K_{Ic}(J)$, MN/m$^{3/2}$	$K_{Ic}(J)/K_{Ic}$
19	125	0.481	2.45	1.32	95.4	1.12	82.5	104.3	1.04
18	110	0.545	2.45	1.33	49.9	1.04	49.9	81.4	1.04
1	76	0.573	2.45	1.34	31.7	1.06	28.8	62.1	1.01
2	76	0.575	2.41	1.34	35.8	1.11	30.1	63.5	1.04
3	76	0.644	2.34	1.34	33.3	1.08	30.1	63.5	1.03
4	76	0.675	2.32	1.34	30.7	1.07	28.7	61.9	1.03
11	4	0.570	2.41	1.35	25.2	1.08	23.6	56.4	1.04
12	4	0.506	2.46	1.35	23.6	1.05	22.6	55.2	1.03
13	4	0.454	2.48	1.35	23.4	1.03	22.3	54.9	1.00

[a] Measured at P_Q.
[b] Measured at $P_Q{}'$.

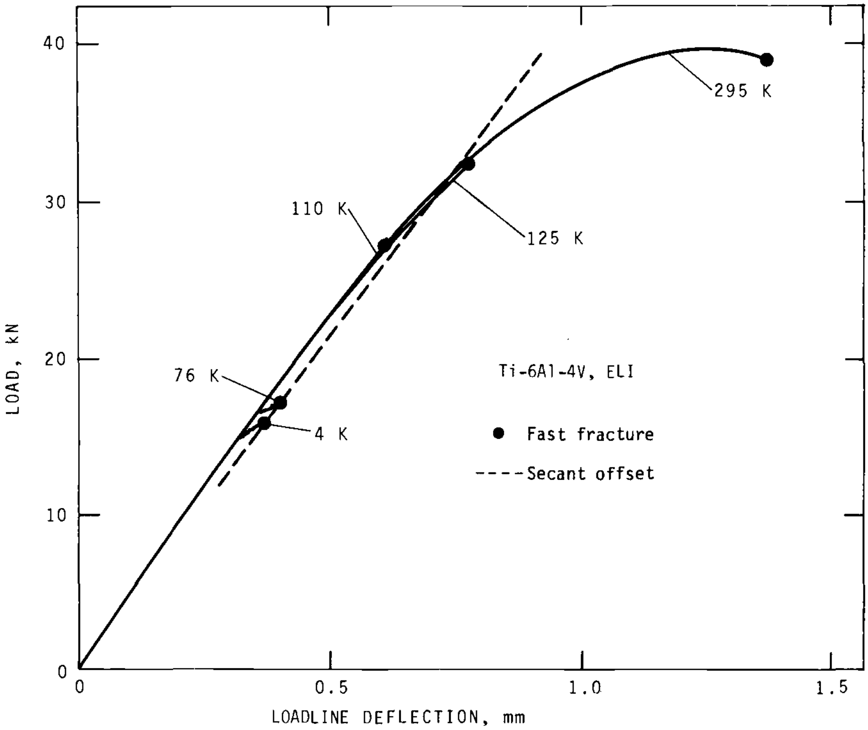

FIG. 7—*Load-deflection records of 2.030-cm-thick compact specimens normalized for* a/W = *0.58.*

this temperature is unambiguous since $P_p = P_Q = P_{\max}$. The linear-elastic K_{Ic} result (78 MN/m$^{3|2}$) is in good agreement with the $K_{Ic}(J)$ value (81.4 MN/m$^{3|2}$) obtained using Eqs 4 and 6. The ratio $K_{Ic}(J)/K_{Ic}$ is 1.04, indicating that the results from two test procedures are equivalent within 4 percent for an ideal linear-elastic P-δ record.

The K_{Ic} data obtained at 76 and 4 K are shown in Table 4. The J-integral was evaluated at the K_{Ic} measurement point, P_Q, and the results denoted J_Q are listed in Table 5. In comparison, the ratios of $K_Q(J)/K_{Ic}$ ranged from 1.03 to 1.12, indicating wider disagreement than observed at 110 K. This apparent disagreement is due to the effects of pop-ins on J-integral calculations. Pop-in phenomena at these lower temperatures violate the assumption of monotonic loading made in the J-integral formulation [*6*]. Complete agreement between J and K measurements is expected only if comparison is made at identical points on a perfectly linear P-δ record. At 76 and 4 K, the $K_Q(J)$ values exceed the values of K_{Ic} because pop-ins prior to P_Q increase the area under the test records without proportionate increases in load.

In this study, errors in J-integral calculations at P_Q due to slight nonlinearity or pop-in were corrected as shown in Fig. 8. According to this procedure, the initial linear slope of the P-δ record is extrapolated up to a point P_Q', which is equal in magnitude to P_Q, and J is calculated from the triangular area $OP_Q'\delta'$

$$J = \frac{\lambda_J}{Bb} \left(\frac{1}{2} P_Q'\delta' \right) \tag{8}$$

where δ' is the hypothetical deflection associated with P_Q', as defined in the figure. Values of J adjusted by measuring at P_Q' are labeled J_{Ic} in Table 5. The correction brings $K_{\text{Ic}}(J)$ and K_{Ic} data into agreement within 4 percent, which is equivalent to the agreement at 110 K where no correction was necessary. The correction procedure was also applied to the test record at 125 K where nonlinearity could be attributed to stable crack extension.

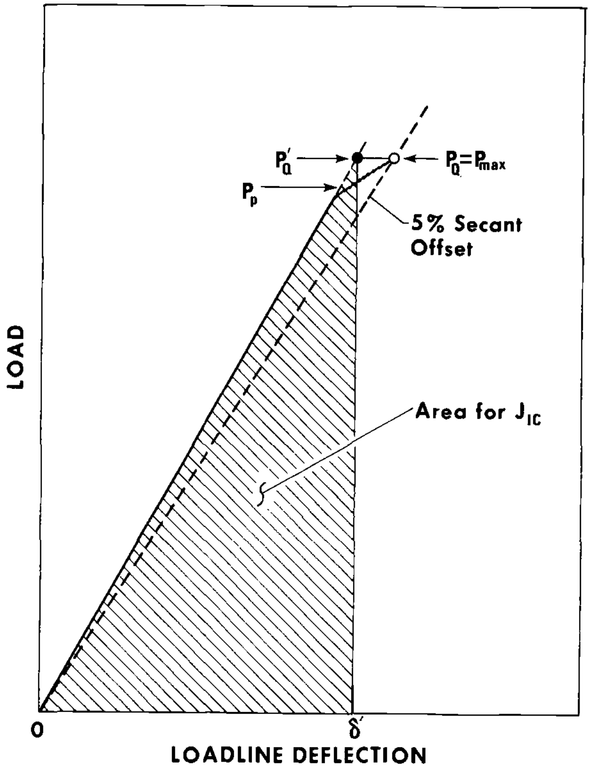

FIG. 8—J_{Ic} calculation, adjusted for effects of pop-in (schematic).

The J-integral calculations above incorporated the values of λ_J which apply to linear-elastic conditions. Using $J = 2A/Bb$, where λ_J is replaced by the constant 2, yields underestimates of the fracture parameters. At 110 K, the critical stress intensity factor converted from $J = 2A/Bb$ underestimated K_{Ic} by 6 percent. At 76 and 4 K, similar calculations at P_Q' yielded conservative errors as high as 10 percent, the results varying as a function of a/W as shown in Fig. 9. For a/W equivalent to 0.6 or greater, the disparity amounts to 4 or 5 percent. Merkle and Corten's expression for J, Eq 4, appears to be more accurate, leading to converted K values that overestimate K_{Ic} by an average of about 3 percent for the range of a/W from 0.45 to 0.70.

Elastic-Plastic Fractures

A single test at 200 K did not yield a K_{Ic} datum. The ASTM Method E 399-74 requirement that $P_{max}/P_Q \leq 1.10$ was not satisfied at this temperature. Nor could $K_{Ic}(J)$ be obtained, since the J_{Ic} measurement point could not be identified from the test record.

At room temperature one specimen was loaded to the point of fast fracture, while six others were unloaded at points along the P-δ diagram. The six corresponding values of J and Δa are shown on the J-resistance curve of Fig. 10. There is some data scatter, but the resistance curve appears to be linear at crack extensions greater than 0.12 mm. Since methods of defining a discrete J_{Ic} measurement point for such a curve have not been standardized, several plausible alternatives are considered.

1. The trend at high Δa may be linearly extrapolated to $\Delta a = 0$, identifying J_{Ic} as the intercept on the J axis [22]. The broken line in Fig. 10 indicates in this case that $J_{Ic} \cong 80$ kJ/m^2.
2. As described elsewhere [9,23], the line $J/2\sigma_{ys}$ may be constructed, its intersection with the resistance curve representing J_{Ic}. Applied to Fig. 10, this method yields $J_{Ic} \cong 88$ kJ/m^2.
3. A significant amount of crack extension, Δa_c, may be defined as critical. Since good results for Ti-6Al-4V alloys were obtained by specifying $\Delta a_c = 1$ percent [11], the same criterion might be applied here. Then, the resistance curve at 1 percent crack extension yields $J_{Ic} \cong$ 100 kJ/m^2.

Summarizing, the J_{Ic} value at room temperature lies in the range 90 ± 10 kJ/m^2, depending on the method applied to select the measurement point from the resistance curve of Fig. 10. The corresponding values of $K_{Ic}(J)$ given by Eq 6 are in the range 105 ± 6 MN/m$^{3|2}$. This range of $K_{Ic}(J)$ is nearly in agreement with room temperature ASTM Method E 399-74 test results for other ELI grade Ti-6Al-4V alloys; values from 102 to 121 MN/m$^{3|2}$ have been reported [24,25]. Using the $K_{Ic}(J)$ value in Eq 2, an estimated 4.0-cm-thick specimen would be required to produce linear-elastic fractures in this material at room temperature.

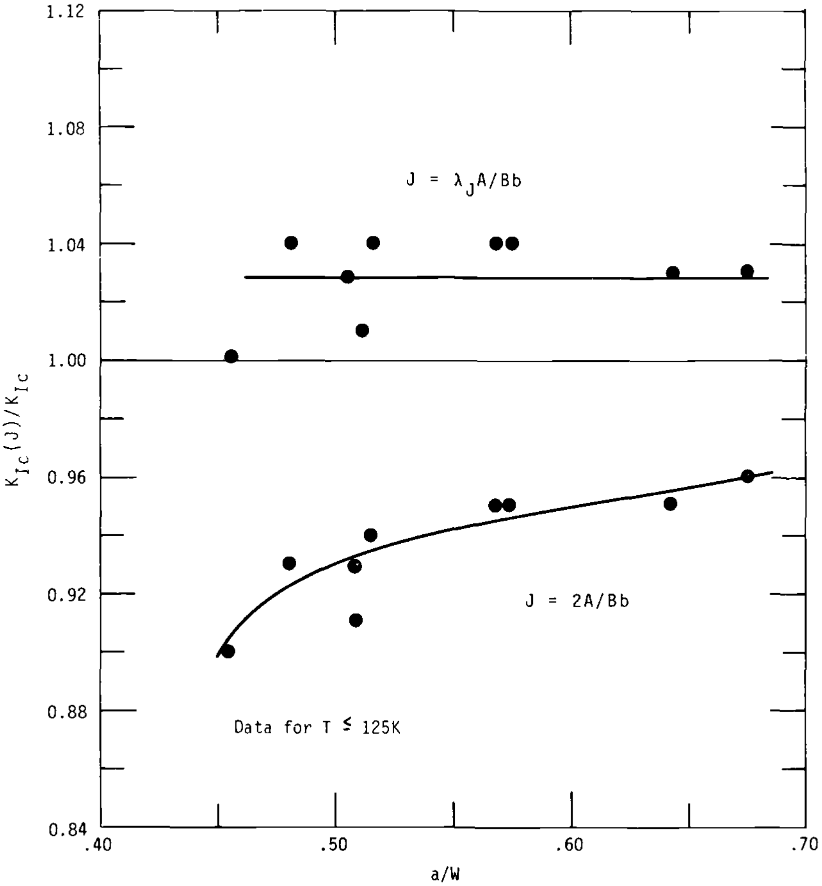

FIG. 9—*Agreement of* K_{Ic} *and J-integral results, as calculated from two equations.*

Effect of Temperature

The specimen strength ratio, R_{Sc}, is listed for each temperature in Table 4. Defined according to ASTM Method E 399-74, R_{Sc} is the ratio of the maximum nominal net-section fracture stress to the tensile yield strength

$$R_{Sc} = \frac{2P_{\max}(2W + a)}{B(W - a)^2\sigma_{ys}} \tag{9}$$

Referring to R_{Sc}, Section 4.1.3 of ASTM Method E 399-74 states: "It is significant as a comparative measure of material toughness when results are compared from specimens of the same form and size, and when this

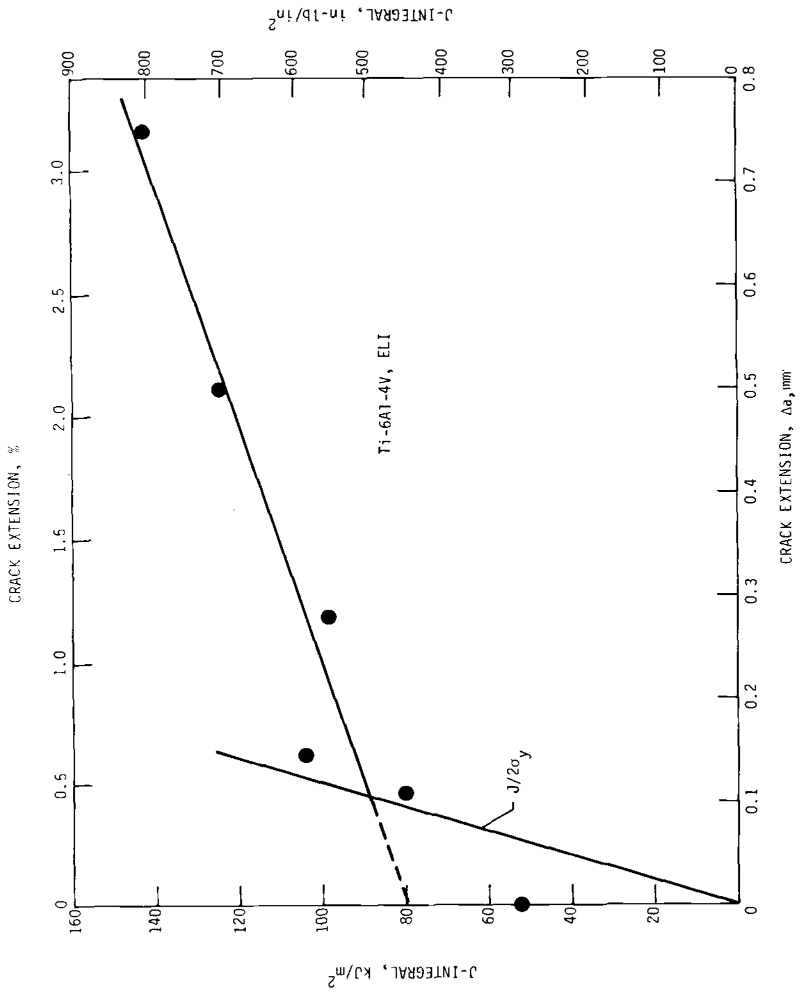

FIG. 10—*J-resistance curve at 295 K.*

size is sufficient that the limit load of the specimen is a consequence of pronounced crack extension prior to plastic instability. . . ."

As a qualitative parameter, R_{Sc} can be used here to rank the effect of temperature on toughness. The observed increase of R_{Sc} between 125 and 295 K implies that J_{Ic} for this material at room temperature should exceed 82.5 kJ/m^2, the J_{Ic} value at 125 K. Consequently, 82.5 kJ/m^2 could be taken as a lower bound for J_{Ic} at room temperature. Critical values from 80 to 100 kJ/m^2 were obtained from Fig. 10 and, although these values vary depending on how the resistance curve is drawn to account for scatter, it appears that the J-integral results at 295 K are consistent with the linear-elastic results at lower test temperatures.

The temperature dependence of K_{Ic} is shown in Fig. 11. The fracture toughness of the ELI alloy remains at a high-shelf level as temperature is reduced from 295 to 125 K, but an abrupt decline of K_{Ic} occurs in the range 125 to 76 K. Temperature reductions in this narrow interval decrease K_{Ic} by 45 percent while temperature reductions from 76 to 4 K decrease K_{Ic} slightly. The abrupt change in behavior between 125 and 76 K constitutes a ductile-to-brittle fracture transition, which, although commonly associated with beta titanium alloys and other body-centered cubic (bcc) and hexagonal close-packed (hcp) materials, has not been documented previously for a Ti-6A1-4V alloy.

The fracture mode and R_{Sc} parameters apparently reflect this fracture transition. Plotted as a function of temperature in Fig. 12, the percent slant fracture displays a trend similar to that of K_{Ic} data. The R_{Sc} values also exhibit a step-like decrease between 125 and 110 K, but the effect is subtle. In contrast to the trends of K_{Ic} and slant fracture modes, R_{Sc} does not exhibit a relatively constant "upper shelf" value.

Discussion

Valid K_{Ic} data for a normal-interstitial grade of Ti-6Al-4V were also shown in Fig. 11. These results were obtained for 2.54-cm-thick compact specimens [*16*]. The normal grade had a microstructure resembling that of the ELI alloy, except that the average alpha grain diameter was 0.006 mm. In comparison, the normal grade exhibits low toughness at each temperature, and it does not exhibit transitional behavior over the range of temperatures investigated.

However, tests at higher temperatures than represented in this study might have revealed a transition in the normal grade. The transition temperature regime should vary with parameters such as grain size and composition. A finer grain size should tend to lower the transition temperature, whereas high impurity content tends to raise it [*26–28*]. Since the properties of titanium alloys are particularly sensitive to interstitial content [*29,30*], it seems possible that the normal grade of Ti-6A1-4V

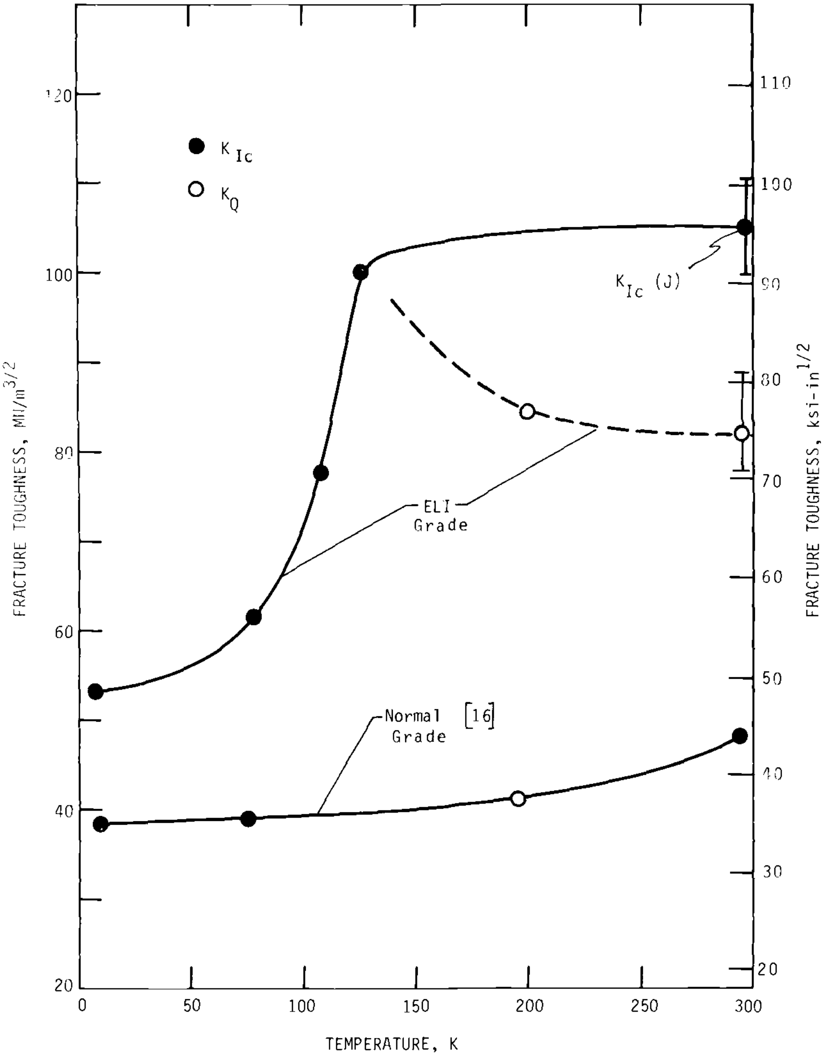

FIG. 11—*Temperature dependence of* K_{Ic} *for Ti-6Al-4V alloys.*

contained a level of embrittling elements sufficient to raise the transition temperature above 295 K.

A quantitative relationship between interstitial content and K_{Ic} values has never been demonstrated, but the difference in toughness between normal and ELI Ti-6Al-4V grades is large. It may seem surprising that there is little difference in crack growth rates, but data for other types of

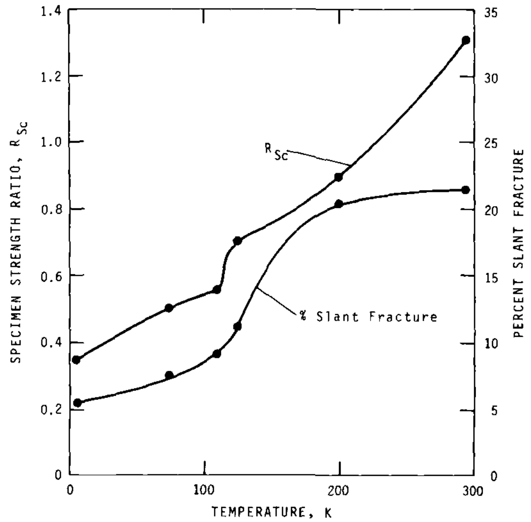

FIG. 12—*Temperature dependence of qualitative fracture parameters for 2.030-cm-thick compact specimens of Ti-6Al-4V, ELI.*

alloys have often led to the conclusion that rates of crack growth at intermediate ΔK values are not highly sensitive to compositional variations [*31,32*].

The temperature independence of fatigue crack growth resistance is also remarkable. Wei and Ritter [*19*] found the crack growth rates of a normal grade of Ti-6Al-4V to be equivalent between 295 and 563 K, while Pittinato's data [2] for a normal grade appear temperature insensitive between 145 and 295 K. The rates from these and other sources [*20,21*] compare quite closely with the data in Fig. 5, supporting the conclusion that the rates for Ti-6Al-4V alloys are relatively constant for over five hundred kelvins.

Cryogenic fracture toughness data for ELI grades of Ti-6Al-4V are available from single-edge-notched or part-through-cracked specimens 0.162 to 0.325 cm thick [*3–5*]. The part-through-cracked specimens simulate surface flaws that occur in service, but the results are considered directly applicable only where service conditions match the specifics of specimen design [*33*]. Some of these data at 77 K are nearly equivalent to the present results for compact specimens while others are not. In any case, the values quoted for nonstandard specimens cannot be termed valid K_{Ic} data until their independence of specimen geometry and flaw shape is proved.

The AMS 4930 specification requires a room temperature K_{Ic} value of at least 60.4 MN/m$^{3/2}$, stating that the ELI alloy is useful at temperatures as low as 20 K. The present alloy amply exceeds this requirement, but the implied limitation to 20 K seems arbitrary. Other structural materials such as ferritic steels are seldom used below their ductile-to-brittle transition temperatures. If the ELI grade of Ti-6A1-4V is an exception, it should be considered useful at any cryogenic temperature; there is only a small change in toughness between 20 and 4 K.

If stable crack extension does not occur, and J_{Ic} is strictly defined as the value of J just prior to crack extension, it seems logical to choose the load point at the first noticeable pop-in, P_p, as the J_{Ic} measurement point. For the tests described here at 76 and 4 K, P_p could be considered a possible measurement point. However, the appearance of load point discontinuities in test records is affected by material and experimental variables, and the identification of such a measurement point is also dependent on judgment in cases where pop-ins are faint and indistinct. The ASTM Method E 399-74 procedure obviates these problems by defining K_{Ic} at P_Q, which corresponds to an effective crack extension of 2 percent [*34*]. Following the standard procedure in this study, P_p could not be taken as the K_{Ic} measurement point for tests at 76 and 4 K. Similarly, the 2 percent point served as a basis for J_{Ic} measurements in the linear-elastic case. Here, it was desirable to maintain consistency with ASTM Method E 399-74 results by measuring J_{Ic} at $P_Q{}'$ as described in the text.

Summary

1. The ELI grade of Ti-6A1-4V exhibits a ductile-to-brittle transition in the temperature interval 125 to 76 K; the fracture toughness significantly exceeds that of a normal grade at all temperatures between 295 and 4 K.

2. The fatigue crack growth rates of Ti-6A1-4V alloys were nearly temperature and purity independent for 10 MN/m$^{3/2}$ $\leq \Delta K \leq$ 50 MN/m$^{3/2}$.

3. The J-integral fracture criterion provided meaningful results for a spectrum of load-deflection behaviors; J_{Ic} data for the elastic-plastic case were consistent with valid K_{Ic} data for this material.

4. Critical values of the J-integral calculated from the equation $J = 2A/Bb$ led to converted K_{Ic} values that appeared to underestimate ASTM Method E 399-74 linear-elastic fracture toughness values by 4 to 10 percent, depending on a/W; the equation $J = \lambda_J A/Bb$ led to modest overestimates of about 3 percent, independent of a/W.

Acknowledgments

This work was sponsored by Kirtland Air Force Base and the Advanced Research Projects Agency; it is a contribution of NBS, not subject to copyright.

The test material and room temperature tensile data were furnished by Beech Aircraft Division in Boulder, and the chemical analysis was performed by Titanium West, Reno, Nev. The elastic properties at room temperature were measured by W. Weston of the NBS Cryogenics Division; E. Ballinger, B. Crockett, and S. Naranjo also aided in data reduction. All of this assistance is appreciated.

References

[*1*] *Handbook on Materials for Superconducting Machinery,* MCIC-HB-04, Metals and Ceramics Information Center, Battelle Columbus Laboratories, Ohio, 1974.
[*2*] Pittinato, G. F., *Metallurgical Transactions,* Vol. 3, 1972, pp. 235–243.
[*3*] Witzell, W. E., "Fracture Data for Materials at Cryogenic Temperatures," Technical Report AFML-TR-67-257, Air Force Materials Laboratory, and AD 825264, General Dynamics-Convair, 1967.
[*4*] Tiffany, C. F. and Lorenz, P. M., "An Investigation of Low Cycle Fatigue Failure Using Applied Fracture Mechanics," Technical Document Report ML-TDR-64-53, Boeing, 1964.
[*5*] Hall, L. R., "Plane-Strain Cyclic Flaw Growth in 2014-T62 Aluminum and 6Al-4V (ELI) Titanium," N69-20265, NASA-CR-62396, Boeing, 1968.
[*6*] Rice, J. R., *Journal of Applied Mechanics, Transactions,* American Society of Mechanical Engineers, Vol. 35, 1968, pp. 379–386.
[*7*] Begley, J. A. and Landes, J. D. in *Fracture Toughness, ASTM STP 514,* American Society for Testing and Materials, 1972, pp. 1–20.
[*8*] Landes, J. D. and Begley, J. A. in *Fracture Toughness, ASTM STP 514,* American Society for Testing and Materials, 1974, pp. 24–39.
[*9*] Landes, J. D. and Begley, J. A. in *Fracture Analysis, ASTM STP 560,* American Society for Testing and Materials, 1974, pp. 170–186.
[*10*] Yoder, G. R. and Griffis, C. A., "J-Integral and the Initiation of Crack Extension in a Titanium Alloy," NRL Report 7662, Naval Research Laboratory, Washington, D. C., 1974.
[*11*] Yoder, G. R. and Griffis, C. A., "Observations on the Use of the J-Integral to Determine Plane-Strain Fracture Toughness from Subsized Specimens to a Titanium-6A1-4V Alloy," NRL Report 7789, Naval Research Laboratory, Washington, D. C., 1974.
[*12*] Rice, J. R., Paris, P. C., and Merkle, J. G. in *Progress in Flaw Growth and Fracture Toughness Testing, ASTM STP 536,* American Society for Testing and Materials, 1973, pp. 231–244.
[*13*] Merkle, J. G. and Corten, H. T., *Journal of Pressure Vessel Technology, Transactions,* American Society of Mechanical Engineers, No. 6, 1974, pp. 1–7.
[*14*] Naimon, E. R., Weston, W. F., and Ledbetter, H. M., *Cryogenics,* Vol. 14, 1974, pp. 246–249.
[*15*] Goode, R. J., *Materials Research and Standards,* Vol. 12, No. 9, 1972, pp. 31–32.
[*16*] Fowlkes, C. W. and Tobler, R. L., "Fracture Testing and Results for a Ti-6A1-4V Alloy at Liquid Helium Temperatures," submitted to *Engineering Fracture Mechanics* for publication.
[*17*] Paris, P. C. in *Fatigue—An Interdisciplinary Approach,* Syracuse University Press, 1964, pp. 107–133.
[*18*] Paris, P. C. and Erdogan, F., *Journal of Basic Engineering, Transactions,* American Society of Mechanical Engineers, Series D., Vol. 85, No. 4, 1963, pp. 528-534.
[*19*] Wei, R. P. and Ritter, D. L., "The Influence of Temperature on Fatigue-Crack Growth in a Mill Annealed Ti-6Al-4V Alloy," NASA-CR-127042, Lehigh University, 1972.
[*20*] Bucci, R. J., Paris, P. C., Hertzberg, R. W., Schmidt, R. A., and Anderson, A. F. in *Stress Analysis and Growth of Cracks, ASTM STP 513,* American Society for Testing and Materials, 1972, pp. 123–140.

[*21*] Yeun, A., Hopkins, S. W., Leverant, G. R., and Rau, C. A., *Metallurgical Transactions*, Vol. 5, 1974, pp. 1833–1844.

[22] Griffis, C. A. and Yoder, G. R., "Application of the J-Integral to Crack Initiation in a 2024-T351 Aluminum Alloy," NRL Report 7676, Naval Research Laboratory, Washington, D. C., 1974.

[*23*] Clarke, G. A., Andrews, W. R., Paris, P. C., and Schmit, D. in *Mechanics in Crack Growth, ASTM STP 590,* American Society for Testing and Materials, 1976, pp. 27–42.

[*24*] McHenry, H. I. and Key, R. E., *Welding Journal,* Vol. 53, 1974, pp. 432–439S.

[*25*] Judy, R. W., Jr., Huber, R. W., and Goode, R., "Fracture Characteristics of Ti-6A1-1Mo and Ti-6A1-4V in 3-inch Section," NRL Report MR 2156, AD 711–586, Naval Research Laboratory, Washington, D. C., 1970.

[*26*] Armstrong, R. W. in *Advances in Materials Research,* H. Liebowitz, Ed., Vol. 4, Interscience, New York, 1970, pp. 101–146.

[*27*] Armstrong, R. W. in *Fracture 1969,* P. Pratt, Ed., Chapman and Hall, London, 1969, pp. 314–326.

[*28*] Stoloff, N. S. in *Fracture—An Advanced Treatise,* H. Liebowitz, Ed., Vol 6, Academic Press, New York, 1969, pp. 1–81.

[29] Frederick, S. F. and Hanna, W. D., *Metallurgical Transactions,* Vol 1, 1970, pp. 347–352.

[*30*] Shannon, J. L., Jr., and Brown, W. F., Jr. in *Applications Related Phenomena in Titanium Alloys, ASTM STP 432,* American Society for Testing and Materials, 1968, pp. 33–63.

[*31*] Barson, J. M., *Journal of Engineering for Industry, Transactions,* American Society of Mechanical Engineers, Vol. 93, 1971, pp. 1190–1196.

[*32*] Johnson, H. H. and Paris, P. C., *Engineering Fracture Mechanics,* Vol. 1, 1968, pp. 3–45.

[*33*] Ehret, R. M., "Assessment of Fracture Mechanics Technology for Space Shuttle Applications," SD–73–SH–0270, Rockwell International, 1973.

[*34*] Srawley, J. E. in *Fracture—An Advanced Treatise,* H. Liebowitz, Ed., Academic Press, New York, 1969, pp. 45–68.

R. E. Lewis,[1] *J. G. Bjeletich,*[1] *T. M. Morton,*[1] *and*
F. A. Crossley [2]

Effect of Cooling Rate on Fracture Behavior of Mill-Annealed Ti-6Al-4V

REFERENCE: Lewis, R. E., Bjeletich, J. G., Morton, T. M., and Crossley, F. A., "**Effect of Cooling Rate on Fracture Behavior of Mill-Annealed Ti-6Al-4V,**" *Cracks and Fracture, ASTM STP 601,* American Society for Testing and Materials, 1976, pp. 371–390.

ABSTRACT: Different cooling rates during duplex-annealing of mill-annealed Ti-6Al-4V 1-in. plate produce essentially indistinguishable microstructures and similar tensile properties, but significantly varying fracture properties. Duplex-annealing was performed by an initial heating at 1775°F (968.3°C) for 1/2 h and air-cooled; then reheated at 1450°F (787.4°C) for 1 h and cooled (1) by water quench, (2) in the air, or (3) in the furnace. Yield strength values, relatively unaffected by the annealing and cooling rate treatments, were grouped at 140±2 ksi (965 ± 14 MPa). Fracture toughness, however, varied from a low of 38 ksi $\sqrt{\text{in.}}$ (42 MPa · $\sqrt{\text{m}}$) in the material with the fastest cooling rate (1) to nearly similar values of 50 and 51 ksi $\sqrt{\text{in.}}$ (55 and 56 MPa · $\sqrt{\text{m}}$) for cooling rates (2) and (3), respectively. The stress-corrosion crack-growth, threshold stress intensities for the three cooling rates were (1) 34 ksi $\sqrt{\text{in.}}$ (37.5 MPa · $\sqrt{\text{m}}$), (2) 30 ksi $\sqrt{\text{in.}}$ (33 MPa · $\sqrt{\text{m}}$), and (3) 22 ksi $\sqrt{\text{in.}}$ (24.2 MPa · $\sqrt{\text{m}}$). Differences in fatigue crack propagation resistance brought about by the three cooling rates are illustrated with safe operating lifetimes obtained by computer simulation for a typical engineering application. The results reveal a fivefold advantage in safe life for air-cooled material. Although the fracture properties exhibited significant variation with cooling rate from the final anneal, light optical microscopy to a magnification of 3000 diameters did not reveal significant microstructural differences. Scanning electron fractographic evidence, however, is consistent with an inference that local ordering, that is, a precipitation process involving Ti_3 Al, is the most probable reason for the furnace-cooled material's more rapid fatigue-crack propagation rates and enhanced susceptibility to stress-corrosion cracking.

KEY WORDS: fractures (materials), mechanical properties, crack propagation, fatigue (materials), stress corrosion, cyclic loads, titanium alloys

The most commonly used titanium alloy for structural applications in high-performance military aircraft is Ti-6Al-4V. This alloy is often used

---

[1] Staff scientist, research scientist, and research scientist, respectively, Materials Sciences, Lockheed Palo Alto Research Laboratory, Palo Alto, Calif. 94304.

[2] Manager, Producibility and Standards, Lockheed Missiles and Space Company, Inc., Sunnyvale, Calif.

in the annealed condition since the combination of mechanical properties and fracture resistance characteristics is more favorable than that found in the solution treated and aged (STA) condition. However, lot-to-lot and heat-to-heat inconsistencies in these properties are often observed and present serious reliability problems. When an annealed material with high value of fracture toughness K_{Ic} is encountered, K_{Iscc} may be lower than usual, indicating increased susceptibility to stress corrosion cracking. The specific reasons for the inconsistent behavior of annealed material are not understood, but unknown variations in processing are believed to be primarily responsible. Existing processing conditions may lack the control required for the production of material with repeatable behavior.

Material quality for high-efficiency applications (for example, the B-1 bomber) is defined primarily by acceptable mechanical properties and specified minimum fracture toughness values. An additional criterion being considered for judging material quality attempts to exploit the dependence of mechanical properties of the material on its microstructure through the use of light optical metallography. Hopefully, reliable performance can be assured if the material can meet acceptable levels of tensile properties and fracture toughness as well as exhibit a desirable microstructure.

The need for consistent, repeatable material behavior in critical aircraft structures, coupled with the continuing challenge to achieve enhanced fracture resistance without compromising material strength, has been the impetus for exploring the merits of various annealing treatments. One such treatment is the duplex annealing of mill-annealed Ti-6Al-4V. This thermal processing was developed for alpha-beta alloys containing 6 percent or more aluminum in order to improve their fracture toughness. The study described in this paper investigates the effects of cooling rates during duplex-annealing of 1-in. Ti-6Al-4V plate on tensile properties, K_{Ic}, K_{Iscc}, fatigue crack propagation rate (da/dN), and microstructure. The practical significance of the measured differences in fracture resistance attributed to cooling rate is illustrated by estimating safe operating lifetimes for a simplified engineering structure using a computer model.

Material

Material for this study was 1-in. plate of standard grade Ti-6Al-4V with a maximum content of 0.2 percent interstitial oxygen. The chemical composition is given in Table 1. The plate material was supplied in the mill-annealed condition per MIL-T-9046. A microstructure approximating as closely as possible that of the 0.75-in. Ti-6Al-4V plate used in the F-14 program, and supplied by the same metal producer, was specified. The as-received microstructure consisted of fine-grain, equiaxed α with some intergranular β. No evidence of acicular α formed from the transformation of β by nucleation and growth was observed.

TABLE 1—*Chemical composition.*

Chemistry, weight percent						
Al	V	Fe	C	H	O	N
6.5	4	0.19	0.02	0.0059	$\leq$0.2	0.027

Thermal Processing

Initially, three samples of the as-received mill-annealed material, of sufficient size to provide all of the required specimens, were heated at a temperature of 1775°F (968.3°C) for a period of ½ h and air-cooled. Each sample was given a second heat treatment at 1450°F (787.1°C). After thermal exposure for 1 h, one sample was cooled by water-quenching, a second by air-cooling, and the final one was permitted to cool in the furnace to 900°F (482.2°C), then air-cooled.

Experimental Procedure

Tensile properties—tensile strength, F_{tu}, 0.2 percent offset yield strength, F_{ty}, percent elongation, and percent reduction in area—were determined from one specimen for each cooling rate condition in accordance with ASTM Tension Testing of Metallic Materials (E 8-69). The tension specimen configuration was the 1-in. (25.4-mm)-gage-length, 0.25-in. (6.4-mm)-diameter ASTM round specimen. The specimen long axis was coincident with the plate long transverse direction. Loads were applied at a strain rate of 0.5 percent per minute to yield, then increased to approximately 2 percent per minute to fracture.

For each of the three cooling rate conditions, three compact tension-type specimens were provided to measure: (1) the fracture toughness index K_{Ic}, (2) the stress-corrosion crack growth threshold K_{Iscc}, and (3) the fatigue crack propagation rate da/dN. The K_{Ic} specimen was used also to provide additional da/dN information. All compact tension specimens were 1 in. (25.4 mm) thick with an H/W ratio of 0.486 and were removed from the parent plate in the TL[3] orientation. The specimen configuration is shown in Fig. 1. To accommodate the test fixture, the K_{Iscc} specimens were fabricated with a threaded hole normal to the crack plane. In all specimens, the starter notch was sharpened to fatigue crack acuity with constant-amplitude, cyclic loads at a stress ratio R of 0.1. The sinusoidal loads were applied with a closed-loop, electrohydraulic fatigue unit. Precrack lengths were nominally 0.75 in. (19 mm) (a/w = 0.3).

After precracking, both the fatigue and K_{Ic} specimens were sinusoi-

---

[3] The first letter designates the direction normal to the crack plane, and the second letter, the expected direction of crack propagation.

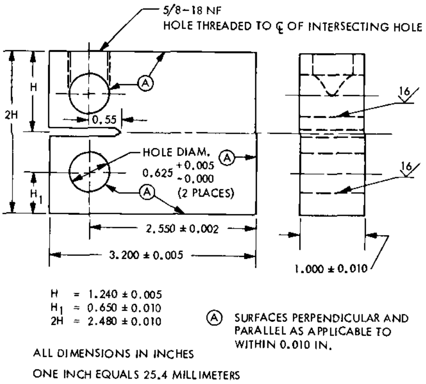

FIG. 1—*Compact tension specimen, 1-in. (25.4-mm) thick,* H/W = *0.486.*

dally loaded at a frequency of 10 to 20 Hz and an R of 0.1. Cyclic loads in the fatigue specimen were adjusted to provide crack growth rate data in the range 10^{-5} to 10^{-3} in. (10^{-4} to 10^{-2} mm) per cycle. The total usable length of the specimen for crack growth was approximately 1 in. (25.4 mm). In the K_{Ic} specimen, the fatigue crack length was extended to between 1.15 and 1.4 in. (29.2 and 35.6 mm) ($0.45 \leq a/w \leq 0.55$). During this crack extension interval, complementary fatigue crack growth rate data, in the range of 10^{-6} to 10^{-5} in. (10^{-5} to 10^{-4} mm) per cycle, were obtained. Crack length was measured optically with a traveling telemicroscope capable of resolving a change of 0.0001 in. (2.5 μm). A graph of increasing crack length with the number of cycles containing a minimum of 40 data points was plotted for the fatigue and K_{Ic} specimens. A smooth line was fitted through contiguous crack length-cycle data, then graphically differentiated. Ten to fifteen differentiations were performed to provide discrete da/dN versus ΔK data points.

Upon completion of fatigue testing, the K_{Ic} specimen was instrumented with a linear voltage differential transformer (LVDT) spanning the mouth of its starter notch and loaded to failure in accordance with the recommendations given in the ASTM Test for Plane-Strain Fracture Toughness of Metallic Materials (E 399-74). The required stress intensity factors were calculated from the following equation

$$K = CP/B\sqrt{a}$$

where

P = load,
B = specimen thickness,
a = average crack length measured from load line, and

C = function expressed in polynomial form [*1*][4] as follows

$$C = 30.96\ (a/W) - 195.8\ (a/W)^2 + 730.6\ (a/W)^3 - 1186.3\ (a/W)^4 + 754.6\ (a/W)^5$$

where W is specimen length measured from the load line.

Loading of precracked K_{Iscc} specimens was accomplished, using load frames specially designed for this purpose. A frame consists of a reacting yoke and a bolt instrumented with strain gages to act as a load cell. The bolt is threaded into the hole provided in one leg of the compact tension specimen. The yoke passes over the bolt and is secured with a loading pin to the opposite leg of the specimen. To load the specimen, a tensile load was applied to the bolt by a test machine and reacted against the yoke. During this loading, an ultrasonic crack follower was attached to the specimen so that increments of crack growth as small as 0.0005 in. (12.7 μm) would be detected. Before load application, a 3.5 percent aqueous solution of sodium chloride (NaCl) was injected into the precrack. The load amplitude was increased slowly until a crack growth rate between 0.01 to 0.1 in. (0.254 to 2.54 mm) per hour was obtained. At the corresponding load, the test machine function was transferred to the load frame by securing a nut on the threaded bolt against the yoke. The load frame crack-opening force is provided by the residual strain energy stored in the loading bolt and yoke.

The specimen and load frame assembly were removed from the test machine and positioned in a small container of the salt solution so that the crack tip and uncracked portion of the specimen were continuously immersed. The positioning of the assembly was such that the load frame was not in contact with the salt water. Since the load frame provides nearly constant crack opening displacement, any extension of the crack is accompanied by a decrease of load in the bolt. Both load and crack length were therefore measured initially and then monitored at periodic intervals. When the crack growth rate decreased to 10^{-6} in. (10^{-5} mm) or less per hour, the crack was assumed to be arrested, and the test was considered complete. After the exposure time required to attain the arrest growth rate (1000 to 1500 h), the crack front was "marked" by the application of a small fatigue load, and the specimen was broken apart in a universal test machine. The threshold value of the stress intensity factor K_{Iscc} is the stress intensity calculated from the load value at crack arrest, that is $da/dt \leq 10^{-6}$ in. (10^{-5} mm) per hour, and the arrested crack average length, as obtained from measurements at 0.25, 0.5, and 0.75 thicknesses.

Metallographic specimens with a surface area of approximately 0.3 in.^{2} (193.6 mm^2) were prepared for light microscopy by electrolytic polish-

---

[4] The italic numbers in brackets refer to the list of references appended to this paper.

ing [2]. The polishing was conducted for 2 min in an electrolytic solution of 400-ml methyl alcohol, 20-ml sulfuric acid (H_2SO_4), 60-g aluminum chloride ($AlCl_3$), and 20-g zinc chloride ($ZnCl_2$); at 30 V and 1 to 1.5 A; and at a temperature of 73°F (23°C). Etching of the specimen was accomplished by immersion for 2 to 3 min in a solution of 2-ml hydrofluoric acid and 100-ml methyl alcohol at room temperature.

Fracture surfaces of each K_{Ic} specimen were examined by means of a scanning electron microscope (SEM). One half of a full specimen was cleaned by immersion in a low-power ultrasonic bath of acetone at room temperature for a period ranging from 5 to 15 min. After cleaning each specimen half was inserted intact into the SEM chamber. The specimen was tilted toward the collector tube so that the angle of incidence (angle between the electron beam and fracture surface normal) was 10 to 30 deg. The acceleration voltage was 10 kV.

Computer Modeling

An iterative computer model of a structure was developed to estimate its life in the presence of a small undetected surface crack. This permitted variations in da/dN, K_{Ic}, and K_{Iscc} for different thermal treatments to be interrelated in practical use-oriented terms. The procedure described in this paper uses the Paris formulation of fatigue crack growth ($da/dN = C\Delta K^x$) and an application of fatigue with a constant R. The same general procedure has also been used for more complex structural applications involving a fatigue spectrum with variable maximum stresses and R values. In these more complex cases, the following Forman formulation of fatigue crack growth

$$da/dN = \frac{C' \, \Delta K^{x'}}{(1 - R)K_{Ic} - \Delta K}$$

has often been used. Segmented Paris formulations have also been useful in which the constants C and x depend not only upon the ΔK range but also upon R.

A diagram of the computational process used is shown in Fig. 2. The material properties upon which the estimation is based are (1) yield strength; (2) criterion for structural failure, that is, K_{Ic} or K_{Iscc}; and (3) constants for segmented Paris equations for da/dN as a function of ΔK. Initial crack depth, initial crack shape, maximum operating stress, and stress ratio can be arbitrarily specified to approximate an intended service application.

The iterative procedure is simple and direct. Values for ΔK and K_{max} are recomputed as the crack depth and length increase by small increments due to applied fatigue stresses. When the crack has grown enough so that the failure criterion is satisfied (for example, $K_{max} = K_{Ic}$), iteration stops. The structure has then "failed" from a crack which grew from the specified initial size to the final size computed in N cycles of fatigue.

Results and Discussion

The tensile, fracture, and K_{Iscc} results for the three cooling rate conditions are given in Table 2. Cyclic crack-growth results are shown in Fig. 3 which is a logarithmic plot of crack growth rate per load cycle da/dN versus the crack tip stress-intensity factor range ΔK. In this figure, the fatigue crack growth rates are exhibited as smooth curves to avoid cluttering of data points. The maximum deviation of the discrete da/dN values from the corresponding curve is less than ±40 percent. Included in both the mechanical property tabulation and the figure exhibiting crack growth rates are data for as-received material. The three different cooling rates did not have a significant effect on the yield and tensile strength of the as-received (mill-annealed) material.

The final anneal of the duplex process, when followed by air or furnace cooling, produced a slightly increased fracture toughness (6 and 8 percent, respectively) compared to the mill-annealed value of 47 ksi $\sqrt{\text{in.}}$ (52 MPa · $\sqrt{\text{m}}$). Cooling from the annealing temperature by water quenching degraded the toughness by about 20 percent compared to the value for the mill-annealed state. However, this decreased toughness was accompanied by a K_{Iscc} value 13 percent greater than that of the air-cooled condition and nearly 55 percent greater than that determined for furnace-cooled material.

From the data presented in Fig. 3, it can be seen that air cooling, *per se,* produced little or no change in the cyclic crack growth compared to the mill-annealed base material. The slightly decreased crack growth rates above a ΔK of 20 ksi $\sqrt{\text{in.}}$ (22 MPa · $\sqrt{\text{m}}$) are, more probably than not, the result of the higher fracture toughness of the air-cooled material. However, both water quenching and furnace cooling resulted in fatigue crack growth rates noticeably different from those measured for the mill-annealed base material. As shown in Fig. 3, furnace cooling had a consistently detrimental effect on the crack growth rate while water quenching produced greatly increased crack growth rates above a stress-intensity range of 18 ksi $\sqrt{\text{in.}}$ (20 MPa · $\sqrt{\text{m}}$). The accelerated growth rate above 18 ksi $\sqrt{\text{in.}}$ (20 MPa · $\sqrt{\text{m}}$ may be attributed to the proximity of the maximum stress intensity to the critical value. The critical stress-intensity value for water quenching was an exceptionally low 38 ksi $\sqrt{\text{in.}}$ (42 MPa · $\sqrt{\text{m}}$).

For a particular engineering application, a specific fracture characteristic (for example, K_{Ic}), may be the only attribute requiring consideration in evaluating the merits of the different cooling rates. In such instances, the decision for preferred cooling rate is straightforward and relatively sim-

I. SPECIFICATION OF INITIAL CONDITIONS

(1)	σ_{ys}	*Material Yield Strength*
(2)	K_{Ic} or K_{Iscc}	Failure Criterion
(3)	C_1, x_1	$da/dN = C\Delta K^x$ where C and x can vary with ΔK as shown below:
	C_2, x_2	
	C_3, x_3	

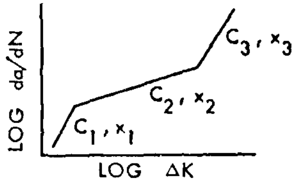

(4)	$a, a/2c$	Initial Crack Depth, Initial Crack Depth/Initial Crack Length
(5)	σ, R	Maximum Stress, Min./Max. Stress

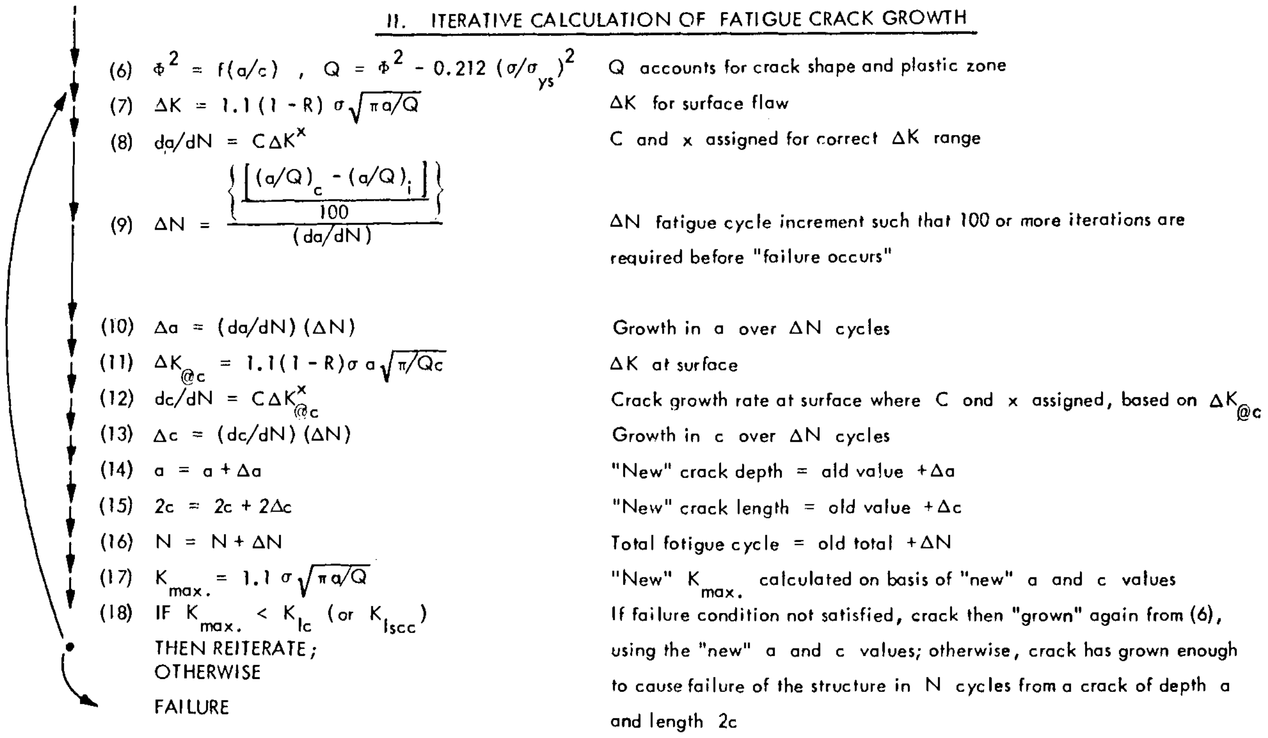

II. ITERATIVE CALCULATION OF FATIGUE CRACK GROWTH

(6)	$\Phi^2 = f(a/c)$, $Q = \Phi^2 - 0.212\,(\sigma/\sigma_{ys})^2$	Q accounts for crack shape and plastic zone
(7)	$\Delta K = 1.1\,(1 - R)\,\sigma\sqrt{\pi a/Q}$	ΔK for surface flaw
(8)	$da/dN = C\Delta K^x$	C and x assigned for correct ΔK range
(9)	$\Delta N = \dfrac{\left\{\dfrac{\left[(a/Q)_c - (a/Q)_i\right]}{100}\right\}}{(da/dN)}$	ΔN fatigue cycle increment such that 100 or more iterations are required before "failure occurs"
(10)	$\Delta a = (da/dN)\,(\Delta N)$	Growth in a over ΔN cycles
(11)	$\Delta K_{@c} = 1.1(1 - R)\sigma\, a\sqrt{\pi/Qc}$	ΔK at surface
(12)	$dc/dN = C\Delta K_{@c}^x$	Crack growth rate at surface where C and x assigned, based on $\Delta K_{@c}$
(13)	$\Delta c = (dc/dN)\,(\Delta N)$	Growth in c over ΔN cycles
(14)	$a = a + \Delta a$	"New" crack depth = old value $+\Delta a$
(15)	$2c = 2c + 2\Delta c$	"New" crack length = old value $+\Delta c$
(16)	$N = N + \Delta N$	Total fatigue cycle = old total $+\Delta N$
(17)	$K_{max.} = 1.1\,\sigma\sqrt{\pi a/Q}$	"New" $K_{max.}$ calculated on basis of "new" a and c values
(18)	IF $K_{max.} < K_{Ic}$ (or K_{Iscc}) THEN REITERATE; OTHERWISE FAILURE	If failure condition not satisfied, crack then "grown" again from (6), using the "new" a and c values; otherwise, crack has grown enough to cause failure of the structure in N cycles from a crack of depth a and length 2c

FIG. 2—*Diagram of the computational process for estimating structural life in presence of a small undetected crack.*

TABLE 2—*Mechanical properties* [a].

Condition	F_{ty}, ksi	F_{tu}, ksi	Elongation, %	Reduction in Area, %	K_{Iscc} (ksi $\sqrt{in.}$)	K_{Iscc} (% of K_{Ic})	K_{Ic} (ksi $\sqrt{in.}$)
MA (mill-annealed condition)	143	151	18	27	. . .[b]	. . .[b]	47
WQ (water-quenched)	141	154	17	37	34	89	38
AC (air-cooled)	138	150	15	28	30	60	50
FC (furnace-cooled)	141	154	18	24	22	42	51

NOTES—One ksi = 6.895 MPa.
One ksi$\sqrt{in.}$ = 1.1 MPa $\cdot\sqrt{m}$.

[a] Data reported are result of individual tests.

[b] Not determined.

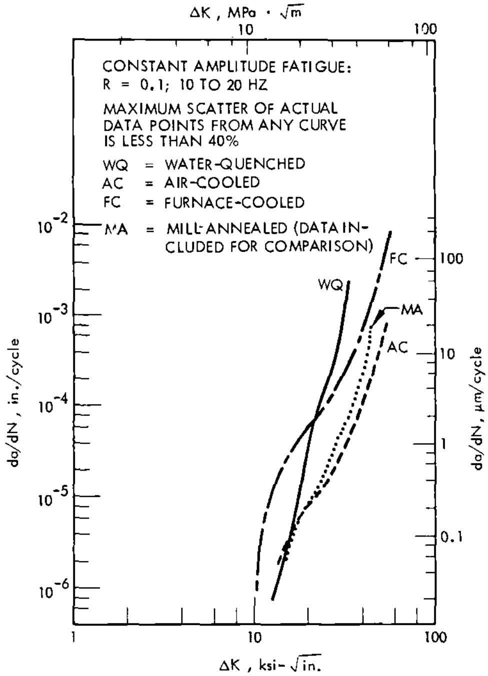

FIG. 3—*Effects of final cooling rate on fatigue crack growth rate in duplex-annealed Ti-6Al-4V, 1-in. plate, 1775°F (968.3°C), 1/2 h, air cooled; and 1450°F (787.4°C), 1 h, cooled as noted.*

ple. However, for any application where the structure is cyclically loaded in service, hence prone to "accidental" failure, consideration must be given to the influence of the cooling rates on all three major fracture properties, that is, K_{Ic}, da/dN, and K_{Iscc}. The effect on each of the fracture properties must be integrated before proper judgment can be made regarding the virtues of any given cooling rate.

The most direct means of performing this evaluation is to determine the resulting safe life of a structure fabricated from cooling-rate processed Ti-6Al-4V material. Although the use of real structures for this purpose is impractical, useful estimates of safe life can be economically made with computer models of crack growth in the structures. In this way, changes in K_{Ic}, da/dN, and K_{Iscc} brought forth by each of the different cooling rates can be interrelated, and a single figure of merit, that is, structure lifetime, assigned for each condition.

The material properties used in this evaluation are given in Table 3. In the computer model, the structure was exposed to constant-amplitude

TABLE 3—*Material properties used for structural life estimation.*

		Failure Criteria		Segmented Paris Fatigue Crack Growth Equation			
Material Condition	0.2% Offset Yield Strength, ksi	K_{Ic},[a] ksi $\sqrt{in.}$	K_{Iscc}, ksi $\sqrt{in.}$	C	X	Lower Limit ΔK, ksi $\sqrt{in.}$	Upper Limit ΔK, ksi $\sqrt{in.}$
MA (mill-annealed condition—as-received)	141	50	. . .	0[b]	. . .	. . .	9.00
				2.14×14^{-14}	7.28	9.00	11.30
				1.32×10^{-11}	4.63	11.30	37.78
				5.69×10^{-24}	12.47	37.78	50.00
WQ (1775°F/0.5 h, air-cooled plus 1450°F/1 h, air-cooled)	141	42	34	0[b]	. . .	. . .	9.00
				2.11×10^{-17}	10.08	9.00	11.68
				1.07×10^{-13}	6.61	11.68	25.54
				1.44×10^{-17}	9.36	25.54	42.00
AC (1775°F/0.5 h, air-cooled plus 1450°F/1 h, furnace-cooled)	138	55	30	0[b]	. . .	. . .	9.00
				1.69×10^{-12}	5.38	9.00	11.68
				2.58×10^{-10}	3.53	15.16	45.16
				2.07×10^{-35}	18.65	45.70	55.00
FC (1775°F/0.5 h, air-cooled plus 1450°F/1 h, furnace-cooled)	141	57	22	0[b]	. . .	. . .	9.00
				1.94×10^{-20}	13.83	9.00	11.57
				1.97×10^{-9}	3.48	11.57	39.13
				1.44×10^{-16}	7.96	39.13	57.00

NOTES—One ksi = 6.895 MPa.
One ksi$\sqrt{in.}$ = 1.1 MPa • $\sqrt{m}$.

[a] K_{Ic} = asymptotic value from *da/dN* testing.

[b] ΔK = 9 ksi-in.$^{0.5}$ (Assumed to be the fatigue crack growth threshold in agreement with indications from the data presented; see Ref *3*).

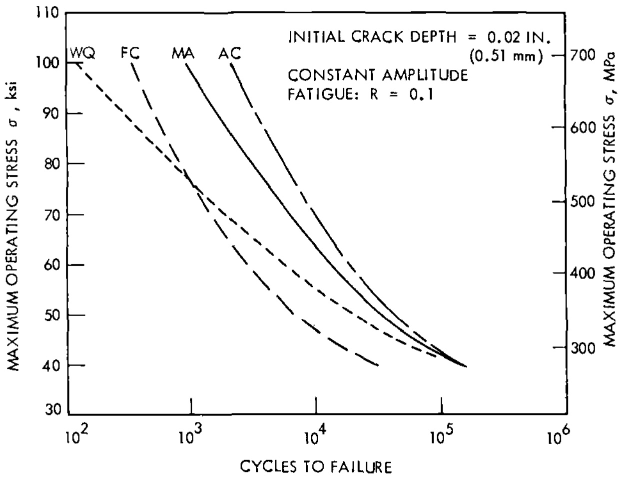

FIG. 4—*Effect of final cooling rate during duplex-annealing on structural life predicted by computer modeling (structural life for mill-annealed condition included for comparison).*

fatigue loads with an R of 0.1. The ratio of initial crack depth-to-crack length, $a/2C$, was 0.15 in all cases. The maximum operating stress and initial crack depth were systematically varied over the ranges most likely to be encountered in realistic situations.

The cycles required to cause failure as a function of maximum operating stress for a given initial crack depth are shown in Fig. 4. The initial crack depth, 0.02 in. (0.51 mm), is well below the level reliably detectable by the state-of-the-art nondestructive inspection (NDI) in large structures. It can be seen from the curves presented in Fig. 4 that duplex-annealed, air-cooled material provides a clear advantage over the other cooling rate conditions as well as the as-received, mill-annealed material. The advantage in cycles to failure ranges from 5 times better than furnace-cooled material at a maximum operating stress of 40 ksi (276 MPa) to 20 times better than water-quenched material at 100 ksi (690 MPa). Safe-life curves for various initial crack depths for furnace-cooled, air-cooled, and water-quenched material were constructed and follow the expected trend. This trend is illustrated in Fig. 5 for air-cooled material only. For computational convenience, each curve in the figure cuts off at the maximum operating stress that corresponds to a fatigue threshold ΔK value of 9 ksi $\sqrt{\text{in.}}$ (10 MPa · $\sqrt{\text{m}}$). When the maximum operating stress is increased from 80 to 100 ksi (552 to 690 MPa), air-cooled material has five to seven times the life of furnace-cooled material in the presence of an initial crack that is 0.005 in. (0.13 mm) deep. With an initial crack

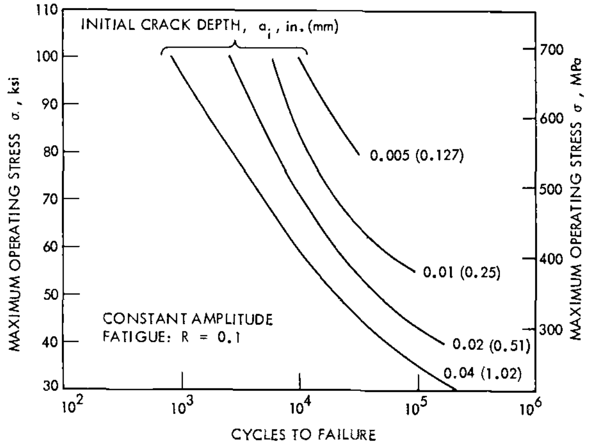

FIG. 5—*Structural lifetime of duplex-annealed and air-cooled Ti-6Al-4V, 1-in. plate for various initial crack depths.*

depth of 0.04 in. (1.02 mm)—sometimes regarded as the reliable limit of NDI detection—and a maximum operating stress of 80 ksi (552 MPa), air-cooled material fails at 2725 cycles while only 80 cycles are required to cause failure of water-quenched material.

A most dramatic illustration of the influence of cooling rate during duplex-annealing on the fracture characteristics of Ti-6Al-4V alloy is presented in Fig. 6. Variation of crack depth with fatigue cycles, from initial to critical size, is portrayed for each cooling-rate condition. For all material conditions shown, the initial crack depth was 0.02 in. (0.51 mm), and the maximum operating stress was 60 ksi (414 MPa). The impact of the advantages in the combined fracture characteristics gained by duplex-annealing and air-cooling is rendered more obvious by the linear coordinates shown in Fig. 6.

In addition to serving as bases for evaluating the merits of a given processing regarding combined fracture properties, Figs. 4, 5, and 6 also clearly illustrate that the effect of variations in these properties on the safe life of a structure can be significant.

Light optical microscopy exhibited similar microstructures for all three cooling rate conditions (Fig. 7). In each case, the microstructure consists mainly of equiaxed α and Widmanstätten $\alpha + \beta$, plus some regions where the primary α grains have an elongated configuration. No metallurgical features, that is, anomalous phases or morphology, that could be identified or correlated with the measured fracture properties, were readily distinguished.

Similar comparisons were performed with scanning microscopy of K_{Ic}

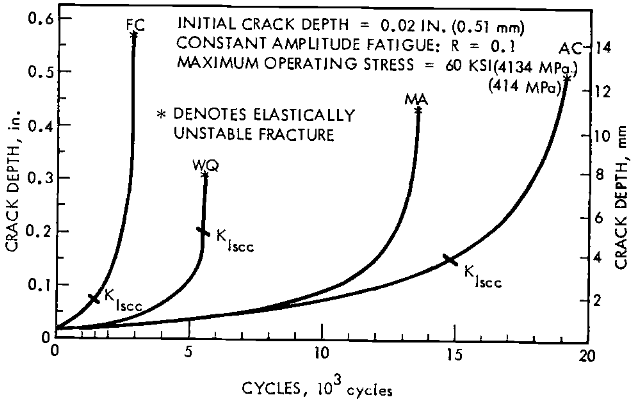

FIG. 6—*Effect of final cooling rate during duplex-annealing on crack depth during life of structure subjected to constant-amplitude fatigue (structural life for mill-annealed condition included for comparison).*

specimens that were fatigue-precracked and monotonically loaded to failure. Two areas located at midthickness on each fracture surface were photographically documented at magnifications of 635 and 2540 diameters. A fatigue region, 0.16 in. (4 mm) before the onset of rapid crack propagation, is displayed in Fig. 8. The macroscopic crack growth rate in this vicinity ranged from 2×10^{-6} in./cycle (5×10^{-5} mm/cycle) at a ΔK of 15 ksi $\sqrt{\text{in.}}$ (16.5 MPa · $\sqrt{\text{m}}$) for air-cooled material to 2×10^{-5} in./cycle (5×10^{-4} mm/cycle) at a ΔK of 14 ksi $\sqrt{\text{in.}}$ (15.4 MPa · $\sqrt{\text{m}}$) for furnace-cooled material. A second area, in the elastically unstable crack growth region of the specimen and 0.08 in. (2mm) beyond the fatigue precrack, is shown in Fig. 9.

The relatively flat appearance of the fatigue-crack surface in the furnace-cooled specimen of Fig. 8 indicates a maximum stress-intensity during fatigue that is a low percentage of the critical value. The absence of distinct fatigue striations and, in some regions, large spacings between suspected striations, suggests minimal resistance to crack propagation. Indeed, the fractographic features observed appear to be more representative of cleavage, a feature usually encountered in static fracture. When the microstructure (Fig. 7) and the subcritical fracture surface (Fig. 8) of the furnace-cooled material are compared, elongated α grains appear to be outlined during subcritical growth.

In contrast, well-developed and closely-spaced striations are in evidence on the fatigue surface of the air-cooled specimen in Fig. 8. Here, the striations dominate the surface, which is more irregular than that found in the furnace-cooled specimen. These observations are consistent with the greater resistance of air-cooled material to fatigue-crack growth.

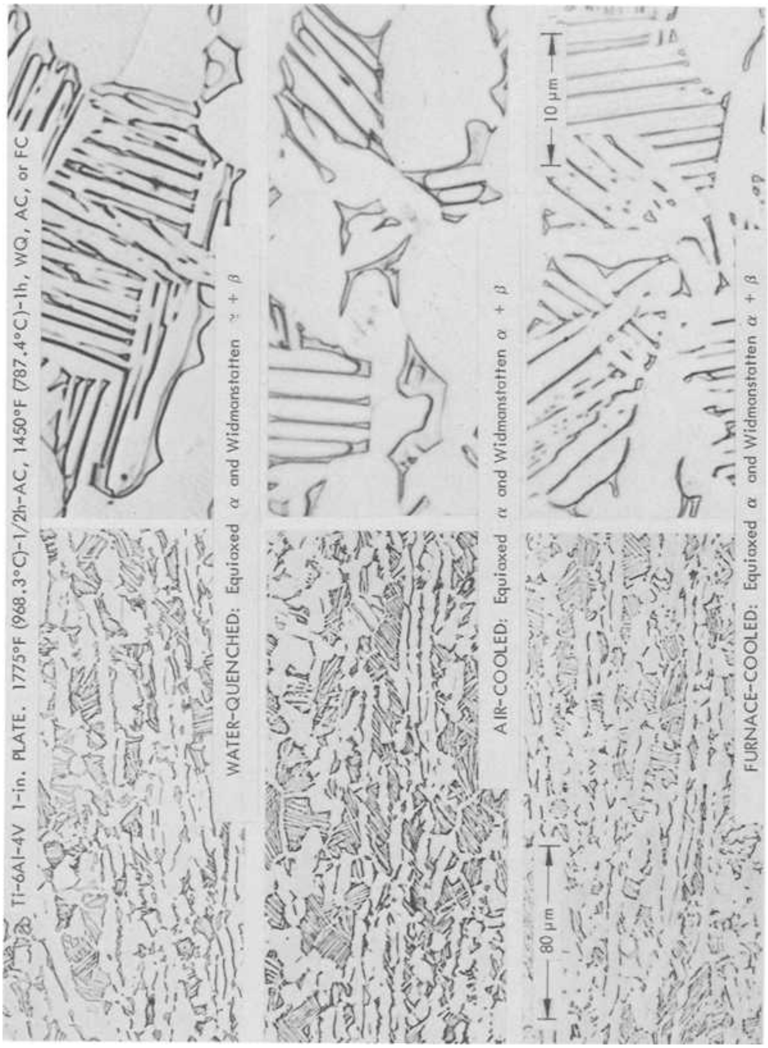

FIG. 7—*Microstructures of Ti-6Al-4V, 1-in. plate cooled from final annealing temperature as indicated (all three microstructures exhibit mixtures of equiaxed α and Widmanstätten α plus β grains).*

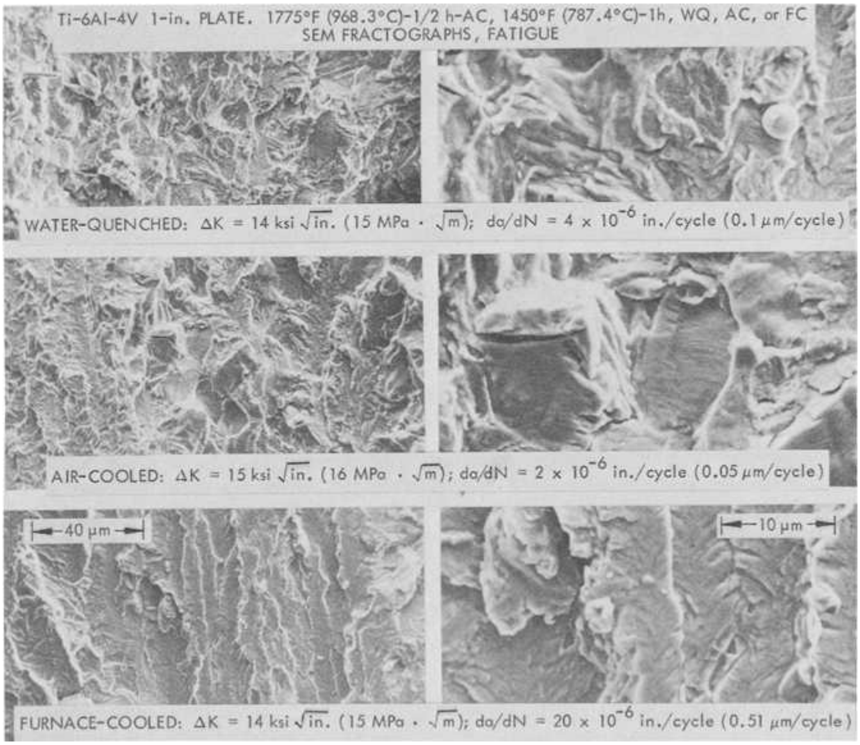

FIG. 8—*Scanning electron micrographs of fatigue surface in each of three conditions cooled from final annealing temperature as indicated (corresponding* ΔK *and* da/dN *values also included).*

There was no distinct indication of α grain boundaries on this fatigue surface.

The fatigue-crack surface of the water-quenched specimen in Fig. 8 exhibits a heterogeneous mixture of features, including some evidence of localized ductile fracture, that is, unarticulated dimple formation, and isolated regions of poorly developed fatigue crack striations. The observed topography of this specimen implies that the crack extended by a combined process of normal fatigue and elastic instability. A tentative conclusion that the stress-intensity at the maximum cyclic stress was critical in many localized sites on the fatigue surface is consistent with the macroscopic measurement of the growth rate and K_{Ic}.

Fractographic differences in the three cooling rate conditions are also observed on the fast fracture surfaces pictured in Fig. 9. The fracture surface of the water-quenched specimen reveals a heterogeneous mix of features but, mainly, indicates cleavage with evidence of elongated dimple formation. Fast fracture was primarily transgranular with a relatively low amount of energy dissipated in plastic deformation.

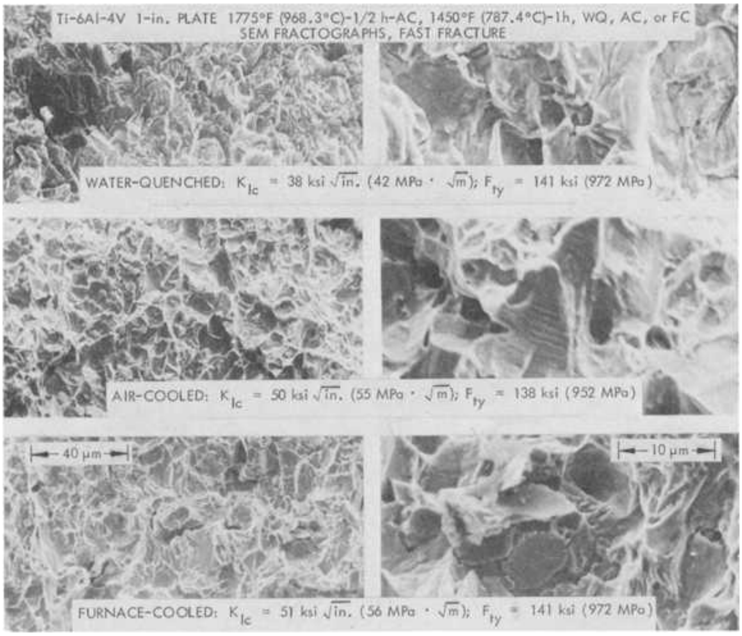

FIG. 9—*Scanning electron micrographs of fast fracture surface in each of three conditions cooled from the final annealing temperature as indicated (corresponding* K_{Ic} *and* F_{ty} *values are also included).*

Higher energy-consuming, ductile-dimple formations dominate the surfaces of both the air and furnace-cooled specimens. However, the dimple formations observed in the air-cooled specimen are more uniform than those found on the surface of the furnace-cooled specimen. Among the large distribution of dimple sizes in the furnace-cooled specimen are small planar fractures of a size comparable to the α-grain size shown in Fig. 7. The primarily disk-shaped fracture areas have relatively featureless surfaces. Only the furnace-cooled specimens showed their presence. The flat and smooth appearance of these platelets is indicative of a low-energy requirement for separation.

Although not directly verified by metallographic examination, the observed anomalous resistance of the furnace-cooled material to subcritical crack growth must be the result of a solid-state reaction. The phenomenon that appears most likely responsible is the local ordering stage of a precipitation process. Consistent with the observed evidence, only subtle fractographic indications of its presence, for example, localized disk-shaped fracture areas with featureless surfaces, would be expected.

It is known that the precipitate Ti_3Al occurs in binary alloys containing

6 percent aluminum [*4–6*]. The detrimental influence of the precipitate on the tensile ductility and Charpy V-notch impact energy of Ti-6Al has been demonstrated by Crossley [*4*]. The precipitation reaction, which takes place preferentially at grain boundaries, is exceptionally sluggish [*7*]. For aging times consistent with commercial heat treatment practice, the precipitate is submicroscopic and coherent. At 1200°F (649°C), the temperature at which kinetics of the precipitation process appear to be most rapid, aging times of the order of 1000 h are required for growth of Ti_3Al particles to micrometre size [*7*]. Vanadium, as well as other isomorphous beta stabilizers, inhibits Ti_3Al precipitation at grain boundaries and appears to make the reaction more sluggish [*7,8*].

It is therefore expected that Ti_3Al, if present in the furnace-cooled Ti-6Al-4V material, is coherent, submicroscopic, and exists in small quantities primarily along grain boundaries. To date, metallographic confirmation of the existence of Ti_3Al precipitate in the suspected regions is lacking. Transmission electron microscopy of several foils taken from furnace-cooled material has not been successful in locating evidence of the precipitate. If the precipitate exists, as such, its submicroscopic size and relatively large spacing between sites where conditions are favorable would partially account for this difficulty. More likely, the precipitate, lacking the necessary atom concentrations, cannot develop beyond an embryonic stage that precedes actual precipitation of a separate Ti_3Al phase. In this case, existence cannot be directly confirmed but only inferred from the observed macroscopic properties and the observed subcritical and critical modes of crack propagation.

Conclusions

The following conclusions have been drawn from the foregoing data and analysis just presented.

1. Variation in cooling rate during the final annealing of Ti-6Al-4V alloy drastically affects fracture properties without affecting tensile properties.

2. Different final cooling rates can produce equivalent toughness material with significantly different subcritical crack growth characteristics. Since subcritical crack growth rates are the major influence affecting the safe life of a structure containing an undetected defect, measurement of K_{Ic} alone provides insufficient information for competent prediction of safe life.

3. The microstructures of material cooled at different rates during final annealing were indistinguishable. However, these cooling rates result in significantly different fracture properties.

4. The degraded subcritical crack growth characteristics, that is, K_{Iscc} and da/dN, of the furnace-cooled material are most probably the result of a difficult-to-detect ordering reaction.

Although not confirmed, the kinetics of Ti_3Al precipitation are believed to be responsible.

Recommendation

Users of annealed Ti-6Al-4V should maintain consistent cooling rates during annealing to produce material with consistent mechanical and fracture properties.

Acknowledgments

This work was supported by (*a*) the Naval Air Systems Command, Contract No. N00019-74-C-0161, "Correlation of Microstructures with Fracture Toughness Properties in Metals," W. T. Highberger, project manager; and (*b*) Lockheed Missiles & Space Company, Inc., Independent Research Funds. The authors express their appreciation to A. T. Davinroy for his invaluable assistance in organizing and conducting the experiments.

References

[1] Wilson, W. K., *Review of Analysis and Development of the WOL Specimen*, Westinghouse Research Report, 67-707-BTLPV-R1, MDR 8, 1967.
[2] Coons, W. C. and Iosty, L. R., "Electrolytic Polishing of Titanium, Its Alloys and Various Other Metals and Alloys," *Microstructural Science*. Vol. 4 July 1976.
[3] Bucci, R. J. et al in *Stress Analysis and Growth of Cracks, Part I, ASTM STP 513*, American Society for Testing and Materials, 1972, pp. 125–140.
[4] Crossley, F. A. and Carew, W. F., *Transactions*, The Metallurgical Society, American Institute of Mining, Metallurgical, and Petroleum Engineers, Vol. 209, 1957, pp. 43–46.
[5] Crossley, F. A., *Transactions*, The Metallurgical Society, American Institute of Mining, Metallurgical and Petroleum Engineers, Vol. 235, 1966, pp. 1174–85.
[6] Namboodhiri, T. K. G. et al, *Metallurgical Transactions*, Vol. 4, 1973, pp. 1323–31.
[7] Crossley, F. A., *Metallurgical Transactions*, Vol. 1, 1970, pp. 1921–29.
[8] Crossley, F. A., *Transactions*, The Metallurgical Society, American Institute of Mining, Metallurgical and Petroleum Engineers, Vol. 245, 1969, pp. 1963–68.

R. D. Margolis,[1] *R. W. Dunlap,*[2] *and H. Markovitz*[2]

Fracture Toughness Testing of Glassy Plastics

REFERENCE: Margolis, R. D., Dunlap, R. W., and Markovitz, H., "**Fracture Toughness Testing of Glassy Plastics,**" *Cracks and Fracture, ASTM STP 601,* American Society for Testing and Materials, 1976, pp. 391–408.

ABSTRACT: Despite widespread use of linear elastic fracture mechanics to describe brittle fracture in glassy plastics, prior work has not established a valid fracture toughness criterion based on the unique aspects of polymer mechanical behavior. In this study, fracture toughness tests on poly(methyl methacrylate) (PMMA) were correlated with crack-tip crazing and fracture surface morphology in order to assess the influence of dissipative processes and crack growth modes on standard toughness test variables. Various K_c criteria were examined for their relevance to PMMA, a material with a velocity dependence of fracture typical of glassy plastics. Since crack-tip crazing is restricted in this material, crack extension is essentially elastic for all normal specimen dimensions and precrack conditions. The load instability at the maximum of the load-displacement record is distinguished from the point of intrinsic instability, which is indicated by the K versus $\dot{a}$ relationship. The load instability leads to a geometry-dependent K_c criterion which can be described analytically, and procedures for measuring a K_c based on intrinsic instability are defined for a standard fracture test. Measured values are in reasonable agreement with estimates derived from K versus $\dot{a}$ in the literature. The implications of the geometric effects on instability are discussed for other materials and specimen geometries.

KEY WORDS: crack propagation, fracture (materials), fracture tests, plastics

Nomenclature

a	Crack length
a_1	Initial crack length
a_2	Crack length at slow-fast transition
a_c	Crack length at the maximum load

---

[1] Manager of engineering and technical service, GRTL Company, Birmingham, Mich. 48010.

[2] Professor of engineering and public affairs, Carnegie Institute of Technology, and professor of mechanics and polymer science, Mellon Institute of Science, respectively, Carnegie-Mellon University, Pittsburgh, Pa. 15213.

$\dot{a}$	Crack speed
B	Specimen thickness
W	Specimen width
P	Load
$P_{\max}$	Maximum load on a load displacement record
Y	Dimensionless geometric stress intensity magnification factor
K	Stress intensity factor
K_c	General critical stress intensity factor
K_{Ic}	Plane strain fracture toughness
$K_c(P_{\max}, a_1)$	Critical stress intensity calculated from the load $P_{\max}$ and crack length a_1
$K_c(P_{\max}, a_2)$	Critical stress intensity calculated from the load $P_{\max}$ and crack length a_2
$K_c(P_{\max}, a_c)$	Critical stress intensity calculated from the load $P_{\max}$ and crack length a_c
$\Delta(a/W)$	Change in relative crack length
σ_{ys}	Yield stress
δ	Crack mouth displacement
Δ	Crosshead displacement per unit length
λ	Specimen compliance

Because of the apparently brittle behavior of most glassy plastics, many attempts have been made to apply the concepts of linear elastic fracture mechanics to these materials. In Marshall and Williams' [*1*][3] recent summary of most fracture work done on poly(methyl methacrylate) (PMMA), engineering values of toughness range from approximately 700 psi (in.)$^{1/2}$ to 1750 psi (in.)$^{1/2}$. This wide variation stems from a failure to assess the variables measured during an engineering fracture toughness test in the context of fundamental fracture phenomena unique to glassy plastics, specifically crack growth dissipative processes (crazing), and the crack velocity dependence of fracture.

Crazing, a form of highly localized plastic deformation, is the dominant mechanism of energy dissipation during crack growth in PMMA and many other glassy plastics [*2*]. Crack-tip crazes are colinear with and extend ahead of the advancing crack and have a wedge-shaped morphology. Also, lenticular-shaped secondary crazes may form on either side of the crack plane. Unlike shear yielding in metals, crazing is controlled primarily by a normal stress criterion [*3,4*]. While the effects of craze morphology on fracture energy have been investigated [*2,5,6*], no studies have related controlled crack tip craze morphologies to the design of valid fracture toughness tests.

---

[3] The italic numbers in brackets refer to the list of references appended to this paper.

Figure 1 summarizes the results of a number of investigations which show the large variation of crack velocity, $\dot{a}$, with applied stress intensity factor, K, in PMMA. Because of the large range of crack velocities during a rising load fracture toughness test, crack speed may be a more fundamental parameter than crack extension against which to measure crack growth resistance for glassy plastics. However, because of the complexity of the measurement, especially at high crack speeds, the type of experiment used to obtain the results summarized in Fig. 1 is too difficult for engineering tests. Also note the discontinuity in the K versus $\dot{a}$ curve at a crack velocity of approximately 1 to 5 in./s. As the crack accelerates above this critical $\dot{a}$, the mode of fracture shifts such that the crack can continue accelerating at a much lower applied K. As a result, during the usual fracture toughness test, a discontinuous increase in velocity is observed which represents an intrinsic fracture instability, unrelated to either the fracture mechanics formalism or the method of specimen loading. The fracture surface morphologies for the two velocity regimes are quite different and can be associated with different molecular processes [*10*].

Given the unique behavior of glassy plastics in terms of crack tip energy dissipation and crack velocity dependence, this study attempts to assess the influence of these phenomena on the design of a simple,

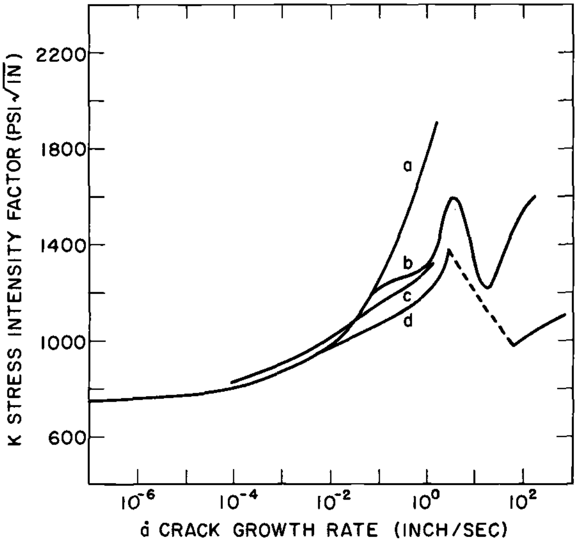

FIG. 1—*Variation of crack velocity with stress intensity factor in PMMA* (a, b, c, *and* d *taken from Refs* 7, 8, 9, *and* 10, *respectively*).

engineering fracture toughness test. Specifically, the linearity of specimen response is related to crack tip crazing, and the crack velocity effect is used to relate crack growth mode to a useful critical fracture criterion.

Procedure

Commercial PMMA was chosen primarily because its crazing and fracture properties have been studied extensively. In addition, PMMA has a relatively simple crack tip craze morphology such that the plastic zone can be easily characterized by the craze length extending ahead of the crack tip. The transparency of PMMA allows visual inspection of the crack and craze at various stages of crack growth.

Standard single edge notch tension (SEN) specimens were machined from the same sheet of ½-in.-thick Plexiglass. Specimen thicknesses were nominally ½ and ¼ in. To investigate the possibility of through-thickness variations in properties, the ¼-in.-thick specimens were machined from both the central portion of the sheet thickness (center cut specimen) and from locations near one face of the sheet (surface cut specimens).

Standard load-displacement (P-δ) records were obtained with instrumentation similar to that recommended by ASTM Test for Plane-Strain Fracture Toughness of Metallic Materials (E 399-72). Crosshead displacement rate was held constant at 0.2 in./min. The initial crack was formed in a fatigue testing apparatus at 30 Hz, where the maximum stress intensity factor during fatigue ranged between 500 psi $(\text{in.})^{1|2}$ and 1200 psi $(\text{in.})^{1|2}$. The range of initial crack lengths, a_1, was $0.20 \leq a_1/W \leq 0.62$, where W is the specimen width.

For each test various combinations of load, P, and crack length, a, were used to calculate critical stress intensity factors. For the SEN specimen with thickness B, the stress intensity factor is given by [*11*]

$$K = \frac{Pa^{1|2}}{BW} Y \tag{1}$$

where

$$Y = 1.99 - 0.41(a/W) + 18.70(a/W)^2 - 38.48(a/W)^3 + 53.85(a/W)^4$$

Each experimentally determined critical stress intensity factor was related to the P-δ curve and fracture surface observations in order to assess its suitability as a fracture criterion.

Crack arrest experiments were also conducted by rapidly unloading specimens after crack extension had started. Since crack extension in PMMA is essentially elastic, this technique is a reliable means by which crack tip conditions characteristic of various levels of stress intensity can be "frozen-in" for microscopic examination.

The crack tip craze length was measured microscopically by cutting the specimen on both sides of the crack plane and examining it as indicated in Fig. 2*a*. Figure 2*b* shows the crack tip of a specimen arrested after a small amount of slow growth. In addition to the direct observation of crack tip crazes (Area C on Fig. 2*b*), craze remnants were often observed directly on fracture surfaces where the crack had undergone a discontinuous change in mode (for example, fatigue precracking to slow growth or slow growth to fast fracture). Such craze remnants were also measured and associated with stress intensity levels just prior to the discontinuity.

Results

Crack-tip Craze Length

Figure 3 shows the length of craze as a function of applied K as determined from actual crazes and from craze remnants on various fracture surfaces. Both fatigue and crack arrest data are included. In addition, data from craze remnants at the transition from slow growth to fast fracture are plotted against estimates of K_c for fast fracture. These estimates will be discussed later. The size of the crack-tip plastic zone is roughly proportional to the square of the applied K, as expected from numerous plastic zone analyses. However, crack-tip plastic zones in PMMA are quite small compared to specimen dimensions. Thus the restrictive conditions imposed on precracking, specimen dimensions, and crack length normally encountered in metals testing are considerably relaxed. For instance, given the requirement that specimen thickness should be at least 2.5 (K_{Ic}/σ_{ys}), or approximately 16 times the plastic zone size (ASTM Method E 399-72), thickness effects should not be observed in PMMA for specimen thicknesses larger than approximately 0.025 in.

Fracture Surface Observations

Figure 4 shows fracture surfaces of a number of specimens with different initial crack lengths. During the fracture test, the crack accelerates from its original position at a_1 through the slow growth region, until a sharp transition to fast fracture occurs at a_2. As the initial crack length increases, the extent of slow growth increases until, for very long initial crack lengths (Fig. 4*d*), no fast fracture occurs at all. For intermediate values of a_1 (Fig. 4*c*), the crack apparently decelerates through the fast fracture region until it resumes slow growth again near the end of the specimen. Figure 5 is a photomicrograph which shows the parabolic markings on the fast fracture surface of a specimen with a long initial crack length. Since the density of parabolic markings has been shown to be roughly proportional to crack velocity and applied K [*12,13*], Fig. 5

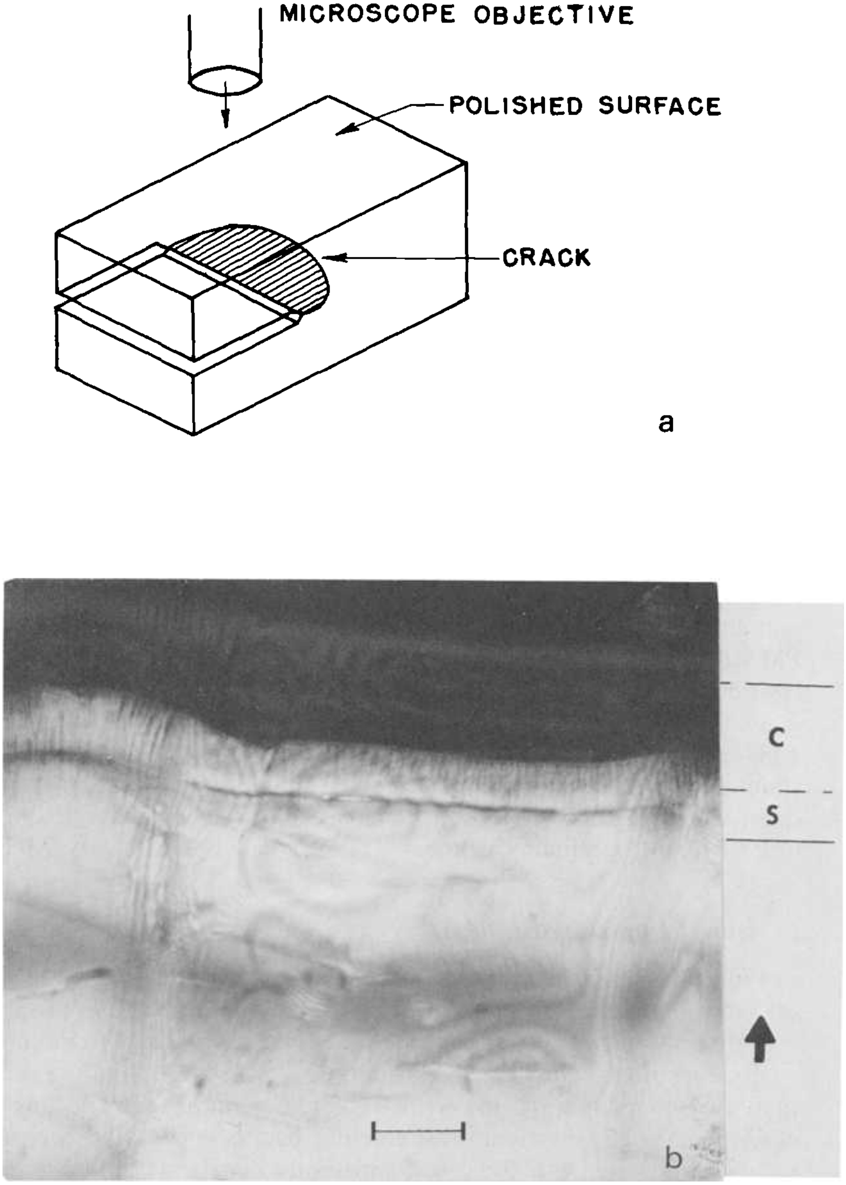

FIG. 2—(a) *Schematic showing method of crack tip observation.* (b) *photomicrograph of an arrested crack tip: F = fatigue precrack region, S = slow crack growth prior to arrest, and C = craze ahead of crack tip. Arrow denotes crack growth direction; marker = 0.001 in.*

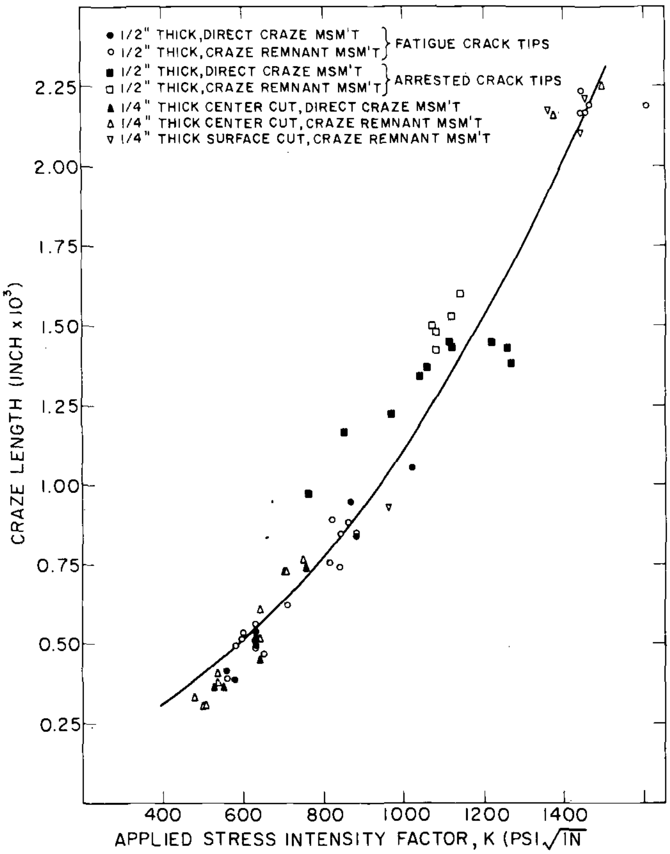

FIG. 3—*Crack tip craze length versus applied stress intensity factor.*

gives further indication that the crack decelerates through the fast fracture region under the influence of a decreasing applied K.

Load-Displacement Records

Typical P-δ curves, arranged in order of increasing initial crack length, are shown in Fig. 6. When crack propagation commences, the curve deviates from a straight line until a load maximum, $P_{\max}$, is reached. At points marked S, the crack velocity reaches such a high value that the recorder can no longer follow the rapidly changing load or displacement signals or both. It is important to note that the specimen has not yet totally separated at Point S.

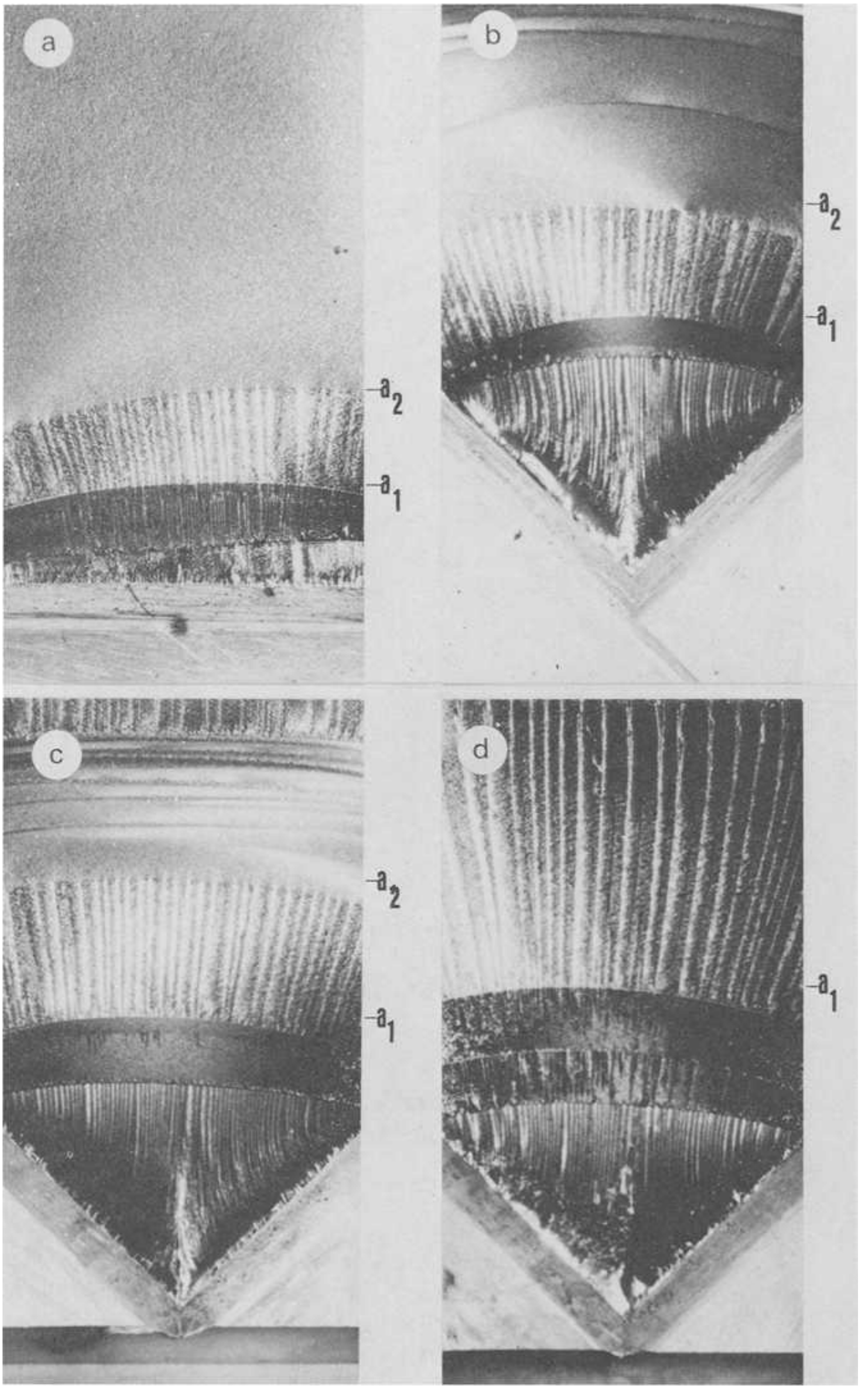

FIG. 4—*Macrofracture surfaces of 1/2-in.-thick specimens. Initial crack lengths:* (a) a_I/W = *0.284,* (b) a_I/W = *0.491,* (c) a_I/W = *0.522, and* (d) a_I/W = *0.584.*

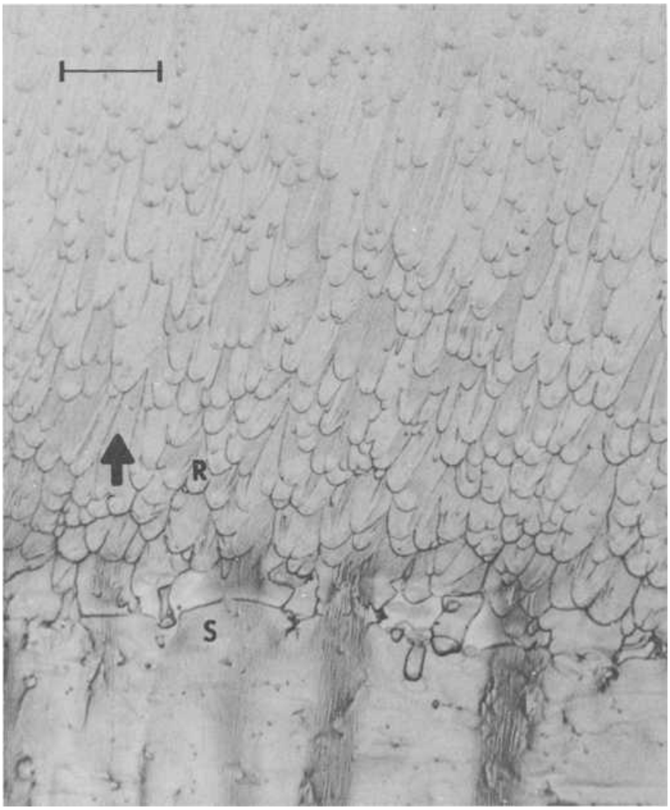

FIG. 5—*Fracture surface near the slow-fast transition: S = slow growth and R = fast fracture. Arrow denotes crack growth direction; marker = 0.005 in.*

One noteworthy feature of the P-δ curve is that there is no clear indication of either when slow crack propagation commences or when the slow-to-fast transition occurs. Unless these points can be unambiguously defined, the definition of a critical condition must necessarily be arbitrary. However, at least a qualitative relation between crack behavior and the P-δ curve can be obtained with the crack arrest experiments described earlier.

The arrested fracture surface shown in Fig. 2*b* reveals a measurable amount of slow crack growth (~ 15 μ) despite the fact that the specimen was arrested in the linear portion of the P-δ curve. Apparently then, crazing near the crack tip does not cause the observed nonlinearity in the P-δ curve, and this deviation from a straight line may be assumed to be due to crack extension alone. Specimens arrested at more advanced points

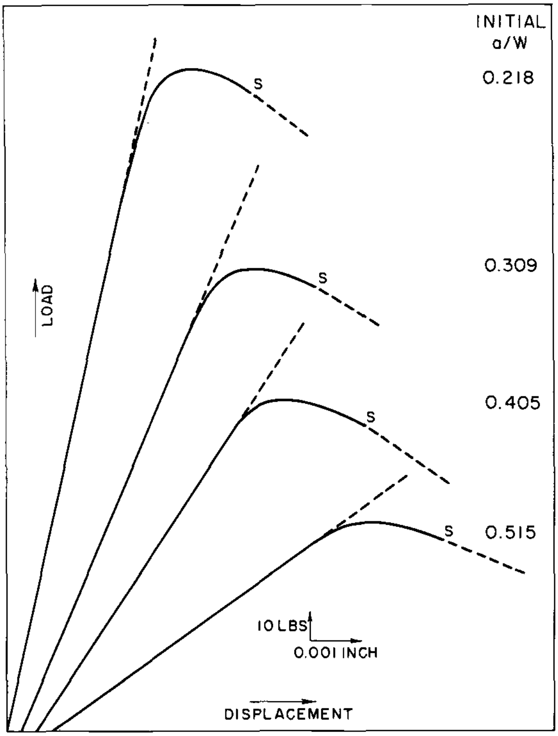

FIG. 6—*Load displacement* (P-δ) *curves for a number of 1/4-in.-thick surface cut fracture specimens.*

along the P-δ curve indicate that slow crack growth operates beyond $P_{\max}$. In fact, the entire fracture toughness test up to the limit of recorder response is confined to the slow growth regime.

Fracture Toughness Test

The measurement of fracture toughness for any material requires a criterion by which a critical condition can be defined on the P-δ curve. Then K_c can be calculated from Eq 1 where a load (P) and crack length (a) are appropriately chosen on the basis of the P-δ curve to define the critical condition. The following criteria were investigated and compared with observations just cited

K_c ($P_{\max}$, a_1)—"slow growth"
K_c ($P_{\max}$, a_2)—"fast fracture"

K_c (P_{max}, a_c)—load instability
K versus ($\Delta a/W$)—crack growth resistance
extrapolated K_c—fast fracture instability

The first two criteria are arbitrary since the observations just presented indicate that neither a_1 nor a_2 can be associated with P_{max}. However, most published data for PMMA are based on such definitions.

In order to define a critical condition based on P_{max}, or a load instability ($dP = 0$), initial slopes of P-δ records were calibrated against crack length and the secant offset method was used to determine the crack length at the load maximum, a_c[*14*]. K_c(P_{max}, a_c) was thus defined, based on the actual conditions at the load instability. The accuracy of the secant offset method for calculating crack lengths in PMMA is illustrated in Fig. 7. Note that the close agreement between computed and measured crack lengths is a further indication that crack extension in PMMA is essentially elastic.

Results on the ½-in.-thick specimens for the first three criteria just listed are plotted against initial crack length in Fig. 8. Data on the ¼-in. specimens are similar. As expected, precrack conditions and specimen thickness had no apparent effect on the results. However, K_c(P_{max}, a_2)

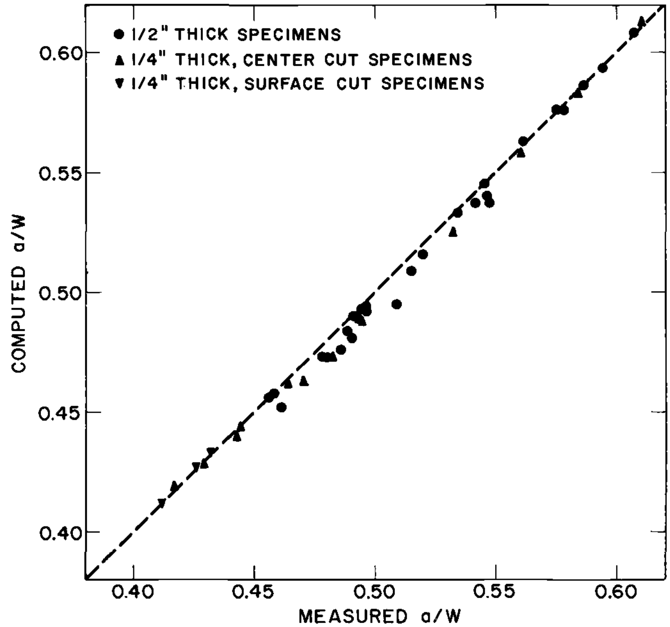

FIG. 7—*Accuracy of the secant offset method of crack length determination; computed* a/W *versus actual* a/W *at arrest.*

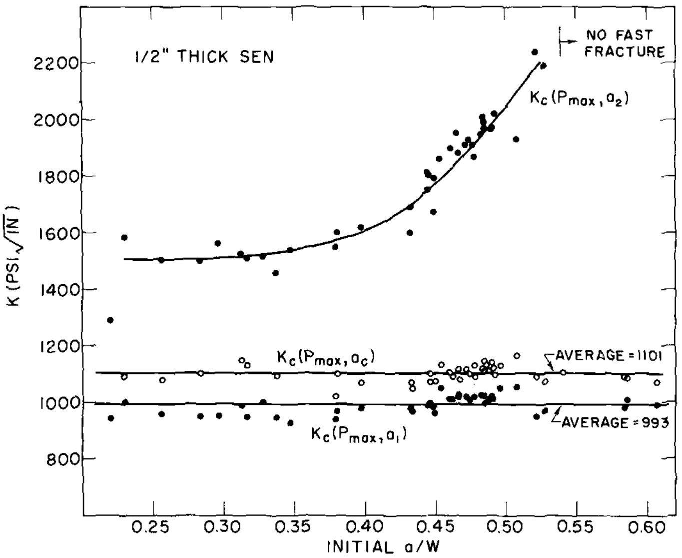

FIG. 8—*Various measures of* K_c *versus initial crack length for the 1/2-in.-thick specimen.*

proved to be quite sensitive to initial crack length. This observation explains much of the wide variation in published data for PMMA. The criterion based on initial crack length, a_1, and the criterion based on crack length at P_{max}, a_c, appear to be independent of all testing variables. Results for all specimen types are shown in Table 1. The slight differences between the ¼ and ½ in. specimens cannot be rationalized on the basis of plasticity effects but rather are due to crack length measurement techniques [*15*].

The secant offset method was also used to generate crack growth resistance curves [*16*], which are shown in Fig. 9 for the ½-in.-thick specimens. Again, the ¼-in. specimen behavior was similar. Note that the curves appear to be linear beyond P_{max} (open circles), and were

TABLE 1—*Data summary:* $K_c(P_{max}, a_1)$ *and* $K_c(P_{max}, a_c)$ *for all specimen types.*

		$K_c(P_{max}, a_1)$		$K_c(P_{max}, a_c)$	
Specimen Type	Number of Tests	Avg psi $\sqrt{in.}$	Standard Deviation, %	Avg psi $\sqrt{in.}$	Standard Deviation, %
1/2 in.-thick	46	993	3.1	1101	2.5
1/4-in. center cut	27	952	3.5	1061	4.2
1/4-in. surface cut	20	951	2.6	1042	2.3

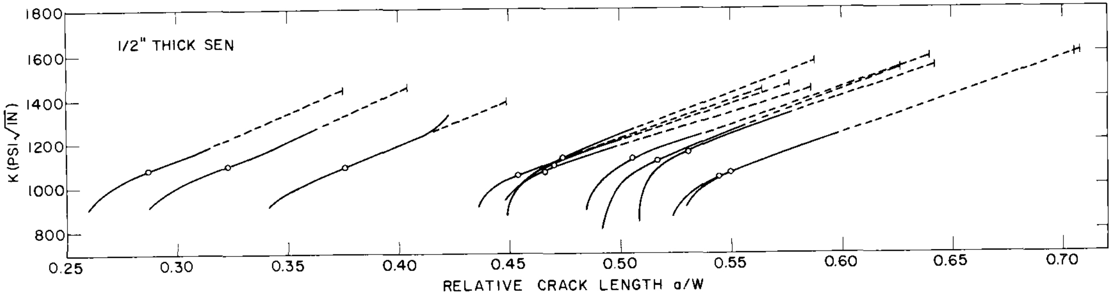

FIG. 9—*Crack growth resistance curves for 1/2-in.-thick specimens; circles denote location of* P_{max}.

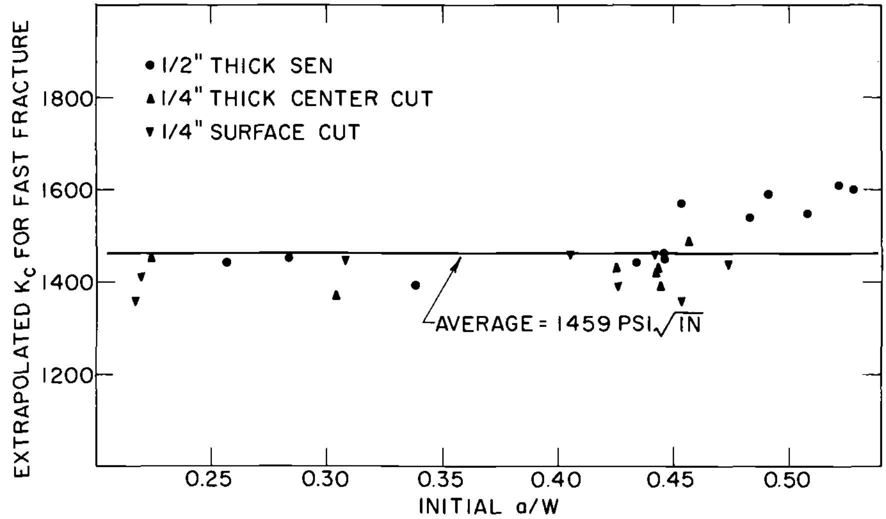

FIG. 10—*Extrapolated* K_c *for fast fracture versus initial crack length.*

therefore extrapolated to a_2, with the K values at these points designated as the extrapolated K_c for fast fracture. Despite the slight dependence on initial crack length shown in Fig. 10, the overall average K_c for fast fracture is 1459 psi (in. ½) with only a 5 percent standard deviation.

Discussion of Instability

The fracture surfaces shown in Fig. 4 indicate that geometry affects the morphology of fracture, as reflected in terms of the extent of slow growth, the existence of the slow-fast transition, and the crack velocity during fast fracture. It therefore seems appropriate to investigate conditions at $P_{\max}$ and during fast fracture in order to understand any possible geometric effects.

Following Clausing [*17*], Eq 1 may be solved for load and differentiated with respect to crack length. Noting that at $P_{\max}$, $dP=0$, an equation for $K_c(P_{\max}, a_c)$ can be obtained

$$K_c(P_{\max}, a_c) = \left[\frac{1}{2(a/W)} + \frac{1}{Y}\frac{dY}{d(a/W)}\right]^{-1} \frac{dK}{d(a/W)} \qquad (2)$$

If the total derivative $dK/d(a/W)$ is interpreted as the slope of the crack growth resistance curve at $P_{\max}$, then Eq 2 indicates that the fracture toughness defined at the load instability is predictably geometry dependent.

Thus, the use of a fracture toughness criterion based on load instability requires that specimens be designed to model the behavior of the structures under consideration. Also, note that Eq 2 is valid for any material, as long as crack extension in the vicinity of $P_{\max}$ is approximately elastic. Furthermore, if the crack growth resistance curve is linear in the region of $P_{\max}$, the equation can be evaluated quite simply for any specimen whose geometry has been characterized by Y (a/W).

The geometric parameter which arises in Eq 2 can also be derived from a consideration of how crack length affects crack velocity, especially in the fast fracture regime. Rewriting Eq 1 to reflect displacement control typical of most fracture toughness tests

$$K = \frac{\Delta}{\lambda} a^{1/2} Y \tag{2}$$

where Δ is the crosshead displacement and λ is the specimen compliance. Noting that for $\dot{a}$ to decrease, $dK/d(a/W)$ must be negative, this equation is then differentiated with respect to (a/W) and $dK/d(a/W)$ is constrained to be negative

$$\frac{1}{\lambda}\frac{d\lambda}{d(a/w)} > \left[\frac{1}{2(a/w)} + \frac{1}{Y}\frac{dY}{d(a/W)}\right] \tag{3}$$

Note that the toughness has no effect on whether the crack will decelerate. Also note that the result is generally applicable as a necessary condition for crack deceleration. In fact, a similar relation has been used to design crack arrest specimens of boron-aluminum composites.[4] As crack length increases, the compliance parameter on the left side of the inequality increases faster and eventually becomes greater than the geometric parameter on the right. Thus, the load carrying capacity of the specimen decreases more rapidly than the geometric factor (Y) can amplify the applied K, and the crack slows down.

The geometric parameter $[1/2(a/W) + 1/Y\ dY/d(a/W)]$ in Eqs 2 and 3 appears to offer a useful characterization of geometric effects on crack behavior and is plotted against (a/W) in Fig. 11 for a number of standard specimen types. The apparent independence of $K_c(P_{\max}, a_c)$ and crack length in this study must be specific to the present experimental circumstances, since the geometry parameter in Fig. 11 differs substantially among various specimen types, although some are reasonably constant in the range of $a/W \approx 0.5$. Generally, however, values of $K_c(P_{\max}, a_c)$ do show some crack length dependence in plane stress tests.

In terms of crack stability, note that for a decelerating crack, Eq 3 requires that the geometric parameter be small relative to the compliance parameter. In Fig. 11, the geometric parameter for the DCB specimen

---

[4] Olster, E. F., private communication.

decreases substantially with a/W while it increases for the CT specimen. This variation is consistent with the general behavior of these specimens; the DCB is inherently stable while the CT specimen promotes unstable crack growth [*17*].

Conclusions

The association of fundamental phenomena such as crack tip crazing and crack velocity effects with the basic variables of a fracture toughness test has established several guidelines for the characterization of fracture in PMMA. It has been demonstrated that, unlike the case for metals, slow stable crack growth in PMMA is essentially brittle (that is, despite microscopic dissipative processes, the macroscopic behavior appears elastic). Also, the sharp transition to fast fracture at a_2, a reflection of the discontinuity in the K versus $\dot{a}$ curve, is not associated with the load

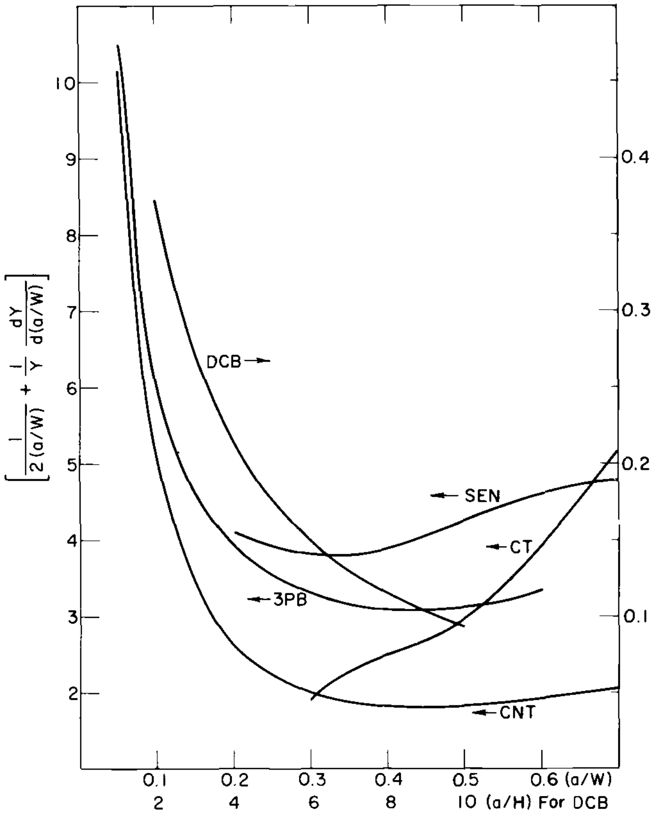

FIG. 11—*Parameter describing the geometry dependent behavior of various specimen types: DCB = double cantilever beam specimen, SEN = single edge notch specimen, CT = compact tension specimen, 3PB = three-point bend specimen, and CNT = center notch tension specimen.*

instability on the P-δ curve. Thus, the following conclusions can be drawn.

1. Specimen size and precracking restrictions for PMMA are considerably less severe than for metals.
2. The previously quoted criteria $K_c(P_{max}, a_1)$ and $K_c(P_{max}, a_2)$ are unnecessarily arbitrary since neither a_1 nor a_2 conincide with P_{max}.
3. Since the extent of slow growth increases with initial crack length, $K_c(P_{max}, a_2)$ varies considerably with a_1. This explains, in part, the variation quoted in the literature.
4. The most reasonable definitions for K_c are based on two uncoupled instabilities, load instability during slow growth, $K_c(P_{max}, a_c)$, and the intrinsic slow-fast transition, K_c (extrapolated).

Specimens can be designed to control both types of unstable crack growth and thus model the behavior of real structures. Finally, it should be noted that the ultimate utility of fracture toughness testing of polymers will most likely be realized for structural engineering plastics whose dissipative processes and crack growth modes are much more complex than those of PMMA. However, the fundamental considerations presented here provide a basis for the development of fracture toughness testing approaches for materials behaving in a more complex manner.

Acknowledgments

This work was supported, in part, by a grant from the Pennsylvania Science and Engineering Foundation.

References

[1] Marshall, G. P. and Williams, J. G., *Journal of Materials Science*, Vol. 8, 1973, p. 138.

[2] Kambour, R. P., *Applied Polymer Symposia*, Vol. 7, 1968, p. 215.

[3] Sternstein, S. S., Ongchin, L., and Silverman, A., *Applied Polymer Symposia*, Vol. 7, 1968, p. 175.

[4] Sternstein, S. S. and Ongchin, L., *Polymer Preprints*, American Chemical Society, Division of Polymer Chemistry, Vol. 10, No. 2, 1969, p. 1117.

[5] Cessna, L. C. and Sternstein, S. S., *Journal of Polymer Science*, Part B, Vol. 3, 1965, p. 825.

[6] Marshall, G. P., Culver, L. E., and Williams, J. G., "The Growth of Cracks and Crazes in Polystyrene: A Fracture Mechanics Approach," Imperial College of Science and Technology, Mechanical Engineering Department, London, 1971.

[7] Marshall, G. P., Culver, L. E., and Williams, J. G., *Plastics and Polymers*, Vol. 37, 1969, p. 175.

[8] *Closed Loop*, MTS Systems Corporation, Vol. 1, No. 5, 1966, p. 3.

[9] Smith, H. L., Stonesifer, F. R., and McKinney, K. R., *Proceedings*, Air Force Conference on Fatigue and Fracture of Aircraft Structures and Materials, AFFDL TR 70-144, Dec. 1969, pp. 395–406.

[10] Broutman, L. J. and Kobayashi, T., "Crack Propagation Studies in Glassy Polymers," AMMRC CR 71-14, AD 736859, Army Materials and Mechanics Research Center 1971.

[11] Brown, W. F., Jr. and Srawley, J. E., *Plane Strain Crack Toughness Testing of High Strength Metallic Materials, ASTM STP 410,* American Society for Testing and Materials, 1966.

[*12*] Cotterell, B., *International Journal of Fracture Mechanics,* Vol. 4, 1968, p. 209.
[*13*] Rosenfield, A. R. and Kanninen, M. F., "The Fracture Mechanics of Glassy Polymers," paper presented at American Society for Metals Symposium on Fracture in Polymers, Cleveland, 16 Oct. 1972.
[*14*] Srawley, J. E., Jones, M. H., and Brown, W. F., Jr., *Materials Research and Standards,* Vol. 7, 1967, p. 262.
[*15*] Margolis, R., "Fracture Toughness Testing of Glassy Plastics," Ph.D. thesis, Carnegie-Mellon University, Pittsburgh, April 1974.
[*16*] *Fracture Toughness Evaluation by R-Curve Methods, ASTM STP 527,* American Society for Testing and Materials, 1973.
[*17*] Clausing, D. P., *International Journal of Fracture Mechanics,* Vol. 5, 1969, p. 211.

S. R. Novak [1] *and J. M. Barsom* [1]

Brittle Fracture (K_{Ic}) Behavior of Cracks Emanating from Notches

---

REFERENCE: Novak, S. R. and Barsom, J. M., "**Brittle Fracture (K_{Ic}) Behavior of Cracks Emanating from Notches,**" *Cracks and Fracture, ASTM STP 601,* American Society for Testing and Materials, 1976, pp. 409–447.

ABSTRACT: Experimental and analytical studies were conducted under AISI sponsorship to determine the influence of short cracks emanating from notches on fracture behavior. All studies were conducted by using concepts of linear-elastic fracture mechanics (LEFM). The experimental studies were conducted on AISI 4340 steel at a high strength level (σ_{ys} = 215 ksi = 1480 MN/m^2) under plane-strain (K_{Ic}) conditions by using various types of fatigue-cracked as well as notched and fatigue-cracked specimens. The analytical studies were conducted by using recently developed theoretical K_I analyses for notched and fatigue-cracked specimens.

The experimental results obtained by using various types of standard fatigue-cracked specimens demonstrated that the basic fracture-toughness behavior of 4340 steel is repeatable and reproducible within a relatively narrow range (K_{Ic} = 70±5 ksi $\sqrt{\text{in.}}$ = 77±5.5 MNm$^{-3/2}$). Limited experimental results on notched and fatigue-cracked double-edge-notched tension (DENT) specimens verified the accuracy of a recent theoretical K_I analysis by Tada. Results for these notched and cracked DENT specimens exhibited good agreement with the baseline K_{Ic} behavior, but two to three times the amount of scatter usually observed in standard K_{Ic} tests (±5 to 10 percent). Tests demonstrated no significant differences in the basic fracture behavior (apparent K_{Ic}) of either pure-tension (DENT) specimens or essentially pure-bending (three-point-bend) specimens when tested with cracks emanating from notches. Apparent K_{Ic} results calculated by using traditional equations, in which the presence of the notch is ignored (treated as a crack of equivalent length), were elevated above the intrisic K_{Ic} level by less than 30 percent for all investigated combinations of specimen type, notch type, and the length of the fatigue crack beyond the notch tip (Δa_F).

The theoretical studies were conducted to develop an analytical criterion

$$\left[\left(\frac{\Delta a_F}{\sqrt{a_N \rho}}\right) = 1/4\right]$$

that predicts the depth beyond which a notch with an emanating crack can be treated as a crack of equivalent length. The engineering significance of this criterion is discussed. For values of the parameter that are greater than the criterion, traditional K_I equations are accurate within ±5 to ±10 percent. For values less than the criterion, the stress-intensity (K_I) at the tip of a short fatigue

---

[1] Senior research engineer and section supervisor, Research Laboratory, United States Steel Corporation, Monroeville, Pa. 15146.

crack (of length Δa_F) emanating from a dull notch (of length, a_N, and radius ρ) is always less severe than a crack of equivalent length, and the use of traditional K_I equations can grossly overestimate the actual K_I at the crack tip. For this short crack-length range, K_I values must be calculated by using appropriate theoretical analyses that account for notch effects in order to minimize the conservative results of traditional analyses.

Included in the present work is a state-of-the-art summary of currently available theoretical K_I analyses for cracks in the near vicinity of notches.

KEY WORDS: crack propagation, brittle fracturing, fractures (materials), cracks, failure analysis, structural integrity

Most premature structural failures are caused by deficiencies in design, fabrication, erection, material selection, or material behavior, or by a combination of these parameters. In the case of sudden or catastrophic fracture, the source of the fracture event can usually be traced to a structural detail, where the combined effects of a discontinuity or stress concentrator and a high applied tensile stress are sufficient to cause fracture. The basic nature of such discontinuities or "notches" may be either (1) mechanical (holes, small-radius fillets, sharp reentrant corners); (2) metallurgical (microstructural changes such as from ferrite-pearlite to martensite in the case of steel), or more commonly; (3) a combination of both mechanical and metallurgical (arc-strikes, flame-cut plate edges).

Regardless of the basic nature of the discontinuity, the applied stress becomes concentrated locally and the sequence of events leading to premature fracture is generally the same for all cyclically loaded structures. For the application of cyclic stresses in service, this sequence corresponds to fatigue-crack initiation, fatigue-crack propagation, and eventual sudden fracture upon attainment of a critical crack size, a_{cr}. This same general sequence prevails regardless of whether the structural component is simple (nonredundant) or complex (redundant), and also regardless of whether residual stresses are present. These conditions merely relate to the rate of change in stress with increasing crack length (structural compliance), the magnitude of the applied stress at fracture, and the extent of overall structural damage due to the fracture.

The successful use of linear-elastic fracture mechanics (LEFM) to accurately predict the critical combination of crack length, a_{cr}, and stress, σ_f, at fracture for brittle materials (plane-strain state of stress) by means of the K_{Ic} parameter is well documented. Many theoretical LEFM relationships currently exist for calculating the stress-intensity factor, K_I, at the tip of a crack located in various body configurations and under various conditions of applied stress, σ, and crack size, a, shape, and orientation [*1–3*].[2] Most such K_I equations relate to the "long crack" or "pure crack" class of problems, in which the crack tip has propagated away from the

---

[2] The italic numbers in brackets refer to the list of references appended to this paper.

crack starter (initial discontinuity or notch) and no account is made (or is necessary) regarding the influence of such a crack starter on K_I. A few additional K_I equations are also available for the "short-crack" class of problems, in which the crack tip is still in the vicinity and under the influence of the initial stress concentrator. This short-crack case is often described as a condition of the crack tip being within the "shadow" of the crack starter (notch) and represents a case where the stress fields of the crack and crack starter interact. Such interactions are specifically accounted for in derivations of K_I for this short-crack class of problems.

If the fracture toughness (K_{Ic}, K_{Id}, K_c) of a structural component is sufficiently high, long cracks can be tolerated in service. That is, such cracks can be easily detected and repairs can be made before fracture has occurred. In contrast, if the fracture toughness is marginal to poor, the existence of short cracks may lead to premature fracture in service.

The accuracy of theoretical K_I equations in predicting the critical conditions at fracture (a_{cr}, σ_f) has been demonstrated experimentally many times for the long-crack (pure crack) class of problems, but the accuracy of existing K_I equations for short cracks in the vicinity of stress concentrators. is currently unknown. Yet overall predictions of minimum structural life depend on such accuracy, even for materials of high fracture toughness, since these predictions rely on correctly characterizing the rate of subcritical crack growth for such short cracks by the mechanisms of fatigue, stress-corrosion cracking, or corrosion fatigue. Moreover, a *large precent of the useful "structural life"* can *actually be spent* during the initiation and early-stage propagation of a crack from a notch in service.[3] Consequently, the accuracy of life prediction relationships depends directly on the accuracy of the K_I characterization for such short-crack problems.

Because of the general importance of this problem, the current investigation was conducted to compare experiment and theory for the conditions of plane-strain fracture, K_{Ic}, of short cracks extending various distances from a preexisting notch. The experimental studies were conducted by using notches with stress-concentration factors, K_t, of 2 and 3, and under otherwise well-defined laboratory conditions—that is, under conditions free of metallurgical discontinuities or residual stress or both. In addition, analytical studies were conducted on specimen geometries other than those used experimentally to determine whether basic relationships could be formulated for characterizing the general nature of K_I for

---

[3] This is particularly true for crack growth due to fatigue or corrosion fatigue, where the crack propagation rate is highly dependent on the stress-intensity fluctuation according to the general relation $da/dN = A\Delta K_I^n$ (where A and n are properties of the material and environment combination evaluated). This is, the ΔK_I value is generally much smaller for short cracks from notches (compared to corresponding long cracks) and the resulting value of da/dN is also much slower, thereby requiring more stress cycles and accounting for a large percentage of the overall structural life.

short cracks emanating from notches. This work was sponsored by the American Iron and Steel Institute (AISI) and was conducted at U. S. Steel Research Laboratory under AISI Project 168.

Materials and Experimental Work

The material used throughout the study was AISI 4340 steel heat-treated to a high strength level ($\sigma_{ys} \cong$ 215 ksi or 1480 MN/m^2). All specimens were obtained from the same 1-in.-thick (2.54-cm) plate. The choice of strength, σ_{ys}, and plate thickness (B = 1.0 in.) was such as to ensure valid K_{Ic} behavior and the complete applicability of LEFM concepts. The plate was divided into four pieces that were heat-treated individually. The chemical composition and mechnical properties obtained from the four pieces are presented in Tables 1 and 2, respectively.

Double-Edge-Notched Tension (DENT) Specimens

The primary objective of the current study was first to establish the basic fracture behavior, K_{Ic}, and then to assess the fracture behavior for specimens with cracks emanating various distances from a mechanical notch with a known stress-concentration factor, K_t. The choice of a double-edge-notched DENT specimen was made to ensure a pure tension stress field, thereby eliminating bending stresses.

All DENT specimens were nominally 1 in. thick (B = 1.00 in.). In addition to the normal narrow-sawcut DENT specimens used for establishing K_{Ic}, two additional notched-type DENT specimens were used in the study, Fig. 1. One specimen contained a deep notch of radius ρ = 0.20 in. (0.5 cm) and the other a semicircular notch of radius ρ = 0.60 in. (1.5 cm), corresponding to K_t values of approximately 3.0 and 2.0, respectively. For each of these latter two notch types, specimens were prepared with different fatigue-crack lengths, Δa_F, beyond the blunt notch tip. The extent of the fatigue cracks was proportioned relative to the notch root radius, ρ. Specifically, for the deep-notch type of specimen with ρ = 0.20 in., duplicate specimens with fatigue-crack lengths of nominally 0, 0.050, 0.100, and 0.200 in. (0, 0.125, 0.25, and 0.50 cm) beyond the notch tip were prepared. For the semicircular-notch type of specimen, duplicate specimens were prepared with fatigue-crack lengths of 0, 0.10, 0.30, and 0.50 in. (0, 0.25, 0.75, and 1.25 cm). The fatigue-crack orientation for all DENT specimens was longitudinal (L-T designation).

The fatigue precracking of all DENT specimens was conducted in a 300-kip (1334 kN) MTS testing machine under R = 0.10 conditions at a frequency of 1 Hz. All DENT specimens were fatigue cracked using a final stress-intensity fluctuation (based on the final crack length, $a = a_T = a_N + \Delta a_F$) in the range ΔK_F = 15.0 to 24.0 ksi $\sqrt{\text{in.}}$ (16.5 to 26.5

TABLE 1—*Chemical composition of 4340 steel tested—percent (Heat 4P3585, Plate 306 296-B) (check analysis).*

C	Mn	P	S	Si	Ni	Cr	Mo	V	Ti	Al Sol	Al Insol	Al Total	N	Co	O_2
0.40	0.70	0.008	0.022	0.33	1.72	0.89	0.22	0.074	<0.005	0.002	0.003	0.005	0.008	0.028	0.0043

TABLE 2—*Mechanical properties of 4340 steel tested*[a] *(Heat 4P3585, Plate 306 296-B).*

Plate Section	Yield Strength (0.2% Offset), ksi	Tensile Strength, ksi	Elongation in 1 in., %		Reduction of Area, %		Charpy V-Notch Energy Absorption, at 80°F, ft•lb
			At Maximum Load	At Fracture	At Maximum Load	At Fracture	
A	215	239	4.7	8.3	6.0	22.6	9
B	216	238	5.0	10.0	7.0	37.5	10
C	215	238	5.7	9.5	10.5	33.9	10
D	214	235	4.7	10.5	6.4	36.5	10

Heat Treatment

Temperature, °*F*	Time at Temperature, h	Type of Cooling
1600	1	air cool
1550	1	oil quench
750	1	air cool

NOTES—Conversion factors: 1 ksi = 6.895 MN/m^2, 1 inch = 25.4 mm, °C = 5/9 (°F − 32), and 1 ft•lb = 1.36 J.

[a] All specimens were taken in the longitudinal orientation. Tensile results are the average obtained from three 0.252-in.-diameter specimens (except for plate section B for which two specimens were tested), and impact results are the average of four standard Charpy V-notch specimens.

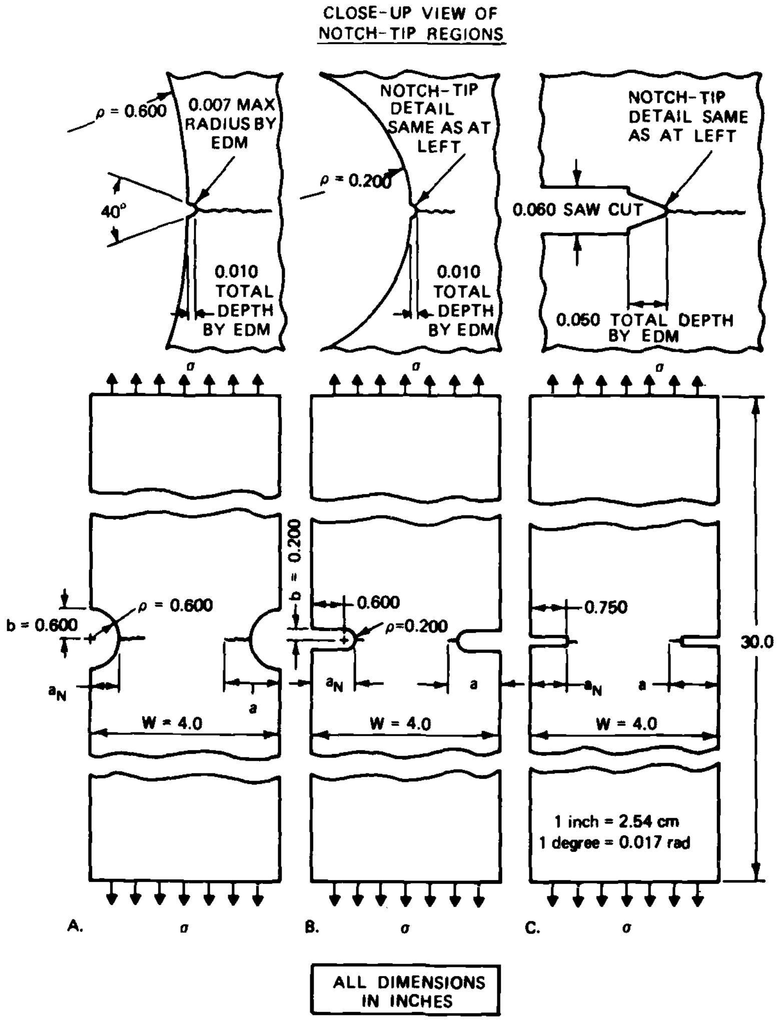

FIG. 1—*Three basic types of double-edge-notched tension (DENT) specimens tested.*

$MNm^{-3|2}$), with the number of stress cycles required being in the range $N = 50\ 000$ to 475 000.

All DENT specimens were tested to fracture under "static" loading conditions $\dot{\epsilon} \cong 10^{-5}\ s^{-1}$ at the crack tip) at room temperature (+72°F or 22°C) by using a 440-kip (1957 kN) Baldwin tension-testing machine. Aside from the basic type of specimen (DENT), all other test conditions were in accordance with ASTM Test for Plane-Strain Fracture Toughness of Metallic Materials (E 399-74T) for standard K_{Ic} testing. Standard load-displacement (P versus V) plots were obtained for each notch by using two double-size NASA clip gages (for V), a hydraulic pressure cell (for P), and an X-Y_1-Y_2 recorder.

Three-Point-Bend Specimens

A secondary objective of the investigation was to conduct a study of the fracture behavior for short cracks emanating from notches by using three-point-bend specimens. This supplementary study was made to complement the primary DENT specimen study just described. However, these tests were basically different in that they were conducted under essentially pure-bending conditions as opposed to the pure-tension conditions for the DENT specimens.

The three-point-bend specimen study was essentially the same as the DENT specimen study in that the same basic notch types, notch orientation (L-T designation), and fatigue-crack extensions (Δa_F) beyond the notch tip were used, Fig. 2. Similarly, the thickness for the three-point-bend specimens was nominally 1 in. (B = 1.00 in.). Standard three-point-bend specimens were first prepared to evaluate K_{Ic}, and then single

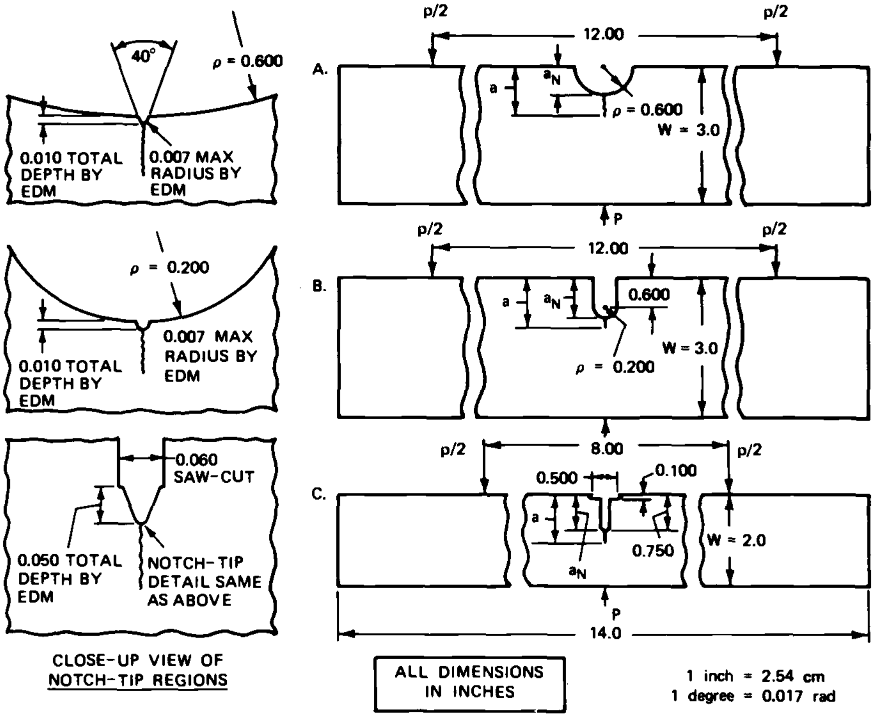

FIG. 2—*Three basic types of three-point bend specimens tested.*

specimens at each of three different Δa_F values beyond the notch tip were prepared for each of the two additional notch geometries.

The fatigue-crack preparation for all 3-point-bend specimens was accomplished by using a high-speed Amsler Vibraphore testing machine under $R = 0.1$ conditions at a frequency of approximately 8000 cpm. All three-point bend specimens were fatigue cracked using a final stress-intensity fluctuation in the range $\Delta K_F = 15.0$ to 30.0 ksi $\sqrt{\text{in.}}$ (16.5 to 33.0 $\text{MNm}^{-3|2}$), with the required number of stress cycles being in the range $N = 80\ 000$ to 700 000.

All three-point-bend specimens were tested to fracture under testing conditions identical with those used for the DENT-specimen study. That is, all 3-point-bend specimens were tested under static loading conditions ($\dot{\epsilon} \cong 10^{-5}\ \text{s}^{-1}$ at the crack tip) and at room temperature ($+72°F$) in the same 440-kip Baldwin tension testing machine. These three-point-bend specimens were tested in accordance with ASTM Method E 399-74T for standard K_{Ic} testing by using the same instrumentation just described for the DENT-specimen study. The three-point loading span (S) to specimen width (W) for these tests corresponded to S:W = 4.0:1.

Compact Specimens (CS)

To evaluate the uniformity of K_{Ic} behavior for several of the 4340 steel plates (heat-treated separately) used in the study, additional fracture-toughness specimens of the compact-specimen (CS)[4] type were prepared. These standard CS specimens were full-thickness ($B = 1.00$ in.) and 1-T in specimen size, Fig. 3, and had the same L-T crack orientation as the DENT and three-point-bend specimens. A select number of the 1-T CS specimens were prepared from the broken halves of DENT specimens at a location as close as possible to the plane of the original fracture.

The CS specimens were all fatigue-precracked by using the high-speed Amsler Vibraphore testing machine under the same conditions just described for the three-point-bend specimens. The CS specimens were tested to fracture in accordance with ASTM Method E 399-74T under testing conditions identical with those just described for both the DENT and the three-point-bend specimens.

K_I *Stress Analyses*

The equation used in calculating K_{I} for the DENT specimen was the basic relation developed earlier by Bowie using complex variable methods [*4*]. This equation has been estimated to be accurate within 1 percent [*4*]. The equations used in calculating K_{I} for the three-point bend and CS specimens were the basic relations that are described in ASTM

---

[4] Formerly referred to as the compact tension (CT) specimen.

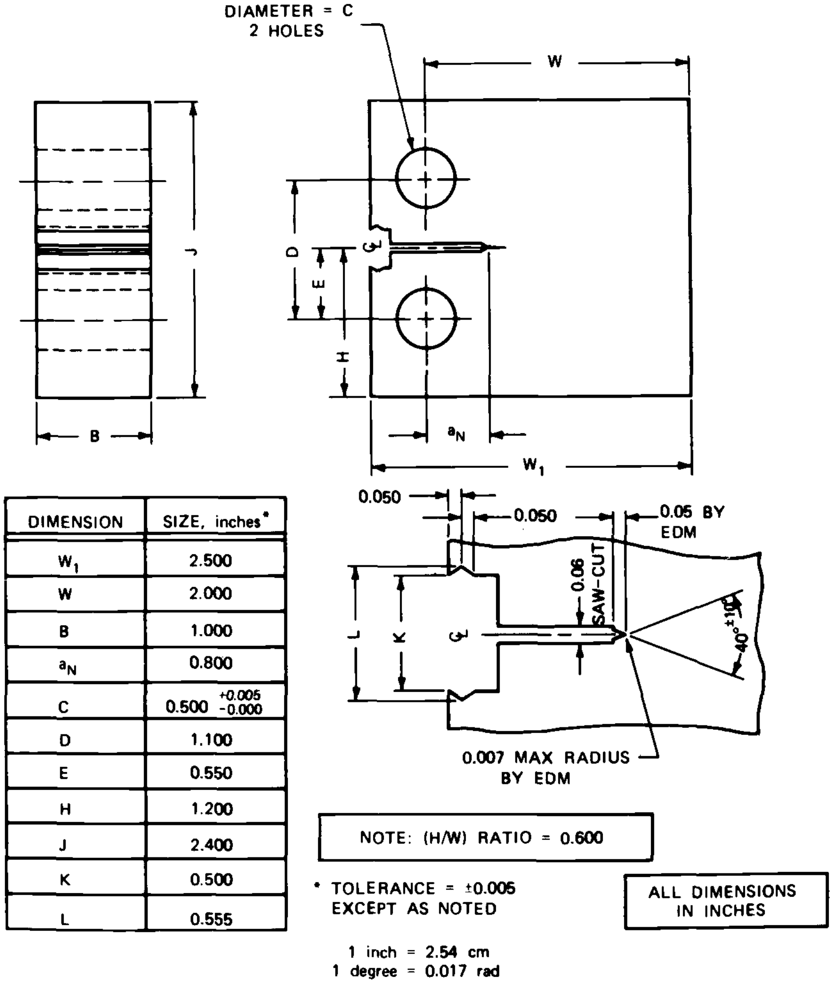

DIMENSION	SIZE, inches*
W_1	2.500
W	2.000
B	1.000
a_N	0.800
C	$0.500\ ^{+0.005}_{-0.000}$
D	1.100
E	0.550
H	1.200
J	2.400
K	0.500
L	0.555

NOTE: (H/W) RATIO = 0.600

* TOLERANCE = ±0.005
EXCEPT AS NOTED

ALL DIMENSIONS
IN INCHES

1 inch = 2.54 cm
1 degree = 0.017 rad

FIG. 3—*1-T compact specimen (CS).*

Method E 399-74T. These three pure crack equations for K_I are the standard relations employed when attempts are made to measure the baseline K_{Ic} behavior of a material using conventional specimen preparation (narrow saw-cut notch with long fatigue crack extension). As such, these pure crack equations are to be distinguished from other K_I analyses available for short cracks emanating from stress raisers such as notches, or "blunt notch" equations, that are given in remaining sections of the present paper.

Results and Discussion

Analytical Considerations

Basic Relationship Between K$_\mathrm{I}$ *and* K$_\mathrm{t}$—The problem of assessing the stress-intensity value for opening mode loading, K_I, can be formulated, because of dimensional-analysis considerations [*1*], in general terms from quantities that are either remote from or local to the tip of a crack, given respectively by

$$K_\mathrm{I} = C_1 \sigma \sqrt{a} \tag{1}$$

or

$$K_\mathrm{I} = \lim_{\rho \to 0} C_2 \sigma_m \sqrt{\rho} \tag{2}$$

where σ is a remotely applied (gross) stress and σ_m is the maximum stress at the tip of a notch of length, a, and acuity, ρ. C_1 and C_2 are constants that depend on the geometry of the body in which the crack is embedded.

Equation 1 represents the traditional LEFM approach to the problem, which is a special case of the general-fracture-mechanics approach represented by Eq 2. This latter equation represents a direct approach to the problem by dealing with the actual parameters occurring at the crack tip, σ_m and ρ, where the fracture process actually occurs, and is applicable to both sharp cracks and to notches.

The basic relationship between K_I and the conventional elastic-stress-concentration factor, $K_\mathrm{t} = \sigma_m/\sigma$, can be assessed by considering both Eqs 1 and 2 for the special case of a long, narrow elliptical notch (approaching a crack), of radius ρ, contained within an infinite sheet subjected to a uniform tensile stress, σ, applied remotely, Fig. 4. For this classical case, the value of the constant in Eq 1 is well known to be $C_1 = \sqrt{\pi}$. Equating both Eqs 1 and 2 and using the relations given in Fig. 4 yields the result $C_2 = \sqrt{\pi}/2$. Thus, Eq 2 may be rewritten as

$$K_\mathrm{I} = \lim_{\rho \to 0} \frac{\sqrt{\pi}}{2} \sigma_m \sqrt{\rho} \tag{3}$$

or, since $K_\mathrm{t} = \dfrac{\sigma_m}{\sigma'}$

$$K_\mathrm{I} = \lim_{\rho \to 0} K_\mathrm{t} \frac{\sigma \sqrt{\pi \rho}}{2} \tag{4}$$

Equation 4 shows that K_I is related to K_t, but only for elastic-stress levels at the notch tip ($\sigma_m \leqq \sigma_\mathrm{ys}$) and theoretically only for the limiting conditions of the notch root radius approaching zero ($\rho \to 0$).

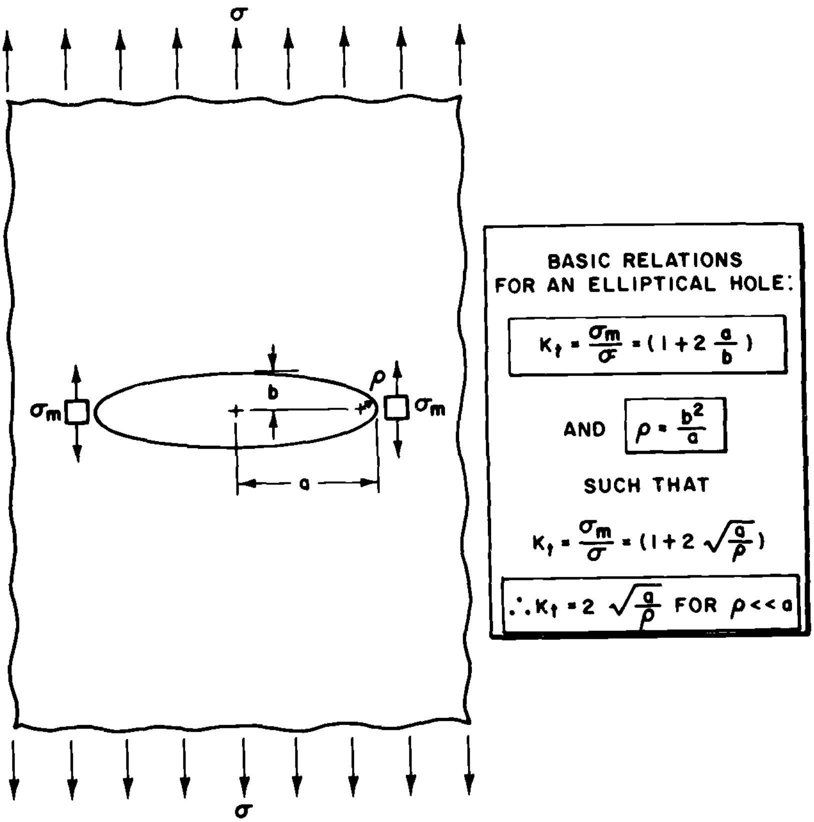

FIG. 4—*Basic relations between theoretical stress-concentration factor,* K_t, *and notch geometry for a long, narrow elliptical notch (approaching a crack) contained in an infinite CCT panel.*

Availability of Theoretical K *Analyses for Cracks in the Vicinity of Notches*—For a cracked body there are three primary modes of loading. These correspond to opening mode, shearing mode, and antiplane shearing mode of the crack faces, described by the symbols I, II, and III, respectively. The specific mode of loading for a cracked body (K_{I}, K_{II}, or K_{III}) is determined primarily by the orientation of the crack and the nature of the applied stress (tension, bending, shear, torsion). Currently, a large number of K_{I}, K_{II}, and K_{III} analyses are available for cracked bodies [*1–3*]. However, most of such K formulations deal with cracks that either are far removed from any boundary of the body or emanate from a straight-sided boundary. That is, only a limited number of existing K formulations are available for short cracks either emanating from or in the near vicinity of stress concentrators such as notches. However, this is the most common condition encountered in real engineering structures because initiation of subcritical crack growth (fatigue, stress-corrosion cracking, corrosion fatigue) is most likely to occur at notches due to stress concentration. Various theoretical studies of K for such short crack problems are currently available in the literature [*5–25*]. The results from most of these studies have been summarized either in the handbook prepared by Sih [*2*] or the one prepared by Tada et al [*3*].

Experimental Results

Baseline K_{Ic} *Behavior*—The specific experimental results obtained in the present study to measure the basic K_{Ic} behavior of the AISI 4340 steel are presented in Table 3. This table shows that the results for the three DENT specimen tests yielded an average value of $K_{Ic} = 68.3$ ksi$\sqrt{\text{in.}}$ (75.1 MNm$^{-3/2}$), and that the results for 4 three-point-bend tests yielded an average value of $K_{Ic} = 71.7$ ksi$\sqrt{\text{in.}}$ (78.9 MNm$^{-3/2}$). These results, obtained under conditions of pure tension and virtually pure bending, respectively, are in excellent agreement.

As can be seen from Table 3, the K_{Ic} results obtained for the DENT and the three-point-bend specimen tests represent the fracture behavior of only two of the four individually heat-treated plates of 4340 steel used in the present study (Plates A and D). To assess the fracture toughness of the remaining two plates of 4340 steel used (Plates B and C) and to further evaluate the K_{Ic} repeatability in general, six additional 1-in.-thick CS specimens were machined and tested. These specimens corresponded to duplicate specimens from three different plates including Plates B and C.

The results for these CS specimen tests are presented in Table 4 and show that the average K_{Ic} value was 70.8 ksi $\sqrt{\text{in.}}$ (77.9 MNm$^{-3/2}$). These results show further that, when one untypically high value is excluded, the remaining five CS results exhibited good repeatability and were all within the range $K_{Ic} = 70.0 \pm 3.9$ ksi $\sqrt{\text{in.}}$ (77.0 ± 4.3 MNm$^{-3/2}$). These specific results also show essentially no variation in the K_{Ic} behavior of the three individually heat-treated plates. In addition, these CS specimen results are in excellent agreement with the results for the preceding DENT and three-point-bend specimen tests. Specifically, the results for all three types of specimens (DENT, three-point bend, and CS) yielded an overall average K_{Ic} value of 70.5 ksi $\sqrt{\text{in.}}$ and, with the exception of a single CS specimen result ($K_{Ic} = 78.1$), were all within the range $K_{Ic} = 70.0 \pm 5.0$ ksi $\sqrt{\text{in.}}$ (77.0 ± 5.5 MNm$^{-3/2}$). These collective results indicate both excellent reproducibility in K_{Ic} values among the three different specimen types and essentially no variation in K_{Ic} behavior for each of the four individually heat-treated plates of 4340 steel used in the present investigation.

The observed variation in K_{Ic} behavior of ±5 ksi $\sqrt{\text{in.}}$ is equivalent to ±7.1 percent relative to the mid-range K_{Ic} value (70.0 ksi $\sqrt{\text{in.}}$). The present results are also in excellent agreement with earlier statistical

TABLE 3—*Summary of baseline* K_{Ic} *behavior determined with basic (narrow saw-cut) specimens.*

Item	Specimen	Plate	$P_{pop\text{-}in}$, lb	P_Q, lb	P_{max}, lb	$K_{pop\text{-}in}$, ksi $\sqrt{in.}$	K_{Ic}, ksi $\sqrt{in.}$	K_{max}, ksi $\sqrt{in.}$
				DENT Specimens [a]				
1	320-3	A	127 200	130 900	130 900	68.9	70.9	70.9
2	320-1	A	NA [b]	125 400	125 400	NA	65.3	65.3
3	320-2	A	NA	126 000	128 640	NA	68.8	70.2
				Three-Point-Bend Specimens [c]				
1	320-3	A	7 750	8 590	8 880	65.0	72.0	74.4
2	320-4	A	7 950	8 440	9 010	64.9	68.9	73.6
3	320-2	D	NA	9 600	9 600	NA	72.2	72.2
4	320-1	D	NA	9 760	9 880	NA	73.5	74.4

[a] Secant-intercept criterion used for 2 percent apparent crack extension at $(2a/W) \cong 0.45$ is $X = 2.5$ percent.

[b] NA = not applicable (pop-in behavior not observed prior to P_Q).

[c] Three-point-bend span length was $S = 8.00$ in. corresponding to $S{:}W = 4.0{:}1$; secant-intercept criterion used for 2 percent apparent crack extension at $(a/W) \cong 0.50$ is $X = 5.0$ percent.

TABLE 4—*Summary of specimen dimensions, fatigue-crack preparation, and* K_{Ic} *results for compact-tension (CS) specimens.*

Item	Specimen	Plate	W, in.	B, in.	a_N, in.	ΔK_F,[a] ksi $\sqrt{\text{in.}}$	N, cycles	a_T, in.	P_Q, lb	P_{max}, lb	K_{Ic},[b] ksi $\sqrt{\text{in.}}$
1	320-2-7	B	2.013	0.913	0.802	21.0	83 000	0.967	9 600	9 780	66.1
2	320-2-9	C	2.015	0.912	0.809	13.9	198 000	0.963	9 590	10 200	66.8
3	320-6-8	D	2.009	0.939	0.804	16.2	123 000	0.958	10 940	10 940	73.8
4	320-6-6	D	2.007	0.938	0.803	17.6	106 000	0.958	11 560	11 560	78.1
5	320-2-6	B	2.011	0.865	0.807	14.4	150 000	0.947	9 580	9 580	69.0
6	320-2-11	C	2.012	0.912	0.805	13.5	216 000	0.941	10 450	10 500	70.7

[a] $\Delta K_F = \Delta P\, F_2\,(a/W)/BW^{1/2}$ where ΔP is the load fluctuation, $a = a_T$ which is the final crack length, and $F_2\,(a/W)$ is a function of the relative crack length, (a/W).

[b] Secant-intercept criterion used for 2 percent crack extension at $(a/W) \cong 0.475$ is $X = 5.0$ percent.

studies of K_{Ic} behavior, where variations of ±5 to ±10 percent relative to the mean K_{Ic} value were observed when large numbers of identical specimens (for a given material) were tested [*26,27*]. The present results and the earlier statistically based variations in K_{Ic} behavior are both only marginally greater than the theoretical minimum variation of ±2.5 percent that might be expected for a perfectly homogeneous material due to limitations in the accuracy of all (typical) experimental measurements and corresponding K_I analyses [*28*].

All thirteen of the K_{Ic} test results obtained with the DENT, three-point-bend, and CS specimens satisfied all the ASTM requirements for the standard K_{Ic} test method.

K_{Ic} *Behavior for Notched Specimens*

General K_{Ic} *Criterion*—The specific criterion used in establishing K_{Ic} corresponds to the point at which the original crack length, a_0, extends by an apparent amount of 2 percent ($\Delta a = 0.02\ a_0$) in the fracture test. For brittle materials, such as the present 4340 steel heat treated to yield strengths in excess of 200 ksi, and for standard K_{Ic} specimens [CS and three-point-bend specimens with relative crack lengths in the range $(a/W) = 0.45$ to 0.55], this occurs when deviation from linearity in the load-displacement (P versus V) test record exceeds a secant-intercept value of 5 percent. The corresponding secant-intercept value for other than standard crack lengths and other specimen types will be different because of specimen compliance considerations. Such considerations have been taken into account in the present study using the earlier results of Brown and Srawley [*4*]. In particular, for DENT specimens with relative crack lengths of $(2a/W) = 0.20$, 0.40, and 0.60, the secant-intercept values corresponding to the 2 percent apparent crack-extension criterion are 1.4, 2.2, and 2.7 percent, respectively. Likewise, for three-point-bend specimens with relative crack lengths of $(a/W) = 0.20$, 0.30, and 0.40, the corresponding secant-intercept values are 3.1, 3.4 and 3.8 percent, respectively.

DENT Specimens—The results obtained for the DENT specimens are presented in Table 5 and Figs. 5 and 6. These results are for DENT specimens prepared under two different conditions of notch geometry ($\rho = 0.20$ in. and $\rho = 0.60$ in.) and for various amounts of fatigue-crack extension beyond the notch tip, Δa_F, for each specimen. Figures 5 and 6 each contain both valid K_{Ic} results (solid data points for Tada analysis) and apparent K_{Ic} results (open data points for Bowie analysis).

The K_{Ic} values presented in Figs. 5 and 6 were calculated by using the analysis for hyperbolically notched DENT specimens by Tada [*15*] (Fig. 7). Figures 5 and 6 show that the average K_{Ic} behaviors for the deep—and shallow—notched specimens are 69.0 ksi $\sqrt{\text{in.}}$ and 73.8 ksi $\sqrt{\text{in.}}$ (75.9 and 81.2 $\text{MNm}^{-3/2}$), respectively. These average K_{Ic} behaviors are both in good agreement with the baseline K_{Ic} behavior established earlier. In addition, the K_{Ic} results for the notched specimens are essentially unaffected by notch radius, ρ, or fatigue crack length, Δa_F, as the Δa_F values become successively smaller. However, the individual K_{Ic} results exhibit a large amount of scatter above and below the average K_{Ic} value for each of the two notched specimen types. The range of these notched-specimen results is more than twice that of the earlier baseline behavior of $K_{Ic} = 70 \pm 5$ ksi $\sqrt{\text{in.}}$ The reasons for the larger amount of scatter in K_{Ic} for the deep—and shallow—notched DENT specimens are unknown. Although somewhat more scatter might be expected strictly on the basis of the additional number of specimens tested,[5] such scatter may be an intrinsic property of notched and fatigue-cracked specimens. Support for this argument can be found in the fact that the notched-specimen results occur both above and below the earlier baseline K_{Ic} behavior, and further, that with increasing Δa_F no significant trends in behavior occur.

The overall agreement between the average K_{Ic} results for the deep and shallow-notched DENT specimens and those of the earlier baseline K_{Ic} behavior is quite good. These experimental results demonstrate that the theoretical K_I analysis by Tada does, indeed, properly account for the interrelationships between notch geometry (notch length, a_N, and notch acuity, ρ), and the extent of fatigue-crack extension beyond the notch tip, Δa_F.

When these same test results for the deep and shallow-notched DENT specimens are analyzed by using the conventional DENT specimen analysis developed earlier by Bowie [*4*], the apparent K_{Ic} values show similar behavior, Figs. 5, 6, and 8. In particular, Fig. 5 shows that the apparent K_{Ic} values calculated by both the Bowie and Tada analyses are virtually identical for the deep-notched ($\rho = 0.20$ in.) specimens. Figure 6 shows that the apparent K_{Ic} values calculated with the Bowie analysis are typically 5 to 10 ksi $\sqrt{\text{in.}}$ (5.5 to 11 $\text{MNm}^{-3|2}$) higher than the corresponding value calculated with the Tada analysis for the shallow-notched ($\rho = 0.60$ in.) specimens. In addition, the difference between the results of the two analyses becomes greater as the fatigue crack extension, Δa_F, becomes smaller. Such results are not unexpected since the Bowie analysis does not account for the presence of notches.[6] Furthermore, even the differences observed for the shallow-notched specimens are still relatively small. The close overall similarity of the apparent K_{Ic} values

---

[5] Another possible source of scatter is that due to eccentricity in loading, a behavior that is virtually impossible to control completely during testing of DENT specimens. However, careful alignment procedures were employed in conducting the present tests for the purposes of minimizing such influence. Consequently, eccentricity is not considered to be a primary source of the observed scatter in the present results.

[6] In K_I calculations with the Bowie analysis, the total crack length is taken as the notch length plus the fatigue ligament ($a_T = a_N + \Delta a_F$). However, variations in the notch width, b, cannot be accounted for with the Bowie analysis.

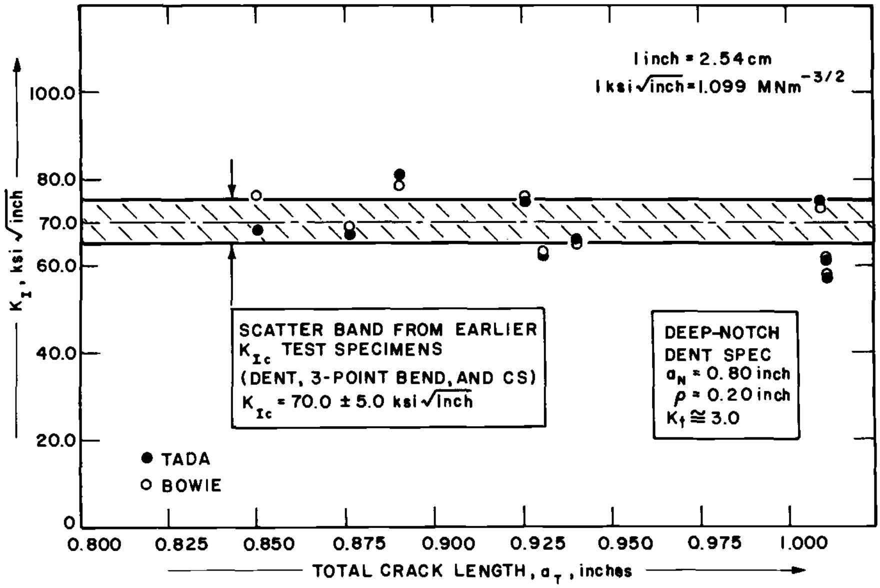

FIG. 5—K_{Ic} *from Tada's analysis and Bowie's analysis (LEFM) versus total crack length for 0.2-in.-radius DENT specimens.*

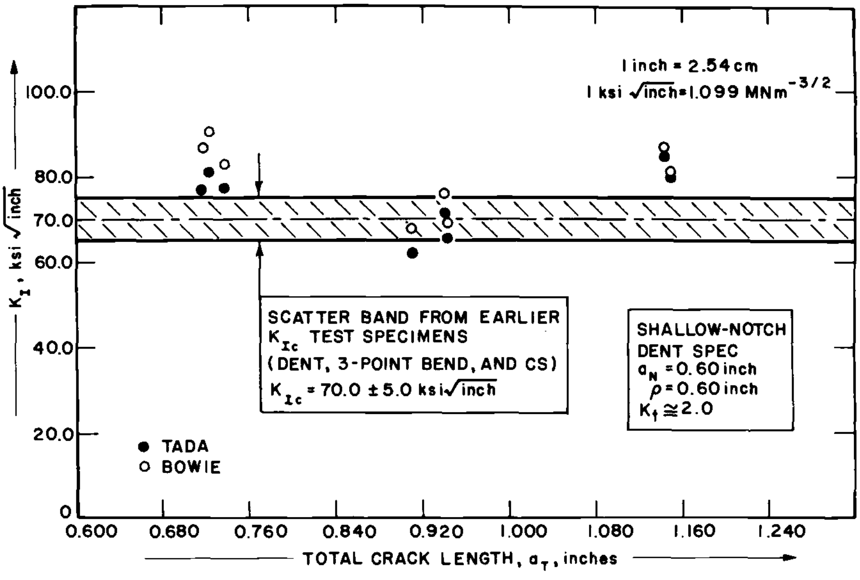

FIG. 6—K_{Ic} *from Tada's analysis and Bowie's analysis (LEFM) versus total crack length for 0.6-in.-radius DENT specimens.*

TABLE 5—*Summary of fracture* (K_{Ic}) *behavior for notched DENT specimens.*

Item	Specimen	Δa_F, in.	P_Q,[a] lb	P_{max}, lb	K_{Ic} Values, ksi $\sqrt{in.}$	
					Tada Analysis[b]	Bowie Analysis[c]
		Deep-Notch DENT Specimen (a_N = *0.080 in.*, ρ = *0.20 in.*, $K_t \cong$ *3.0*)				
4	320-6	0.213	93 240	93 240	61.2	61.6
5	320-1	0.213	91 120	97 560	57.2	57.4
6	320-10	0.213	120 720	120 720	74.9	75.3
7	320-12	0.141	110 280	110 280	65.7	65.5
8	320-9	0.128	130 920	130 920	74.5	76.0
9	320-11	0.133	106 800	106 800	61.7	63.2
10	320-7	0.091	138 000	138 000	80.5	78.3
11	320-2	0.078	116 400	136 680	67.2	68.9
12	320-4	0.052	136 440	136 440	68.3	76.0
13	320-3	0	NA	>440 000	NA	NA
14	320-5	0	272 000	>440 000	NA	156(253)[d]
15	320-8	0	NA	>440 000	NA	NA
		Shallow-Notch DENT Specimen (a_N = *0.60 in.*, ρ = *0.60 in.*, $K_t \cong$ *2.0*)				
16	320-3	0.549	126 200	126 200	79.9	81.1
17	320-2	0.542	134 900	134 900	85.2	86.6
18	320-11	0.344	126 500	126 500	65.6	69.0
19	320-12	0.339	139 500	161 100	71.6	75.9
20	320-6	0.311	127 050	127 050	62.1	68.2
21	320-10	0.140	175 000	180 400	77.4	83.2
22	320-8	0.128	193 000	201 600	81.1	90.4
23	320-9	0.117	186 000	186 000	76.4	86.7
24	320-5	0	NA	>440 000	NA	NA
25	320-7	0	NA	>440 000	NA	NA
26	320-1	0	NA	>440 000	NA	NA

NOTES—Specimen and parent-plate relationships were as follows:

Plate A—Items 5, 11, 12, and 13;
Plate B—Items 4, 10, 14, and 15;
Plate C—Items 6, 7, 8, 9, 16, 17 and 26; and

Plate D—Items 18, 19, 20, 21, 22, 23, 24, and 25.

[a] P_Q is the value of the load at a given secant intercept on the load versus COD record. The value of the secant for a particular case is determined from the compliance of the specimen and corresponds to 2.0 percent crack extension [4]. For the specimens tested, the secant value ranged from 2.1 to 2.7 percent.

[b] $K_I = \sigma \sqrt{\pi \Delta a_F} \cdot F \left(\frac{\rho}{a_N}, \frac{a_N}{W/2}, \frac{a_T}{W/2} \right)$ where σ is the nominal gross stress calculated from P_Q; Δa_F, ρ, a_N, W, and a_T are specimen dimensions, shown in Fig. 1; and the function, F, can be found in Fig. 7 [3].

[c] $K_I = \frac{P\, a_T^{1/2}}{B\, W} Y$ where $P = P_Q$ and a_T, B, and W are specimen dimensions (also see Fig. 1); Y is a function of $(2a_T/W)$ as given in Ref. 4.

[d] The apparent K values cited do not represent fracture, but merely behavior observed in the test corresponding to the 2 percent apparent crack-extension criterion (secant value, $X = 2.3$ percent) and to maximum load capability of the tension testing machine used ($P_{max} = 440$ kips) as follows

$$K_Q = 156 \text{ ksi} \sqrt{\text{in.}} \text{ where } P = P_Q = 272 \text{ kips and } X = 2.3 \text{ percent}$$

and

$$K_{I,max} = 253 \text{ ksi} \sqrt{\text{in.}} \text{ where } P = P_{max} = 440 \text{ kips and } X = 22.7 \text{ percent}$$

No visible crack extension was observed at maximum load capacity ($P = 440$ kips), and it is likely that fracture would not have occurred until much higher load levels were attained. Although LEFM concepts are not applicable and K_I calculations are not valid because of the absence of a sharp crack at the notch tip ($\Delta a_F = 0$), and further, because the observed behaviors represent plasticity rather than actual stable crack extension, the results provide a general perspective of apparent K_I behavior that can occur for the limiting condition of zero crack extension initially at the tip of a notch ($\Delta a_F = 0$).

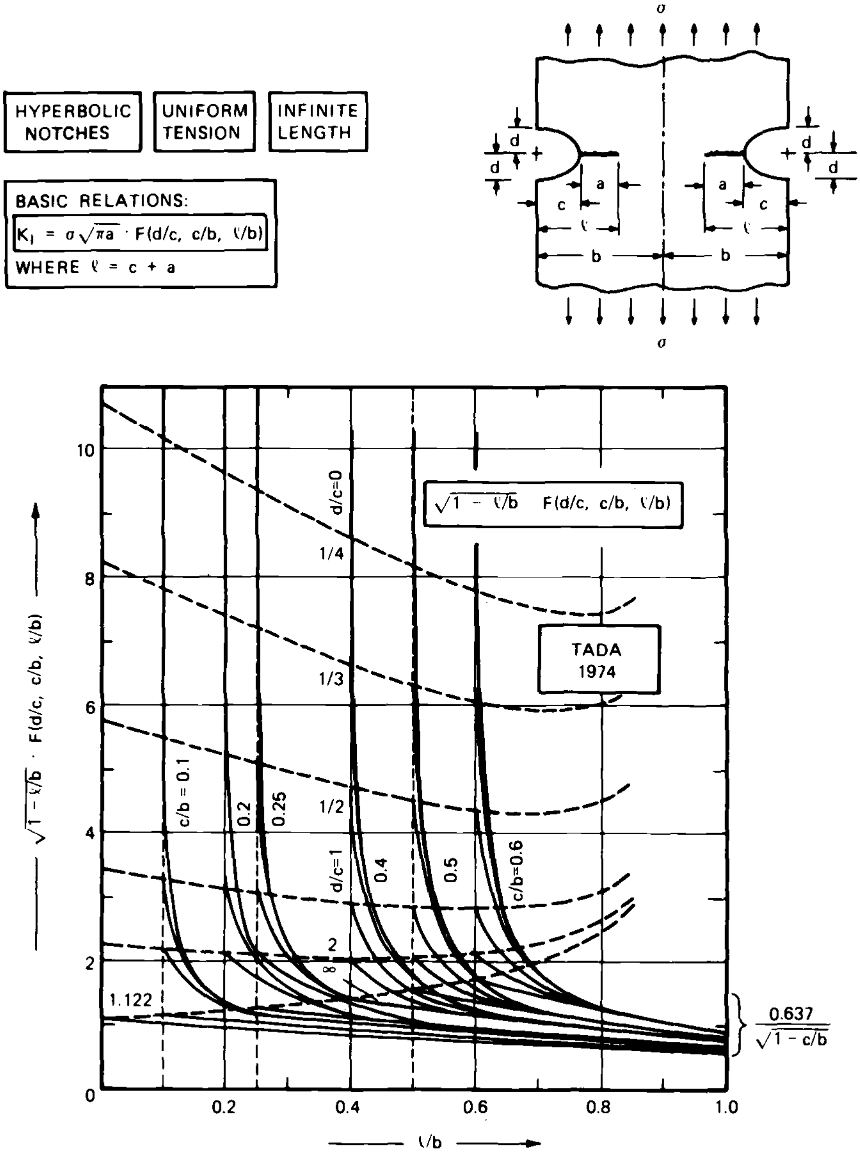

FIG. 7—*K_I solutions available from Tada, 1974, for cracks emanating from hyperbolic notches contained by finite (width) double-edge-notched tension (DENT) sheets.*

calculated with both the Tada and Bowie analyses is also surprising, particularly the K_{Ic} values for the smaller values of Δa_F.

The reasons that such results are surprising are two-fold. First, it is well known that the use of total crack lengths that are less than the

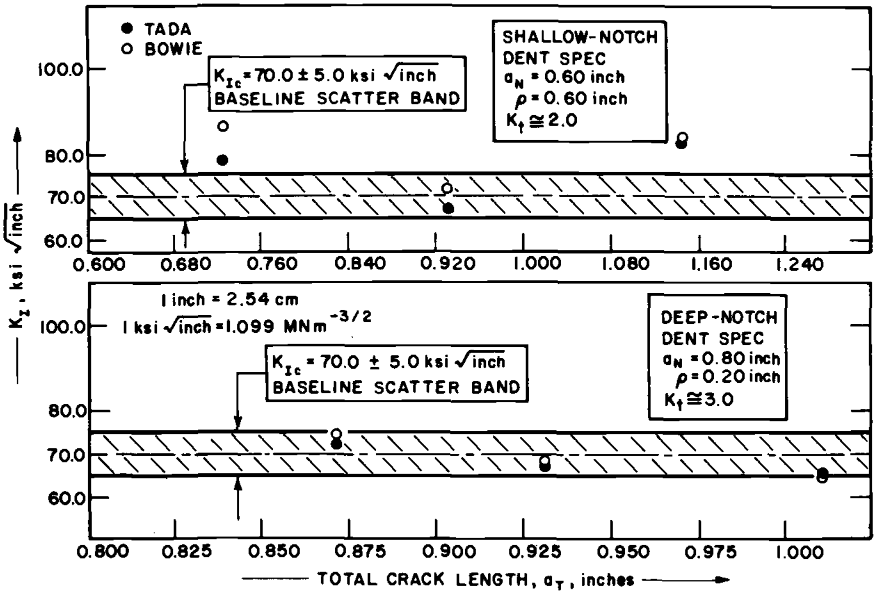

FIG. 8—*Average* K_I *values calculated from Tada's analysis and Bowie's analysis versus average total crack length for 0.6 and 0.2-in.-radius DENT specimens.*

minimum value (a_{min}) required for a valid K_{Ic} can lead to elevation of the apparent K_{Ic} value,[7] and further, that the extent of such overestimates of K_{Ic} can be substantial for very short crack lengths [*4,29,30*]. Second, relatively long fatigue-crack ligaments. Δa_F, beyond the notch tip are specified in ASTM Method E 399 for standard K_{Ic} tests in order to ensure no influence of the notch itself. That is, the Δa_F value should extend beyond a 30-deg ($\pi/6$ rad) included angle which completely encompasses the notch tip.

The minimum total crack length required for a valid K_{Ic} for the 4340 steel tested is $a_{min} = 2.5\ (K_{Ic}/\sigma_{ys})^2 = 0.265$ in. (6.73 mm). The minimum fatigue-crack ligaments corresponding to the 30-deg included-angle criterion for the $\rho = 0.20$-in. and $\rho = 0.60$-in. specimens are 0.573 and 1.718 in. (14.6 and 43.6 mm), respectively.

In the present tests, the Δa_F values used were substantially shorter than *either* of the two minimum crack-length criteria just given. In the specific case of the a_{min} criterion, the actual Δa_F values, taken as the total crack length in the Tada analysis, ranged as low as one fifth to less than one half

---

[7] The elevation effect relates to the critical event for fracture (K_{Icr}, K_{IE}, K_c), which is determined by specific in-plane specimen dimensions, $W - a$ and W, and not to the K_Q value, which can occur prematurely ($K_Q < K_{Ic}$) as a direct result of gross plasticity at the crack tip.

of the $a_{\min}$ value of 0.265 in. for the $\rho = 0.20$-in. and $\rho = 0.60$-in. specimens, respectively. In the case of the 30-deg included-angle criterion, the actual Δa_F values employed in the current tests ranged to less than one tenth of the respective minimum values required for each notched specimen type, Table 5. Despite the use of such small Δa_F values, essentially no effect was observed in the resulting K_{Ic} values calculated on the basis of either the Tada or Bowie analysis. The overall significance of these short-crack-length experimental results will be discussed relative to practical engineering and general analytical treatments of the problem in subsequent sections of this paper.

Three-Point-Bend Specimens—The results for the three-point-bend specimens prepared with notch conditions similar to those for the preceding DENT specimens are presented in Table 6 and Fig. 9. No theoretical K_I analysis currently exists to account for the presence of notches under bending conditions. That is, the results presented in Fig. 9 were calculated in a manner similar to that of a standard three-point-bend K_{Ic} test, thereby ignoring notch width, b, and notch acuity, ρ (but not notch length, a_N). Because of both the lack of a theoretical K_I analysis to account for notch effects and the supplementary nature of these three-point-bend specimen tests relative to the primary DENT study, only one specimen was tested for each condition. This limited number of tests was

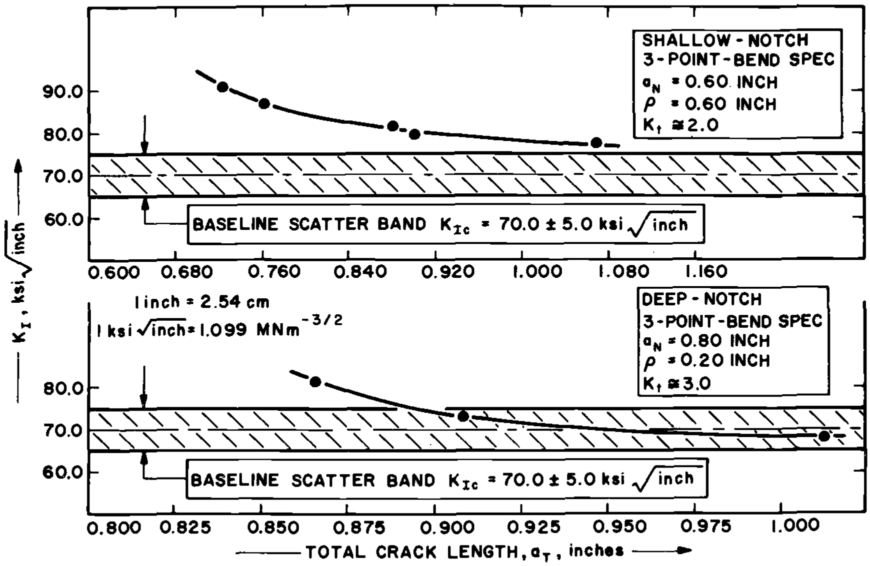

FIG. 9—*Apparent* K_{Ic} *versus average total-crack length for 0.6 and 0.2-in.-radius three-point-bend specimens.*

TABLE 6—*Summary of fracture* (K_{Ic}) *behavior for notched three-point-bend specimens.*

Item	Specimen	Δa_F, in.	P_Q,[a] lb	P_{max}, lb	Apparent K_{Ic},[b] ksi $\sqrt{\text{in.}}$
	Deep-Notch Three-Point-Bend Specimen (a_N = 0.80 in., ρ = *0.20 in.*, $K_t \cong$ *3.0*)				
5	320-3	0.214	16 690	18 950	68.2
6	320-1	0.108	19 620	21 420	73.3
7	320-2	0.066	22 670	22 670	81.6
	Shallow-Notch Three-Point-Bend Specimen (a_N= *0.60 in.*, ρ = *0.60 in.* $K_t \cong$ *2.0*)				
8	320-3	0.470	18 350	19 000	77.8
9	320-1	0.301	21 640	21 640	79.8
10	320-2	0.283	22 820	22 820	81.9
11	320-6-8	0.136	26 000	26 000	86.9
12	320-6-12	0.126	28 000	28 000	90.9

NOTES—Specimen and parent-plate relationships were as follows:
Plate A—Item No.'s 5, 6, 7, 8, 9, and 10, and
Plate D—Item No.'s 11 and 12.
Conversion factors were
1 in. = 25.4 mm,
1 lb = 0.454 kg, and
1 ksi $\sqrt{\text{in.}}$ = 1.099 $\text{MNm}^{-3/2}$

---

[a] P_Q is the value of the load at a secant intercept of ~3.5 percent in the load versus COD (P versus V) record, and corresponds (from compliance, Ref *4*) to 2.0 percent crack extension.

[b] $K_I = Y \cdot 6Ma_T^{1/2}/B\,W^2$, where Y is a function of (a_T/W) as given in Ref *4*, M is the value of the applied moment (three-point-span = 12.0 in.), and a_T, B, and W are specimen dimensions (see Fig. 2).

judged to be sufficient to evaluate the basic effects of notches under conditions of essentially pure bending.

Figure 9 shows that the apparent K_{Ic} results for the deep-notched (ρ = 0.20 in.) three-point-bend specimens range between 68 and 82 ksi $\sqrt{\text{in.}}$ (75 and 90 $\text{MNm}^{-3/2}$), and are in the same general range as the results obtained on the same basis earlier for the corresponding DENT specimens, Fig. 5. However, these limited three-point-bend results indicate a consistent trend of slightly increasing apparent K_{Ic} with decreasing fatigue-crack ligament, Δa_F, as might be expected. This same trend exists and is more pronounced for the shallow-notched (ρ = 0.60 in.) specimens, Fig. 9, which exhibit apparent K_{Ic} values in the range 77 to 90 ksi $\sqrt{\text{in.}}$ (85 to 99 $\text{MNm}^{-3/2}$). Although these results for the shallow-notched specimens tested in three-point bending are quite similar to the results for the counterpart DENT specimens (Bowie analysis), Fig. 6, the trend appears to be more consistent.

Engineering Significance of Notched-Specimen Results

All the results for the DENT and three-point-bend specimen tests can be directly compared on the same basis, as shown in Figs. 10 and 11 for the deep and shallow-notched specimens, respectively. That is, all of these results were calculated on the basis of the corresponding K_I analyses that do not account for notch effects [*4*]. In addition, the apparent K_{Ic} values are normalized with respect to the average K_{Ic} behavior (70 ksi $\sqrt{\text{in.}}$) and are plotted against the ratio of fatigue-crack extension, Δa_F, and the notch-tip radius, ρ.

Figure 10 shows that the apparent K_{Ic} results for the deep-notched (ρ = 0.20 in.) DENT and three-point-bend specimens are all essentially in the range $K_{Ic} = 70 \pm 10$ ksi $\sqrt{\text{in.}}$ These deep-notched specimen results indicate twice as much scatter as the baseline K_{Ic} results, but otherwise show no significant trends over the entire nominal testing range from $(\Delta a_F/\rho) = 1/4$ to 1. Figure 11 shows that the apparent K_{Ic} results for the corresponding shallow-notched (ρ = 0.60 in.) specimens also exhibit scatter over the same nominal range, $(\Delta a_F/\rho) = 1/4$ to 1. However, the apparent K_{Ic} results for these blunt-notched specimens generally fall either within the primary K_{Ic} scatter band (70 ± 5 ksi $\sqrt{\text{in.}}$ or between this range and a value (91 ksi $\sqrt{\text{in.}}$) that is 30 percent above the average K_{Ic} value.

Figures 10 and 11 show that the basic fracture behavior for short cracks emanating from notches is not influenced significantly by the nature of the applied stress. That is, although greater scatter in apparent K_{Ic} values (calculated on the same basis of ignoring notch presence) is observed experimentally, the basic fracture behavior is approximately the same under conditions of both pure tension (DENT specimens) and essentially pure bending (three-point-bend specimens).

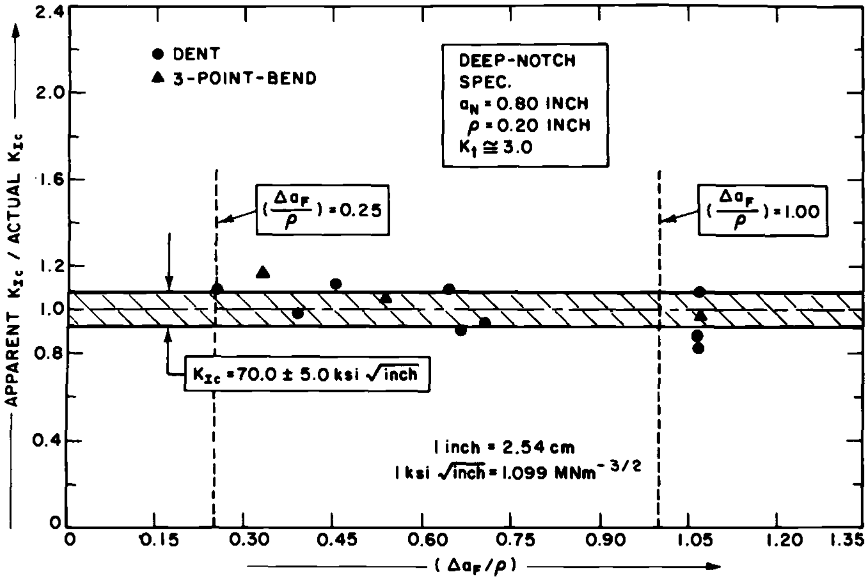

FIG. 10—*Normalized* K_{Ic} *versus normalized fatigue-crack length for 0.2-in.-radius DENT and three-point-bend specimens.*

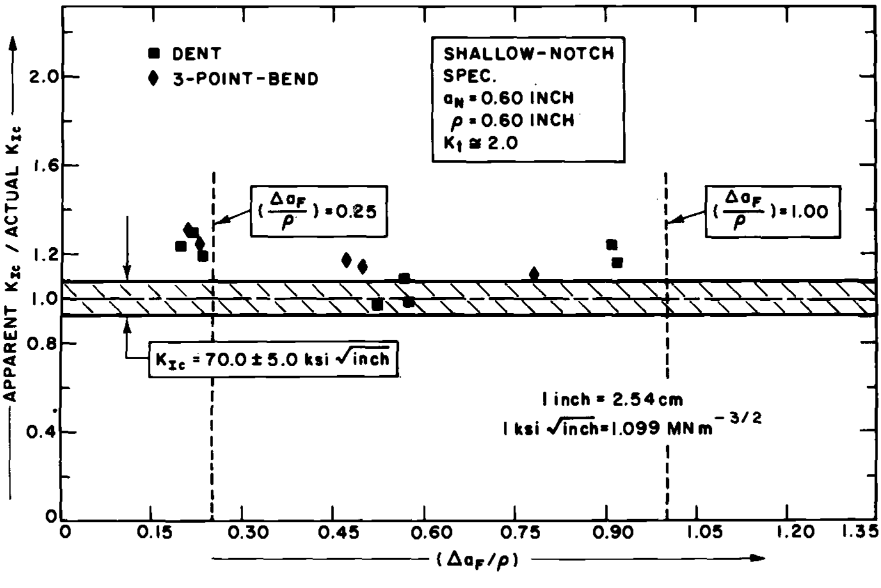

FIG. 11—*Normalized* K_{Ic} *versus normalized fatigue-crack length for 0.6-in.-radius DENT and three-point-bend specimens.*

The results in Figs. 9, 10 and 11 suggest that very small fatigue-crack extensions beyond a notch tip ($\Delta a_F < 1/4\ \rho$) may be quite significant in elevating the apparent K_{Ic} value above the intrinsic K_{Ic} level (when traditional K_I analyses are used).[8] Conversely, these results indicate that once a fatigue crack has extended a distance of one notch-tip radius beyond the tip of the notch ($\Delta a_F > \rho$), the influence of the notch may be disregarded under LEFM conditions. Between these limits ($(\Delta a_F/\rho) = 1/4$ to 1), the effects of the notch can result in elevating the apparent K_{Ic} value between 0 and 30 percent above the intrinsic K_{Ic} level, depending on the specific conditions.

From an engineering standpoint the present results are useful in indicating that, under certain conditions, the presence of notches can be disregarded when attempts are made to predict the conditions at fracture for a structural component in service. That is, once the baseline K_{Ic} behavior of the structural component is known, the assumptions of plane-strain fracture at K_{Ic}, disregarding notch effects,[9] will result in a calculated value of critical flaw size at fracture, a_{cr}, that ranges between being correct to being slightly in error on the conservative side.

For very short fatigue-crack extensions beyond a notch tip, $(\Delta a_F/\rho) < 1/4$, the predicted value of a_{cr} will be conservative (less than actual a_{cr}) because the apparent K_{Ic} at fracture will be elevated above K_{Ic}.[10] For crack extensions that are relatively large, $(\Delta a_F/\rho) > 1$, fracture will occur near K_{Ic}, and the corresponding prediction of a_{cr} will be essentially correct. In the interim region, $(\Delta a_F/\rho) = 1/4$ to 1, the values of a_{cr} calculated on this basis may range from being correct to being conservative. Such calculated a_{cr} values may be as much as 1.30 to 1.70 times smaller than the actual a_{cr} value, as a result of the apparent K_{Ic} value being elevated by 15 to 30 percent, respectively, above the intrinsic K_{Ic} level due to the presence of a notch. Such errors are both conservative and quite small in relation to the order-of-magnitude range (a_{cr} = 0.001 to 100 in., or 0.025 mm to 2.54 m) of values normally considered in typical engineering situations.

The present results indicate that the repeatability in the fracture level (apparent K_{Ic}) for notched and fatigue-cracked specimens appears to be somewhat less than that observed in routine K_{Ic} tests on the same material. That is, the scatter in the apparent K_{Ic} for identical notched and cracked specimens appears to be on the order of two to three times that observed in normal K_{Ic} tests (±10 to ±20 percent as opposed to ±5 to

---

[8] See, for example, the result in Table 5, which indicates superficially high K_I values (K_Q = 156 ksi $\sqrt{\text{in.}}$ and $K_{I,max}$ = 253 ksi $\sqrt{\text{in.}}$) without fracture for a deep-notch DENT specimen tested with no fatigue-crack extension beyond the notch tip ($\Delta a_F = 0$).

[9] Total crack length taken as notch depth plus fatigue-crack extension ($a_T = a_N + \Delta a_F$).

[10] The critical flaw size at fracture, a_{cr}, depends on the square of the critical stress-intensity value at fracture. Thus, in general terms, $a_{cr} = A\ (K_{Icr}/\sigma_{ys})^2$ where A is a constant that is determined by specific specimen geometry.

±10 percent), with the apparent K_{Ic} values generally lying either within ±10 percent of the average K_{Ic} value or above this range. The present results suggest that, from an engineering point of view, the existence of notches needs to be considered only when the fatigue-crack extension beyond the notch tip is less than one half the notch-tip root radius, $(\Delta a_F/\rho) < 1/2$. In this relatively short crack-length range, precise K_I analyses that take notch effects into account are required [5–25].

Analytical Comparisons for Cracks Emanating from Notches

The results given in the preceding section are applicable *only* to the specific types of notches studied experimentally. Attempts to determine the general applicability of the preceding conclusions can be made through comparisons of existing analytical solutions for K_I. For example, Bowie's analysis for cracks emanating from a circular hole contained in a large plate subjected to uniform tension [5] can be compared with the classical analysis of an infinite CCT specimen on the basis of a relative crack extension, $(\Delta a_F/\rho)$, Fig. 12. This figure shows that when a crack has extended from a circular hole by an amount equal to one fourth of the hole radius, the K_I value calculated with either analysis is the same (a K_I ratio of 1.00). For longer cracks, $(\Delta a_F/\rho) > 1/4$, the K_I value given by the more accurate Bowie analysis differs by less than ±5 percent from that calculated on the basis of the infinite CCT specimen analysis. From the standpoint of accuracy required in most engineering calculations and actual variation typically found in pertinent mechanical properties of a given material (±5 to ±10 percent for K_{Ic} and σ_{ys}), the two K_I analyses are essentially identical for $(\Delta a_F/\rho) \geqq 1/4$.

The Bowie analysis for a hole is a special case of the more general and more precise analysis by Newman for cracks emanating from various types of elliptical notches contained in a large plate subjected to uniform tension [6,7]. K_I values calculated from the Newman analysis can again be compared with those calculated from the infinite CCT specimen analysis. The ratio of K_I values given by these two analyses can be plotted against crack extension, Δa_F, measured in relation to both notch tip radius, ρ, and notch depth, a_N, as shown in Figs. 13 and 14, respectively. These figures show that, if a general relationship is being sought, *neither* the $(\Delta a_F/\rho)$ or the $(\Delta a_F/a_N)$ parameter is correct for characterizing the extent of crack extension, since the sequence of intercept values occurring at a K_I ratio of 1.00 becomes *reversed* in going from one plot to the other.

Results in Fig. 15 show that a common intercept value (at a K_I ratio of 1.00) can be found to characterize all the elliptical notches considered when crack extension is characterized in terms of the square root of the notch radius times notch depth. In particular, the curves for all the elliptical notches considered pass through a K_I ratio of 1.00 when $(\Delta a_F/\sqrt{a_N\rho})$ is approximately equal to 1/4. For crack extensions *greater than*

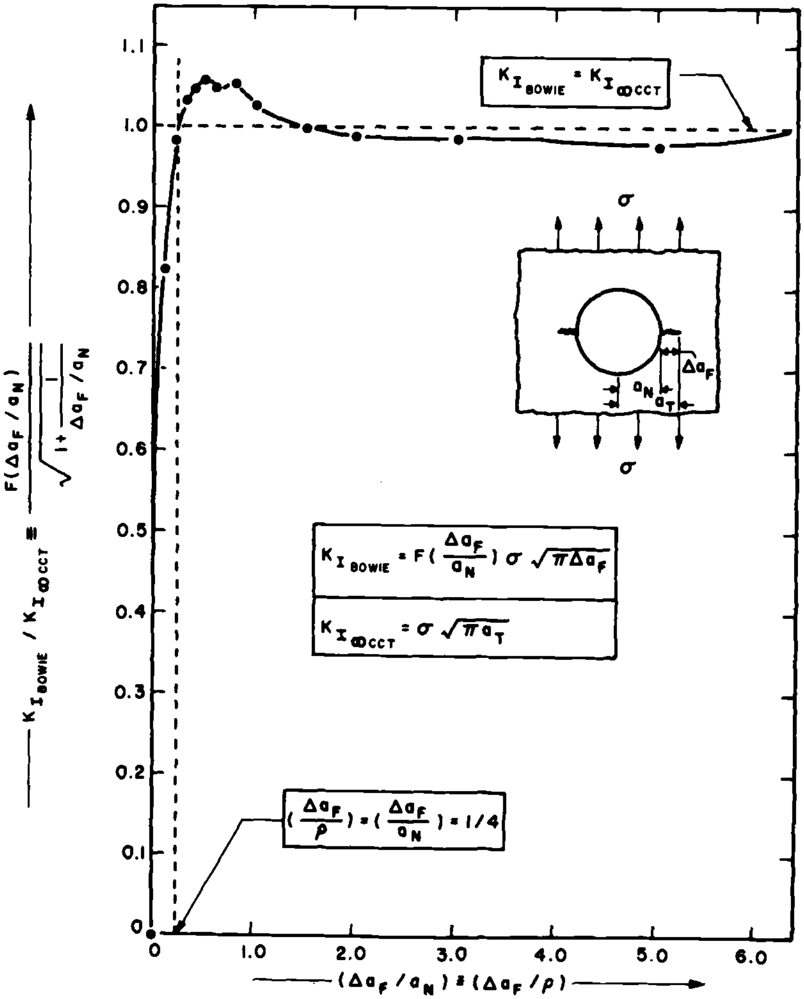

FIG. 12—K_I *ratio for cracks emanating from a hole contained in an infinite CCT specimen subjected to uniform tension applied remotely.*

or equal to this intercept value, $(\Delta a_F/\sqrt{a_N\rho}) \geqq 1/4$, the K_I ratio is always between the limits of 1.00 [11] and 1.10. That is, *above* the intercept value the K_I values calculated with the more precise Newman analysis are either equal to or slightly higher than corresponding K_I values calculated on the basis of the classical infinite CCT specimen analysis. Conversely, if K_I calculations are made with the infinite CCT specimen analysis for the region *above* the intercept point, $\Delta a_F \geqq 1/4\ \sqrt{a_N\rho}$, such values will be

---

[11] The value of 1.00 corresponds to the limiting condition attained for all notch types when Δa_F becomes large.

either precise or conservative by an amount less than 10 percent, depending on specific conditions.

Similar types of analytical comparisons can be made for other types of notch geometries when precise K_I analyses exist that account for notch effects. An analysis by Tada [*15*] currently exists for the case of cracks emanating from various elliptical notches contained in a semi-infinite sheet subjected to uniform tension. Calculations of K_I with this analysis can be compared with those of the standard semi-infinite SENT specimen analysis (which ignores notch width and acuity). Calculations on this basis are presented in relation to the normalized crack-extension parame-

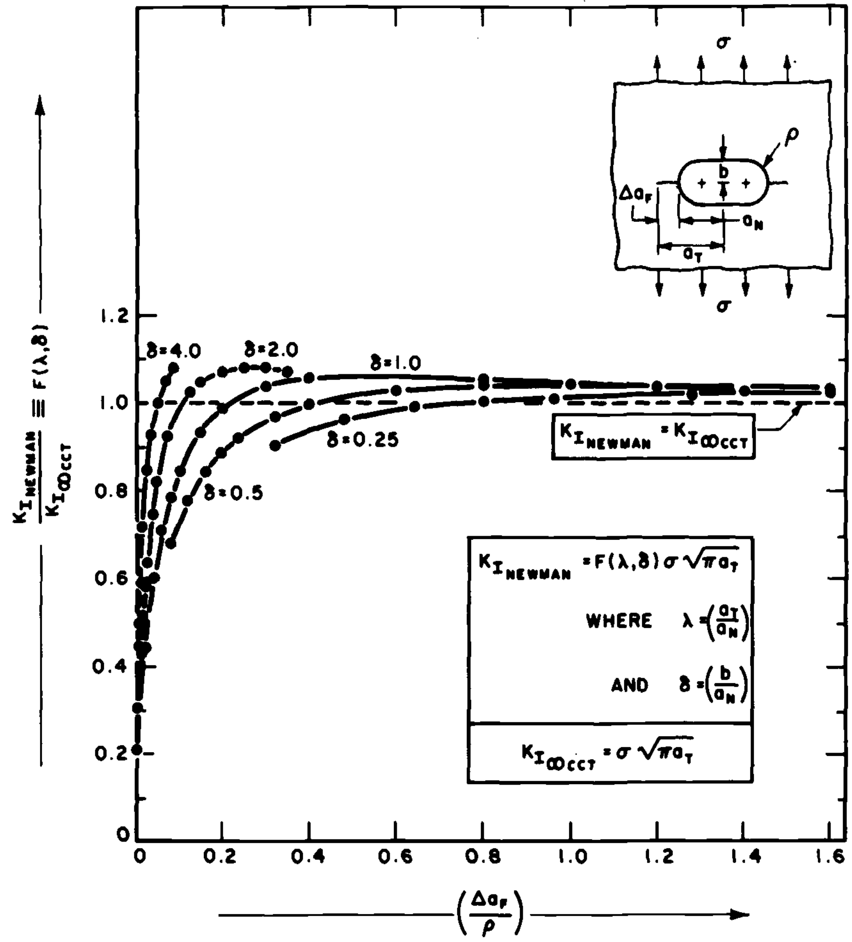

FIG. 13—K_I *ratio for cracks emanating from various elliptical holes contained in an infinite CCT specimen subjected to uniform tension applied remotely.*

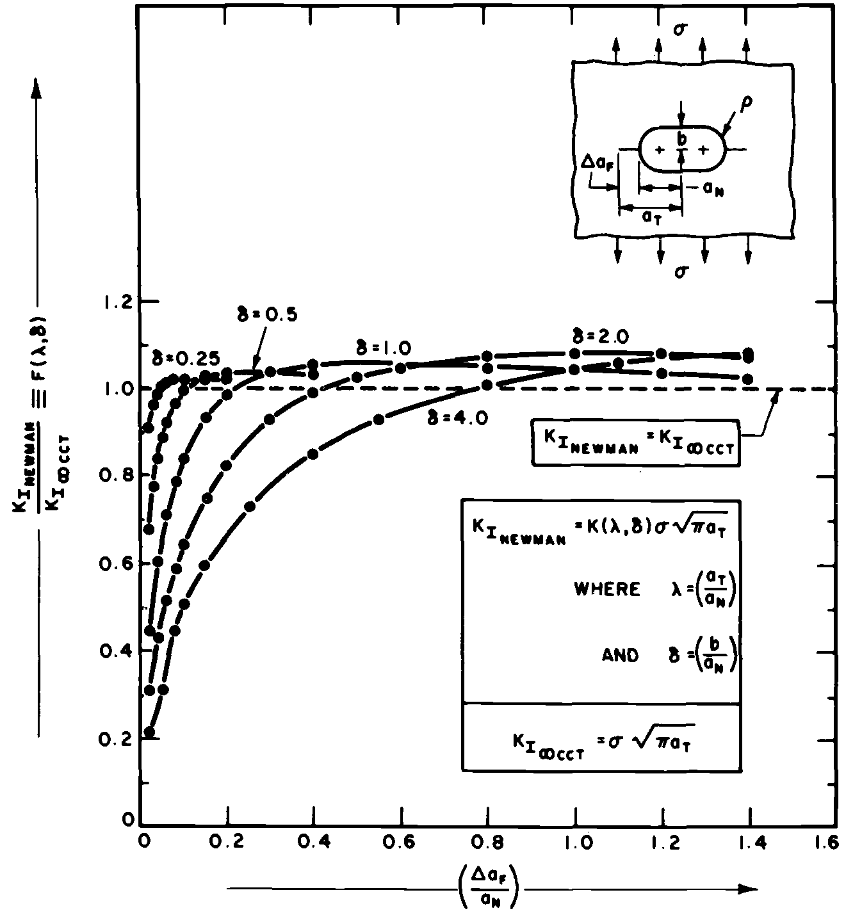

FIG. 14—K$_I$ *ratio for cracks emanating from various elliptical holes contained in an infinite CCT specimen subjected to uniform tension applied remotely.*

ter determined previously ($\Delta a_F/\sqrt{a_n\rho}$) for three notch conditions, Fig. 16. This figure shows that at the point where ($\Delta a_F/\sqrt{a_N\rho}$) = 1/4, the K_I ratios range between 0.93 and 1.00, with the lowest value occurring for a semi-circular notch condition [δ = (b/a_N) = 1.00]. For notches that are more blunt than a semi-circular notch, the corresponding K_I ratios are consistently less (for example, K_I ratios of 0.90 and 0.86 for δ = 2.00 and δ = 4.00, respectively). However, blunt notches of this type (δ > 1.00) are generally *not* of primary concern in most engineering structures because the extent of stress concentration is quite low. In addition, blunt notches of this type in a cyclically loaded structure will generally result in initiation of a large number of cracks around the periphery of the notch tip

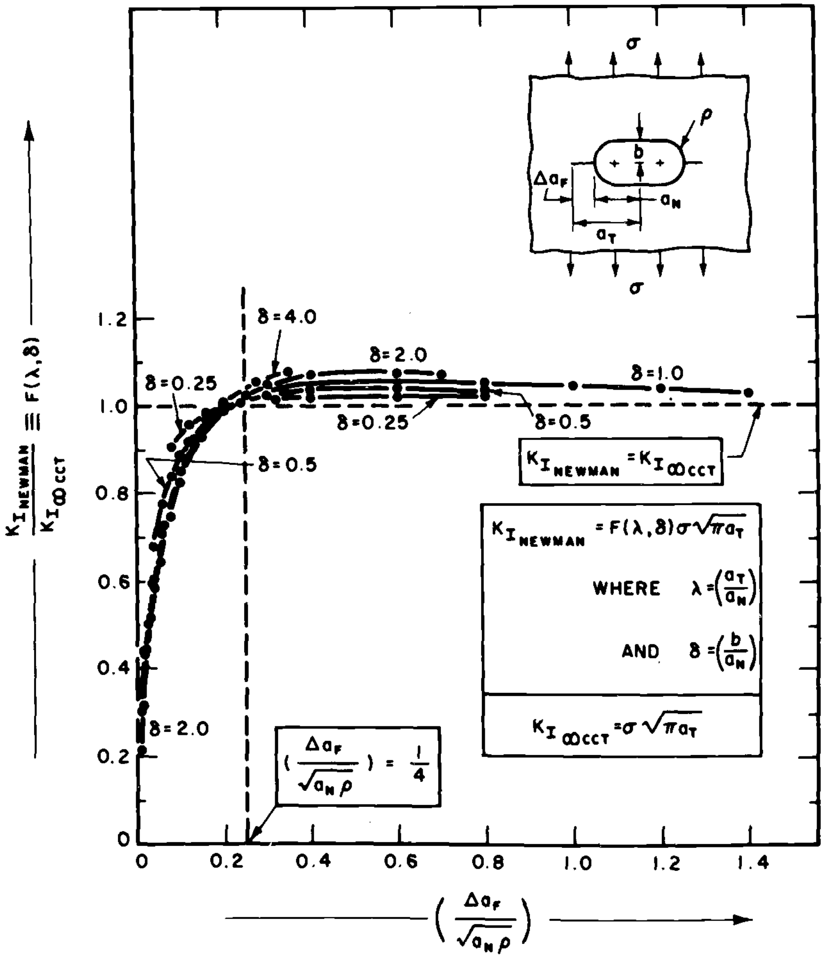

FIG. 15—K_I *ratio for cracks emanating from various elliptical holes contained in an infinite CCT specimen subjected to uniform tension applied remotely.*

(rather than a single crack), thereby preventing the application of LEFM concepts, even for a brittle material, until a single crack becomes dominant.

The results of Fig. 16 can be considered as the limiting condition for an infinite DENT specimen containing elliptical notches. That is, these results correspond to $(2a/W) \cong 0$. The extent of influence for a finite specimen width can be examined by using the Tada analysis for a hyperbolically notched DENT specimen, Fig. 7, and the corresponding Bowie analysis for a regular DENT specimen [*4*]. For the case of cracks emanating from semi-circular notches that are each 5 percent of the

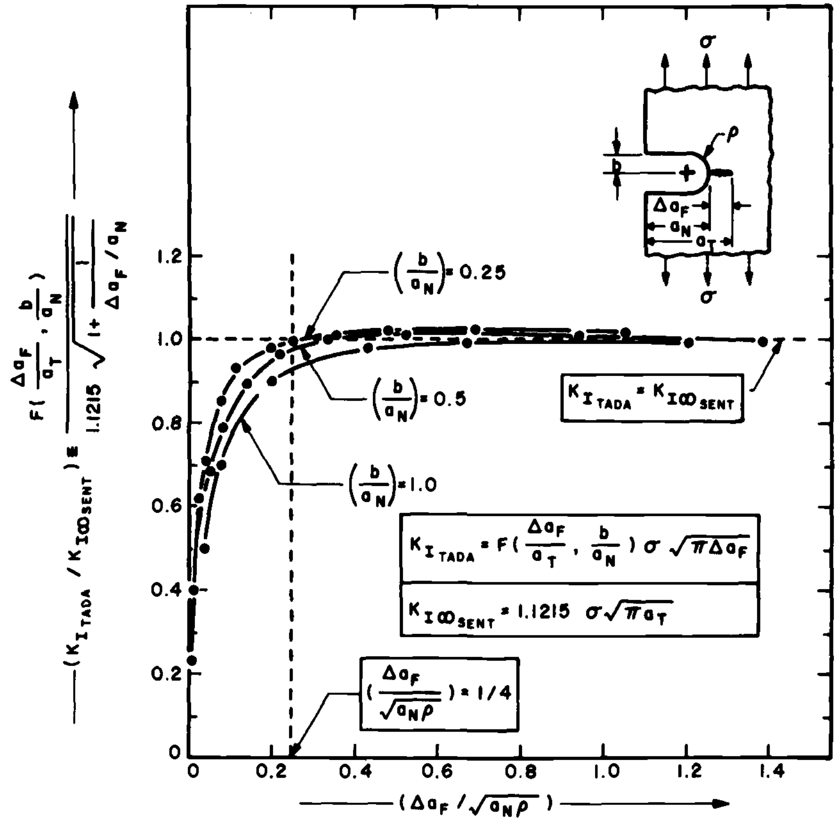

FIG. 16—K_I ratio for cracks emanating from various semi-elliptical notches contained in a semi-infinite SENT specimen subjected to uniform tension applied remotely.

specimen width [$\delta = 1.00$ and $(2a/W) = 0.10$], the K_I ratio at the intercept value of $(\Delta a_F/\sqrt{a_N\rho}) = 1/4$ is 0.95, Fig. 17. For the case of semicircular notches that are each 20 percent deep [$\delta = 1.00$ and $(2a/W) = 0.40$], the corresponding K_I ratio is 0.87. For semicircular notches that are even deeper, the corresponding K_I ratio would be even less, Table 7. This behavior is to be expected since it reflects increasing disturbance in the elastic-stress field at each crack tip caused by the presence of the opposing notch. These results indicate that the effects of a finite specimen width on the general analytical criterion developed are minimal, and further, that the corresponding effects of opposing notches for a finite-width DENT specimen can be neglected, or considered as second-order, until the notches become quite deep, [$(2a/W) \geqq 0.40$].

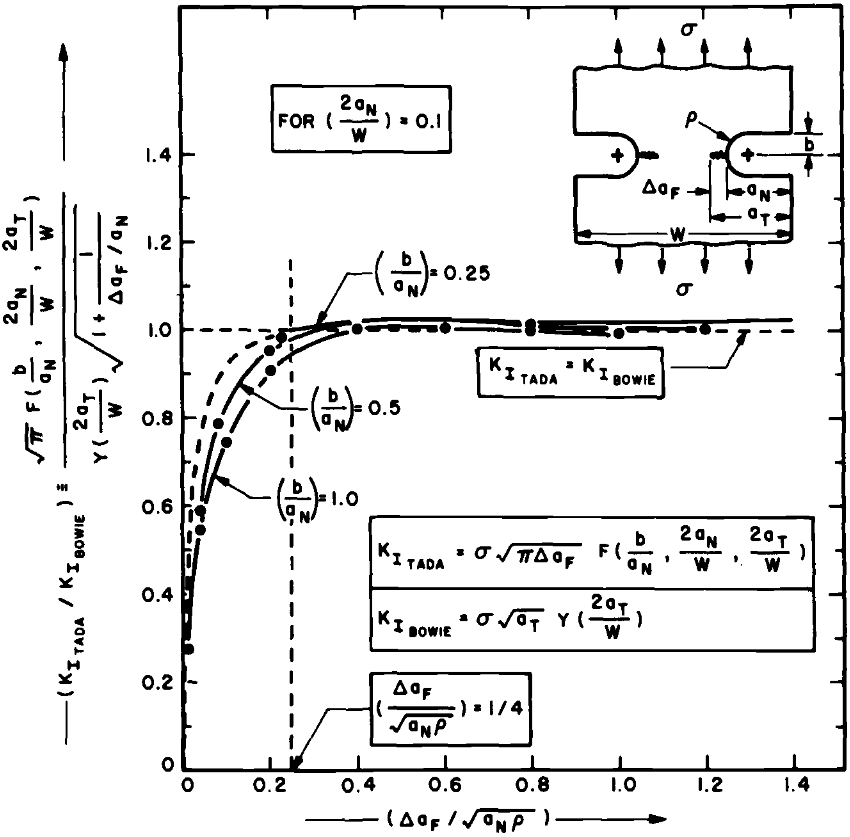

FIG. 17—K_I *ratio for cracks emanating from various hyperbolic notches contained in a DENT specimen of finite width subjected to uniform tension applied remotely.*

Significance and Applicability of Analytical Criterion Developed

The results of the analytical comparisons made in the previous section are summarized in Figs. 15, 16, and 17 (as well as in Table 7). These results indicate that a general analytical criterion, $(\Delta a_F/\sqrt{a_N \rho}) = 1/4$, can be used to determine the point at which the geometry of a notch with an emanating crack can be neglected. That is, when crack extensions are such that $\Delta a_F \geqq 1/4 \sqrt{a_N \rho}$, calculations of K_I made on the basis of an appropriate K_I analysis that *does not* account for notch effects will be within ±5 to ±10 percent of calculations made by using a precise K_I analysis that *does* account for notch geometry. This level of accuracy appears to be sufficient for most engineering calculations since typical variations in the mechanical properties of a given structural material (E, σ_{ys}, K_{Ic}) are of the same order.

TABLE 7—*Ratio of* K_I *values obtained from analyses considering notch effects to* K_I *values obtained from analyses considering only total crack length.*

		$[K_I$ Ratio $\equiv K_I$ (Notched and Cracked)$/K_I$ (Cracked Only)$]$											
		Notched and Cracked Infinite CCT [a] for $(\Delta a_F/\sqrt{a_N\rho})$ =			Notched and Cracked Semi-Infinite SENT [b] for $(\Delta a_F/\sqrt{a_N\rho})$ =			Notched and Cracked DENT [c] $(2a_N/W) = 0.10$ for $(\Delta a_F/\sqrt{a_N\rho})$ =			Notched and Cracked DENT [c] $(2a_N/W) = 0.40$ for $(\Delta a_F/\sqrt{a_N\rho})$ =		
Item	$\delta \equiv (\frac{b}{a_N})$	0.25	0.50	1.00	0.25	0.50	1.00	0.25	0.50	1.00	0.25	0.50	1.00
1	0.25	1.01	1.02	1.02	0.99	1.02	1.02	1.00	1.03	1.02	0.94	0.98	1.00
2	0.50	1.01	1.04	1.03	0.98	1.01	1.01	0.98	1.02	1.00	0.93	0.98	1.01
3	1.00	1.01	1.06	1.04	0.93	0.98	0.99	0.95	1.01	1.00	0.87	0.95	0.97
4	2.00	1.02	1.08	1.05	0.90	0.94	0.98	0.91	0.95	0.99	0.90	0.97	1.01
5	4.00	1.04	1.10	1.06	0.86	0.93	0.98	0.94	0.96	1.00	1.06	NA	NA

NOTE—NA = not applicable. This set of values of $(2a_N/W)$, $(\Delta a_F/\sqrt{a_N\rho})$, and δ represents a specimen for which the crack length is greater than the uncracked ligament.

[a] K_I ratio $= K_{I\ \mathrm{Newman}}/K_{I\infty\mathrm{CCT}} \equiv F\ (a_T/a_N,\ b/a_N)$ where F is a K calibration function of the specimen geometry (see Fig. 15).

[b] K_I ratio $= K_{I\ \mathrm{Tada}}/K_{I\infty\mathrm{SENT}} \equiv \dfrac{F(\Delta a_F/a_T,\ b/a_N)}{1.1215\,[1 + 1/\Delta a_F/a_N)]^{1/2}}$ where F is a K calibration function of the specimen geometry (see Fig. 16).

[c] K_I ratio $= K_{I\ \mathrm{Tada}}/K_{I\ \mathrm{Bowie\ DENT}} \equiv \dfrac{\pi^{1/2}\,F(b/a_N,\ 2a_N/W,\ 2a_T/W)}{Y \times 2a_T/W[1 + 1/(\Delta a_F/a_N)]^{1/2}}$ where F and Y are K calibration functions of the specimen geometry.

(See Figs. 7 and 17)

The analytical criterion developed appears to be generally applicable to elliptical, parabolic, or hyperbolic notches so long as the notch is semi-circular or sharper ($\delta \leqq 1.00$). The criterion should be valid under the same conditions required for any K_I analysis—that is, for a sharp crack, small-scale yielding at the crack tip, and when LEFM concepts are otherwise applicable. Accordingly, the criterion is applicable for various states of stress (plane-strain, transitional, plane-stress) and for cracks that propagate as a result of any of the subcritical-crack-growth processes (fatigue, stress-corrosion cracking, corrosion fatigue).

If engineering applications require either (1) greater accuracy (that is, errors of less than ±5 to ±10 percent in K_I), (2) consideration of notches that are more blunt than a semi-circular notch ($\delta > 1.00$), or (3) determination of the effects of an opposing notch or free surface in close proximity (for example, a finite DENT specimen with deep notches, $2a/W \geqq 0.40$), an alternative point beyond which the notch presence can be disregarded is $(\Delta a_F/\sqrt{a_N\rho}) = 1/2$, as shown in Table 7.

For cracks shorter than either of the cited intercept values, $(\Delta a_F/\sqrt{a_N\rho}) < 1/4$, the precise K_I analysis corresponding to the particular notch and loading conditions must be used. If such an analysis does not exist, a close approximation can be obtained by using the equation

$$K_I = 1.122\ K_t\ \sigma\ \sqrt{\pi \Delta a_F} \qquad (5)$$

As shown in an analysis by Tada [*15*], Eq 5 becomes more accurate for very short crack lengths ($\Delta a_F \rightarrow 0$) emanating from a semi-elliptical notch tip located at the free surface of a semi-infinite SENT specimen. A general analytical expression for K_t values of such semi-elliptical notches has been determined by Tada [*15*]. A general analytical expression for K_t values at the tips of elliptical notches contained in an infinite CCT specimen is included in Fig. 4, and corresponding K_t values for elliptical notches contained in a finite-width CCT specimen are included in the stress-intensity handbook prepared by Tada et al [*3*]. Expressions for K_t values of various types of notches and stress conditions can be found in the works of Neuber [*31*], Peterson [*32*], and Savin [*33*].

Summary and Conclusions

Results are presented for experimental and analytical studies of the influence of short cracks, emanating from notches, on the fracture-toughness of brittle materials. The experimental studies were conducted on a high-strength AISI 4340 steel (σ_{ys} = 215 ksi = 1480 MN/m^2) under plane-strain conditions, and included evaluation of K_{Ic} behavior by using standard fatigue-cracked specimens and notched and fatigue-cracked specimens. The primary experimental study consisted of testing DENT specimens that contained either a semicircular notch ($\rho = 0.60$ in. or 1.5 cm, and $K_t \cong 2.0$) or a relatively deep notch ($\rho = 0.20$ in. or 0.5 cm, and $K_t \cong 3.0$). For each notch condition, the extent of fatigue crack extension, Δa_F, beyond the notch tip was proportional to the notch root radius, ρ, the ratio $\Delta a_F/\rho$ ranging from 1/4 to 1 for a number of DENT specimens. Additional three-point-bend specimens with identical notch preparation were also tested. The analytical studies were conducted by using recently developed theoretical K_I analyses for a number of notched and fatigue-cracked specimens. All results were analyzed in terms of LEFM concepts and under conditions free of residual stress. The results can be summarized as follows.

1. The basic plane-strain fracture behavior of AISI 4340 steel heat-treated to specific conditions was found to be both quite repeatable and reproducible, with the results for tests conducted with each of three different specimen types (DENT, three-point bend, and CS) essentially contained within the range $K_{Ic} = 70 \pm 5$ ksi $\sqrt{\text{in.}}$ (77 + 5.5 $\text{MNm}^{-3|2}$).

2. A recent theoretical K_I analysis by Tada for hyperbolically notched and cracked DENT specimens was experimentally verified over a limited experimental range for relatively short crack extensions, Δa_F.

3. The fracture behavior of notched and fatigue cracked DENT specimens evaluated with the Tada analysis exhibited average K_{Ic} values that were in good agreement with the baseline K_{Ic} behavior. Although the results exhibited greater scatter in K_{Ic} (by factors of two to three) than usually observed in normal K_{Ic} tests (± 5 to ± 10 percent), no significant trends were otherwise observed over the experimental range investigated.

4. The basic behavior of short cracks emanating from notches showed no significant differences relative to fracture (apparent K_{Ic}) under conditions of either pure tension (DENT specimens) or essentially pure-bending (three-point-bend specimens).

5. Apparent K_{Ic} values calculated by using traditional K_I equations, in which notch effects are ignored, were elevated above the intrinsic K_{Ic} level (70 ksi $\sqrt{\text{in.}}$) by less than 15 to 30 percent, depending on specific conditions, for both DENT and three-point-bend specimens. Such relatively small elevations occurred despite the fact that the Δa_F values for each notch condition ranged to less than 10 percent of the corresponding minimum value specified in ASTM Method E 399 to assure no influence of the notch in a standard K_{Ic} test—30-degree ($\pi/6$ rad) included-angle criterion.

6. Calculations of critical flaw size (a_{cr}), made for the current tests on the basis of using traditional equations (not accounting for notch effects) and an assumption of fracture at $K_{Ic} = 70$ ksi $\sqrt{\text{in.}}$, would result in estimates that are either correct or conservative by factors of < 1.30 to 1.70—errors that are relatively small in view of the five orders of

magnitude usually considered in typical engineering studies (a_{cr} = 0.001 to 100 in., or 0.025 mm to 2.54 m).

7. An analytical criterion, $(\Delta a_F/\sqrt{a_N \rho}) = 1/4$, has been developed to predict the point at which the geometry of a notch (of length, a_N, and radius, ρ) with an emanating crack (of length Δa_F) can be safely neglected. For crack extensions such that $\Delta a_F \geqq 1/4 \sqrt{a_N \rho}$, calculations of K_I made on the basis of an appropriate traditional K_I analysis (not accounting for notch effects) will be accurate within ±5 to ±10 percent. The analytical criterion developed appears to be generally applicable to elliptical, parabolic, or hyperbolic notches so long as the notch is semicircular or sharper ($\delta \leqq 1.00$) and conditions of LEFM are otherwise applicable.

8. Comparisons of existing theoretical K_I analyses indicate that a notch with an emanating crack is always less severe than a crack of the same total length when geometry values are less than the analytical criterion developed. The K_I value at the tip of a short crack emanating from a notch can be substantially less than that for a crack of equivalent length when $\Delta a_F < 1/4 \sqrt{a_N \rho}$.

9. A summary is presented of all currently known theoretical K_I analyses for cracks in the vicinity of notches (both emanating from and in the near vicinity of notches). Such analyses have primary significance, from an engineering standpoint, for very short cracks that are less than the analytical criterion developed, $(\Delta a_F/\sqrt{a_N \rho}) = 0$ to $1/4$, since the use of traditional K_I analyses can lead to substantial overestimates of K_I in this short-crack-length range.

The experimental and analytical results of the present study are applicable to fracture behavior as well as to various forms of subcritical crack growth (fatigue, stress-corrosion cracking, and corrosion fatigue). The analytical criterion developed should be valid under the same conditions required for any K_I analysis (sharp crack, small-scale yielding, and LEFM concepts being otherwise applicable) and have applicability under various states of stress (plane-strain, transitional, plane-stress).

Disclaimer

It is understood that the material in this paper is intended for general information only and should not be used in relation to any specific application without independent examination and verification of its applicability and suitability by professionally qualified personnel. Those making use thereof or relying thereon assume all risk and liability arising from such use or reliance.

References

[*1*] Paris, P. C. and Sih, G. C. in *Fracture Toughness Testing and Its Applications, ASTM STP 381,* American Society for Testing and Materials, April 1965, pp. 30–83.

[*2*] Sih, G. C., *Handbook of Stress-Intensity Factors for Researchers and Engineers,* Institute of Fracture and Solid Mechanics, Lehigh University, Bethlehem, Pa., 1973.

[*3*] Tada, H., Paris, P. C., and Irwin, G. R., Eds., *Stress Analysis of Cracks Handbook,* Del Research Corporation, Hellertown, Pa., 1973.

[*4*] Brown, W. F., Jr., Srawley, J. E., *Plane Strain Crack Toughness Testing of High Strength Metallic Materials, ASTM STP 410,* American Society for Testing and Materials, Dec. 1967, pp. 1–129.

[*5*] Bowie, O. L., ''Analysis of an Infinite Plate Containing Radial Cracks Originating From the Boundary of an Internal Circular Hole,'' *Journal of Mathematics and Physics,* Vol. 35, 1956.

[*6*] Newman, J. C., Jr., ''Stress Analysis of Simply and Multiply Connected Regions Containing Cracks by the Method of Boundary Collocation,'' Masters thesis, Virginia Polytechnic Institute, 1969.

[*7*] Newman, J. C., Jr., ''An Improved Method of Collocation for the Stress Analysis of Cracked Plates With Various Shaped Boundaries,'' NASA TN D-6376, NASA Technical Note, National Aeronautics and Space Administration, Aug. 1971.

[*8*] Berezhnitskii, L. T., *Soviet Materials Science,* Vol. 2, 1966, pp. 16–23.

[*9*] Nishitani, H. and Isida, M., *Transactions,* Japanese Society for Mechanical Engineers, No. 212, 1969, p. 131.

[*10*] Neal, D. M., *International Journal of Fracture Mechanics,* Vol. 6, 1970, pp. 393–400.

[*11*] Isida, M., *Engineering Fracture Mechanics,* Vol. 2, No. 1, July 1970, pp. 61–79.

[*12*] Isida, M., in *Methods of Analysis and Solutions of Crack Problems,* G. C. Sih, Ed. Noordhoff, Holland, 1973.

[*13*] Isida, M., *Engineering Fracture Mechanics,* Vol. 5, No. 3, Sept. 1973, pp. 647–665.

[*14*] Doran, H. E. and Buchwald, V. T., *Journal of the Institute of Mathematics and Its Applications,* Vol. 5, 1969, pp. 91–112.

[*15*] First supplement to *Stress Analysis of Cracks Handbook,* Tada, H., Paris, P. C., and Irwin, G. R., Eds., Del Research Corporation, Hellertown, Pa., 1974.

[*16*] Erdogan, F. and Gupta, G. D., ''Inclusion Problem with a Crack Crossing the Boundary,'' Lehigh University Technical Report, IFSM-73-34, 1973.

[*17*] Perlman, A. B. and Sih, G. C., *International Journal of Engineering and Science,* Vol. 5, No. 11, Nov. 1967, pp. 845–867.

[*18*] Papioannou, S. G., ''A Finite Element Method for Calculating Stress Intensity Factors and Its Application to Composites,'' M. S. thesis, Lehigh University, 1972.

[*19*] Creager, M. and Paris, P. C., *International Journal of Fracture Mechanics,* Vol. 3, 1967, pp. 247–252.

[*20*] Yokobori, T., Ichikawa, M., Konosu, S., and Takahashi, R., *Reports of the Research Institute for Strength and Fracture of Materials,* Tohoku University, Sendai, Japan, Vol. 8, No. 1, Nov. 1972, pp. 1–17.

[*21*] Wilson, W. K. *Transactions,* American Society of Mechanical Engineers, *Journal of Pressure Vessel Technology,* 1974, pp. 1–6.

[*22*] Sih, G. C. *Transactions,* American Society of Mechanical Engineers, *Journal of Applied Mechanics,* Vol. 32, 1975, p. 51.

[*23*] Sih, G. C., et al, Report No. AFML-TR-70-112, Part II, U.S. Air Force Contract Report, 1971.

[*24*] Clark, W. G., Jr., in *Fracture Toughness and Slow-Stable Cracking, ASTM STP 559,* American Society for Testing and Materials, 1974, pp. 205–224.

[*25*] Barsom, J. M. and McNicol, R. C., in *Fracture Toughness and Slow-Stable Cracking, ASTM STP 559,* American Society for Testing and Materials, 1974, pp. 183–204.

[26] Brown, W. F., Jr., and Srawley, J. E., *Plane Strain Crack Toughness Testing of High-Strength Metallic Materials, ASTM STP 410,* American Society for Testing and Materials, Dec. 1967, p. 26.
[27] McCabe, D. E., *Journal of Materials,* Vol. 7, No. 4, Dec. 1972, pp. 449–454.
[28] Orange, T. W. in *Fracture Analysis, ASTM STP 560,* American Society for Testing and Materials, 1974, pp. 122–133.
[29] Freed, C. N., *Engineering Fracture Mechanics,* Vol. 1, No. 4, April 1970, pp. 729–731.
[30] Orange, T. W., *Engineering Fracture Mechanics,* Vol. 3, No. 1, July 1971, pp. 53–69.
[31] Neuber, H., *Kerpspennung Slehre,* Springer, Berlin, 1937 and 1958; English translation available from Edwards Bros., Ann Arbor, Mich.
[32] Peterson, R. E., *Stress Concentration Design Factors,* John Wiley and Sons, Inc., New York, 1953.
[33] Savin, G. N., *Stress Distribution Around Holes (Naukova Dumke),* Press, Kiev, 1968 (in Russian); NASA Technical Translation, NASA TT F607, 1970.

R. C. Labbens,[1] *J. Heliot,*[1] *and A. Pellissier-Tanon* [2]

Weight Functions for Three-Dimensional Symmetrical Crack Problems

---

REFERENCE: Labbens, R. C., Heliot, J, and Pellissier-Tanon, A., "**Weight Functions for Three-Dimensional Symmetrical Crack Problems,**" *Cracks and Fracture, ASTM STP 601,* American Society for Testing and Materials, 1976, pp. 448–470.

ABSTRACT: The knowledge of weight functions would be of great help for the solution of three-dimensional crack problems. A numerical method of computation of these functions by finite elements is developed, starting from the simple consideration of concentrated forces applied to the crack and the energy released by local extensions of the crack.

Particular attention is paid to the consideration of the asymptotic value of the weight functions at the crack tip, which allows the definition of dimensionless weight functions and makes the numerical calculation easier.

Special weight functions are considered for the case when the applied stress depends on one coordinate only.

The method is checked by comparing the computed weight function for a penny-shaped crack in an infinite solid with the known closed form solution. It seems that the accuracy obtained could allow for solution of engineering problems; however this should be checked by other tests especially in the region of the singularity.

The computing time, however, is long because of the large number of nodes needed in three-dimensional bodies, and the calculation is costly. It seems advisable to investigate the possibilities of other methods of solution of elasticity problems, such as the method of boundary integral equations, for changing the order of magnitude of the computing time and the cost of the calculation.

KEY WORDS: crack propagation, fracture properties, stresses, elastic theory, weight function, cracks, fractures (materials), three dimensional

Nomenclature

P, P_i A point on the crack surface
P' A point on the crack front

---

[1] Scientific manager and research engineer, respectively, Creusot-Loire, Paris, France.
[2] Research consultant, Framatome, Courbevoie, France.

ρ, θ	Polar coordinates of P with respect to P' and the tangent to the crack front
dS (P)	A small area of the crack surface around the Point P
F	A normal force applied at P
p (P)	A normal pressure function of P
K_F (P,P')	Stress intensity factor at P' resulting from forces F applied at P
G (P,P')	Influence function at P' depending upon P
M (P,P')	Bueckner's weight function
h (P,P')	Rice's weight function
g (P,P')	Nondimensional influence function
δs	A small arc of the crack front at P'
δn	A small displacement of P'normal to the crack front
δA (P')	A small extension of the crack surface resulting from δs and δn
P	Potential energy
E'	E modulus of elasticity in plane stress $E/(1 - \nu^2)$ in plane strain
a	In a semi-infinite crack distance from P to the crack front
b	In a penny-shaped crack, radius of the crack
b, α	In a penny-shaped crack, polar coordinates of P'
r, β	In a penny-shaped crack, polar coordinates of P

The authors offered a method for the numerical calculation of weight functions for two-dimensional problems, which reduces the calculation of stress intensity factors for the solution of very simple integrals at the Eighth National Symposium on Fracture Mechanics [*1*] [3]. This method provided practical applications to engineering problems for the rather elaborate weight function concept developed by Bueckner [*2*] and Rice [*3*].

The weight functions also apply to three-dimensional problems [*2,3*] and to a cracked solid. When they are known, the stress intensity factor under any load at every point of the crack front can be calculated by a simple surface integral. These functions would be very useful for the problem of a semi-elliptical crack in any solid, subjected to a variable stress field, such as thermal stresses, or similar problems.

A great deal of valuable work has been done by several authors in the calculations of stress intensity factors in such three-dimensional situations, algebraically or numerically. Among these authors, Shah and Kobayashi [*4*] studied the problem of an elliptical crack in an infinite solid under an arbitrary normal loading, which is close to the present problem. The same authors also developed solutions for elliptical cracks under tension or bending in semi-infinite solids or plates [*5,6*] and an approximate solution for corner cracks under a linearly varying pressure [*7*].

---

[3] The italic numbers in brackets refer to the list of references appended to this paper.

This paper discusses weight functions which can be numerically calculated for any smooth crack in any solid, such as pressure vessels and nozzles, so that stress intensity factors can be calculated under rapidly variable stresses, for example, thermal stresses. This is limited to symmetrical and symmetrically loaded bodies.

Three-dimensional problems are much more difficult than two-dimensional problems, since a weight function exists for every point along the crack front and is a two-variable function of the two coordinates of the points of the loaded contour (which in this paper is reduced to the surfaces of the crack).

Special attention is given to the asymptotic values of the weight functions at the crack front in order to make the numerical calculations easier. This permits a definition of dimensionless functions which are the same for all homothetic geometries.

Weight and Influence Functions

Let us consider a plane crack in a solid with a front of any reasonably smooth shape and a pair of symmetric opening forces at Point P on the crack surfaces (Fig. 1). Symmetry with respect to the y-z plane is assumed.

These forces produce a stress intensity factor K_F (P,P') at Point P' of the crack front.

The stress intensity factor per unit force is

$$G\ (P,P') = \frac{K_F\,(P,P')}{F} \tag{1}$$

in an influence function. For an opening pressure p (P) applied on the crack sides, the stress intensity factor is an integral calculated on one side of the crack

$$K\ (P') = \int_s G\ (P,P')\,p\ (P)\,d\,S\ (P) \tag{2}$$

The influence function is proportional to the weight function defined by Bueckner and by Rice. With Bueckner's and Rice's normalizations these are, respectively

$$M\ (P,P') = \frac{\pi}{2}\ G\ (P,P')$$

and

$$h\ (P,P') = \frac{1}{2}\ G\ (P,P')$$

In this paper, the influence function G (P, P') will be considered, and the transposition to weight function is straight forward.

With the pair of concentrated forces, F, a local extension of the crack at P' (Fig. 2)

$$\delta A \ (P') = \frac{1}{2} \ \delta s \cdot \delta n$$

results in an increase of the opening, $2\delta w_F$ (P), and a potential energy variation

$$\delta P = -\frac{F}{2} \cdot 2\delta w_F \ (P) = -\frac{K_F{}^2(P,P')}{E'} \delta A \ (P')$$

It follows that

$$G \ (P,P') = \frac{K_F \ (P,P')}{F} = \frac{E'}{K_F \ (P,P')} \frac{\delta w_F \ (P)}{\delta A \ (P')} \tag{3}$$

This is equivalent to Rice's definition of three-dimensional weight functions [3]. It is clear that G (P,P') is zero when the forces, F, act at a point along the crack front other than P'.

Semi-Infinite Crack in an Infinite Solid

The value of K for a semi-infinite crack in an infinite solid subjected to a pair of opening forces at P (Fig. 3) is given by the expression [8]

$$K_F \ (P,P') = \frac{\sqrt{2} F}{(\pi a)^{3|2}} \cdot \frac{1}{1 + \left(\frac{y}{a}\right)^2}$$

After some trigonometric transformations

$$G \ (P,P') = \frac{K_F \ (P,P')}{F} = \frac{\sqrt{2}}{(\pi a)^{3|2}} \sin^2\theta = \frac{\sqrt{2 \sin\theta}}{(\pi \rho)^{3|2}} \tag{4}$$

For any crack in any solid, Eq 4 yields the asymptotic value of G (P,P') when $P \rightarrow P'$ (Fig. 4).

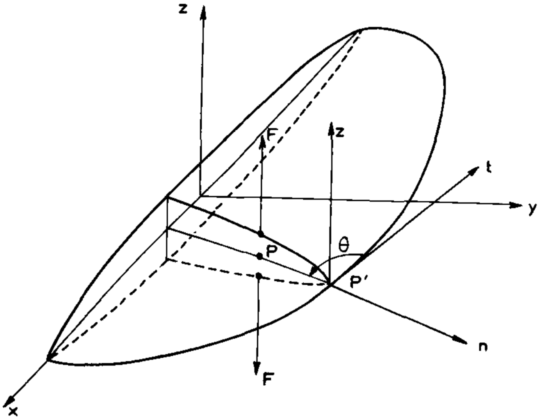

FIG. 1—*A crack loaded by a pair of normal forces.*

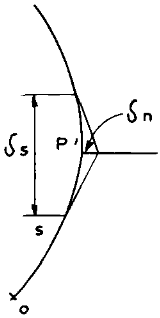

FIG. 2—*Small extension of a crack.*

In order to avoid this singularity, a nondimensional and nonsingular function

$$g\ (P,P') \ = \ \frac{(\pi\rho)^{3|2}}{\sqrt{2}\ \sin\theta} G\ (P,P') \tag{5}$$

was defined for purposes of numerical calculation. It is equal to one for this infinite crack, or for any crack in the limit

$$\lim_{P \longrightarrow P'} g\ (P,P') = 1$$

regardless of the direction θ along which P arrives at P'; $g\ (P,P')$ is zero all along the crack tip except at P' where it is one.

Penny-Shaped Crack in an Infinite Solid

The problem of a pair of forces at P on a penny-shaped crack in an infinite solid has also been solved [8] (Fig. 5).

For this geometry

$$\frac{K_F\ (P,P')}{F} = \frac{1}{\pi\sqrt{\pi b}} \cdot \frac{\sqrt{b^2 - r^2}}{\rho^2} \qquad (6)$$

with

$$r^2 = b^2 + \rho^2 - 2b\rho \sin\theta$$

or

$$\frac{K_F\ (P,P')}{F} = \frac{1}{\pi\sqrt{\pi b}} \cdot \frac{\sqrt{2b\rho \sin\theta - \rho^2}}{\rho^2} \qquad (7)$$

If $P \rightarrow P'$, $\rho \rightarrow 0$, and Eq 7 reduces to Eq 4.

The same limit is obtained by letting b approach infinity.

For the penny-shaped crack, the function $g\ (P,P')$ of Eq 5 is

$$g\ (P,P') = \frac{(\pi\rho)^{3|2}}{\sqrt{2}\sin\theta} G\ (P,P') = \sqrt{1 - \frac{\rho}{2b \sin\theta}}$$

Its values are plotted on Fig. 6; the sections by constant θ are parabolas.

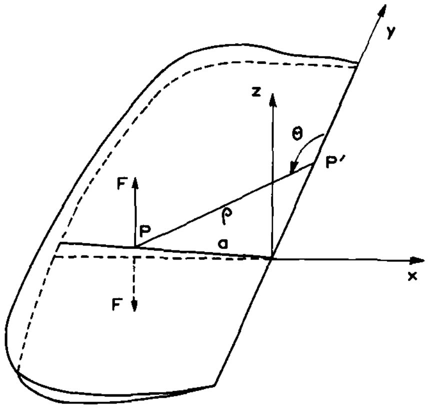

FIG. 3—*A semi-infinite straight crack.*

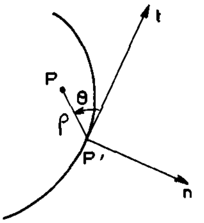

FIG. 4—*A small portion of a curved crack.*

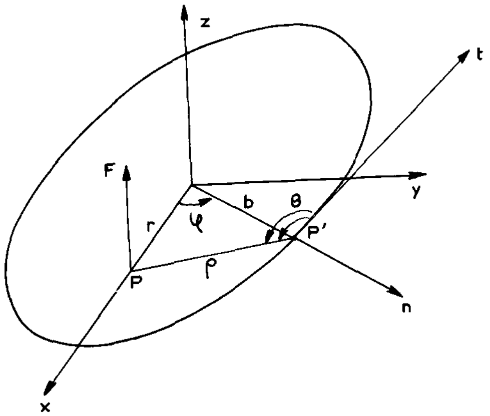

FIG. 5—*A penny-shaped crack.*

Consistency with the Displacements of Bueckner's Fundamental Fields

Bueckner has shown [*2*] that the weight functions are the singular displacements of so-called "fundamental fields," which produce an infinite energy in a small volume. Such a field is generated by a pair of concentrated forces applied very near the crack tip [*9*].

The displacements of such fields with an infinite crack in an infinite solid (Fig. 7) are asymptotic values for any crack in any solid. Kassir and Sih [*10*] gave the more general expressions for displacements due to a pair of forces applied at a distance, a, from the crack tip. Therefore, the displacement in the z-direction for any Point M of the solid is

$$w = -2\;(1-\nu)\,f + z\,\frac{\partial f}{\partial z}$$

with

$$f(r',\phi,y) = -\frac{F}{2\mu\pi^2}\,\frac{1}{\rho'}\,\text{arc tan}\left[\frac{2\sqrt{ar'}}{\rho'}\quad\sin\frac{\phi}{2}\right]$$

$$\rho'^2 = \overline{QM}^2 = (x+a)^2 + y^2 + z^2$$

When

$$a \rightarrow 0, Q \rightarrow P', \rho' \rightarrow P'M = \frac{r'}{\cos\psi}$$

$$\lim_{a\rightarrow 0} f\,(r',\,\psi,\,y) = -\frac{F\sqrt{a}}{\mu\pi^2}\,\frac{\sqrt{r'}}{\rho'^2}\,\sin\frac{\phi}{2} =$$

$$-\frac{F\sqrt{a}}{\mu\pi^2}\,\frac{\sqrt{\cos\psi}\cdot\sin\frac{\phi}{2}}{\rho'^{3|2}}$$

For Point P on the crack surface (Fig. 7)

$$\phi = \pm\,\pi \quad \rho' = \rho \quad \psi = \theta - \frac{\pi}{2}$$

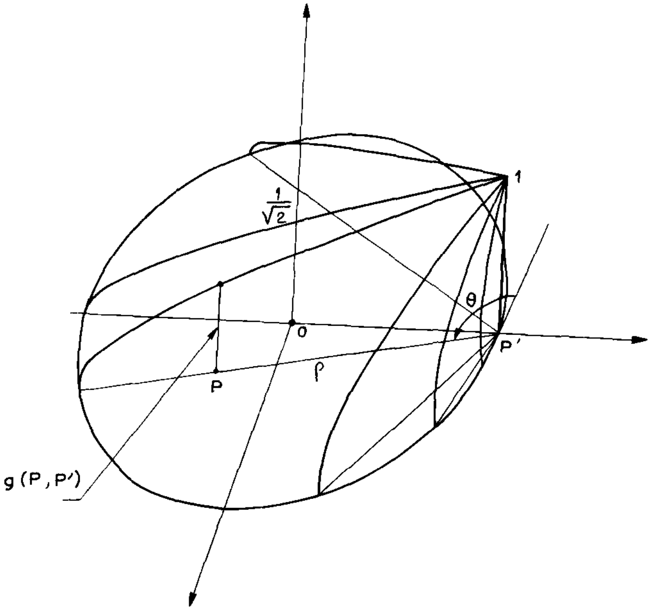

FIG. 6—*Values of* g(P,P′) *for a penny-shaped crack.*

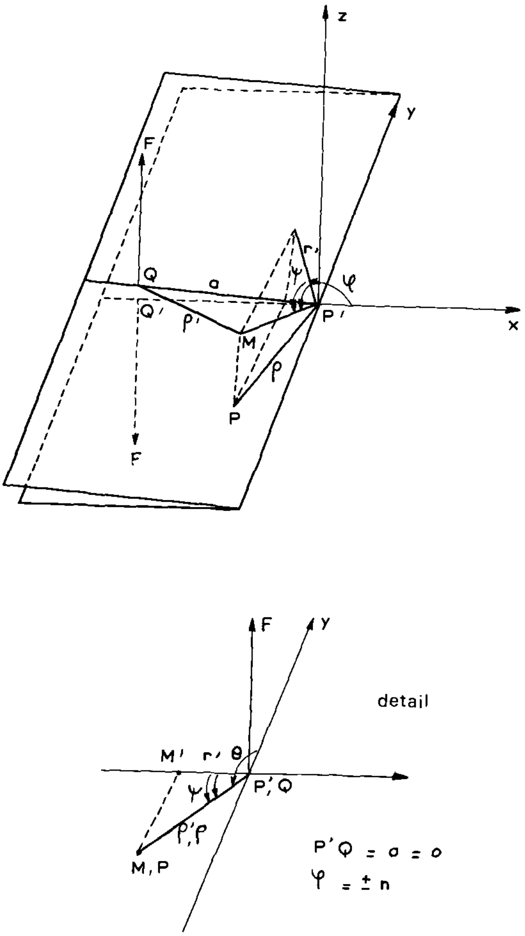

FIG. 7—*A semi-infinite straight crack.*

$$w^+ = \sqrt{\frac{2}{\pi}}\,\frac{2\,(1-\nu^2)}{E}\,F\sqrt{a}\,\frac{\sqrt{2}\,\sin\theta}{(\pi\rho)^{3|2}} \tag{8}$$

If the strength of the Bueckner type singularity $F\sqrt{a}$ is given the value and the dimension of $\pi E/4\ (1-\nu^2)$

$$w^+ = \sqrt{\frac{\pi}{2}}\,\frac{\sqrt{2}\,\sin\theta}{(\pi\rho)^{3|2}}$$

is actually the symptotic value of the weight function in the Bueckner's definition. This is consistent with Eq 4.

Strength of the Singularity

One may be surprised by the singularity $\rho^{-3|2}$.

Calculating the stress intensity factor $K(P')$ according to Eq 2 leads to the expression

$$K\ (P')\ = \frac{1}{\pi}\sqrt{\frac{2}{\pi}}\int_S p(P)\ g(P,P')\sqrt{\frac{\sin\theta}{\rho}}\,d\rho d\theta$$

which can be integrated, for when $P \rightarrow P'$, $g\ (P,P') \rightarrow 1$.

If $P \rightarrow P'$ along the crack front, θ and ρ are zero together with

$$\lim \frac{\rho}{\sin\theta} = R$$

where R is the radius of curvature of the crack front.

The elements of the integral along the crack front contribute for nothing to $K(P')$, but the elements near P' away from the tangent contribute strongly on account of $\rho^{-1|2}$

Outline of the Numerical Calculation

Only a general outline of the steps involved in the computational program are presented here.

1. The Code TITUS [*11*] for elasticity problems was utilized. Because the number of nodes in three-dimensional problems is usually large (1400 for modeling one fourth of a penny-shaped crack, among which 56 were located on the crack surface), it was necessary to condense groups of elements into superelements.

The objective was to calculate the nondimensional function $g\ (P,\ P')$ for a certain number of crack sizes, each of them resulting from the preceding one by a smooth closure along the crack front.

The indices used in the following discussion are defined as i = nodes on the crack surface, (1), (2), . . . = crack fronts, and p = particular i on a crack front.

2. The first step is the calculation of the stress intensity factor resulting at any point $P'^{(1)}$ of the largest crack front, denoted (1), from a pair of normal forces, F_i, applied at the node, P_i, on the crack surfaces (Fig. 8).

Arbitrary pairs of forces, F_i, are applied at the n nodes, P_i, and for this calculation only the forces, $\delta_{ij}\ F_j$, are kept, so that no forces other than F_i applied at P_i remain.

To calculate $K\ (P_i,\ P'^{(1)})$, a small normal displacement, δ_n, is introduced at $P'^{(1)}$. This displacement is small when compared to the adjacent elements of the crack front. The potential energy released by this extension can be calculated by the stiffness matrix derivation method developed by Parks [*12*]. If the potential energy release rate is in direct relation with $K\ (P_i,\ P'^{(1)})$ by

$$\frac{K^2\ (P_i, P'^{(1)})}{E'} = -\frac{\delta P}{\delta A(P'^{(1)})}$$

it is easy to calculate the function $G\ (P_i,\ P'^{(1)})$ and the nondimensional function $g\ (P_i,\ P'^{(1)})$.

This method was proven to be efficient and accurate [*12*] and its main advantage is that it avoids calculations in the whole body for the original and the slightly extended crack fronts. Actually, one node on the crack front and eventually a few others in the adjacent area are displaced. Results of these calculations showed that with a normal displacement, smaller than one thousandth of the dimension of the adjacent elements of the crack front, the potential energy release rate was independent of the normal displacement. Displacing only one node gave as accurate results as were obtained by displacing a few nodes.

The nondimensional function can be calculated as just described for the largest crack considered.

3. In order to arrive at the next smaller crack front, denoted (2), closure forces, $\alpha_p F_p$, are applied at nodes, p, along the new crack front. They are determined by the condition that at nodes p the opening of the crack (1) under the action of the force F_i applied at P_i and forces $\alpha_p F_p$ is zero. If $w_{pi}^{(1)}$ is the displacement of node p under the action of force F_i, the condition is

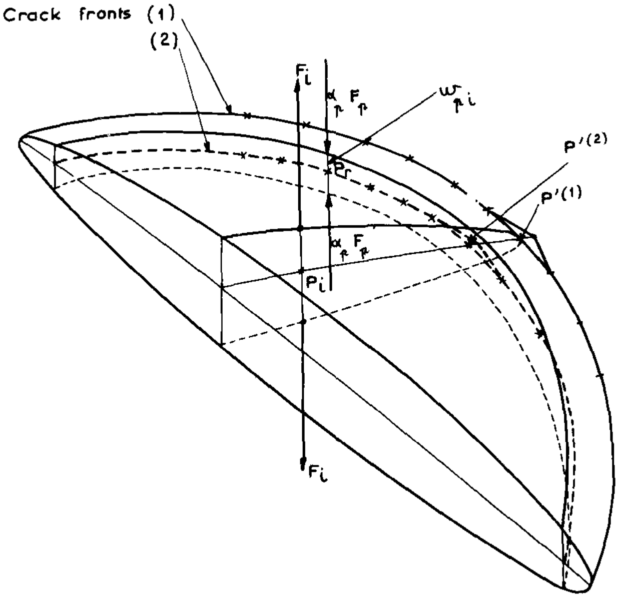

FIG. 8—*Forces applied on the crack surface; closure forces.*

$$w_{pi}^{(1)} + \alpha_p w_{pp}^{(1)} = 0$$

The combination of the forces, F_i, to be used for the second crack front in which the forces must be nonzero only at node i and at nodes p is therefore determined by

$$(\delta_{ij} + \alpha_p \delta_{pj}) F_j$$

The calculations for the second crack front are then reduced to a calculation with the former front and the new combination of applied forces. The nondimensional function is computed by giving a small normal displacement to node $P'^{(2)}$.

Subsequent fronts may be considered by adding new closure forces, etc. One computer run yields the influence functions or the nondimensional functions for the desired number of crack fronts generated from each other by a smooth closure.

One difficulty with this method is that a finer mesh is necessary near the center of the crack if one wishes to keep a significant number of nodes on the rather short crack fronts.

4. Only ordinary elements were used to reduce the number of nodes, and this gave rather poor accuracy near the crack tip. An improvement can be obtained, with no significant increase in computing time, by using isoparametric elements with many degrees of freedom near the crack tip. Moreover, interpolation is possible since the value of the nondimensional function is known on the crack front.

5. The major difficulty in the numerical solution involves solving a large number of equations for unknown displacements. For example, the model for the penny-shaped crack contained 1400 nodes with three degrees of freedom, leading to a set of 4200 simultaneous equations. Here, division into superelements with a maximum number of nodes between 300 and 600 is necessary.

Calculated Weight Function for a Penny-Shaped Crack in an Infinite Solid

1. The first attempt to check the validity of the program was performed on a penny-shaped crack in an infinite solid, because the influence function for this problem is given in closed form by Eq 6.

Other problems could have been considered for this check, because the stress intensity factors for a certain number of three-dimensional problems have been calculated by several other authors. But, to our knowledge, it seems that three-dimensional weight functions were calculated only for a semi-infinite crack and a penny-shaped crack in an infinite solid. Such verification should be made if the method can be further developed.

To reduce the number of elements, forces of equal magnitude were applied at four symmetrical points, P in Fig. 9. For Point P_l in the first quadrant

$$G\,(P_1, P') = \frac{\sqrt{b^2 - r^2}}{\pi\,\sqrt{\pi b}}\left(\frac{1}{\rho_1^2} + \frac{1}{\rho_2^2} + \frac{1}{\rho_3^2} + \frac{1}{\rho_4^2}\right)$$

and the nondimensional function

$$g\,(P_1,P') = \sqrt{\frac{b^2 - r^2}{2b\,\sin\theta_1}}\,\rho_1^{3/2}\left(\frac{1}{\rho_1^2} + \frac{1}{\rho_2^2} + \frac{1}{\rho_3^2} + \frac{1}{\rho_4^2}\right) \qquad (9)$$

The computed values of $g\,(P_1,\ P')$ are compared with those resulting from Eq 9.

2. The infinite solid was replaced by a cylinder of radius $4b$ and height $12b$. Because of its symmetrical form, only one eighth of this cylinder had to be modeled (Fig. 10).

Figures 11 and 12 show the mesh in the plane of the crack and in the meridional plane. The total number of nodes was about 1400, with 164 located in the plane of the crack and 56 on the crack surface.

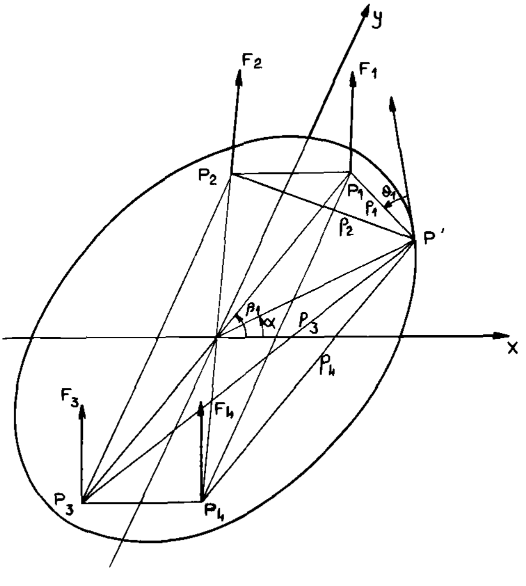

FIG. 9—*Four symmetrical forces applied to a penny-shaped crack.*

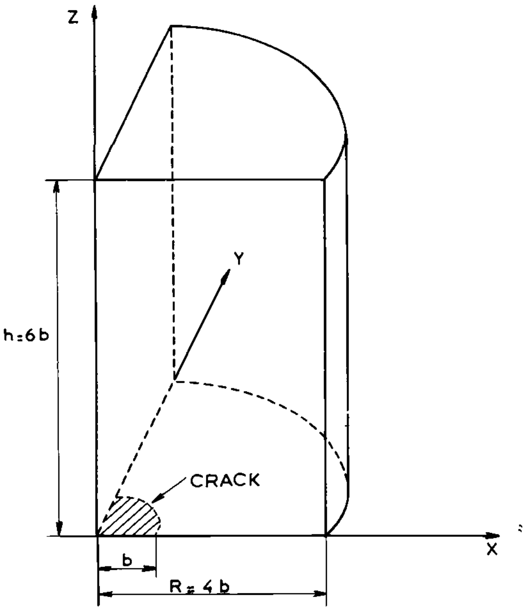

FIG. 10—*Cylinder modeling an infinite solid with a penny-shaped crack.*

The nondimensional function, $g(P,P')$, was computed for equidistant positions of P' on the crack front, $\alpha = 0$ or $90°$, $\alpha = 22.5$ or $67.5°$, and $\alpha = 45°$.

The results are presented in Figs. 13, 14, and 15. Each figure shows the weight functions at P′ for forces applied at P on the meridional lines defined by $\beta = 0$, 22.5, 45, 67.5, or 90°.

The results for $\alpha = 67.5°$ and $\alpha = 90°$ are obtained by symmetry with respect to the meridional line $\beta = 45°$.

The following values of $g\ (P,P')$ were known in advance: (*a*) on the crack front, zero, except for P at P'; (*b*) for P at P', $g\ (P',P') = 1$, except that $g\ (P_1',P_1') = g\ (P_2',P_2') = 2$; and (*c*) at the center, $g\ (0,P') = 2\sqrt{2}$.

3. The values of the nondimensional function for $\alpha = 0$ obtained from the numerical analysis are compared with the closed form solution in Table 1.

It can be seen that the accuracy is better than 3 percent if $r/b \leqslant 0.7$; about 5 percent if $r/b = 0.8$; and between 10 and 15 percent if $r/b = 0.9$ except near P', especially at Nodes 10, 13, and 14 (these nodes are in the region of a rapid variation of the function, from zero along the crack tip to 2 at P' ($\beta = 0$)). It seems that the mesh should be finer in this region.

This inaccuracy for $r/b \geqslant 0.8$ can be corrected by an interpolation

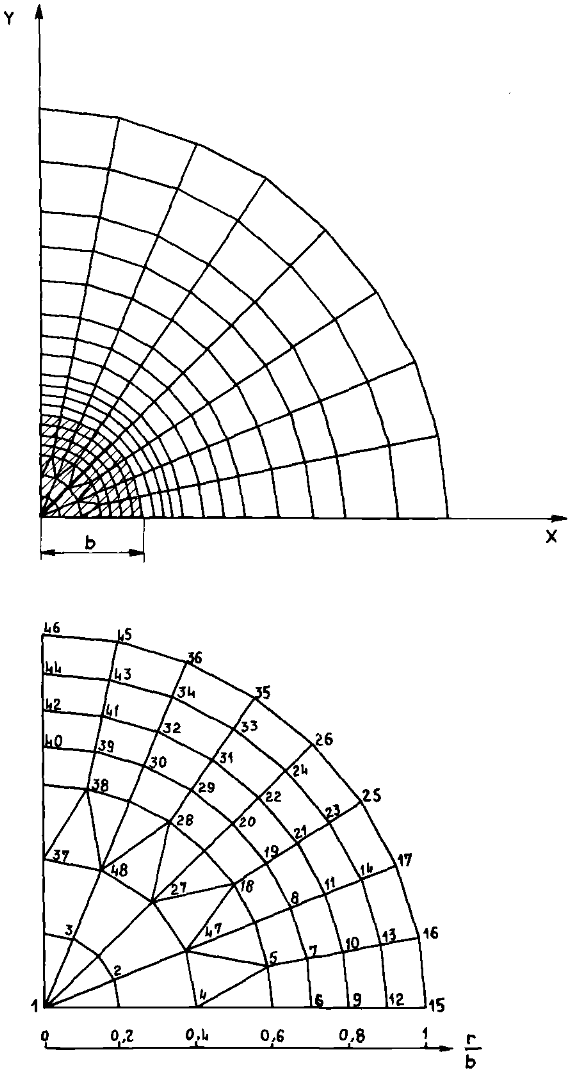

DETAIL OF THE CRACK

FIG. 11—*Mesh in the plane of the crack.*

between the accurate values at $r/b = 0.7$ and the known values on the crack front, which is zero everywhere except at P' where it is two.

However, it seems advisable to improve the accuracy near P' since,

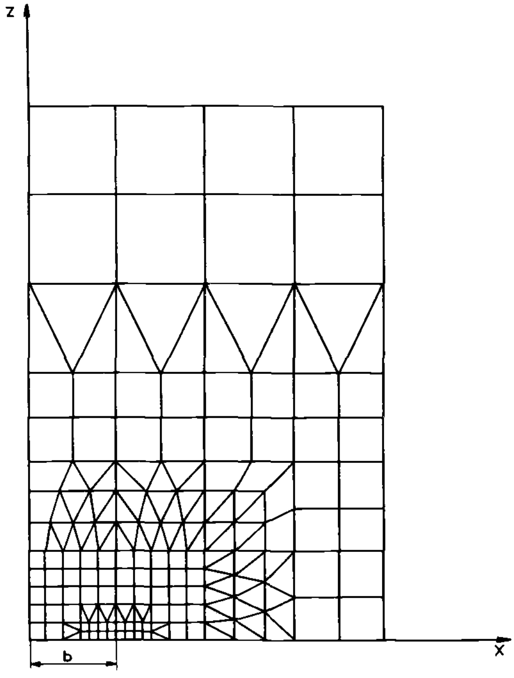

FIG. 12—*Mesh in a meridional plane.*

because of the singularity of the weight function at P', this area may contribute more than other regions to the value of K.

4. The computer time for the calculation of the penny-shaped crack problem was 75 min for a first attempt; this run yielded the functions for five crack sizes. Some improvement in this run time can be expected. However, because of the large number of nodes in three-dimensional bodies, it must be expected that the computer time will be rather long for any problem.

The time also depends on the code, and improvements would be possible if the codes were more appropriate to this particular problem.

Solution of two-dimensional problems requires a much shorter computer time. For example, the weight functions for a cracked strip or a circular crack in a cylinder were obtained in about 100 s. This calculation yielded the weight functions for all crack lengths [*1*].

Even if more calculation experience were acquired and more efficient codes were used, it seems that applying the finite element method to the solution of three-dimensional crack problems would require long computer times, because of the large number of nodes involved.

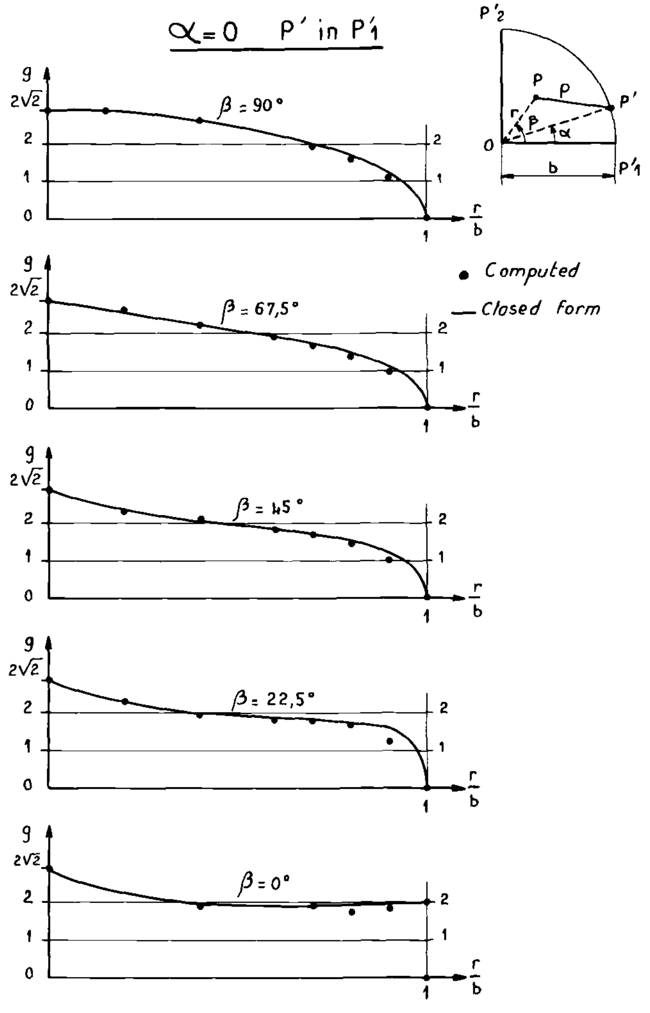

FIG. 13—*Values of* g (P,P′) *for* P′ *at* $\alpha = 0$ *and* 90°.

5. The function $g\ (P,P')$ was also calculated for smaller cracks using the closure process as described earlier, and the accuracy was of the same order of magnitude as before. This confirms the capability of getting functions for several cracks from one computer run; but, as stated previously, a refined mesh is necessary to keep a significant number of nodes on the reduced crack fronts.

TABLE 1—*Values of* g (P$_i$,P′) − P′ *defined by* $\alpha = 0°$.

Nodes, P_i	g_{FEM} Computed	g_c, Closed Form	$\frac{g_{FEM}}{g_c}$
1	2.870	2.828	1.014
2	2.276	2.264	1.005
3	2.590	2.513	1.030
4	2.064	1.980	1.042
5	2.024	1.890	1.070
6	1.874	1.901	0.986
7	2.075	1.877	1.105
8	2.036	1.819	1.119
9	1.758	1.920	0.915
10	2.181	1.868	1.167
11	1.866	1.747	1.067
12	1.856	1.954	0.949
13	0.606	1.822	0.333
14	1.270	1.565	0.811
18	1.893	1.843	1.026
19	1.787	1.754	1.019
20	1.671	1.707	0.978
21	1.450	1.619	0.896
22	1.448	1.523	0.950
23	1.167	1.345	0.868
24	1.057	1.200	0.880
27	2.105	2.057	1.023
28	1.809	1.859	0.973
29	1.663	1.697	0.979
30	1.677	1.736	0.966
31	1.393	1.476	0.943
32	1.401	1.483	0.944
33	1.025	1.123	0.912
34	1.007	1.102	0.913
37	2.623	2.592	1.012
38	1.999	2.054	0.973
39	1.775	1.837	0.966
40	1.947	2.019	0.964
41	1.463	1.552	0.942
42	1.600	1.697	0.943
43	1.042	1.137	0.916
44	1.129	1.232	0.916
47	2.089	1.994	1.047
48	2.240	2.228	1.005

Particular Problem of an Applied Stress Function of *x* only

If the applied stress is a function of *x* only (Fig. 16), then

$$K(P') = \int_0^1 \sigma(x) \left[\int_{y_1(x)}^{y_2(x)} G(x,y;\, x',y'(x')dy \right] dx$$

or

$$K(P') = \int_0^1 \sigma(x)\, H_x(x;\, x')dx$$

where $H_x\ (x;\ x')$ is given in conjunction with Eq 5 by

$$H_x\ (x;\ x') = \int_{y_1(x)}^{y_2(x)} \frac{\sqrt{2\sin\theta}}{(\pi\rho)^{3|2}}\ g(x,y;\ x')d\theta$$

using the substitutions

$$\rho = \frac{x' - x}{-\cos(\theta+\alpha)}$$

$$y - y' = -\ (x' - x)\ \tan(\alpha + \theta)$$

$$dy = -\ (x' - x)\frac{d\ \theta}{\cos^2(\alpha+\theta)}$$

one arrives at

$$H_x\,(x;x') = -\ \frac{1}{\pi}\sqrt{\frac{2}{\pi}}\,\frac{1}{\sqrt{(x'-x)}}\int_{Q_1}^{Q_2}\left[\frac{\sin\theta}{-\cos(\alpha+\theta)}\right]^{1|2} \times\ g(x,y;\ x')d\theta \tag{10}$$

It is easy to see that this integral exists when $x \rightarrow x'$. It is possible to define a nondimensional function

$$h_x\ (x;\ x') = \sqrt{(x' - x)}\,H_x\ (x;\ x')$$

and

$$K\ (P') = \int_0^1 \frac{h_x(x;\ x')}{\sqrt{(x' - x)}}\ \sigma\ (x)dx$$

However, the number of nodes necessary in the calculation is not very different from what it would be with an applied stress function of x and y, and the computer time remains long.

Mixed-Mode Problems

If the restriction of symmetry is applied, then only pure modes and symmetrical bodies can be considered. The calculations are restricted to loads applied to the crack faces and are sufficient to solve any K problem. However, the weight function concept, as developed by Bueckner, can be used for any load or mixed-mode problem.

As stated by Paris and McMeeking [9], the displacement calculations of a fundamental field gives the solutions for any load applied to any contour. By considering around each Point P', a small sphere on which the displacements can be calculated and imposed, the numerical accuracy might be improved. In this case, however, a fine mesh would be necessary near the small sphere, and it is likely that due to the large number of nodes long computer times is necessary.

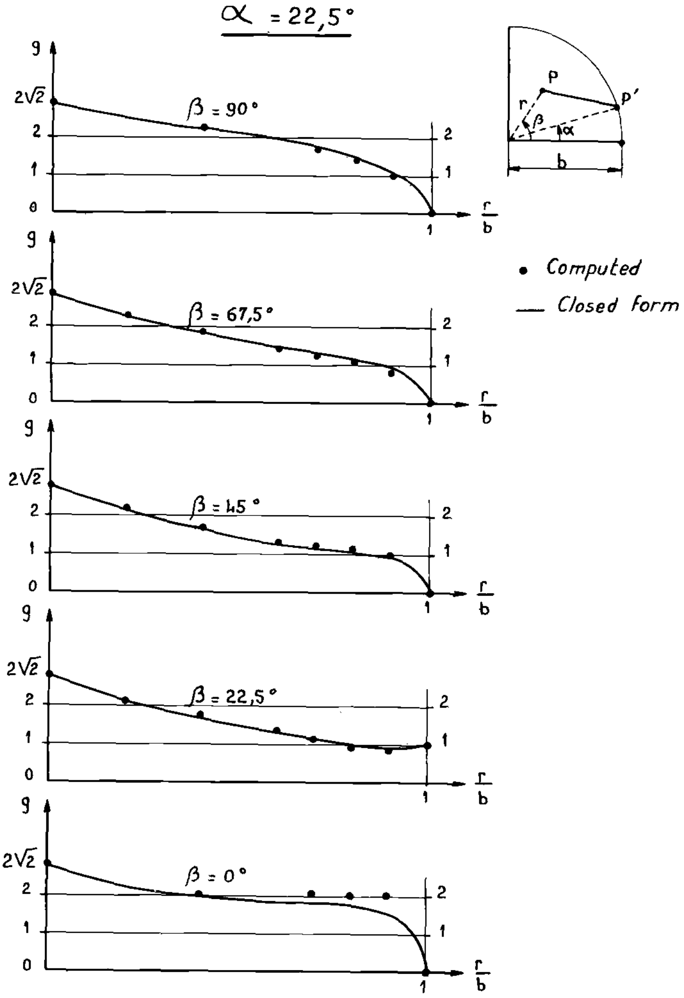

FIG. 14—*Values of* g(P, P') *for* P' *at* α = *22.5 and 67.5°.*

The tabulation of mixed mode functions on an arbitrary contour might be long and difficult. For this reason, it seems appropriate to limit the loaded contour to the crack surfaces.

Conclusions

A finite element method for computing three-dimensional weight or influence functions has been developed, where the closure method yields functions for several crack fronts from one computer run.

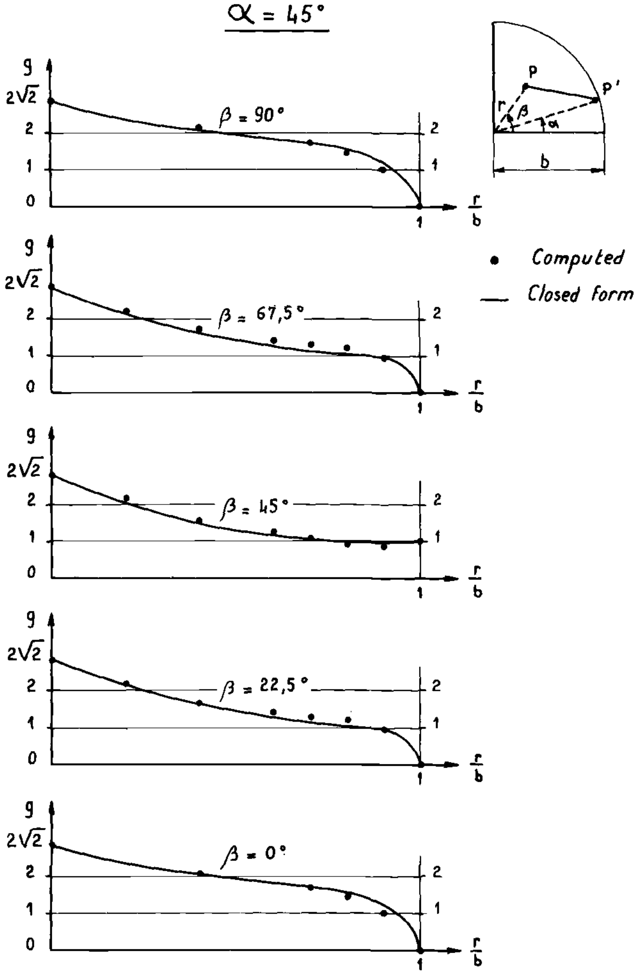

FIG. 15—*Values of* g(P, P') *for* P' *at* $\alpha = 45°$.

This method was used to solve a penny-shaped crack problem, and the numerical results were compared with known closed-form solution.

The computer figures can be corrected by an interpolation between the accurate points and the crack front where the values of the function are known. However, an improvement in accuracy is desirable near the point at which K is calculated; this would probably require more elements in the area. Further tests are needed to determine the actual accuracy in this area.

The required computer time was rather long, which makes the calcula-

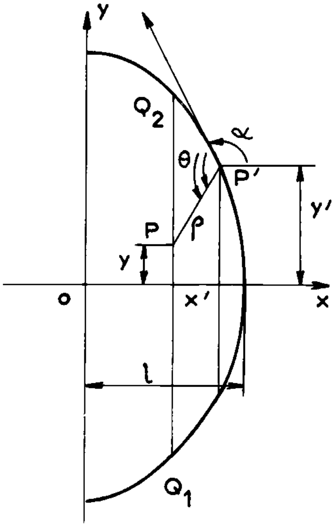

FIG. 16—*A crack loaded by a stress function of* x *only.*

tion expensive. This can be attributed to the large number of nodes for three-dimensional problems, which makes it necessary to divide the body into a number of superelements. The time can be somewhat reduced by improving the codes. However, due to the high number of nodes the effect would be nominal.

Because any method for solving elasticity problems can be used to calculate stress intensity factors and weight functions, it is advisable to investigate the suitability of methods other than finite elements, such as the method using boundary-integral equations [*13,14*] which might result in shorter computer time and cheaper calculations. However, the number of elements on the crack surface is likely to increase, resulting in better accuracy near the crack tip.

Acknowledgments

The authors acknowledge the helpful discussions with G. R. Irwin, University of Maryland; J. R. Rice, Brown University; and D. Radenkovic, Ecole Polytechnique, Paris. This research was partially supported by Délégation Générale à la Recherche Scientifique et Technique, under Contract 74.7.0750.

References

[*1*] Labbens, R. C., Pellissier-Tanon, A., and Heliot, J. in *Mechanics of Crack Growth, ASTM STP 590,* American Society for Testing and Materials, 1976, pp. 368–384.
[2] Bueckner, H. F. in *Methods of Analysis and Solutions of Crack Problems,* G. C. Sih, Ed., Noordhoff, 1973, Chapter 7.
[*3*] Rice, J. R., *International Journal of Solids and Structures,* 1972, p. 751.
[*4*] Shah, R. C. and Kobayashi, A. S., *Engineering Fracture Mechanics,* 1971, p. 71.
[*5*] Shah, R. C. and Kobayashi, A. S., *International Journal of Fracture,* 1973, p. 133.
[*6*] Shah, R. C. and Kobayashi, A. S. in *Stress Analysis and Growth of Cracks, ASTM STP 513,* American Society for Testing and Materials, 1971, p. 3.
[7] Kobayashi, A. S. and Enetanya, A. N. in *Mechanics of Crack Growth, ASTM STP 590,* American Society for Testing and Materials, 1976, pp. 477–495.
[*8*] Tada, H., Paris, P. C., and Irwin, G. R., *The Stress Analysis of Cracks Handbook,* Del Research Corporation, Hellertown Pa., 1973.
[*9*] Paris, P. C. and McMeeking, R. M., *International Journal of Fracture,* 1975, p. 354.
[*10*] Kassir, M. D. and Sih, G. C., *Three Dimensional Crack Problems,* Noordhoff, 1975.
[*11*] Hasselin, G., Heliot, J., and Vouillon, C., Paper M 2/3, 2nd International Conference on Structural Mechanics in Reactor Technology, Berlin, 1973.
[*12*] Parks, D. M., *International Journal of Fracture,* Dec. 1974, p. 481.
[*13*] Cruse, T. A., *The Surface Crack: Physical Problems and Computation Solutions,* American Society of Mechanical Engineers, Nov. 1972, pp. 153, 170.
[*14*] Lachat, J. C. and Watson, J. O., *Symposium on Boundary Integral Equation Method,* American Society of Mechanical Engineers, June 1975.

P. C. Paris,[1] *R. M. McMeeking,*[1] *and H. Tada* [2]

The Weight Function Method for Determining Stress Intensity Factors

---

REFERENCE: Paris, P. C., McMeeking, R. M., and Tada, H., "**The Weight Function Method for Determining Stress Intensity Factors,**" *Cracks and Fracture, ASTM STP 601,* American Society for Testing and Materials, 1976, pp. 471–489.

ABSTRACT: An alternate method to those of Bueckner and Rice is presented for the derivation of the two-dimensional weight function for determining crack tip stress intensity factors. The weight function has $r^{-1/2}$ type displacement singularity at the crack tip. It is shown that this singular field can be formulated using Westergaard stress functions in a manner similar to the method used for $r^{1/2}$ type fields in crack tip displacements.

A straight-forward approach for obtaining weight functions for cracked finite bodies is presented. This technique can be combined in a simple fashion with the finite element method. As an example, a weight function for the SEN strip is obtained in this manner. Moreover, closed form infinite body weight functions are also developed and used to derive some well-known stress intensity factor formulas.

KEY WORDS: crack propagation, fractures (materials), cracks, weighting functions, stress intensity factors

Bueckner [*1*] [3] has devised a method of determining stress intensity factor solutions, which has also been discussed by Rice [2]. The method depends mainly on the reciprocal theorem and other energy-method like considerations. The method may also be extended to computations of displacements in a manner almost identical to that in Ref *3* (see Appendix B of Ref *3*). Earlier similar "Green's Function" approaches are also found in Refs *4* through *6*. For an elegant presentation of the method in all generality the reader is referred to Refs *1,2,7,8*. However, in this section a more direct derivation of those results will be given. Nevertheless, a new approach to deriving weight functions will be presented in the

---

[1] Visiting professor and research assistant, respectively, Division of Engineering, Brown University, Providence, R. I. 02912.

[2] Staff scientist, Del Research Corporation, Hellertown, Pa.

[3] The italic numbers in brackets refer to the list of references appended to this paper.

second and third sections which do not require prior familiarity with weight functions. Therefore, the reader may prefer to simply note the results of this first section, Eqs 8 and 9, before proceeding directly into the later sections.

The analysis to follow will show that if the complete solution (for its stress intensity factor and displacements) to a crack problem for one loading system is known, then the solution (for K) for the same cracked configuration with any other loading may be obtained directly from the known solution. To show this consider a cracked body with loads, P_1, $P_2 \ldots P_N$, as the independently applied loads. From well-known results and definitions (for example, see pp. 1.10–1.12 and Appendixes A and B of Ref *3*), the Griffith energy rate, $\mathcal{G}$, is

$$\mathcal{G} = \frac{\partial U}{\partial a}\bigg|_P = \frac{1}{2} \sum_{i=1}^{N} \sum_{j=1}^{N} \frac{\partial C_{ij}(a)}{\partial a} P_i P_j = \frac{1}{2} \sum_{i=1}^{N} P_i \frac{\partial u_i}{\partial a} \tag{1}$$

where the displacements of loading points, u_i, can be written in terms of elastic compliance coefficients, $C_{ij}(a)$ as functions of crack length, a

$$u_i = \sum_{j=1}^{N} u_i^j = \sum_{j=1}^{N} C_{ij}(a) P_j \tag{2}$$

because of the reciprocal theorem $C_{ij} = C_{ji}$, which was used in writing the preceding equations.

Now on the other hand, the Griffith energy rate may be written in terms of stress intensity factors (see Ref *3*, p. 1.12) as

$$\mathcal{G} = \frac{K^2}{E'} = \frac{1}{E'} \sum_{i=1}^{N} \sum_{j=1}^{N} k_i(a) k_j(a) P_i P_j \tag{3}$$

since the stress intensity factor, K, is linearly dependent on the loads, P_i, or

$$K = \sum_{i=1}^{N} K_i = \sum_{i=1}^{N} k_i(a) P_i \tag{4}$$

In this analysis E' is the effective modulus of elasticity; E, for plane stress or $E/1 - \nu^2$ for plane strain, and K_i the stress intensity factor for the ith load.

Now equating the double sums in both results for $\mathcal{G}$,[4] that is, Eqs 1 and 4, and noting that since this must be true for any values of the loads, P_1, $P_2 \ldots P_N$, the coefficients must be identical term by term, then

---

[4] As suggested by J. R. Rice, private communication, 1974.

$$\frac{k_i(a)k_j(a)}{E'} = \frac{1}{2}\frac{\partial C_{ij}(a)}{\partial a} \tag{5}$$

Let a full solution be known for just one of the loads, say P_m. Then rearranging the latest result

$$k_i(a) = \frac{E'}{2}\frac{\partial C_{im}(a)}{\partial a}\frac{1}{k_m(a)}$$

or from Eq 4

$$k_i(a) = \frac{E'}{2}\frac{\partial C_{im}(a)}{\partial a}\frac{P_m}{K_m} \tag{6}$$

By saying the solution is known for a load, P_m, it is meant that K_m is known and C_{im} is known since the displacements, u_i^m, for the load at P_m are presumed to be known and from Eq 2

$$C_{im} = \frac{u_i^m}{P_m}$$

Combining Eqs 4 and 6

$$K = \sum_{i=1}^{N} k_i(a)P_i = \frac{E'}{2}\frac{P_m}{K_m}\sum_{i=1}^{N}\frac{\partial C_{im}(a)}{\partial a}P_i \tag{7}$$

Thus K can be found for loads, P_i, from results obtained from just one load, P_m. This is the desired result.

For arbitrary distributed tractions $T(s)$ over a surface, s, instead of discreet forces, P_i, the form of the result, Eq 7, becomes

$$K = \int h_m\,(s,a)\,T(s)\,ds \tag{8}$$

where $h_m(s,a)$ is the "weight function" as determined entirely from the solution for a load (or loading system) characterized by m. For this result it is noted that

$$h_m(s,a) = \frac{E'}{2K_m(a)} \times \frac{\partial u^m(s,a)}{\partial a} \tag{9}$$

where $u^m(s,a)$ are displacements at s in the direction of the tractions $T(s)$ but caused only by the loading system characterized by m.

A Special Method of Determining the Weight Function, Mode I

In a two-dimensional problem let loading State **1** be the known loading state (corresponding to *m*) where concentrated forces, P_1, are applied on the crack surface at a distance, *c*, from the crack tip. Let loading State **2** (for the same configuration) be one of arbitrary tractions for which it is desired to determine K_2. By the reciprocal theorem

$$P_1 u_2 = \int T_2 u_1 ds \tag{10}$$

where the displacements *u* form reciprocal work products (for example, ι_{22} is the displacement at the location of P_1 in the direction of P_1 but due to loading State **2**) see Fig. 1.

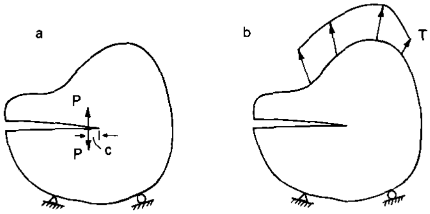

FIG. 1—*An elastic body with two states of loading:* (a) *State 1 and* (b) *State 2.*

Now, presume that the distance, *c*, from the crack tip to the loading forces in State **1** is very small (that is, approaching zero compared to other dimensions). Then the displacement u_2 will be within the crack tip stress field for State **2** or [*3*]

$$u_2 = 2v \Big|_{\substack{r = c \\ \theta = \pi}} = \frac{4\sqrt{2}}{\sqrt{\pi} E'} K_{12} \sqrt{c} \tag{11}$$

Note that due to the symmetrical (with respect to the crack) force system selected for State **1** only Mode I fields contribute work-producing displacements, u_2, thus the *K* being computed here is only the Mode I component. Substituting Eq 11 and rearranging Eq 10 gives

$$K_{12} = \frac{\sqrt{\pi} E'}{4\sqrt{2}} \frac{1}{P_1 \sqrt{c}} \int T_2 u_1 ds \tag{12}$$

Now as *c* diminishes to zero let $P_1 \sqrt{c}$ remain a finite constant, choosing for later convenience

$$\frac{P_1 \sqrt{c}}{\pi} = B_1 \tag{13}$$

The Westergaard stress function for State **1** with the distances to boundaries very (infinitely) large compared to c is [*3*]

$$Z = \frac{P\sqrt{c}}{\pi(z + c)\sqrt{z}} \tag{14}$$

which upon substituting Eq 13 and letting c approach zero is appropriate. This leads to a local crack tip field situation in State **1** of

$$Z_{11}(z) = B_1/z^{3|2} \tag{15}$$

since as c approaches zero, the effects of the boundaries may be neglected. Again, substituting results into Eq 12 gives

$$K_{12} = \frac{E'}{4\sqrt{2\pi}\, B_1} \int T_2 u_1{}^1 ds \tag{16}$$

where T_2 are the applied tractions and $u_1{}^1$ are now the corresponding displacements without applied loads, due to inserting a local Mode I singularity of $z^{-3|2}$ type [5] of strength B_1 as in Eq 15 at the crack tip where K_2 is desired. The weight function is then

$$h_{1m}(a,s) = \frac{E' u_1{}^1\,(a,s)}{4\sqrt{2\pi}\, B_1} \tag{17}$$

Bueckner [*1*] obtained a similar result by a less direct approach.

It is easy to visualize inserting the local singularity described by Eq 15 into a finite element scheme to determine resulting displacements $u_1{}^1$ (a,s), for all mesh points with no other loads present. This has distinct advantages over other finite element methods since the solution generated applies to *all* possible loadings. The advantage also applies when results are obtained using collocation or direct solutions employing this method.

This derivation has proceeded to consider Mode I only, and the resulting stress intensity factor in Eq 16 is of a Mode I type. However, it is possible to replace State **1** with its Mode II or Mode III counterparts and rederive results for K_{II} and K_{III}, as well as K_{I}, as follows.

---

[5] Let the $z^{-3|2}$ singularity be known as the "Bueckner Type" with its strength appropriately denoted as "B."

Mode II and Mode III Weight Functions

By repeating the derivation of the preceding section, that is, Eq 10 through Eq 17, but replacing State **1** on Fig. 1 with its Mode II or Mode III counterpart, as shown on Figs. 2*a* and *b*, then weight functions may be developed directly for Mode II and Mode III stress intensity factors. The results are shown in the following equations.

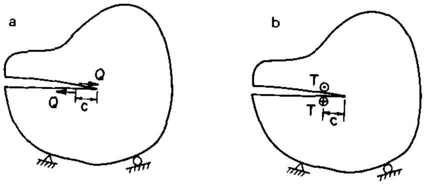

FIG. 2—*Alternate states of load for Modes II and III.*

Mode II

$$K_{II2} = \frac{E'}{4\sqrt{2\pi}\,B_{II}} \int T_2 u_1{}^{II} ds \tag{18}$$

where $u_1{}^{II}$ is now caused by inserting a local field of the Bueckner type at the crack tip of interest, that is

$$Z_{II1}(z) = B_{II}/z^{3|2} \tag{19}$$

Mode III

$$K_{III2} = \frac{G}{2\sqrt{2\pi}\,B_{III}} \int T_2 u_1{}^{III} ds \tag{20}$$

where G is the shear modulus and $u_1{}^{III}$ is caused by inserting the Bueckner singularity

$$Z_{III1}(z) = B_{III}/z^{3|2} \tag{21}$$

Therefore, it is equally easy to insert Mode II and Mode III singularities in problems to obtain the Mode II and Mode III weight functions

$$h_{IIm}(a,s) = \frac{E' u_1{}^{II}(a,s)}{4\sqrt{2\pi}\,B_{II}} \tag{22}$$

and

$$h_{IIIm}(a,s) = \frac{G\, u_1{}^{III}(a,s)}{2\sqrt{2\pi}\,B_{III}} \tag{23}$$

where now Eq 8 may be applied individually for each of the three modes of stress intensity factors.

For displacement boundary conditions see Appendix I.

Near Tip Bueckner Displacement Fields

The displacement fields may be computed for Bueckner type singularities, that is (see Eqs 15, 19, and 21)

$$Z(z) = B/z^{3|2}$$

for each mode. Making use of the usual r, θ coordinates measured from the crack tip, the results for plane strain displacement are as follows.

Mode I

$$\begin{aligned} u &= \frac{B_I}{G\sqrt{r}} \cos \frac{\theta}{2}\left[2\nu - 1 + \sin \frac{\theta}{2} \sin \frac{3\theta}{2}\right] \\ v &= \frac{B_I}{G\sqrt{r}} \sin \frac{\theta}{2}\left[2 - 2\nu - \cos \frac{\theta}{2} \cos \frac{3\theta}{2}\right] \\ w &= 0 \end{aligned} \tag{24}$$

Mode II

$$\begin{aligned} u &= \frac{B_{II}}{G\sqrt{r}} \sin \frac{\theta}{2}\left[2 - 2\nu + \cos \frac{\theta}{2} \cos \frac{3\theta}{2}\right] \\ v &= \frac{B_{II}}{G\sqrt{r}} \cos \frac{\theta}{2}\left[1 - 2\nu + \sin \frac{\theta}{2} \sin \frac{3\theta}{2}\right] \\ w &= 0 \end{aligned} \tag{25}$$

Mode III

$$\begin{aligned} u &= 0 \\ v &= 0 \\ w &= \frac{B_{III}}{G\sqrt{r}} 2 \sin \frac{\theta}{2} \end{aligned} \tag{26}$$

For plane stress for Modes I and II replace ν by $\nu/(1 + \nu)$ and also note then $w \neq 0$.

For generating weight functions these fields should be inserted locally at the crack tip where K is desired. They are then the actual weight function displacements which should be used for loads near by the crack tip.

For a semi-infinite crack in an infinite body, they are the weight function displacements for the whole problem (two-dimensional problems). Some examples will follow making use of these results for very simple problems so as to illustrate the method. The power of the method is however only fully appreciated with more complicated problems when combined with numerical, finite element, and other procedures.

Closed-Form Weight Functions

Closed forms for Westergaard stress functions, Z and $\bar{Z}$, can be written to form weight function displacement fields throughout a body. The technique of finding such stress functions is much the same as for normal crack stress analysis problems except that the crack tip, for which the weight function is desired, will have a $z^{-3/2}$ (in Z) of strength B. Some examples are as follows (each applies to all three Modes I, II, and III)

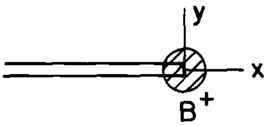

$$\begin{Bmatrix} Z_{\mathrm{I}}(z) \\ Z_{\mathrm{II}}(z) \\ Z_{\mathrm{III}}(z) \end{Bmatrix} = \begin{Bmatrix} B_{\mathrm{I}} \\ B_{\mathrm{II}} \\ B_{\mathrm{III}} \end{Bmatrix} \frac{1}{z^{3/2}} \qquad (27)$$

$$\begin{Bmatrix} \bar{Z}_{\mathrm{I}}(z) \\ \bar{Z}_{\mathrm{II}}(z) \\ \bar{Z}_{\mathrm{III}}(z) \end{Bmatrix} = - \begin{Bmatrix} B_{\mathrm{I}} \\ B_{\mathrm{II}} \\ B_{\mathrm{III}} \end{Bmatrix} \frac{2}{z^{1/2}} \qquad (28)$$

Note, all Z and $\bar{Z}$ expressions apply to all three modes as indicated here.

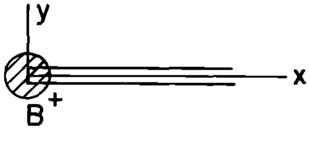

$$Z(z) = \frac{iB}{z^{3/2}} \qquad (29)$$

$$\bar{Z}(z) = -\frac{2iB}{z^{1/2}} \qquad (30)$$

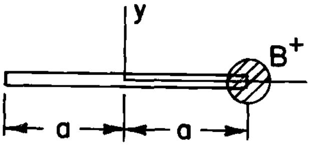

$$Z(z) = \frac{B\sqrt{2a}}{(z-a)^{3/2}\,(z+a)^{1/2}} \qquad (31)$$

$$\bar{Z}(z) = -B\sqrt{\frac{2}{a}}\left(\frac{z+a}{z-a}\right)^{1/2} \qquad (32)$$

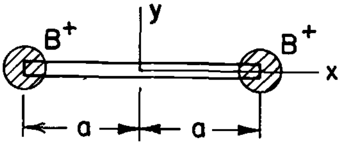

$$Z(z) = \frac{2B\sqrt{2a}\,z}{(z^2 - a^2)^{3/2}} \quad (33)$$

$$\bar{Z}(z) = \frac{-2B\sqrt{2a}}{(z^2 - a^2)^{1/2}} \quad (34)$$

Symmetric about y-axis. Note, remove 2 to get K at one crack tip.

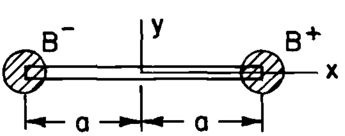

$$Z(z) = \frac{B(2a)^{3/2}}{(z^2 - a^2)^{3/2}} \quad (35)$$

$$\bar{Z}(z) = \frac{-2B\sqrt{2a}}{(z^2 - a^2)^{1/2}} \times \frac{z}{a} \quad (36)$$

Skew symmetric about y-axis. Note, remove 2 to get K at one crack tip.

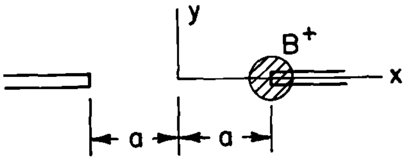

$$Z(z) = \frac{B\sqrt{2a}}{(a - z)^{3/2}(a + z)^{1/2}} \quad (37)$$

$$\bar{Z}(z) = B\sqrt{\frac{2}{a}}\left(\frac{a + z}{a - z}\right)^{1/2} \quad (38)$$

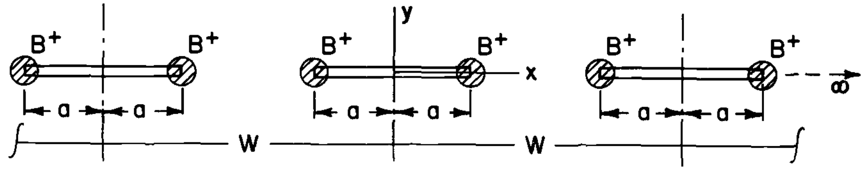

$$Z(z) = \frac{2B\left(\frac{\pi}{w}\cos\frac{\pi a}{w}\right)^{3/2}\left(2\sin\frac{\pi a}{w}\right)^{1/2}\sin\frac{\pi z}{w}}{\left(\sin\frac{\pi z}{w} - \sin\frac{\pi a}{w}\right)^{3/2}\left(\sin\frac{\pi z}{w} + \sin\frac{\pi a}{w}\right)^{3/2}} \quad (39)$$

$$\bar{Z}(z) = \frac{-2B\left(\frac{2\pi}{w}\tan\frac{\pi a}{w}\right)^{1/2}\cos\frac{\pi z}{w}}{\left[\left(\sin\frac{\pi z}{w}\right)^2 - \left(\sin\frac{\pi a}{w}\right)^2\right]^{1/2}} \quad (40)$$

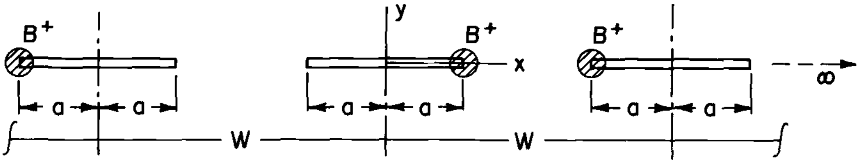

$$Z(z) = \frac{B\left(\frac{\pi}{w}\cos\frac{\pi a}{w}\right)^{3/2}\left(2\sin\frac{\pi a}{w}\right)^{1/2}}{\left(\sin\frac{\pi z}{w} - \sin\frac{\pi a}{w}\right)^{3/2}\left(\sin\frac{\pi z}{w} + \sin\frac{\pi a}{w}\right)^{1/2}} \tag{41}$$

$$\bar{Z}(z) = B\left\{\frac{-\left(\frac{2\pi}{w}\tan\frac{\pi a}{w}\right)^{1/2}\cos\frac{\pi z}{w}}{\left[\left(\sin\frac{\pi z}{w}\right)^{2} - \left(\sin\frac{\pi a}{w}\right)^{2}\right]^{1/2}} + i\cot\frac{\pi a}{w}\left(\frac{\pi}{w}\sin\frac{2\pi a}{w}\right)^{1/2}\Pi_c\left[\sin^{-1}\left(\frac{\sin\frac{\pi z}{w}}{\sin\frac{\pi a}{w}}\right), 1, \sin\frac{\pi a}{w}\right]\right\}$$

$$\Pi_c[\phi,n,k] = \int\frac{d\phi}{(1-n\sin^2\phi)(1-k^2\sin^2\phi)^{1/2}} \tag{42}$$

An Example of Finite Element Results

As mentioned earlier, weight function displacements can be obtained using finite element analysis by putting a small hole at the crack tip and inserting the Bueckner type field as boundary conditions on the hole. That is using Eqs 24 (or Eqs 25 or 26) as boundary conditions on the hole, with all other surfaces stress free in order to determine the State **1** displacements, u_1.

As an example, consider the single edge cracked strip for which a variety of loadings are available with previously tabulated results [*9,3*]. The particular strip selected here is (see Fig. 3), $a = b/2$, $2h = 6b$ with circular hole at the crack of radius, $r = 0.006944b$ and $\nu = 0.3$. A mesh of 352 elements and 398 nodes was used as shown on Fig. 3 (with the inner circles of elements removed and enlarged for clarity).

The table gives results obtained by simply inserting the displacement field, Eq 24, at 25 points on the upper half of the hole, and constraining

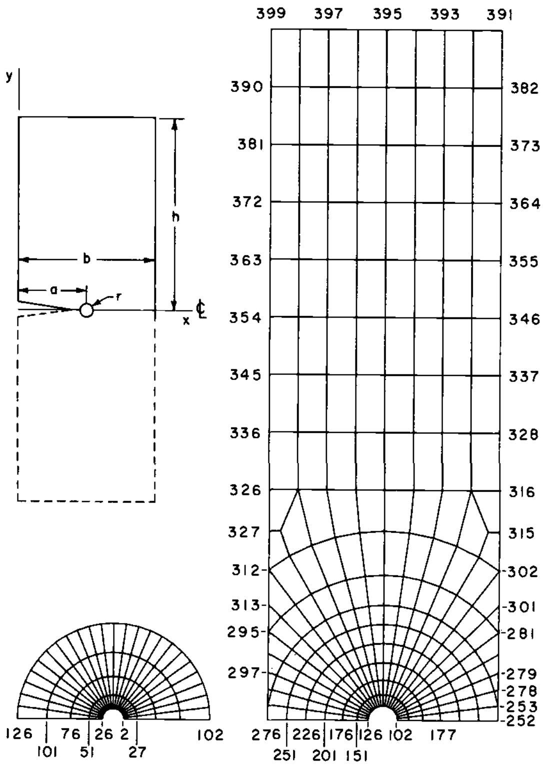

FIG. 3—*A single-edge cracked strip with a circular hole at the crack radius.*

points on the crack plane ahead of the crack to remain on that plane. In this manner only half of the problem needs to be treated by finite elements. The points on Table 1 are numbered as indicated on the mesh in Fig. 3 and located by coordinates x/b and y/b. The corresponding components of the displacements, u_1, for use in the integral to obtain K_{I2} are

$$\bar{u}/b = \frac{E'(u_1)_x}{2\sqrt{2\pi}\, B_I b} \tag{43}$$

$$\bar{v}/b = \frac{E'(u_1)_y}{2\sqrt{2\pi}\, B_I b}$$

so that K_{I2} may be obtained from components of tractions for one half of a problem (with respect to crack plane symmetry)

$$K_{I2} \int (T_x\bar{u} + T_y\bar{v})\, ds \tag{44}$$

TABLE 1—*Weight function displacements for an edge cracked strip.*

	$\left(\frac{a}{b} = 0.5,\ \frac{h}{b} = 3, \nu = 0.3,\ \frac{r}{b} = 0.006944\right)$			
Point	x/b	y/b	$\bar{u}/b$	$\bar{v}/b$
2	0.5069	0	−2.736	0
27	0.5156	0	−1.767	0
102	0.5625	0	−0.595	0
177	0.75	0	0.285	0
26	0.4931	0	−0.000003	9.575
51	0.4844	0	−0.232	7.066
76	0.4722	0	−0.269	5.930
101	0.4566	0	−0.297	5.395
126	0.4375	0	−0.319	5.187
151	0.3888	0	−0.319	5.229
176	0.3264	0	−0.346	5.670
201	0.25	0	−0.368	6.374
226	0.1666	0	−0.385	7.214
251	0.0833	0	−0.393	8.084
276	0	0	−0.396	8.960
297	0	0.207	1.795	8.971
295	0	0.3837	3.719	8.956
313	0	0.5	4.988	8.933
312	0	0.6516	6.634	8.908
327	0	0.820	8.453	8.890
326	0	1.00	10.401	8.887
336	0	1.25	13.116	8.887
345	0	1.50	15.838	8.889
354	0	1.75	18.563	8.891
363	0	2.00	21.289	8.892
372	0	2.25	24.015	8.892
381	0	2.50	26.740	8.892
390	0	2.75	29.466	8.892
399	0	3.00	32.191	8.892
397	0.25	3.00	32.191	6.166
395	0.50	3.00	32.191	3.441
393	0.75	3.00	32.191	0.715
391	1.0	3.00	32.191	−2.010
382	1.0	2.75	29.466	−2.010
373	1.0	2.50	26.740	−2.010
364	1.0	2.25	24.015	−2.010
355	1.0	2.00	21.289	−2.010
346	1.0	1.75	18.564	−2.011
337	1.0	1.50	15.838	−2.012
328	1.0	1.25	13.109	−2.015
316	1.0	1.0	10.371	−2.017
315	1.0	0.820	8.386	−2.015
302	1.0	0.6516	6.515	−1.980
301	1.0	0.50	4.819	−1.912
281	1.0	0.3837	3.525	−1.744
279	1.0	0.207	1.774	−1.249
278	1.0	0.134	1.228	−0.865
253	1.0	0.0653	0.904	−0.437
252	1.0	0	0.805	0

NOTE—($\bar{u}$ and $\bar{v}$ values for all 398 mesh points are available from the authors).

Using this formula and Table 1, the following accuracies are observed in comparative results for various loadings:

(*a*) uniform tension applied at the ends ~ 2.9 percent (see Ref *3*, p. 2.10),

(*b*) uniform pressure on the crack surface ~ < 4.9 percent,

(*c*) pure bending (moment applied anywhere beyond, $y/b = 1.5$) ~ 3.2 percent (see Ref *3*, p. 2.13),

(*d*) four-point bending (with loads at $y/b = 1$ and 3) ~3.2 percent, and

(*e*) three-point bending (with a span of $4b$) ~3.6 percent (see Ref *3*, p. 2.16).

This is only an example and better accuracies may be produced by finer finite element meshes. However, Table 1 allows the reader to calculate K_I results of comparable accuracies for any loading for this configuration. Its advantages and generality are thus obvious.

This same method applies, of course, to Mode II and Mode III simply using the proper fields, Eqs 25 and 26, as just implied. Moreover, it is obviously applicable to residual stress, thermal stress, and body force problems via simple superposition or direct application. The method is also open to three-dimensional finite element applications.

Closed Form Examples

Example 1

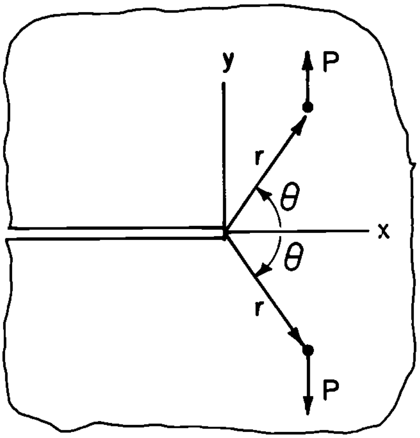

Consider an infinite sheet with a semi-infinite crack with a pair of equal and opposite forces (per unit thickness), P, as shown. The stress solution with a Bueckner type Mode I singularity (and no loading forces) is, as in Eq 27.

$$Z_{\text{II}}(z) = \frac{B_{\text{I}}}{z^{3|2}}(\text{any } z) \tag{45}$$

The stress intensity factor for the loads shown may be computed from

$$K_{\text{I}} = \frac{E'}{4\sqrt{2\pi}\,B_{\text{I}}}\int T_2 u_1{}^{\text{I}}\,ds \tag{46}$$

Now because of x-axis symmetry

$$\textstyle\int T_2 u_1{}^{\text{I}}\,ds = 2P \times v_1\,(\text{r},\theta) \tag{47}$$

The usual displacement relationships apply [*3*] or

$$2Gv_1 = 2(1 - \nu)\text{Im}\bar{Z}_{\text{I1}} - y\,Re\,Z_{\text{I1}} \tag{48}$$

where for plane stress ν can be replaced by $\nu/(1 + \nu)$. Substituting Z_{I1} and taking $z = re^{i\theta}$, etc. (see also Eq 24)

$$v_1 = \frac{B_{\text{I}}}{G\sqrt{r}}\sin\frac{\theta}{2}\left[2(1 - \nu) - \cos\frac{\theta}{2}\cos\frac{3\theta}{2}\right] \tag{49}$$

continuing the substitutions

$$K_{\text{I}} = \frac{P}{(1 - \nu)\sqrt{2\pi r}}\sin\frac{\theta}{2}\left[2(1 - \nu) - \cos\frac{\theta}{2}\cos\frac{3\theta}{2}\right] \tag{50}$$

For the special case $r = b$ and $\theta = \pi$, the result is as usual [*3*]

$$K_{\text{I}} = \frac{2P}{\sqrt{2\pi b}} \tag{51}$$

and for the special case $r = y_0$ and $\theta = \frac{\pi}{2}$ the result is easily obtained

$$K_{\text{I}} = \frac{P}{\sqrt{\pi y_0}}\left[\frac{5 - 4\nu}{4 - 4\nu}\right] \tag{52}$$

Therefore, it is seen that in this case getting the K_{I} through the weight function method gives direct algebraic access to a simpler form for some uses.

Note also from Eqs 25 and 26 that no Mode II or Mode III work is done by the forces, P, with these displacements, so $K_{\text{II}} = K_{\text{III}} = 0$.

Example 2

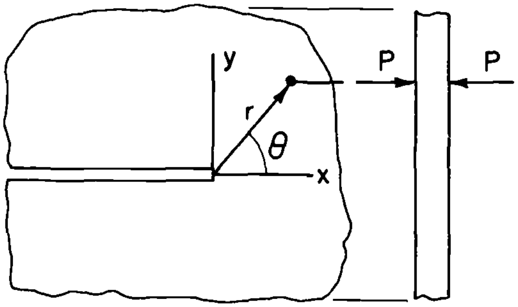

Consider a crack tip in a sheet which is subject to pinching forces, P, as shown. The (thinning) displacement per unit thickness is

$$u_1 = -\varepsilon_z = \frac{\nu}{E}(\sigma_x + \sigma_y) \tag{53}$$

which from the Westergaard stress function analysis becomes for

Mode I

$$u_1 = \frac{2\nu}{E} Re\, Z_{\mathrm{I}} \tag{54}$$

Mode II

$$u_1 = -\frac{2\nu}{E} Im\, Z_{\mathrm{II}} \tag{55}$$

for both modes

$$Z(z) = \frac{B}{z^{3|2}} = \frac{B}{r^{3|2}}\left(\cos\frac{3\theta}{2} - i\sin\frac{3\theta}{2}\right) \tag{56}$$

where substituting these results into Eqs 16 and 18 gives

$$K_{\mathrm{I}} = \frac{\nu P}{2\sqrt{2\pi}\,R^{3|2}}\cos\frac{3\theta}{2}$$

$$K_{\mathrm{II}} = \frac{-\nu P}{2\sqrt{2\pi}\,R^{3|2}}\sin\frac{3\theta}{2} \tag{57}$$

Acknowledgments

This work was principally accomplished at Brown University under support from the National Science Foundation—Materials Research Laboratory and the Atomic Energy Commission. The many suggestions of J. R. Rice are gratefully acknowledged as contributing much to this work.

APPENDIX I

Weight Functions for Displacement Boundary Condition

The previous derivations of weight functions assumed that all boundary conditions in State **2** are force loadings except for constraints just sufficient to eliminate rigid body modes. However, the reactions at those constraints are constituents of the forces T_2 applied to the weight function for computing K_2. The weight function for State **2** may be derived for boundary conditions of forces T_2 on the surface S_T and displacements u_2 on the surface S_u by imposing in State **1** boundary conditions of zero displacements on S_u. Then following in the same derivation as before Eq 16 becomes

$$K_{I2} = \frac{E'}{4\sqrt{2\pi}\,B_I}\left(\int_{S_T} T_2 u_1^I ds - \int_{S_u} P_1^I u_2 ds\right) \tag{58}$$

where $u_1{}^I$ are the displacements in the altered State **1**, arising from the Bueckner type singularity of strength B_I at the crack tip, and $P_1{}^I$ are the reactions in the altered State **1** arising at S_u due to the Bueckner type singularity. The Mode II and Mode III forms may be derived straight forwardly as before. Note that a problem with displacement boundary conditions on one part of the boundary requires a different weight function from a problem with displacement boundary conditions on another part of the boundary.

APPENDIX II

A Suggestion on Analytical Improvement of Numerical Solutions for Weight Functions

In the numerical weight function example given here and the preceding analysis, it was demonstrated that imposing only the Bueckner field of displacements (Eq 24, etc.) upon a hole at the crack tip gave reasonable results. However, the full weight function solution for a body of finite dimensions in general may be written as

$$Z = \frac{B + B_1 z + B_2 z^2 + B_3 z^3 + \ldots}{z^{3/2}} \tag{59}$$

where: B_1, B_2, B_3, . . ., along with the addition of an appropriate state of uniform stress, are adjusted to suit the exterior boundary conditions. Thus, it is noted that using the Bueckner type singularity alone imposed inside a hole is imposing only the leading singularity. It thus appears that retaining all the singular terms, that is

$$Z = \frac{B + B_1 z}{z^{3/2}} \tag{60}$$

would be a better approximation and lead to improvements in numerical analysis. The additional term is $B_1/z^{1/2}$ which is noted to be the usual type of crack tip stress singularity where

$$B_1 = \frac{K}{\sqrt{2\pi}} \tag{61}$$

Therefore, selecting the appropriate value of B_1 for a given B is noted to require the determination of a crack tip stress intensity factor. The appropriate approach may be viewed as a superposition as shown in Fig. 4.

The actual solution desired is shown in Fig. 4*a* where both B and K are imposed through the implied field of Eqs 60 and 61 as displacement boundary conditions inside the hole. However, the appropriate value of K in terms of B (linear dependence) is not yet known. However, Fig. 4*a* can be regarded as the superposition of Fig. 4*b* and *c*. Now 4*b* is the infinite body solution with the Bueckner singularity alone imposed, whose exact solution is expressed by Eq 60 (with $B_1 = 0$). For the actual finite body in 4*b* we find tractions T_b on the boundary. Then in 4*c* we apply these tractions in a reversed sense, that is, $T_c = -T_b$ so that the superposition of 4*b* and *c* give the proper boundary conditions for 4*a*. The resulting K in 4*c* due to tractions T_c is the desired result.

Numerically the procedure is as follows:

1. Determine an initial (approximate) weight function imposing a Bueckner field, B, (only) within the hole in Fig. 4*a*. Note that the result is like the numerical example given in the paper.

2. Use the resulting initial weight function in Step 1 and the tractions T_c as determined from Fig. 4*b*, that is $-T_b$ to determine K.

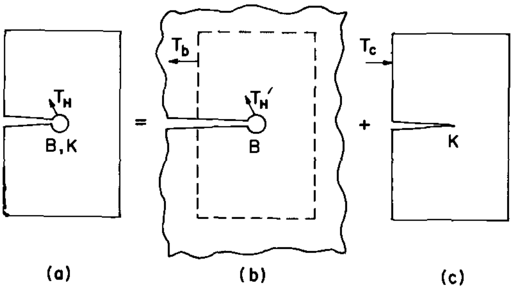

FIG. 4—*Superposition of loadings to determine and improve weight function.*

3. Impose the displacement field implied by K within the hole in Fig. 4*a* to get displacement corrections for the weight function in Step 1.

4. Combine the weight function displacements and corrections in Steps 1 and 3 to get the final weight function.

An additional improvement in computational ease can be gained in this procedure when using appropriate finite element programs for computation. The computation of K in Fig. 4*c*, that is, Step 2, from the initial weight function in Step 1 requires computation of the integral of tractions, $-T_b$, through weight function displacements, u_a, of the form

$$-\int u_a T_b ds \qquad (62)$$

around the exterior boundary. However, by reciprocal theorem between Figs. 4*a* and *b*, it is found that

$$-\int u_a T_b ds = \int (T_{\mathrm{H}} - T_{\mathrm{H}}') u_{\mathrm{H}} ds \qquad (63)$$

where T_{H} are the resulting tractions at the hole due to imposed displacements in the hole in Step 1. The tractions, T_{H}, are normally available from the finite element results. T_{H}' are the tractions at the hole in Fig. 4*b* which are purely from the Bueckner type field which can easily be stored for computation, and u_{H} are the Bueckner field displacements of both Figs. 4*a* and *b* (already stored). Either form may be used, but it appears that for repeated computation on many configurations the form of the right-hand side of Eq 63 has advantages over the left.

Thus, it appears to be possible to make a very simple computation for K and a single repetition of the original weight function computation to obtain an improved weight function. Consequently, this suggestion is made for those interested in exploring the maximum possible computational accuracy obtainable through the methods in this work.

References

[1] Bueckner H. F., *Zeitschrift für Angewandte Mathemetik und Mechanik,* Band 46, 1970, Seite 529–545.
[2] Rice, J. R., *International Journal of Solids and Structures,* Vol. 8, 1972, pp. 751–758.
[3] Tada, H., Paris, P. C., and Irwin, G. R., *The Stress Analysis of Cracks Handbook,* Del Research Corporation, Hellertown, Pa. 1973.
[4] Paris, P. C., "The Mechanics of Fracture Propagation and Solutions to Fracture Arrester Problems," Document D2-2195, The Boeing Company, 1957.
[5] Barenblatt, G. I., in *Advances in Applied Mechanics,* Academic Press, New York, Vol. vii, 1962, p. 55.
[6] Sih, G. C., Paris, P. C., and Erdogan, F., "Crack Tip Stress Intensity Factors for Plane Extension and Plate Bending Problems," *Journal of Applied Mechanics, Transactions,* American Society of Mechanical Engineers, Vol. 29, 1962.
[7] Bueckner, H. F., *Zeitschrift für Angewandte Mathemetik und Mechanik,* Vol. 51, 1971, pp. 97–109.
[8] Bueckner, H. F., "Field Singularities and Related Integral Representations," *Methods of Analysis and Solutions of Crack Problems,* G. C. Sih, Ed. Noordhoff International Publishing, Chapter 3, 1972.

[9] Paris, P. C. and McMeeking, R. M., ''Efficient Finite Element Methods for Stress Intensity Factors Using Weight Functions,'' *International Journal of Fracture Mechanics,* April 1975.

D. E. Macha,[1] *W. N. Sharpe, Jr.,*[2] *and*
A. F. Grandt, Jr.[1]

A Laser Interferometry Method for Experimental Stress Intensity Factor Calibration

REFERENCE: Macha, D. E., Sharpe, W. N., Jr., Grandt, A. F., Jr., "**A Laser Interferometry Method for Experimental Stress Intensity Factor Calibration,**" *Cracks and Fracture, ASTM STP 601,* American Society for Testing and Materials, 1976, pp. 490–505.

ABSTRACT: A laser interferometry crack tip opening displacement measurement technique has been developed and is described here. This interferometric displacement gage was used to measure displacements near the crack tip in flawed specimens. Measured displacements were then converted to stress intensity factor calibration curves by means of the linear elastic fracture mechanics displacement equations. Application of this procedure to compact and edge-cracked aluminum specimens resulted in experimental stress intensity factor calibrations that agreed well with theoretical predictions for these two geometries.

KEY WORDS: crack propagation, fractures (materials), lasers, interferometry

The stress intensity factor, K, is the linear elastic fracture mechanics parameter which characterizes crack behavior in many materials [*1*][3]. As indicated by Eq 1, K relates remote load σ, crack length a, and flaw geometry $F(a)$ into a quantity having the units of stress times the square root of length.

$$K = \sigma \sqrt{\pi a}\, F(a) \qquad (1)$$

The determination of K as a function of crack length for a particular geometry is referred to as a K-calibration. Since the stress intensity factor

---

[1] Materials research engineers, Air Force Materials Laboratory, Wright-Patterson Air Force Base, Ohio 45433.

[2] Professor, Department of Metallurgy, Mechanics, and Materials Science, Michigan State University, East Lansing, Mich. 48824.

[3] The italic numbers in brackets refer to the list of references appended to this paper.

allows the engineer to evaluate cracked structures, recent efforts have been directed toward cataloging existing K-calibrations [*2,3*].

The purpose of this paper is to present a new experimental technique for obtaining K-calibrations based on laser interferometry measurements of in-plane displacements in the vicinity of the crack tip. The technique is demonstrated and evaluated by comparing measurements with well-established theoretical predictions for edge-cracked and compact specimens.

K-calibrations may be determined by analytical or numerical, finite element, or experimental methods [*1*]. The analytical or numerical techniques are often restricted to fairly simple flaw geometries. The finite element methods can handle relatively complicated geometries and, if proper precautions are taken regarding the stress singularity at the crack tip, produce K-calibrations of acceptable accuracy. Experimental K-calibrations can be obtained by compliance techniques [*4*], photoelasticity [*5*], fracture toughness measurements [*6*], crack growth rate methods [*7*], and by measurements of displacements (or strains) in the vicinity of the crack tip. Experimental techniques are valuable for establishing K-calibrations on actual components under service conditions and in situations where complicated geometry or loading configurations make other approaches difficult.

In the crack tip displacement method one measures the displacement at some point near the crack tip as a function of remote load and then computes K from the elastic displacement relations [*8*]. For Mode I loading, the appropriate equations are given by

$$u_x = \frac{K_I}{G}\sqrt{\frac{r}{2\pi}}\cos\frac{\theta}{2}\left[\frac{1-\nu}{1+\nu} + \sin^2\frac{\theta}{2}\right] \tag{2}$$

$$u_y = \frac{K_I}{G}\sqrt{\frac{r}{2\pi}}\sin\frac{\theta}{2}\left[\frac{2}{1+\nu} - \cos^2\frac{\theta}{2}\right] \tag{3}$$

for conditions of plane stress, and by

$$u_x = \frac{K_I}{G}\sqrt{\frac{r}{2\pi}}\cos\frac{\theta}{2}\left[1 - 2\nu + \sin^2\frac{\theta}{2}\right] \tag{4}$$

$$u_y = \frac{K_I}{G}\sqrt{\frac{r}{2\pi}}\sin\frac{\theta}{2}\left[2 - 2\nu + \cos^2\frac{\theta}{2}\right] \tag{5}$$

for plane strain. Here u_x and u_y are the x and y components of displacement at a point near the crack tip located by the polar coordinates (r, θ) as shown in Fig. 1, while G is the shear modulus and ν is Poisson's ratio. Corresponding relations are given for Mode II and Mode III types of loading [*8*].

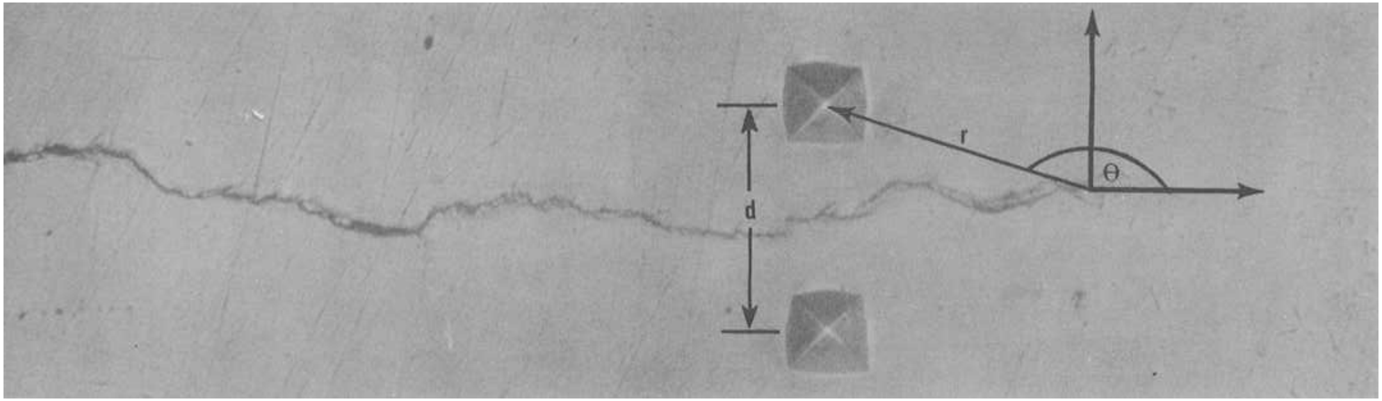

FIG. 1—*Photomicrograph of a fatigue crack defining the crack tip coordinates and showing the surface indentations with* r = *0.061 mm.* θ = *163 deg, and* d = *0.050 mm.*

The crack tip displacement method requires a technique capable of measuring small displacements very near the crack tip. As a rule of thumb, these displacement relations are regarded to be sufficiently accurate within a distance $a/20$ from the crack tip, where a is the crack length [9]. Adams [10] used a photographic technique to measure the relative displacement of identifiable surface markings astride a fatigue crack and only 76 μm apart. His technique, though somewhat laborious, could be used to obtain K. Elber [11] developed an accurate clip gage with gage length of 1.27 mm that could be used for K-calibrations of larger specimens. Dudderar and Gorman [12] made K measurements in thin PMMA sheet specimens using holographic interferometry to measure the displacement perpendicular to the sheet. Their technique is applicable only to thin transparent models. Sommer [13] and Crosley et al [14] measured the crack displacements inside glass models by optical interferometry and used them to calculate K. The advantage of interior displacement measurements near the crack tip is offset by the transparency requirement of the specimen.

Evans and Luxmoore [15] used the laser speckle method to measure inplane displacements on the specimen surface and compare the measured values with those predicted by theory. A brittle plastic specimen was used, but the technique works on metals as well. Displacements as small as 0.02 μm at a distance of 25 μm from the crack tip were obtained. Their results show a great deal of scatter, and the experimental procedures are rather tedious; presumably these disadvantages will be overcome with further development of this new technique. The measurement procedure reported herein is a refinement of the laser interferometric technique reported earlier [16]. Displacements of 0.02 μm at 50 μm from the crack tip are measurable with this technique.

Prior to describing the experimental method, it is useful to rearrange the elasticity equations into a form more convenient for the experimental data. Combining Eqs 1 and 3, one obtains

$$F(a) = \frac{G}{f(\theta)} \sqrt{\frac{2}{ra}} \frac{u_y}{\sigma} \tag{6}$$

Here $f(\theta)$ is the angle dependent term in Eq 3. The plane stress form for u_y was chosen here since all of the displacement measurements were made on the specimen surface.

Plastically deformed material left in the wake of a propagating fatigue crack can cause crack closure [11], a phenomena characterized by an initial nonlinear load-displacement response. Once the opening load [11] is reached, however, behavior is again elastic. Thus, when the slope u_y/σ in Eq 6 is taken from the linear portion of the load displacement record following the opening load, an elastic stress intensity factor calibration is obtained. The interferometric displacement gage employed here has the sensitivity necessary to determine this opening load (see, for example, Ref *17*).

The interferometric displacement gage is briefly described, along with the data acquisition and reduction procedures, in the following sections. Displacement measurements were made at various distances from the crack tip on edge-cracked and compact specimens, and the K values obtained show good agreement with theoretical values.

Experimental Procedures

Interferometric Displacement Gage

The principles of the interferometric displacement gage (IDG) employed here have been described in detail in Ref *18*. Only a basic review of the technique follows here. Shallow reflective indentations are pressed into the polished surface of the specimen on either side of the crack as shown in Fig. 1. When coherent light impinges upon the indentations, it is diffracted back at an angle, α_0, with respect to the incident beam as shown schematically in Fig. 2. Since the indentations are placed close together, the respective diffracted beams overlap resulting in interference fringe patterns on either side of the incident laser beam. A photograph of a typical interference fringe pattern is given in Fig. 3.

In observing the fringe pattern from a fixed position at the angle α_0, fringe movement occurs as the distance, d, between the indentations

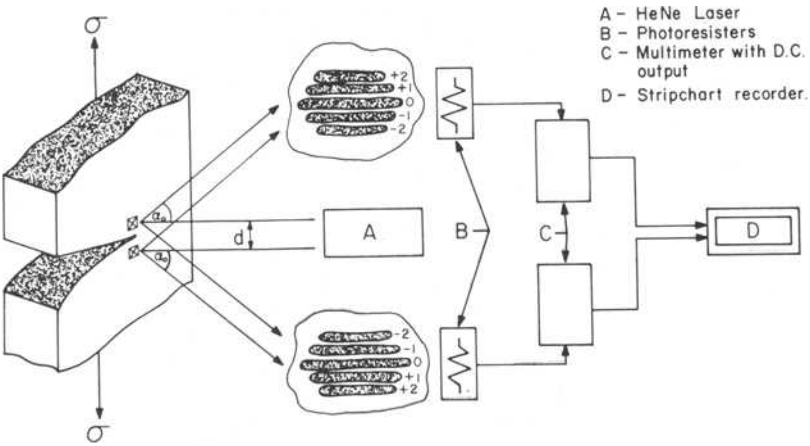

FIG. 2—*Schematic showing fringe pattern generation and recording technique, with nominal values of* d = *0.050 mm and* α_0 = *44 deg.*

changes. Application of a tensile load, causing the distance between the indentations to increase, results in positive fringe motion towards the incident beam. Conversely, the removal of the tensile load results in negative fringe motion away from the incident beam.

The relationship between the indentation spacing and the fringe order shown schematically in Fig. 2 is [*19*]

$$d \sin \alpha_0 = m\lambda \tag{7}$$

Here m is the fringe order, d the spacing between indentations, λ the wave length of the incident beam, and α_0 the angle between the incident and reflected beams, thus defining the zeroth fringe order.

The relationship between the change in indentation spacing, δd, and the change in fringe order at the fixed observation point, δm, is given by Eq 8

$$\delta d = \delta m \ \lambda / \sin\alpha_0 \tag{8}$$

It is this relationship that serves as the basis for the IDG.

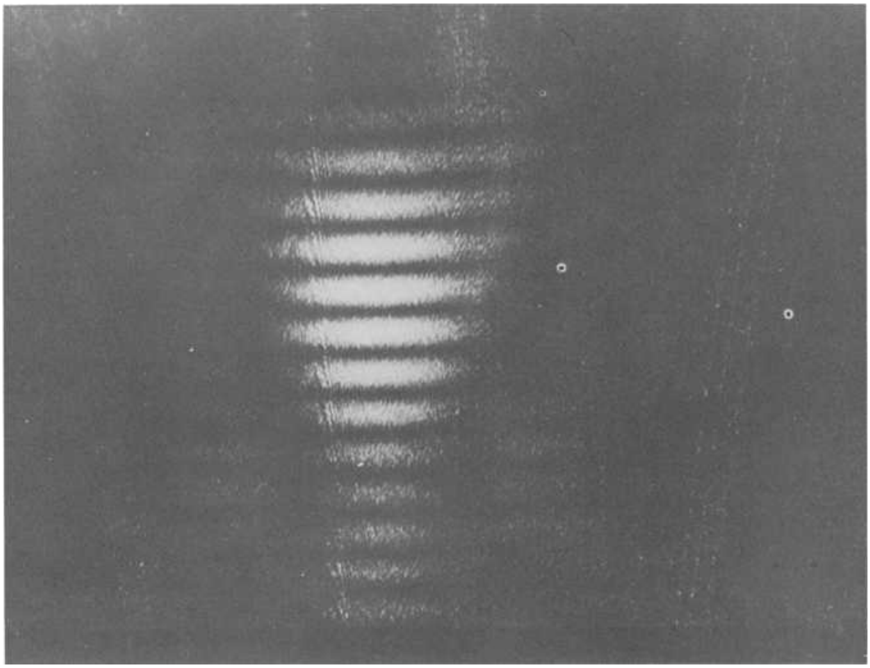

FIG. 3—*Typical interference fringe pattern.*

Specimen Geometry and Preparation

Crack tip opening displacement (CTOD) measurements were conducted on standard compact specimens made of 2024-T851 aluminum (yield stress = 450 MPa) and single-edge-cracked plate specimens made of 7075-T651 aluminum (yield stress = 535 MPa). Drawings of the specimen geometries are shown in Fig. 4. The fracture toughness of the 2.54-cm-thick 2024-T851 specimens was 23 MPa · $m^{1|2}$ and approximately 50 MPa · $m^{1| 2}$ for the 0.31-cm-thick 7075-T651 members.

The preparation of the specimen surface is critical for generating usable fringe patterns since the patterns are degraded by stray reflections surrounding the indentations. A flat surface was attained on the compact specimens by lapping on a metal lapping wheel with 10.5-μm powder suspended in oil. The surface was subsequently polished with a 5-μm diamond paste. Since it was physically impossible to lap the surface of the single edge cracked specimens with the lapping wheel, the specimen surfaces were buffed with a series of commercially available buffing rouges. In all cases, the buffing direction was normal to the crack growth direction.

Fatigue cracks were initiated and grown in all specimens with a Schenke resonant fatigue testing machine. The maximum applied load and load ratios ($R = P_{\text{min}}/P_{\text{max}}$) used for crack growth are listed in Tables 1 and 2.

The reflective indentations were applied to the specimen surface with a Lietz microhardness tester. The indenter is a square based pyramidal diamond with face angles of 136 deg. The application load in all cases was 50 g with an average time of application of 15 s. To apply the indentations, the specimen is mounted at a 45-deg angle on the microhardness tester micrometer stage in order that the indenter edges be normal and parallel to the crack growth direction. The crosshairs in the x-y micrometer stage of the microhardness tester allow placement of the

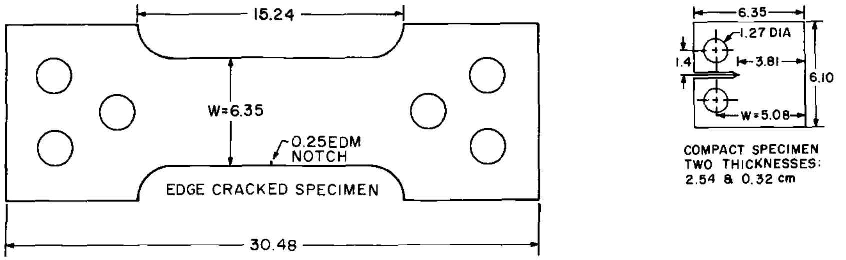

FIG. 4—*Single edge cracked and compact specimen geometries. (All dimensions in centimetres.)*

TABLE 1—*Experimental data for compact specimens (2024-T851 aluminum).*

Specimen	Thickness B, cm	Cyclic Load		Crack Length, a, cm	r, mm	$KBW/P\sqrt{a}$	
		$P_{\max(N)}$	R			Experimental	Theoretical
1	2.540	6230	0.1	2.149	0.056	11.758	11.963
				2.149	0.501	11.975	11.963
				2.149	1.500	12.061	11.963
				2.540	0.056	14.171	13.629
				2.540	0.501	11.600	13.629
				2.540	1.500	13.529	13.629
				2.918	0.056	15.606	16.297
				2.918	0.501	16.832	16.297
				2.918	1.500	16.697	16.297
				3.429	0.056	23.343	23.226
				3.429	0.501	24.388	23.226
				3.429	1.500	25.666	23.226
8–1	0.312	780	0.1	2.019	0.056	10.525	11.553
				2.019	0.501	11.630	11.553
				2.019	1.500	10.659	11.553
				2.393	0.056	13.654	12.886
				2.393	0.501	12.505	12.886
				2.393	1.500	12.859	12.886
				2.939	0.056	14.966	16.430
				2.939	0.401	19.172	16.430
				2.939	1.500	17.902	16.430
				3.432	0.056	23.582	23.143
				3.432	0.401	25.345	23.143
				3.432	1.450	24.271	23.143
8–2	0.300	780	0.1	1.765	0.045	10.981	10.970
				1.765	0.614	10.881	10.970
				1.765	1.187	10.481	10.970
				2.443	0.057	13.199	13.123
				2.443	0.358	13.554	13.123
				2.443	1.453	14.672	13.123

TABLE 2—*Experimental data for edge cracked specimens (7075-T6 aluminum).*

Specimen	Thickness, B, cm	Cyclic Load		Crack Length, a, cm	r, mm	$KBW/P\sqrt{a}$	
		$P_{\max(N)}$	R			Experimental	Theoretical
17	0.559	24 500	0.1	0.518	0.056	2.031	2.063
				0.518	0.501	1.882	2.063
17	0.559	14 500	0.1	1.641	0.079	2.389	2.709
				1.641	0.501	2.419	2.709
				1.641	1.500	2.345	2.709
				2.553	0.069	3.296	3.754
				2.553	0.608	3.247	3.754
				2.553	1.494	3.115	3.754
18	0.626	24 500	0.1	0.475	0.056	2.109	2.050
				0.475	0.501	2.106	2.050
		14 500	0.1	1.524	0.142	2.636	2.679
				1.524	0.640	2.762	2.679
				1.524	1.590	2.679	2.679
				2.540	0.056	3.564	3.734
				2.540	0.700	4.025	3.734
				2.540	1.600	3.765	3.734
				3.500	0.090	5.974	6.006
				3.500	0.625	5.589	6.006
				3.500	1.317	6.221	6.006
19	0.572	24 500	0.1	0.495	0.056	2.451	2.056
				0.495	0.501	2.010	2.056
		14 500	0.1	1.499	0.056	2.518	2.596
				1.499	0.501	2.473	2.596
				1.499	1.200	2.272	2.596
				2.535	0.071	4.231	3.726
				2.535	0.507	3.761	3.726
				2.535	1.307	3.704	3.726

indentations in the desired location. A typical application of the indentations is shown in Fig. 1, where $x = -50$ μm and $d = 50$ μm. After application of the indentations, r and θ were measured with the ocular scale in the microhardness tester, locating the gage points with respect to the crack tip.

Data Acquisition and Reduction

The fringe motion recording technique for monitoring CTOD employed an economical and simple system shown schematically in Fig. 2. It consists of a coherent light source, two photoresistor detectors, two multimeters with d-c voltage output, and a dual-channel stripchart recorder.

The light source utilized for this work was a Spectra Physics Model 134, 3-mW HeNe laser. The laser has a beam wavelength (λ) of 0.6328 μm. The diffracted fringe patterns were received by two CdS bulk effect photoresistors mounted on multiaxis vernier stages to allow accurate and reproducible positioning of the cell relative to the fringe pattern. The active face of each photoresistor was masked, leaving a 0.1-mm slit (which was smaller than the fringe spacing) to distinguish individual fringes. Each photoresistor was connected to a multimeter to allow monitoring of the fringe motion and to provide a d-c voltage output. The d-c output of the voltmeter was used to drive a stripchart recorder.

The stages with the photoresistors were mounted on a frame attached to an Instron testing machine. The laser was mounted on a tripod; relative motion or vibration was no problem as the equipment was mounted on a very solid floor. After mounting the specimen in the loading fixture, it was cycled through the appropriate loading schedule to allow alignment of the fixtures. It was found that for CTOD measurements at a distance of 50 μm from the tip the total fringe motion was small enough to require manual tracking of the fringe pattern. At distances larger than 50 μm, the large amount of fringe motion permits an automatic fringe motion recording technique. In both data acquisition techniques, the specimen was preloaded prior to aligning the photoresistors to a fringe maximum, allowing elimination of most rigid body motion encountered in loading. The remaining rigid body motion was accounted for in the data reduction program.

Displacements at 50 μm from Crack Tip

With the load fixture aligned and a preload applied to the specimen, the interfringe spacing for each pattern was measured by sweeping the photoresistor across the pattern. The detectors were aligned with the slit at a fringe maximum and the vernier stage readings recorded for each photoresistor. The specimen load was then increased a predetermined increment. While loading, the fringe motion was visually monitored and the detectors relocated on their respective maxima. The new vernier stage reading was recorded at the increased load. The incremental load and fringe motion was recorded throughout the load sequence. Since the fringe spacing is known in terms of distance on the vernier stage, the displacement of a fringe maximum from its original position may easily be converted to δm by dividing by the fringe spacing. Measured values of α_0 and the given value of λ then complete the data required to compute displacement δd via Eq 8. The displacement obtained from the two detectors was averaged to eliminate rigid body motion [*18*]. A typical plot of the linear portion of the load versus displacement data is given in Fig. 5.

The calibration factor for a set of measurements is $\lambda/\sin \alpha_0$ divided by the original fringe spacing. The wave length λ is precise, and the relative uncertainty of $\sin \alpha_0$ is about 0.8 percent. However, the initial fringe spacing (in units of distance on the stage) is established by subtracting the location of fringe maxima positions and is thus slightly more than 1 percent. One is faced then with a fixed relative uncertainty of 2 percent in the calibration factor. Fringe motion, δm of Eq 8, is also established by subtraction and its relative uncertainty is quite large at small values of displacement; dropping off to about 10 percent at 0.3 μm and 1 percent at 2 μm.

Displacements Greater Than 50 μm from Crack Tip

When determining CTOD at distances greater than 50 μm from the crack tip, an automatic fringe motion tracking technique was employed. With the specimen fixtures aligned and the specimen preloaded, the photosensitive detectors were positioned on a fringe maximum. The specimen was then automatically loaded to the predetermined maximum load. As the fringes pass the stationary detector the resistance of the element changes, giving a trace on the stripchart recorder of the passing fringe intensity. A typical stripchart recording of fringe motion is shown in Fig. 6. These data were correlated on a time base with the load history from the Instron chart paper, and then reduced to the desired load-displacement data.

A simple computer program was written for inputs λ, α_0, δ_m, and load-time data. Fringe motion values of 0, ½, 1, 1½, etc. were read from the stripchart record with a digitizing table. Three pairs of load-time data were entered from the Instron chart and used to define a polynomial giving the load as a function of time. Thus, by digitizing a specific value of δ_m, the displacement δ_d was calculated and the corresponding time at that displacement used in the load function polynomial to determine the

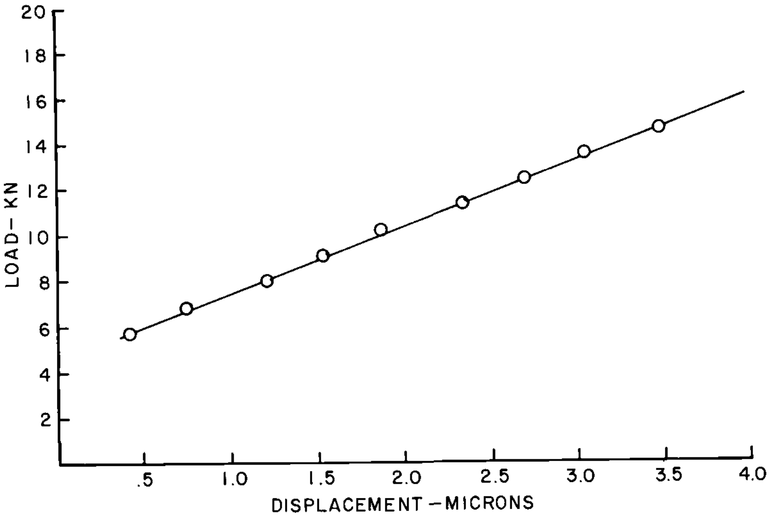

FIG. 5—*Linear portion of a typical load-displacement curve.*

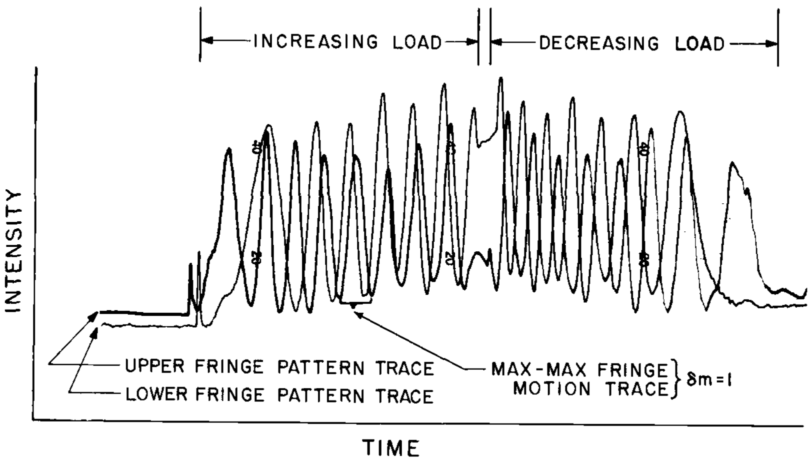

FIG. 6—*Typical stripchart recorder trace of fringe motion.*

load. In this manner, load-displacement data for both the upper and lower fringe patterns were calculated. The program plots both the upper and lower fringe pattern load-displacement curves, then averages the two curves and plots the resulting average, curve, as shown in Fig. 7. The

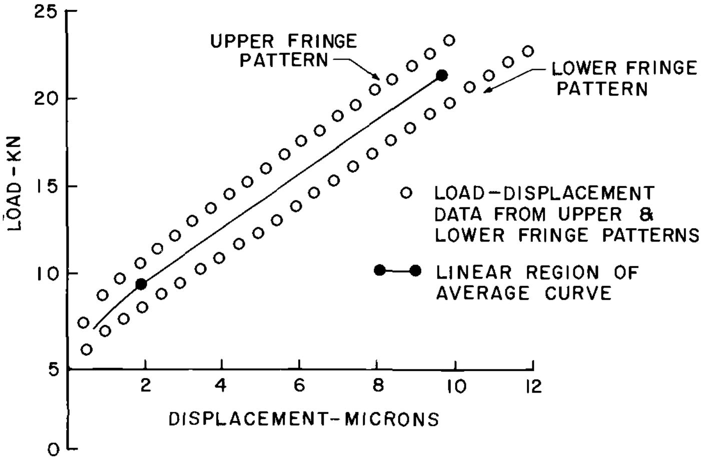

FIG. 7—*Typical load-displacement curve determined from upper and lower fringe patterns.*

relative uncertainty of displacements measured more than 50 μm from the crack tip quickly drops to the approximately 2 percent associated with the calibration factor because such a large number of fringes are measured.

Results and Discussion

The interferometric technique described here was used to obtain experimental K-calibrations for edge-cracked and compact specimens. Since these geometries have been thoroughly studied by other experimental and analytical means, they provide a known baseline to which the interferometry method can be compared. The results of this study are summarized in Tables 1 and 2 and Figs. 8 and 9. As seen in Tables 1 and 2, three compact and three edge-cracked specimens were examined. For almost every crack length considered, displacements were measured at three positions behind the crack tip (nominally 0.05, 0.5, and 1.5 mm). Figures 8 and 9 show that there was no systematic trend associated with the measurement location, r, from the crack tip, although some a/r ratios were as small as 10. In addition, the difference between theoretical and experimental results showed no systematic trend with variations in either a/W or specimen thickness.

Figure 7 shows a complete load displacement curve with the initial nonlinear region associated with fatigue crack closure and the linear portion after the crack faces are completely separated. Care was taken in the data reduction scheme to ensure that the linear portion of the curve

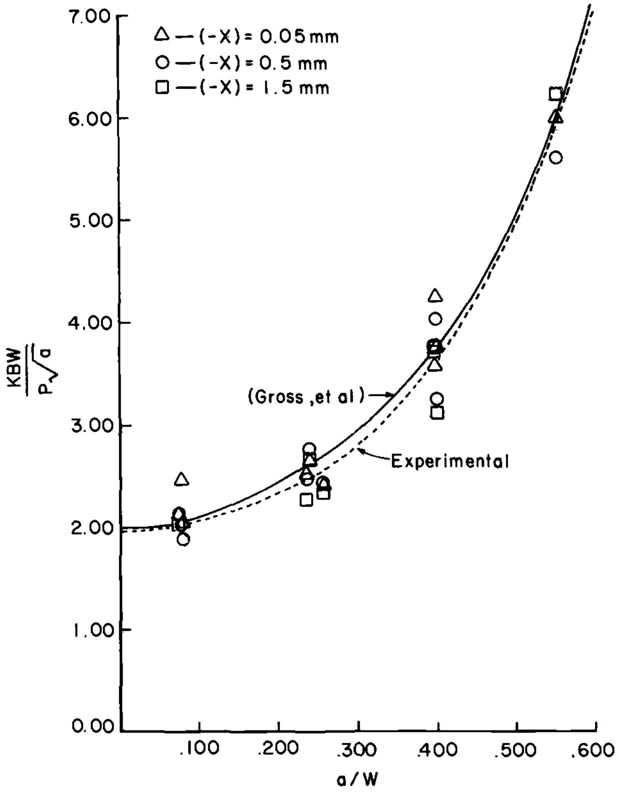

FIG. 8—*Comparison of experimental K-calibration for single-edge cracked specimens with theoretical results.*

was used in Eq 6 to compute the stress intensity factor calibration curve. Thus, by using the linear slope of the load displacement curve, one may measure *K* in actual components while accounting for possible residual stresses induced during the precracking procedure.

As seen in Figs. 8 and 9, individual *K* measurements scatter about previously established results [*20,21*]. For the edge-cracked specimens, the maximum difference between a single measured and theoretical value is 19 percent. The maximum difference in average values for a given crack length is 14 percent. Individual points in the compact specimen varied by as much as 15 percent while the average at each crack length agreed to within 6 percent. These variations among the experimental data indicate that several measurements should be taken in order to establish a reliable K-calibration from CTOD measurements.

The fact that the actual cracks examined here were not perfectly

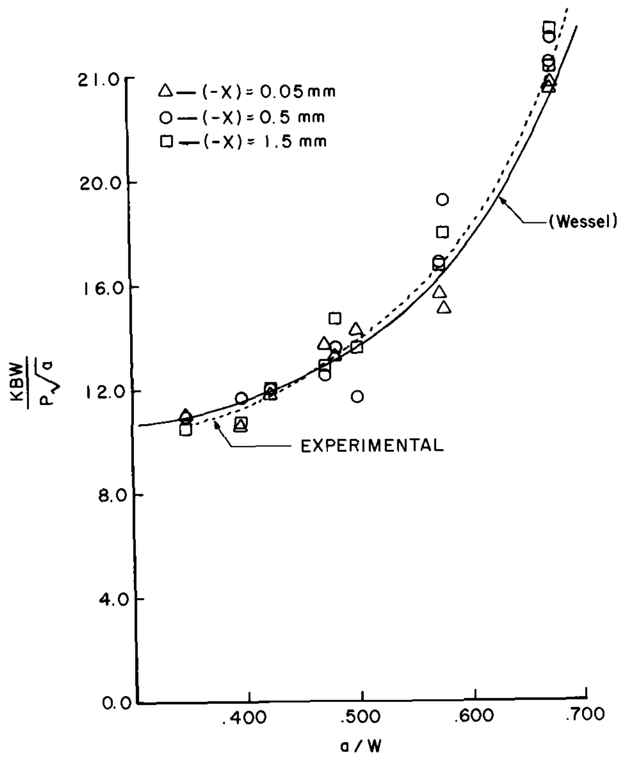

FIG. 9—*Comparison of experimental K-calibration for compact specimens with theoretical results.*

straight on a microscale as assumed in the derivation of Eqs 2 thru 5, presents a likely source of error. As seen in Fig. 1, for example, a meandering crack makes it particularly difficult to precisely define a local coordinate system at the crack tip. Thus, any deviations from a mathematically straight crack introduces possible errors in defining r and θ which are then reflected in $F(a)$ through Eq 6. This discrepancy between ideal and actual cracks is also borne out by the fact that actual flaws were not perfectly planar through the specimen thickness. In addition, it was also not possible to apply loads to the specimen that exactly match the boundary conditions of the theoretical analyses.

Although there may be considerable scatter in individual measurements, the entire collection of data can be utilized to generate a useful K-calibration. As seen in Figs. 8 and 9, for example, fourth degree least squares representations of the data agree within 5 percent of theoretical predictions throughout the range of crack lengths studied for both geometries. Thus, the results of these experiments indicate that a K-calibration curve fitted to crack tip opening displacement data obtained by laser interferometry can be expected to be accurate within ± 5 percent.

References

[*1*] Broek, D., *Elementary Engineering Fracture Mechanics,* Noordhoff International Publishing, The Netherlands, 1974.

[*2*] Tada, H., Paris, P. C., and Irwin, G. R., *The Stress Analysis of Cracks Handbook,* Del Research Corporation, Hellertown, Pa., 1973.

[*3*] Sih, G. C., *Handbook of Stress Intensity Factors,* Lehigh University, Bethlehem, Pa., 1973.

[*4*] Bubsey, R. T., Fisher, D. M., Jones, M. H., and Srawley, J. E., "Compliance Measurements," *Experimental Techniques in Fracture Mechanics,* A. S. Kobayashi, Ed., The Iowa State University Press, Ames, Iowa, 1973.

[*5*] Marloff, R. H., Leven, M. M., Ringler, T. N., and Johnson, R. L., *Experimental Mechanics,* Vol. 11, No. 12, 1971, pp. 529–539.

[*6*] Hall, L. R. and Finger, R. W., *Proceedings,* Air Force Conference on Fatigue and Fracture of Aircraft Structures and Materials, Technical Report AFFDL-TR-70-144, Wright-Patterson AFB, Ohio, Sept. 1970, pp. 235–262.

[*7*] James, L. A. and Anderson, W. E., *Journal of Engineering Fracture Mechanics,* Vol. 1, April 1969, pp. 565–568.

[*8*] Paris, P. C. and Sih, G. C. in *Symposium on Fracture Toughness Testing and Its Application, ASTM STP 381,* American Society for Testing and Materials, 1965 pp. 30–81.

[*9*] Kobayashi, A. S., *Experimental Techniques in Fracture Mechanics,* The Iowa State University Press, Ames, Iowa, 1973.

[*10*] Adams, N. J. I., *Engineering Fracture Mechanics,* Vol. 4, 1971, pp. 543–554.

[*11*] Elber, W. in *Damage Tolerance in Aircraft Structures, ASTM STP 486,* American Society for Testing and Materials, 1971, pp. 230–242.

[*12*] Dudderar, T. D. and Gorman, H. J., *Experimental Mechanics,* Vol. 13, No. 4, 1973, pp. 145–149.

[*13*] Sommer, E., *Engineering Fracture Mechanics*, Vol. 1, 1970, pp. 705–718.

[*14*] Crosely, P. B., Mostovoy, S., and Ripling, E. J., *Engineering Fracture Mechanics,* Vol. 3, 1971, pp. 421–433.

[*15*] Evans, W. T. and Luxmore, A., *Engineering Fracture Mechanics,* Vol. 6, 1974, pp. 735–743.

[*16*] Sharpe, W. N., Jr. and Grandt, A. F., Jr., "A Laser Interferometric Technique for Crack Surface Displacement Measurements," *Proceedings*, 20th International Instrumentation Symposium on the Instrument Society of America, Albuquerque, N. Mex., May 1974.

[*17*] Sharpe, W. N., Jr. and Grandt, A. F., Jr. in *Mechanics of Crack Growth, ASTM STP 590,* American Society for Testing and Materials, pp. 302–320.

[*18*] Sharpe, W. N., Jr., *International Journal of Nondestructive Testing,* Vol. 3, 1971, pp. 56–76.

[*19*] Jenkins, F. A. and White, H. E., *Fundamentals of Optics,* McGraw-Hill, New York, 1957.

[*20*] Gross, B., Srawley, J. E., and Brown, W. F., Jr., "Stress Intensity Factors for a Single-Edge-Notch Tension Specimen by Boundary Collocation of a Stress Function," NASA Technical Note D-2395, National Aeronautics and Space Administration, 1964.

[*21*] Wessel, E. T., "State of the Art of the WOL Specimen for K_{IC} Fracture Toughness Testing," *Engineering Fracture Mechanics,* Vol. 1, No. 1, June 1968.

J. L. Swedlow [1]

Criteria for Growth of the Angled Crack

REFERENCE: Swedlow, J. L., "**Criteria for Growth of the Angled Crack,**" *Cracks and Fracture, ASTM STP 601*, American Society for Testing and Materials, 1976, pp. 506–521.

ABSTRACT: Mixed mode fracture in two dimensions has been of recent interest via study of a crack at an arbitrary angle to the axis of applied load. Three criteria for growth under tensile loads are reviewed and, although they proceed on distinct bases, give similar results. A corollary to a minimum energy hypothesis is inferred. A compression model is suggested and examined in terms of two criteria. Comparisons to data, to the extent they are available, are considered; observations on the nature of the data are followed by suggestions for further research.

KEY WORDS: crack propagation, fractures (materials), criteria, growth, mixed mode

The angled crack problem has been discussed in the literature for well over a decade, and the last several months have been host to a significant rise in the rate of publication. While it is not our purpose only to review this literature, looking at pertinent results tends to clarify both their interrelation and their meaning to the potential user. The basic problem derives from the situation sketched in Fig. 1: a crack is oriented at an angle β to the direction of load, and one seeks both the direction θ along which the crack begins to grow and the magnitude of loading $\bar{\sigma}$ at which growth starts. The center-cracked plate is not the only configuration that may be examined; it has however, become normative for study of the angled crack problem and that pattern is followed here, for planar analysis. Exceptions involving edge cracks have been reported recently [*1*,*2*].[2] It may be noted that the special case $\beta = 90$ deg is allied to the configuration used in conventional fracture testing as described, for example, in ASTM Standard Method of Test for Plane-Strain Fracture

---

[1] Professor, Department of Mechanical Engineering, Carnegie Institute of Technology, Pittsburgh, Pa. 15213.

[2] The italic numbers in brackets refer to the list of references appended to this paper.

Toughness of Metallic Materials (E 399-74). This case is then used as a reference situation against which findings for $\beta < 90$ deg are normalized.

Where $\beta = 90$ deg, it is usually assumed—and observed—that a crack grows in a self-similar manner, that is, the crack's length merely extends. For $\beta < 90$ deg, similarity is lost in that growth begins in a direction other than the original inclination of the crack. In terms of Fig. 1, $\theta \neq 0$. Forecasting θ, the direction of initial crack growth for any value of β, has proceeded on a number of bases. The simplest is that the stress field generated by the pre-existing crack, in terms of one parameter or another, is controlling and the angular behavior of that parameter should be examined at or near the crack tip. Alternatively, the crack is represented by a slender ellipse (or a narrow slot) and the resultant stress field is appropriately scrutinized. Third, the crack is modeled as shown in Fig. 1 plus a short extension in some direction, and behavior of this configuration is then studied.

For tensile loading ($\bar{\sigma} > 0$), each approach gives its own distinctive result, but it is interesting to note that the differences among them are small. Moreover, all such results are qualitatively similar to the experimental information we have found in the literature to the point that there is little operational basis for preferring any one approach over the others. For compressive loading ($\bar{\sigma} < 0$), not all the procedures just outlined have been applied and, of those which have, rather poor correlation to physical behavior is to be observed. We note further that most of the

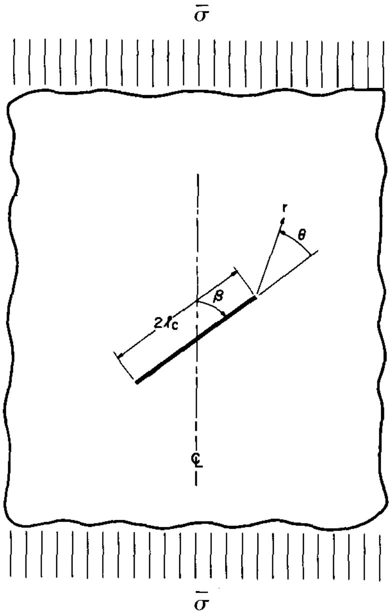

FIG. 1—*Problem geometry and associated coordinates.*

experiments involved fairly brittle materials[3] and the data tend to be scattered.

Analyses involving a line crack plus a short extension at some angle to it have been pursued by several people [*3–8*] but only a few [*5–7*] have applied their results to the present problem, and then only for tensile loads. Some of the work [*4,6*] has been criticized [*7,9*] and it appears at this point that Palaniswamy and Knauss [*7*] give the most comprehensive statement of this model of the angled crack problem. They compare the potential energy of the line crack plus extension to that of the line crack alone, in effect performing a classical Griffith analysis [*10*]. The angle θ for which the rate of change of potential energy with respect to crack length (at vanishing amounts of extension length) is minimal, is then selected as the preferred direction of growth. Experimental results for a swollen polyurethane elastomer are also given [*7*]; the scatter is modest and agreement with analytical predictions is fair but not total. Thus, the conceptual basis is proper and the quality of prediction seems little better than that of much simpler procedures, outlined in the following section.

Analysis involving a slender ellipse admit a more classical statement of stresses, following Kolosoff [*11*] or, more conveniently, Timoshenko and Goodier [*12*]. This approach differs from those using a line crack in three respects: no stress singularity is encountered, extension may emanate from points other than at the very end of the crack, and compressive loading does not lead directly to interference of the crack's flanks. While the first feature is useful in analyzing the stress field, the import of the latter two is not clear as the ellipse is allowed to shrink to a line crack. Certainly this approach was used by Griffith [*10*] but, since he had assumed a self-similar growth pattern whereby the ellipse or its limit, the crack, replicates itself, the issues associated with transforming a smooth surface to a crack point were circumvented. Nonetheless, Cotterell [*13*] and Sih [*14*] have used this shape in certain of their analyses, but their results are viewed potentially as problematic in terms of poor correlation to experiment.

Analyses of the line crack itself admit the simplest representation of near-tip stresses and thereby have proven popular. For tensile loading, two parameters of this stress field have been examined to predict θ and $\overline{\sigma}$. Erdogan and Sih [*15*] were evidently the first to look at hoop stress (σ_θ in Fig. 1) at the crack tip and find θ such that this quantity achieved a maximum; their predictions were strongly supported by limited data on polymethylmethacrylate (PMMA). Subsequently, Ewing and Williams pursued this idea but evaluated the hoop stress at a small distance from the crack tip [*1,2,16,17*]; a considerable amount of data (also on PMMA) were generated in support of the analysis, albeit with some scatter. Some discussion of this work should be noted [*18,19*]. Sih and his coworkers

---

[3] Thus justifying the elastic analyses typically employed for this problem.

then argued in favor of a direction for which the strain energy density is minimal—on the basis that this corresponds to a maximum in potential energy—and have reported analytical results for a variety of cases, together with a limited selection of data already in the literature [*14,20,23*]. It is not clear whether the strain energy density is to be evaluated at the edge of an elliptical perforation [*14*], at the tip of a crack [*20*], or a small distance from it [*22*]. The result is nonetheless sensitive to Poisson's ratio, as addressed briefly by Finnie and Weiss [*24*].

These two approaches involve different levels of complexity in actual use but give qualitatively similar results for tensile loading, in two dimensions. Maximum hoop stress seems a bit primitive when compared to the lessons of linear elastic fracture mechanics, but it may be less so if the distance at which the hoop stress is examined is viewed as a disposable parameter that tends to characterize the material under test. Minimum strain energy density is problematic owing in part to its correspondence to a maximum potential energy: one normally regards this quantity as the integral of field variables over some domain rather than itself a point or field quantity as implied by Sih. In addition, strain energy density is insensitive to the sign of loading ($\bar{\sigma} \gtrless 0$) yet Sih repeatedly gives distinct predictions for tensile ($\bar{\sigma} > 0$) and compressive ($\bar{\sigma} < 0$) excitation, but fails to cite a sorting condition [*14,20–23*].

Indeed, the case of compression has some intrinsic interest [*25*]. For a line crack, the crack's faces inescapably tend to close on themselves—leading to a potential incompatibility—yet Sih and Cha [*23*] state that ". . . this will not affect the results quantitatively." Cotterell [*13*] avoids the difficulty by working with a slender ellipse and a narrow slot, and his predictions do not conform especially well to his experimental results. McClintock and Walsh [*26*] modified the Griffith theory to account for the effects of crack closure in compression, including friction along the crack faces, but these effects were shown by Hoek and Bieniawski [*25*] to differ from those assumed, at least in certain glasses and rocks. More to the point of interest here is the distinctive behavior Sih predicts for compression in the absence of a basis whereby strain energy density in compression is distinguished from that in tension, the analysis being otherwise unchanged. Unlike Sih's forecast for tensile loading, his results for compression show no real similarity to other predictions or to Cotterell's data [*13*].

We thus come to two main issues. The first is the procedure to be used with the minimum strain energy density criterion whereby distinct predictions for tensile and compressive loadings are obtained. Second, we seek means for modeling the compression case such that any incompatibility is obviated and a qualitatively more realistic prediction is made. Both points are addressed in the sequel and, in passing, we observe some reason for the tendency of experimental data to be scattered.

Tensile Loading

We turn first to the situation in Fig. 1 for $\bar{\sigma} > 0$. Although a full solution to the stress problem is available [*12*], its form is cumbersome for our purpose. A preferred representation derives from Williams's analysis [*27*] whereby stresses local to the crack tip are given by

$$
\begin{aligned}
\sigma_r &= \left[K_{\mathrm{I}}/\sqrt{(2\pi r)}\right]\left[\frac{5}{4}\cos\frac{\theta}{2} - \frac{1}{4}\cos 3\frac{\theta}{2}\right] + \\
&\left[K_{\mathrm{II}}/\sqrt{(2\pi r)}\right]\left[-\frac{5}{4}\sin\frac{\theta}{2} + \frac{3}{4}\sin 3\frac{\theta}{2}\right] + \sigma_t\cos^2\theta \\
\sigma_\theta &= \left[K_{\mathrm{I}}/\sqrt{(2\pi r)}\right]\left[\frac{3}{4}\cos\frac{\theta}{2} + \frac{1}{4}\cos 3\frac{\theta}{2}\right] + \\
&\left[K_{\mathrm{II}}/\sqrt{(2\pi r)}\right]\left[-\frac{3}{4}\sin\frac{\theta}{2} - \frac{3}{4}\sin 3\frac{\theta}{2}\right] + \sigma_t\sin^2\theta \\
\tau_{r\theta} &= \left[K_{\mathrm{I}}/\sqrt{(2\pi r)}\right]\left[\frac{1}{4}\sin\frac{\theta}{2} + \frac{1}{4}\sin 3\frac{\theta}{2}\right] + \\
&\left[K_{\mathrm{II}}/\sqrt{(2\pi r)}\right]\left[\frac{1}{4}\cos\frac{\theta}{2} + \frac{3}{4}\cos 3\frac{\theta}{2}\right] - \sigma_t\sin\theta\cos\theta
\end{aligned}
\qquad (1)
$$

in which

$$
\begin{aligned}
K_{\mathrm{I}} &= \bar{\sigma}\ \sqrt{(\pi\ell_c)}\sin^2\beta \\
K_{\mathrm{II}} &= \bar{\sigma}\sqrt{(\pi\ell_c)}\sin\beta\cos\beta \\
\sigma_t &= \bar{\sigma}\ (\cos^2\beta - \sin^2\beta)
\end{aligned}
\qquad (2)
$$

where ℓ_c is the crack's half-length and $\bar{\sigma} = +1$. For reference, the energy density is

$$W = (1/2G)\ \{[(\kappa + 1)/8]\ (\sigma_r + \sigma_\theta)^2 - \sigma_r\sigma_\theta + \tau_{r\theta}{}^2\} \qquad (3)$$

having used G for the shear modulus, $\kappa = (3 - \nu)/(1 + \nu)$ in plane stress, and ν is Poisson's ratio. This localized analysis limits the range of r over which Eq 1 may be used (see Fig. 1 for definition of the various coordinates). In all the numerical work reported in the following discussion, $\nu = 0.3$ and $E = 2\ (1 + \nu)\ G = 10^7$.

With this simple representation, we have examined σ_θ and W for extrema over the range -180 deg $\leq \theta \leq 180$ deg, with[4] $r = 0.0002$, 0.002, and 0.02, and $\beta = 5, 10, \ldots 90$ deg. While selected results are given in the following figures, it is instructive first to look at the variation of these quantities with θ itself. Using $r = 0.002$ and $\beta = 70$ deg,

---

[4] Since $\ell_c = 1$, these values are effectively for r/ℓ_c.

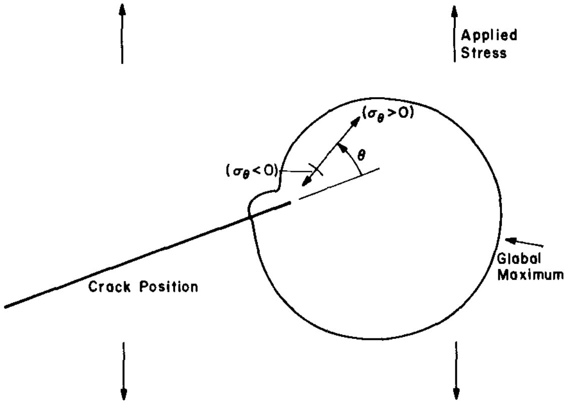

FIG. 2*a*—*Histogram of hoop stress for tensile loading, β = 70 deg,* r *= 0.002.*

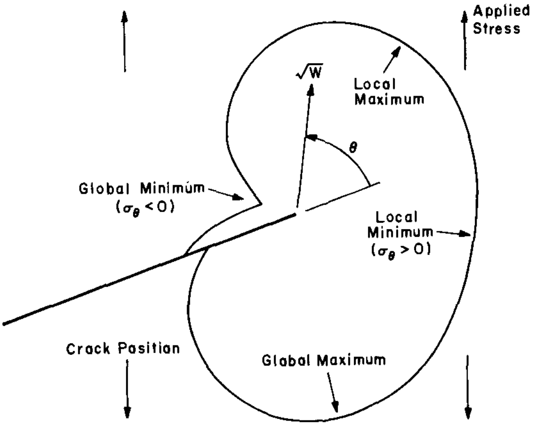

FIG. 2*b*—*Histogram of strain energy density for tensile loading, β = 70 deg,* r = *0.002.*

histograms of σ_θ and $\sqrt{W}$ are sketched in Fig. 2*a* and *b*. It is seen that σ_θ is null at $\theta \doteq \pm 180$ and about 76 deg, it has minima at about -179 and 113 deg, and there is a maximum at about -30 deg. No null values of $\sqrt{W}$ appear, and there are four extrema as delineated on Fig. 2*b*.

Certain observations are in order at this point. Were we to seek a maximum hoop stress, the result would be unequivocal as there is only one such extremum. Two minima in W (or, equivalently, $\sqrt{W}$) occur, one local and the other global, and we have no *a priori* basis for selecting one over the other. If we take Sih's first hypothesis [*20*] literally, we would choose the maximum at θ about 143 deg as this should correspond to a global maximum of potential energy. It is to be noted, however, that Sih selects the local minimum at $\theta \sim -27$ deg where the associated hoop stress is tensile. On the other hand, the global minimum occurs where the hoop stress is compressive. Taking this point a step further, if we merely change the sign of $\bar{\sigma}$ in the foregoing development, the sign of σ_θ is reversed in the histogram of Fig. 2*a*, but that in Fig. 2*b* is not. It follows that the global minimum in W is associated with a tensile hoop stress if $\bar{\sigma} < 0$ in Eqs 1 and 2; not too coincidentally, it is this minima that Sih uses for compressive loading. Thus, it would seem that Sih's first hypothesis[5] should have a corollary statement to the effect that this minimum need not be global but that it must be associated with a tensile hoop stress. Results of the type depicted in Fig. 2*a* and *b* have been examined over the full range of parameters used in this study, and the applicability of the corollary is confirmed. Evidently, Sih et al have employed this condition to sort tensile from compressive results but, to our knowledge, have not articulated it [*14,20–23*].

We also note that the scatter characteristic of experimental data in the literature tends to be explicable in terms of the histograms of Figs. 2*a* and *b*. The extrema we have examined to this point tend to be rather shallow so that small variations in local material strength as may arise from variations in thickness or the substructure of the material itself can influence measured results. It should be no surprise, therefore, to find scatter in data even where close control is maintained over a series of test specimens.

With this background, we may look at predicted directions of initial crack growth and loads to failure. Using the maximum hoop stress criterion, θ as a function of β is shown in Fig. 3 for r = 0.0002, r =

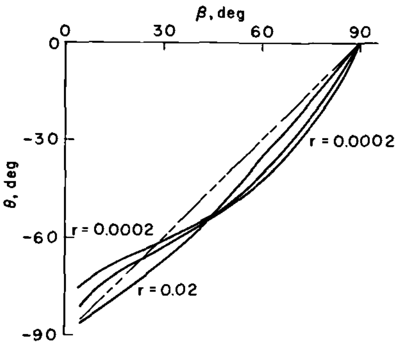

FIG. 3—*Angle of initial crack growth versus crack inclination using hoop stress criterion, tensile loading.*

---

[5] Stated in Ref *20* as: "The crack will spread in the direction of maximum potential energy density" or, equivalently, "crack initiation will start in a radial direction along which the strain energy density is a minimum."

0.002, and $r = 0.02$, together with a line that represents growth precisely normal to the applied load ($\beta - \theta = 90$ deg). The distance r is seen to have a modest influence on the shape of the curve and, in practice, would probably be used to characterize the particular material under test. Analogous plots, derived from the minimum strain energy density criterion and modified by the corollary just indicated, are shown in Fig. 4; these results correspond to Sih's predictions in, for example, Ref *20*. For reference, we show θ as a function of β derived from purely a global minimum of strain energy density in Fig. 5 and, not surprisingly, it may be observed that these curves correspond to Sih's predictions for compressive loading. We disregard these curves in the sequel since they violate the proposed corollary for tensile loading and, as discussed later, involve an incompatibility under compressive loading. Relative load to failure is plotted in Fig. 6 for the $r = 0.002$ curves of Fig. 3 and 4. The hoop stress criterion gives a lower failure load, one fairly insensitive to crack inclination in the range 60 deg $< \beta <$ 90 deg, while the modified strain energy density criterion increases monotonically with β decreasing from 90 deg. The curves are not dramatically different; further, they are similar to that found by Palaniswamy and Knauss [*7*], and all correspond to the pattern of behavior suggested by physical measurements [*2,7,16,17*]. Finally, we observe that, subject to a certain assumption of continuity, Nuismer suggests that the theory of Ref *7* gives results identical to maximum stress theory for $r = 0$ [*28*]. Bilby and Cardew, however, disagree with Nuismer's argument as a result of independent analyses [*29*].

Compressive Loading

As just indicated, it is inappropriate to replace $\bar{\sigma}$ by $-\bar{\sigma}$ in Eqs 1 and 2 as a model of compressive loading. We disallow a negative value of K_I

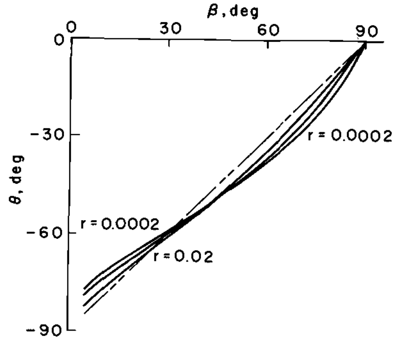

FIG. 4—*Angle of initial crack growth versus crack inclination using modified strain energy criterion, tensile loading.*

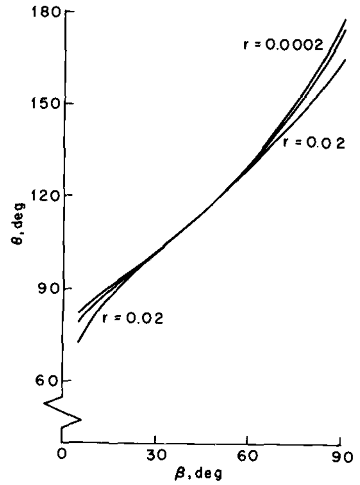

FIG. 5—*Angle of initial crack growth versus crack inclination using minimum strain energy criterion, tensile loading.*

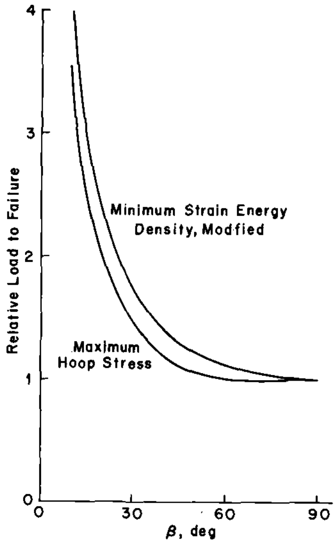

FIG. 6—*Relative load to failure versus crack inclination for tensile loading,* r = *0.002.*

which leads to the opposite of crack opening, that is, to the crack closing on itself with material adjacent to the crack's flanks merging. An alternate and preferred model of response therefore suppresses K_I and, in addition, allows for transfer of the compression across the crack. Moreover, friction along the crack faces is permissible, and we use here a simple Coulomb representation. We thus write in place of Eqs 1 and 2 the expressions

$$\begin{aligned}
\sigma_r &= \left[K_{\mathrm{II}}/\sqrt{(2\pi r)}\right]\left[-\frac{5}{4}\sin\frac{\theta}{2}+\frac{3}{4}\sin 3\frac{\theta}{2}\right] \\
&\quad + \bar{\sigma}\,(\sin^2\theta-\mu\sin 2\theta)\sin^2\beta+\sigma_t\cos^2\theta \\
\sigma_\theta &= \left[K_{\mathrm{II}}/\sqrt{(2\pi r)}\right]\left[-\frac{3}{4}\sin\frac{\theta}{2}-\frac{3}{4}\sin 3\frac{\theta}{2}\right] \\
&\quad + \bar{\sigma}\,(\cos^2\theta+\mu\sin 2\theta)\sin^2\beta+\sigma_t\sin^2\theta \\
\tau_{r\theta} &= \left[K_{\mathrm{II}}/\sqrt{(2\pi r)}\right]\left[\frac{1}{4}\cos\frac{\theta}{2}+\frac{3}{4}\cos 3\frac{\theta}{2}\right] \\
&\quad + \bar{\sigma}\,(\sin\theta\cos\theta-\mu\cos 2\theta)\sin^2\beta-\sigma_t\sin\theta\cos\theta
\end{aligned} \tag{4}$$

where $\bar{\sigma} = -1 < 0$, μ is the coefficient of friction, and

$$\begin{aligned}
K_{\mathrm{II}} &= \bar{\sigma}\sqrt{(\pi\ell_c)}\,(\sin\beta\cos\beta-\mu\sin^2\beta) \\
\sigma_t &= \bar{\sigma}\,(\cos^2\beta-\sin^2\beta)
\end{aligned} \tag{5}$$

Note that Eqs 4 and 5 imply along the crack faces, either that sliding motion is impending (in which case μ is a static coefficient) or that motion is occurring (and μ is a kinetic value). Preassigning a numerical value of μ precludes consideration of frictional force less than the limiting value at which motion is impending, however. In the terminology of Eq 5, we may consider only those cases for which $\cot\beta \geq \mu$.

Following the pattern used for tensile loading, we examine first histograms of σ_θ and $\sqrt{W}$ (using Eq 3), and sketches appear in Fig. 7. It is seen that hoop stress has two maxima, the larger near 93 deg being selected as the likely direction of initial crack growth. The energy density has three minima but, using the proposed corollary to Sih's first hypothesis, only one is acceptable, that at about 95 deg. We observe also the shallowness of these two extrema and the previous remark anticipating data scatter carries over to this situation.

Scrutiny of the numerical results over a range of the parameters r, β, and μ allows generalization of the foregoing, and the results appear in the next five figures. Directions of initial crack growth for the same three values of r but frictionless crack surfaces are shown in Fig. 8, and for three moderate levels of friction in Fig. 9, all based on the maximum hoop stress criterion. Using the minimum strain energy density criterion,

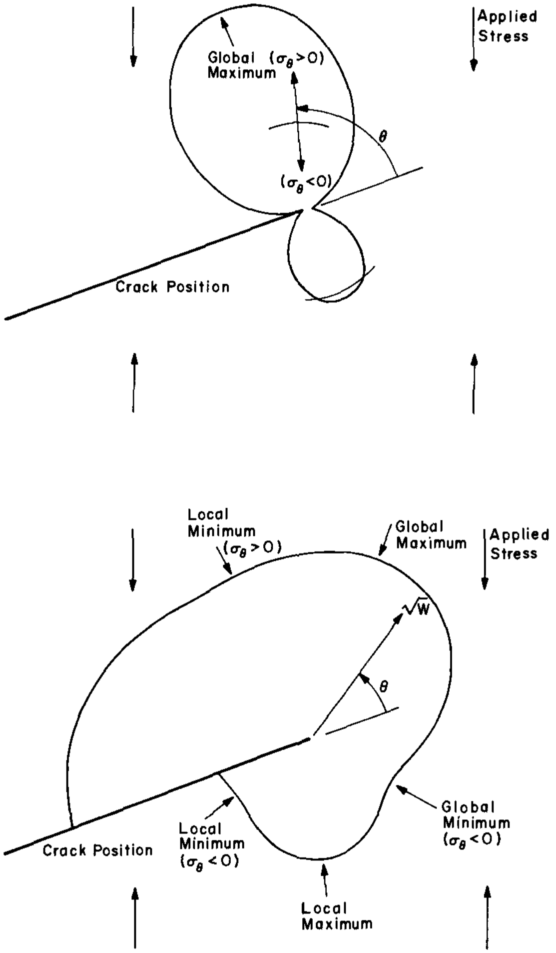

FIG. 7—(a) *Histogram of hoop stress for compressive loading,* β = *70 deg,* r = *0.002,* μ = *0.3.* (b) *Histogram of strain energy density for compressive loading,* β = *70 deg,* r = *0.002,* μ = *0.3*

we obtain the curves sketched in Figs. 10 and 11. In both, the solid (and dotted) curves correspond to values of θ derived from use of a global minimum and a sharp discontinuity is evident. Except for $r = 0.02$, which may be too large for the simplified analysis represented by Eqs 4 and 5, the upper solid curves together with the dashed curves result from use of the modified strain energy criterion, that is, from imposing the corollary.

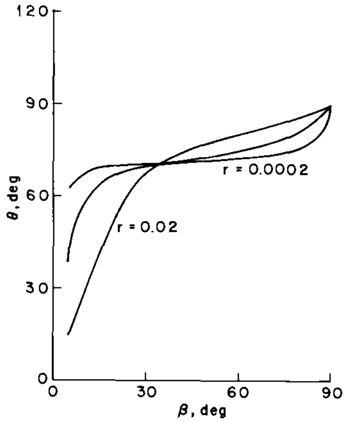

FIG. 8—*Angle of initial crack growth versus crack inclination using hoop stress criterion, compressive loading, frictionless surfaces.*

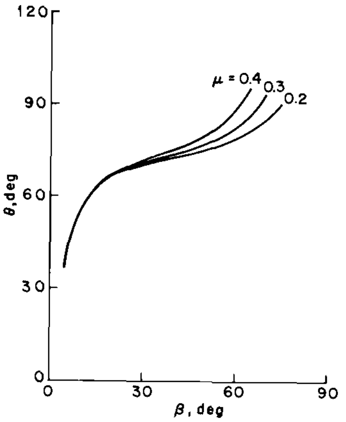

FIG. 9—*Angle of initial crack growth versus crack inclination using hoop stress criterion, compressive loading,* r = *0.002, with friction.*

Finally, in Fig. 12 we have the predicted load to failure for $r = 0.002$ and $\mu = 0.3$. The results for the two criteria are indistinguishable to the scale sketched, and the curve is virtually a perfect parabola whose axis is at $\theta = 40$ deg.

Clearly, the differences between the predictions of the two criteria are modest at most. It is striking to note, however, that both indicate a range

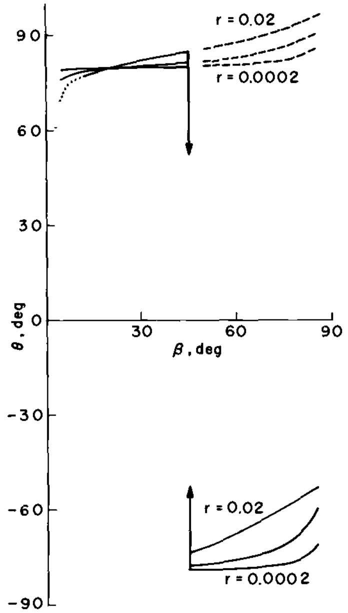

FIG. 10—*Angle of initial crack growth versus crack inclination using minimum strain energy criterion, compressive loading, frictionless surfaces.*

of θ that is compatible with Cotterell's data [6] [*13*]. Figures 9 and 11 suggest that suitable choices of r and μ will bring the predictions in line with these experimental results provided that analysis for cot $\beta<\mu$ is carried through. While we have not performed a study of the type developed by Palaniswamy and Knauss [7] pertinent to compressive loading, the implication from the tensile results is that it could provide results similar to those given here. It is therefore anticipated that the nature of the model used for the case of compression is more central to rationalization to Cotterell's data than the particular criterion selected to complete the study.

Concluding Remarks

It would thus appear that the criterion of minimum strain energy density requires in addition to its two hypotheses a corollary statement to the effect that the energy minimum must be accompanied by a tensile hoop stress. There is every indication that such a requirement has been used in

---

[6] See also the sketches in the second of Ref *24*.

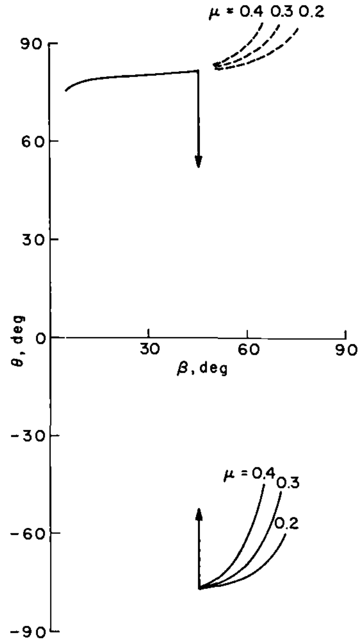

FIG. 11—*Angle of initial crack growth versus crack inclination using minimum strain energy criterion, compression loading,* r = *0.002, with friction. Solid curves correspond global minima, dashed curves to minima with tensile hoop stress.*

conjunction with this work but not stated. Second, we observe that an alternate, if simplified, model of the compression case leads to qualitatively realistic predictions, at least insofar as we have been able to find data in the literature. Third, the angular distribution of various quantities we have examined appears, at least within the context of the simple analyses given here, to indicate that physical data will tend to be scattered. In the absence of load configurations which reduce, in a manner of phrasing, the shallowness of extrema as they appear on a histogram, this result is unavoidable. To the extent that this occurs, there can be little basis of an operational sort to opt for any one of the various criteria over the others. Finally, it is worth repeating that the foregoing pertains to the two-dimensional case and no firm basis for generalization to three-dimensional circumstances presents itself.

Further work in this problem area might well be directed toward designing experiments which tend to narrow the scatter band of the data. This may involve multiaxial loading or loading plus appropriate kinematic excitation. Applications to a broader range of materials are then in order inasmuch as the design situations where such capability would be

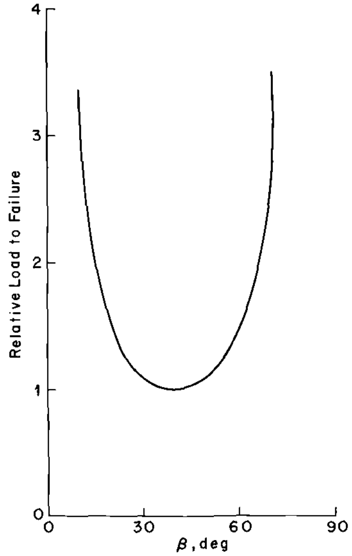

FIG. 12—*Relative load to failure versus crack inclination for compressive loading, using hoop stress and strain energy criterion,* r *= 0.002,* μ *= 0.3.*

useful involve, typically, ductile metallic alloys, structures with residual stresses, and material anisotropy as found, for example, in heavily cold worked alloys or advanced fiber composites. For an illuminating example, see Ref *30*. What we have now is a selection of procedures which give qualitatively satisfactory planar results in a few materials, but it is difficult to say which one is superior insofar as physical fidelity is concerned.[7] Answering this point in terms of accurate but economical analysis and in terms of a broad data base is very much in order.

Acknowledgements

This work has benefitted from conversations with Professors G. C. Sih and J. G. Williams, and their influence is gratefully acknowledged. Computer time was provided by Carnegie-Mellon University.

References

[*1*] Ewing, P. D. and Williams, J. G., *International Journal of Fracture,* Vol. 10, 1974, p. 135.

[2] Ewing, P. D., Swedlow, J. L., and Williams, J. G. "Further Results on the Angled Crack Problem," *International Journal of Fracture,* Vol. 12, 1976, pp. 85–93.

---

[7] This point is noted in the second of Ref *19*.

[3] Sanday, S. C., Ph.D. thesis, Department of Civil Engineering, Carnegie-Mellon University, 1967.

[4] Andersson, H., *Journal of the Mechanics and Physics of Solids,* Vol. 17, 1969, pp. 405–417; see also, Vol. 18, 1970, p. 437.

[5] Palaniswamy, K., Ph.D. thesis, Graduate Aeronautical Laboratories, California Institute of Technology, 1972.

[6] Hussain, M. A., Pu, S. L., and Underwood, J. H. in *Fracture Analysis, STP 560,* American Society for Testing and Materials, 1974, pp. 2–28.

[7] Palaniswamy, K. and Knauss, W. G., "On the Problem of Crack Extension in Brittle Solids under General Loading," Report SM 74-8, Graduate Aeronautical Laboratories, California Institute of Technology, 1974.

[8] Montulli, L. T., private communication, Feb. 1975.

[9] Palaniswamy, K. and Knauss, W. G., *International Journal of Fracture Mechanics,* Vol. 8, 1972, pp. 114–117.

[10] Griffith, A. A., *Philosophical Transactions of the Royal Society,* Vol. A221, 1920, pp. 163–198.

[11] Kolosoff, G., Ph.D. thesis, Dorpat, 1909.

[12] Timoshenko, S. P. and Goodier, J. N., *Theory of Elasticity,* 3rd ed., McGraw-Hill Book Co., New York, 1970 pp. 191–194.

[13] Cotterell, B., *International Journal of Fracture Mechanics,* Vol. 8, 1972, pp. 195–208.

[14] Sih, G. C. in *Prospects of Fracture Mechanics,* Noordhoff International Publishing, Leyden, 1975, pp. 85–102.

[15] Erdogan, F. and Sih, G. C., *Journal of Basic Engineering,* Vol. 85D, 1963, pp. 519–525.

[16] Williams, J. G. and Ewing, P. D., *International Journal of Fracture Mechanics,* Vol. 8, 1972, pp. 441–446.

[17] Ewing, P. D. and Williams, J. G., *International Journal of Fracture,* Vol. 10, 1974, pp. 537–544.

[18] Finnie, I. and Saith, A., *International Journal of Fracture,* Vol. 10, 1973, pp. 484–486.

[19] Sih, G. C. and Kipp, M. E., *International Journal of Fracture,* Vol. 10, 1974, pp. 261–265; See also, authors' closure, Vol. 10, 1974, p. 265.

[20] Sih, G. C. in *Methods of Analysis and Solutions of Crack Problems,* Noordhoff International Publishing, Leyden, 1973, pp. xxi–xlv.

[21] Sih, G. C., *Handbook of Stress-Intensity Factors,* Lehigh University, Bethlehem, 1973, pp. vi–xl.

[22] Sih, G. C., *International Journal of Fracture,* Vol. 10, 1974, pp. 305–321.

[23] Sih, G. C. and Cha, B. C. K., *Engineering Fracture Mechanics,* Vol. 6, 1974, pp. 699–723.

[24] Finnie, I. and Weiss, H. D., *International Journal of Fracture,* Vol. 10, 1974, pp. 136–138; see also, author's closure, Vol. 10, 1974, pp. 279–283.

[25] Hoek, E. and Bieniawski, Z. T., *International Journal of Fracture Mechanics,* Vol. 1, 1965, pp. 137–155.

[26] McClintock, F. A. and Walsh, J. B., *Fourth U.S. Congress of Applied Mechanics,* American Society of Mechanical Engineers, New York, 1963, pp. 1015–1021.

[27] Williams, M. L., *Journal of Applied Mechanics,* Vol. 24, 1957, pp. 109–114.

[28] Nuismer, R. J., *International Journal of Fracture,* Vol. 11, 1975, pp. 245–250.

[29] Bilby, B. A. and Cardew, G. E., *International Journal of Fracture,* Vol. 11, 1975, pp. 708–712.

[30] Williams, J. G. and Birch, M. W., in this volume.

Wan-liang Hu [1] *and H. W. Liu* [1]

Crack Tip Strain—A Comparison of Finite Element Method Calculations and Moiré Measurements

REFERENCE: Hu, Wan-liang and Liu, H. W., "**Crack Tip Strain—A Comparison of Finite Element Method Calculations and Moiré Measurements,**" *Cracks and Fracture, ASTM STP 601,* American Society for Testing and Materials, 1976, pp. 522–534.

ABSTRACT: The moiré crack tip strain measurements made on double-edge-notched specimens loaded into the region of general yielding are compared with the finite element method (FEM) calculations. If the ratio of specimen thickness and the total net cross-sectional width, $(W\text{-}2a)/t$, is equal to or more than ten, the bulk of the strain measurements agree well with the results of the plane stress calculations except in the small area close to the crack tip. The crack tip region is stiffened by the triaxial state of stress, and the deformation within the stiffened zone is less than that calculated for the plane stress model. The region affected by the crack tip stiffening extends to a distance from the crack tip equal to specimen thickness. This crack tip stiffened zone is imbedded in the characteristic plane stress zone if $(W\text{-}2a)/t$ is larger or equal to ten.

KEY WORDS: crack propagation, comparison, measure and integration, strain distribution, cracks, aluminum alloys, elastoplastics, numerical analysis

The finite element method (FEM) has been used to calculate crack tip stresses and strains in elasto-plastic plates [*1–3*].[2] Most of the calculations are either in the plane strain or plane stress condition. All of these calculations indicate the existence of stress and strain singularities at a crack tip. Swedlow and Underwood [*4*] have compared the calculated crack tip strains with the measured strains. The general qualitative trends of the calculations and measurements agree well with each other.

Rice and Rosengren [*5*] and Hutchinson [*6*], using the deformation plasticity theory, have made analytical calculations. They found that the characteristic stress and strain singularities at a crack tip are related to the

---

[1] Research assistant and professor, respectively, Department of Chemical Engineering and Materials Science, Syracuse University, Syracuse, N. Y. 13210.

[2] The italic numbers in brackets refer to the list of references appended to this paper.

strain hardening exponent of a material if the material obeys the power law strain hardening.

Underwood and Kendall [*7*], Kobayashi [*8*], and Ke and Liu [*9*] have made extensive crack tip strain and crack opening displacement measurements with the moiré method. These measurements clearly indicate the three dimensional characteristics of crack tip deformation [*9*]. In the region far away from the crack tip, the deformation seems to be in the plane stress condition. Close to the crack tip, the stiffening effect is evident.

Sih [*10*] and Kobayashi [*11*] have made analytical calculations of the three dimensional crack tip stresses and strains in an elastic solid. To date, a very limited number of three dimensional elasto-plastic calculations have been made [*12,13*]. In this study, plane stress finite element calculations are made and modeled by kinematically coupled plane stress and plane strain layers for the elements near the crack tip. The results of the calculations are compared with the strain measurements made by Ke and Liu [*14*] using moiré techniques. The agreement of the calculations and the measurements is good.

Qualitative Discussion on the Three Dimensional Characteristics of Crack Tip Deformation

Most of the analytical and numerical calculations are made either for plane stress or plane strain conditions. If a plate is very thick, a plane strain analysis is applicable; whereas, if a plate is very thin, plane stress analysis is often used. For either model, one assumes that the stresses and strains are independent of plate thickness.

The plane strain and plane stress analyses are idealized models. The stresses and strains near the crack tip of a plate are in reality much more complicated. The region closer to a crack tip has higher strains and tends to contract more, but the crack tip region is constrained from contract by the region of lower strains further away from the crack tip. This constraint resists thickness contraction and induces the tensile stress in the direction of plate thickness, σ_{zz}. Along the crack front and in the interior of a very thick plate, the thickness contraction is negligibly small, and the state of deformation approaches that of plane strain. On the plate surface, the traction must be zero; therefore, the conditions of plane stress prevail. For a cracked thick plate, the state of stresses and strains changes gradually, from that of plane stress on the specimen surface to that of plane strain in the interior. This is true if the plastic zone size is small enough in comparison to the plate thickness.

It is also clear that the rate of transition from the state of plane stress on the surface to the state of plane strain in the interior depends upon the strain gradient induced from geometrical irregularities. If the gradient is high, the transition is fast; conversely, if the gradient is low, the transition is slow. If there is no strain gradient in the plane of a plate, there is no constraint from the deformation in the plate thickness direction to induced σ_{zz} regardless of how thick the plate is. Close to a crack tip, the strain gradient is steep, and the rate of transition is fast. As the distance from crack tip increases, the strain gradient decreases, and the thickness of the transition layer increases. Far away from the crack tip, the state of stresses and strains throughout the plate thickness is essentially that of plane stress.

A schematic picture of the plane strain plastic zone in a thick plate near a crack tip is shown in Fig. 1. If a plate is thick enough, the size of the plane strain zone starts from zero on the plate surface and grows to the fully developed size in the interior. There is a transition region between the plane stress region on the plate surface and the plane strain region in the interior of a thick plate. In the interior of a thick plate, the plane strain plastic zone, $r_{p\epsilon}$, coincides with r_p. Close to the plate surface, r_p becomes bigger, but $r_{p\epsilon}$ becomes smaller. The length of the fully developed plane strain region, 2η, relative to the size of the transition region, depends upon the size of the plastic zone relative to the plate thickness. For a thicker plate and a smaller r_p, η is longer. Within the transition region and the plane strain plastic region, the hydrostatic tensile stress, that is, $(\sigma_{xx} + \sigma_{yy} + \sigma_{zz})/3$, increases and the effective stress decreases, thereby reducing the overall plastic deformation. It can be said that the crack tip region is "stiffened" against plastic deformation.

In the case of small scale yielding, the size of the plane strain zone depends upon the quantity $(K/\sigma_Y)^2/t$. For a valid K_{Ic} test, the value of the quantity must be less than 0.4, that is, at this value, and "effective" plane strain zone exists for the fracture test. At a higher value of the quantity, the "stiffening" effect is less. In the region of general yielding, the stiffening effect will be greatly reduced.

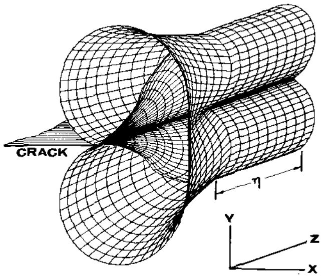

FIG. 1—*Schematic diagram showing half of the plastic zone; the plane strain plastic zone is imbedded.*

Finite Element Calculation

In this study, FEM are used to calculate the crack tip deformation. The stiffening effect at a crack tip is modeled by a composite matrix. The results are compared with the moiré strain measurements made by Ke and Liu [*14*] on 2024-0 aluminum alloy specimens. The measurements were made on 4 and 8 in.-wide double-edge-notched specimens of 0.125, 0.25 and 0.5 in. thick. The elongations of a 7-in. gage length over the cracked section were also measured.

The incremental theory of plasticity is used. Von Mises' yield criterion and Prandtl-Reuss' flow rule are employed. The constitutive equation for the analysis of the elasto-plastic behavior of the material is

$$\dot{\epsilon}_{ij} = \frac{1+\nu}{E}\dot{\sigma}_{ij} - \frac{\nu}{E}\dot{\sigma}_{kk}\delta_{ij} + \frac{9}{4}\frac{S_{k\ell}\dot{\sigma}_{k\ell}}{\bar{\sigma}^2 H'} S_{ij} \tag{1}$$

where

H' = slope of the curve in a plot of the effective stress, $\bar{\sigma}$, versus effective plastic strain $\bar{\epsilon}^p$,

$\dot{\sigma}_{ij}$, $\dot{\epsilon}_{ij}$ = stress and strain increments, and

S_{ij} = deviatoric stresses.

$\bar{\sigma}$ and $\bar{\epsilon}^p$ are defined as

$$\bar{\sigma} = \sqrt{\frac{3}{2} S_{ij}S_{ij}} \tag{2}$$

and

$$\bar{\epsilon}^p = \sqrt{\frac{2}{3} \epsilon_{ij}^p \epsilon_{ij}^p} \tag{3}$$

where ϵ_{ij}^p are the plastic strains.

Figure 2 shows the uniaxial tensile stress-strain curve of Batch C aluminum alloy. The Young's modulus, E, and the Poisson's ratio, ν, are 11×10^6 psi and 0.34, respectively. The yield stress, σ_Y, is 7260 psi, and the strain hardening exponent, n, is 0.315. The stress-strain relations used in the calculation are

$$\begin{aligned} \sigma &= E\epsilon \quad \text{for} \quad \sigma \leq \sigma_Y, \text{ and} \\ \sigma &= k\,\epsilon^n \quad \text{for} \quad \sigma \geq \sigma_Y, \end{aligned} \tag{4}$$

where $K = E^n \sigma_Y^{(1-n)}$. These relations represent a good material characterization as shown in Fig. 2.

If Eq 1 were expanded and inverted, the stress increments could be expressed in terms of strain increments for both plane stress and plane strain cases. It is convenient to express the relations in matrix form

$$\begin{aligned} [\dot{\sigma}] &= [D_\sigma] \times [\,\dot{\epsilon}\,] \quad \text{for plane stress, and} \\ [\dot{\sigma}] &= [D_\epsilon] \times [\,\dot{\epsilon}\,] \quad \text{for plane strain.} \end{aligned} \tag{5}$$

The matrix vectors consisting of the planal components of the incremental stress and incremental strain are defined as

$$[\,\dot{\sigma}\,] = \begin{bmatrix} \dot{\sigma}_{xx} \\ \dot{\sigma}_{yy} \\ \dot{\tau}_{xy} \end{bmatrix} \quad \text{and } [\dot{\epsilon}] = \begin{bmatrix} \dot{\epsilon}_{xx} \\ \dot{\epsilon}_{yy} \\ \dot{\gamma}_{xy} \end{bmatrix} \tag{6}$$

$[D_\sigma]$ and $[D_\epsilon]$ are symmetrical coefficient matrices, respectively, for plane stress and plane strain cases. The explicit forms of $[D_\sigma]$ and $[D_\epsilon]$ have been reported by Swedlow [*15*].

A plane stress calculation is made. Figure 3 shows a quarter of the double-edge-notched specimen and the element mesh with 265 nodes and 468 linear displacement triangular elements. At the far end, a uniform displacement was applied as the excitation parameter. The dimension of the element closest to the crack tip is 0.0035 in. All the results presented in this study are far away from the crack tip in comparison with the smallest element size. A finer mesh calculation gives the same results.

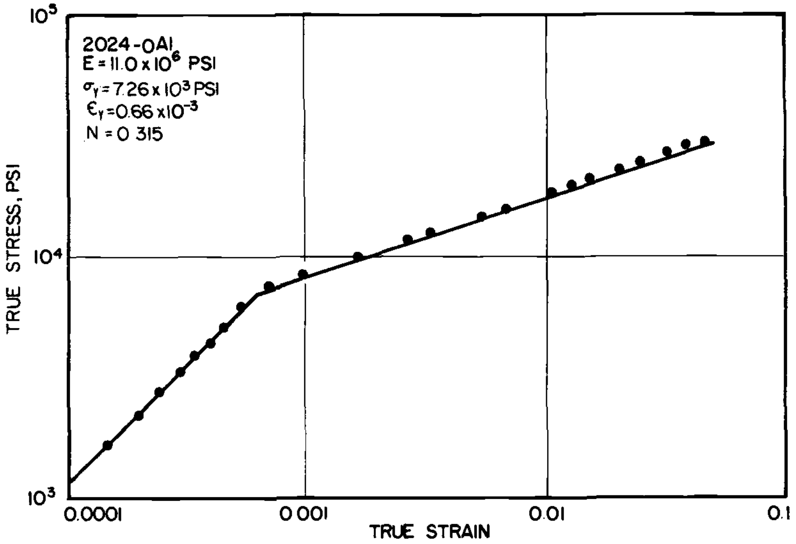

FIG. 2—*Uniaxial tensile stress-strain curve for 2024-0 aluminum alloy, Batch C.*

The dashed lines in Fig. 4 shows the calculted ϵ_{yy} along the crack line for plane stress case as compared with the measured values made on the 0.25-in.-thick specimen. The agreement between the calculated and the measured values is very good in the region more than 0.25 in. away from the crack tip. It is interesting to note that the plate is also 0.25 in. thick. In the region, r is less than 0.25 in.; the measured values are less than the calculated ones. The crack tip region is stiffened by the triaxial state of stress in the interior of the plate. The stiffened region in the interior restrains the plastic deformation on the specimen's surface. Even though the state of stress on the surface is that of plane stress, the measured strains are much less than those of the calculated plane-stress values. Ke and Liu [*14*] have made similar measurements on specimens made of other materials at various thicknesses. All their results clearly show changes of slopes in a log-log plot of ϵ_{yy} against distance from the crack tip at two points along the crack line. One takes place at $t/2$, the other changes at t, where t is the specimen thickness. The measurements seem

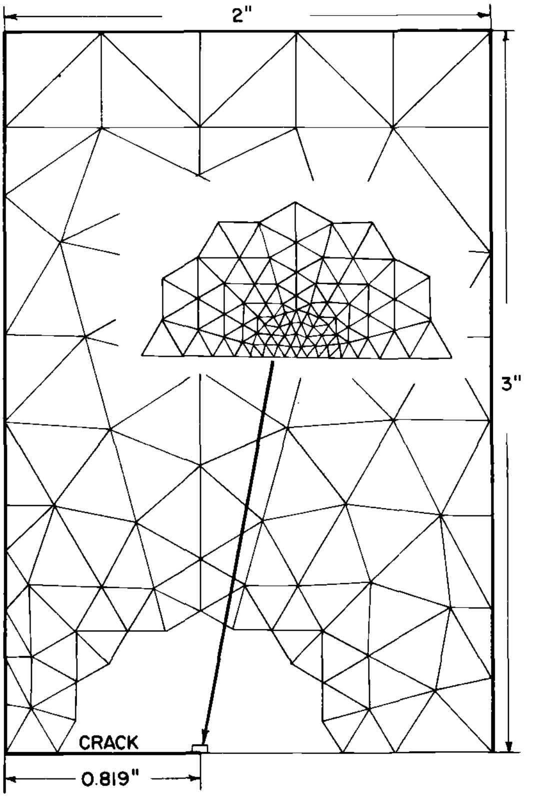

FIG. 3—*Finite element representation of first quadrant of the specimen. The details of elements near crack tip are inserted.*

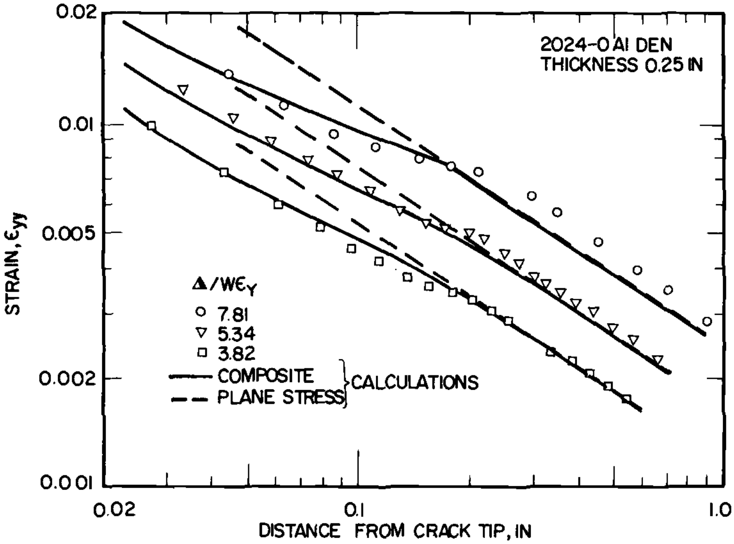

FIG. 4—*Comparison of calculated* ϵ_{yy} *versus the experimental measurements for a 0.25-in.-thick double-edge-notched 2024-0 Batch C aluminum.*

to indicate that the zone from the crack tip to a distance equal to the half of the specimen thickness is stiffened. With this in mind and the discussion given previously, we proceed to modify the stiffness matrices of the elements close to the crack tip. Figure 5 shows the modification zone within which the stiffness matrix of each element is modified to reflect the stiffening effect of the plane strain plastic zone. The modification zone in both x and y directions extends to $t/2$.

It is assumed that the degree of stiffening is equivalent to a certain size of the "plane strain zone" in the crack tip region. It is further assumed, for the sake of simplicity, that the shape and the size of this modification zone remain the same throughout the loading. For each of the elements within the modification zone, a linear combination of $[D_\sigma]$ and $[D_\epsilon]$ replaces $[D_\sigma]$. This composite matrix $[D]$ is defined as

$$[D] = \Omega[D_\epsilon] + (1 - \Omega)\,[D_\sigma] \tag{7}$$

where Ω is the mixing parameter whose value changes linearly with the distance from the crack tip. For the 0.25-in.-thick plate, the value of Ω changes from 0.04 at the crack tip to zero at the boundary of the modification zone. The value of Ω, for the 0.5-in.-thick plate is 0.08 at the crack tip. Outside of the modification zone $[D]$ is equal to $[D_\sigma]$; thus $[D]$ is used to construct the stiffness matrix. The values of Ω are deter-

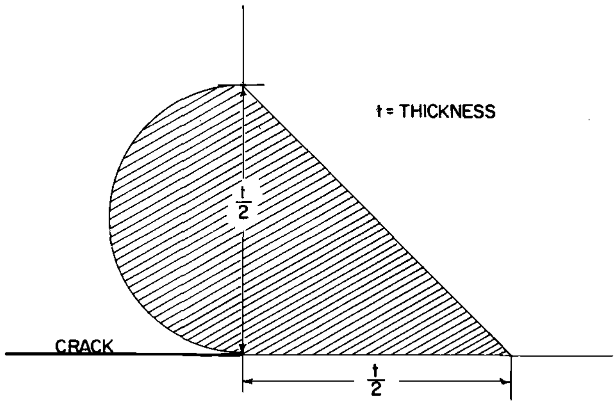

FIG. 5—*Region of modification within which the stiffness matrix of each element is modified.*

mined by trial and error so as to make the calculated strains, ϵ_{yy}, match with the measurements.

For each element inside the modification zone, the strain increment in z direction is reduced to

$$\dot{\epsilon}_{zz} = (1 - \Omega) \times \left[\frac{1 - 2\nu}{E}(\dot{\sigma}_{xx} + \dot{\sigma}_{yy}) - \dot{\epsilon}_{xx} - \dot{\epsilon}_{yy}\right] \tag{8}$$

For each element in this zone there are two sets of stress increments, one for plane stress and one for plane strain. These two sets of stress increments could be obtained from the strain increments following Eq 5. The resulting stresses are then used to generate separately the $[D_\sigma]$ and $[D_\epsilon]$ for the next loading step.

Figure 4 also shows the results of the composite mode calculation for the 0.25-in.-thick plate as denoted by the solid lines. It is to our surprise that a very small plane strain state could make such a significant change in ϵ_{yy}.

Similar calculations and measurements are also made for the 0.5-in.-thick specimen. The results are shown in Fig. 6. The two sets of experimental points for the two cracks of the same double-edge-notched specimen at the same elongation of the cracked section are shown. The difference of these two sets of measurements is possibly caused by the internal crack configuration and by a slight bending. Additional plane stress calculations are made for different batches of the aluminum alloy

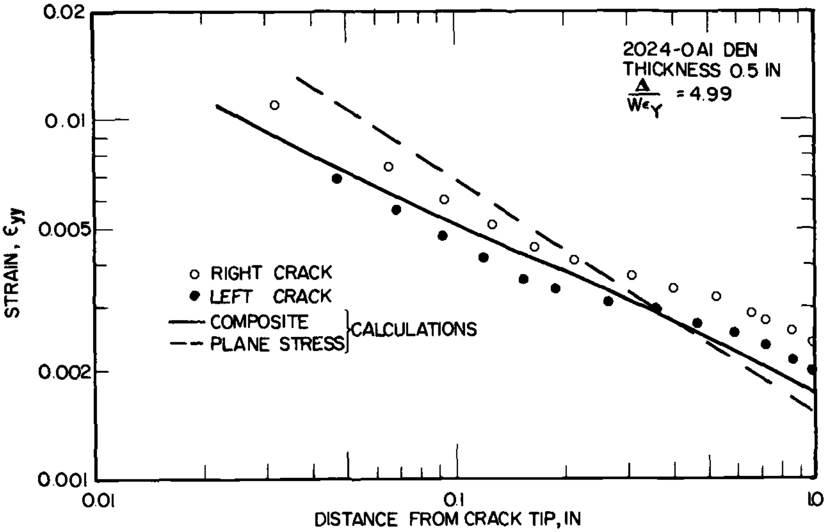

FIG. 6—*Comparison of calculated* ϵ_{yy} *versus the experimental measurements for a 0.5-in.-thick double-edge-notched 2024-0 Batch C aluminum.*

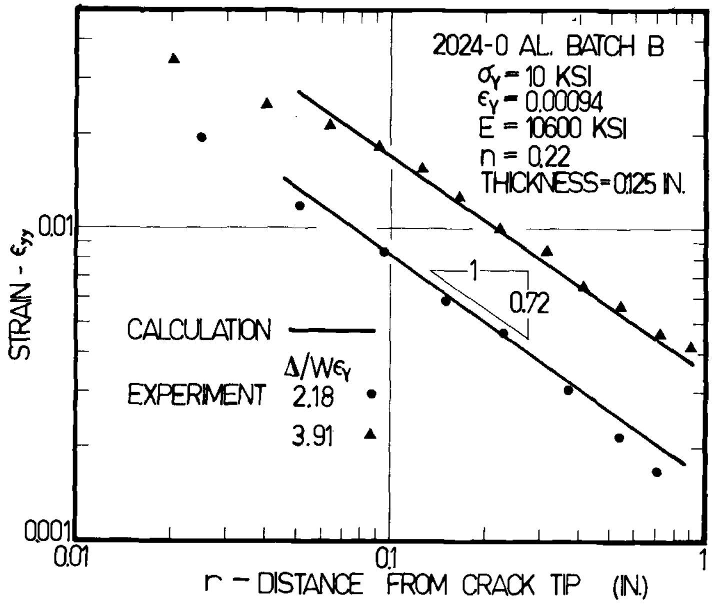

FIG. 7—*Comparison of calculated* ϵ_{yy} *versus the experimental measurements for a 0.125-in.-thick double-edge-notched 2024-0 Batch B aluminum.*

with slightly different yield strengths and strain hardening exponents. The comparison with the strain measurements are shown in Fig. 7 and 8.

Figure 9 compares the load-elongation curves of both the pure plane stress calculation and the composite mode calculations for both 0.25 and 0.5-in.-thick specimens with the experimental data. The elongation, Δ, measurements were made over a gage length of 7 in. The vertical dimension of the area used for the calculations, as seen in Fig. 3, is 3 in., which corresponds to a gage length of 6 in. Therefore, the average strain of the top most elements were added to make up the total calculated elongation for the plot in Fig. 9.

The good agreement of these curves with the measurements indicates that the major part of the specimen is under plane stress condition. The experimental load-elongation curve of the 0.5-in.-thick specimen is only ten percent higher than the calculated plane stress curve. Although the near tip stress and strain distribution is affected considerably by the crack tip stiffening, but the overall compliances of the specimens have not changed much.

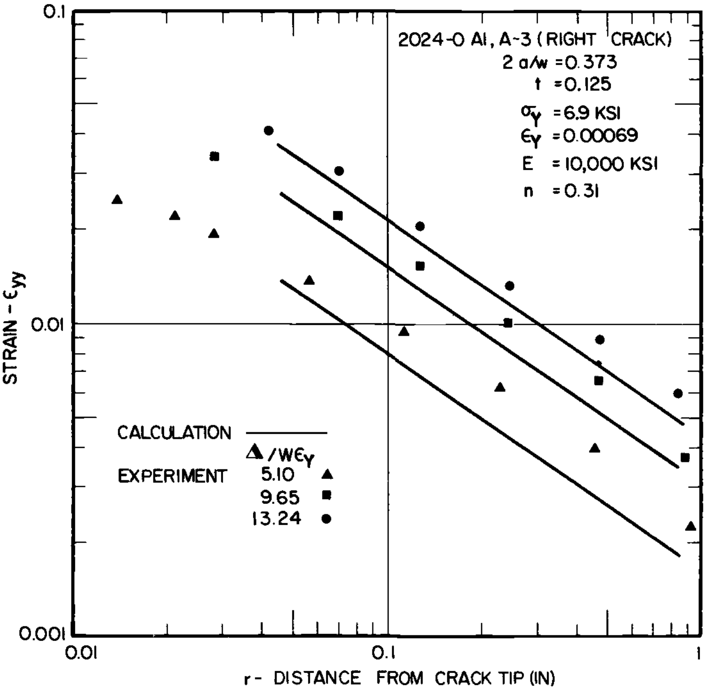

FIG. 8—*Comparison of calculated* ϵ_{yy} *versus the experimental measurements for a 0.125-in.-thick double-edge-notched 2024-0 Batch A aluminum.*

Discussions

A careful analysis of the experimental data and of the calculated results in Fig. 4 indicates that the crack tip deformation is characterized by two important regions: close to the crack tip, the deformation is affected by the crack tip stiffening zone; further away from the crack tip, the deformation is primarily that of plane stress. A transition region exists between them. The slope of the curves in the plane stress region is −0.68 which is very close to that given by the analytical calculations of Rice and Rosengren [5] and Hutchinson [6], −0.76. The results in Fig. 4, show that in the characteristic plane stress zone, the strain ϵ_{yy} can be written as

$$\epsilon_{yy} = K_\epsilon/r^m \tag{9}$$

where K_ϵ can be considered as the strain intensity factor, and in this case m is 0.68.

The slopes of the curves in the stiffened zone are somewhat less, and the values are close to −0.53. Further away from the plane stress zone, close to the center of the specimen, the curves level off. The agreement of the experimental data with both the plane stress calculation and the composite mode calculation in Fig. 4 is very good.

In Fig. 6, the measurements and the calculated strains of a 0.5-in.-thick plate are shown. The overall agreement between the measurements and the calculations is good. In the crack tip stiffened region, the calculated strains agree well with the measurements. The intermediate region between the stiffened region and the plane stress region is much longer. It extends to r, approximately equal to 0.5 in. The total ligament, $(W - 2a)$, of the specimen is only 2.4 in. The plane stress region is not large enough to show the characteristic slope of the strain curve. The results in Fig. 6 lead us to conclude that in order to observe the characteristic slope of a

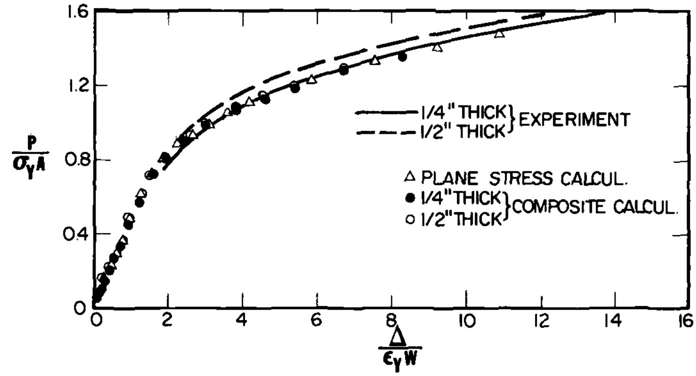

FIG. 9—*Load-elongation curves of both the pure plane-stress calculation and the composite calculation compared with the experiment data.*

plane stress region in an experiment, the total ligament of a double-edge-notched specimen should be ten times or more than the specimen thickness. If a bending load exists such as in the case of a wedge opening load (WOL) type specimen, the ligament should be even wider. It is also clear that in the case of small scale yielding, in order to observe the characteristic slope of a plane stress plastic zone, the size of the plastic zone should also be five times or more than the thickness.

If the ligament is wide enough, the crack tip stiffening zone is imbedded in the characteristic plane stress zone. The maximum tensile stress in the stiffening zone is increased above that of the plane stress calculation and the deformation, on the other hand, is reduced. The stiffening effect is strongly controlled by the plate thickness. Therefore, the results of the measurements and the calculations suggest that for the specimens of the same thickness with the same stress and strain fields in the characteristic plane stress zones, the stresses and strains in the stiffened zones must be the same.

At the outset, it should be recognized that the composite mode calculation is not intended as an exact three dimensional calculation for the crack tip stresses and strains. The degree of the crack tip stiffening is adjusted by trial and error to fit the experimental data. The important purpose of the calculation is to qualitatively show the extent of the three dimensional effect.

One of the important results of the calculation is to reveal that the extent of the plane strain plastic zone is very limited for a specimen loaded considerably into the region of general yielding. For example, for the 0.25-in.-thick specimen, in the composite finite element calculation, the value of Ω is only 0.04. This can be interpreted as meaning that the equivalent plane strain plastic zone at the crack tip is only four percent of the plate thickness. However, this is not to say that the actual length of the plane strain zone is four percent of the crack front. Rather, it means that the buildup of the triaxial state of stresses and the restraining of plastic deformation at the crack tip are equivalent to a four percent plane strain zone. It is doubtful that in the 0.25-in.-thick plate at these load levels, the true plane strain condition exists at the crack tip. This observation casts a serious doubt on the premise that a small specimen can be used to measure plane strain fracture toughness for a very ductile and tough material. Comparing the load-elongation curves in Fig. 9, it is also found that the extent of the plane strain zone is very limited. At the same elongation, the applied stresses of the experimental curve for the ½-in.-thick specimen are only ten percent higher than the plane stress curve. The extent of the plane strain zone is much smaller than expected.

The stresses and strains in the characteristic plane stress zone is used by Hu et al [*16*] to obtain the equivalent stress intensity factor of a small laboratory specimen loaded considerably into the region of general yielding.

Summary and Conclusions

The crack tip is stiffened by the triaxial state of stresses in the interior of a plate. In the crack tip stiffened zone, the plastic deformation is less than the calculated strains using the plane stress model. Further away from the crack tip, the strain measurements agree with the plane stress calculation exceedingly well. If the total ligament width in more than ten times plate thickness, that is, $(W - 2a) > 10t$, the crack tip stiffened zone is imbedded in the characteristic plane stress zone. For the specimens of the same thickness with the same stresses and strain fields in the characteristic plane stress zone, the stresses and strains in the stiffened zones of all the specimens must be the same.

References

[*1*] Swedlow, J. L., Williams, M. L., and Yang, W. E., *Proceedings,* First International Conference on Fractography, Sendai, Vol. 1, 1965, pp. 259–282.
[*2*] Chan, S. K., Tuba, I. S., and Wilson, W. K., *Engineering Fracture Mechanics,* Vol. 2, 1970, pp. 1–17.
[*3*] Marcal, P. V. and King, I. P., *International Journal of Mechanical Sciences,* Vol. 9, 1967, pp. 143–155.
[*4*] Underwood, J. H., Swedlow, J. L., and Kendall, D. P., *Engineering Fracture Mechanics,* Vol. 2, 1971, pp. 183–196.
[*5*] Rice, J. R. and Rosengren, A. F., *Journal of the Mechanics and Physics of Solids,* Vol. 16, 1968, pp. 1–12.
[*6*] Hutchinson, J. W., *Journal of the Mechanics and Physics of Solids,* Vol. 16, 1968, pp. 337–347.
[*7*] Underwood, J. H. and Kendall, D. P., "Measurement of the Strain Distribution in the Region of a Crack," presented to ASTM Committee E-24 on Fracture Testing of Metals, March 1967.
[*8*] Kobayashi, A. S., Engstrom, W. L., and Simon, B. R., *Experimental Mechanics,* Vol. 9, No. 4, 1969, pp. 163–170.
[*9*] Ke, J. S. and Liu, H. W., "Moiré Technique," *Experimental Techniques in Fracture Mechanics,* Vol. 2, Society for Experimental Stress Analysis, monograph series, to be published.
[*10*] Sih, G. C., *International Journal of Fracture Mechanics,* Vol. 7, 1971, p. 39.
[*11*] Kobayashi, A. S., "Stress Intensity Factors for Some Surface Flaw Problem," presented at the U. S.-Japan Joint Seminar on Strength and Structure of Solid Materials, Minnowbrook, N. Y., Oct. 1974.
[*12*] Levy, N. and Marcal, P. V., "Three-Dimensional Elastic-Plastic Stress and Strain Analysis for Fracture Mechanics, Phase I: Simple Flawed Specimens," HSST Technical Report 12, Heavy Section Steel Technology, 1970.
[*13*] Levy, N. and Marcal, P. V., "Three-Dimensional Elastic-Plastic Stress and Strain Analysis for Fracture Mechanics, Phase II: Improved Modelling," HSST Technical Report 17, Heavy Section Steel Technology, 1971.
[*14*] Ke, J. S. and Liu, H. W., *Engineering Fracture Mechanics,* Vol. 5, 1973, pp. 187–202.
[*15*] Swedlow, J. L., "A Procedure for Solving Problems of Elasto-Plastic Flow," Report SM-73, Department of Mechanical Engineering, Carnegie-Mellon University, Pittsburgh, Pa., Sept. 1971.
[*16*] Hu, W., Kuo, A. S., Liu, H. W., *Proceedings,* 12th Annual Meeting, Society of Engineering Science, 1975, pp. 219–231.

M. J. G. Broekhoven [1]

Theoretical and Experimental Analysis of Crack Extension at Nozzle Junctions

REFERENCE: Broekhoven, M. J. G., "**Theoretical and Experimental Analysis of Crack Extension at Nozzle Junctions,**" *Cracks and Fracture, ASTM STP 601,* American Society for Testing and Materials, 1976, pp. 535–558.

ABSTRACT: Due to the complexity of both geometry and stress distribution, the analysis of cracks in the transition region of nozzle-to-cylinder junctions, where local peak stresses promote crack extension, constitutes one of the most complicated problems in a fracture mechanics based design procedure as adopted in the American Society of Mechanical Engineers (ASME) *Boiler and Pressure Vessel Code* (Section III, Appendix G) for nuclear pressure vessels. Results of studies on this subject are scarce. This paper reviews results obtained in the last two years within a Netherlands cooperative research program mainly directed at the nozzle corner crack problem and covers both theoretical and experimental investigations. Significant conclusions from these studies are also presented.

KEY WORDS: crack propagation, fractures (materials), nozzles, fatigue (materials), pressure vessels, finite elements, stress intensity factors

Availability of sufficiently accurate procedures for the quantitative determination of the fatigue crack growth rate and fracture behavior of cracks is a prerequisite for those structures whose failure (either leakage or fracture) can lead to severe personal or economic dangers or both, such as aircraft and spacecraft structures and nuclear or (petro) chemical pressure vessels. The extreme consequences of fracture of light-water reactor pressure vessels (Fig. 1) have, over the past decennia, spawned extensive research in the field of fracture analysis of heavy section steel structures. This has resulted in the widespread application of linear elastic fracture mechanics (LEFM) technology for this type of structure, requiring the calculation of crack tip stress field intensity factors (K-factors) appropriate for the geometry and loading system of concern. Application of

---

[1] Laboratory for Thermal Power and Nuclear Engineering, Delft University of Technology, Delft, The Netherlands.

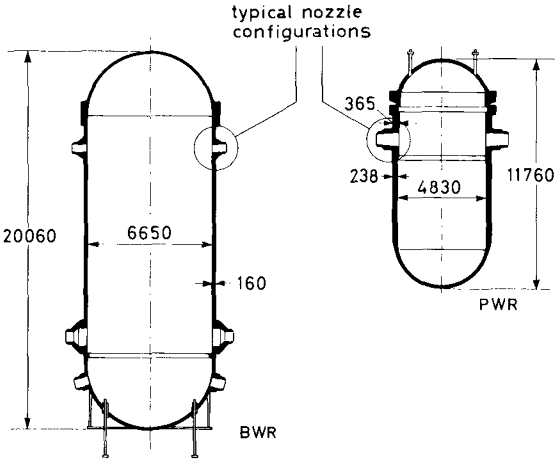

FIG. 1—*Characteristic dimensions (mm) of 1000 MWe boiling water and pressurized water reactor pressure vessels.*

LEFM has been adopted for the design of nuclear pressure vessels in the American Society of Mechanical Engineers (ASME) *Boiler and Pressure Vessel Code,* [*1*].[2] In short, this appendix requires that for a postulated surface defect, the (highly temperature dependent) fracture toughness exceeds the relevant K-factor by a given safety factor under all relevant loading conditions. The postulated elliptical surface defect has a depth of one quarter of the section thickness, up to a maximum of 75 mm and a length of six times that depth.

Cracks developing from discontinuities (perforations in plate or shell structures, such as the nozzle-cylinder junctions which are the subject of the present study) are of special concern because the high local stresses associated with such discontinuities, reaching peak values at inside nozzle corners of over 2.5 times the maximum membrane stress in the undisturbed cylinder under internal pressure loading, considerably decrease the tolerable crack size. However, determination of K-factors for nozzle corner cracks is hampered both by the complex geometry (Fig. 2) and by the complex local stress distribution (Fig. 3). As elucidated in Fig. 2, the problem comprises a quarter elliptical or circular crack, bounded by the curved surface of the inside nozzle wall, the doubly curved surface of the nozzle radius, the curved inside surface of the vessel wall, and a complex shaped back surface. Figure 3 shows a typical picture of the stress distribution perpendicular to the crack plane for the uncracked situation, as obtained from a finite element analysis. Evidently the most dangerous crack orientation is in the x-y plane of Fig. 2.

These figures also elucidate the differences with the hole corner crack

---

[2] The italic numbers in brackets refer to the list of references appended to this paper.

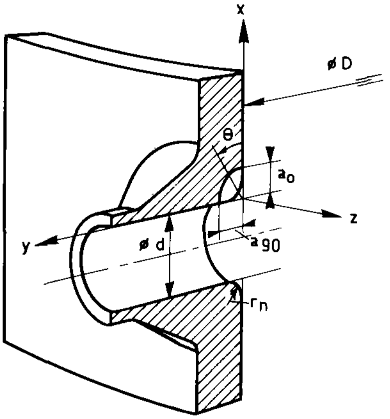

FIG. 2—*Nozzle-to-cylinder junction with corner crack.*

problem that has received considerable attention (for examples, see Refs *2–6*) because of its significance in aircraft engineering. Although the hole corner crack configuration may be considered as a fair approximation to the nozzle corner crack, as first proposed by Yukawa [*7*], the geometrical deviations and associated deviations of local stress distribution make the use of such a similarity model rather speculative.

Whereas Ref *1* provides definite procedures for calculating K-factors for less complicated crack geometries in pressure vessels, the complexity of the nozzle corner crack and the resulting scarcity of appropriate data have hampered the establishment of such procedures for cracks at nozzle junctions. Therefore, reference is made to an approximation procedure [*8*], based on results from a finite element analysis [*9*] and experimental data from burst tests on epoxy model vessels [*10*].

Because of the scarcity of LEFM-based studies on nozzle corner cracks, this subject has been adopted as main area of research within a Netherlands cooperative research program [*11*], started in late 1972. In spite of the restricted applicability of LEFM in view of the high toughness of nuclear pressure vessel steels and the possibility of local yielding at nozzle transitions, the program has been based on application of LEFM in order to conform to American Society of Mechanical Engineers (ASME) Codes [*1*]. Moreover, it was felt that the difficult LEFM problem should be solved before starting an elastic-plastic treatment. Also, it was anticipated that the availability of an accurate linear elastic solution can be of considerable importance for assessing elastic-plastic failure behavior over the full range of elastic, contained yielding, and full yield fracture behavior (for example, see Ref *12*).

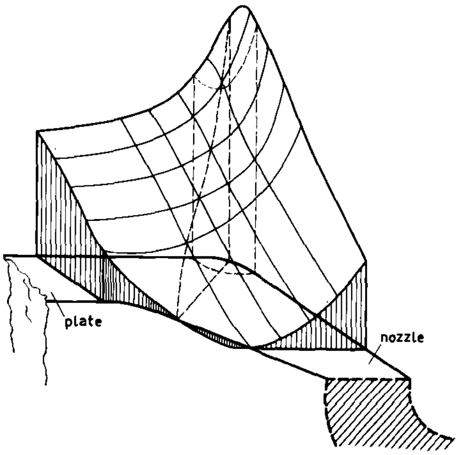

FIG. 3—*Stress distribution perpendicular to section with crack (nozzle on plate, uniaxial loaded).*

Some results obtained within this program are provided in Refs *13–16*. This paper reviews results obtained in the last two years by the author and his co-workers using finite element, analytical, and experimental studies. The status of the work as of mid-1975 is as follows. The finite element studies in the first instance had to provide highly accurate K-values for a series of cracks in a specific nozzle geometry [*14,15*]. These values should serve as reference data for subsequent studies aimed at an economical optimization of the finite element computations for design purposes [*15,17*]. The reference data should also serve to check the applicability and accuracy of simplified and advanced analytical K-factor computation procedures [*13,16*]. The experimental investigations, including fatigue crack growth experiments [*13,16*] and fracture studies (in progress) of nozzle models, aim at the evaluation of the applicability of the theoretical data for assessing real crack extension behavior at nozzle junctions.

Practical considerations were instrumental in selecting nozzle-on-flat-plate models (Fig. 4) under uniaxial loading for the experiments; the deviation from the nozzle-on-pressurized-cylinder configuration does not affect the complex character of the problem regarding geometry and stress distribution. For reasons of comparison the theoretical investigations concern the same geometry, but computational results for nozzle-on-cylinder geometries are presented as well. The results presented concern two nozzle geometries, denoted "N5" and "A," as shown in Fig. 5 (scaled to equal thickness of the vessel wall). Both are BWR-nozzles; N5 is the main coolant inlet nozzle of the Dutch Dodewaard 50 MWe vessel, whereas Nozzle A is the geometry analyzed by Rashid and Gilman [*9*] by the finite element technique.

Because of its scope, this paper is descriptive, leaving out mathematical details; where appropriate, reference is made towards other reports on the subject.

Finite Element Studies

Analysis

All computations have been performed using the Automated System for Kinematic Analysis (ASKA) (Version 5.1) [*18*] as installed on the intermediate size computer (IBM 360/65) available at that time at Delft University's Computing Center.

The model investigated (a scale model of Nozzle N5 on a flat plate) is shown in Fig. 6. Whereas most computations concern uniaxial (1:0) loading, similar to the experiments, a separate run was made for the case of biaxial (1:½) loading. This biaxially loaded nozzle-on-flat-plate configuration constitutes an accurate simulation of the real nozzle-on-pressurized cylinder configuration. [*19,20*]. Because of symmetry, only one half of the geometry had to be analyzed. The maximum membrane

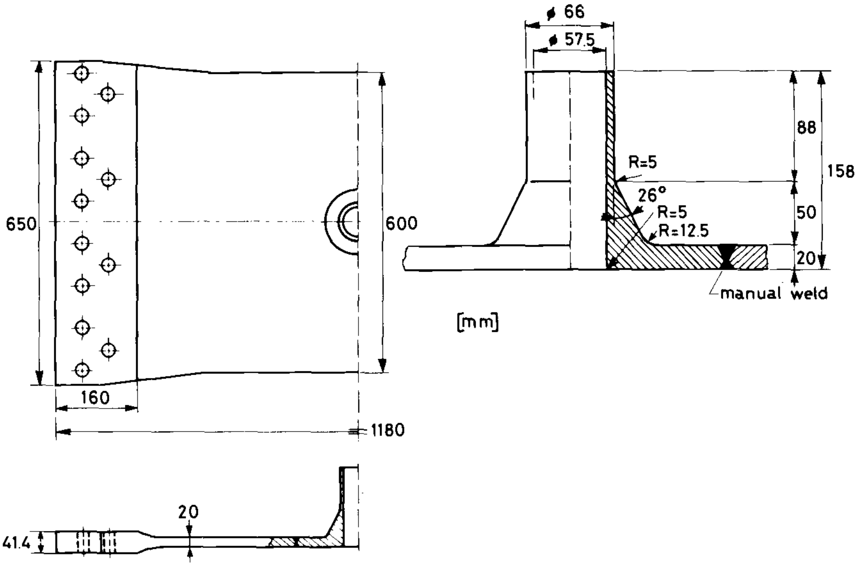

FIG. 4—*Typical nozzle-on-flat-plate model (N5/A508).*

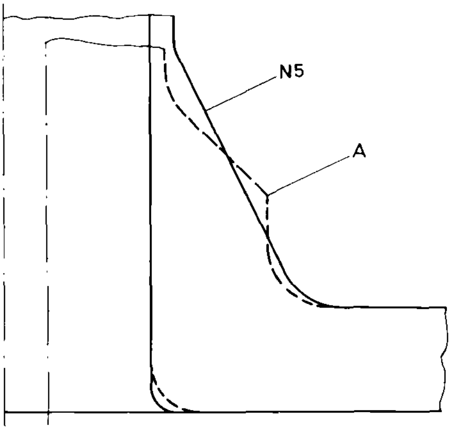

FIG. 5—*Comparison of the geometries of Nozzle N5 and Nozzle A.*

stress perpendicular to the crack plane is 1 N/mm^2, $E = 20.7 \times 10^4$ N/mm^2, $\nu = 0.3$. Figure 7 shows the mesh for the plane containing the cracks ($\psi = 0$), and Fig. 8 shows the mesh used for areas remote from the crack region. The five crack fronts described by the mesh of Fig. 7 were chosen equal to those observed in fatigue experiments with a similar nozzle as will be presented later in the paper. Higher order elements were used to obtain an optimal approximation of the singular crack tip stress and strain fields, mainly HEXEC-27 elements (27 nodes, incomplete quartic, with parabolic curved edges) and PENTAC-18 elements (18 nodes, incomplete cubic, with parabolic curved edges) for the transition from fine to coarse mesh.

The resulting total number of over 7000 unknowns in relation to the capacity of the available computer facility necessitated the use of a substructuring option, available within the ASKA system. The three level substructuring schematization shown in Fig. 9 was selected partially on the basis of practical considerations, for example, allowable job sizes. However, instrumental in the choice of the hypernets (100. . . .600) was the fact that such choice yielded the opportunity to analyze 6 geometries (1 uncracked and 5 with cracks of step-wise increasing size) by only changing the relatively small hypernet (about 670 unknowns versus 2029 in Subnet 1) through inserting all crack surface nodes in this hypernet. This yielded a considerable reduction in total computation costs. Details of the computational procedures and techniques, with particular reference to mesh generation, recursive substructuring, and computational costs are described elsewhere [*14*].

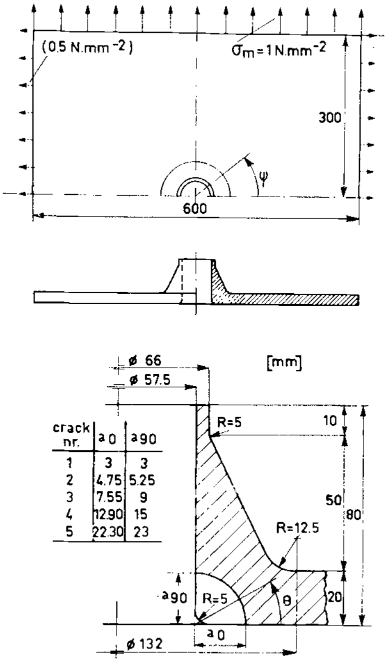

crack nr.	a_0	a_{90}
1	3	3
2	4.75	5.25
3	7.55	9
4	12.90	15
5	22.30	23

FIG. 6—*Nozzle N5 on flat plate; finite element model.*

The disturbance of stresses and displacements due to the introduction of a crack damps out with distance from the cracked region, so that in general a surface remote from and enclosing this region can be determined where these parameters are almost unaffected by the crack. An analysis of the enclosed region only, with fixed boundary conditions (stresses, displacements) derived from an analysis of the uncracked structure, then yields almost the same results as obtainable from an analysis of the entire structure, but at considerably lower costs, in particular, if use is made of a special purpose relatively cheap finite element program to derive those boundary conditions. (Such a program, denoted CASPA, using geometrically axissymmetrical ring elements with six-node triangular cross section with a Fourier series solution for displacements and stresses, has been developed in the author's laboratory [*19,20*].) The loss of accuracy inherent to such a procedure may be roughly estimated from the proportional change of the stresses or displacements at the candidate boundaries due to introduction of the crack within an analysis of the entire structure.

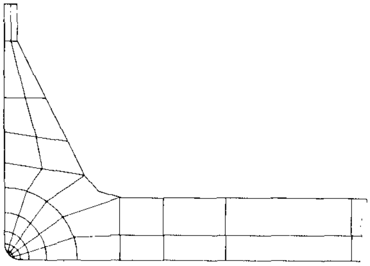

FIG. 7—*Finite element schematization in ψ = 0-deg plane (with crackfronts).*

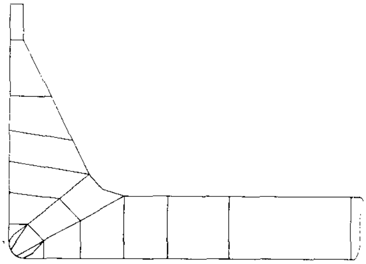

FIG. 8—*Finite element schematization in ψ = 180-deg plane.*

From the previous analysis of one half of the structure the proportional changes of the displacements due to introduction of the Cracks 1 through 5 (Fig. 6) in the planes ψ = 45 and 90 deg, respectively (Fig. 9), could be obtained readily. Based on these numbers, it was estimated that restricting the analysis to one quarter of the structure should introduce an error in the order of 1 percent, and to 1/8 of the structure in the order of 4 percent for Crack 3 (which has a crack depth exceeding the ASME postulated design defect size). Therefore, a separate analysis was performed for the part of the structure indicated in Fig. 10, loaded on its interfaces with prescribed displacements as obtained from the analysis of the entire uncracked structure. (Evidently, by application of fixed prescribed displacements the true K-factors will be underestimated, whereas fixed prescribed stresses (nodal loads) will yield an overestimate. Prescribed displacements were chosen for practical reasons, and they would yield an idea about the nonconservatism). The analysis required generation of two new subnets (A and B instead of 1 and 2, Fig. 10) and a new mainnet 10; the finite element schematization within the new subnets was equal to the original schematization. Total computer costs involved in this analysis were less than one quarter of those for the original analysis.

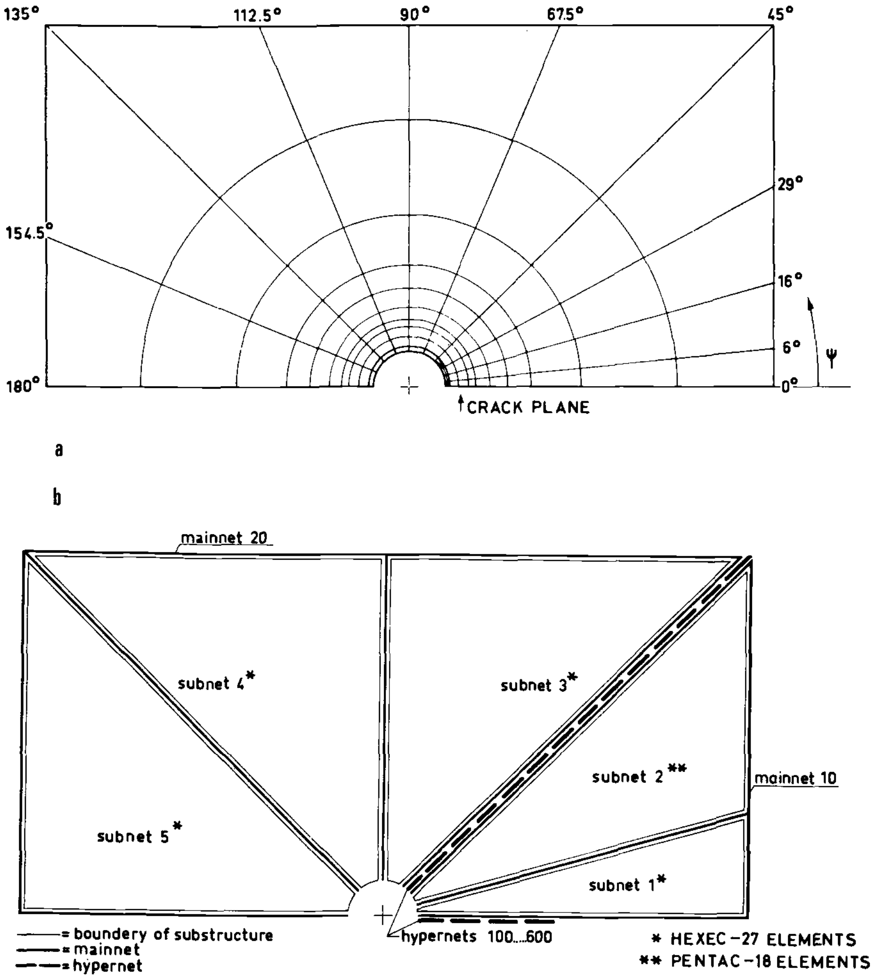

FIG. 9—(a) *Top view of mesh;* (b) *schematization in subnets, mainnets, and hypernets.*

Derivation of K-factors

K-factors have been derived from the results of the previous analyses by several procedures documented in the literature [*9,21*]; details are given in Ref *14*.

The so-called stress and displacement methods require the substitution of near crack tip stresses or displacements resulting from the finite element treatment in analytical expressions, relating these crack tip field parameters with the K-factor. This procedure has the advantage that a

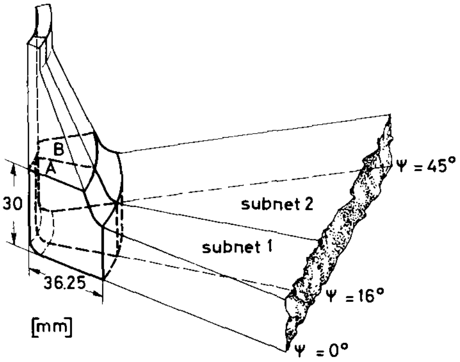

FIG. 10—*Part of the structure treated in a separate analysis.*

straightforward solution for one single crack problem suffices and that it results in local K-factors; thus, the full K-factor variation results along a crackfront. However, the disadvantage is that it generally requires a large number of relatively small elements around the crack front to arrive at a sufficiently accurate approximation of the near crack tip singular stress and displacement field. As elucidated later in this paper, however, fairly accurate results have been obtained in the present study for Cracks 2, 3, and 4 with a relatively coarse mesh (characteristic element size at the crack front about 0.7 to 0.4 times characteristic crack depth), by the use of elements with an incomplete quartic displacement field.

The results of the stress and displacement methods can be considerably improved by the use of special crack tip elements with a built in $\sqrt{r}$ singularity to reproduce the known form of the analytical solution in the near tip region, instead of the commonly used polynomial interpolation functions, for examples, see Refs *22* and *23*. However, such special elements are not generally available in existing finite element programs and their incorporation by the user may cause considerable difficulty in large programs such as ASKA. The use of modified standard elements, that is, elements with mid-side nodes in a quarter position so that a $\sqrt{r}$ singularity is introduced [*24,25*] has yielded considerably improved solutions in 2-D studies performed at the author's laboratory, using the MARC Analysis Research Corporation finite element system. However, application of similarly modified 3-D elements in the present ASKA-based study so far has been hampered by operational difficulties.

Energy methods require the calculation of the strain energy release rate associated with crack extension, which can be simply converted into a K-factor. This procedure yields accurate results even for relatively coarse meshes around the crack front, and therefore is much more suitable, in particular, for 3-D crack problems. However, it requires the solution for at least two different cracks. The required crack extension can be simulated by releasing nodes on the crack front, so that the crack extends to the next nodal point in front of the original crack front,[3] or by forward translation of crack front nodal points in the plane of the crack. Such crack extension can be simulated either for the entire crack front, that is, by releasing or translating all nodes on it (the "global energy method," as applied in Ref *9*) or for a part of the crack front, that is, by releasing or translating one or a few crack front nodes (the "local energy method"). The first procedure results in a global K-factor, that is, one averaged along the crack front. If the K-factor varies along the crack front (generally true for 3-D configurations), a global K-factor has only restricted significance. The second procedure yields local K-factors. For rather coarse meshes, application of the local energy method by releasing one or a few crack front nodes generally causes such a strong alteration of the originally smooth crack front that the significance of the resulting local K-factors becomes doubtful; a slight translation of those nodes will yield much more accurate results. Generally, both the global and local energy methods require complete stress analysis runs for both the original and the new (disturbed) mesh, which, for large structures, leads to extreme computation times, especially when crack extension is simulated in a series of steps. Considerable reduction of computational costs can then be achieved by using substructuring, either by locating the nodal points to be released in a mainnet or by treating the relatively small part of the mesh that has to be altered (by releasing or translating nodes) as a substructure. Changes in the geometry then only require the regeneration of a modified mainnet or substructure respectively.

Taking full advantage of the finite element formulation, Parks [*26*] developed an optimal procedure for application of the (either global or local) energy method, termed the stiffness derivative procedure. He showed that the change of potential energy associated with an alteration of the crack front can be calculated from the vector of displacements for the original cracked configuration (which requires a normal stress analysis run) and the change of the stiffness matrix of a ring of elements surrounding the disturbed part of the crack front due to the alteration. As the element stiffness matrices for the original cracked configuration have already been generated in the normal stress analysis run, only the stiffness matrices of a relatively small number of elements connected to the translated node(s) have to be regenerated. This procedure can be applied

---

[3] If higher order elements are used, as in the present study, it is necessary to release all midside and midface nodes in the crack plane of any element for which one node is released; otherwise, an unstable K solution with considerable deviation from the true solution is obtained.

with relatively coarse meshes, and is particularly advantageous for computing local K-factors for complicated 3-D configurations.

Within the present study, the displacement method has been applied for all five crack fronts in the analysis of the entire structure. In this analysis, also, the global energy method has been applied; stepwise extension of the crack front to form Cracks 1 to 5 has been simulated by releasing the relevant nodes. Because all crack surface nodes were inserted in the hypernet, this required only the analysis of this relatively small net. Parks' stiffness derivative procedure has been applied for all nodal points on the five crack fronts to obtain local K-factors for both the entire structure as well as for the part of the structure treated in a separate analysis. The analysis of the entire structure using Parks' method involved both uniaxial (1:0) and biaxial (1:0.5) loading. The other analyses have been restricted to uniaxial loading.

Results and Conclusions

The K-factors resulting from the several analyses have been plotted in Figs. 11 and 12, together with results obtained with the semianalytical

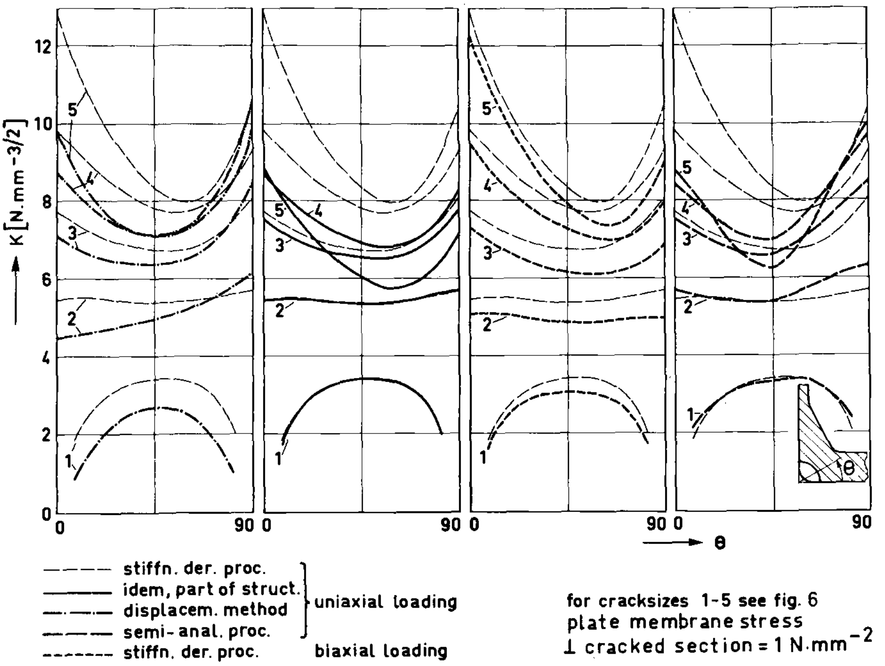

FIG. 11—*Comparison of nozzle corner crack K-factors (as function of θ) from various procedures.*

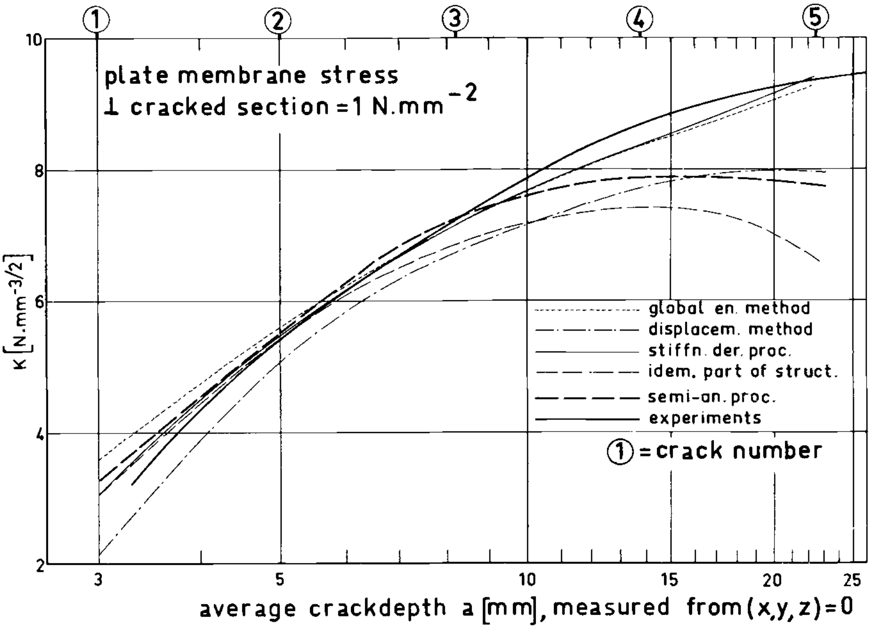

FIG. 12—*Comparison of nozzle corner crack K-factors (averaged along the crack fronts) from various procedures (uniaxial loading).*

procedure described in the next section. Figure 11 shows the variation of *K* along all five crack fronts as a function of θ. The results of the stiffness derivative procedure (analysis of one half of the structure, uniaxial loading) are shown in all four panels of this figure as a basis for comparison; results from other procedures appear, one each, in the various panels. Figure 12 shows K-values *averaged* along the crack fronts versus *average* crack depth; this figure also includes experimental data discussed later in this paper.

Restricting the discussion to the finite element results, the following conclusions can be made.

1. Results of the global energy method and average values of the stiffness derivative procedure are in close agreement (Fig. 12), as expected. The deviation for very small cracks, in fact only Crack 1, is due to the fact that the global energy method cannot cope accurately with the extension from a zero crack situation to a part circular surface crack.

2. Results of the displacement method, though too low for the whole range of crack sizes investigated, show reasonable agreement with the results of the stiffness derivative procedure for cracks of intermediate depth. This fair agreement seems to be fully attributable to the capability

of the applied higher order elements to approximate the near-tip displacements, in spite of the relatively coarse mesh applied.

3. Contrarily, the stress method yielded meaningless results, which therefore have been omitted here. The main reason for this seems that the finite element method is based on displacements, yielding stress fields of lower accuracy than the displacement fields; moreover, the program gives displacements at all nodes but stresses only at corner nodes, thus yielding insufficient stress data for appropriate application of the stress method.

4. Analysis of a suitably chosen small part of the structure (less than ⅛ instead of half the structure, Fig. 10) with fixed boundary displacements obtained from an analysis of the uncracked structure yields accurate results for the cracks of main concern here (Cracks 1 to 4), at much lower costs.

5. Results obtained by the stiffness derivative procedure for the cases of uniaxial and biaxial loading show a very good qualitative agreement (Fig. 11). As expected, K-factors for the biaxial loading case are lower for all cracks investigated.

6. The results show good qualitative agreement with the results of finite element studies of nozzle corner cracks published recently by other investigators [*27–29*]; a quantitative comparison is hampered by the differences between the nozzle and crack geometries studied.

7. Based on figures regarding computational costs gathered in the course of these studies, guidelines could be developed regarding improvement of the substructuring schematization which, for the present case, should lead to savings in computation times of well over 50 percent [*14*].

Analytical Studies

As elucidated previously, the complexity of the nozzle corner crack problem rules out the possibility for establishing exact analytical solutions, thereby making application of numerical techniques mandatory. However, the extreme computational costs associated with the use of finite elements seem to make application of that method prohibitive for practical design purposes, although considerable reduction seems possible as indicated previously and elsewhere [*17*]. This has led to studies aimed at the derivation of K-factors of sufficient accuracy by analytical approximations. Numerous approximate analytical solutions, several of which have been proposed in the literature, can be obtained by simplifying the geometry or the stress distribution or both to some extent, thus allowing application of existing analytical solutions for less complicated configurations. Mainly directed towards the hole corner crack problem, such procedures generally use the Bowie solution for through cracks from a hole in a flat plate together with solutions for embedded circular or elliptical cracks, with corrections for free surfaces taken from the literature [*30*]. The applicability of such approximations is discussed elsewhere [*6*], giving comparisons of several approximation procedures with results of 3-D photoelastic experiments, concluding an overall rather poor agreement.

For nozzle corner cracks the accuracy of simplified analytical approximations depends on the size of the crack relative to the corner radius and to the nozzle inside diameter. For very shallow cracks at the nozzle corner surface an infinitely long or a semi or part circular or elliptical surface crack may be a fair geometrical approximation, and K-factors for such approximated geometries may be obtained with fair accuracy using existing solutions for complex loaded 2-D or 3-D surface cracks. For deeper cracks, taking a quarter circular or elliptical shape, one has to rely upon approximation procedures similar to those used for hole corner cracks. However, whereas the true *uncracked* geometry and stress distribution are accurately accounted for in the Bowie solution which generally forms part of the approximation procedures for hole corner cracks, so that remaining deviations from the exact solution stems from erroneous accounting for both the fact that the real crackfront is curved instead of straight (as in the Bowie solution) as well as for the influence of the free surfaces, the true *uncracked* geometry and stress distribution for the nozzle junction configuration deviate considerably from the hole-in-plate configuration, thus making the Bowie solution less relevant for the nozzle corner crack problem and thereby adding an extra source of errors if hole corner crack approximation procedures are applied to nozzle corner cracks. Although the applicability of such rather simple approximation procedures deserves further investigation be it already because of the negligible computational costs involved (some results are presented in Ref *16*), the above reasoning indicates that possible accurate results should be attributed at least partly to coincidence and that their general application requires verification with accurate finite element results for a suitable range of various designs.

The constituents that characterize the complexity of the nozzle corner crack problem, that is, the elliptical shape of the crackfront, the complicated free surfaces, and the complex uncracked stress distribution, indicate that an optimal approximation may be arrived at by advanced solutions for complex loaded elliptical cracks together with procedures that enable the introduction of free surfaces (the latter requirement stems from the fact that no closed-form solutions exist for semi- or quarter-circular or elliptical cracks). This has led to the development of the so-called semianalytical procedure, first presented in a provisional form in Ref *13* and subsequently in Ref *16*. In the interest of emphasizing results and due to necessary space limitations, we have omitted details of the procedure given elsewhere [*16*] and only some typical results are shown. Additional details of the procedure appear in an internal report [*31*].

Results for Nozzle N5 on a flat plate under uniaxial loading have been presented in Figs. 11 and 12, together with finite element results, and experimental results that will be discussed later in the paper. Good agreement between the semianalytical results and accurate finite element results is shown in the right-hand panel of Fig. 11 for Cracks 1 to 3. As shown in this figure and Fig. 12, the semianalytical results yield an increasing underestimation of the finite element results for crack depths exceeding about 50 percent of the unreinforced wall thickness; however, further steps may improve the agreement. Figure 13 shows a comparison of average K-factors derived by the semianalytical procedure for Nozzle A on a pressurized cylinder with average K-factors obtained by Rashid and Gilman [*9*] for the same configuration, using the global energy method in a finite element treatment. The semianalytical results were derived from both the version of the program that deals with small semicracks as well as the version that deals with the larger quarter cracks. Both curves can be readily connected with a single smooth curve. Maximum deviations occur for crack depths below the postulated [*1*] quarter thickness crack depth. However, rather than attributing these deviations only to inaccuracies within the semianalytical procedure they may also be partially due to inaccuracies within the procedure applied in Ref *9*. In that study, K-factors have been attached to "effective crack lengths" that are smaller than the true crack lengths for which they have been calculated within the finite element scheme, because such a proce-

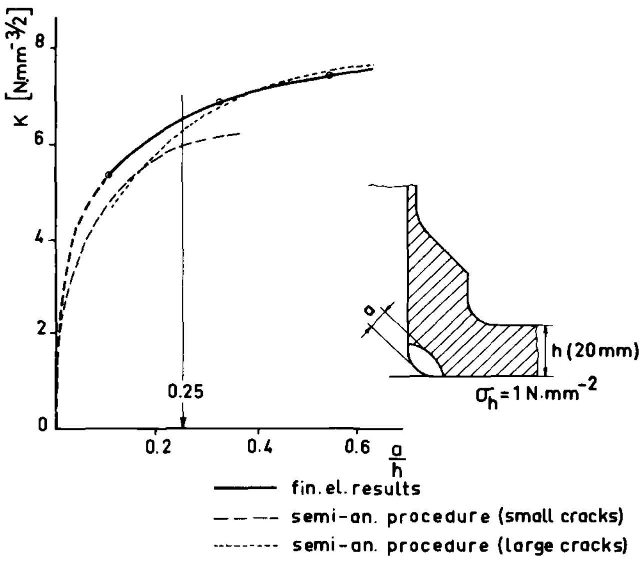

FIG. 13—*Comparison of results of semianalytical procedure with finite element results* [9] *Nozzle A.*

dure was found to yield better agreement with accurate analytical results for some 2-D cases studied. Apart from objections that could be made to the application of tendencies in 2-D studies to the results of a 3-D treatment, one of the two 2-D examples shown in Ref *9* indicated that for very small cracks the use of such an effective crack length decreases the agreement with analytical results. Much better agreement is obtained using the true crack length. If, as an intermediate solution, the curve representing the finite element results of Ref *9* in Fig. 13 is shifted to the right over one quarter of the distance between two subsequent crack fronts in the finite element schematization, indicated by the dots, instead of over one half of this distance (which should bring back the curve for effective crack lengths to a position relevant for the true crack lengths), then very good agreement with the semianalytical results is observed over the whole range of crack lenghts.

Although more data seem required to warrant definite conclusions regarding the applicability of the semianalytical procedure and its accuracy, the results obtained so far clearly indicate its potential to obtain accurate K-factor distributions for quarter circular of elliptical nozzle corner cracks with average depths up to well over the quarter thickness crack depth, at very low costs. Some further improvement may be expected from the application of more appropriate free surface correction factors whereas extension of the range of applicability to much deeper cracks requires the determination of appropriate correction factors to cope with the doubly connected character of the geometry and the increasing influence of the reinforced part of the nozzle. The only solution to the latter problem seems to be the empirical derivation of such factors from comparison with accurate finite element results.

Experimental Investigations

Experimental Procedure

The experiments, aimed at investigating the applicability of the theoretical results for real crack extension processes, concern monitoring of the growth of corner cracks in nozzle-on-flat-plate models under uniaxial fatigue loading. Based on the principle illustrated in Fig. 14, the crack growth rate data from these model tests can be translated to apparent K-factors as a function of crack depth using da/dN versus ΔK curves for the same material. This principle, also used by other investigators, for example, Refs *32* and *33*, has been chosen mainly because it permits the experimental determination of apparent K-factors for a series of cracks of continuously increasing size in a single experiment. The notation "apparent K-factor" is associated with the simplifying assumption used within

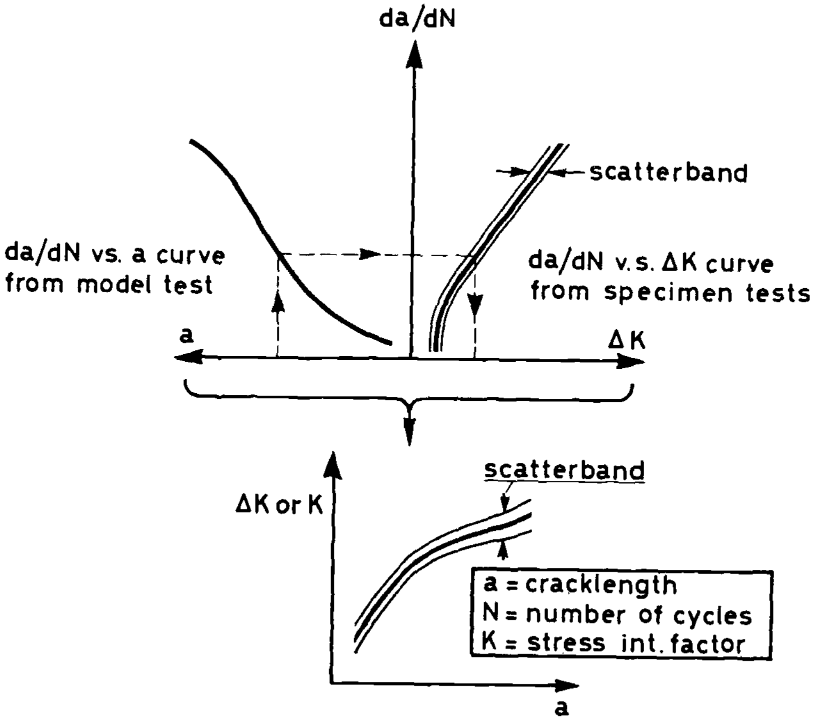

FIG. 14—*Principle of experimental technique to determine* K *as function of* a.

this procedure, that is, that a specific crack growth rate is uniquely related to a specific ΔK value at the same R ($=K_{min}/K_{max}$) ratio, irrespective of such factors as geometry, K-history, surface layer effects, etc.

Some practical considerations, such as accessibility for continuous accurate crack growth monitoring, available loading equipment, and production costs, were instrumental in selecting uniaxially loaded nozzle-on-flat-plate models (Fig. 4) for the experiments. The deviation from the nozzle-on-pressurized (and thus biaxially loaded) cylinder configuration does not affect the complex character of the problem, as mentioned previously. Results of 3 model tests concerning the same nozzle (N5) are reported. One model, already available at the start of the present program from other investigations [*19*], is entirely manufactured from a common construction steel (St42); the other two consist of a nozzle of A508 Cl 2 material welded into a flat plate of St52 steel. Manufacturing of these latter models involved premachining of an oversized nozzle and plate, manual arc welding, stress relief annealing, nondestructive testing, and machining of all surfaces to final dimensions. Initial part-circular cracks were provided by spark erosion with crack depths measured from the surface at $\theta = 45$ deg of about 1 mm. The models were load cycled in a 1 MN Amsler fatigue machine at about 8 Hz (maximum loads 0.692 MN (St42 model) and 0.942 MN (A508 models); $R = 0.1$). Crack growth rates were monitored at the inside nozzle surface and at the plate surface using a microscope in a special optical arrangement which enabled a crack tip localization generally within some hundredths of a millimetre. In order to eliminate the laborious and time consuming visual observations, two procedures for automatic crack growth monitoring were elaborated, using two robot photo cameras and two television cameras. Some details are presented in Ref *16*. The da/dN versus ΔK data have been obtained by standard procedures for both nozzle materials applied, using four-point bend specimens.

Results and Discussion

From interpreting the model test results by the procedure of Fig. 14, it followed that the difference between the apparent K-factors at $\theta = 0$ and 90 deg, respectively, was within a few percent for crack depths up to about 25 mm. A similar minor variation of the apparent K-factors all along the crack fronts, that is, for $0 < \theta < 90$ deg, then follows from the

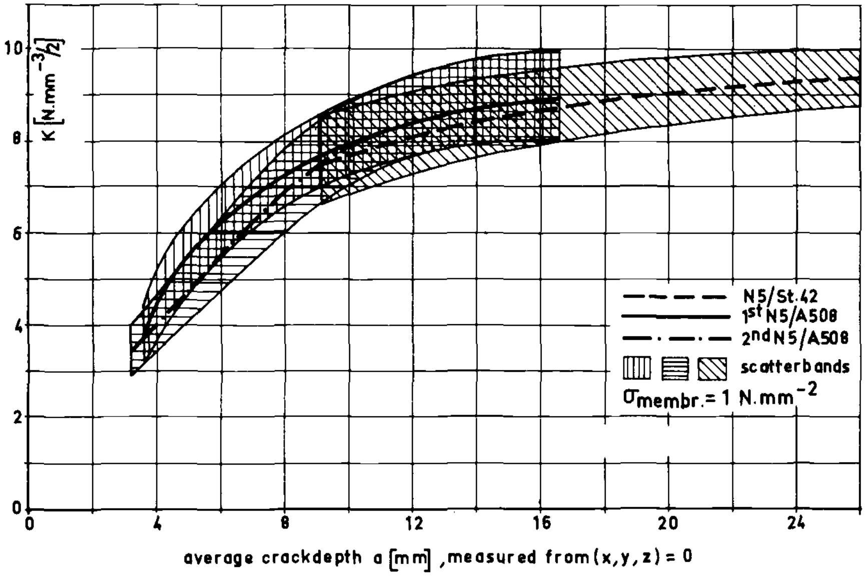

FIG. 15—*Apparent K-factors from experiments, Nozzle N5.*

assumption that the crack fronts maintain an approximately quarter elliptical shape during the total fatigue crack growth process. This assumption is supported by experimental evidence from other investigations, for examples, see Refs *10, 34,* and *35,* and by a marking detected at the crack surface of the St42 model (the other two models have been kept intact for subsequent fracture tests). Because of the minor variations of the apparent K-factor along the crack fronts these factors have been plotted as values averaged for $\theta = 0$ and 90 deg versus average crack depths in Fig. 15, together with their scatterbands. (Due to insufficiently polished surfaces no growth data for $a < 9$ mm have been obtained for the St42 model.) A best fit curve through the data represented in Fig. 15 has been drawn in Fig. 12, thus allowing for a comparison of average apparent K-factors with theoretical results described before.

Taking into account the data scatter generally associated with fatigue crack growth experiments, the mutual agreement between the experimental results from the three model tests shown in Fig. 15 seems very good, especially because the results concern models of different materials, tested at fatigue load levels that differed by approximately 30 percent. The strong variation of K-factors along the crack fronts that resulted from both the finite-element analyses as well as the semianalytical procedure, with maximum differences of over 50 percent, is not at all reproduced by the apparent K-factors that result from the fatigue experiments. As mentioned already, the latter factors show only a minor variation, values in the neighborhood of $\theta = 90$ being slightly higher than those at $\theta = 0$ deg. This difference qualitatively is in agreement with the fact that along the line $\theta = 90$ deg the normal stresses in the uncracked geometry exceed the normal stresses along the line $\theta = 0$ deg. A further discussion regarding the comparison of theoretical and experimental results is provided in the next section.

General Conclusions and Discussion

Recent advances regarding finite element method applications for complex 3-D crack problems enables an accurate computation of the full K-factor variation along quarter elliptical crack fronts in nozzle junctions, in particular if use is made of the stiffness derivative procedure [*26*]. Considerable reduction of required computation time can be achieved by the use of a suitable substructuring scheme, whereas a further considerable reduction without unacceptable loss of accuracy can be obtained by restricting the analysis to a small part of the structure only, with fixed boundary conditions obtainable from an economical finite element treatment of the uncracked structure. Mesh coarsening should yield an additional decrease of computation time, and the accuracy of the results can be improved by the use of special crack tip elements which can be obtained by a simple modification of existing elements. Investigations regarding these latter two subjects are in progress. The results of these finite element studies show a strong variation of the K-factors along the crack fronts. However, they do not show the rapid fall-off of the K-factor close to the free surfaces, as predicted in [*36*]; this should require a much finer mesh in those areas.

A semianalytical procedure for computing the full K-factor variation along part-elliptical crack fronts in nozzle junctions has been indicated. This procedure yields results that are in good agreement with accurate finite elements results for the crack sizes of main concern, that is, crack depths up to about one third of the unreinforced wall thickness, at very much lower costs (in the order of a few percent of the cost associated with a finite element treatment). For larger cracks, this procedure becomes less accurate and requires further elaboration. This procedure is capable of approximately reproducing near free surface effects as mentioned before by using appropriate free surface correction factors derived from studies that account for such effects.

Experimental results in terms of apparent K-factors obtained by fatigue testing cracked nozzle models show only a minor variation of the apparent K-factor along the crackfront, with slightly higher values at the inside nozzle surface where the uncracked stresses are highest. Evidently this discrepancy stems from the fact that crack growth rate data obtained from standard specimen tests cannot be used to predict accurately local fatigue crack extension for complex crack problems. Predictions of fatigue crack extension based on calculated K-factors and standard test data would yield a shape of the crack fronts quite different from those observed in practice. Close observation of the results obtained in this present study and elsewhere, for example, in Ref *35*, even indicates that the crack growth rate has a minimum at the free surfaces where the crack front shows an inside curvature. At the present, no complete picture exists regarding the causes of this discrepancy. Several factors that may contribute to it can be considered.

1. After a short period of ''predicted'' crack extension in accordance with the computed local K-factors the shape of the crack front is changed; thus, the K-factor distribution is changed. Predictions of subsequent crack growth should be based on the new shape and the new K-factor distribution. Such a step-wise procedure can be simulated in a finite element treatment, although that would be extremely expensive. The expectation, however, that minor changes of the crack shape will cause so much alteration of the K-factor variation that originally high values will be lowered and the other way round so that more or less constant values result seems very speculative, although some equalizing process may occur in reality.

2. The thickness dependent state of stress at the crack front, that is,

plane stress versus plane strain, influences the fatigue crack growth rate. However, specimens were used with about the same thickness as for the nozzle models, whereas no noticeable thickness dependency has been observed at tests in the thickness range of concern here.

3. Complications regarding the near-surface K-factors as mentioned before, that is, the very rapid drop-off of the K-factor near the free surfaces [*36*] and, moreover, the change of the strength of the singularity in that region as studied by Benthem [*37*] are not accounted for in the present theoretical results. However, their influence seems to be restricted to a rather thin surface layer only, whereas the discrepancy mentioned before occurs along the entire crack front. Besides, to some extent these complications occur as much in the models as in the specimens.

4. Crack closure effects (for example, see Ref *38*) may play an important role. The state of plane stress near the free surfaces allows for larger plastic zones than at interior parts of the crack front; the larger plastic deformations near the free surfaces yield more crack closure, and this effect is reinforced because of the higher calculated K-factors near the free surfaces. Such a reinforced crack closure at the free surfaces should reduce the effective part of ΔK, thus causing a more uniform effective K-factor distribution along the crack front. Preliminary experimental and theoretical results obtained recently at the author's laboratory seem to support this explanation. In view of such an explanation it seems rather striking that the average apparent K-factors from the fatigue experiments are in very close agreement with the average theoretical K-factors.

Further study regarding the factors mentioned previously seems required, with emphasis on the influence of crack closure effects. Evidently the significance of the strong variation of K along the crack front with respect to fracture behavior constitutes another important problem. Fracture tests of the fatigue-cracked models, now in progress, are aimed at studying this aspect. Preliminary results, indeed, indicate the dominant role of the maximum theoretical K-factor for fracture in the linear elastic regime.

Acknowledgments

The work reported here has been performed mainly within the framework of the Netherlands cooperative research program BROS [*11*], partly sponsored by the Dutch Ministry of Economic Affairs with Rotterdam Dockyard Company as main contractor. The efforts of graduate students who participated in this work have been much appreciated. The author thankfully acknowledges the very valuable contributions of his colleagues M. Hartevelt, M. G. v.d. Ruijtenbeek and H. A. C. M. Spaas. Encouragement of D. G. H. Latzko has been much appreciated.

References

[1] *ASME Boiler and Pressure Vessel Code,* Section III, Appendix G, American Society of Mechanical Engineers, 1974.

[2] Hall, L. R. and Finger, R. W., *Proceedings,* Air Force Conference on Fatigue and Fracture of Aircraft Structure and Materials, AFFDL TR-70-144, 1970, pp. 235–264.

[3] Broek, D., Nederveen, A., and Meulman, A., "Applicability of Fracture Toughness Data to Surface Flaws and to Corner Cracks at Holes," Report NLR-TR-71033 U, National Aerospace Laboratory, NLR, Netherlands, Jan. 1971.

[4] Liu, A. F., *Engineering Fracture Mechanics,* Vol. 4, 1972, pp. 175–179.

[5] Hsu, T. M. and Liu, A. F., "Stress Intensity Factors for Truncated Elliptical Cracks," paper presented at the Seventh National Symposium on Fracture Mechanics, American Society for Testing and Materials, Aug. 1973.

[6] McGowan, J. J. and Smith, C. W. in *Mechanics of Crack Growth, ASTM STP 590,* American Society for Testing and Materials, 1976, pp. 460–476.

[7] Yukawa, S., "Evaluation of Periodic Proof Testing and Warm Prestressing Procedures for Nuclear Reactor Vessels," Heavy Section Steel Technology Progress Report HSSTP-TR-1, General Electric Company, Schenectady, N.Y., 1969.

[8] Pressure Vessel Research Committee Ad Hoc Group on Toughness Requirements, "PVRC Recommendations on Toughness Requirements for Ferritic Materials," *Welding Research Council Bulletin,* No. 175, Aug. 1972.

[9] Rashid, Y. R. and Gilman, J. D, *Proceedings,* First Structural Mechanics in Reactor Technology Conference, Paper G 2/6, Berlin, Sept. 1971.

[10] Derby, R. W., *Experimental Mechanics,* Vol. 12, No. 12, 1972.

[11] Broekhoven, M. J. G., "The Dutch Cooperative Research Program 'BROS'—Fracture Analysis Research on Nozzle Intersections," Report MMPP-84, Laboratory for Thermal Power and Nuclear Engineering, Delft University of Technology, Delft, The Netherlands, Dec. 1973.

[12] Sumpter, J. D. G. and Turner, C. E., "Fracture Analysis in Areas of High Nominal Strain," *Proceedings,* Second International Conference on Pressure Vessel Technology, Paper II–79, San Antonio, 1973.

[13] Broekhoven, M. J. G., "Analysis of a Nozzle-Corner Crack Problem," Second Structural Mechanics in Reactor Technology Conference, Paper G 4/7, Berlin Sept. 1973.

[14] Broekhoven, M. J. G. and Spaas, H. A. C. M., "Application of the Finite Element Technique to a Complex 3-D Elastic Problem (Nozzle Junction with Cracks)," Report MMPP–101, Laboratory for Thermal Power and Nuclear Engineering, Delft University of Technology, Delft, The Netherlands, Aug. 1974.

[15] Broekhoven, M. J. G., "Computation of Stress Intensity Factors for Nozzle Corner Cracks by Various Finite Element Procedures," *Proceedings,* Third Structural Mechanics in Reactor Technology Conference, Paper G 4/6, London, Sept. 1975.

[16] Broekhoven, M. J. G. and Ruijtenbeek, M. G. V. D. "Fatigue Crack Extension in Nozzle Junctions—Comparison of Analytical Approximations with Experimental Data," *Proceedings,* Third Structural Mechanics in Reactor Technology Conference, Paper G 4/7, London, Sept. 1975.

[17] Broekhoven, M. J. G., Maaren, W. V., Ruijtenbeek, M. G. V. D., and Spaas, H. A. C. M., "Comparative Finite Element Studies of a Complicated 3-D Crack Problem with Emphasis on Cost Reduction," Report MMPP-127, Laboratory for Nuclear Engineering, Delft University of Technology, Delft, The Netherlands, 1975.

[18] Schrem, E. and Roy, J. R., "An Automatic System for Kinematic Analysis, Part 1," IUTAM Colloquium on High Speed Computing of Elastic Structures, University of Liège, 23-28 Aug. 1970.

[19] Campen, D. H. van, "Some Applications of Engineering Mechanics in Pressure Vessel Analysis," Ph.D. thesis, Delft University of Technology, Delft, The Netherlands, May 1972.

[20] Campen, D. H. van and Spaas, H. A. C. M., *Nuclear Engineering and Design,* Vol. 21, 1972, pp. 368–395.

[21] Chan, S. K., Tuba, I. S., and Wilson, W. K., *Engineering Fracture Mechanics,* Vol. 2, 1970, pp. 1–17.

[22] Wilson, W. K. in *Mechanics of Fracture—Part I,* G. C. Sih, Ed., Noordhoff International, 1973, pp. 484–515.

[23] Tracey, D. M., *International Journal of Fracture Mechanics,* Vol. 9, 1973, pp. 340–343.

[24] Barsoum, R. S., *International Journal of Fracture Mechanics,* Vol. 10, No. 4, 1974, pp. 603–605.

[25] Neale, B. K., *International Journal of Fracture Mechanics,* Vol. 11, No. 1, 1975, pp. 177–178.

[26] Parks, D. M., *International Journal of Fracture Mechanics,* Vol. 10, No. 4, Dec. 1974, pp. 487–502.

[27] Hellen, T. K. and Dowling, A. R., *International Journal of Pressure Vessels and Piping,* Vol. 3, No. 1, 1975, pp. 57–74.

[28] Schmitt, W., *International Journal of Pressure Vessels and Piping,* Vol. 3, No. 2, 1975.

[29] Reynen, J., "Analysis of Cracked Pressure Vessel Nozzles by Finite Elements," *Proceedings,* Third Structural Mechanics in Reactor Technology Conference, Paper G 5/1, London, Sept. 1975.

[30] "The Surface Crack—Physical Problems and Computational Solutions," J. L. Swedlow, Ed., presented at the Winter Meeting, American Society of Mechanical Engineers, 1972.

[31] Broekhoven, M. J. G., "Theoretical and Experimental Study of Crack Extension at Nozzle Junctions," Report MMPP-134, Laboratory for Thermal Power and Nuclear Engineering, Delft University of Technology, Delft, The Netherlands, Oct. 1975.

[32] Sommer, E. and Ratwani, R., "Experimental Investigations of Part-Through Cracks in Plate and Thick-Walled Shells," *Proceedings,* Second Structural Mechanics in Reactor Technology Conference, Paper G 4/3, Berlin, Sept. 1973.

[33] James, L. A. and Anderson, W. E., *Engineering Fracture Mechanics,* Vol. 1, No. 3, 1969, p. 565.

[34] Pickett, A. G. and Grigory, S. C., "Cyclic Pressure Tests of Full-Size Pressure Vessels," *Welding Research Council Bulletin,* No. 135, Nov. 1968.

[35] Miyazono, S. and Shibata, K., "Crack Propagation Characteristics in the Nozzle Corners of a Pressure Vessel Steel Model of Light Water Reactor," *Proceedings,* Third Structural Mechanics in Reactor Technology Conference, Paper G 4/8, London, 1975.

[36] Hartranft, R. J. and Sih, G. C. in *Mechanics of Fracture—Part I,* G. C. Sih, Ed., Noordhoff International, 1973, pp. 179–238.

[37] Benthem, J. P., "Three-Dimensional State of Stress at the Vertex of a Quarter-Infinite Crack in a Half-Space," Report WTHD 74, Laboratory of Engineering Mechanics, Delft University of Technology, Delft, The Netherlands, Sept. 1975.

[38] Elber, W. in *Damage Tolerance in Aircraft Structures, ASTM STP 486,* American Society for Testing and Materials, 1971, pp. 230–242.

J. E. Srawley[1] *and B. Gross*[1]

Side-Cracked Plates Subject to Combined Direct and Bending Forces

REFERENCE: Srawley, J. E. and Gross, B., "**Side-Cracked Plates Subject to Combined Direct and Bending Forces,**" *Cracks and Fracture, ASTM STP 601,* American Society for Testing and Materials, 1976, pp. 559–579.

ABSTRACT: The opening mode stress intensity factor and the associated crack mouth displacement are comprehensively treated using planar boundary collocation results supplemented by end-point values from the literature. Data are expressed in terms of dimensionless coefficients of convenient form which are functions of two dimensionless parameters, the relative crack length, and a load combination parameter which uniquely characterizes all possible combinations of tension or compression with bending or counterbending. Accurate interpolation expressions are provided which cover the entire range of both parameters. Application is limited to specimens with ratios of effective half-height to width not less than unity.

KEY WORDS: crack propagation, bending, fracture tests, stress intensity factor, boundary collocation analysis, crack mouth opening.

Nomenclature

a	Crack length (or depth), see Fig. 1
B	Specimen thickness, see Fig. 1
c_1, c_2	Numerical coefficients in Eq 11
E	Young's modulus
E'	Effective modulus, see Discussion section
H	Effective half-height of specimen
K	Stress intensity factor (Mode I in this context)
M	Moment of complentary couple
P	Resultant applied force
s	Distance of knife edge from crack mouth (see section on Crack Mouth Displacement Slopes)
v	Crack mouth displacement

---

[1] Head, Fracture Mechanics Section, and materials engineer, respectively. National Aeronautics and Space Administration, Lewis Research Center, Cleveland, Ohio 44135.

W	Specimen width, see Fig. 1
α	Relative crack length, a/W
Γ	Dimensionless stress intensity coefficient
Δ	Dimensionless crack mouth displacement coefficient
θ	Displacement combination parameter, arctan (v_M/v_P)
ν	Poisson's ratio
σ	Stress
ω	Load combination parameter, arctan (σ_M/σ_P)

Subscripts

I	Opening mode of crack tip deformation
M	Value for net section bending ($\omega = 1$)
P	Value for net section tension ($\omega = 0$)

This paper is a comprehensive treatment of the opening mode stress intensity factor, K_I, and the associated crack mouth displacement, v, for quasiplanar rectangular specimens with single-side cracks of any uniform depth, loaded in any manner that can be represented sufficiently well by a linear distribution of normal forces across each end boundary. To justify such a representation of simple, practical methods of load application, the ratio of effective half-height to width of the specimen should not be less than unity, preferably substantially greater for higher accuracy of application of the displacement data. The treatment of shorter specimens would require more refined, nonlinear modeling of the actual loading force distribution so that the interaction with the crack stress field would be adequately approximated.

Results of certain cases covered here have been published previously by the present authors and others [*1,2*].[2] However, these previous results are not sufficient for a comprehensive treatment of the subject. The results of this study constitute a homogeneous body of data which were subjected to linear regression analysis to estimate consistency and precision.

In this treatment, the distribution of normal forces across an end boundary is characterized by the statically equivalent combination of resultant force, chosen to act through mid-net section, and the complementary couple. Either the force, or the couple, or both, can act in a positive sense so as to cause the crack to open in the vicinity of the tip (tension or bending), or can act in a negative sense to cause the crack to tend to close near the tip (compression or counterbending). For some load combinations, the effect on the crack mouth is the same as at the tip; for others, such as combined tension and counterbending, it may be opposite. In general, the force and the couple are to be regarded as independent

---

[2] The italic numbers in brackets refer to the list of references appended to this paper.

variables. Commonly, however, in a practical testing, when force is applied by a single actuator, there is a proportional relation between the force and the couple which depends on the line of action of the force and on the relative crack length.

The data are given in the form of dimensionless coefficients, $\Gamma(K_I)$ and $\Delta(v)$, which are both functions of two dimensionless parameters, the relative crack length, α, and the load combination parameter, ω, equal to arctan $(6M/P(W - a))$, where P is the magnitude of the resultant force, M is the moment of the complementary couple, W is the specimen width, and a is the crack length. Both Γ and Δ are linear functions of the quantity tan $(\pi/4 - \omega)$, and the coefficients of the linear equations are finitely bounded functions of α which are expressed as rational algebraic functions for interpolation purposes. The ratio H/W, of the half-height to width of the specimen is the third independent parameter which would be expected to have an appreciable effect on the values of Γ and Δ if it were less then unity. For the values considered, 1, 2, and 4, however, the effect on Γ was found to be practically negligible, and the effect on Δ, erratic and of the order of 5 percent at the most.

The primary data for values of the relative crack length, α, other than the end points, 0 and 1, were obtained by the boundary collocation method of analysis as described in Ref *3*; the end point values were obtained from Refs *2* or *4* except in one case which is discussed later.

The purpose of this study is to serve as a prerequisite for the development of new test methods for measurement of such properties of materials as fracture toughness, fatigue crack propagation resistance, and stress corrosion crack propagation resistance. The potential advantages of the full range of load combinations has by no means been thoroughly explored, nor has the possibility that the property of interest might be significantly dependent on the mode of loading. This possibility follows from the fact that the crack tip plastic zone characteristics will certainly be affected.

In the application of results of planar analysis it is useful to distinguish between two types of quasiplanar practical plate specimens, as shown in the cross section in Fig. 1: (*a*) edge-cracked, and (*b*) face-cracked. In either case the crack length, or depth, must be practically uniform if the planar analysis is to apply accurately. Both kinds of specimens are necessary so that tests can be conducted with cracks oriented in different directions with respect to material texture, in particular, in the direction that cracks have been found to occur in service of a structural member. One particular use of the face-cracked specimen follows from regarding it as the extreme case of the widely used part-through cracked or surface-cracked type of specimen Fig. 1(*c*). The analysis of part-through cracked specimens is essentially three-dimensional and presents difficulties which are not yet satisfactorily resolved [*5*]. The present results provide a bound on the three-dimensional analysis and, are, therefore a useful guide as to

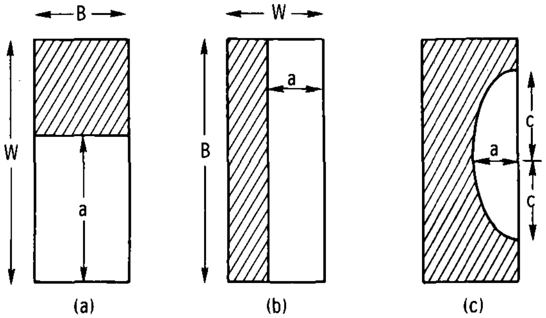

FIG. 1—*Cross sections through crack planes of rectangular plate specimens with* (a) *edge crack,* (b) *face crack, and* (c) *part-through semielliptical crack. Note that the width dimension,* W, *is always taken to be in the same direction as the crack length,* a, *and the thickness,* B, *taken to be normal to that direction.*

its accuracy. Moreover, tests of face-cracked specimens *can* provide a useful check on the reliability of tests of part-through cracked specimen or serve to substitute for them when convenient.

Boundary Collocation Analysis

Boundary collocation analyses were conducted for two different, but equivalent, types of end boundary conditions, as shown in Fig. 2(*a*). The first type is a linear distribution of normal tractions across the end boundary, as shown at the top of the figure. The second type consists of uniform distributions of shear stress along prolongations of the side boundary, as shown at the bottom of the figure. Both distributions are statically equivalent to the combination of resultant force, P, which acts through mid-net section and complementary couple of moment, M. The use of these two distinct types of boundary conditions provided a check of the consistency of the method. It was found that the same results could be obtained with either type, but the analysis had to be carried considerably further to reach satisfactory convergence when the second (shear) type of boundary condition was used. Satisfactory convergence is approached by successive runs with increasing numbers of boundary stations until there is no significant variation in the result. The complete set of results presented here was obtained, therefore, with the first (normal stress) type of boundary conditions, and a substantial number of these results were confirmed with the second type. The purpose of Fig. 2(*b*) is to show other equivalent expressions of the load combination, a linear distribution of normal tractions across the net section, and a pair of parallel forces acting at the corners. These expressions serve conceptual purposes; they are of no concern to the boundary collocation analysis.

The boundary collocation procedure used has been described in Ref 3,

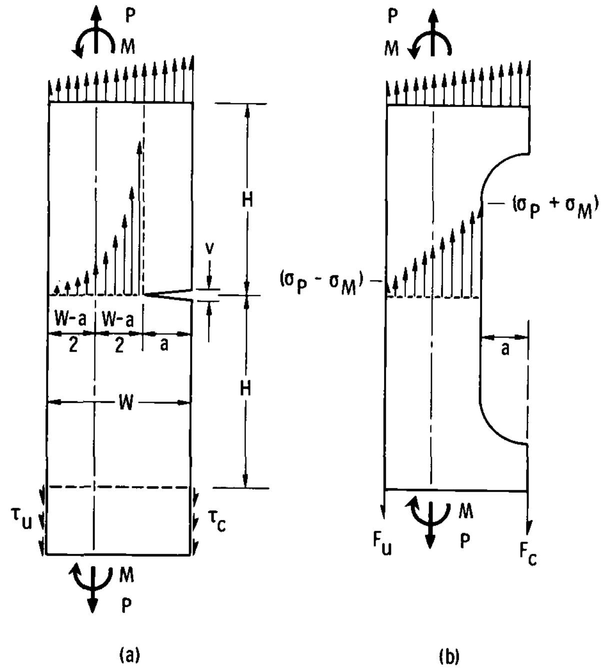

FIG. 2—*Specimen model dimensions, equivalent end boundary conditions, and stress distributions.* (a) *Boundary collocation model showing normal tractions case at top and shear tractions case at bottom.* (b) *Equivalent linear net stress distribution model showing equivalent force pair at bottom.*

and in greater detail in Ref *6*. Briefly, a stress function which satisfies the necessary conditions on the crack boundary surface takes the form of an infinite series with unknown coefficients. This series is truncated, and the remaining coefficients are determined from the conditions that the stress function and its derivative must satisfy the imposed boundary conditions at a finite number of selected boundary stations. The derivation of the boundary values of the stress function and its derivative for the present cases are given in the Appendix. The number of undetermined coefficients can be equal to or less than twice the number of boundary stations. If it is less, then an overdetermined system of simultaneous equations results, and this set of equations is solved by a least squares best fit technique. This procedure has the advantage of introducing smoothing into the numerical analysis and has been adopted as a normal routine. The value of the stress intensity factor is directly proportional to the coefficient of the first term of the series, which is singular and dominates the stress and displacement fields in the vicinity of the crack tip. Satisfactory convergence of this coefficient is sufficient to accurately obtain the stress intensity factor. Displacements at points not close to the crack tip involve all the coefficients, not equally but with successively diminishing importance. Consequently, the analysis must be carried considerably further to obtain satisfactory values of displacements than to obtain the stress intensity factor.

Form and Use of Results

The values obtained by boundary collocation of the stress intensity coefficient, $\Gamma = \Gamma(a, \omega) = K_I/(\sigma_P + \sigma_M) \sqrt{a(1 - \alpha)}$, are listed in Table 1; those of the crack mouth displacement coefficient, $\Delta = \Delta(\alpha, \omega) = E'v/(\sigma_P + \sigma_M) \cdot a$, are similarly listed in Table 2. As mentioned previously, these forms of dimensionless coefficients were chosen because of their particular suitability for interpolation over the entire range of the two principal dimensionless variables: $\alpha = a/W$, and $\omega = \arctan (\sigma_M/\sigma_P) = \arctan (6M/P\ (W - a))$. The form of Γ is essentially due to Koiter [*4*] and [*7*], and that of Δ is the natural complement. Discussion of the properties and use of these coefficients now follows.

The value of the stress intensity factor, K_I, for any combination of forces is obtained, like a component of stress, by direct superposition. In the present case the value of K_I for the combination of resultant force, P, and couple of moment, M, is

$$K = K_P + K_M = (\Gamma_P \sigma_P + \Gamma_M \sigma_M)\sqrt{a(1 - \alpha)} \tag{1}$$

where the subscript I has now been dropped on the understanding that the present context refers exclusively to the first or opening mode of crack extension, and where

σ_P = $P/B(W - a)$ is the component of normal net stress due to P,
σ_M = $6M/B(W - a)^2$ is the component of normal net stress due to M,
Γ_P = $K_P/\sigma_P \sqrt{a(1-\alpha)}$ is the stress intensity coefficient for uniform normal net stress, as given in Table 1 for $\omega = 0$, and
Γ_M = $K_M/\sigma_M \sqrt{a(1-\alpha)}$ is the stress intensity coefficient for pure bending net stress distribution, as given in Table 1 for $\omega = \pi/2$.

The combined stress intensity coefficient is defined as

$$\Gamma = K/(\sigma_P + \sigma_M)\sqrt{a(1-\alpha)} \tag{2}$$

$$= (\sigma_P \Gamma_P + \sigma_M \Gamma_M)/(\sigma_P + \sigma_M) \tag{3}$$

$$= (\Gamma_P + \Gamma_M \tan \omega)/(1 + \tan \omega) \tag{4}$$

where

$$\tan \omega = \sigma_M/\sigma_P = 6M/P(W - a)$$

TABLE 1—*Boundary collocation values of the stress intensity coefficient, Γ, obtained with normal traction boundary conditions.*

		For $\alpha (= a/W)$ Values of							
		0.1	0.2	0.3	0.4	0.5	0.6	0.7	0.8
H/W	ω	$\Gamma = K_I/(\sigma_P + \sigma_M)\sqrt{a(1-\alpha)}$							
4	0	1.470	1.164	0.961	0.822	0.725	0.659	0.614	0.581
	$\pi/4$	1.528	1.252	1.064	0.930	0.832	0.759	0.704	0.662
	$\pi/2$	1.585	1.339	1.167	1.039	0.938	0.858	0.794	0.743
2	0	1.466	1.164	0.961	0.822	0.725	0.659	0.613	0.580
	$\pi/4$	1.523	1.251	1.064	0.930	0.832	0.758	0.704	0.661
	$\pi/2$	1.583	1.339	1.167	1.038	0.938	0.858	0.794	0.742
1	0	1.468	1.163	0.961	0.822	0.725	0.659	0.614	0.580
	$\pi/4$	1.526	1.250	1.065	0.932	0.832	0.758	0.704	0.661
	$\pi/2$	1.582	1.338	1.168	1.039	0.938	0.858	0.794	0.741

TABLE 2—*Boundary collocation values of the crack mouth opening coefficient, Δ, obtained with normal traction boundary conditions.*

		For α (= a/W) Values of							
		0.1	0.2	0.3	0.4	0.5	0.6	0.7	0.8
H/W	ω	$\Delta = E'v/(\sigma_P + \sigma_M)a$							
4	0	3.800	2.770	1.855	1.055	0.331	−0.358	−1.035	−1.730
	$\pi/4$	4.125	3.405	2.763	2.223	1.757	1.335	0.934	0.540
	$\pi/2$	4.450	4.040	3.670	3.390	3.183	3.027	2.903	2.810
2	0	3.690	2.735	1.850	1.055	0.331	−0.357	−1.037	−1.733
	$\pi/4$	3.985	3.321	2.741	2.220	1.757	1.335	0.933	0.532
	$\pi/2$	4.400	3.960	3.675	3.381	3.183	3.027	2.901	2.800
1	0	3.860	2.780	1.855	1.055	0.327	−0.367	−1.044	−1.740
	$\pi/4$	4.200	3.420	2.763	2.225	1.763	1.337	0.929	0.536
	$\pi/2$	4.550	4.060	3.670	3.394	3.190	3.032	2.903	2.795

Similarly, for the crack mouth displacement, v

$$v = v_P + v_M = (\sigma_P \; \Delta_P + \sigma_M \; \Delta_M)a/E' \tag{5}$$

where

$\Delta_P = E'v_P/\sigma_P a$,
$\Delta_M = E'v_M/\sigma_M a$, and
$E' = E$, Young's modulus, for plane stress, or $E/(1 - \nu^2)$ for plane strain, where ν is Poisson's ratio.

The effective value of E' for a practical specimen will lie between these limits and will depend on the ratios a/W and B/W. It is best established by direct experiment on actual specimens or scaled-up models.

Also, the combined crack mouth displacement coefficient is defined as

$$\Delta = E'v/(\sigma_P + \sigma_M)a \tag{6}$$
$$= (\sigma_P \, \Delta_P + \sigma_M \, \Delta_M)/(\sigma_P + \sigma_M) \tag{7}$$
$$= (\Delta_P + \Delta_M \tan \omega)/(1 + \tan \omega) \tag{8}$$

The advantage of the form of the parameter ω is that every possible state of load combination corresponds to one, and only one, value of ω in the range $0 \leq \omega \leq 2\pi$. Figure 3 shows how the four kinds of mixed load combinations might be obtained with a single actuator. Also, eight special cases can be distinguished as follows.

ω	$\tan \omega$	State of Load Combination
0	0	simple net tension
$\pi/4$	1	balanced tension and bending
$\pi/2$	∞	simple net bending
$3\pi/4$	-1	balanced bending and compression
π	0	simple net compression
$5\pi/4$	1	balanced compression and counterbending
$3\pi/2$	$-\infty$	simple counterbending
$7\pi/4$	-1	balanced counterbending and tension

Equations 4 and 8 can be expressed in linear form

$$\Gamma = (\Gamma_P + \Gamma_M)/2 + (1 - \tan \omega)(\Gamma_P - \Gamma_M)/2(1 + \tan \omega)$$
$$= (\Gamma_P + \Gamma_M)/2 + (\Gamma_P - \Gamma_M) \tan(\pi/4 - \omega)/2 \tag{9}$$

$$\Delta = (\Delta_P + \Delta_M)/2 + (\Delta_P - \Delta_M)\tan(\pi/4 - \omega)/2 \tag{10}$$

These linear equations enable the results given in Tables 1 and 2, for three values of ω, to be subjected to linear regression analysis, which provides an objective measure of their precision. The sample size of three is minimal, but Eqs 9 and 10 are true functional relations, not statistical ones, and the three values of the independent variable, $\tan(\pi/4 - \omega) = 1$,

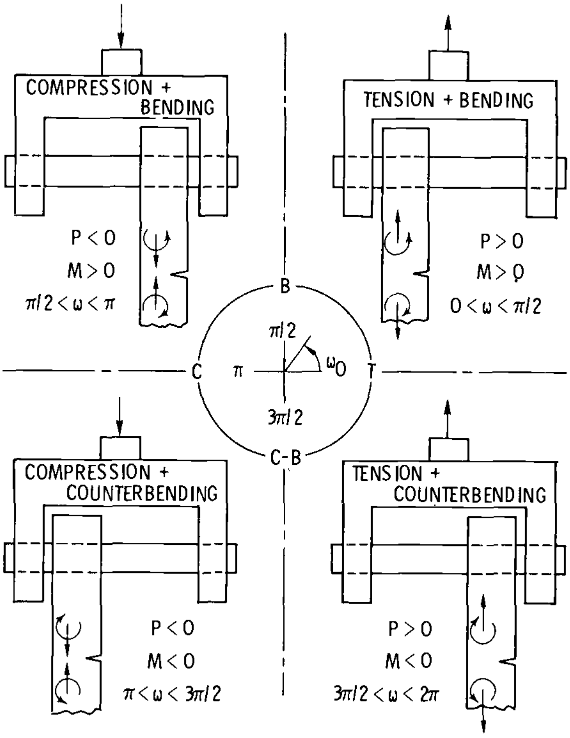

FIG. 3—*Illustration of the four kinds of combined load.*

0, and -1, are exact; consequently, any variation about the regression line is attributable solely to scatter of the boundary collocation values of the dependent variable, Γ or Δ.

The measure of precision calculated was the ratio of the standard error of the estimate to the mean of the three values of the dependent variable, Γ or Δ. The standard error of the estimate is the positive square root of that part of the variance of the dependent variable not accounted for by its regression on the independent variable. The precision of the values of Γ in Table 1 is better than 0.1 percent in all cases. In Table 2, the precision of the values of Δ is also better than 0.1 percent when H/W is 4. But when H/W is 2 or 1, about half of the results are less precise, the worst being hardly better than 1 percent. These less precise results are for $\alpha = 0.1$, 0.2, 0.3, or 0.8, not for intermediate values, which reflects the fact that the boundary collocation method is subject to greater round-off errors when the relative crack length is either small or large.

Since both Γ and Δ are linear in the parameter $\tan(\pi/4 - \omega)$, they are linearly related to one another. By elimination of the common parameter in Eqs 9 and 10

$$\Gamma = c_1 + c_2 \ \Delta \tag{11}$$

where

$$2c_1(\alpha) = \Gamma_P + \Gamma_M - (\Delta_P + \Delta_M)\ (\Gamma_P - \Gamma_M)/(\Delta_P - \Delta_M)$$
$$c_2(\alpha) = (\Gamma_P - \Gamma_M)/(\Delta_P - \Delta_M)$$

Alternatively, Eq 11 can be inverted to give Δ as a linear function of Γ. Either equation can be used in a similar manner to Eqs 9 and 10 for linear regression analysis. The correlation coefficients for Eq 11 were better than 0.99999 in all cases, and the precisions of the regression lines were better than 0.1 percent for $H/W = 4$. It is, therefore, apparent that the boundary collocation values of Γ and Δ are highly consistent.

There is a further linear relation for the ratio $\Gamma/\Delta = Ka^{1/2}/E'v\ (1 - \alpha)^{1/2}$, which is useful when the crack mouth displacement is the controlled variable in fatigue crack generation or crack extension resistance experiments. Let $v_M/v_P = \tan\theta = (\Delta_M/\Delta_P)\tan\omega$, then it is easily shown that

$$2(\Gamma/\Delta) = (\Gamma_P/\Delta_P + \Gamma_M/\Delta_M) + (\Gamma_P/\Delta_P - \Gamma_M/\Delta_M)\tan(\pi/4 - \theta) \tag{12}$$

End-Point Values and Interpolation Expressions

The combined coefficients Γ and Δ are exact functions of the parameter ω by definition, Eqs 4 and 8, but the particular coefficients in these equations, namely: $\Gamma_P = \Gamma(\alpha,0)$, $\Gamma_M = \Gamma(\alpha,\pi/2)$, $\Delta_P = \Delta(\alpha,0)$, and $\Delta_M = \Delta(\alpha,\pi/2)$, are unknown functions of the parameter α. Therefore it is desirable to provide suitable interpolation expressions for these coefficients. These expressions should agree exactly with the end-point values of the coefficients at $\alpha = 0$ and 1, which may be assumed to be known very accurately. They should also be acceptably consistent with the end-point slopes, $d\Gamma/d\alpha$ and $d\Delta/d\alpha$, though not so stringently as to impose undue complexity on the forms of the interpolation functions. Finally, they should agree with the intermediate values of the coefficients and should not deviate systematically from those values. The intermediate values used in the study of interpolation expressions were those obtained by linear regression analysis of the boundary collocation results for $H/W = 4$, which therefore involve the results for all three values of ω in Tables 1 and 2.

The various end-point values are given in Table 3, each with a symbol in brackets to identify its source. Ten of these values were obtained from either Ref *2* or *4*. Estimates of the other six were obtained by extrapolation of functions of the variables such that the slopes of the plots were nearly constant near one or the other of the end points. These estimates are identified by the symbol [*T*] for text. One of them is the coefficient $\Delta(1,0)$, and its value of -3.26 is estimated to be accurate within about 1 percent. The other five are end-point slopes, and may be somewhat less accurate, but are correspondingly less important for the present purpose. It was established that the order of $d\Delta/d\alpha$ at $\alpha = 0$ is $-1/0^{1/2}$ for both values of ω from the fact that plots of Δ against $\alpha^{1/2}$ approach a common slope of -5.4 as α approaches zero.

TABLE 3—*End-point values of the coefficients and their derivatives.*[a]

ω	α	Γ		$d\Gamma/d\alpha$		Δ		$d\Delta/d\alpha$	
0	0	1.9887	[*4*]	−6.96	[*4*]	5.84	[2]	order $(-1/0^{1/2})$	[*T*]
0	1	0.5204	[2]	−0.4	[*T*]	−3.26	[*T*]	−9.1	[*T*]
$\pi/2$	0	1.9887	[*4*]	−5.40	[*4*]	5.84	[2]	order $(-1/0^{1/2})$	[*T*]
$\pi/2$	1	0.6629	[*4*]	−0.332	[*4*]	2.64	[2]	−1.6	[*T*]

NOTE—[*T*] = source in text.

Interpolation expressions of general conic form which cover the full range of α from 0 to 1 are discussed by Bentham and Koiter [*4*] for the case of Γ_M and also for the case of uniform tension applied remotely across the gross section, which corresponds in present terms to the combined load case where $\omega = \arctan(3\alpha/(1 - \alpha))$. In each case, these authors determined the six disposable coefficients of the conic form from the values of Γ at the end points and those of its first and second derivatives, without recourse to any intermediate values. Since the values of these coefficients are not given in Ref *4*, the present authors determined them from the data of that reference, but found that the resulting expressions were not in sufficiently good agreement with the boundary collocation data. A modified approach was tried then in which only the end point values of Γ and its first derivative were employed, the remaining two conditions required to determine the six coefficients being obtained from the boundary collocation data. This approach was no more successful than the first, so it was concluded that the general conic form was not the most appropriate for the present purpose.

Other forms of interpolation functions are given by Tada et al [*2*] for both Γ_M and Δ_M and for the corresponding coefficients for the combined load case of uniform gross tension. These functions, however, do not agree sufficiently well with the present boundary collocation results, though they do agree with the less extensive results of Refs *1* and *8*. Consequently, it was considered necessary to explore other forms of interpolation expressions. The most satisfactory interpolation expressions devised were the rational algebraic functions which follow

$$\Gamma_P = 1.9887 - 1.468\,\alpha - 4.76\,\alpha(1 - \alpha)/(1 + \alpha)^2 \qquad (13)$$

$$\Gamma_M = 1.9887 - 1.326\,\alpha - (3.49 - 0.68\,\alpha + 1.35\,\alpha^2)\alpha(1 - \alpha)/(1 + \alpha)^2 \qquad (14)$$

$$\Delta_P = 5.84 - 9.1\,\alpha - 4.1\,\alpha^{1/2}(1 - \alpha)^{3/2}/(1 + 0.1435\,\alpha) \qquad (15)$$

$$\Delta_M = 5.84 - 2.3\,\alpha - 3.42\,\alpha^2 + 2.52\,\alpha^3 - 4.1\,\alpha^{1/2}(1 - \alpha)^{3/2}/(1 + 0.1435\,\alpha) \qquad (16)$$

In each of these expressions the leading coefficient is the value of the function for $\alpha = 0$, and the remaining coefficients are related by the value for $\alpha = 1$, so that each expression has four or less independent numerical coefficients to fit eight boundary collocation values. Moreover, Eqs 13 and 14 are devised to have features in common, as are Eqs 15 and 16, so that the general interpolation expressions which correspond to Eqs 4 and 8 each have only five independent numerical coefficients to fit twenty-four boundary collocation values (Tables 1 and 2 for $H/W = 4$). The interpolation expressions, therefore, involve considerable smoothing of the boundary collocation results. For all six expressions, the algebraic mean of the deviations of the boundary collocation values is less than 0.1 percent, and the deviations are unsystematic. For Eqs 4, 13, and 14, the individual deviations are within plus or minus 0.5 percent, except for $\alpha = 0.1$ where the equations overestimate the boundary collocation values by about 1 percent. It is quite possible that these boundary collocation values for such short cracks are in error to that extent. For Eqs 8, 15, and 16, the individual deviations are all within plus or minus 1 percent. From these various considerations it is concluded that the interpolation expressions given here are sufficiently precise and reliable for practical purposes.

Crack Mouth Displacement Slopes

It is sometimes convenient to use separate knife edges, which are attached to the specimen by screws or adhesive, for mounting the clip gage which is used to measure the crack mouth displacement. In such cases it is necessary to know the values of the displacement coefficient, Δ_s, at some small distance, s, away from the crack mouth. For this reason, values of the crack mouth opening slope $d\Delta/dx$ were obtained and are listed in Table 4. The distance x is measured away from the specimen edge along the extension of the crack line. Then, at a position $x = s$, the value of the displacement coefficient $\Delta_s = \Delta_0 + s\, d\Delta/dx$, where Δ_0 is the value of Δ at the crack mouth as given in Tables 2 and 3, or by Eqs 8, 15, and 16. In Table 4, the values obtained by boundary collocation, for $\alpha =$ 0.1 to 0.8, are somewhat less accurate than those of the displacement coefficient itself in Table 2. The reason is that to obtain the derivative

TABLE 4—*Values of the crack mouth opening slope* $d\Delta/d(x/w)$.

	For ω Values of		
	0	$\pi/4$	$\pi/2$
a/w	$d\Delta/d(x/W) = (E'W/\sigma a)dv/dx$		
0	48	48	48
0.1	15.3	18.2	21.1
0.2	6.6	9.3	12.0
0.3	2.6	5.3	8.0
0.4	0.44	3.2	6.0
0.5	−0.84	2.0	4.9
0.6	−1.7	1.2	4.2
0.7	−2.3	0.63	3.6
0.8	−2.9	0.27	3.4
0.9	. . .	. . .	. . .
1.0	−3.26	−0.31	2.64

involves taking the difference between the displacement at the crack mouth and that at some small distance along the crack. The relative error of this difference is likely to be considerably greater than that of either displacement. To obtain the derivatives with substantially greater accuracy would require that the boundary collocation analysis be carried considerably further. This was not considered to be warranted since it should not be necessary for the supplementary term $s\ d\Delta/dx$ to exceed about one tenth of the principal term Δ_0. As a practical rule, the distance s should not exceed one-tenth of the crack length.

The value in Table 4 for $\alpha = 0$ was obtained by extrapolation of the inverse square roots of the boundary collocation values to their common value. The values for $\alpha = 1$ are the same as the values for Δ_0 because the crack tip and the "hinge point" are then located at the back surface of the specimen.

Discussion

The present authors published stress intensity and crack mouth displacement coefficients, Refs *1* and *8*, respectively, for side-cracked specimens loaded in uniform tension across the gross section. This boundary condition is equivalent to tensile loading through frictionless pins located at mid-width, as shown by the inset in Fig. 4, and it involves the relation: $\sigma_M/\sigma_P = \tan \omega = 3\alpha/(1 - \alpha)$. In this figure, the straight lines correspond to Eq 9 with coefficients obtained from the interpolation expressions, Eqs 13 and 14. The points marked by circles on this chart are boundary collocation values of Γ for uniform gross tension which are derived either from Ref *1* or recent supplementary results. The maximum deviation of any of these points from the corresponding line is less than 1

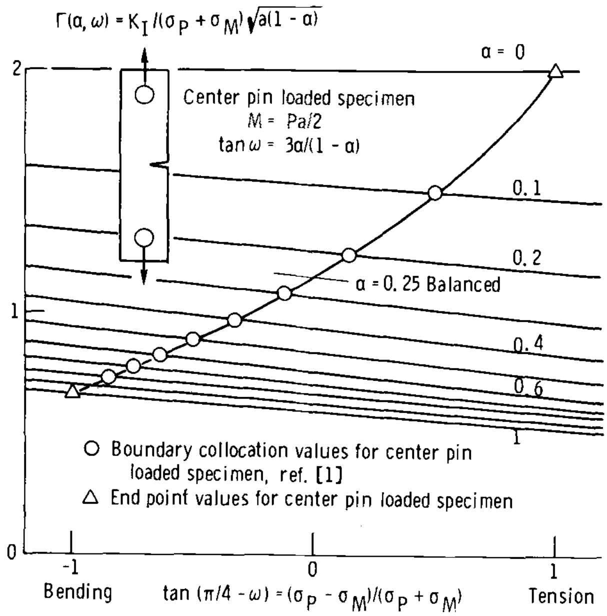

FIG. 4—*Stress intensity coefficient,* Γ, *versus the function tan* ($\pi/4 - \omega$) *of the load combination parameter,* ω. *The straight lines are the results of the present work for* $\omega = 0, \pi/4$, *and* $\pi/2$. *The superimposed points are from earlier work on the case for which tan* $\omega = 3\alpha/(1 - \alpha)$.

percent. Thus the earlier results for this special case are in very good agreement with the interpolation expressions presented here.

Figure 4 also illustrates the point that the state of loading for center pin loaded specimens varies from net tension ($\omega = 0$) when $\alpha = 0$ to net bending ($\omega = \pi/2$) when $\alpha = 1$. At $\alpha = 1/4$, the value of ω is $\pi/4$, and the net bending stress is exactly equal to the net tension stress; for greater values of α, the bending stress is predominant. Evidently, a face-cracked specimen loaded in this manner does not represent the extreme case of a part-through cracked specimen, as has sometimes been assumed mistakenly. For this purpose, the specimen would have to be loaded in such a manner as to maintain uniform net tension for all values of α. Alternatively, it might be more practical to load the specimen to maintain uniform displacement across the width at some appropriate distance from the crack. These two alternatives are not exactly equivalent, of course, and might produce significantly different test results. This is a matter for further investigation.

Figure 5 is the chart of the crack mouth opening displacement coeffi-

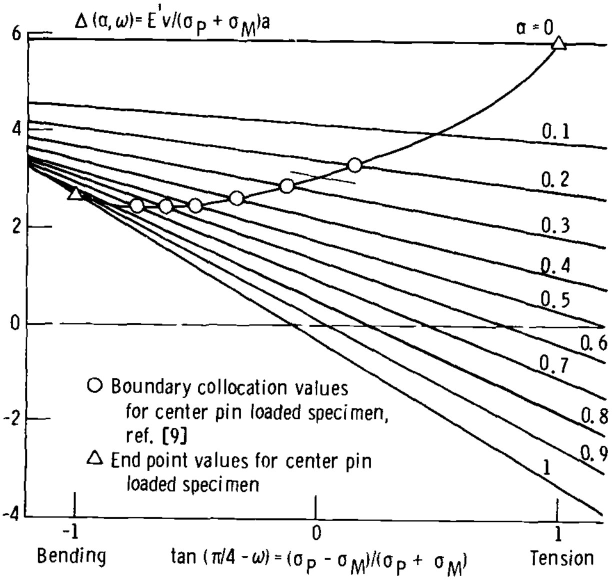

FIG. 5—*Crack mouth displacement coefficient,* Δ, *versus tan* ($\pi/4 - \omega$). *The straight lines are the results of the present work; the superimposed points are from earlier work on the case for which tan* $\omega = 3\alpha/(1 - \alpha)$.

cient Δ which corresponds to Fig. 4. The straight lines represent Eq 10 and the coefficients were obtained from the interpolation expressions, Eqs 15 and 16. The circles represent boundary collocation results for uniform gross tension taken from Ref *8*. The deviations of these earlier results from the lines are less than 1/2 percent, except at $\alpha = 0.7$ which is 2 percent below the corresponding line. It is notable that these values of Δ for uniform gross tension do not differ greatly from those for net bending (tan $(\pi/4 - \omega) = -1$), but are in strong contrast to the values for uniform net tension (tan$(\pi/4 - \omega) = 1$). Whereas the minimum value of Δ for gross section tension is 2.4 at $\alpha = 0.7$, that for net section tension is -3.26 at $\alpha = 1$.

The reason for the rapid decrease of Δ with increase of α under net section tension is that the equivalent combination of force and couple causes counterbending of the two parts of the specimen on either side of the crack, and this counterbending is greater the longer the crack. In consequence, although the crack tip is always opened by this mode of loading (the stress intensity is always positive), the crack mouth displacement is negative when α exceeds about 0.65. In practice, the crack is usually simulated by a pointed slot or notch from which extends a short fatigue crack. The slot mouth displacement, therefore, can be negative. It is important to appreciate, however, that the present results do not apply if there is contact along any part of the crack faces, because this would induce compressive contact stresses which were not imposed in the present boundary collocation analysis. The effect of such contact stresses can be analyzed by various methods if their magnitude and distribution can be determined.

The crack mouth displacement data are needed for several different purposes, such as in the procedure of ASTM Test for Plane-Strain Fracture of Metallic Materials (E 399-74) for determination of the K_{Ic} plane strain fracture toughness or for displacement control of fatigue cracking in an electrohydraulic closed-loop loading system. Another important purpose, less commonly appreciated, is for analysis of test results when the measured force applied to a cracked specimen is complemented by an unmeasured bending moment. This can occur unintentionally if loading fixtures are designed with insufficient care or appreciation of the nature of the stress distribution imposed on the specimen by the fixture. It will occur when force is transmitted to a face-cracked specimen by wedge or hydraulic grips in order to obtain a uniform distribution of end displacement across the specimen width.

The compliance of the specimen, vB/P, can be measured by recording P against v while the specimen is lightly loaded and unloaded. Then, providing that the crack length is accurately known and practically uniform, the value of tan ω and thus σ_M can be determined as follows from Eq 6

$$\frac{E'v}{(\sigma_P + \sigma_M)a} = \Delta(\alpha,\omega) = \frac{\sigma_P\, \Delta_P(\alpha) + \sigma_M\, \Delta_M(\alpha)}{(\sigma_P + \sigma_M)} = \frac{E'v}{(1 + \tan\omega)\sigma_P a}$$
$$= \frac{\Delta_P + \tan\omega\, \Delta_M}{1 + \tan\omega} \quad (17)$$

Therefore

$$\tan\omega = \frac{\sigma_M}{\sigma_P} = \frac{(E'v/\sigma_P a) - \Delta_P}{\Delta_M}$$
$$= \frac{(E'Bv/P)(1 - \alpha)/\alpha - \Delta_P}{\Delta_M} \quad (18)$$

Since the value of α is known, those of Δ_P and Δ_M can be obtained from Eqs 15 and 16, respectively, vB/P is determined experimentally, so that it only remains to determine the value of E' in order to obtain the value of tan ω from Eq 18, and hence the value of σM. The quantity E' is equal to $E/(1 - x^2)$, where E is Young's modulus and x is equal to 0 for a homogeneous state of generalized plane stress, and is equal to Poisson's ratio for a homogeneous state of plane strain. In practice, the value of x for most metallic materials is between 0 and 0.3, depending upon the three parameters: α, ω, and $B/(W - a)$, but independent of size scale. For a given specimen form and material the value of x can be determined from a series of compliance experiments in which the accurate values of α and ω are known. It seems likely that a systematic series of such experiments with several different materials might reveal generalities about the dependence of x on the three dimensionless parameters and on Poisson's ratio. The authors are not aware of the existence of such information at the present time.

Summary

Comprehensive information is presented on the opening mode stress intensity factor, K_I, and on the associated crack mouth displacement, v, for quasiplanar rectangular specimens with single transverse side cracks of any uniform depth, loaded in any manner that can be represented sufficiently well by a linear distribution of normal forces across each end boundary. The data for values of the relative crack length, α, other than the end points, 0 and 1, were obtained by boundary collocation analysis; the end point values were available from the literature, except in one case which was obtained by a reliable method of extrapolation.

The information is given in the form of dimensionless coefficients, Γ (K_I) and $\Delta(v)$, which are both functions of two principal dimensionless parameters, α, and the load combination parameter, ω. Both Γ and Δ are linear functions of the quantity $\tan(\pi/4 - \omega)$, and the coefficients of the linear equations are finitely bounded functions of α. Rational algebraic interpolation expressions are given for these functions of α which fit the primary data within the precision of that data and are considered to be accurate to within 1 percent or better. The effect on Γ and Δ of the third dimensionless parameter, the ratio H/W of half-height to width of the specimen, is shown to be very weak providing that it exceeds unity.

The purpose of the information is to serve as a prerequisite for the development of new test methods for measurement of such properties of materials as fracture toughness, fatigue crack propagation resistance, and stress corrosion crack propagation resistance. The potential advantages of the full range of load combinations (tension or compression combined with bending or counterbending) has by no means been thoroughly explored, nor has the possibility that the property of interest might be significantly depending on the mode of loading. This possibility follows from the fact that the characteristics of the crack tip plastic zone will certainly be affected.

APPENDIX

Stress Function and Stress Function Boundary Conditions for Side-Cracked Plates

The form of the stress function in terms of the polar coordinates, r and ϕ as shown in Fig. 6, is

$$X(r,\phi) = \sum_{n=1}^{\infty} r^{n+1/2} A_{2n-1} \left[\cos(n-3/2)\phi - \left(\frac{2n-3}{2n+1}\right)\cos\left(n+\frac{1}{2}\right)\phi\right] + r^{n+1} A_{2n}[\cos(n-1)\phi - \cos(n+1)\phi] \qquad (19)$$

Its application is discussed in detail elsewhere [3]. The values of the stress function, X, and its normal derivatives, $\partial X/\partial x$ and $\partial X/\partial y$, along the prescribed model boundaries (AB, BC, and CD in Fig. 6*a* and AB, BB′, B′C′, C′C, and CD in Fig. 6*b*) are derived from known boundary tractions as shown in Fig. 6, and are as follows.

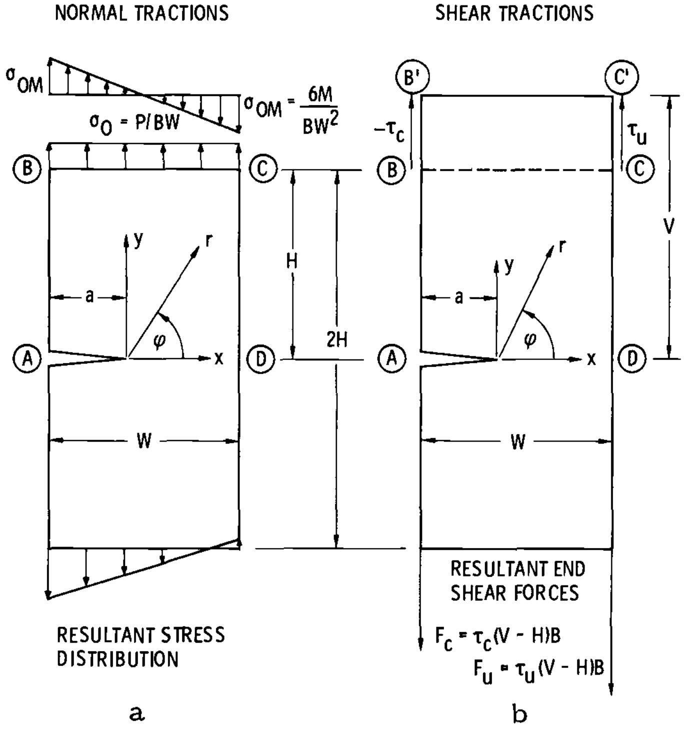

FIG. 6—*Alternative boundary collocation models.*

From the load condition of Fig. 6*a* where $P = \sigma_0 BW$ and $M = BW^2\sigma_{0M}/6$.
Along AB

$$X = 0 \tag{20}$$

$$\frac{\partial X}{\partial x} = 0 \tag{21}$$

Along BC

$$X = \frac{P}{BW}\left(\frac{x^2}{2} + ax + \frac{a^2}{2}\right) - \frac{12M}{BW^3}\left(\frac{a^3}{6} + \frac{a^2x}{2} + \frac{ax^2}{2} + \frac{x^3}{6}\right)$$

$$+ \frac{6M}{BW^2}\left(\frac{x^2}{2} + ax + \frac{a^2}{2}\right) \tag{22}$$

$$\frac{\partial X}{\partial y} = 0 \tag{23}$$

Along CD

$$X = \frac{PW}{2B} + \frac{M}{B} \tag{24}$$

$$\frac{\partial X}{\partial x} = \frac{P}{B} \tag{25}$$

From the load conditions of Fig. 6*b* where τ_c and τ_u are the uniformly distributed side shear tractions, we have the following equations.

Along AB

$$X = 0 \tag{26}$$

$$\frac{\partial X}{\partial x} = 0 \tag{27}$$

Along BB′

$$X = 0 \tag{28}$$

$$\frac{\partial X}{\partial x} = \tau_c(y - H) \tag{29}$$

Along B′C′

$$X = \tau_c(V - H)(x + a) \tag{30}$$

$$\frac{\partial X}{\partial y} = 0 \tag{31}$$

Along C′C

$$X = \tau_c(V - H)W \tag{32}$$

$$\frac{\partial X}{\partial x} = \tau_u(V - y) + \tau_c(V - H) \tag{33}$$

Along CD

$$X = \tau_c(V - H)W \tag{34}$$

$$\frac{\partial X}{\partial x} = (\tau_u + \tau_c)(V - H) \tag{35}$$

References

[*1*] Gross, B. and Srawley, J. E., "Stress Intensity Factors for Single-Edge Notch Specimens in Bending or Combined Bending and Tension," NASA TN D-2603, National Aeronautics and Space Administration, Washington, D.C., Jan. 1965.

[2] Tada, H., Paris, P. C., and Irwin, G. R., "The Stress Analysis of Cracks Handbook," Del Research Corporation, Hellertown, Pa., 1973.

[*3*] Gross, B. and Mendelson, A., *International Journal of Fracture,* Vol. 8, No. 3, Sept. 1972, pp. 267–276.

[*4*] Bentham, J. T. and Koiter, W. T. in *Mechanics of Fracture: I—Methods of Analysis and Solution of Crack Problems,* G. C. Sih, Ed., Noordhoff International Publishers, Leyden, The Netherlands, 1973, pp. 159–162.

[*5*] *The Surface Crack: Physical Problems and Computational Solutions,* J. L. Swedlow, Ed., American Society of Mechanical Engineers, New York, 1972.

[*6*] Gross, B. "Some Plane Problem Elastostatic Solutions for Plates Having a V-Notch," NASA TM X-69370, National Aeronautics and Space Administration, Washington, D. C., Jan. 1970.

[*7*] Koiter, W. T. "Stress Intensity Factors for Sheet Strips Under Tensile Loads," Mechanical Engineering Laboratory Report 314, Delft University of Technology, The Netherlands, 1965.

[*8*] Gross, B., Roberts, E., Jr., and Srawley, J. E., *International Journal of Fracture,* Vol. 4, No. 3, Sept. 1968, pp. 267–276; Errata, Vol. 6, No. 1, Mar. 1970, p. 87.